ASME
SETTING THE STANDARD

Journal of Fluids Engineering

Published Bimonthly by ASME

VOLUME 128 • NUMBER 3 • MAY 2006

Transactions of the ASME, Journal of Fluids Engineering (ISSN 0098-2202) is published bimonthly (Jan., Mar., May, July, Sept., Nov.) by The American Society of Mechanical Engineers, Three Park Avenue, New York, NY 10016. Periodicals postage paid at New York, NY and additional mailing offices.
POSTMASTER: Send address changes to Transactions of the ASME, Journal of Fluids Engineering, c/o THE AMERICAN SOCIETY OF MECHANICAL ENGINEERS, 22 Law Drive, Box 2300, Fairfield, NJ 07007-2300.
CHANGES OF ADDRESS must be received at Society headquarters seven weeks before they are to be effective. Please send old label and new address.
STATEMENT from By-Laws. The Society shall not be responsible for statements or opinions advanced in papers or ... printed in its publications (B7.1, Par. 3).

TECHNICAL PAPERS

(Contents continued on inside back cover)

This journal is printed on acid-free paper, which exceeds the ANSI Z39.48-1992 specification for permanence of paper and library materials. ♾™
♻ 85% recycled content, including 10% post-consumer fibers.

TECHNICAL BRIEFS

DISCUSSION

The ASME Journal of Fluids Engineering is abstracted and indexed in the following:

Applied Science & Technology Index, Chemical Abstracts, Chemical Engineering and Biotechnology Abstracts (Electronic equivalent of Process and Chemical Engineering), Civil Engineering Abstracts, Computer & Information Systems Abstracts, Corrosion Abstracts, Current Contents, Ei EncompassLit, Electronics & Communications Abstracts, Engineered Materials Abstracts, Engineering Index, Environmental Engineering Abstracts, Environmental Science and Pollution Management, Excerpta Medica, Fluidex, Index to Scientific Reviews, INSPEC, International Building Services Abstracts, Mechanical & Transportation Engineering Abstracts, Mechanical Engineering Abstracts, METADEX (The electronic equivalent of Metals Abstracts and Alloys Index), Petroleum Abstracts, Process and Chemical Engineering, Referativnyi Zhurnal, Science Citation Index, SciSearch (The electronic equivalent of Science Citation Index), Shock and Vibration Digest, Solid State and Superconductivity Abstracts, Theoretical Chemical Engineering

Analysis of Spatiotemporal Variations and Flow Structures in a Periodically Driven Cavity

S. Sriram

Abhijit P. Deshpande[1]
e-mail: abhijit@che.iitm.ac.in

S. Pushpavanam

Department of Chemical Engineering,
Indian Institute of Technology Madras,
Chennai-600 036, India

The time-dependent fluid flow in a square cavity was studied using model fluids of glycerol-water solution at different frequencies and amplitudes of motion of the top plate. The range of Reynolds numbers in our investigation varied from 5 to 3700. The experiments were carried out in a square cavity with a periodically driven lid, and planar velocity measurements were obtained using particle image velocimetry. The flow was driven by moving the top surface of the cavity in a simple harmonic motion. The aspect ratio, defined as the ratio of cavity length to the cavity height, is unity. The ratio of cavity spanwise width to the length of the cavity is 0.2. The temporal variation of velocity at fixed locations in the cavity exhibits a periodic variation. The basic frequency of the fluid motion at a point in the flow domain was observed to be the same as that of plate motion for low Reynolds number Re. However, existence of dominant secondary frequencies was observed along the central vertical plane. The velocity variation as a function of time at a fixed position and the velocity profiles along horizontal and vertical planes are also quantitatively described. These were compared to computational fluid dynamics (CFD) simulations based on the finite volume technique. Comprehensive details of the flow as a function of Reynolds number are analyzed. The evolution of secondary vortices at different plate positions as a function of Reynolds number is also presented. The planar velocity measurements acquired are indicative of the flow behavior in a periodically driven cavity with a narrow span width even at high Re. At very low Re, the flow throughout the periodically driven cavity qualitatively resembles the classical steady lid-driven cavity flow. At high Re, the entire cavity is occupied with multiple vortices. The qualitative features of the bulk flow observed are valid even for cavities with infinite span width. [DOI: 10.1115/1.2173289]

Keywords: periodically driven cavity, particle image velocimetry, periodicity, secondary vortex, CFD simulations

1 Introduction

The study of the dynamics of the fluid motion in a lid-driven cavity is a classical problem in fluid mechanics. It serves as a benchmark or case study for understanding complex flows with closed circulation. It acts as an idealized representation of many industrial-processing applications, such as short-well and flexible blade coaters. In recent years, the flow in a periodically driven cavity has been examined extensively for different operating conditions. Time periodic cavity flows can be viewed as prototypes for studying mixing processes.

O'Brien [1] theoretically and numerically studied the oscillatory box flow and the results were consistent with their earlier experimental results. The flow within a two-dimensional (2D) closed finite square cavity, driven by a sliding wall that executes sinusoidal oscillation, was treated by Soh and Goodrich [2]. Later, Iwatsu et al. [3] studied flow driven by a torsionally oscillating lid in a square cavity through numerical simulations for a wide range of Reynolds numbers and frequencies of the oscillating lid. They reported that at low frequencies the effect of the lid motion penetrates a larger depth into the cavity, and flow is similar to the steady driven cavity flow at the maximum plate velocity. At high frequencies, however, the flow was confined within a thin layer near the oscillating lid. Iwatsu et al. [4] analyzed the three-dimensional (3D) flow structures in a cubic cavity with an oscillating lid by numerical simulations. They studied the effect of frequency on the penetration depth. They reported the presence of the secondary flows at low frequencies, illustrating the 3D nature of the flow. Vogel et al. [5] studied the vortex dynamics of the flow in a rectangular cavity driven by harmonic oscillation of the bottom wall using flow visualization and digital particle image velocimetry measurements. They examined the stability of the basic state and found the limits within which the system can be approximated as 2D and can be used as a surface viscometer.

In spite of various investigations described above, quantitative information of the entire flow field for a wide range of parameters is not available for periodically driven cavity flows. Many researchers have studied the mixing of Newtonian and viscoelastic fluids in time periodic cavity flows. Chien et al. [6] experimentally studied laminar mixing using glycerol as the working fluid in a 2D periodic cavity by analyzing a material line and blob deformation. It was found that the efficiency of the mixing strongly depends on the frequency of oscillation of the wall. Niederkorn and Ottino [7] also carried out experimental and computational investigations on mixing of viscoelastic fluids in a cylindrical geometry with eccentricity. They studied the effect of elasticity of the fluid on the rate of stretching under different flow conditions. Fluid mixing in 2D and 3D time periodic cavity flows as a function of rheological fluid parameters was studied using numerical computations by Anderson et al. [8]. They found the existence of good mixing regions for Newtonian fluids and bad mixing regions in case of shear thinning fluids. Detailed study of the flow structures in a periodic cavity is hence important in understanding and determining the efficiency of the mixing process.

Mixing of viscoelastic fluids is important in a variety of indus-

[1]Author to whom correspondence should be addressed.

Contributed by the Fluids Engineering Division of ASME for publication in the JOURNAL OF FLUIDS ENGINEERING. Manuscript received October 3, 2005; final manuscript received November 16, 2005. Assoc. Editor: Timothy J. O'Hern.

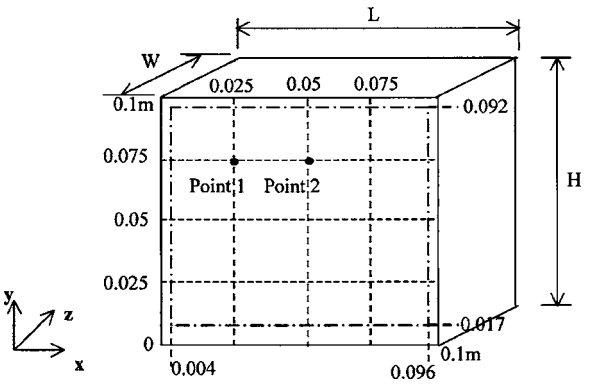

Fig. 1 Geometric details of the cavity

trial applications, such as processing of polymers and melts. The mixing is efficient only when the fluid particles move and follow pathlines spanning larger regions in the cavity. In many of the polymer processing operations, the quality of the final product is greatly dependent on the flow and mixing of the polymer. These processes frequently involve cavities with narrow gaps with periodically moving boundaries. Therefore, we have chosen a periodically driven cavity with narrow spanwise direction to characterize the flow features. In order to obtain an understanding of the flow behavior, this work focuses on flow structures with Newtonian fluids. Velocity measurements in different planes were made at various experimental conditions using a particle image velocimeter. The periodicity of the flow, comprehensive features of the flow, and variation of velocity components along horizontal and vertical planes in the flow field are presented. The experimental results were compared to 2D and 3D computational fluid dynamics (CFD) simulations based on the finite volume method using a commercial package FLUENT 6.1.

2 Materials and Methods

The experiments were conducted in a periodically driven cavity [5]. The walls are made of acrylic sheets of 0.6 cm thickness. The length L of the cavity (along the x direction) is 0.1 m, the height H measured (in the y direction) is 0.1 m, and the spanwise width W of the cavity is 0.02 m (in z direction) (Fig. 1). The aspect ratio defined as the ratio of length to height (L/H) of the cavity is unity in our study.

Figure 2 shows a front view of the cavity (A) and the experimental set up. The top plate (B) was designed to move to and

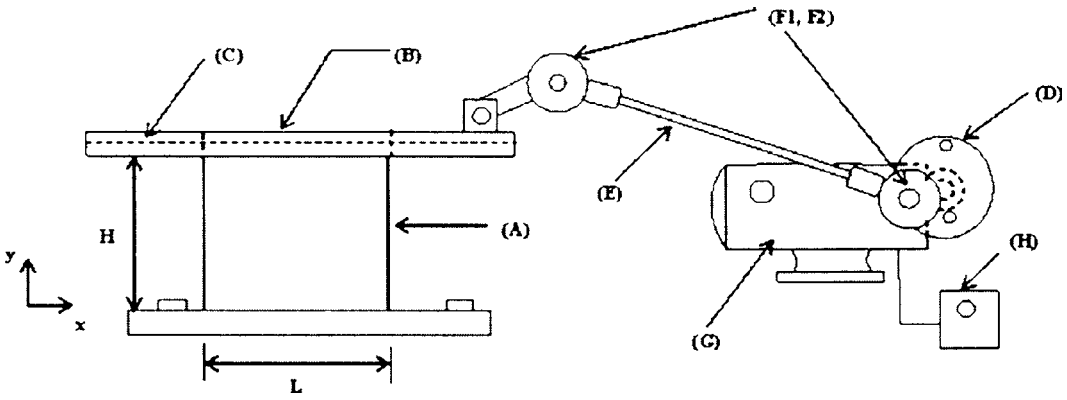

Fig. 2 Schematic diagram of the experimental setup: (A) cavity, (B) top plate, (C) guide plate arrangement, (D) drive wheel, (E) connecting rod assembly, (F1, F2) ball bearings, (G) permanent magnet DC motor, and (H) thyristor drive

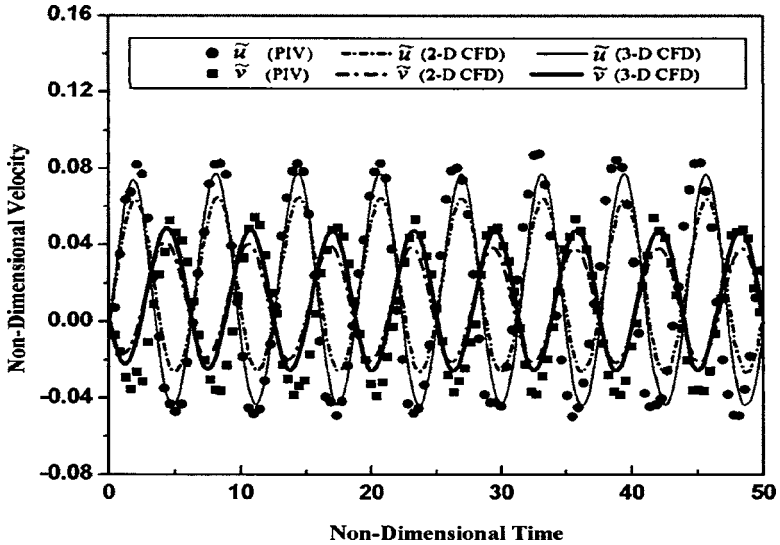

Fig. 3 Comparison of temporal variation of $\tilde{u}$ and $\tilde{v}$ at point 1 in the cavity from the PIV measurements with CFD simulations (μ=0.0235 Pa s, Re=348, St=845)

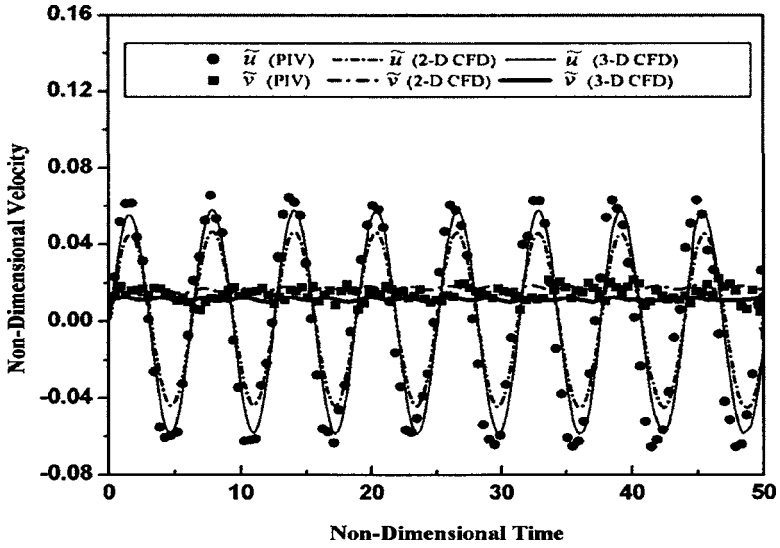

Fig. 4 Comparison of temporal variation of $\tilde{u}$ and $\tilde{v}$ at point 2 in the cavity from the PIV measurements with CFD simulations (μ=0.0235 Pa s, Re=348, St=845)

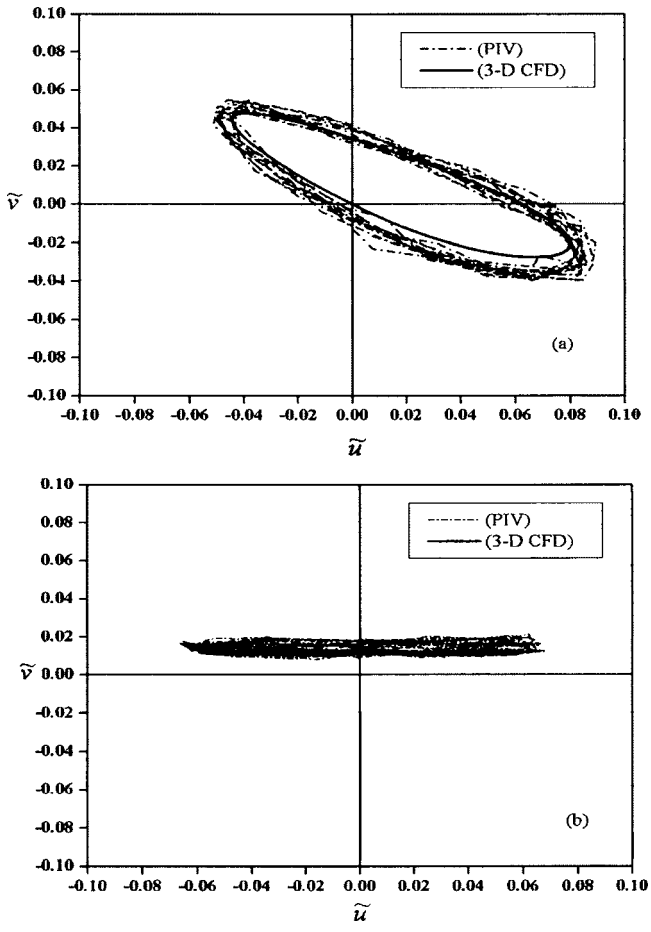

Fig. 5 Trajectories of $\tilde{u}$ and $\tilde{v}$ from PIV measurements and 3D CFD simulations (*a*) point 1 and (*b*) point 2 (μ=0.0235 Pa s, Re=348, St=845)

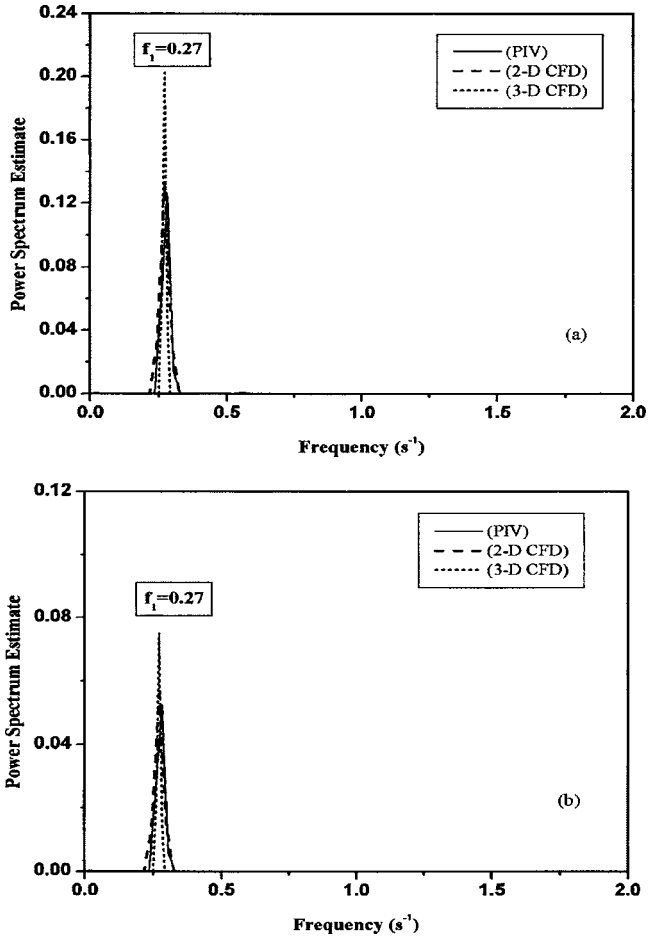

Fig. 6 Power spectra of *x* and *y* component velocities from experimental measurements and CFD simulations at point 1 (*a*) $\tilde{u}$ and (*b*) $\tilde{v}$ (μ=0.0235 Pa s, Re=348, St=845)

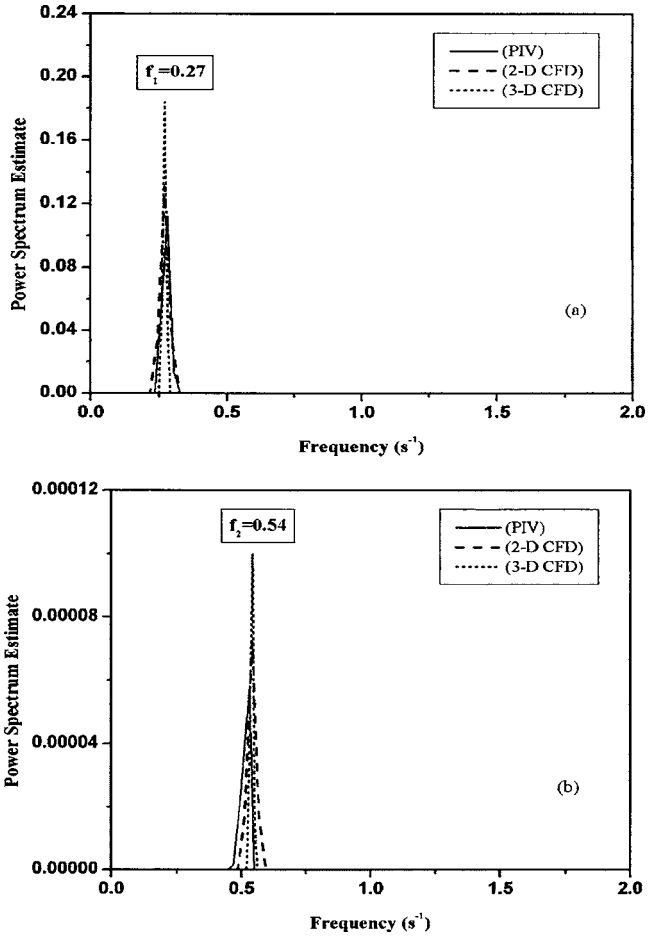

Fig. 7 Power spectra of *x* and *y* component velocities from experimental measurements and CFD simulations at point 2 (*a*) $\tilde{u}$ and (*b*) $\tilde{v}$ (μ=0.0235 Pa s, Re=348, St=845)

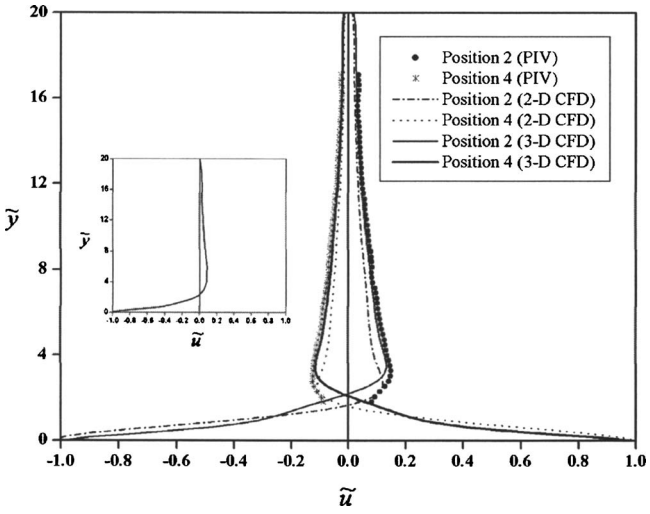

Fig. 8 Comparison of velocity profiles of $\tilde{u}$ measured at the central *z* plane at plate positions 2 and 4 along *x*=0.05 with CFD simulations (μ=0.0235 Pa s, ω=1.7 (s^{-1}), Re=348, St=845). The simulation result of Iwatsu et al. [3] at plate position 2 (ω=1, Re=400) is given as the inset.

from along the x direction. This was rendered possible with a guide plate (C) arrangement. The periodic motion of the top plate was achieved with a drive wheel (D) and connecting rod (E) assembly. Ball bearings (F1, F2) were used for attaching each end of the connecting rod as well as to support the drive wheel. A permanent magnet DC motor (G) was used to turn the drive wheel. The speed of the motor was controlled by a thyristor drive (H). The plate frequency was varied using the thyristor drive. The amplitude (maximum displacement) of the top plate motion was set by the radius at which the connecting rod was attached to the drive wheel. For this, several holes at different radial positions were provided in the drive wheel (D). The position of a marker on the top plate was tracked over a period of time. The velocity of the plate was confirmed as a sinusoidal function using image analysis

$$U_p = A\omega \sin(2\pi ft) \tag{1}$$

where A represents the amplitude of the plate (m) and ω is the angular frequency, which is given by $2\pi f$ where f is the measured frequency of the plate motion (s^{-1}). The experiments were conducted at three different amplitudes 0.04 m, 0.05 m, and 0.06 m and five different angular frequencies 0.83, 1.04, 1.25, 1.70, and 2.51 s^{-1}. The dimensionless Reynolds number is defined as $\mathrm{Re}=(U_{\max}\rho H)/\mu$, and the Stokes number is defined as $\mathrm{St}=\omega\rho H^2/\mu$. Here, the maximum velocity of the plate ($U_{\max}=A\omega$) is the velocity scale, ρ is the fluid density, and μ is the viscosity of the fluid. The penetration depth (i.e., the distance up to which the momentum penetrates in the cavity in relation to the depth of the cavity) is an important parameter. Thus, depth of the cavity (H) is chosen as the length scale for our problem.

We chose our experimental fluid as commercial 99% glycerol. The experiments were carried out with different viscosities of the glycerol-water solutions. The viscosities were measured at 25 °C using a rheometer Physica MCR-301, and the corresponding viscosities were found to be 0.0047 Pa s (40 vol %), 0.0143 Pa s (60 vol %), 0.0235 Pa s (70 vol %), 0.0366 Pa s (75 vol %), 0.147 Pa s (95 vol %), and 0.771 Pa s (99 vol %). The volume percent reported here is for glycerol. The samples were tested by applying shear rate from 0 to 100 s^{-1} in ramp mode using a coaxial cylinder measuring system.

2.1 Experimental Technique. Particle image velocimetry (PIV), a nonintrusive technique, was used to get accurate quantitative information of the instantaneous planar velocity field (LaVision GmBH, Germany). The fluid was seeded with hollow glass

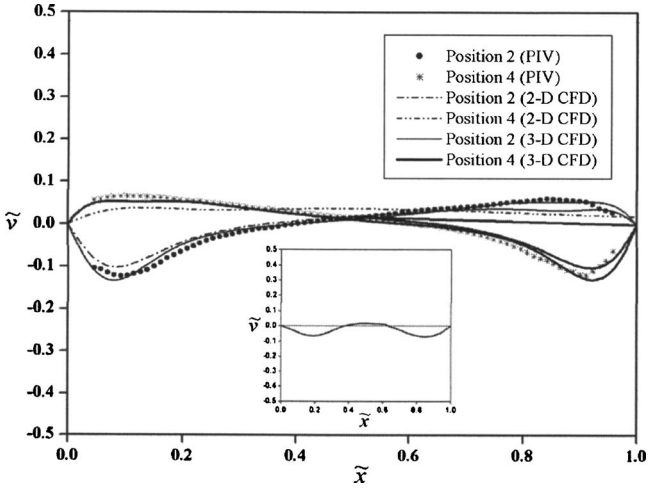

Fig. 9 Comparison of velocity profiles of $\tilde{v}$ measured at the central *z* plane at plate positions 2 and 4 along *y*=0.075 from PIV measurements with CFD simulations (μ=0.0235 Pa s, ω=1.7 (s^{-1}), Re=348, St=845). The simulation result of Iwatsu et al. [3] at plate position 2 (ω=1, Re=400) is given as the inset.

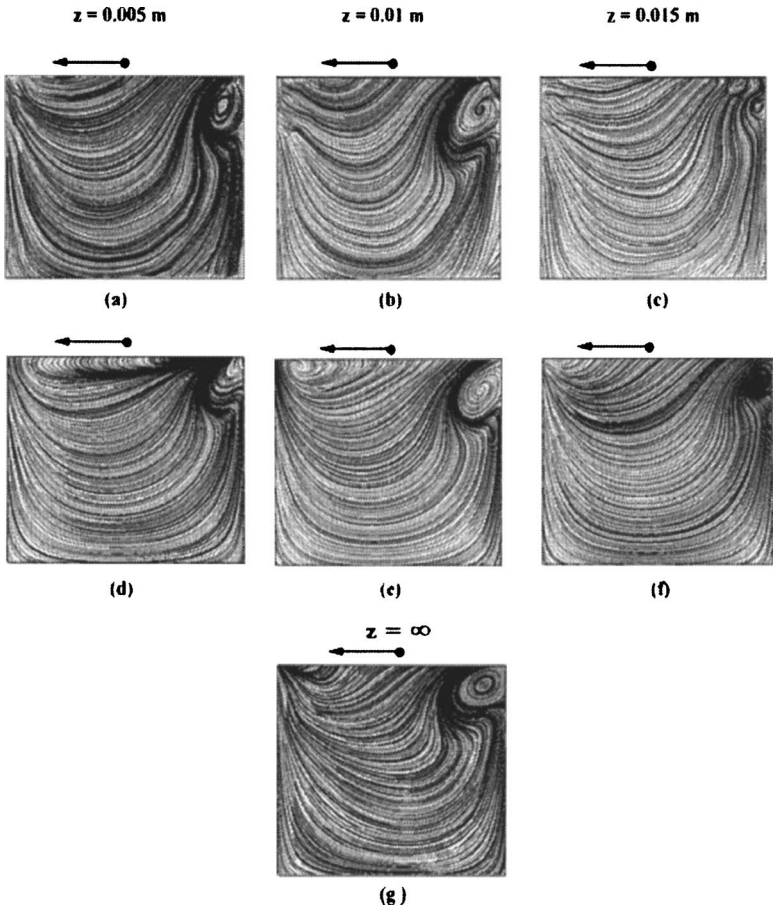

Fig. 10 Flow variation in different *z* planes at plate position 2: comparison of the streamline patterns from PIV planar measurements and CFD simulations (*a*–*c*) PIV, (*d*–*f*) 3D CFD, and (*g*) 2D CFD (μ=0.0143 Pa s, Re=1040, St=2024). The arrow indicates the instantaneous position and direction of the plate.

particles of 5–10 μm size, supplied by LaVision. The PIV measurements were made using 1 mm thick Nd:YAG laser sheet, of 120 mJ pulse energy, and 532 nm wavelength, to illuminate the plane of interest. The light scattered by the particles were recorded with FlowMaster-3S charge coupled device (CCD) camera (1280×1024 pixels, 8 Hz) from LaVision. The PIV acquisition rate was 4 Hz.

The 2D velocity field measurements in the x-y plane (u, velocity in x direction; v, velocity in y direction) were done in a field of view 0.094 m $\times$ 0.075 m located symmetrically around the center. Two images were taken within a short interval of time. Each image was subdivided into interrogation windows of 32×32 pixel in size. The size of each pixel was 2.94 mm $\times$ 2.34 mm. The cross-correlation function for each interrogation window was used to obtain a two-dimensional shift. Subsequent division by the time interval between two consecutive images yields the velocity components in the imaging plane. The time interval between two laser pulses for various experiments varied between 0.014 and 0.11 s. The vector fields were calculated with an overlap of 50%, and the calculated vectors were postprocessed by setting an allowable vector range, which was specified for each velocity component. All the vectors outside this range were removed. The gaps arising from such a rejection were filled by interpolation. A median filter, which computes a median vector from eight neighboring vectors was used. The image analysis was carried out using Davis 6 software (LaVision).

The motion of the top plate was measured experimentally. Since this motion is periodic, the velocities at different points in the flow field also show temporal variations. The flow field is, hence, a function of position and time. We are interested in a quantitative comparison of the results of our experiments to numerical simulations. We describe the flow field at four different top plate positions. At position 1, the plate moves from the extreme right toward the center. Position 2 corresponds to the plate at the center of the cavity moving toward the left, and position 4 corresponds to the plate at the center of the cavity moving toward the right. At both positions 2 and 4, the plate velocity is at the maximum, though in the opposite direction. The plate position, when it moves from the left extreme toward the center is called position 3. The experimental data were collected after the system reached a terminal state, i.e., after the initial transients had decayed.

2.2 Computational Technique. The CFD simulations were performed using FLUENT 6.1. The 2D and 3D geometries were made using GAMBIT 2.1. The grid independency was ensured by meshing the geometry with different spacing between the cells. The quad map-type grid with 50,000 cells was chosen for 2D computations and 266,000 cells for 3D computations for detailed studies. A periodic boundary condition on the top plate was imposed using an externally defined macro, and the other faces of the cavity were considered as solid stationary walls. The convective flow terms were discretized using second-order upwind scheme. The coupled implicit time formulation was used with second-order accuracy. The time step used was 0.025 s for comparison to temporal variation of experimental data.

3 Results and Discussion

The planar measurements were made in a periodically driven cavity using PIV over a broad range of parameters. The area of experimental investigation is shown in dashed lines in Fig. 1. The measurements in x-y plane were done at different z planes $z=0.005$, 0.01, and 0.015 m (i.e., at a quarter, half, and three quarters width). The magnitudes of u and v at different points were extracted from the instantaneous velocity fields. All the results discussed in this work were obtained after the decay of initial transients and after the system had achieved a terminal periodic state. The instantaneous planar velocity fields at each plate position were averaged over ten measurements and used for the analysis. The nondimensional velocities are defined as $\tilde{u}=u/U_{\max}$ and $\tilde{v}=v/U_{\max}$, respectively. Time is nondimensionalized with the frequency of the plate motion, $\tilde{t}=t\omega$. In Sec. 3, experimental results are presented for Re=348 and are compared to the simulations. Subsequently, the discussion is included for results at all the Re investigated in this work.

3.1 Discussions on Flow Characteristics at Re=348. In Figs. 3 and 4, we depict typical periodic variation of $\tilde{u}$ and $\tilde{v}$ at points 1 and 2, respectively, for Re=348 (points are shown in Fig. 1). We see the sinusoidal variation of $\tilde{u}$ and $\tilde{v}$ at both the points. Point 1 is closer to the top corner, and the flow is equally dominant in both the directions at this point. Consequently, the magnitudes of both the components are significant. There exists a phase lag between $\tilde{u}$ and $\tilde{v}$ at point 1. Point 2 lies in the central plane, where the flow is significant in x direction. Therefore, $\tilde{v}$ is much smaller than $\tilde{u}$. The results based on the 2D as well as 3D CFD simulations are also shown in Figs. 3 and 4. The experimental results match well with the simulation predictions at both these points. It should be noted that qualitative agreement in terms of relative magnitudes and quantitative agreement in terms of cyclicity is obtained when 2D simulations are compared to the experimental PIV measurements. Magnitudes of maximum velocity are under-predicted by the 2D simulations. However, better agreement was observed with the 3D simulations. This is due to flow in the z direction, which is not accounted for in 2D simulations. The variation of velocity fields in the z direction as well as possible impact of the relative magnitude of the span width is discussed later.

To highlight the periodic terminal state and further to compare experimental measurements with simulations, phase trajectories at points 1 and 2 are shown in Fig. 5. The trajectories are closed curves, confirming the periodic nature of the terminal state. In Fig. 5(a), there is only one loop for the phase plane trajectory of point 1. This indicates that during a cycle both the velocity components are periodic, and in a cycle, each of them has only one maximum and one minimum. Additionally, the phase lag of approximately half a cycle is apparent from the figure. Figure 5(b) shows the behavior at point 2 that $\tilde{u}$ exhibits one maximum and one minimum while $\tilde{v}$ exhibits two maxima and two minima. This underscores the presence of dominant secondary frequency in the $\tilde{v}$ at point 2.

Figures 6 and 7 show the comparison of power spectra of $\tilde{u}$ and $\tilde{v}$ at points 1 and 2 obtained from PIV measurements and CFD simulations. Figures 6 and 7(a) show a peak frequency at $f_1=0.27\ s^{-1}$, imposed plate frequency. However, Fig. 7(b) shows that the vertical velocity component has the peak frequency, $f_2=0.54\ s^{-1}$, which is double the imposed plate frequency. The dominance of the secondary frequency in the central vertical plane was observed at other Re as well.

The velocity profiles of $\tilde{u}$ from the PIV measurements along vertical plane $x=0.05$ are shown in Fig. 8. The profiles are depicted for plate position 2 and plate position 4, when the plate velocity is maximum. In Fig. 8, the vertical coordinate is nondimensionalised by the scale, $\tilde{y}=(0.1-y)/(2v/\omega)^{1/2}$, where $(2v/\omega)^{1/2}$ is the scaling factor [9]. It is seen that $\tilde{u}$ is maximum near the plate and gradually decays along the depth of the cavity. Moreover, the velocity profiles at positions 2 and 4 are symmetric with respect to the central y plane ($y=0.05$) because of the symmetry of the domain and the sinusoidal variation of the plate velocity. At this Re, the flow is in the opposite direction to the plate motion in a larger fraction of the cavity. This implies that only in a smaller fraction of the cavity next to the plate, are the velocities generally higher and in the direction of the plate motion. The velocity profile of $\tilde{v}$ along $y=0.075$ at plate positions 2 and 4 are depicted in Fig. 9. The horizontal coordinate in Fig. 9 is nondimensionalised by the scale, $\tilde{x}=x/L$, where L is the length of the cavity. Profiles of $\tilde{v}$ at positions 2 and 4 are mirror images, about $x=0.05$. These profiles are also compared to 2D as well as 3D CFD simulations, which are shown as the curves in Figs. 8 and 9. Results from both the simulations are in qualitative agreement with the experimental results. However, the 3D simulations match quantitatively with the experimental results. Similar velocity profiles from 2D numerical simulations were reported by Iwatsu et al. [3] and are shown as insets in Figs. 8 and 9.

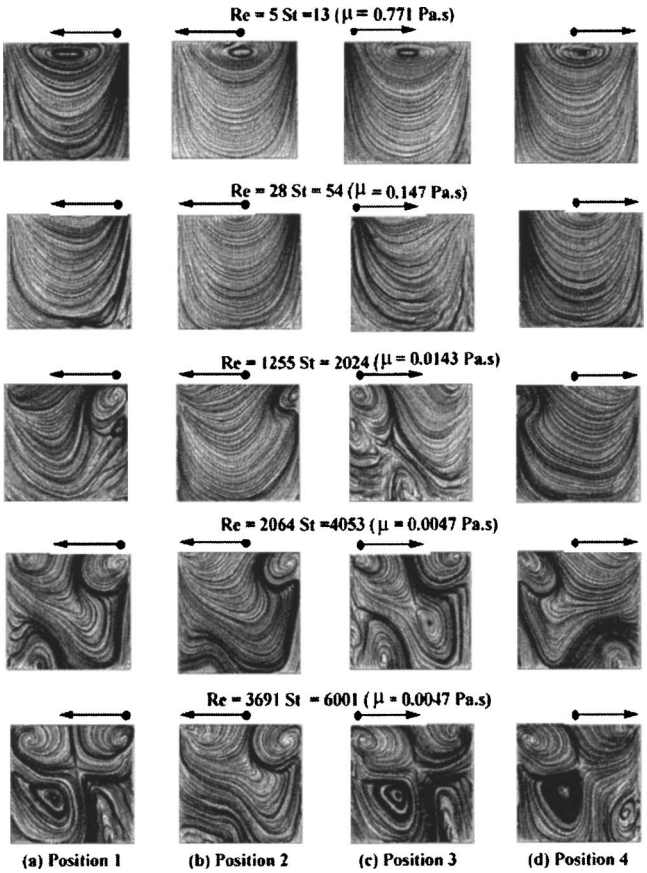

Fig. 11 Streamlines of velocity fields from planar measurements at the central *z* plane showing the representative evolution of flow as a function of Re and St at different plate positions. The arrow indicates the instantaneous position and direction of the plate.

3.2 Effect of Span Width Direction. The planar experimental measurements as well as CFD simulations were done at different z planes and at different Re. The flow variation in the different z planes (plate position 2 at Re=1040) is shown in the streamline plots from PIV measurements as well as CFD simulations in Figs. 10(a)–10(f). In the figures, the arrow indicates the instantaneous position and direction of the plate. It should be noted that the z plane locations are midplane and two planes equidistant from the midplane and the walls. The characteristic feature in all the

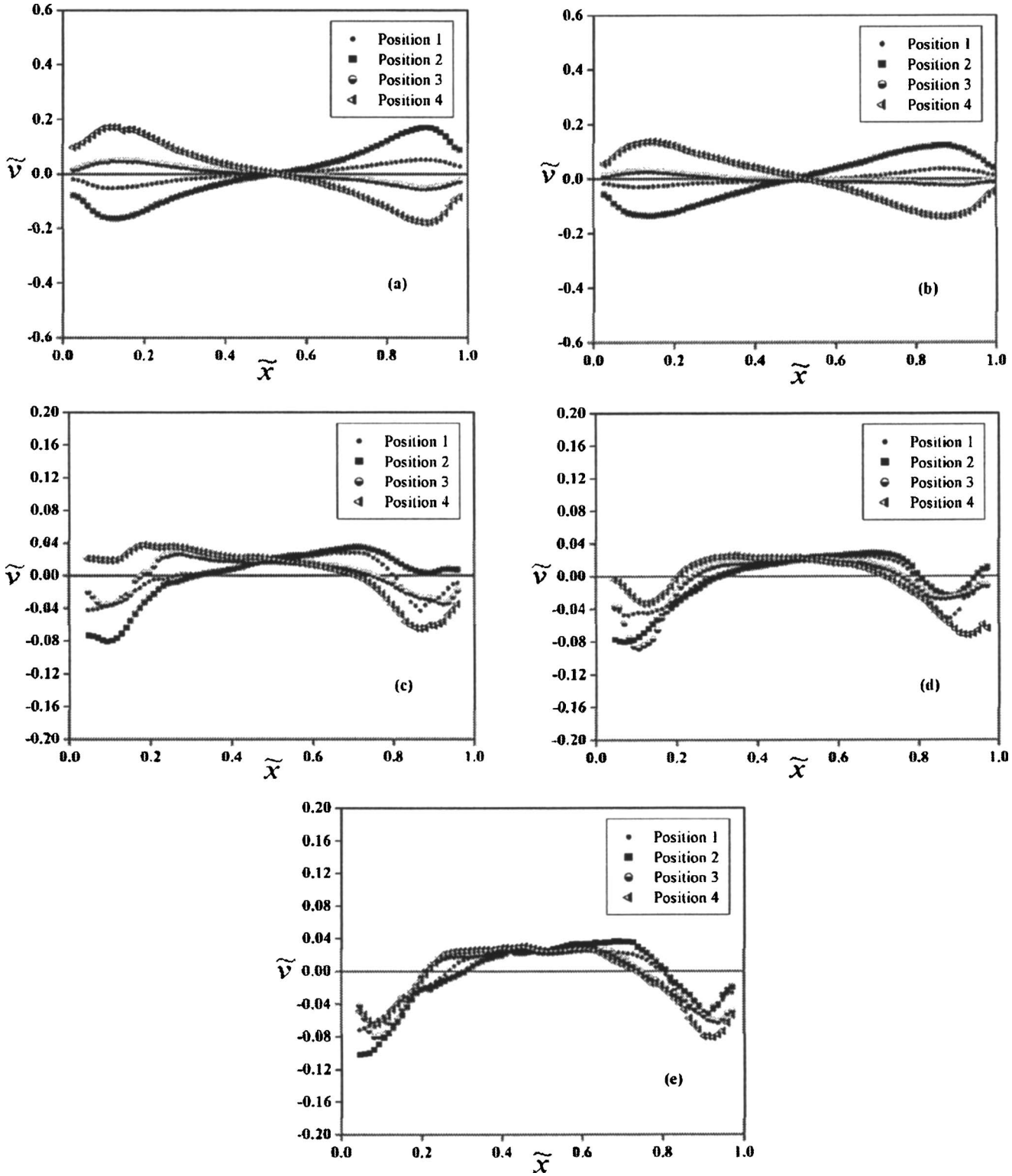

Fig. 12 Profiles of the experimentally measured nondimensionalized vertical component velocity in the central *z* plane along the horizontal plane *y*=0.075 for different Re, St: (*a*) Re=5, St=13 (μ=0.771 Pa s), (*b*) Re=28, St=54 (μ=0.147 Pa s), (*c*) Re=1255, St=2024 μ=0.0143 Pa s (μ=0.0143 Pa s), (*d*) Re=2064, St=4053 (μ=0.0047 Pa s), and (*e*) Re=3691, St=6001 (μ=0.0047 Pa s)

streamline plots is a strong circulation region in the top right corner. It is noteworthy that the differences at the three planes exist in terms of the size of the region. Naturally, 2D and 3D simulations also differ in the same respect. Even though there is a variation in the *z* direction at large Re, the planar measurements acquired are reasonably accurate in depicting the flow. Similar observations could be made for other plate positions and for different Re.

To investigate the impact of span width on flow structure in the cavity, 3D simulations were also performed for cavities of differ-

ent span width, $W=0.01$ m and $W=0.03$ m (recall span width of experimental cavity was 0.02 m). Even at high Re, the z velocity is nearly zero through out the cavity with $W=0.01$ m and increases with the increase in the span width. However, the x component velocity is almost the same with all the span widths. The streamline patterns at different conditions are qualitatively similar, and they are in good agreement with the 2D simulations regardless of span width of the cavity. This observation was also highlighted with results discussed earlier (Re=348), where the 2D simulations agreed qualitatively with 3D simulations as well as experimental measurements.

Overall, these results highlight the effect of finite span width on the quantitative variation of pointwise velocity and flow structure. We have analyzed the differences at all Re through measurements at different z planes and simulations with different widths. Experimental measurements were carried out at planes defined by $z=0.005$, 0.01, and 0.015 m. The different widths for which simulations were carried out were $W=0.01$, 0.02, 0.03 m and ∞ (2D simulations imply infinite span width). Based on the observations, it can be concluded that similar qualitative features of the flow are observed in all the cases. In the next section, we present variation in the flow structure and velocity at different planes as functions of Re.

3.3 Discussion of Results at Different Re. In order to visualize the overall flow patterns, the streamline plots from the experimental data for different plate positions (discussed in Sec. 2.1) at different Re are shown in Fig. 11. In this figure the arrow indicates the instantaneous position and direction of the plate. We can observe that at very low Re(=5), the streamlines are similar at all the plate positions. For instance, there is only a primary vortex that fills up the entire cavity. In addition, at all the plate positions, the flow resembles that in a steady lid-driven cavity (LDC). Similar results were reported by Iwatsu et al. [3]. At Re=28 as well, the primary vortex fills the entire cavity at all the plate positions. The fluid near the top plate is driven in the same direction as that of the lid motion and a counterflow exists below the top layer as discussed earlier. At Re=1255, the primary vortex observed at plate positions 2 and 4 evolves into counterrotating secondary vortices at positions 1 and 3, respectively. At higher Re(=2064), the corner recirculation region that is dominant at positions 1 and 3 is observed in the vicinity of the side wall at positions 2 and 4 as well. Therefore, the size as well as persistence of the recirculation region increases with Reynolds number. When the Reynolds number was further increased to 3691, the whole cavity flow can be described as a combination of multiple counterrotating vortices. These experimentally determined flow patterns are in good agreement with the simulation results of Iwatsu et al. [3].

To examine the velocity variation quantitatively, the velocity distribution along the horizontal plane $y=0.05$ at different Re is plotted in Figs. 12(a)–12(e). The y component of velocity ($\tilde{v}$) is taken from the experimental measurements at the central plane ($z=0.01$) at Re=5, 28, 1255, 2064, and 3691. The larger the Re, larger is the magnitude of velocity. However, $\tilde{v}$ is lower at larger Re. Comparing velocity profiles at Re of 5 and 28 (Figs. 12(a) and 12(b)), we can observe that the flow is qualitatively similar. As mentioned earlier, streamline patterns as well as velocity profiles at these Re are very similar to those in a steady LDC. Considerable differences are observed at higher Reynolds numbers, with velocity profiles displaying significant variation along x. However, variation with respect to plate position is smaller at higher Re. This is in good agreement with the observation made earlier that, at high Re the streamline patterns observed at plate position 1 and 3 persist for positions 2 and 4 as well. The presence of multiple vortices in the cavity is highlighted with multiple regions of positive and negative $\tilde{v}$. Evolution of flow structure, such as reported in this work, and the detailed characterization of secondary flows is important for fundamental understanding and as well as for mixing applications.

4 Conclusions

The periodic oscillatory flow in a square cavity has been studied under different experimental conditions using particle image velocimetry. Based on the variation in plate velocity and fluid viscosity, flow in a range of Reynolds numbers (5–3700) was analyzed. The temporal variation of the flow at characteristic points presented dictates the sinusoidal nature of the flow. The frequency content of the flow was investigated by means of power spectrum analysis. The spatial variation of the flow along the central vertical plane was largely in the horizontal direction. Differing planes of symmetry in velocity profiles were observed for horizontal and vertical velocity components. At very low Re, the flow structure is qualitatively similar to the steady lid-driven cavity. The presence of secondary recirculating regions was observed at high Re. The measurements were also done at different planes in the spanwise direction to assess the effect of finite span width on the flow behavior. The experimental measurements were compared to the 2D and 3D computational fluid dynamic simulations. Based on all the results, it can be concluded that planar measurements and 2D simulations lead to a qualitative understanding of the flow behavior in the cavity under investigation. Measurements at different planes along with 3D simulations lead to quantitative information about the flow structure and velocity fields.

Acknowledgment

The financial support given by the DST (FIST) is acknowledged. We would like to thank A. Srikanth and Abhilash Narayanan for their experimental and analysis help. We also thank J. Desinghu for providing experimental assistance.

References

[1] O'Brien, V., 1975, "Unsteady Cavity Flows: Oscillatory Flat Box Flows," ASME J. Appl. Mech., **42**, pp. 557–563.
[2] Soh, W. H., and Goodrich, J. W., 1988, "Unsteady Solution of Incompressible Navier-Stokes Equations," J. Comput. Phys., **79**, pp. 113–134.
[3] Iwatsu, R., Hyun, J. M., and Kuwahara, K., 1992, "Numerical Simulations of Flows Driven by a Torsionally Oscillating Lid in a Square Cavity," ASME J. Fluids Eng., **114**, pp. 143–151.
[4] Iwatsu, R., Hyun, J. M., and Kuwahara, K., 1993, "Numerical Simulations of Three Dimensional Flows in a Cubic Cavity With an Oscillating Lid," ASME J. Fluids Eng., **115**, pp. 680–686.
[5] Vogel, M. J., Hirsa, A. H., and Lopez, J. M., 2003, "Spatial-Temporal Dynamics of a Periodically Driven Cavity Flow," J. Fluid Mech., **478**, pp. 197–226.
[6] Chien, W. L., Rising, H., and Ottino, J. M., 1986, "Laminar and Chaotic Mixing in Several Cavity Flows," J. Fluid Mech., **170**, pp. 355–37.
[7] Niederkorn, T. C., and Ottino, J. M., 1993, "Mixing of a Viscoelastic Fluid in a Time-Periodic Flow," J. Fluid Mech., **256**, pp. 243–268.
[8] Anderson, P. D., Galaktionov, O. S., Peters, G. W. M., Van De Vosse, F. N., and Meijer, H. E. H., 2000, "Mixing of non-Newtonian Fluids in a Time-Periodic Cavity Flows," J. Non-Newtonian Fluid Mech., **93**, pp. 265–286.
[9] Schlichting, H., 1979, *Boundary Layer Theory*, McGraw-Hill, New York, pp. 93–94.

Masahiro Murayama
Undergraduate student

Yoshiki Yoshida[1]
Associate Professor
e-mail: kryoshi@kakuda.jaxa.jp

Yoshinobu Tsujimoto
Professor

Osaka University,
Graduate School of Engineering Science,
1-3, Machikaneyama,
Toyonaka, Osaka 560-8531,
Japan

Unsteady Tip Leakage Vortex Cavitation Originating From the Tip Clearance of an Oscillating Hydrofoil

Tip leakage vortex cavitations originating from the tip clearance of an oscillating hydrofoil were observed experimentally. It was found that the delay between the unsteady and the steady-state results of the tip leakage vortex cavitation increase, and that the maximum cavity size decreases when the reduced oscillating frequency increases. To simulate the unsteady characteristics of tip leakage vortex cavitation, a simple calculation based on slender body approximation was conducted taking into account the effect of cavity growth. The calculation and experimental results of the cavity volume fluctuation were found to be in qualitative agreement. [DOI: 10.1115/1.2173290]

Introduction

It is recognized that cavitation instabilities, such as cavitation surge and rotating cavitation, are caused by the unsteady characteristics of cavitation, i.e., mass flow gain factor and cavitation compliance. Cavitations in unshrouded pump impellers can be classified into three types: cavitation on the blade surface, cavitation in the tip leakage flow, and cavitation in back-flow vortices. For the blade cavitation, unsteady characteristics have been extensively studied, and it is now possible to predict the mass flow gain factor and cavitation compliance theoretically [1,2]. However, few studies have been performed on the unsteady cavitation characteristics in the tip leakage flow, although it seems that such cavitation in this plays an important role in cavitation instabilities.

In a preliminary study [3], we presented tip leakage vortex cavitation results for a fixed hydrofoil. In the present investigation, we focus on the cavity response, i.e., variation of the size and the location of the cavity, to the frequency of an oscillating hydrofoil. Unsteady cavitation on the blade surface of oscillating hydrofoils has been extensively studied [4–6] with regard to unsteady attached cavitation of the propeller in the wake of a ship, but only a limited number of results are related to the tip vortex cavitation under unsteady conditions. To our knowledge, the only results available on the subject are those of Mckenney et al. [7] and Boulon et al. [8] regarding a hydrofoil without tip clearance.

Rains [9] first proposed the application of slender body approximation to the tip leakage vortex. In this method, a 3-D tip leakage flow is simulated by a 2-D unsteady crossflow. Chen et al. [10] applied this method to a compressor tip clearance flow by using the vortex method. Watanabe et al. [11] recently extended this method to include the effects of cavity growth, and Higashi et al. [3] have applied Watanabe's method to the tip leakage vortex cavitation of a fixed hydrofoil. In the present study, Watanabe's method is further applied to the unsteady tip leakage vortex cavitation of an oscillating hydrofoil. The influences of the reduced oscillating frequency were examined by comparison of the experimental results with the calculations.

Experimental Apparatus and Procedures

The experiments were conducted in the cavitation tunnel shown schematically in Fig. 1. The tunnel is a closed loop and the cavitation number, σ, is adjusted by using a vacuum pump connected to the top of the pressure control tank. The cavitation number was kept constant at $\sigma=1.0$ throughout the present experiments. The cross section of the test section was rectangular, the height and the width were 70 and 100 mm, respectively, and the length was 500 mm as shown in Fig. 2. Both the sidewall and the top wall of the test section were made of transparent acrylic resin to allow systematic visualization. A convergent with an area reduction ratio of 4.65 was situated upstream of the test section. The water was deaerated by setting the pressure at 5 kPa for more than 12 h before the experiments. Although the free stream velocity, U, was varied between 2.9 and 5 m/s, the effect of the Reynolds number ($\mathrm{Re}=UC/\nu=2.6-4.5\times10^5$) on the test results could not be observed in this range. Therefore, the free stream velocity was kept constant and equal to 5 m/s throughout the experiments.

Figure 3 shows the geometry of the tested hydrofoil. It consists of a smooth 3 mm thick stainless steel flat plate with a surface roughness of about 1 μm. The chord C was 90 mm, the span H was 67 mm, and the design tip clearance was 3 mm (the actual value was 2.95 mm). Both the leading and the trailing edges were rounded with a radius of 1.5 mm. As with the findings by Gearhart [12], with a square tip, "gap cavitation" in the clearance between the tip and the wall and "sheet vortex cavitation" in the shear layer of the leakage jet clearly appeared. To remove these types of cavitation, the pressure side corner of the tip was rounded to a radius of 3 mm, as shown in Fig. 3 [13,14].

The oscillating mechanism is shown schematically in Figs. 4 and 5. A three-bar linkage oscillates the hydrofoil in a nearly sinusoidal motion as shown in Fig. 5. It provides a pitching motion of the hydrofoil around the mid-chord "O" in Fig. 3 at a dimensional frequency, f, up to 16 Hz, which corresponds to a reduced frequency, $k=2\pi fC/(2U)=\omega C/(2U)$, up to 0.9. The unsteady angle of attack $\alpha(t)$ is represented by $\alpha(t)=\alpha_m+\Delta\alpha\times\sin(2\pi ft)$. Tests conducted for different couples of α_m and $\Delta\alpha$ have shown that the characteristics of the unsteady tip leakage vortex cavitation are conserved. Thus, all the results presented here are for a mean angle of attack, α_m, of 4 deg and an oscillating amplitude of the angle of attack, $\Delta\alpha$, of 2 deg. The tip flow was visualized with high-speed video camera operating at 250 frames/s, and with a photo camera with a strobe light providing an exposure of 20 μs.

[1]Author to whom correspondence should be addressed. Current address: Japan Aerospace Exploration Agency, Institute of Aerospace Technology, Kakuda Space Center, Koganezawa 1, Kimigaya, Kakuda, Miyagi 981-1525, Japan.

Contributed by the Fluids Engineering Division of ASME for publication in the JOURNAL OF FLUIDS ENGINEERING. Manuscript received February 23, 2004; final manuscript received October 20, 2005. Assoc. Editor: Georges L. Chahine.

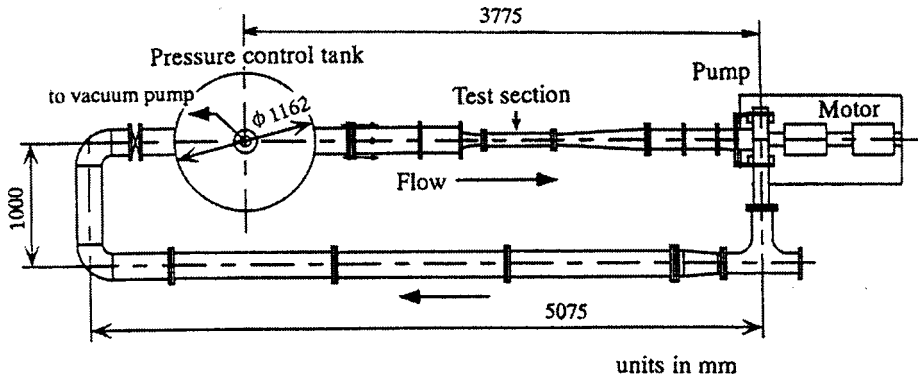

Fig. 1 Top view of the cavitation tunnel

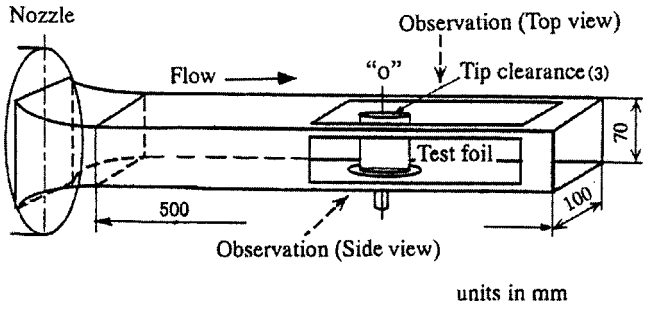

Fig. 2 Scheme of the test section

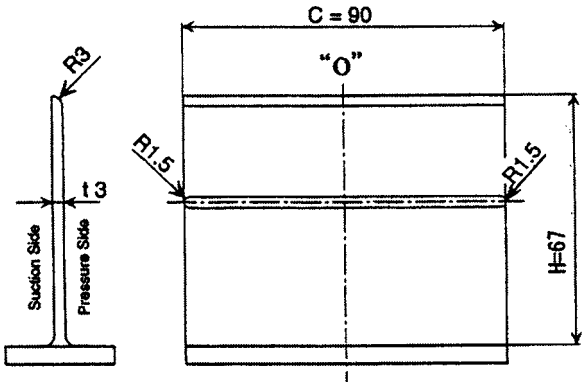

Fig. 3 Configuration of the flat plate hydrofoil

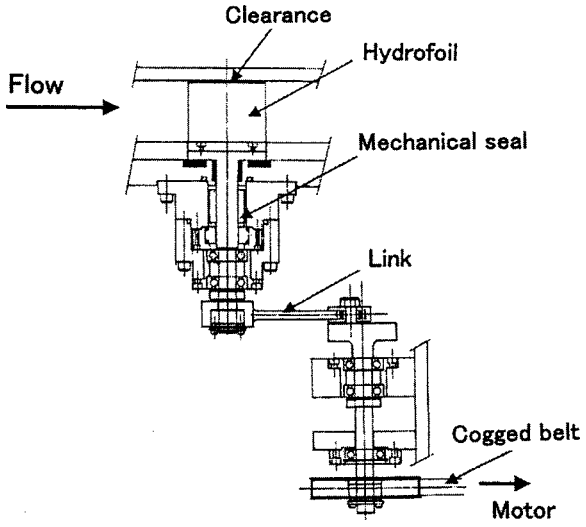

Fig. 4 Cross section of the equipment used to produce the pitching oscillation

Experimental Results

Observation of the Tip Leakage Vortex Cavitation. Figure 6 shows photos of the tip leakage vortex cavitation observed from the top of the test section at various angles of attack, i.e., α=2, 4(+), 6, 4(−), and 2 deg sequentially, for the reduced frequencies

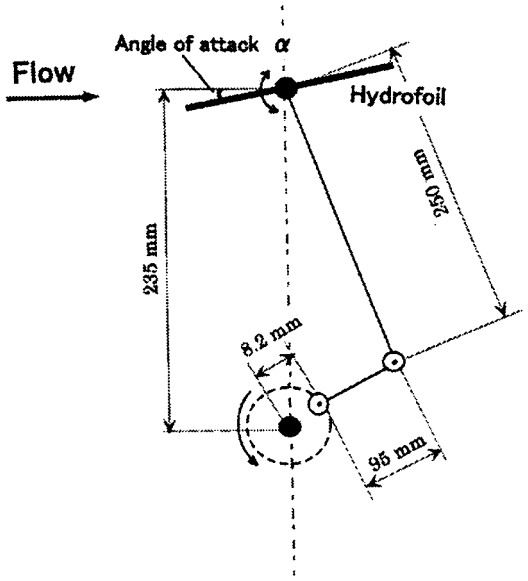

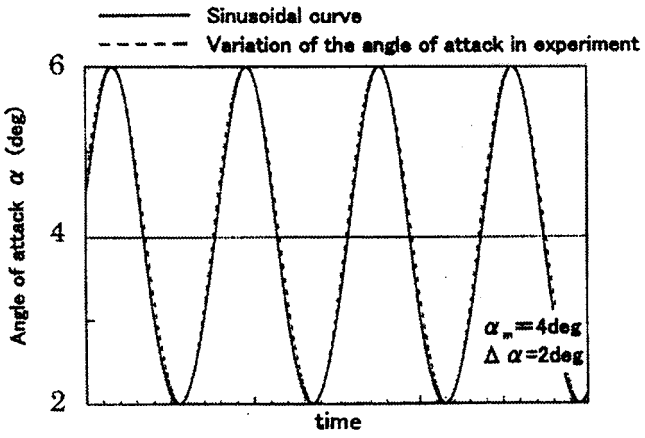

Fig. 5 Schematic showing the three-bar linkage used to produce the oscillation of the angle of attack, and variation of the angle of attack compared with the sinusoidal curve, for α_m =4 deg and $\Delta\alpha$=2 deg

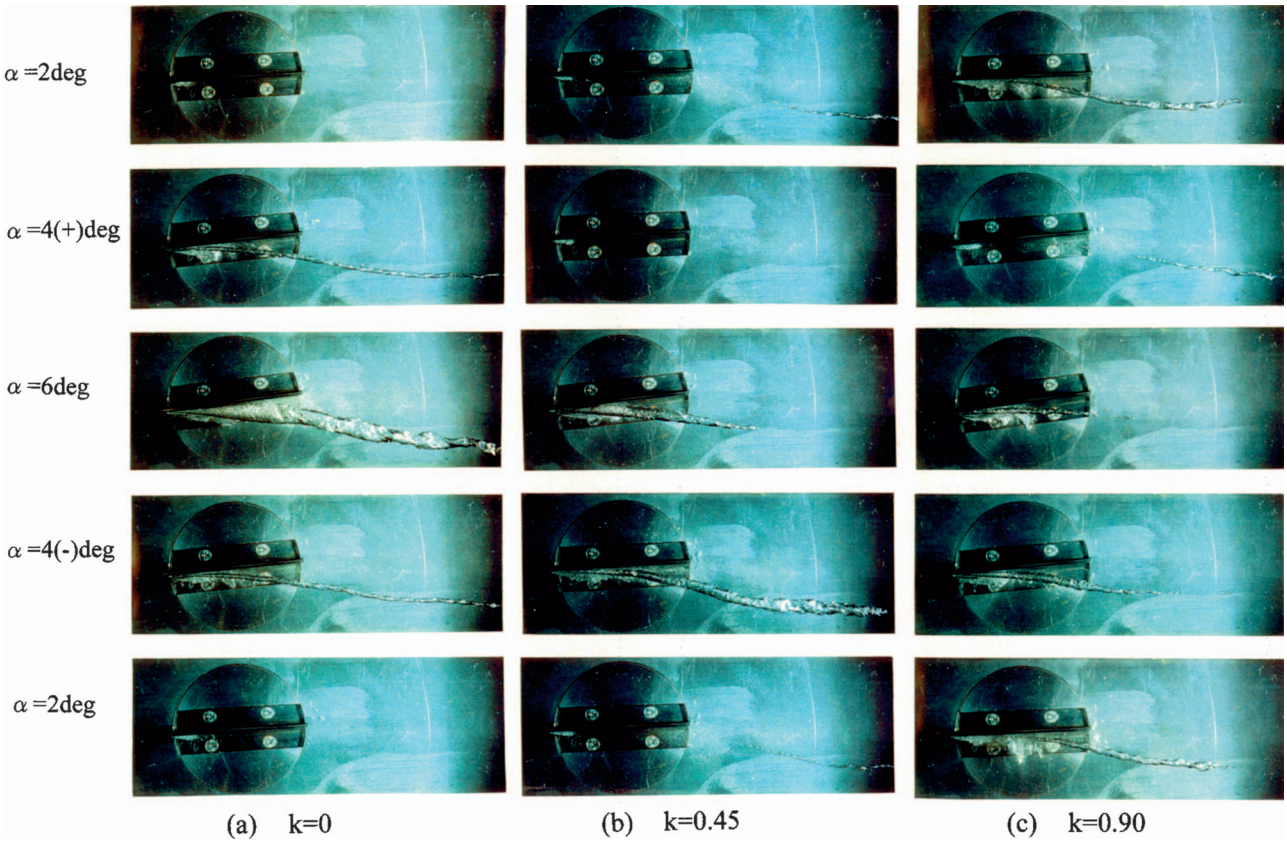

Fig. 6 Photographs of the tip leakage vortex cavitation with various frequencies, for $k=0,0.45,0.90$, $\sigma=1.0$, $\alpha_m=4$ deg and $\Delta\alpha=2$ deg (uncertainty in $\alpha=0.1$ deg, $k=0.005$). (*a*) $k=0$. (*b*) $k=0.45$. (*c*) $k=0.90$.

$k=0$ (steady) and $k=0.45,0.90$, (unsteady), at the cavitation number $\sigma=1.0$. The plus (+) or minus (−) sign next to the angle of attack indicates that it is increasing or decreasing, respectively. Hereafter, we focus on the influence of the oscillating frequency on the cavity size, i.e., the typical radius of cylindrical tip vortex cavitation and the location, i.e., trajectory of the tip vortex cavitation.

Steady Condition ($k=0$). In Fig. 6(*a*), it is shown that at $\alpha=2$ deg, tip leakage vortex cavitation is not observed, although a limited blade cavitation at the leading edge occurs. At $\alpha=4$ deg, a very long cylindrical vortex cavitation develops with unchangeable radius. Notice that the cavity extends beyond the viewing window. At $\alpha=6$ deg, cavitation in the shear layer of the leakage jet occurs near the tip clearance, rolls up into the vortex, and feeds the cavity, resulting in a considerable increase in its size. Again, the tip vortex cavitation twists and convects beyond the viewing window. The angle made by the foil and the trajectory of the cavity increases as the angle of attack increases. These results are reasonable because the pressure difference across the tip clearance as well as leakage flow increases at a larger angle of attack. Other results for the steady condition have been presented elsewhere [3].

Unsteady Condition ($k=0.45$ and 0.90). Figure 6 shows that the critical angle of attack, for which the length and radius of the tip vortex cavitation are the largest, varies from $\alpha=6$ deg (at $k=0$) to $\alpha=4(-)$ deg (at $k=0.45$) and $\alpha=2$ deg (at $k=0.90$). It was also found that the cavitation in the shear layer of the leakage jet does not appear for the unsteady conditions, and that the cavity length and radius decrease remarkably with an increase in the oscillating frequency. As opposed to the results for the steady condition, at which the tip leakage vortex cavitation at $\alpha=2$ deg cannot be observed, for the unsteady condition at $k=0.90$ and $\alpha=2$ deg, the tip leakage vortex cavitation is seen downstream of the foil.

Variation of the Cavity Radius. To obtain a better understanding of the influence of the oscillating frequency on the cavitation behavior, the cavity radius, R, of the tip leakage vortex cavitation and the cavity length, l, of the attached cavitation on the blade surface were measured with the high-speed video pictures from the top and side views as shown in Figs. 7(*a*) and 7(*b*). Because the radius and length of the cavitation fluctuated considerably even at the same angle of attack, the measurements were averaged over 20 frames of the high-speed video for the same angle of attack. Table 1 shows the standard deviation of cavity radius at $Z/C=0.5$, 1.0 and cavity length at mid-span, at $k=0$ ($\alpha=6$ deg), 0.45 ($\alpha=5(-)$ deg), and 0.90 ($\alpha=4(-)$ deg).

Figure 7(*c*) shows the radius of the tip vortex cavity (assumed to have a circular cross section) at the foil mid-chord $Z/C=0.5$ and at the trailing edge $Z/C=1.0$ as a function of the reduced time (instantaneous angle of attack) for various reduced frequencies up to $k=0.90$. In addition, the length of the attached cavity was measured at the foil mid-span for each instantaneous angle of attack, as shown in Fig. 7(*b*). This is only an indication of the length of the attached cavity because near the tip clearance the length was shorter than that at the mid-span for all cases due to the tip clearance flow. Figure 7(*d*) shows the length of the attached cavitation as a function of the reduced time (instantaneous angle of attack) for the various reduced frequencies.

Figure 7(*c*) shows that the delay between the unsteady and the steady-state results increase when the reduced frequency increases. The cavity size develops slowly when the angle of attack increases; it shrinks rapidly when the angle of attack decreases. In addition, the maximum radius of tip leakage vortex cavitation decreases if the oscillating frequency is increased. As a result, the amplitude of the fluctuation of the radius for $k=0.90$ is half that for $k=0$. Such aspects, i.e., the delay between the unsteady and the steady-state results and the reduction of the amplitude of the

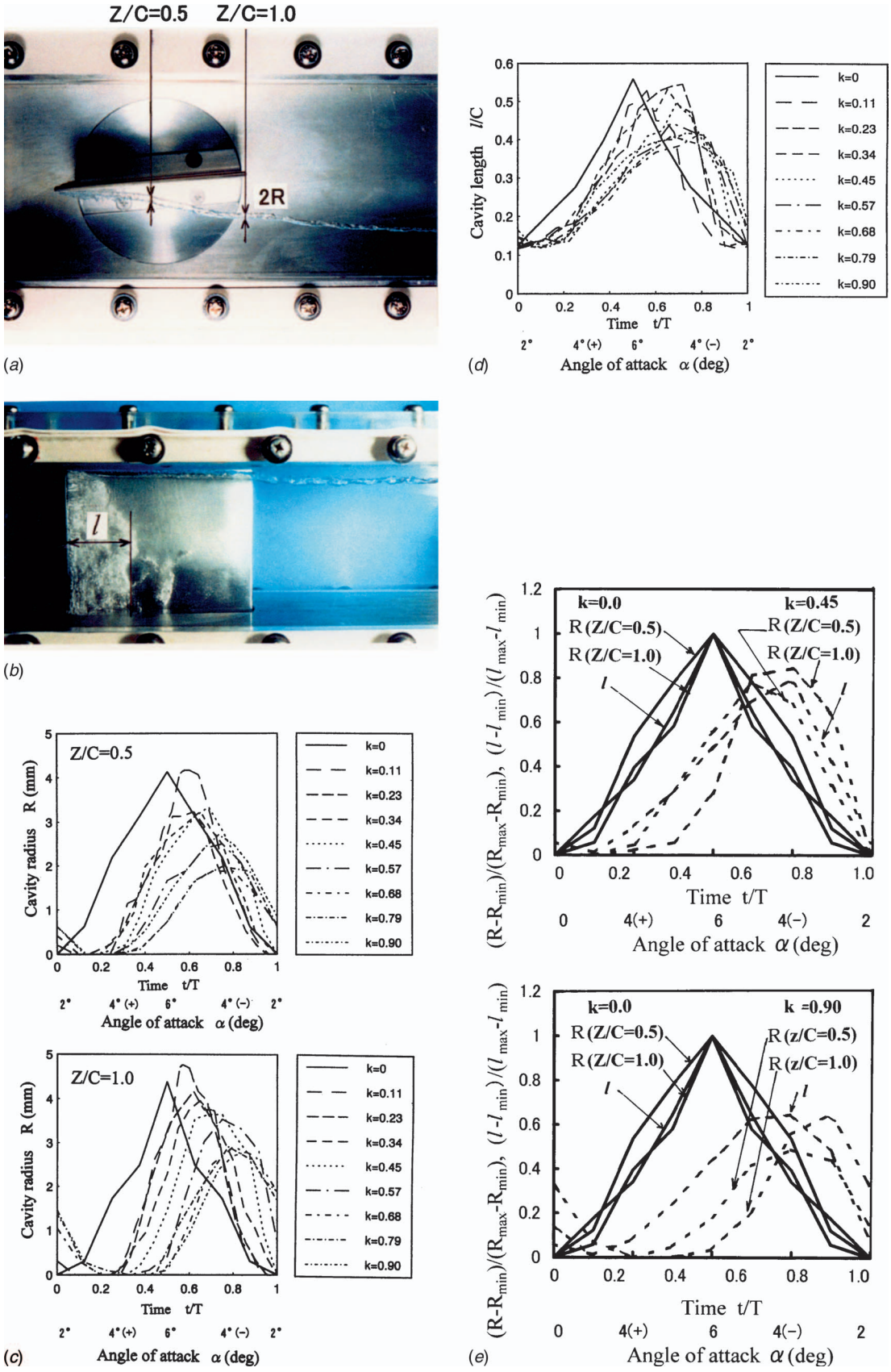

Fig. 7 (*a*) Cavity radius *R* of the tip leakage vortex cavitation at $Z/C=0.5$ and $Z/C=1.0$. (*b*) Blade cavity length *l* on the blade surface at mid-span. (*c*) Influence of the oscillating frequency on variation of the cavity radius *R* at $Z/C=0.5$ and $Z/C=1.0$, for $\sigma=1.0$, $\alpha_m=4$ deg, and $\Delta\alpha=2$ deg (uncertainty in $R=0.2$ mm, $\alpha=0.1$ deg, $k=0.005$). (*d*) Influence of the oscillating frequency on variation of the cavity length *l* at mid-span, for $\sigma=1.0$, $\alpha_m=4$ deg, and $\Delta\alpha=2$ deg (uncertainty in $l/C=0.02$, $\alpha=0.1$ deg, $k=0.005$) at $k=0.45$ and $k=0.90$ (*e*) Comparison of the delay of cavity radius *R* of the tip vortex cavitation with cavity length *l* at mid-span, for $\sigma=1.0$, $\alpha_m=4$ deg, and $\Delta\alpha=2$ deg (uncertainty in $\alpha=0.1$ deg, $k=0.005$) at $k=0.45$ and $k=0.90$.

Table 1 Standard deviation of cavity $\sigma(R)$ and cavity length $\sigma(l/C)$

	k=0	k=0.45	k=0.90
σ (R) (mm) at Z/C=0.5	0.60 (α = 6 deg)	0.56 (α = 5 (-)deg)	0.45 (α = 4 (-) deg)
σ (R) (mm) at Z/C=1.0	0.68 (α = 6 deg)	0.61 (α = 5 (-) deg)	0.57 (α = 4 (-) deg)
σ (l/C) at mid-span	0.09 (α = 6 deg)	0.10 (α = 5 (-) deg)	0.07 (α = 4 (-) deg)

cavity radius, are analogous to the unsteady behavior of the length of the attached cavitation at the mid-span as shown in Fig. 7(*d*). Figure 7(*e*) shows comparison of the normalized cavity radius (Z/C=0.5, 1.0) with the normalized cavity length (mid-span) at k=0.45 and k=0.90. The amount of the delay and decrease of the amplitude for the attached cavitation was almost the same as that of the tip vortex cavitation.

Outline of the Analytical Method

Tip leakage vortex cavitation occurs in the low pressure region of the vortex core formed by the rolling up of the shear layer between the tip leakage flow and the main flow (provided the local pressure is the vapor pressure). To explain the calculation method, we illustrate crossflow planes **A**, **B**, **C**, and **D** at different chordwise locations **a**, **b**, **c**, and **d**, respectively, as shown in Fig. 8. Location **a** is at the leading edge and **d** is at the trailing edge. The tip leakage flow starts at location **a**. As the crossflow plane moves through the foil, the vortices representing the shear layer are shed into the main flow from the tip of the foil. The vortices roll up in the subsequent cross sections, as illustrated in planes **B**, **C**, and **D**.

We assume that the crossflow plane moves downstream with the free stream velocity U. Hence, the distance between the planes analyzed is $\Delta S = U \times \Delta t$, where Δt is a time increment. The following assumptions were made in the present calculation. The velocity of the tip leakage jet on the crossflow plane at location S is simply assumed to be $U_j = (2\Delta p/\rho)^{1/2}$, where Δp is the instantaneous pressure difference across the tip clearance. The pressure difference Δp is assumed to consist of the steady component, Δp_m, related to the mean angle of attack, α_m, and the unsteady component, Δp_u, related to the amplitude of the oscillating angle of attack, $\Delta\alpha$. The steady component, Δp_m, is estimated from a noncavitating 2-D incompressible inviscid flow calculation around a thin foil. The unsteady component, Δp_u, is estimated from the unsteady airfoil theory described below.

The analytical method used to calculate the noncavitating flow around an oscillating foil in an ideal fluid has been given by Kármán and Sears [15]. Here, we use the results of 2-D noncavitating flow analysis available from Fung [16] to evaluate the unsteady pressure difference across the blade. Figure 9(*a*) shows the coordinate used in the following theoretical calculation. The motion and the foil are defined as follows. The foil surface is represented by $\xi = \cos(\theta)$, so that the leading edge is $\xi = -1$ and the trailing edge is $\xi = +1$. If we assume the pitching motion around the mid-cord at $\xi = 0$, the displacement η of the foil surface can be represented as

$$\eta = -\Delta\alpha \times \xi \times \exp(i\omega t), \quad \omega = 2\pi f \tag{1}$$

The unsteady pressure distribution on the foil is expressed as follows [16]:

$$p_u = \rho U^2 \times \Delta\alpha \times \left\{ -\left[\left(1 + \frac{ik}{2}\right) C(k) - \frac{ik}{2} \right] \tan\frac{\theta}{2} - 2ik \sin\theta + \frac{1}{4}k^2 \sin 2\theta \right\} \times e^{i\omega t} \tag{2}$$

where $k(=2\pi fC/(2U) = \omega C/(2U))$ is the reduced frequency, and $C(k)$ is the Thedorsen function. Typical unsteady pressure distribution on the blade is shown in Fig. 9(*b*). The unsteady component of the pressure difference Δp_u is calculated from p_u using Eq. (2).

A vortex method was used for the calculation on the crossflow plane. A source $q_j = 2 \times U_j$ is distributed at the tip clearance, which represents the tip leakage jet. The discrete free vortices Γ, representing the shear layer between the tip leakage jet and the main flow, are released from the corner of the tip. The strength of the vortices is determined as $\Gamma = U_j^2 \times \Delta t/2$ from the leakage jet velocity U_j.

In this calculation, a single cylindrical cavity starts to develop at the location of the minimum pressure, when the pressure first becomes lower than the vapor pressure p_v. The growth of this cylindrical cavity, radius R, on the crossflow plane is determined

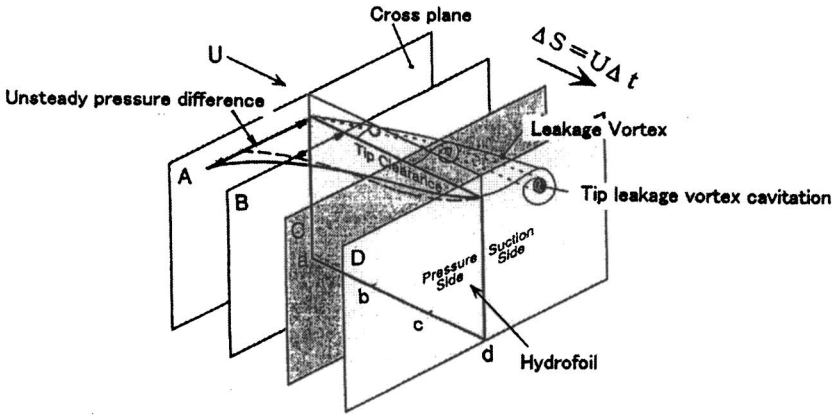

Fig. 8 Sketch for explanation of the cross plane and the unsteady pressure difference across the tip clearance

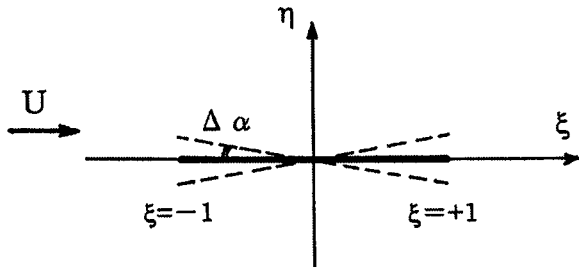

(a) Pitching oscillation of flat plate foil

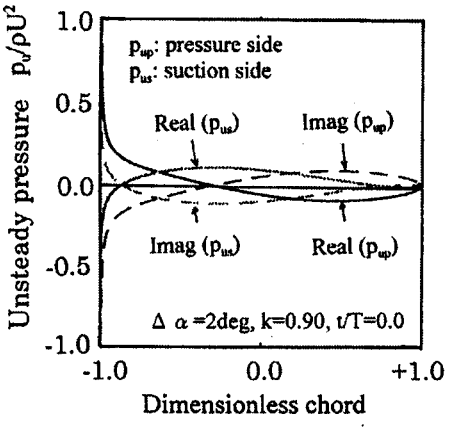

(b) Unsteady pressure distribution

Fig. 9 Coordinate of the pitching oscillation of a thin flat plate foil and typical unsteady pressure distribution for $\Delta\alpha=2$ deg, $k=0.90$, and $t/T=0$. (*a*) Pitching oscillation of flat plate foil. (*b*) Unsteady pressure distribution.

by the unsteady version of Bernoulli equation. The effect of the cavity is represented by a source $q_b=2\pi R\times dR/dt$ at the center of the rolled-up vortex. The effects of the sidewall of the test section are ignored for simplicity. Boundary conditions on the upper wall and the foil surface are satisfied by introducing the mirror image of singularities within $0\leqslant S/C\leqslant 1.0$. However, the mirror image with respect to the foil surface is not considered at $S/C>1.0$ where there is no foil. The initial radius of the cavity is set to be $R/C=0.00011$, and the time increment is $\Delta t=(C/U)/2000$ in the present calculations.

Calculation Results

Cavitation Behavior. Figure 10 shows the projection of the cavity on a plane normal to the foil, as shown in the visualizations of Fig. 6, calculated for steady ($k=0$) and unsteady conditions ($k=0.45, 0.90$) at $\sigma=1.0$, $\alpha_m=4$ deg, and $\Delta\alpha=2$ deg.

First, for the steady condition ($k=0$), the cavity size is larger at a larger angle of attack. This general behavior agrees well with the experimental results, except that the tip leakage vortex cavitation grows rapidly near the leading edge at $\alpha=2$ deg. It seems that the estimation of the steady pressure difference, Δp_m, across the tip clearance estimated from the 2-D inviscid flow analysis is responsible for the overestimation. However, the present 2-D unsteady flow model based on a slender body approximation can qualitatively predict the location and the size of the cavity for the steady condition.

For the unsteady conditions ($k=0.45$ and 0.9), the tip vortex cavitation grows to a maximum at $\alpha=6-4(-)$ deg. From these results, it is clear that the cavity development is delayed behind the foil oscillation. Here, focusing on the instance of $\alpha=2$ deg, it can be observed that the tip leakage vortex cavitation grows again downstream for the unsteady conditions ($k=0.45, 0.90$), although it disappears near the trailing edge for the steady condition ($k=0$). These characteristics qualitatively agree with unsteady experimental results as shown in the visualization of Fig. 6.

Figure 11(*a*) compares the trajectory of the cavity for the steady and unsteady conditions. For the steady condition ($k=0$), the

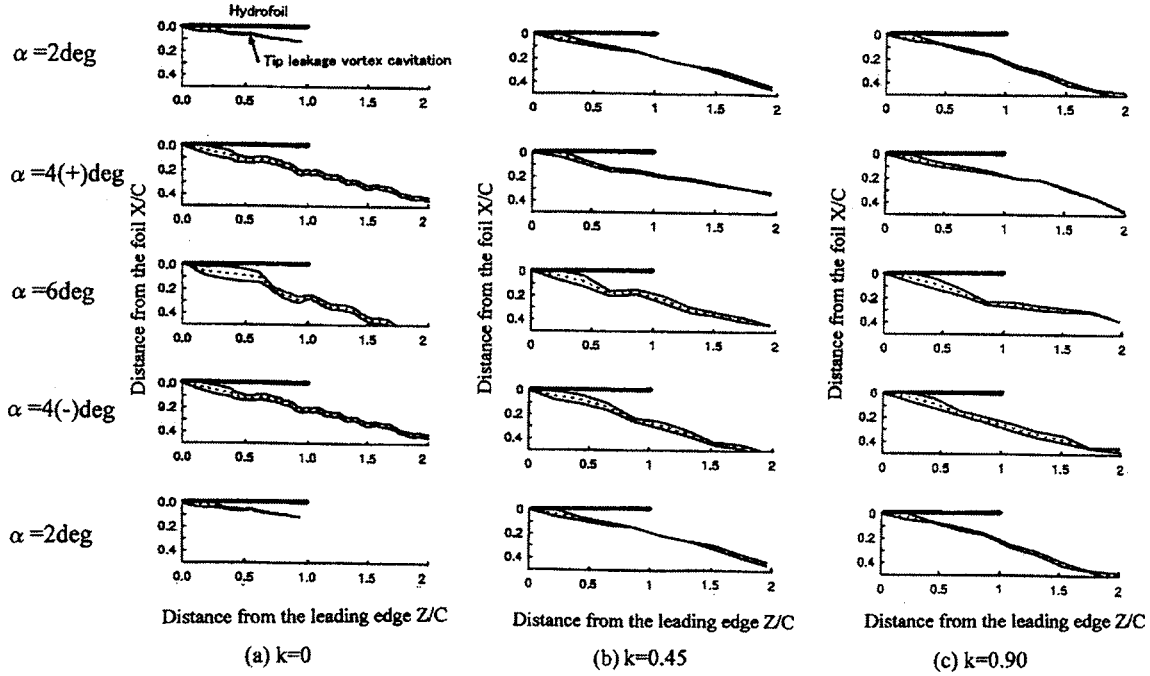

Fig. 10 Calculation results of the tip leakage vortex cavitation with various oscillating frequencies, for $k=0, 0.45, 0.90$, $\sigma=1.0$, $\alpha_m=4$ deg, and $\Delta\alpha=2$ deg, compared with the experimental results shown in Fig. 6. (*a*) $k=0$, (*b*) $k=0.45$, (*c*) $k=0.90$.

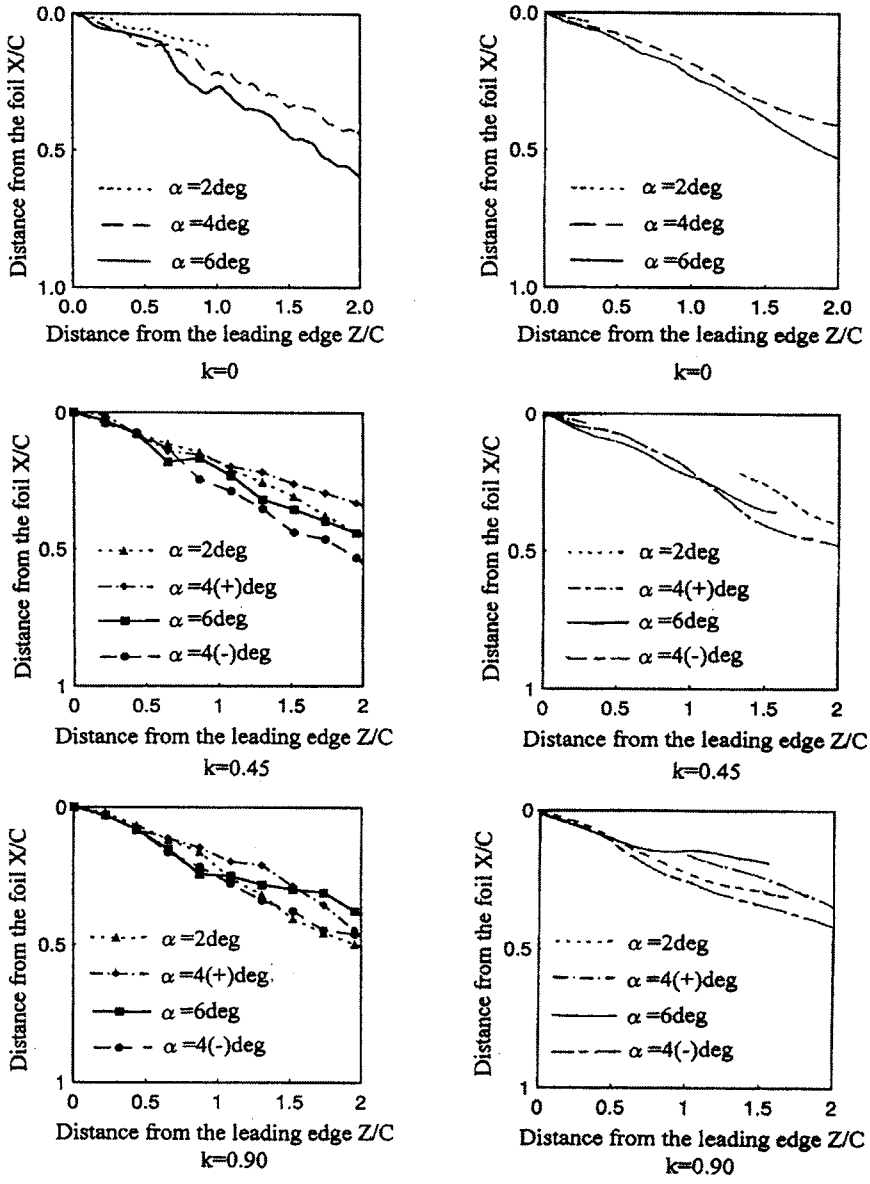

Fig. 11 Cavity trajectory at various angles of attack for $k=0, 0.45, 0.90$, $\sigma=1.0$, $\alpha_m=4$ deg, and $\Delta\alpha=2$ deg (experimental uncertainty in X/C, $Z/C=0.05$, $\alpha=0.1$ deg, $k=0.005$). (*a*) Calculation, (*b*) Experiment.

angle made by the foil and the trajectory of the cavity increase with increasing angle of attack. For the unsteady conditions, the cavity trajectory becomes meandering with increasing oscillating frequency. For the unsteady condition $k=0.90$, the trajectory at $\alpha=2$ deg is far from the foil, and the trajectory at $\alpha=6$ deg is close to the foil at $Z/C=2.0$. This is contrary to the situation for the steady condition. Figure 11(*b*) shows the trajectory of the cavity in the experiments at the same condition as that in the calculations. Similar behavior of the cavity trajectory could be observed in the experiments.

Cavity Volume. Figure 12 shows the variation of the estimated cavity volume compared with experimental results. Both cavity volumes were estimated by integrating of the partial cylindrical cavity from the leading edge ($Z/C=0$) to twice the chord length ($Z/C=2.0$). In this estimation, it was assumed that the cavity shape is cylindrical. Although the agreement between the experiment and calculation is not sufficient quantitatively, the same tendency can be found with respect to the influence of the oscillating frequency. That is, (a) the delay between the unsteady and the steady-state results increase, and (b) the maximum volume of the cavity decreases when the reduced frequency increases.

Discussions

Tip leakage vortex cavitation occurs in lower pressure region in the vortex core formed by rolling up of the shear layer. Therefore, let us examine the vortices representing the shear layer that eventually rolls up to the tip leakage vortex core. In the present calculation, the discrete free vortices Γ are released from the corner of the tip on the crossflow plane. The total amount of the shed vortices was calculated and compared between the steady ($k=0$) and the unsteady ($k=0.9$) condition.

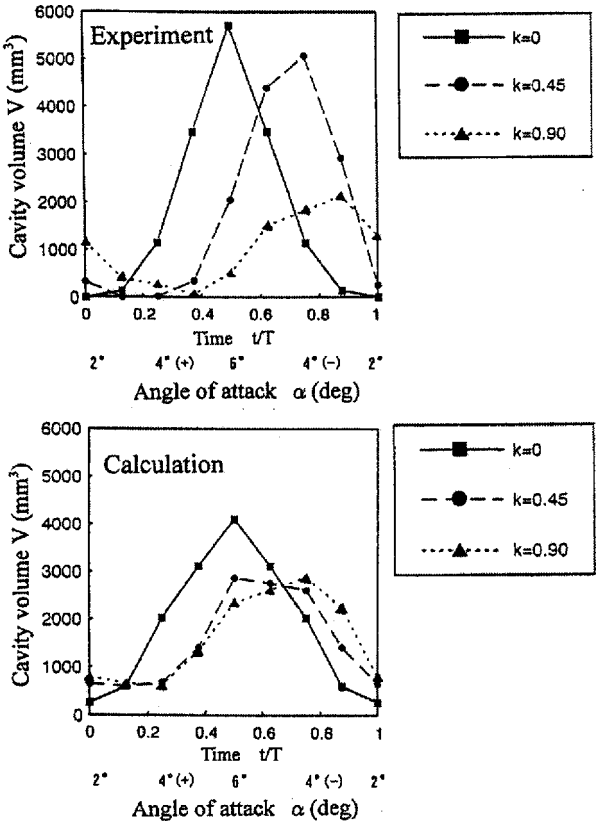

Fig. 12 Comparison of the variation of the cavity volume between the experiments and calculations, for $k=0, 0.45, 0.90$, $\sigma=1.0$, $\alpha_m=4$ deg, and $\Delta\alpha=2$ deg. Cavity volume is limited from the leading edge to the length of the two chords (experimental uncertainty in $V=200$ mm^3, $\alpha=0.1$ deg, $k=0.005$). (*a*) Experiment. (*b*) Calculation.

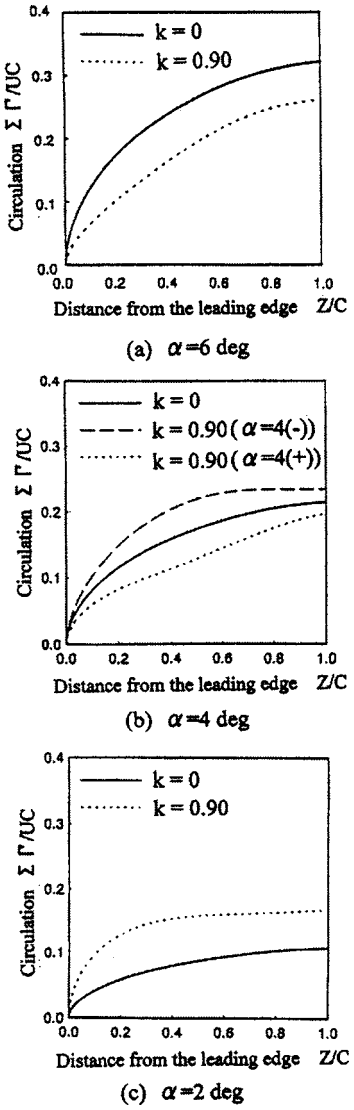

Fig. 13 Total amount of the shed vortices $\Sigma\Gamma/UC$ compared between steady ($k=0$) and unsteady ($k=0.90$) condition, for $\sigma=1.0$, $\alpha_m=4$ deg and $\Delta\alpha=2$ deg

Figure 13 shows the increase of the total amount of the shed vortices, $\Sigma\Gamma/UC$, on the crossflow plane from the leading edge to the trailing edge. These figures show the increase at the instant angle of attack $\alpha=6$, 4(+), 4(−), and 2 deg, respectively, when the crossflow plane reaches the trailing edge at $Z/C=1.0$. Here, we focus on the circulation, i.e., the total amount of the shed vortices $\Sigma\Gamma/UC$ at the trailing edge ($Z/C=1.0$). Figure 14 presents a comparison of the circulation for the steady ($k=0$) and unsteady ($k=0.90$) conditions. For the steady condition $k=0$, this value is theoretically equal to $\Sigma\Gamma/UC=C_L/2=\pi\times\sin\alpha$ (C_L: lift coefficient of the flat plate foil) at $Z/C=1.0$. Comparing the unsteady result with the steady one, it was found that (a) at $\alpha=6$ deg, $\Sigma\Gamma/UC$ for the unsteady condition is less than that for the steady condition. While (b) at $\alpha=4(-)$ deg, $\Sigma\Gamma/UC$ for the unsteady condition is larger than that for the steady condition. To the contrary, at $\alpha=4(+)$ deg, $\Sigma\Gamma/UC$ for the unsteady condition is less than that for the steady condition, and (c) at $\alpha=2$ deg, $\Sigma\Gamma/UC$ for the unsteady condition is larger than that for the steady condition. These tendencies of $\Sigma\Gamma/UC$ at $Z/C=1.0$ agree with those of the unsteady cavity radius, R, observed at $Z/C=1.0$ as shown in Fig. 7(*c*).

From these results, it can be concluded that the circulation of the tip leakage vortex core consisting of the shed vortices becomes smaller for the unsteady states than for the steady one. Also, the fluctuation of the total amount of vortices is delayed behind the oscillation of the angle of attack. It can be inferred that the unsteady behavior of the pressure difference across the tip clearance is responsible for the characteristics of the circulation of the tip leakage vortex and affects the growth and the decay of the unsteady tip vortex cavitation.

Conclusions

The results obtained in the present study can be summarized as follows:

1. When the reduced frequency of the oscillating hydrofoil increases, the delay between the unsteady and the steady-state results of the tip vortex cavitation increases, and the maximum volume of that decreases. These characteristics were observed both in the experiment and the calculation.
2. The present 2-D unsteady flow model based on a slender body approximation can qualitatively predict the unsteady behavior of the tip leakage vortex cavitation of the oscillating hydrofoil.
3. The unsteady behavior of the pressure difference across the tip clearance influences the circulation of the tip vortex core and affects the growth and the decay of the unsteady tip leakage vortex cavitation.

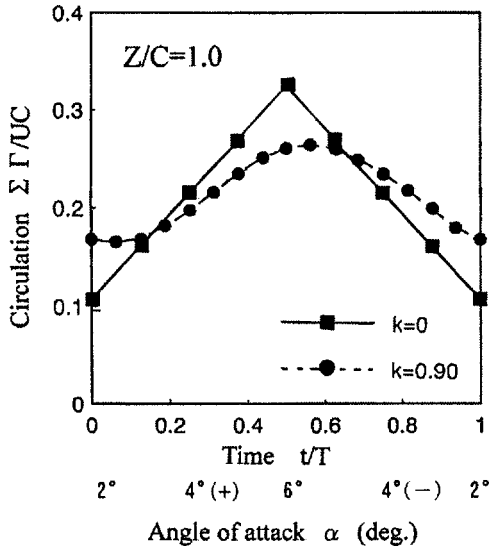

Fig. 14 Comparison of the circulation $\Sigma\Gamma/UC$ on the crossflow plane at the trailing edge ($Z/C=1.0$) between the steady ($k=0$) and unsteady ($k=0.90$) condition, for $\sigma=1.0$, $\alpha_m=4$ deg, and $\Delta\alpha=2$ deg

Acknowledgment

The authors would like to express their sincere gratitude to Seiji Higashi for his valuable advice regarding calculations, and Dr. Tatsuro Kudo of the National Maritime Research Institute who showed them many reports on unsteady cavitation in propellers.

Nomenclature

C = chord
$C(k)$ = Thedorsen function
C_L = lift coefficient=Lift/$(\rho U^2 C/2)$
f = frequency
H = span
i = imaginary unit
k = reduced frequency=$2\pi fC/(2U)=\omega C/(2U)$
l = cavity length of the blade cavitation
p = pressure
p_1 = pressure at inlet
p_v = vapor pressure
Δp = pressure difference across the tip clearance
Δp_m = mean component of pressure difference across the tip clearance
Δp_u = unsteady component of pressure difference across the tip clearance
q_j = strength of source representing the leakage jet
q_b = strength of source representing the cavity growth
R = radius of the cavity
Re = Reynolds number=UC/ν
S = distance along the chord
ΔS = increment of S
T = period
t = time
Δt = time increment
ξ, η = coordinates, defined in Fig. 9
U = free stream velocity
U_j = velocity of leakage jet flow
V = cavity volume
X = distance from the foil
Z = distance from the leading edge
α = angle of attack
$\Delta\alpha$ = amplitude of the angle of attack
α_m = mean angle of attack
Γ = strength of vortices
ν = kinematic viscosity
ρ = density
σ = cavitation number=$(p_1-p_v)/(\rho U^2/2)$, or standard deviation
ω = angular velocity of oscillating foil

References

[1] Brennen, C. E., 1978, "Bubbly Flow Model for Dynamic Characteristics of Cavitating Pumps," J. Fluid Mech., **89**, pp. 234–240.
[2] Otsuka, S., Tsujimoto, Y., Kamijo, K., and Furuya, O., 1996, "Frequency Dependence of Mass Flow Gain Factor and Cavitation Compliance of Cavitating Inducers," ASME J. Fluids Eng., **118**, pp. 400–408.
[3] Higashi, S., Yoshida, Y., and Tsujimoto, Y., 2002, "Tip Leakage Vortex Cavitation From the Tip Clearance of a Single Hydrofoil," JSME Int. J., Ser. B, **45**, pp. 662–671.
[4] Tanibayashi, H., and Chiba, N., 1977, "Unsteady Cavitation of Oscillating Hydrofoil," Mitsubishi Tech. Bull., **117**, pp. 1–10.
[5] Miyata, H., Tamiya, S., and Kato, H., 1972, "Pressure Characteristics and Cavitation on an Oscillating Hydrofoil," J. Soc. Naval Architects of Japan (in Japanese), **132**, pp. 107–115.
[6] Franc, J. P., and Michel, J. M., 1988, "Unsteady Attached Cavitation on an Oscillating Hydrofoil," J. Fluid Mech., **198**, pp. 171–189.
[7] Mckenney, E. A., and Hart, D. P., 1993, "Experimental Determination of Bound Circulation and Shed Vorticity Induced by an Oscillating Hydrofoil," ASME FED-Vol. 153, *Cavitation and Multiphase Flow*, pp. 87–91.
[8] Boulon, O., Franc, J. P., and Michel, J. M., 1997, "Tip Vortex Cavitation on an Oscillating Hydrofoil," ASME J. Fluids Eng., **119**, pp. 752–758.
[9] Rains, D. A., 1954, "Tip Clearance Flows in Axial Flow Compressors and Pumps," California Institute of Technology, Hydrodynamics and Mechanical Engineering Laboratories, Lab. Rep. No. 5.
[10] Chen, G. T., Greitzer, E. M., Tan, C. S., and Marble, F. E., 1991, "Similarity Analysis of Compressor Tip Clearance Flow Structure," ASME J. Turbomach., **113**, pp. 260–271.
[11] Watanabe, S., Seki, H., Higashi, S., Yokota, K., and Tsujimoto, Y., 2001, "Modeling of 2-D Leakage Jet Cavitation as a Basic Study of Tip Leakage Vortex Cavitation," ASME J. Fluids Eng., **123**, pp. 50–56.
[12] Gearhart, W. S., 1966, "Tip Clearance Cavitation in Shrouded Underwater Propulsors," J. Aircr., **3**, pp. 185–192.
[13] Ido, A., and Uranishi, K., 1991, "Tip Clearance Cavitation and Erosion in Mixed-Flow Pumps," FED (Am. Soc. Mech. Eng.), Vol. **119**, pp. 27–29.
[14] Laborde, R., Chantrel, P., and Mory, M., 1997, "Tip Clearance and Tip Vortex Cavitation in Axial Flow Pump," ASME J. Fluids Eng., **119**, pp. 680–685.
[15] Von Kármán, T. H., and Sears, W. R., 1938, "Airfoil Theory for Non-Uniform Motion," J. Aeronaut. Sci., **5**, pp. 379–389.
[16] Fung, Y. C., 1969, *An Introduction to the Theory of Aeroelasticity*, Dover Publication, Inc., New York, p. 401.

Hironori Horiguchi
Graduate School of Engineering Science,
Osaka University,
1-3 Machikaneyama, Toyonaka,
Osaka, 560-8531, Japan
e-mail: horiguti@me.es.osaka-u.ac.jp

Yury Semenov
Institute of Technical Mechanics,
National Academy of Science and
National Space Agency of Ukraine,
15, Leshko-Popel' St.,
Dniepropetrovsk, 49005, Ukraine
e-mail: relcom@semenov.dp.ua

Masataka Nakano
Technical Development and Engineering Center,
Turbo and Hydraulic Machinery Department,
Ishikawajima-Harima Heavy Industries Co., Ltd.,
1 Shin-nakahara, Isogo, Yokohaha,
Kanagawa, 235-8501, Japan
e-mail: masataka_nakano@ihi.co.jp

Yoshinobu Tsujimoto
Graduate School of Engineering Science,
Osaka University,
1-3 Machikaneyama, Toyonaka,
Osaka, 560-8531, Japan
e-mail: tujimoto@me.es.osaka-u.ac.jp

Linear Stability Analysis of the Effects of Camber and Blade Thickness on Cavitation Instabilities in Inducers

It has been shown by experimental and numerical studies that various cavitation instabilities occur in inducers for rocket engines when the cavity length exceeds about 65% of the blade spacing. On the other hand, it has been pointed out by an experimental study that the cavitation instabilities occur when the pressure gradient near the throat becomes small to some degree. The present study is motivated to examine the latter criterion based on pressure gradient for cavitation instabilities from the viewpoint of theoretical analysis. For this purpose, analyses of steady flow and its stability were carried out for cavitating flow in cascades with circular arc and plano-convex blades by a singularity method based on closed cavity model. It was found that the criterion based on the cavity length for the occurrence of cavitation instabilities is more adequate than the criterion based on the pressure gradient. It was also found that the steady cavity length and the stability of the flow in both cascades can be practically correlated with a parameter $\sigma/[2(\alpha-\alpha_0)]$, *where* σ *is a cavitation number,* α *is an angle of attack, and* α_0 *is a shockless angle of attack.* [DOI: 10.1115/1.2173291]

Introduction

High-speed turbomachinery, such as turbopumps for rocket engines, is operated under cavitating condition. Cavitation can become unstable even at the design flow rate, and unsteady cavitation seriously reduces the reliability of the rocket engine system. Therefore, the prediction of the possible cavitation instabilities and the understanding of their characters are required for the improvement of the reliability.

The analyses of steady cavitation flow in inducers and its stability have been made by the authors [1,2]. The results show that various modes of cavitation instabilities can occur when the steady cavity length reaches about 65% of the blade spacing of the impeller. Actually, some of those modes predicted have been also found in experiments [3,4].

On the other hand, it has been suggested by an experimental study [5] that the cavitation instabilities can occur when the pressure gradient near the throat becomes small to some degree as the values of $\sigma/(2\alpha)$ decreases, where σ is a cavitation number and α is an angle of attack. To examine this from the standpoint of theoretical analysis, the analyses of steady flow and its stability are carried out for cavitating flow in cascades with circular arc and plano-convex blades by a singularity method based on a closed-cavity model.

First, the effects of camber and blade thickness are discussed. Then, the relation between the pressure gradient on the suction surface of a blade near the throat and the occurrence of cavitation instabilities is examined. Based on the results for the cascades with various solidity and stagger, we discuss which is more adequate for the criterion of stability, the steady cavity length, or the pressure gradient at the cavity trailing edge.

Contributed by the Fluids Engineering Division of ASME for publication in the JOURNAL OF FLUIDS ENGINEERING. Manuscript received July 25, 2004; final manuscript received October 25, 2005. Assoc. Editor: Georges L. Chahine.

In high-speed turbopumps, the backflow vortex cavitation and tip vortex cavitation, as well as the blade surface cavitation treated here can occur, and the flow field is generally three-dimensional. So, the effect of the three-dimensionality of the flow and cavitation may not be negligible. However, only two-dimensional blade surface cavitation is considered here to obtain fundamental characteristics.

Model for Present Analysis

We consider a cascade with the spacing h and the stagger angle β as shown in Fig. 1, with a mean flow of magnitude U and the angle of attack α. The cascade has circular arc blades as shown in Fig. 1 or plano-convex blade shown in Fig. 2. To simplify the problem, it is assumed that the outlet duct length is infinite and no velocity fluctuation exists at downstream infinity. The inlet duct length L is assumed to be finite and set to be $100C$ in the present study. The inlet duct is connected to a space with constant total pressure p_t along AB at the duct inlet. The complex conjugate velocity fluctuation there is denoted by $\tilde{N}e^{i\beta}e^{j\omega t}$, where $\tilde{N}$ represents the amplitude of axial velocity fluctuation.

The camber line of the circular arc blades is given by

$$y = \frac{\Omega\xi}{2}\left(1 - \frac{\xi}{C}\right) + Ih\cos\beta, \quad 0 \leqslant \xi \leqslant C$$

$$(I = -\infty, \ldots, -1, 0, 1, \ldots, \infty) \tag{1}$$

where Ω is an angle subtended by the tangents to the blade at the leading and trailing edges. In the present study, Ω is assumed to be small as is the angle of attack α. From the blade geometry, a relation exists between Ω and maximum camber t

$$\Omega = 8\frac{t}{C} \tag{2}$$

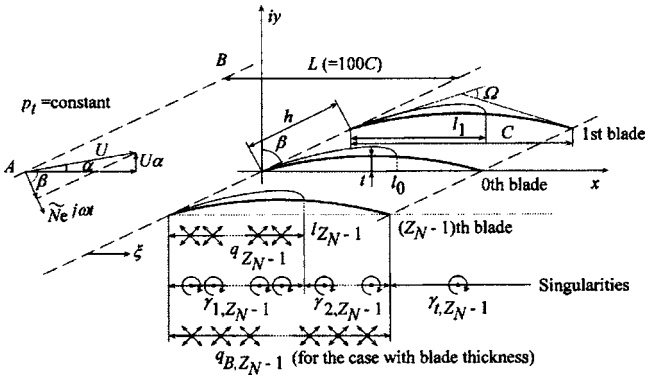

Fig. 1 Schematic of the cascade with circular arc blades

To study the effects of the blade thickness, we consider a cascade with plano-convex blades shown in Fig. 2. The shape of the suction surface of the blade is given by Eqs. (1) and (2), where t is the maximum blade thickness for the case of plano-convex blade.

The index of blades n is defined by taking account of the periodicity of blade row for the inducer with blade number Z_N: the blade on the x-axis is given the index zero, the index increases in a positive direction of the y -axis, and the index of Z_Nth blade returns to zero.

In the present study, the partial cavitation with cavity length l_n on the nth blade is considered. The velocity disturbance due to the blades and cavities can be represented by source distributions q_n on the cavity region, vortex distributions $\gamma_{1,n}$ and $\gamma_{2,n}$ on the blade region, and trailing vortices $\gamma_{t,n}$ on the wake surface of the blades. For the plano-convex blades, source distributions $q_{B,n}$ on the blade region are used to represent the effects of blade thickness. These singularities are distributed on the chords, and their extensions on the assumption that the cavity thickness, the camber, and the flow disturbance are small. Then, the complex velocity $w(z,t)$ can be obtained by integrating the velocities induced by these singularities along the chords and their extensions. The detailed expression of $w(z,t)$ is shown in Appendix A.

We divide the strength of singularities and the cavity length into the steady and unsteady components as follows:

$$q_n(s_1) = q_{s,n}(s_1) + \tilde{q}_n(s_1)e^{j\omega t}$$

$$\gamma_{1,n}(s_1) = \gamma_{1s,n}(s_1) + \tilde{\gamma}_{1,n}(s_1)e^{j\omega t}$$

$$\gamma_{2,n}(s_2) = \gamma_{2s,n}(s_2) + \tilde{\gamma}_{2,n}(s_2)e^{j\omega t}$$

$$q_{B,n}(s_1) = q_{Bs,n}(s_1)$$

$$q_{B,n}(s_2) = q_{Bs,n}(s_2)$$

$$\gamma_{t,n}(\xi) = \tilde{\gamma}_{t,n}(\xi)e^{j\omega t}$$

$$l_n = l_{s,n} + l_n e^{j\omega t}$$

$$(n = 0, \ldots, Z_N - 1) \tag{3}$$

where s_1 and s_2 are the coordinates stretching with the variable cavity length l_n and defined by

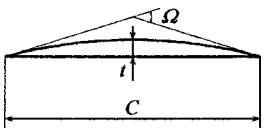

Fig. 2 Plano-convex blade

$$s_1 = l_n/\xi \quad (0 \leq s_1 \leq 1, 0 \leq \xi \leq l_n, n = 0, 1, \ldots, Z_N - 1) \tag{4}$$

$$s_2 = \{\xi - (2l_n - C)\}/(C - l_n) \quad (1 \leq s_2 \leq 2, l_n \leq \xi \leq C, n = 0, 1, \ldots, Z_N - 1) \tag{5}$$

$\omega = \omega_R + j\omega_I$ is the complex frequency with the real part ω_R and the imaginary part ω_I signifying the frequency and decay rate, respectively.

In the present study, the chamber angle Ω is assumed to be small, as well as the angle of attack α. Because of the linearization based on this assumption, the right-hand side of the boundary conditions, Eqs. (B5) and (B7), becomes 0 for unsteady components. As a result, the value of unsteady source $\tilde{q}_{B,n}$ becomes zero.

The velocity around the cascade is divided into the uniform steady component $(U, U\alpha)$, the steady disturbance (u_s, v_s), and the unsteady disturbance $(\tilde{u}, \tilde{v})$ components as follows:

$$u = U + u_s + \tilde{u}e^{j\omega t}$$

$$v = U\alpha + v_s + \tilde{v}e^{j\omega t} \tag{6}$$

Here, it is assumed that $\alpha \ll 1$, $U \gg |u_s|$, $|v_s| \gg |\tilde{u}|$, $|\tilde{v}|$ and linearization is made on these assumptions.

Boundary Conditions

Boundary conditions are applied on the coordinates s_1 and s_2 stretching with the variable cavity length l_n.

Boundary Condition on Cavity Surface. The pressure on the cavity surface $(z = mhe^{i(\pi/2-\beta)} + l_m s_1 + 0i, \quad 0 \leq s_1 \leq 1, \quad m = 0, 1, \ldots, Z_N - 1)$ is assumed to be constant and equal to the vapor pressure p_v. The index m is the number of the blade on which the boundary conditions are applied. The linearized momentum equation on the cavity surface is given by

$$\frac{\partial u_{c,m}}{\partial t} + U\frac{\partial u_{c,m}}{\partial \xi} = 0 \tag{7}$$

Solving Eq. (7) in consideration of Eq. (4), we obtain the velocity $u_{c,m}(s_1)$ on the cavity surface as follows:

$$u_{c,m}(s_1) = U + u_{cs} + \tilde{u}_{c,m}e^{-j(\omega l_{s,m}/U)s_1}e^{j\omega t} \tag{8}$$

Equation (8) leads to the following boundary condition:

$$\text{Real}[w(mhe^{i(\pi/2-\beta)} + l_m s_1 + 0i, t)] = U + u_{cs} + \tilde{u}_{c,m}e^{-j(\omega l_{s,m}/U)s_1}e^{j\omega t}, \quad 0 \leq s_1 \leq 1 \tag{9}$$

The velocity on the cavity surface is related with the pressure at $\xi = -L$ as follows, by the unsteady Bernoulli's equation between $\xi = 0$ and $\xi = -\infty$ and the momentum equation for the fluid between $\xi = -L$ and $\xi = -\infty$, which oscillates uniformly with the amplitude $\tilde{N}$

$$u_{cs} = \frac{p_{-Ls} - p_v}{\rho U} = \frac{\sigma U}{2} \tag{10}$$

$$\frac{\partial\left[\Phi_{0,m} - \Phi_{-\infty} - \lim_{b\to\infty}\{(b - L\cos\beta)\tilde{N}\}\right]}{\partial t} + U\tilde{u}_{c,m} - U\tilde{N}\cos\beta = \frac{\tilde{p}_{-L}}{\rho} \tag{11}$$

where p_{-Ls} and p_v are the pressure at the upstream boundary, $\xi = -L$, and the vapor pressure, respectively. b is a distance along the axis of cascade between the leading edge of blade and the upstream. σ is the cavitation number and defined as $2(p_{-Ls} - p_v)/(\rho U^2)$. $\Phi_{0,m}$ and $\Phi_{-\infty}$ are the velocity potentials at the leading edge of mth blade and $\xi = -\infty$, respectively. By the assumption that the flow around the cascade is connected to a space with a constant total pressure along AB at a distance L from the leading edge, we can obtain

$$\tilde{p}_{-L} = -\rho U \tilde{N} \cos\beta \tag{12}$$

Equations (10) and (11) with Eq. (12) give the tangential velocity u_{cs} and $\tilde{u}_{c,m}$ on the cavity surface.

Boundary Condition on Blade Surface. On the wetted blade surface, the flow should be tangential to the blade. This boundary condition can be expressed by using the y-component velocity. The practical expression of the boundary condition is given in Appendix B.

Cavity Closure Condition. The cavity thickness η_m should satisfy the following kinematic condition:

$$\frac{\partial \eta_m}{\partial t} + \frac{1}{l_m}\left(U - s_1 \frac{dl_m}{dt}\right)\frac{\partial \eta_m}{\partial s_1} = q_m(s_1), \quad (0 \leqq s_1 \leqq 1) \tag{13}$$

The cavity thickness is separated into steady and unsteady components as follows:

$$\eta_m(s_1) = \eta_{s,m}(s_1) + \tilde{\eta}_m(s_1)e^{j\omega t} \tag{14}$$

Equation (13) with Eqs. (3) and (14) is separated into steady and unsteady components after linearization. By integrating these equations, we obtain

$$\eta_{s,m}(s_1) = \frac{l_{s,m}}{U}\int_0^{s_1} q_{s,m}(s_1')ds_1' \tag{15}$$

$$\tilde{\eta}_m(s_1) = \frac{l_{s,m}}{U}\int_0^{s_1} \tilde{q}_m(s_1')e^{-j(\omega l_{s,m}/U)(s_1 - s_1')}ds_1' + \frac{\tilde{l}_m}{U}\int_0^{s_1}\left(1 + j\frac{\omega l_{s,m}}{U}s_1'\right)q_{s,m}(s_1')e^{-j(\omega l_{s,m}/U)(s_1 - s_1')}ds_1' \tag{16}$$

The cavity closure conditions for steady and unsteady components are as follows:

$$\eta_{s,m}(1) = 0 \tag{17}$$

$$\tilde{\eta}_m(1) = 0 \tag{18}$$

Kutta's Condition. The pressure difference across the blade is assumed to vanish at the trailing edge. From the difference of momentum equations on the pressure and suction surfaces of the blade after linearization, we can represent the above assumption by the following equation:

$$\frac{\partial}{\partial t}\left[\int_0^1 \gamma_{1,m}(s_1)l_m ds_1 + \int_1^2 \gamma_{2,m}(s_2)(C - l_m)ds_2\right] + U\gamma_{2,m}(2) = 0 \tag{19}$$

Equation (19) is equivalent to Kelvin's circulation conservation law and signifies that the vortex wake of strength $\gamma_{2,m}(2)$ is shed from the trailing edge with the mean velocity U, corresponding to the change of the blade circulation.

For the case that the trailing free vortex of the strength $\tilde{\gamma}_{t,m}(\xi)$ is transported on the freestream, it can be related with $\tilde{\gamma}_{2,m}(2)$ as follows:

$$\tilde{\gamma}_{t,m}(\xi) = \tilde{\gamma}_{2,m}(2)e^{-j(\omega/U)(\xi - C)} \tag{20}$$

Downstream Condition. In the case that the downstream duct length is assumed to be infinite, the downstream flow-rate fluctuation is suppressed due to the infinite inertia effect. Then, the continuity equation can be given by

$$\tilde{N} + \frac{1}{Z_N h}\sum_{n=0}^{Z_N - 1}\left\{\int_0^1 \tilde{q}_n(s_1)l_n ds_1\right\} = 0 \tag{21}$$

Closure Condition for q_B. The unknowns $q_{Bs,m}$, which represent the blade thickness, should satisfy the following equation:

$$\int_0^1 q_{Bs,m}(s_1)l_m ds_1 + \int_1^2 q_{Bs,m}(s_2)(C - l_m)ds_2 = 0 \tag{22}$$

Procedure of Calculation

The unknowns are the steady and unsteady components of strength of source and vortexes, $q_m(s_1)$, $q_{Bs,m}(s_1)$, $q_{Bs,m}(s_2)$, $\gamma_{1,m}(s_1)$, $\gamma_{2,m}(s_2)$, the cavity length l_m, the velocity $u_{c,m}$ on the cavity surface, and the amplitude of the inlet velocity fluctuation $\tilde{N}$. These are determined by the boundary conditions mentioned above. The strength of singularities are specified at discrete points, $s = S_{1,k}(k = 1 \sim N_C)$ on the cavity surface and $S_{2,k}(k = 1 \sim N_B)$ on the wetted surface in the coordinates s_1, s_2, stretching with the variable cavity length l_m as unknowns. The locations of the singularity specifications, $S_{1,k}$ and $S_{2,k}$ are given as follows so that they distribute densely near the leading and trailing edges of the cavity and the blade.

$$S_{1,k} = \frac{l_{s,m}}{2}\left[1 - \cos\left(\frac{\pi}{N_C - 1}(k-1)\right)\right] \quad (0 \leqq S_{1,k} \leqq 1, k = 1, \ldots, N_C) \tag{23}$$

$$S_{2,k} = 1 + \frac{1}{2}\left[1 - \cos\left(\frac{\pi}{N_L}\cdot k\right)\right] \quad (1 < S_{2,k} \leqq 2,\ k = 1, \ldots, N_B) \tag{24}$$

The strength of singularities is basically assumed to be linear between these discrete points. However, near the leading and trailing edges of cavity, the singular behavior of linearized cavitating flow obtained by Geurst [6] is taken into account, as employed by Kerwin et al. [7]. More specifically, the strength of singularities are assumed to be $q_n(s_1) \sim s_1^{(-1/4)}$ and $\gamma_{1,n}(s_1) \sim s_1^{(-1/4)}$ near the leading edge of cavity and blade, and $q_n(s_1) \sim (1 - s_1)^{(-1/2)}$ and $\gamma_{2,n}(s_2) \sim (s_2 - 1)^{(-1/2)}$ near the trailing edge of cavity. The boundary conditions are applied at the middle of the discrete points. After linearization, the boundary conditions are reduced as follows to the system of linear equations for the unknowns except $l_{s,m}$ and ω.

For steady components,

$$\begin{bmatrix} \\ A_s(l_{s,m}) \\ \\ \end{bmatrix}\begin{Bmatrix} q_{s,m}(S_{1,1}) \\ \vdots \\ \gamma_{1s,m}(S_{1,1}) \\ \vdots \\ \gamma_{2s,m}(S_{2,1}) \\ \vdots \\ q_{Bs,m}(S_{1,1}) \\ \vdots \\ q_{Bs,m}(S_{2,1}) \\ \vdots \\ \sigma \end{Bmatrix} = \begin{Bmatrix} \\ \mathbf{B}_s \\ \\ \end{Bmatrix}$$

$$(m = 0, 1, \ldots, Z_N - 1) \tag{25}$$

and for unsteady components,

$$\begin{bmatrix} \\ A_u(l_{s,m},\omega) \\ \\ \end{bmatrix} \begin{Bmatrix} \tilde{q}_m(S_{1,1}) \\ \vdots \\ \tilde{\gamma}_{1,m}(S_{1,1}) \\ \vdots \\ \tilde{\gamma}_{2,m}(S_{2,1}) \\ \vdots \\ \tilde{u}_{c,m} \\ \vdots \\ \tilde{l}_m \\ \vdots \\ \tilde{N} \end{Bmatrix} = \begin{Bmatrix} \\ 0 \\ \\ \end{Bmatrix}$$

$$(m = 0, 1, \ldots, Z_N - 1), \tag{26}$$

where $A_s(l_{s,m})$ and $A_u(l_{s,m},\omega)$ are coefficient matrices, $\mathbf{B}_s$ is a constant vector. The values of unknowns on mth blade are shown by the index $m(=0,1,\ldots,Z_N-1)$.

The steady flow is determined by solving Eq. (25). In the present study, the cavity length $l_{s,m}(m=0,\ldots,Z_{N-1})$ are determined for a given value of σ. For this purpose, a repetitive method is used. First, we assume the values of $l_{s,m}(m=0,\ldots,Z_{N-1})$ and the values of other unknowns are determined from Eq. (25) without using the closure condition. Then the cavity thickness at the cavity trailing edge is calculated. If the cavity thickness is calculated to be positive/negative, a longer/shorter cavity length is assumed for the next iteration. This process is repeated until we obtain the closure condition. Equation (26) is a homogeneous system of linear equations. The determinant of the coefficient matrix $A_u(l_{s,m},\omega)$ should satisfy

$$|A_u(l_{s,m},\omega)| = 0 \tag{27}$$

so that a nontrivial solution can be obtained. The complex frequency $\omega=\omega_R+j\omega_I$ is determined from Eq. (27). Thus, the angular frequency ω_R and the stability of cavitation depend on the steady cavity length $l_{s,m}$ or, equivalently, σ.

The numbers of discrete points, N_C and N_B are set to be 37 in the present study. The steady cavity length obtained with $N_C=N_B=37$ agrees with that with $N_C=N_B=100$ to second or third places of decimals. Thus, $N_C=N_B=37$ is considered to be sufficient for the discussions in the present study.

Results and Discussions

Steady Cavity Length. Figure 3 shows the steady cavity length in the cascades with circular arc blades, plano-convex blades and flat plate blades. The solidity C/h is 2, the stagger angle β is 80 deg and the number of blades Z_N is 3. The values of l_s/h $(=l_{s,m}/h, m=0,1,2)$ are plotted against $\sigma/(2\alpha)$ in Fig. 3(*a*), where α is an angle of attack. $\sigma/(2\alpha)$ is used instead of σ for comparison of the results to the steady cavity length for the cascade with flat plate blades, which is the function of $\sigma/(2\alpha)$. It is found that the steady cavity length is smaller for larger camber and blade thickness, and the difference of the effects of the camber and blade thickness is small for the steady cavity length. Symbols in Fig. 3(*a*) show the onset point of the rotating cavitation [8] obtained by the stability analysis. The value of $\sigma/(2\alpha)$ at the onset of the rotating cavitation is smaller for larger camber and blade thickness. The rotating cavitation occurs for the steady cavity length longer than the 65% of blade spacing.

The steady cavity length l_s/h plotted against $\sigma/[2(\alpha-\alpha_0)]$ is shown in Figs. 3(*b*) and 3(*c*) for the cascades with circular arc blades and plano-convex blades, respectively. α_0 is a shockless angle of attack for noncavitating flow; the values of α_0 are shown in each figure. From these results, the steady cavity length can be practically correlated with $\sigma/[2(\alpha-\alpha_0)]$ for both cascades.

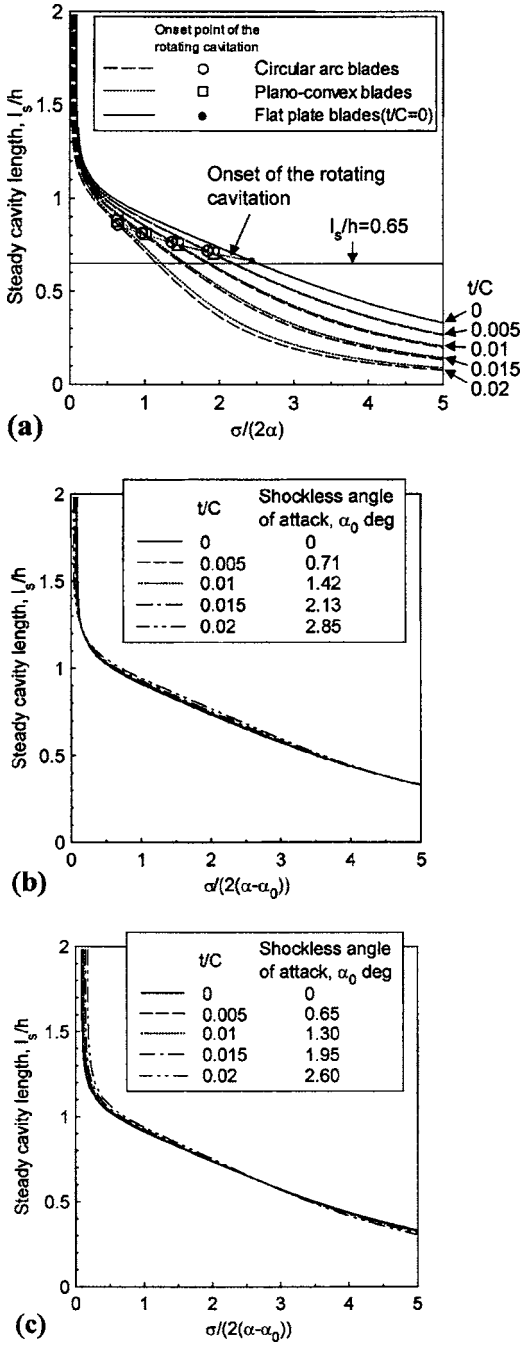

Fig. 3 Steady cavity length in the cascade with circular arc blades and plano-convex blades, $C/h=2$, $\beta=80$ deg, $\alpha=5$ deg: (*a*) l_s/h versus $\sigma/(2\alpha)$, (*b*) l_s/h versus $\sigma/[2(\alpha-\alpha_0)]$ in the cascade with circular arc blades, and (*c*) l_s/h versus $\sigma/[2(\alpha-\alpha_0)]$ in the cascade with plano-convex blades

Stability Analysis. Figures 4–6 show the Strouhal number St of unstable modes with negative ω_I and the phase difference $\theta_{n,n+1}$ for the cascades with flat plate blades, circular arc blades, and plano-convex blades, respectively. The Strouhal number in the present study is based on the steady cavity length l_s and defined as follows:

$$\mathrm{St} = \frac{\omega_R/2\pi}{U/l_s} \tag{28}$$

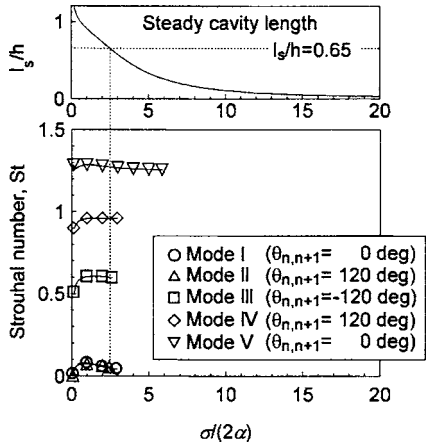

Fig. 4 Strouhal number of destabilizing roots for the cascade with flat plate blades. C/h=2, β=80 deg

Many unstable modes are obtained, but only lower order modes are shown in Figs. 4–6. Modes I and V are the cavitation surge modes with same phase for all blades. Modes I and V are the modes whose Strouhal numbers are dependent and independent on the length L of the inlet duct, respectively.

Modes II–IV correspond to the modes of the rotating cavitation.

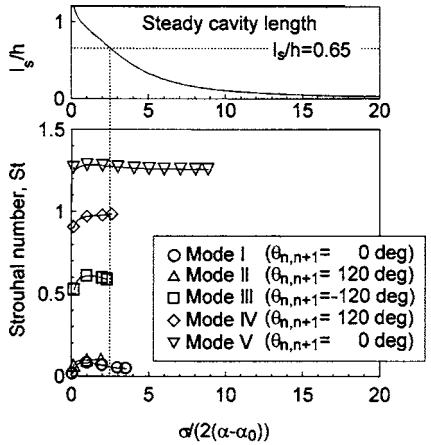

(a) t/C=0.01 (α_0=1.42 deg)

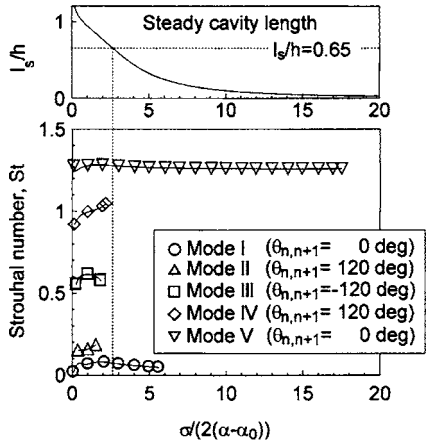

(b) t/C=0.02 (α_0=2.85 deg)

Fig. 5 Strouhal number of destabilizing roots for the cascade with circular arc blades. C/h=2, β=80 deg, α=5 deg: (*a*) t/C =0.01 (α_0=1.42 deg) and (*b*) t/C=0.02 (α_0=2.85 deg)

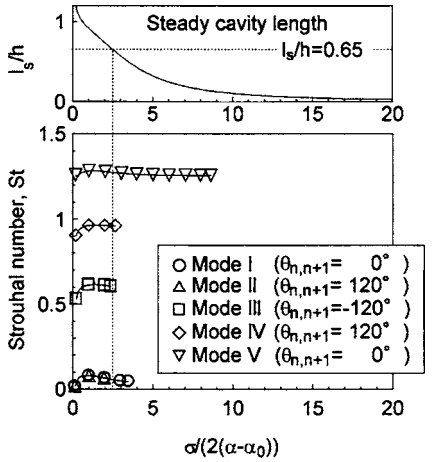

(a) t/C=0.01 (α_0=1.30 deg)

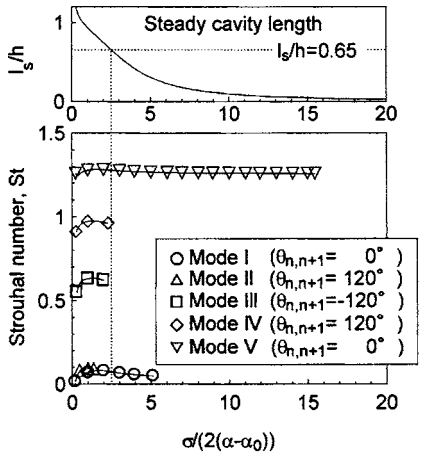

(b) t/C=0.02 (α_0=2.60 deg)

Fig. 6 Strouhal number of destabilizing roots for the cascade with plano-convex blades, C/h=2, β=80 deg, α=5 deg: (*a*) t/C=0.01 (α_0=1.30 deg) and (*b*) t/C=0.02 (α_0=2.60 deg)

From the phase difference $\theta_{n,n+1}$, we can identify that mode II represents the forward rotating cavitation, modes III and IV represent the backward rotating cavitation and higher-order mode of forward rotating cavitation, respectively.

Figures 5(*a*) and 5(*b*) show the results on the cascades with circular arc blades whose cambers t/C equal 0.01 and 0.02, respectively. From Figs. 4, 5(*a*), and 5(*b*), it is found that as the value of t/C increases, the values of $\sigma/[2(\alpha-\alpha_0)]$ at the onset of modes II–IV, corresponding to the rotating cavitation decrease, and those of modes I and V, corresponding to the cavitation surge increase.

Figures 6(*a*) and 6(*b*) show the results on the cascades with plano-convex blades whose thicknesses t/C equal 0.01 and 0.02, respectively. As the value of t/C increases, the values of $\sigma/[2(\alpha-\alpha_0)]$ at the onset of modes II–IV decrease and those of modes I and V increase as well as the case of the cascades with circular arc blades.

As shown in Figs. 4–6, various unstable modes appear for the steady cavity length longer than 65% of the blade spacing. This means that the steady cavitation with the cavity longer than 65% of the blade spacing is unstable also for the case with the camber and blade thickness. Since the cavity length l_s/h is correlated with $\sigma/[2(\alpha-\alpha_0)]$ as shown in Fig. 3, the onset of the cavitation instabilities is basically correlated with this parameter.

Effect of the Length of Inlet Duct. Figure 7 shows the Strou-

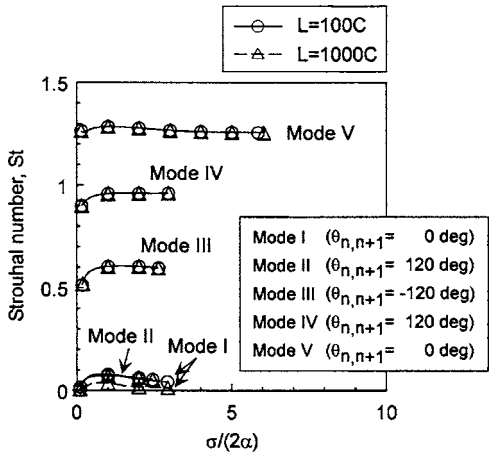

(a) Strouhal number of Mode I - V

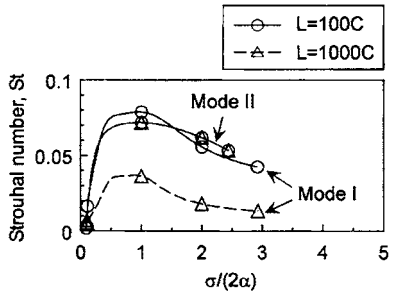

(b) Strouhal number of Mode I and II

Fig. 7 Effect of the length of inlet duct for the Strouhal number in the cascade with flat plate blades; $C/h=2$, $\beta=80$ deg: (*a*) Strouhal number of modes I–V and (*b*) Strouhal number of modes I and II

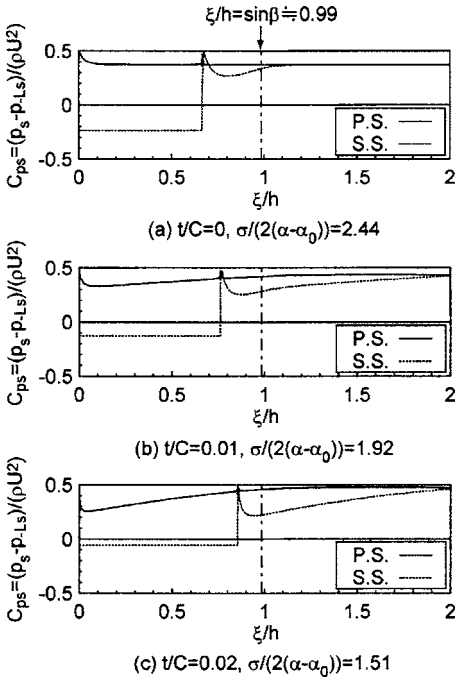

Fig. 8 Steady pressure distribution on the suction surface of a blade in the cascades with flat plate blades ($t/C=0$) and circular arc blades at the onset of the rotating cavitation, $C/h=2$, $\beta=80$ deg, $\alpha=5$ deg: (*a*) $t/C=0$, $\sigma/[2(\alpha-\alpha_0)]=2.44$, (*b*) $t/C=0.01$, $\sigma/[2(\alpha-\alpha_0)]=1.92$, and (*c*) $t/C=0.02$, $\sigma/[2(\alpha-\alpha_0)]=1.51$

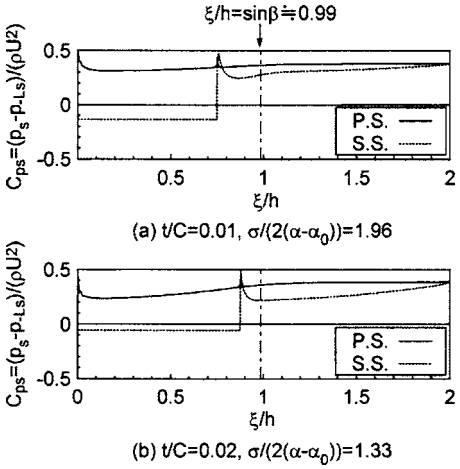

Fig. 9 The same as Fig. 8, for the cascades with plano-convex blades: (*a*) $t/C=0.01$, $\sigma/[2(\alpha-\alpha_0)]=1.96$ and (*b*) $t/C=0.02$, $\sigma/[2(\alpha-\alpha_0)]=1.33$

hal number of the unstable modes and phase difference $\theta_{n,n+1}$ for the length of inlet duct $L=100C$ and $1000C$ in the cascade with flat plate blades. It is found that the Strouhal number of mode I is significantly affected by the duct length.

The total of the fluctuating cavity volume in mode I is quite larger than that in other modes [2]. Therefore, the mass flow fluctuation in mode I is larger. Thus, the Strouhal number of mode I is significantly affected by the inlet duct length.

Steady Pressure Distribution and Pressure Gradient on Blade. Figures 8 and 9 show the steady pressure distributions on the circular arc and plano-convex blades, respectively, at the onset of the rotating cavitation. Figure 8(*a*) shows the pressure distribu-

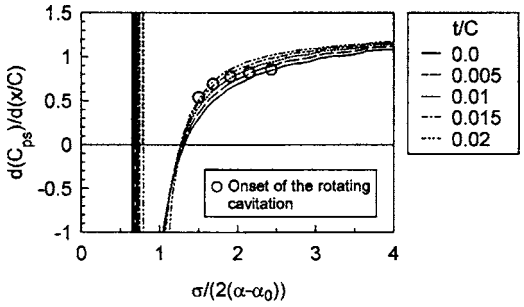

(a) Cascade with circular arc blades

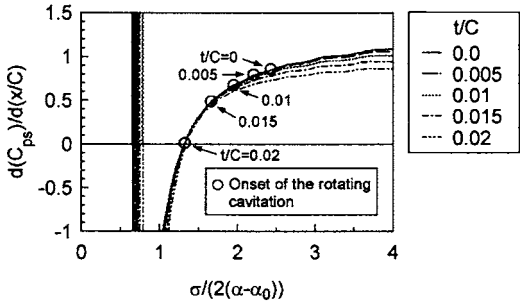

(b) Cascade with plano-convex blades

Fig. 10 Pressure gradient on the suction surface of a blade at $\xi=h\sin\beta$, $C/h=2$, $\beta=80$ deg, $\alpha=5$ deg: (*a*) cascade with circular arc blades and (*b*) cascade with plano-convex blades

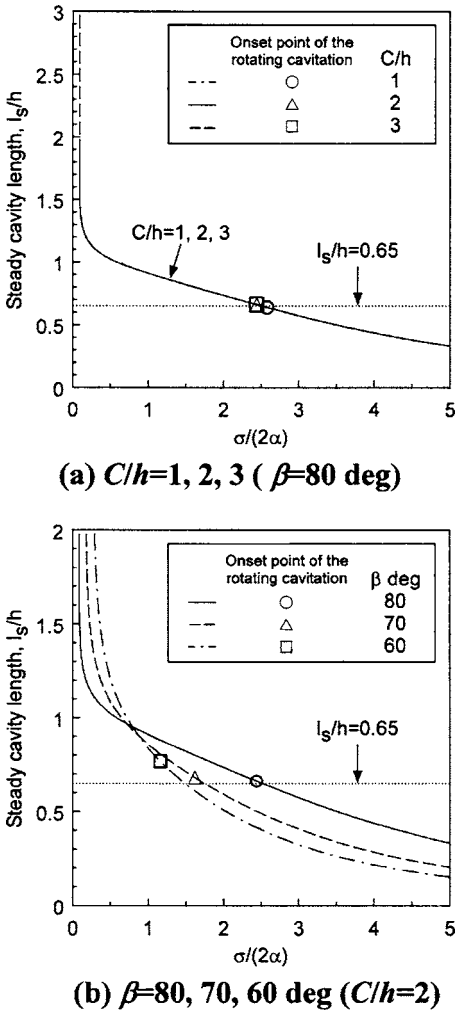

Fig. 11 Steady cavity length in the cascade with flat plate blades: (*a*) $C/h=1,2,3$ ($\beta=80$ deg) and (*b*) $\beta=80,70,60$ deg ($C/h=2$)

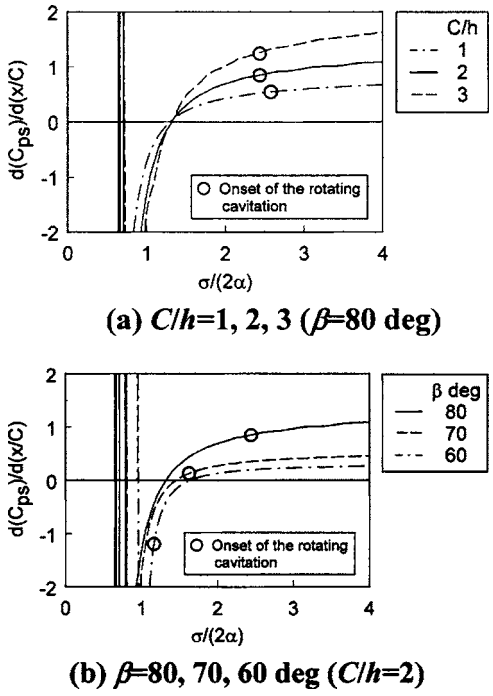

Fig. 12 Pressure gradient on the suction surface of a blade at $\xi=h\sin\beta$ in the cascade with flat plate blades; $\alpha=5$ deg: (*a*) $C/h=1,2,3$ ($\beta=80$ deg) and (*b*) $\beta=80,70,60$ deg ($C/h=2$)

tion on a blade of the cascade with flat plate blades. The regions with constant pressure $C_p=-\sigma/2$ in Figs. 8 and 9 correspond to cavities. The pressure coefficient C_p approaches 0.5 near the cavity trailing edge. This is caused by the flow stagnation due to the applied linear closed-cavity model.

Here, we consider the pressure gradient at the throat $\xi/h=\sin\beta$, where the effect of the flow stagnation at the cavity trailing edge is insignificant. The dotted-dashed lines at $\xi/h=\sin\beta\fallingdotseq 0.99$ in Figs. 8 and 9 represent the location of the throat of cascade.

Figure 10 shows the steady pressure gradients on the suction surface of blades at the throat, $\xi/h\fallingdotseq 0.99$. Figures 10(*a*) and 10(*b*) are for the cascades with circular arc blades and plano-convex blades, respectively. As the value of $\sigma/[2(\alpha-\alpha_0)]$ decreases, the pressure gradient $d(C_p)/d(x/C)$ decreases. The negative slope is caused by the flow stagnation near the cavity trailing edge. The sharp increase near $\sigma/[2(\alpha-\alpha_0)]\fallingdotseq 0.65-0.75$ corresponds to the shift between cavity surface and the stagnation point.

The ○ in Figs. 10(*a*) and 10(*b*) shows the onset point of the rotating cavitation corresponding to mode II. The rotating cavitation occurs when the pressure gradient becomes small to some degree. The values of critical pressure gradient $d(C_p)/d(x/C)$ at the onset of rotating cavitation are almost constant and $0.6\sim 0.8$ for $t/C=0-0.02$ in the cascade with circular arc blades. However, the value of critical pressure gradient changes largely for the cascade with plano-convex blades.

Effects of Solidity and Stagger on the Critical Pressure Gradient for the Onset of Rotating Cavitation. Figure 11 shows the steady cavity length in the cascade with flat plate blades. Figure 11(*a*) shows the cavity length for the cascade with $C/h=1,2,3$ and $\beta=80$ deg. Figure 11(*b*) shows the cavity length in the cascade with $C/h=2.0$ and $\beta=80$, 70, 60 deg. The onset points of rotating cavitation are shown in these figures. It was found that the rotating cavitation occurs when the cavity is longer than 65% of the blade spacing in all cascades.

Figure 12 shows the steady pressure gradient on the suction surface of blades at the throat, $\xi/h=0.99$ in the cascade with flat plate blades. Figure 12(*a*) is for the cascades with $C/h=1,2,3$ and $\beta=80$ deg and Fig. 12(*b*) is for the cascades with $C/h=2$ and $\beta=80$, 70, 60 deg. It was found in Fig. 12(*a*) and 12(*b*) that the distribution of the pressure gradient is significantly affected by the solidity C/h and the stagger β. The values of critical pressure gradient at the onset of rotating cavitation also changes significantly for C/h and β.

Through the above discussions on the pressure gradient, it was found that the values of the pressure gradient at the onset of rotating cavitation are affected by the blade thickness, solidity, and stagger of cascades. Therefore, the criterion based on the cavity length for the occurrence of cavitation instability is more adequate than the criterion based on the pressure gradient.

Conclusions

The analyses of steady cavitating flow in cascades and its stability were carried out to investigate the effects of the camber and blade thickness, and the relation between the pressure gradient on the suction surface of a blade near the throat and the occurrence of cavitation instabilities.

In the analysis of the steady flow, it was found that the steady cavity length is shorter for the larger camber and blade thickness and the difference of the effects of the camber and blade thickness is small for the steady cavity length. It was also found that the steady cavity length can be practically correlated with a parameter $\sigma/[2(\alpha-\alpha_0)]$ for the cascades with circular arc blades and plano-convex blades, where α_0 is a shockless angle of attack.

In the stability analysis, various modes of cavitation instabilities appear for the cavity longer than 65% of the blade spacing in both cascades with circular arc blades and plano-convex blades. From this fact, the criterion based on the steady cavity length is considered to be adequate for the occurrence of the cavitation instabilities for both cascades as well as for the cascade with flat plate blades. Since the cavity length is correlated with the parameter $\sigma/[2(\alpha-\alpha_0)]$, cavitation instabilities are also correlated with the parameter.

The steady pressure gradient on the suction surface of a blade near the throat was calculated. When the pressure gradient became small to some degree, the rotating cavitation occurred. However, the values of critical pressure gradient at the onset of rotating cavitation are affected by the blade thickness, solidity, and stagger of cascades. Therefore, the criterion of cavitation instability is more adequate than the criterion based on the pressure gradient.

Acknowledgment

The authors would like to express their sincere gratitude to Tadashi Arifuku for helpful discussion. This study was supported by a Grant-in Aid for Scientific Research (A) from the Japan Society for the Promotion of Science. This support is greatly acknowledged.

Nomenclature

A = coefficient matrix
$\mathbf{B}$ = constant vector
C = chord length
C_p = pressure coefficient, $(p-p_{-Ls})/(\rho U^2)$
f = function defined by Eq. (4)
h = blade spacing
I = arbitrary integer number
i = imaginary unit in space, $i^2=-1$
j = imaginary unit in time, $j^2=-1$
L = distance between the leading edge of the blade and the space with constant total pressure, $100C$
l = cavity length
N = amplitude of upstream axial velocity fluctuation
N_C, N_B = number of discrete points on s coordinate
p_{-L} = pressure at $\xi=-L$
p_t = total pressure at $\xi=-L$
p_v = vapor pressure
q = strength of source
q_B = strength of source which represents blade thickness
S = location of discrete point on s-coordinate
St = Strouhal number, $(\omega_R/(2\pi))/(U/l_s)$
t = maximum camber or maximum length between suction surface and chord or time
U = upstream mean velocity
U_T = peripheral velocity (moving speed) of cascade, $U\sin(\alpha+\beta)$
u = x component of flow velocity
v = y component of flow velocity
w = complex velocity, $u-iv$
Z_N = number of blade
z = complex coordinate, $x+iy$
α = angle of attack
α_0 = shockless angle of attack
β = stagger angle
Φ_0 = velocity potential at the leading edge of blade
$\Phi_{-\infty}$ = velocity potential at upstream infinity
γ = strength of vortex
η = cavity thickness
$\theta_{m,n}$ = phase angle of the fluctuation of cavity length on nth blade relative to mth blade
ξ = distance from the leading edge along chord
ρ = density of fluid
σ = cavitation number, $2(p_{-Ls}-p_v)/(\rho U^2)$
ω = complex angular frequency, $\omega_R+j\omega_I$
ω_R = angular frequency
ω_I = decay ratio

Superscript

$\tilde{}$ = unsteady component

Subscripts

1, 2 = index of cavitating and non-cavitating region in terms of s-coordinate
c = cavity surface
k = index of discrete point
m,n = blade index
s = steady component
t = trailing free vortex
u = unsteady component

Appendix A: Complex Velocity

The complex velocity is given by

$$w(z,t) = u - iv = Ue^{-i\alpha} + \tilde{N}e^{i\beta}e^{j\omega t} + \frac{1}{2\pi}\sum_{n=0}^{Z_N-1}\left[\int_0^1 \{q_n(s_1) + i\gamma_{1,n}(s_1) + q_{B,n}(s_1)\}\right.$$
$$\times\{f_n(z,l_n s_1) - f_n(-L + ae^{i(\pi/2-\beta)}, l_n s_1)\} l_n ds_1$$
$$+ \int_1^2 \{i\gamma_{2,n}(s_2) + q_{B,n}(s_2)\}\{f_n(z,(C-l_n)s_2 + (2l_n - C)) - f_n(-L + ae^{i(\pi/2-\beta)}, (C-l_n)s_2 + (2l_n - C))\}$$
$$\left.\times(C-l_n)ds_2 + i\int_C^\infty \gamma_{t,n}(\xi)\{f_n(z,\xi) - f_n(-L + ae^{i(\pi/2-\beta)}, \xi)\}d\xi\right] \quad \text{(A1)}$$

$$f_n(z,\xi) = \frac{\pi}{Z_N h} e^{-i(\pi/2-\beta)} \cot\left\{ \frac{\pi}{Z_N h}(z-\xi)e^{-i(\pi/2-\beta)} - \frac{n}{Z_N}\pi \right\} \tag{A2}$$

The function $f_n(z,\xi)$ represents the effects of infinite number of singularities of equal strength located at $z=\xi+IZ_N h e^{j(\pi/2-\beta)}$, $I=-\infty,\ldots,-1,0,1,\ldots,\infty$. The strength of singularities is specified on these coordinates s_1 and s_2 moving in accord with the variable cavity length l_n. In the present analysis with larger $L(=100C)$, $f(-L+ae^{i(\pi/2-\beta)},\xi)$ is approximated to $-\pi e^{i\beta}/h$, where a is an arbitrary constant.

Appendix B: Boundary Conditions on Blade Surface

The y component of velocity on circular arc blade is given by

$$(U+u_s+\tilde{u}e^{j\omega t})\frac{dy}{dx} = (U+u_s+\tilde{u}e^{j\omega t})\frac{\Omega}{2}\left(1-2\frac{\xi}{C}\right) \approx \frac{U\Omega}{2}\left(1-2\frac{\xi}{C}\right) \quad (\because \text{Eq. (1)}) \tag{B1}$$

Therefore, the following boundary conditions should be satisfied.

For the cascade with circular arc blades,

$$-\text{Imag}[w(mhe^{i(\pi/2-\beta)}+l_m s_1-0i,t)] = \frac{U\Omega}{2}\left(1-2\frac{l_m s_1}{C}\right), \quad (0\leqslant s_1\leqslant 1) \tag{B2}$$

$$-\text{Imag}[w\{mhe^{i(\pi/2-\beta)}+(C-l_m)s_2+(2l_m-C)\pm 0i,t\}] = \frac{U\Omega}{2}\left(1-2\frac{(C-l_m)s_2+(2l_m-C)}{C}\right), \quad (1\leqslant s_2\leqslant 2) \tag{B3}$$

For the cascade with plano-convex blades,

$$-\text{Imag}[w(mhe^{i(\pi/2-\beta)}+l_m s_1-0i,t)] = 0, \quad (0\leqslant s_1\leqslant 1) \tag{B4}$$

$$-\text{Imag}[w(mhe^{i(\pi/2-\beta)}+l_m s_1+0i,t)] = \frac{U\Omega}{2}\left(1-2\frac{l_m s_1}{C}\right), \quad (0\leqslant s_1\leqslant 1) \tag{B5}$$

$$-\text{Imag}[w\{mhe^{i(\pi/2-\beta)}+(C-l_m)s_2+(2l_m-C)-0i,t\}] = 0, \quad (1\leqslant s_2\leqslant 2) \tag{B6}$$

$$-\text{Imag}[w\{mhe^{i(\pi/2-\beta)}+(C-l_m)s_2+(2l_m-C)+0i,t\}] = \frac{U\Omega}{2}\left(1-2\frac{(C-l_m)s_2+(2l_m-C)}{C}\right), \quad (1\leqslant s_2\leqslant 2) \tag{B7}$$

where Imag$[w]$ means the imaginary part of w.

References

[1] Horiguchi, H., Watanabe, S., Tsujimoto, Y., and Aoki, M., 2000, "A Theoretical Analysis of Alternate Blade Cavitation," ASME J. Fluids Eng., **122**(1), pp. 156–163.

[2] Horiguchi, H., Watanabe, S., and Tsujimoto, Y., 2000, "A Linear Stability Analysis of Cavitation in a Finite Blade Count Impeller," ASME J. Fluids Eng., **122**(4), pp. 798–805.

[3] Huang, J. D., Aoki, M., and Zhang, J. T., 1998, "Alternate Blade Cavitation on Inducer," JSME Int. J., Ser. B, **41**(1), pp. 1–6.

[4] Tsujimoto, Y., 2001, "Simple Rules for Cavitation Instabilities in Turbomachinery," *Proc. 4th International Symposium on Cavitation*, The University of Michigan and the California Institute of Technology, Pasadena, pp. 1–16.

[5] Wegner, M., Acosta, A. J., and Tsujimoto, Y., 2003, "Panel Discussion on Inducer Design Criteria," J. Test. Eval., **9**(4), pp. 229–237.

[6] Geurst, J. A., 1959, "Linearized Theory for Partially Cavitated Hydrofoils," Int. Shipbuild. Prog., **6**(60), pp. 369–384.

[7] Kerwin, J. E., Kinnas, S. A., Wilson, M. B., and McHugh, J., 1986, "Experimental and Analytical Techniques for the Study of Unsteady Propeller Sheet Cavitation," *Proc. of 16th Symposium on Naval Hydrodynamics*, National Academy Press, Washington, DC, pp. 387–414.

[8] Kamijo, K., Shimura, T., and Watanabe, M., 1977, "An Experimental Investigation of Cavitating Inducer Instability," *Proc. Winter Annual Meeting*, ASME, New York, ASME Paper No. 77-WA/FW-14, pp. 1–9.

Characteristics of Small Vortices in a Turbulent Axisymmetric Jet

Sudhaker Chhabra

Pablo Huq[1]

Ajay K. Prasad[2]
e-mail: prasad@me.udel.edu

Department of Mechanical Engineering,
University of Delaware,
Newark, DE 19716-3140

Characteristics of small vortices were studied in axisymmetric jets wherein the Kolmogorov scale was approached by progressively decreasing the Reynolds number while still maintaining turbulent flow. A periodic forcing introduced far upstream of the jet nozzle ensured that the jet was turbulent. A vortex eduction tool was developed and applied to the high-pass filtered 2D velocity field in the axial plane of a turbulent jet while varying Re between 140 and 2600. Vortex population, energy, vorticity, and rms (root-mean-square velocity fluctuations) of the high-pass filtered field were measured to elucidate vortex characteristics. The observed population of vortices decreases dramatically at the Kolmogorov scale. The observed increase in vortex population with decreasing vortex size appears to be in accord with the space-filling argument, in that the vortex population in a two-dimensional domain should grow as R^{-2}. The energy density curve obtained from vortex statistics reproduces the $-5/3$ slope for the inertial subrange, and the high-pass filtered field accounts for approximately two-thirds of the total rms.
[DOI: 10.1115/1.2173292]

Introduction

Turbulent flow is comprised of eddies, ranging in size from the Kolmogorov scale (η) at the small end of the spectrum to the integral scale (b) at the large end. In most turbulence studies, the velocity signal is acquired using pointwise techniques, such as hot-wire anemometry [1,2] or laser-Doppler anemometry [2], and the time-resolved velocity signal record is analyzed to extract its spectral content. The small probe volume in these techniques is well suited to obtain measurements at even the smallest scales in the flow. In contrast, in the current research, we determine the characteristics of small eddies in a turbulent axisymmetric jet using the particle image velocimetry (PIV) measurement technique. We use a vortex eduction tool to identify vortices in the high-pass filtered 2D velocity field of a turbulent flow and extract their statistical properties, such as population density, size, circulation, and energy. We have previously applied this tool to extract vortex statistics from velocity measurements in the axial plane of a self-similar turbulent axisymmetric jet [3]. In a subsequent paper, an improved version of the tool was used to measure the variation of circulation and vorticity within vortex cores [4]. The properties of large engulfing eddies that typically reside at the jet edge were explored in [5].

An obvious difficulty with using PIV to explore the smallest flow scales is a lack of spatial resolution; it is difficult to obtain data using PIV at scales approaching the Kolmogorov scale in typical turbulent flows. One solution is to employ techniques akin to micro-PIV, where the flow is examined at sufficiently high magnifications to resolve the smallest scales. However, instead of applying progressively larger magnifications and exploring the Kolmogorov scale in that manner, our approach is to employ successively smaller jet Reynolds numbers and increase the Kolmogorov scale to the point that it becomes visible to our recording configuration wherein the spatial resolution is unchanged throughout.

At the outset, it is useful to briefly review the characteristics of vortices of various sizes. Starting from the integral scale, successive generations of eddies may be assigned a size br^n ($n=0,1,2,\ldots$, and r is some factor smaller than unity). Space-filling considerations [6] imply that the number of eddies of a particular generation will grow as r^{-3n} in three-dimensional space; in a two-dimensional domain, an r^{-2n} relationship is expected. Energy is introduced at the integral scales and flows down the cascade to be eventually removed at the Kolmogorov scale by viscous dissipation. According to Kolmogorov theory, the rate at which energy is produced by Reynolds stresses is identical to the rate at which it is dissipated by viscous stresses [6], implying that it is also identical to the energy flux down the cascade.

At a given Reynolds number, the energy density increases with wave number k until it reaches a peak value at the integral scale [7]. Subsequently, the energy density diminishes monotonically as the wave number increases. As described in [8] this energy is finally dissipated by viscosity. Hence, the total energy E of vortices of size k should depend on the dissipation rate ε, k, and kinematic viscosity ν

$$\frac{E(k)}{\nu^{5/4}\varepsilon^{1/4}} = \frac{E(k)}{v^2\eta} = f(k,\eta) \tag{1}$$

Here, η is the Kolmogorov scale defined as $\eta=(\nu^3/\varepsilon)^{1/4}$ and v is the Kolmogorov velocity defined as $v=(\nu\varepsilon)^{1/4}$.

The centerline energy dissipation rate for axisymmetric jets is given by $\varepsilon=0.5u_c^3/(z-z_0)$ [2], where u_c is the centerline velocity, and $(z-z_0)$ is the downstream distance from the virtual origin of the jet. The integral scale for turbulent jets is of the order of the local jet width b, given by the $1/e$ point of the Gaussian profile approximation to the time-averaged streamwise velocity in a jet. (For the purpose of our study, it is adequate to assume that the integral scale is equal to b.) Substituting for ε in the expression for η, we obtain

$$\eta = \left(\frac{\nu^3(z-z_0)}{0.5u_c^3}\right)^{1/4} \tag{2}$$

Noting also that for an axisymmetric jet, Re based on nozzle diameter (d) and nozzle exit velocity (u_o) is $\approx 1.7bu_c/\nu$, we can write

$$\frac{\eta}{b} = 3\left(\frac{1}{\mathrm{Re}}\right)^{3/4} \tag{3}$$

These expressions are useful for designing the jet experiment and selecting operating parameters as described next. We also describe the details of the vortex eduction tool whereby 2D vector maps obtained using PIV are high-pass filtered to extract their

[1]College of Marine Studies, University of Delaware.
[2]Corresponding author.

Contributed by the Fluids Engineering Division of ASME for publication in the JOURNAL OF FLUIDS ENGINEERING. Manuscript received September 10, 2004; final manuscript received October 25, 2005. Review conducted by Joseph Katz.

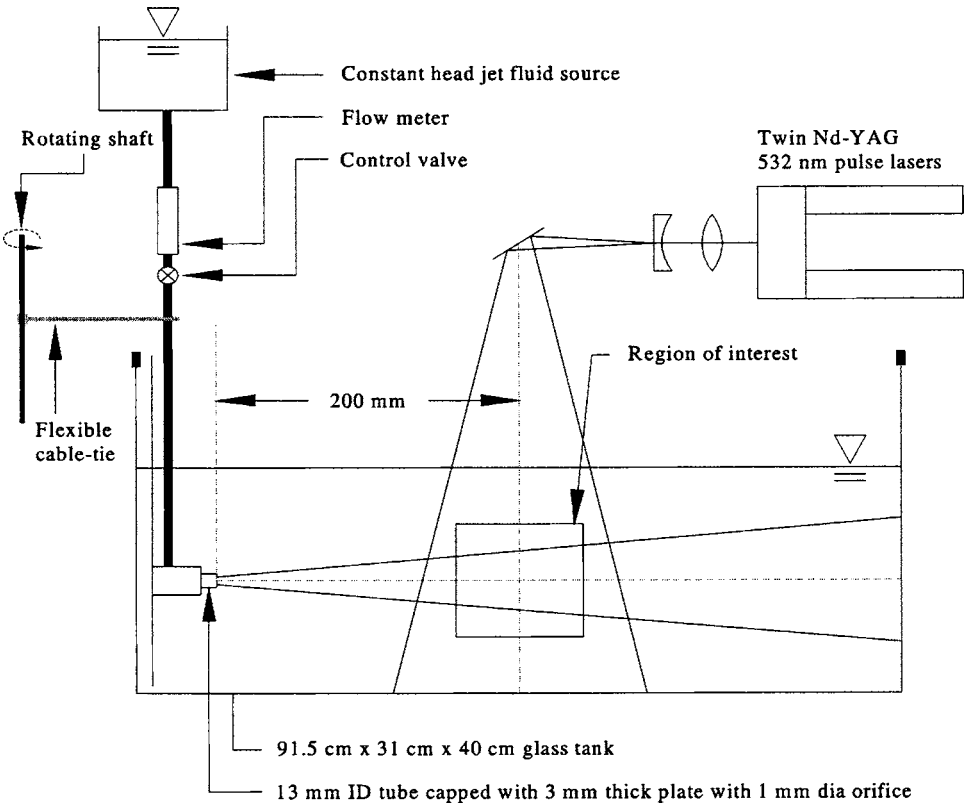

Fig. 1 Schematic of experimental setup

high-frequency content in the form of vortices. Vortex populations, vorticity, and energy distributions are examined and compared to results available in the literature.

Experimental Setup and Measurement Techniques

PIV measurements were conducted in a rectangular glass tank 91.5 cm×31 cm×40 cm high, housing a jet-nozzle assembly mounted to one side of the tank, as shown in Fig. 1. The nozzle assembly consisted of a cylinder (13 mm ID and 46 mm long) capped by a 3 mm thick end plate; a 1 mm dia hole drilled at the center of the end plate served as the jet orifice. One of the challenges in this study was to ensure that the jet remained turbulent even at Reynolds numbers as low as 140. This was achieved by applying a periodic perturbation on the jet supply tubing as will be described shortly. Our nozzle was specifically designed such that this perturbation was not damped by the time the jet emerged from the orifice. The nozzle-cylinder was connected via flexible tubing, a valve, and rotameter to a constant head fluid source mounted on an adjustable height platform. The flow rate and, hence, the Reynolds number for the jet were controlled by adjusting the height of the platform and the valve opening. During experiments, the height of host fluid in the glass tank was equal to the tank width (31 cm), and the nozzle was positioned at the center of this square cross section at one end of the tank, as shown in Fig. 1. The dimensions of the tank relative to the jet nozzle diameter were comparable to previous jet experiments conducted in our laboratory [3–5] and ensured that the finiteness of the host fluid did not influence jet development in any measurable way. Deionized water was used as the working fluid for both the jet and the host. Both fluids were seeded with fluorescent PIV tracer particles (40 μm).

As shown in Fig. 1, PIV measurements were conducted in an axial plane of the jet over a region of interest centered 200 mm downstream from the nozzle. The region of interest was illuminated by twin Nd-YAG lasers (*Continuum* Surelite II) and providing 30 mJ per pulse at a wavelength of 532 nm. The laser beams were passed through a sheet-forming module and steering optics to produce a 1 mm thick vertical laser sheet that was directed downward into the tank through the top surface as shown in Fig. 1. A 10-bit *LaVision* Imager Intense PIV/LIF (laser-induced fluorescence) camera, with a 1376×1040 pixel array was oriented orthogonal to the illuminated plane. The camera magnification was set to capture a width of the jet corresponding to approximately ±1.5b about the jet axis. The view field was set to 140 mm wide for all measurements. A long-wave pass filter was mounted on to the camera lens during PIV measurements to block elastic scattering of laser light while allowing fluorescence to pass through and improve the overall signal quality.

The time separation between laser pulses (4–10 ms, depending on the operating Reynolds number) was chosen to maximize in-plane particle displacement (reducing random error) while still restricting out-of-plane particle motion to acceptable levels. Double-frame images were acquired at 0.5 Hz. The Reynolds number was varied from 140 to 2600. An ensemble of 200 instantaneous velocity fields was acquired for each Reynolds number to compute vortex statistics.

To ensure turbulent flow for even small Reynolds numbers, the jet was tripped by applying a periodic disturbance (4–15 Hz, based on the operating Reynolds number) in the following manner. A flexible nylon self-locking cable tie (Gardner Bender, Part No. 46-108, 20 cm long×2.5 mm wide×0.8 mm thick) was attached to the shaft of a variable speed motor. The cable tie was trimmed to a final length of 15 cm and positioned to impact the flexible jet supply tubing approximately 18 cm (i.e., 180 nozzle diameters) upstream of the nozzle. The low level of the applied forcing and its distance from the nozzle made it far less dominant compared to other jet forcing methods, such as [9] who describe radically altered jets produced by axial and circumferential excitations applied *directly* at the nozzle exit. Furthermore, the Strouhal number ($St=fd/u_o$) of the applied forcing in our experiments

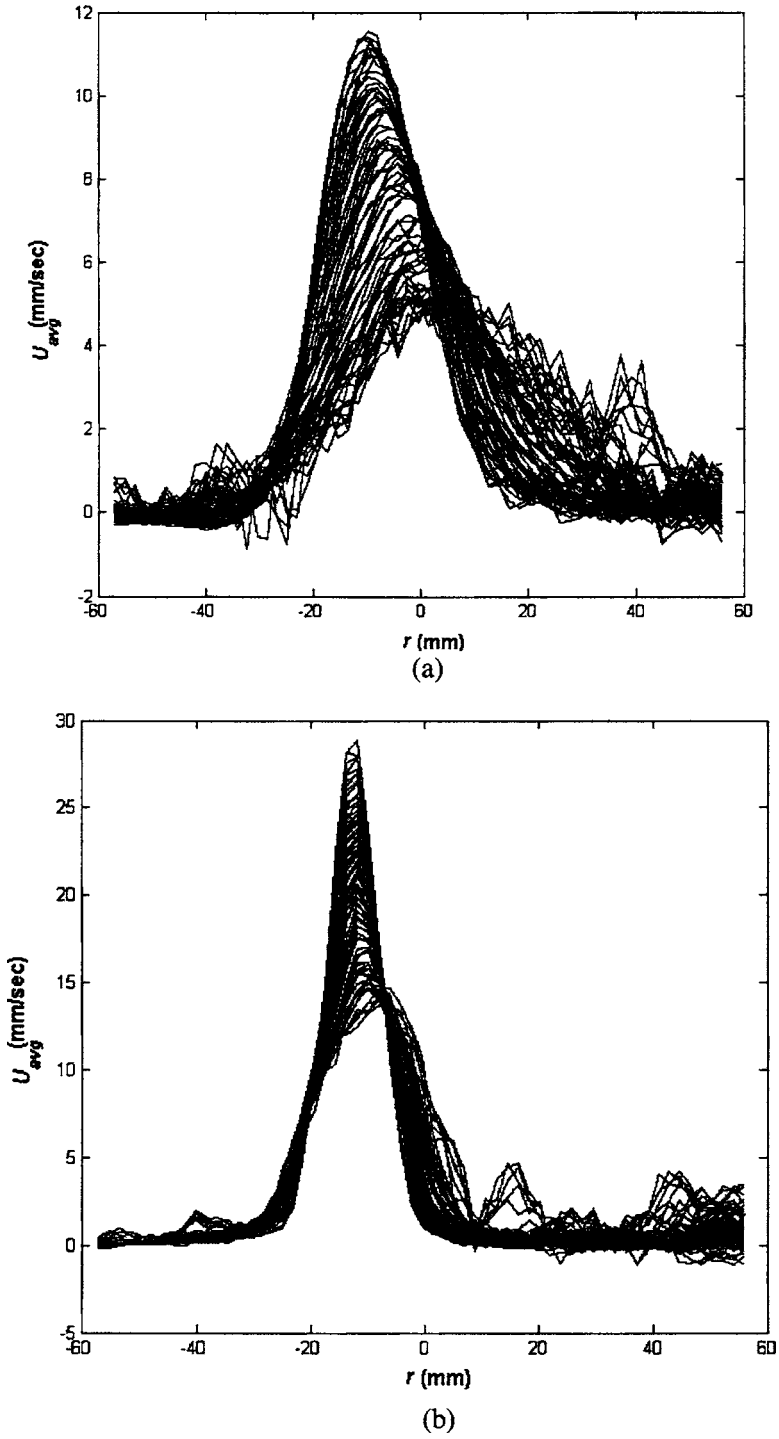

Fig. 2 Time-averaged streamwise velocity profiles for Re=250: (*a*) perturbation turned on (turbulent jet) and (*b*) perturbation turned off (laminar jet)

was in the range of 0.005–0.03, which is one to two orders of magnitude smaller than the "preferred frequency" required to radically alter jet behavior [9].

In our experiments, the revolutions per minute (rpm) of the variable speed motor and, hence, the frequency of the applied disturbance was selected after careful visual evaluation of the jet behavior. A small amount of sodium hydroxide and thymolphthalein (an indicator that turns blue for pH$\geqslant$8.5 and is colorless otherwise) was added to the jet supply reservoir to visualize the jet emerging into the host fluid and confirm that the jet remained turbulent even at the smallest Reynolds numbers employed in this study. When the jet fluid underwent turbulent mixing with the host, its pH dropped below the threshold value rendering it colorless. The use of this pH-indicator method allowed an effective visualization of the turbulent nature of the emerging jet even during a PIV run, without incurring a buildup of dye in the tank that would impair PIV recording.

In addition to visual evaluation of the jet, time-averaged axial velocity profiles were plotted at various downstream locations for all the Reynolds numbers used in the study. Figure 2 shows two dramatically different plots for U_{avg} for Re=250. The first plot corresponds to the turbulent jet (perturbation has been turned on),

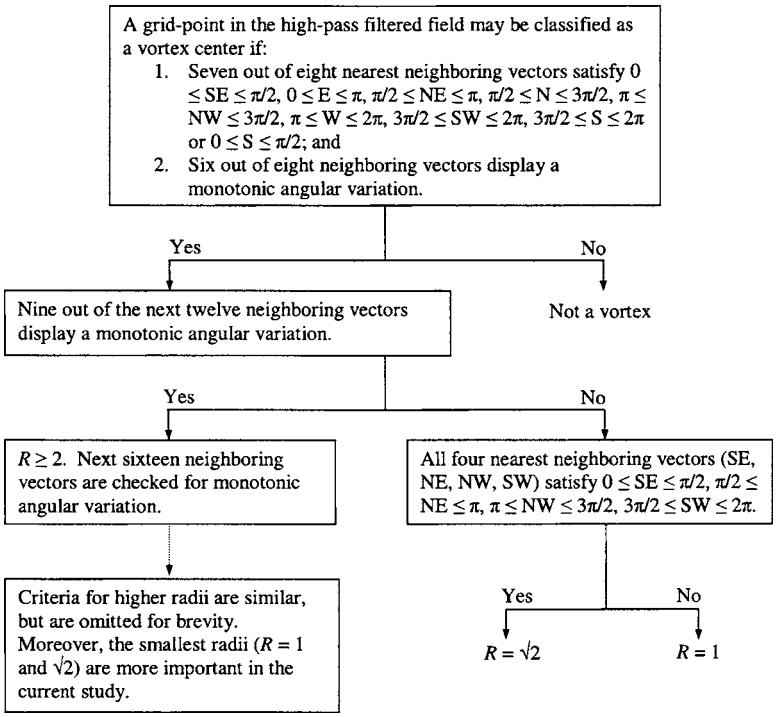

Fig. 3 Flow chart for identifying a vortex center and determining its radius

and the second plot corresponds to the laminar jet (perturbation is off). The centerline velocity is substantially smaller for the turbulent case (10 mm/s max) relative to the laminar case (25 mm/s max), which is the expected behavior. The laminar jet is also very narrow due to minimal mixing with the ambient fluid. On the other hand, the turbulent jet displays the typical rapid mixing with the ambient fluid and spreads laterally at the typical rate for turbulent jets. As an aside, note that both the turbulent and laminar jets lean slightly to the right as they proceed downstream (which actually means downward in the experimental situation because the jet is horizontally directed from left to right). This is because it is difficult to accurately match the jet density to the host density and the effect is more pronounced at low Re. However, since our vortex eduction technique uses the high-pass filtered velocity field, this slight tilt has a negligible effect on the vortex statistics that are of interest in this paper.

The velocity profile for even the smallest Reynolds number resembled those for higher Reynolds numbers. Furthermore, the two characteristic constants for turbulent jets (the centerline velocity decay constant B_u and the jet spread rate c) were calculated for all Re used in the study and found to be close to values commonly quoted in the literature (B_u=5.7, c=0.1) for turbulent jets. Finally, rms profiles for all Re were plotted for each downstream distance. Turbulent jet literature quotes the ratio of the rms to the mean velocity at about 0.25 at the centerline. Our rms results provide a value that is very close to that expected for turbulent jets.

Cross correlation, with double-pass grid refinement was used for PIV processing, resulting in a final interrogation spot size of 32×32 pixels with 50% overlap. The resolution of the square grid of the resulting vector fields was 1.63 mm. The particle displacement measurement error is about 0.1 pixels, which corresponds to a relative error in the velocity measurement of about 1–2% at the centerline.

Vortex Education Technique

A high-pass filtering technique [3,10] was used for educing vortices that were identified using the definition provided by [11]. First, the instantaneous velocity field is smoothed using a Gaussian kernel. The resulting field is thus low-pass filtered. Next, the high-pass filtered field is obtained by subtracting the low-pass filtered field from the instantaneous field, exposing the vortices. The standard deviation of the smoothing Gaussian kernel was set to three grid units, and the filter was truncated at five grid units [5]. An automated method was employed for counting the number of vortices as described in [5]. Briefly, a point in the high-pass filtered field was identified as a vortex center if the neighboring vectors displayed a monotonic variation in angular orientation from 0 to 2π while moving in a closed path around it; specific details for the identification of the smallest radii (1 and $\sqrt{2}$) are presented in Fig. 3. Details for higher radii are similar, but are omitted for brevity and also because the smallest radii are the focus of the current study. The robustness of the education technique can be confirmed by the good comparison between the educed vortices and the corresponding standard vorticity plot (see Fig. 5, Ref. [4]). In addition to the algorithm described in [5] and in Fig. 3, it was also necessary to employ one additional criterion in the present work. At low Reynolds numbers, the magnitude of the vectors in the high-pass filtered field falls to <0.1 pixels, which is comparable to the error in the PIV measurement. In order to circumvent the detection of spurious vortices from such vector fields, we set a threshold value for the average velocity magnitude within a vortex of 0.07 pixels, in order to accept a vortex as a valid one. Our automated code identifies vortices of sizes 1, $\sqrt{2}$, 2, $\sqrt{5}$, $\sqrt{8}$, 3, 10, and $\sqrt{13}$ grid units (each radius value is the square root of the sum of the squares of two integers). The outermost radial position that passed the check mentioned in Fig. 3 was marked as the radius R of that vortex. Vortex radius (R), rotational sense (clockwise or counterclockwise), and circulation (Γ) were measured directly, and energy (E) and vorticity (ω) were derived. Circulation is defined as

$$\Gamma = \oint u' \cdot ds \tag{4}$$

where u' is the high-pass filtered velocity vector. Energy density is calculated as

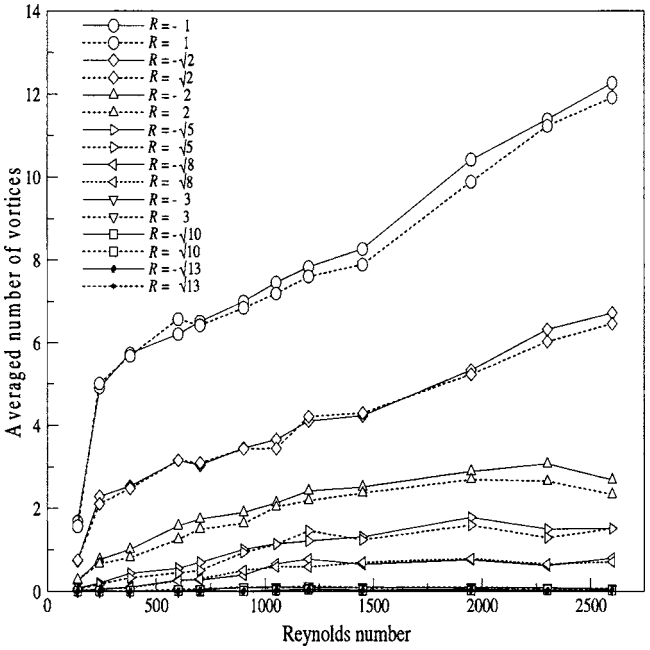

Fig. 4 Variation of number of vortices (per frame) with Reynolds number. Negative radius values in the legend correspond to clockwise eddies.

$$E(k) = \frac{c_1 \Gamma^2}{k} \tag{5}$$

where k is the wave number and c_1 is a constant. (We have set $c_1 = 1$ for the energy plots presented in this paper.) Vorticity is calculated as

$$\omega = \frac{\Gamma}{R^2} \tag{6}$$

Results and Discussions

The vortex education tool described earlier (Fig. 3) was used to explore the variation of vortex populations for various Re and vortex radius R. In Fig. 4, we plot vortex populations sorted by vortex radius against Re. The plot contains three important results: (i) The vortex populations for clockwise[3] and counterclockwise eddies are almost identical, which is expected from symmetry considerations and thus lends confidence to our eduction tool; (ii) For a given Re, the vortex population decreases continuously with increasing radius, which is consistent with the space-filling hypothesis (we will explore this aspect in greater detail shortly); and (iii) For a given vortex radius, the vortex population decreases monotonically as Re is decreased (especially for vortices of smaller radii), with a precipitous drop in population at the smallest Re of 140. The dramatic decay in number of vortices of small radii ($R = \pm 1, \pm\sqrt{2}$) below Re=250 indicates that these eddies are approaching the Kolmogorov scale, beyond which viscosity suppresses eddy formation. Equation (3) indicates that $\eta \approx 1.47$ mm (see also Table 1) for Re=140 at a midframe downstream distance of $200d$, which compares well with the smallest vortex size in Fig. 4. The number of vortices for larger radii also decreases for Re <250, but the change is not as significant as it is for smaller radii.

Figure 5 is simply a rearrangement of the data in Fig. 4, in that we now plot vortex populations sorted by Re against vortex radius. The vortex population (N) and the vortex radius (R) are normalized by their corresponding values for $R=1$, respectively.

[3]Clockwise eddies are denoted by negative radius values in the legend in Fig. 4.

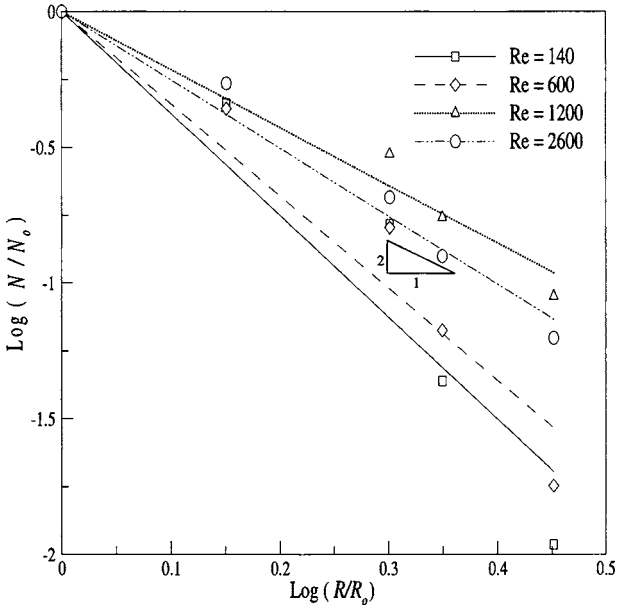

Fig. 5 Linear fits for ratio of vortex population and radius

Table 1 Kolmogorov scale at the centerline of round jets at $z/d=200$ for different Reynolds numbers

Reynolds number	Kolmogorov scale (mm)
140	1.47
240	1
380	0.7
600	0.49
700	0.43
900	0.37
1050	0.33
1200	0.29
1450	0.26
1950	0.21
2300	0.18
2600	0.16

The experimental data (for $R<3$) are reasonably fit by straight lines with slopes ranging from −2.1 for Re=1200 to −3.7 for the lowest Re of 140. Large vortices are sparse at low Re, and therefore, there is a greater sampling error associated with their populations.[4] Consequently, we focus on the data for Re=1200 (slope=−2.1) and 2600 (slope=−2.5) in Fig. 5. Both their slopes are close to −2. This result appears to be in accord with the space-filling argument, in that the vortex population in a two-dimensional domain should grow as R^{-2} when moving from one vortex size to the next.

Kinetic energy of the vortices of different size is plotted in Figs. 6 and 7. Essentially, the energy density curve reaches a maximum at a wave number corresponding to the integral scale and decreases for higher wave numbers. The energy density plot in Fig. 6 was obtained as follows. First, we summed the total energy contained by all vortices of a given radius in the entire record. Next, we divided this total by the number of frames to get the average energy for that vortex radius per frame; the average en-

[4]It should be noted that slopes of the Re=140 and 600 lines are close to 2 if vortices of larger radii are ignored.

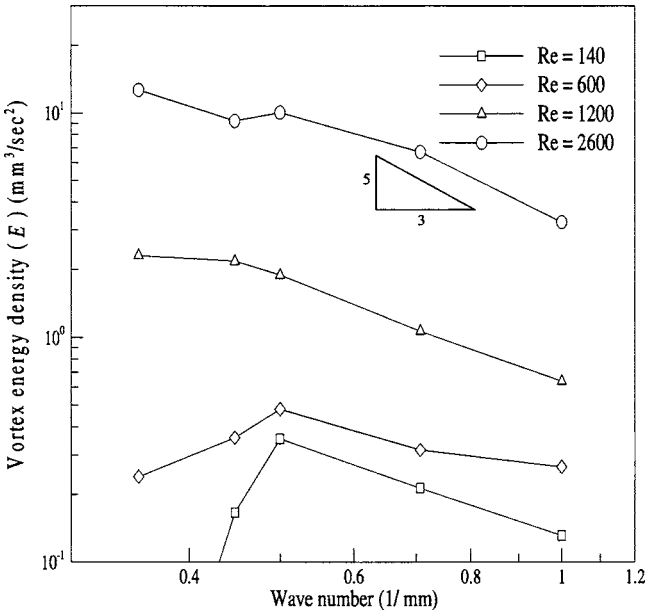

Fig. 6 Variation in vortex energy with vortex size (energy averaged per frame)

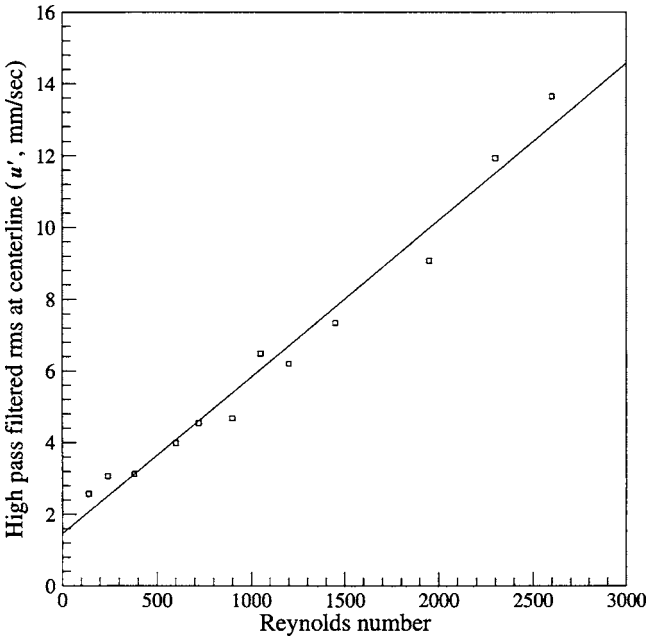

Fig. 8 Variation of centerline rms (u') of high-pass filtered velocity field with Reynolds number

ergy per unit area was then obtained by dividing by the area of the frame. Finally, because the energy of all eddies of size $2\pi/k$ is proportional to $E(k)$ times the width of the energy spectrum, which is k [7], we can obtain $E(k)$ by dividing the average energy per unit area by k. The energy plots shown in Fig. 6 match fairly well with theory that predicts a $E(k)$ versus k slope of $-5/3$ in the inertial subrange. Figure 6 indicates a slope of about -1.3 for the larger Re values. As expected, energy values decrease with Reynolds number for every wave number. Figure 7 presents the energy data of Fig. 6 in dimensionless form (energy density is normalized by $u_c^2 b$). The energy density curve indicates a reasonably good collapse for wave numbers greater than $0.1b/R$.

Typically in turbulence studies, rms of the velocity signal is measured directly, using a pointwise technique, such as hot-wire anemometry or laser-Doppler anemometry. Here, we extract rms of the high-pass filtered velocity using PIV measurements with good spatial resolution but limited temporal resolution. The rms of the high-pass filtered streamwise velocity (u') at the centerline is plotted against Reynolds number in Fig. 8; the data are fit well by a straight line. A linear relationship is to be expected because all velocities scale with the local centerline velocity u_c, which, in turn, is proportional to Re. Note that the fit to the data does not pass through the origin, suggesting that a small portion of the measured rms may arise from noise in the velocity data. The slope of the line is 0.0044 mm/s. Using the well-known correlation for *total* (i.e., across all wave numbers) rms at the centerline ($u'/u_c = 0.25$, which can be rewritten as $u'/\mathrm{Re} = 0.15\, \upsilon/b$), it is readily

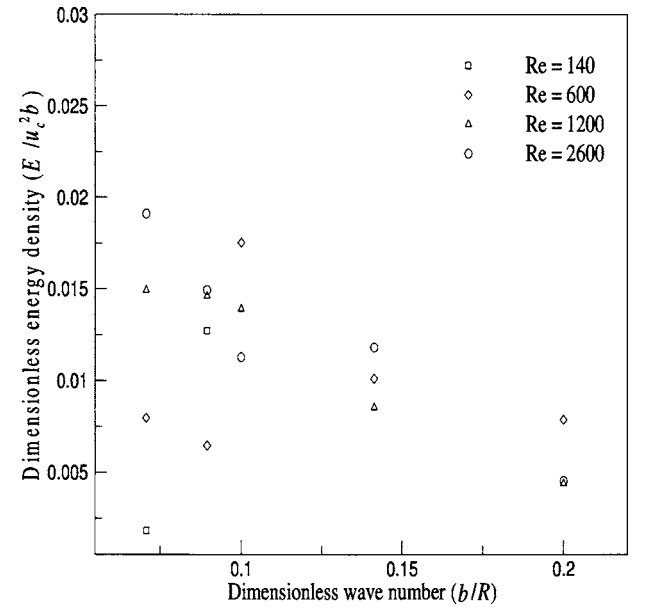

Fig. 7 Variation of nondimensional vortex energy with vortex size

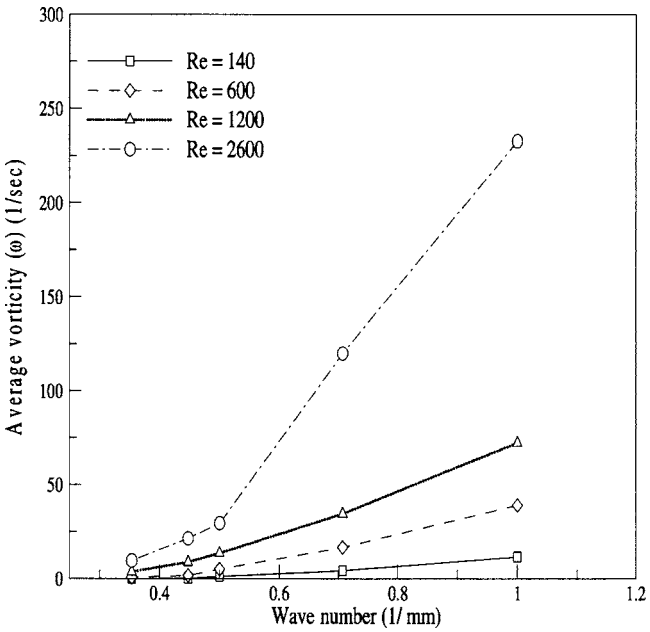

Fig. 9 Variation in average vorticity with vortex size

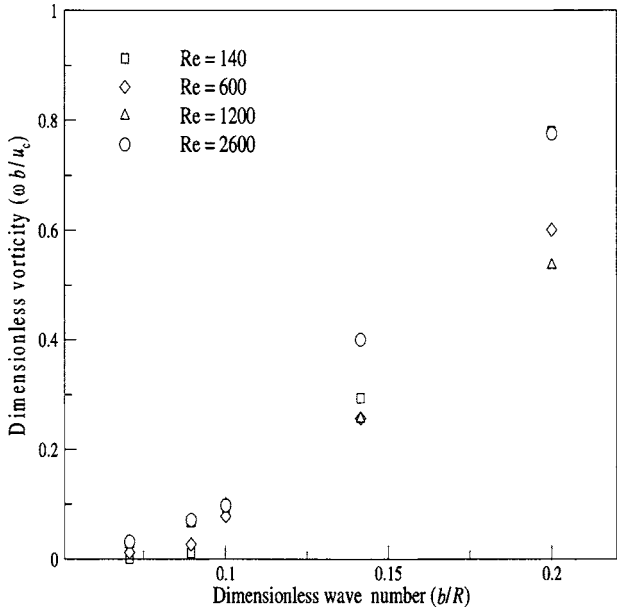

Fig. 10 Variation of nondimensional vorticity with vortex size

shown that the slope of u' versus Reynolds number should be 0.0075 mm/s for our experimental conditions. The difference between the two slopes is contributed by the low-pass field, which carries the remainder of the rms with it. For the size of the filter used in our study, we can conclude that approximately two-thirds of the total rms (or about half the total energy) is carried by the high-pass filtered field.

Vorticity (averaged over 200 frames) sorted by Reynolds number is plotted against vortex size in Figs. 9 and 10. It is evident that vorticity increases with k and that the relative increase in the vorticity is greater for larger Reynolds numbers (Fig. 9). When Fig. 9 is replotted in dimensionless form in Fig. 10, the data collapse quite well and confirm that vorticity increases with wave number.

Conclusions

Characteristics of small vortices in turbulent jets are obtained by applying a vortex education tool to high-pass filtered $2D$ velocity fields. Vortex characteristics are obtained at scales approaching the Kolmogorov scale by employing jets at low Reynolds numbers at which they would ordinarily be laminar. The jets are forced to remain turbulent at these low Re's by applying a periodic perturbation to the jet fluid. Results show that the vortex population drops substantially when the eddy size approaches the Kolmogorov scale. Vortex populations sorted by Reynolds number are consistent with the space-filling argument in two dimensions. The energy density varies with wave number as $-5/3$ for the inertial subrange, and vorticity increases with wave number. For the size of the filter used in our study, approximately two-thirds of the total rms (or about half the total energy) is carried by the high-pass filtered field.

References

[1] George, W. K., and Baker, C. B., 1980, "Analysis of Hot-Wire-Measurements in Turbulent Jets," Bull. Am. Phys. Soc., **25**(9), p. 1074.
[2] Hussein, H. J., Capp, S. P., and George, W. K., 1994, "Velocity Measurements in a High Reynolds Number, Momentum-Conserving Axisymmetric Turbulent Jet," J. Fluids Mech., **258**, pp. 31–75.
[3] Agrawal, A., and Prasad, A. K., 2002, "Properties of Vortices in the Self-Similar Turbulent Jet," Exp. Fluids, **33**, pp. 565–577.
[4] Agrawal, A., and Prasad, A. K., 2003, "Measurements Within Vortex Cores in a Turbulent Jet," ASME J. Fluids Eng., **125**, pp. 561–568.
[5] Agrawal, A., and Prasad, A. K., 2002, "Organizational Modes of Vortices in an Axisymmetric Turbulent Jet," Flow, Turbul. Combust., **68**, pp. 359–377.
[6] Frisch, U., 1995, *Turbulence: The Legacy of A. N. Kolmogorov*, Cambridge University Press, Cambridge, England.
[7] Hinze, J. O., 1959, *Turbulence: An introduction to Its Mechanism and Theory*, McGraw-Hill, New York.
[8] Tennekes, H., and Lumley, J. H., 1972, *A First Course in Turbulence*, The MIT Press, Cambridge, MA.
[9] Reynolds, W. C., Parekh, D. E., Juvet, P. J. D., and Lee, M. J. D., 2003, "Bifurcating and Blooming Jets," Annu. Rev. Fluid Mech., **35**, pp. 295–315.
[10] Adrian, R. J., Christensen, K. T., and Liu, Z.-C., 2000, "Analysis and Interpretation of Instantaneous Turbulent Velocity Fields," Exp. Fluids, **29**, pp. 275–290.
[11] Robinson, S. K., Kline, S. J., and Spalart, P. R., 1989, "Quasi-Coherent Structures in the Turbulent Boundary Layer. Part II: Verification and New Information From a Numerically Simulated Flat-Plate Boundary Layer," *Near Wall Turbulence, Proceedings of Zaric Memorial Conference*, S. J. Kline and N. H. Afgan, eds., Hemisphere, New York, pp. 218–247.

Sensitivity Analysis of Entrance Design Parameters of a Backward-Inclined Centrifugal Fan Using DOE Method and CFD Calculations

A. Behzadmehr
Mechanical Engineering,
University of Sistan & Baluchestan,
Zahedan, Iran

Y. Mercadier

N. Galanis

Génie Mécanique,
Université de Sherbrooke,
Québec Canada

Centrifugal fans with an electric motor included in the hub are commonly used in HVAC (heating, ventilation, and air conditioning) systems. A design of experiments (DOE) has been performed to study the effect of the entrance conditions of a backward-inclined centrifugal fan on its efficiency. The parameters involved are the base radius of the motor hub, the radius of the fan entry section, the deceleration factor throughout the entry zone (from the entry of the fan to the entry of the blade), and the solidity factor. Numerical simulation coupled with the DOE has been used for the sensitivity analysis of the entrance parameters. Initially, a complete factorial plan (2^4) *was performed to screen the most influent parameters and interactions. This has shown that the motor's cap radius, as well as its interactions with other parameters, is not significant. A second DOE, using composite central design (CCD which has a second order of accuracy) has then been performed on the remaining parameters (radius of the fan entry section, deceleration factor, and the solidity factor). The effects of these parameters and their interactions on the fan efficiency are now presented. A linear regression with three parameters has been performed to establish the efficiency distribution map. The methodology employed is validated by comparing the predicted results from the DOE and those from the numerical simulation of the corresponding fan.* [DOI: 10.1115/1.2173293]

1 Introduction

Small centrifugal fans and blowers have been used extensively in home appliances and heating, ventilation, and air conditioning (HVAC) systems. Flow in a centrifugal fan is a complex three-dimensional phenomenon, involving boundary layer, separation, secondary flow, turbulence, etc. Also, the geometry is often complex and asymmetric. These geometrical parameters have significant effects on the performance of centrifugal fans and blowers. Many studies have been concerned with blade and volute geometry, but few are dedicated to the entrance parameters and, above all, to the combined effects of these parameters. The design of a centrifugal fan is traditionally based on dimensionless analysis. Two well-known classical books of Stepanoff [1] and Eck [2] treat design in this manner. Many experimental and theoretical research efforts have been made in this field in order to explore and understand the behavior of flow through a machine. However, most of the theoretical works only consider nonviscous flow through the fan in order to simplify such a complex problem; details of such an approach are discussed by the authors in [1,2]. Recently, through use of improving facilities available for performing the numerical calculations, more researchers have been interested in considering viscous flow modeling by solving the Navier-Stokes equations. Computational fluid dynamics (CFD) tools can help us to understand the flow-field variations throughout a machine and are also very efficient for the study of the effects of geometrical parameters on the performance of fans and blowers. These enable the researcher to achieve suitable parameters, corresponding to the desired machine performance. The question remains however, what are the suitable parameters? What is the effect of each parameter and what is the overall effect of the interaction of these parameters on the performance of the machine?

Many works in the literature have been found using numerical simulation for the study of flow fields in a turbomachine (however, published works on small fans and blowers are in number limited). Among them, Rai and Madavan [3] has used three-dimensional (3D) Navier-Stokes equations to numerically study the rotor-stator interaction. Zhang et al. [4] analyzed 3D viscous flow within a backswept centrifugal impeller using Navier-Stokes equations and k-ε turbulent model. Strickland et al. [5] presented a numerical simulation for the study of flow field inside a centrifugal pump. Lin and Huang [6] designed and numerically simulated a small forward-curved centrifugal fan. They found a good agreement between the experimental and numerical results. Gonzalez et al. [7] showed that numerical simulation is capable of capturing the details of the flow field throughout a centrifugal pump due to the impeller-volute interaction. Choi et al. [8] used CFD tool integrated with an optimization code to improve the design of an automotive fan; they selected limited independent parameters (two parameters related to the radial distribution of the sweep angle of an axial fan) in order to maximize the pressure coefficient and to also minimize the production of turbulent kinetic energy. As the numbers of iterations required to converge the optimization code depend on the number of variables employed, they used a limited number of parameters. Recently, Yu et al. [9] numerically studied the flow field for a centrifugal fan using the multiple reference frame method. They analyzed the effect of the blade inlet angle and the impeller gap on the fan performance.

As seen in the foregoing paragraphs, all of the earlier published works have been aimed at understanding the behavior of flow inside a machine and its interaction with its solid parts or at trying to optimize a particular machine by considering some pertinent

Contributed by the Fluids Engineering Division of ASME for publication in the JOURNAL OF FLUIDS ENGINEERING. Manuscript received September 28, 2004; final manuscript received October 7, 2005. Review conducted by Joseph Katz.

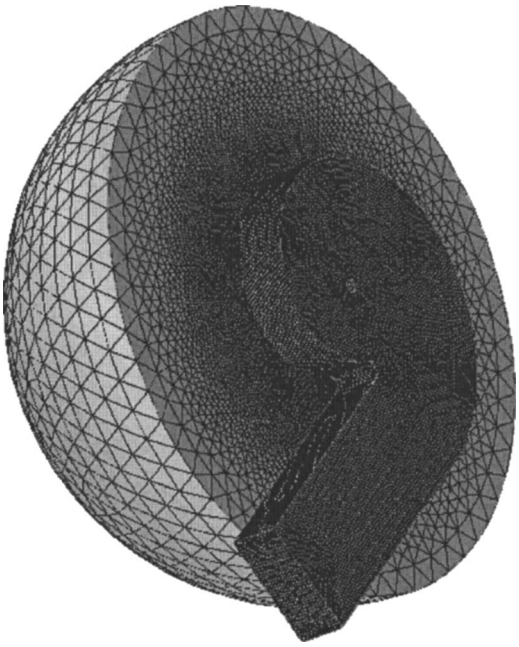

Fig. 1 Sketch of the fan unstructured mesh (hemisphere is added to inlet)

parameters. But as we know, there is no published work that studies the weight and effect of each design parameter (e.g., entry region variables, blade design parameters, and collector and volute parameters) on the general performance of a turbomachine and, in particular, a centrifugal fan.

Therefore, the purpose of this present paper is to study and understand the weight and effects of the entrance region parameters of a backward-inclined centrifugal fan on the fan's efficiency. Thus, the cap of the motor (an electric motor mounted inside the hub and rotating the fan), entrance radius, deceleration factor through the entry zone, and the solidity factor were chosen to study their weight and their effects as well as their interactions on the efficiency of the centrifugal fan. Therefore, a first design of experiments (DOE) has been planned based on a complete factorial method. The result of this first DOE is refined, using the central composite design (CCD) method. The fan response to each configuration of the parameters is calculated, numerically, by using a validated numerical code.

2 Model Description and Numerical Procedures

2.1 Geometry and Grid. A geometrical discretization of a backward-inclined centrifugal fan is created using the commercial software GAMBIT. It consists of the entry region, rotor and the volute. In order to simulate the real inlet condition, a large hemisphere is added to the entry region for the purpose of imposing inlet boundary conditions. Unstructured tetrahedral cells are used for the meshing of all regions. It is constructed using more than a million cells (1,047,501). A general view of the geometry and grids are shown in Figs. 1 and 2.

2.2 Mathematical Formulations and Numerical Procedure. Three-dimensional elliptical forms of the governing equations (continuity and Navier-Stokes equations) for incompressible flows are used as primitive variables:

$$\frac{\partial U_j}{\partial X_j} = 0 \tag{1}$$

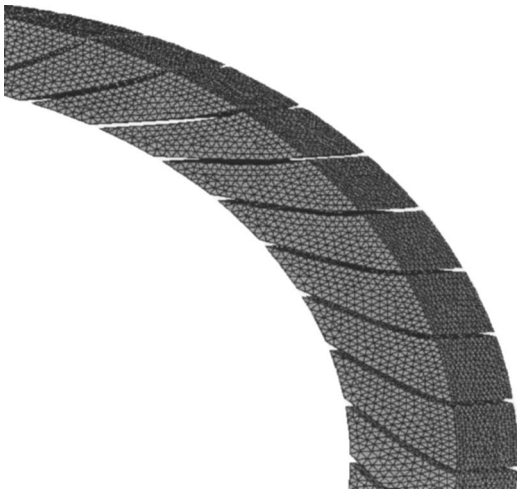

Fig. 2 Detail of the rotor mesh

$$\rho \frac{\partial}{\partial X_j}(U_j U_i) = -\frac{\partial P}{\partial X_i} + \frac{\partial}{\partial X_j}\left[\mu\left(\frac{\partial U_i}{\partial X_j} + \frac{\partial U_j}{\partial X_j}\right) - \rho\overline{u_i u_j}\right] \tag{2}$$

Since the temperature is constant, the energy conservation equation is not used and the fluid properties are assumed to be constant. The standard k-ε turbulent model is chosen for the modeling of the effects of turbulence while a wall function is used to resolve the near wall flows. The commercial software FLUENT is used to resolve the set of equations based on the control volume method. In order to have more accuracy, second-order upwind is selected for the advection terms and the SIMPLE method is performed for the pressure-velocity coupling. A steady-state multiple reference frame modeling is used in the calculations to simulate the flow behavior in different zones (rotating and stationary zones) while the unsteady interaction effects were neglected. This method seems to provide a savings in computer time by a factor of about 10 [10] and the same degree of accuracy of the unsteady calculations using the sliding mesh method based on Refs. [11,12]. Also, recently Yu et al. [9] have used the multiple reference frame method for modeling a centrifugal fan. They showed that good agreement between the numerical and experimental results was obtainable.

2.3 Boundary Conditions. Centrifugal fan geometry consists of three different zones: the entrance, the rotor, and the volute. The inlet region and the volute are considered on a stationary frame, whereas the rotor zone is studied on a rotating frame. Surfaces between the entry zone and the rotor (surfaces corresponding to the blades entry) and surfaces between the rotor and the volute (surfaces corresponding to the blades exit) are defined interfaces, needed for the relative velocity of the rotor. Uniform velocity normal to the hemisphere surface is imposed as the inlet boundary condition while the turbulence intensity is assumed to be 1% and the turbulent viscosity ratio equal to 1, corresponding to the prevailing low-turbulence air condition. There are some rotating walls included in the inlet zone; thus, they are considered as rotating walls in the stationary frame. The rotor walls related to the rotor zone are selected as nonrotating walls in their frame (rotating frame). The outflow boundary condition, with a mass balance correction, is imposed at the volute outlet.

Convergence of the solution is determined by monitoring the normalized residuals for each dependent variable. The solution is considered converged when these normalized residuals reduce to 1×10^{-3} and the mass residual decreases to 1×10^{-6}.

2.4 Validation of Numerical Simulations. In order to validate the numerical code, grid-independent tests have been done and the calculated results compared to the experimental results.

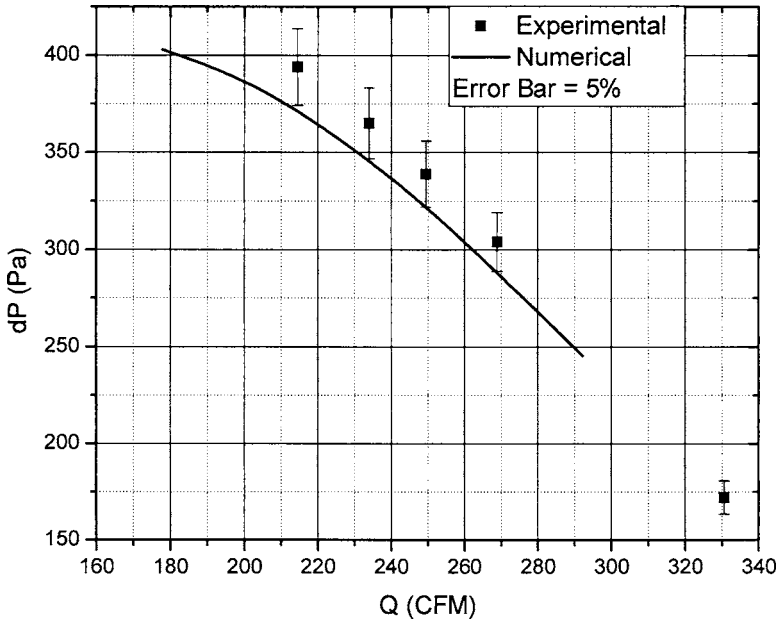

Fig. 3 Comparison of the numerical simulation with the experimental measurements

Experimental data were obtained using the ANSI/AMCA Standard 210-99 "Laboratory Method of Testing Fans for Aerodynamic Performance Rating" [13].

At different mass flow rates (see Fig. 3), the pressure difference between the inlet of the fan and the exit of the volute were compared and the concordance between the numerical results and the experimental results are within 5%.

3 Design of Experiment and Results Analysis

Design of experiment (DOE) was performed on k variables at more than two levels in order to understand their weights and effects on the plan [14]. A 2^k factorial design was chosen to construct the design of experiment this is a design with the k factor each at two levels. Therefore, for a 2^k-design, the complete model would contain 2^k-1 effects. Four parameters (related to the entrance design of the centrifugal fan) were chosen to study their effects and their interactions' effects on the fan efficiency. The selected parameters are (A) the radius of the cap of the motor (motor installed in the fan and a cylindrical shape assumed for it (see Fig. 4), (B) the radius of the entrance (see Fig. 4), (C) deceleration factor (from the inlet section to the blade inlet), and (D) the solidity factor. The angle of attack and the blade inlet diameter are related to the deceleration and the solidity factor following the method presented by Eck [2] and used in this study to generate the geometry. Table 1 summarizes the two levels of each factor (the lower level is identified by −1 and the higher one by +1). Based on the parameters and the number of levels, a factorial design table is prepared and shown in Table 2. The response of these variables (fan efficiency) is obtained by the corresponding numerical simulation solutions. Therefore, a series of numerical simulations has been performed for different combinations of these parameters and their levels ($2^4=16$ tests), while other fan design parameters, such as blade exit angle, external diameter, blade profile (constant thickness blade), etc., are considered to be constant. For example, the first row shows the level of each parameter at the first test, i.e., A=−1, B=−1, C=−1, and D=−1, which means (see Table 1): A=1.27 cm, B=0, C=0.7 and D=2. The analysis of variance for these four parameters at two levels is highlighted in Table 3 (interactions of the higher degree, ABC, ABD, and BCD are neglected). The sum of squares used for testing the hypothesis, that a main effect or an interaction is negligible, is presented on the first row (ss). The degree of freedom (DOF) appears in the second row while the variance (s^2) is shown in the third row. These values have been obtained following the method presented by Montgomery [14]. In this experiment plan, the Fisher factor (F_0), shown in the next row, is equal to 6.61 for a 95% confidence level (i.e., the method used to produce the confidence interval yields a correct statement 95% of the time). The

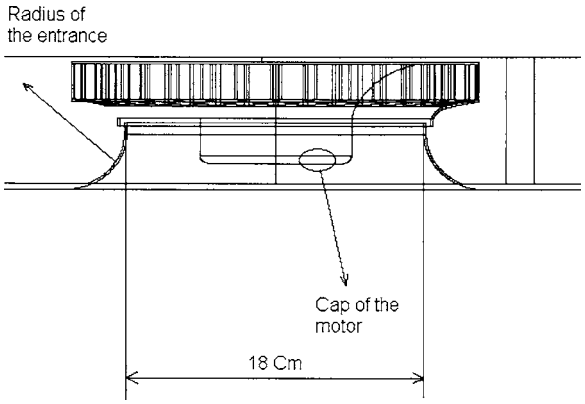

Fig. 4 Entrance nomenclature

Table 1 Parameters and their two levels value for the complete factorial model

Factors	Parameters	Level 1 (-1)	Level 2 (+1)
A	Radius of the head of the motor	1.27 (cm)	2.54(cm)
B	Radius of the entry section	0	1.27 (cm)
C	Deceleration factor	0.7	1
D	Solidity factor	2	3

Table 2 Level of the parameters for each test

Test Number	Factors and Interactions														
	A	B	C	D	AB	AC	AD	BC	BD	CD	ABC	ABD	ACD	BCD	ABCD
1	-1	-1	-1	-1	1	1	1	1	1	1	-1	-1	-1	-1	1
2	-1	-1	-1	1	1	1	-1	1	-1	-1	-1	1	1	1	-1
3	-1	-1	1	-1	1	-1	1	-1	1	-1	1	-1	1	1	-1
4	-1	-1	1	1	1	-1	-1	-1	-1	1	1	1	-1	-1	1
5	-1	1	-1	-1	-1	1	1	-1	-1	1	1	1	-1	1	-1
6	-1	1	-1	1	-1	1	-1	-1	1	-1	1	-1	1	-1	1
7	-1	1	1	-1	-1	-1	1	1	-1	-1	-1	1	1	-1	1
8	-1	1	1	1	-1	-1	-1	1	1	1	-1	-1	-1	1	-1
9	1	-1	-1	-1	-1	-1	-1	1	1	1	1	1	1	-1	-1
10	1	-1	-1	1	-1	-1	1	1	-1	-1	1	-1	-1	1	1
11	1	-1	1	-1	-1	1	-1	-1	1	-1	-1	1	-1	1	1
12	1	-1	1	1	-1	1	1	-1	-1	1	-1	-1	1	1	-1
13	1	1	-1	-1	1	-1	-1	-1	-1	1	-1	-1	1	1	1
14	1	1	-1	1	1	-1	1	-1	1	-1	-1	1	-1	-1	-1
15	1	1	1	-1	1	1	-1	1	-1	-1	1	-1	-1	-1	-1
16	1	1	1	1	1	1	1	1	1	1	1	1	1	1	1

Table 3 Analysis of variance for the complete factorial model

Analysis of Variance											
	Mean	A	B	C	D	AB	AC	AD	BC	BD	CD
SS	3.1E-01	9.9E-04	7.5E-02	5.4E-02	1.0E-01	1.3E-06	3.9E-04	1.6E-03	1.4E-02	1.9E-02	3.7E-02
DF	15	1	1	1	1	1	1	1	1	1	1
s^2		9.9E-04	7.5E-02	5.4E-02	1.0E-01	1.3E-06	3.9E-04	1.6E-03	1.4E-02	1.9E-02	3.7E-02
F (Confidence)	(95%) F_0= 6.61	0.49	36.92	26.92	50.45	0.00	0.19	0.81	7.10	9.26	18.41
Effect		NS	S	S	S	NS	NS	NS	S	S	S
S: significant, NS: Non-significant											

Table 4 Parameters and their level for CCD

Runs	Radius of the entry section (cm)	Deceleration	Solidity	Efficiency	
				Simulation 1	Simulation 2
1	1.016	0.8	1.7	0.59	0.56
2	1.016	0.8	2.3	0.57	0.58
3	1.016	1.2	1.7	0.62	0.62
4	1.016	1.2	2.3	0.56	0.57
5	1.524	0.8	1.7	0.57	0.58
6	1.524	0.8	2.3	0.56	0.57
7	1.524	1.2	1.7	0.56	0.58
8	1.524	1.2	2.3	0.50	0.52
9	1.27	1	2	0.60	
10	0.910844	1	2.0	0.60	
11	1.629156	1	2.0	0.58	
12	1.27	0.7172	2.0	0.53	
13	1.27	1.2828	2.0	0.54	
14	1.27	1	1.5757	0.60	
15	1.27	1	2.4243	0.59	

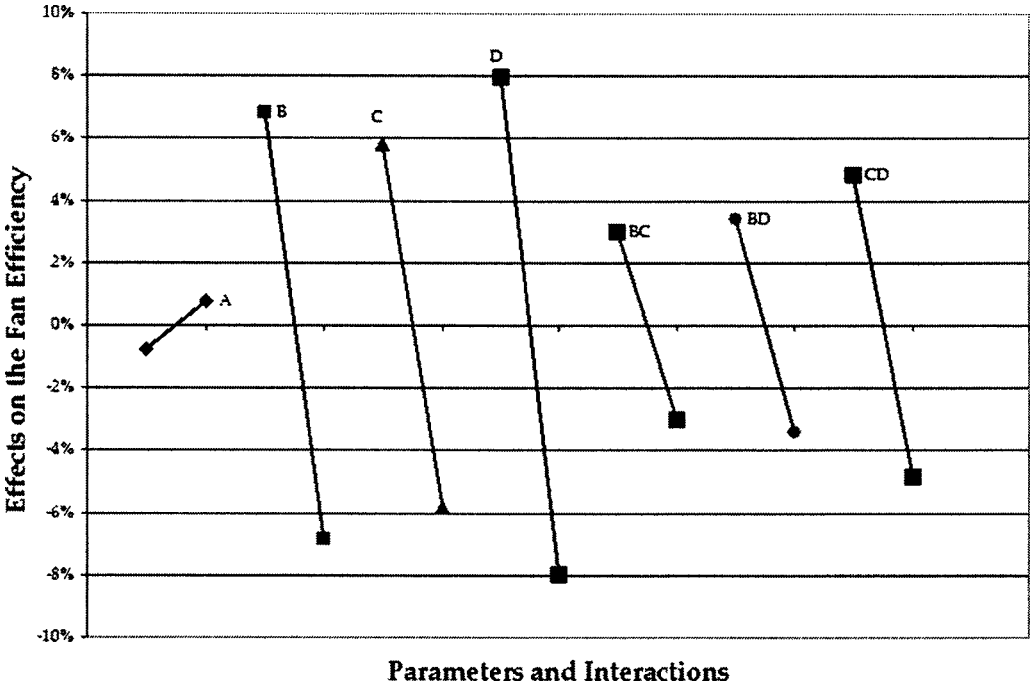

Fig. 5 Response of the first DOE (complete factorial model)

estimated F values for the parameters B, C, D and the interactions BC, BD, and CD are greater than F_0, which means these parameters and interactions are statistically significant.

Figure 5 shows the response of these four parameters and the previously mentioned three significant interactions on the fan efficiency. As shown in this figure, parameter A (the radius of the motor cap) compared to the other parameters (B, C, and D) has no significant effect on the efficiency of the fan. However, the interactions BC, BD, and CD are very important. The results of the first DOE show the region of the greatest influence on the fan efficiency. The parameters B, C, and D, as well as the interaction BC, BD, and CD have positive effects on their lower level (−1). But if all of the parameters stay at their lower levels (−1), their interactions can not stay at their lower level because it becomes a positive value $(-1\times-1=1)$, corresponding to the higher level. Therefore, an interesting region can not be constructed based on the lower level of all of these parameters. Thus, the region of the optimum condition would be constructed based on the lower level of the parameters B and D and the higher level of parameter C, since the latter effect is less important. This also allows for having lower levels for the interactions BC and CD, which have a positive effect.

At this stage, another DOE has been planned to refine the region of the optimum condition. Instead of a factorial design, a central composite design (CCD) [14] is chosen for the new plan. This will enable us to study the behaviour of the parameters and their interactions by the second order of accuracy.

Table 4 summarizes the parameters and their levels for the CCD. It is seen that the two levels of parameters B and D are around their lower level in the first DOE, whereas parameter C is close to its higher level, as was explained earlier. To construct the CCD plan, 15 tests are needed. Eight tests must be performed at two levels to construct the factorial plan (in order to reduce numerical error in the regression, these eight test have been calculated twice with two different schemes, so that for these eight tests in Table 4, two response values are written), six runs at another two levels to establish the axial points ($2k$), and one test at another condition to establish the center point are also needed. The analysis of variance for these parameters is shown in Table 5. The estimated Fisher factor shows that factor C and interactions BD and BCD are not important. However interactions BC and CD have significant effects. Also, it shows that the interaction effects of BC, BD, and CD are significant with a 95% confidence level.

The result of this analysis is shown in Fig. 6: the entrance radius (B) and the solidity factor (D), as well as the interactions BC and CD are all very important. It is interesting to note that the

Table 5 Analysis of variance for CCD

Analysis of Variance								
	Mean	B	C	D	BC	BD	CD	BCD
SS		3.42E-03	1.53E-04	4.08E-03	2.27E-03	1.43E-04	2.62E-03	7.30E-08
DF	15	1	1	1	1	1	1	1
s^2		3.42E-03	1.53E-04	4.08E-03	2.27E-03	1.43E-04	2.62E-03	7.30E-08
F (Confidence)	(95%) 3.46	24.68	1.11	29.48	16.40	1.03	18.94	0.00
Effect		S	NS	S	S	NS	S	NS
S: significant, NS: Non-significant								

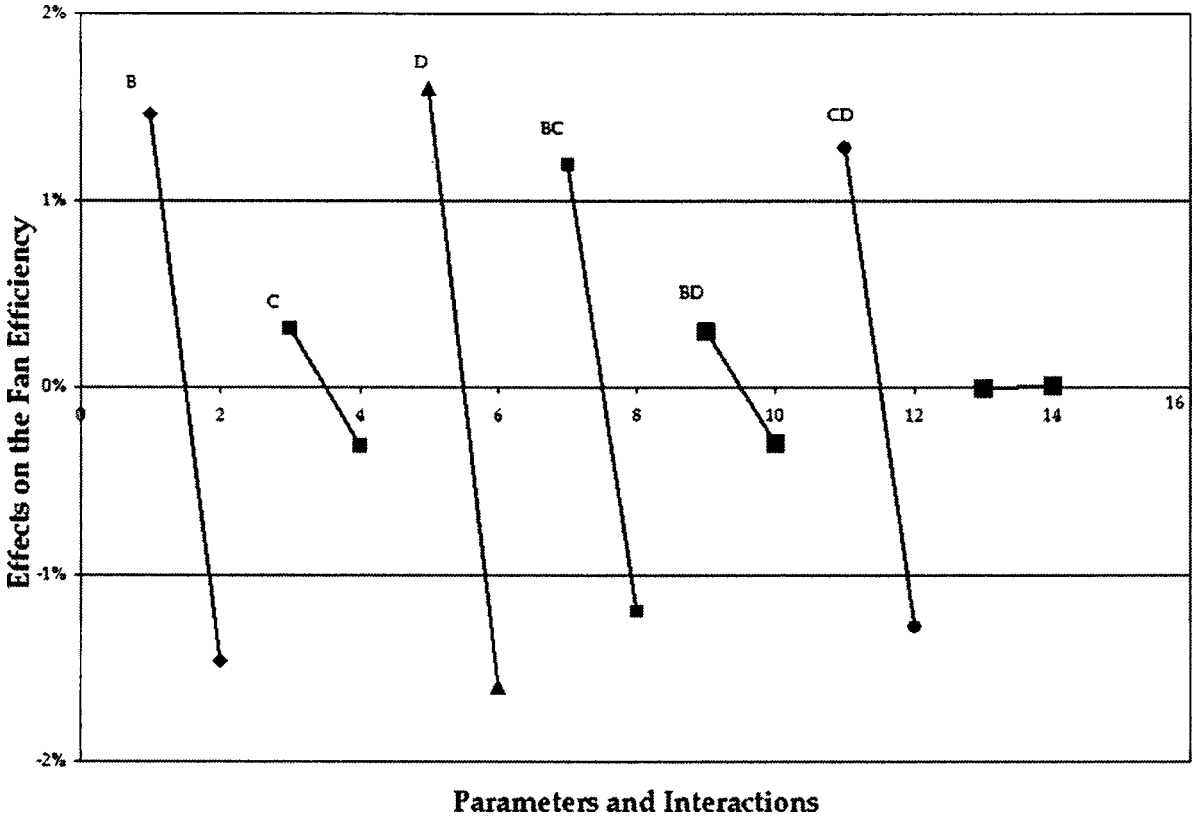

Fig. 6 Response of the CCD

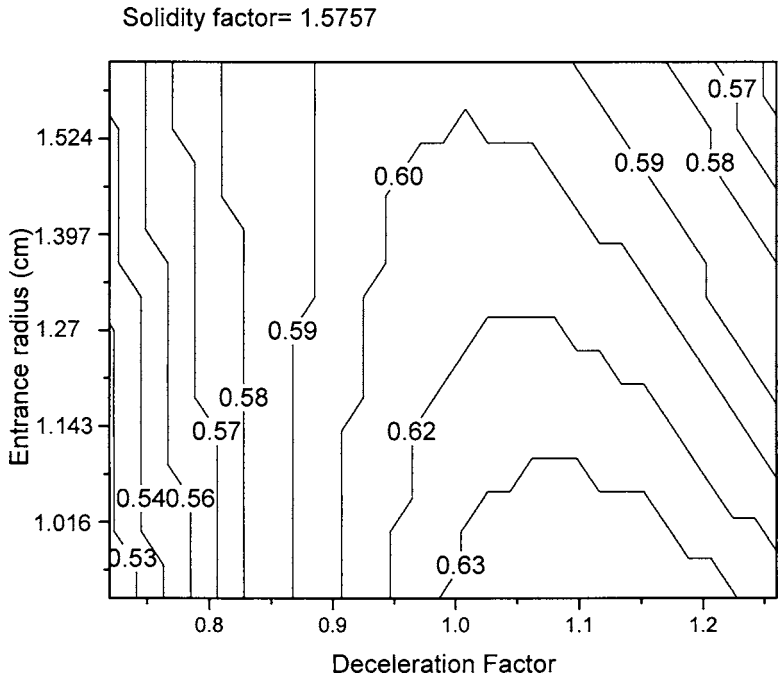

Fig. 7 Contour of efficiency map for the solidity factor 1.5757

parameter C (deceleration factor) has not as significant an effect as its interactions with the entrance radius (BC) and the solidity factor (CD). This is because of an indirect effect of the deceleration factor (C) on the blade angle of attack and inlet diameter. All the parameters and interactions BC and CD have a positive effect at their lower levels and a negative effect at their higher levels. This means that to have a positive interaction effect, one of the main parameters (B, C, or D) should stay at its lower level (less-effective position). Since the deceleration factor (C) has a less important effect than the other two, it is chosen to stay at its higher level and, consequently, the interactions BC and CD can stay at their positive effect position.

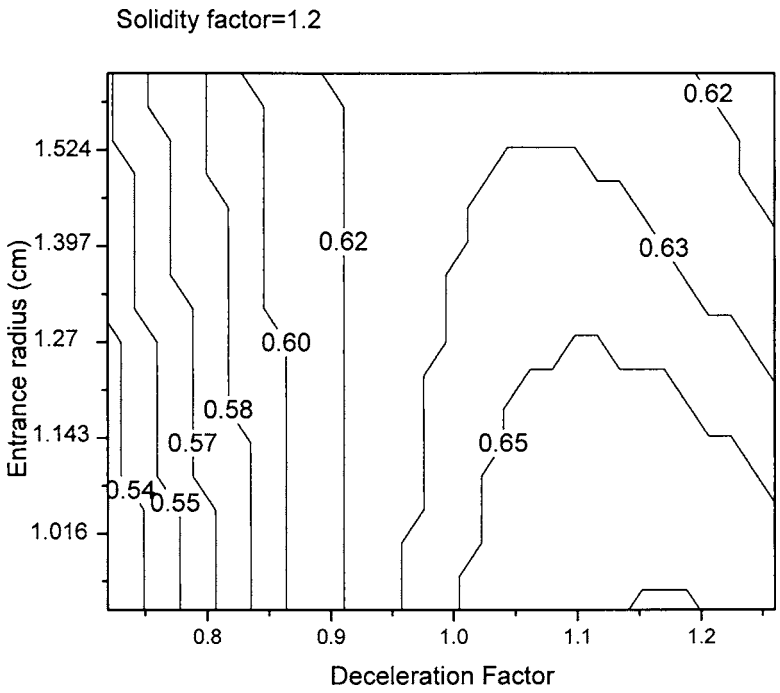

Fig. 8 Contour of efficiency map for the solidity factor 1.2

4 Optimum Design

A linear regression with the three factors (B, C, and D) has been done to find the response surface. A contour map presenting different efficiency regimes has been drawn, based on the variations of the deceleration factor (C) and the entrance radius (B) for different values of the solidity factor (D). Figure 7 shows such a contour for the solidity factor of 1.5757 (lower level); increasing the deceleration factor (parameter C goes to its higher level) and keeping the entrance radius (B) around its lower level (1.016 cm), the maximum efficiency region appears for this solidity factor. Then by decreasing the solidity factor to 1.2, a region of higher efficiency appears. This is shown in Fig. 8, a region of 65% efficiency which could not be seen in the case of $D=1.5757$. However, as it is shown in Fig. 9, increasing the solidity factor to 1.8 causes a reduction in the efficiency. This is confirmed that the movement direction required to achieve a higher efficiency is toward the lower value of the solidity factor. These contours show that the optimum region, having maximum efficiency based on the entrance parameters, is a region for which $B \leq 1.016$ cm, $1 < C < 1.2$ and $D < 1.7$.

In order to validate the procedure, a geometrical condition (which gives specific value to each entrance parameter) in the

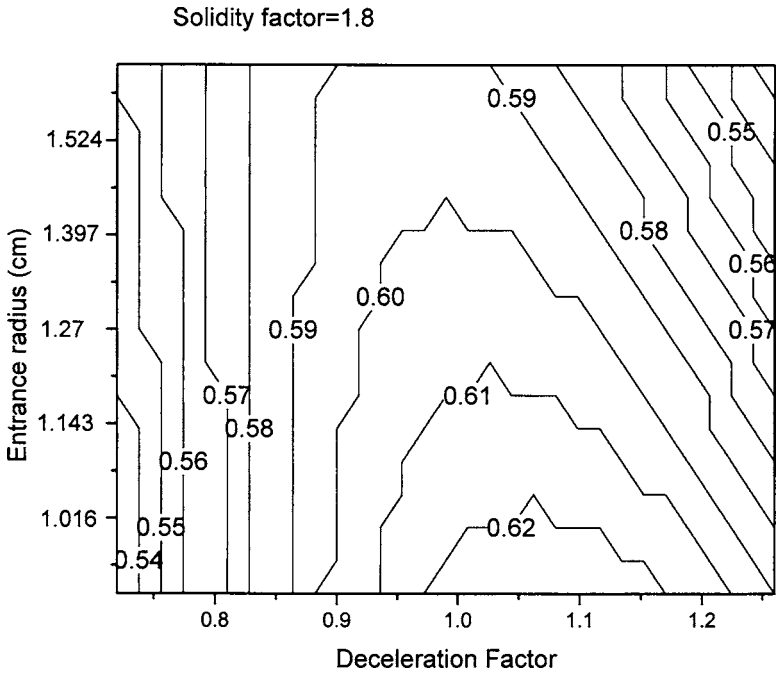

Fig. 9 Contour of efficiency map for the solidity factor 1.8

region of 63–64% efficiency, was chosen (see Fig. 7). The corresponding fan was configured, based on the following values:

Entrance radius (B) = 0.9108 cm

Deceleration factor (C) = 1.1267

Solidity factor (D) = 1.5757

Then the fan was simulated numerically and the efficiency obtained equal to 62%. This confirms that the efficiency map obtained using the DOE methodology is reliable with good precision.

5 Conclusion

The design of experiments (DOE) has been performed in order to study the effect of the entrance geometry of a backward-inclined centrifugal fan on the efficiency of the fan. Numerical simulation has been used to determine the efficiency of the fan for different configurations of the entrance parameters. These entrance parameters consist of the radius of the cap of the motor used for rotating the fan, the radius of the entry section, a deceleration factor throughout the entry zone (from the entry of the fan to the entry of the blade), and the solidity factor. The first DOE (complete factorial model) specifies the region of the most important effects. It shows that the motor's cap, as well as its cross-interactions with the other parameters, is not significant. However, the effects of three other parameters and their interactions are important. Therefore, a region of positive effect on fan efficiency is established. A second DOE (central composite design (CCD), which has a second-order accuracy) has also been performed on the three most important parameters (radius of the entry to the fan, deceleration factor, and the solidity factor). CCD is focused on the regions that have positive effects on the fan efficiency. A linear regression on three factors at three levels shows the map of different efficiency regions based on these three important parameters. A higher-efficiency region appears when the entrance radius is smaller than 0.9108 cm, deceleration varies around 1.1, and the solidity factor is lower than 1.7. The effects of each principal parameter and their interaction have been discussed, and the regions of various efficiencies are presented on a contour format. The methodology is validated by comparing the predicted result of DOE and the numerical simulation on a specific fan.

Acknowledgment

The authors thank the Natural Science and Engineering Research Council of Canada for its financial support.

Nomenclature

K = number of factors
P = pressure (Pa)
U, u = time-mean and fluctuating velocity (m s^{-1})

Greek symbols

μ = dynamic viscosity (N s m^{-2})
ρ = density (kg m^{-3})

References

[1] Stepanoff, A. J., 1957, *Centrifugal and Axial Flow Pumps: Theory, Design & Application*, Wiley, New York.
[2] Eck, B., 1973, *Fans Design and Operation of Centrifugal, Axial-Flow, and Cross-Flow Fans*, Oxford, Pergamon Press, New York.
[3] Rai, M. M., and Madavan, N. K., 1990, "Multi-Airfoil Navier-Stokes Simulations of Turbine Rotor-Stator Interaction," ASME J. Turbomach., **112**(3), pp. 377–384.
[4] Zhang, M. J., Pomfret, M. J., and Wong, C. M., 1996, "Three-Dimensional Viscous Flow Simulation in a Backswept Centrifugal Impeller at the Design Point," Comput. Fluids, **25**(5), pp. 497–507.
[5] Stickland, M. T., Scanlon, T. J., Fernandez-Francos, J., Blanco-Marigorta, E., and Parrondo, J., 2002, "A Numerical and Experimental Analysis of Flow in a Centrifugal Pump," *Proceedings of the 2002 ASME Joint U.S.-European Fluids Engineering Conference*, Montreal, Quebec Canada, pp. 703–708.
[6] Lin, S. C., and Huang, C. L., 2002, "An Integrated Experimental and Numerical Study of Forward-Curved Centrifugal Fan," Exp. Therm. Fluid Sci., **26**, pp. 421–434.
[7] Gonzalez, J., Fernandez, J., Blanco, E., and Santolaria, C., 2002, "Numerical Simulation of the Dynamic Effect Due to Impeller-Volute Interaction in a Centrifugal Pump," ASME J. Fluids Eng., **124**, pp. 348–354.
[8] Choi, J. H., Kim, K. Y., and Chung, D. S., 1997, "Numerical Optimization for Design of an Automotive Cooling Fan," SAE, Heat Exchanges for Automotive Design, **1262**, pp. 73–77.
[9] Yu, Z., Li, Song, He, W., Wang, W., Huang, D., and Zhu, Z., 2005, "Numerical Simulation of Flow Field for a Whole Centrifugal Fan and Analysis of the Effects of Blade Inlet Angle and Impeller Gap," HVAC&R Res., **11**(2), pp. 263–283.
[10] Luo, J. Y., Issa, R. I., and Gosman, D., 1994, "Prediction of Impeller Induced Flows in Mixing Vessels Using Multiple Frames of References," Inst. Chem. Eng. Symp. Ser., **136**, pp. 549–556.
[11] Lane, G. L., Rigby, G. D., and Evans, G. M., 2001, "Pressure Distribution on the Surface of Rushton Turbine Blades: Experimental Measurements and Prediction by CFD," J. Chem. Eng. Jpn., **34**(5), pp. 613–620.
[12] Bujalski, W., Jaeorski, Z., and Nienow, A. W., 2002, "CFD Study of Homogenization With Dual Rushton Turbines: Comparison With Experimental Results: Part II: The Multiple Reference Frame," Chem. Eng. Res. Des., **80**(1), pp. 97–104.
[13] ANSI/AMCA Standard 210-99, "Laboratory Method of Testing Fans for Aerodynamic Performance Rating," Air Movement and Control Association International Inc., www.amca.org
[14] Montgomery, D. C., 2001, *Design and Analysis of Experiments*, Wiley, New York.

Steady and Unsteady Radial Forces for a Centrifugal Pump With Impeller to Tongue Gap Variation

José González
e-mail: aviados@uniovi.es

Jorge Parrondo

Carlos Santolaria

Eduardo Blanco

Universidad de Oviedo,
Área de Mecánica de Fluidos,
Campus de Viesques,
33271 Gijón (Asturias), Spain

Experimental and numerical studies are presented on the steady and unsteady radial forces produced in a single volute vaneless centrifugal pump. Experimentally, the unsteady pressure distributions were obtained using fast response pressure transducers. These measurements were compared with equivalent numerical results from a URANS calculation, using the commercial code FLUENT. *Two impellers with different outlet diameters were tested for the same volute, with radial gaps between the blade and tongue of 10.0% and 15.8% of the impeller radius, for the bigger and smaller impeller diameters, respectively. Very often, pump manufacturers apply the similarity laws to this situation, but the measured specific speeds in this case were found to be slightly different. The steady radial forces for the two impellers were calculated from both the measured average pressure field and the model over a wide range of flow rates in order to fully characterize the pump behavior. Again, a deviation from the expected values applying the similarity laws was found. The data from the pressure fluctuation measurements were processed to obtain the dynamic forces at the blade passing frequency, also over a wide range of flow rates. Afterwards, these results were used to check the predictions from the numerical simulations. For some flow rates, the bigger diameter produced higher radial forces, but this was not to be a general rule for all the operating points. This paper describes the work carried out and summarizes the experimental and the numerical results, for both radial gaps. The steady and unsteady forces at the blade passing frequency were calculated by radial integration of the pressure distributions on the shroud side of the pump volute. For the unsteady forces, the numerical model allowed a separate analysis of the terms due to the pressure pulsations and terms related to the momentum exchange in the impeller. In this way, the whole operating range of the pump was studied and analyzed to account for the static and dynamic flow effects. The unsteady forces are very important when designing the pump shaft as they can produce a fatigue collapse if they are not kept under a proper working value.* [DOI: 10.1115/1.2173294]

Introduction

Knowledge of the radial forces is fundamental to understanding the dynamic working conditions of a centrifugal pump. The main goal of this paper is to determine such forces both on a steady and unsteady basis. The flow inside a centrifugal pump is quite complex and it is always dominated by the geometrical constraints which impose a strongly 3D structure.

The fluid flow inside a centrifugal pump is characterized by a circumferentially nonuniform unsteady pattern, mostly associated with the rotation frequency and, especially, the blade-passing frequency [1]. Fluctuations at the blade-passing frequency are the result of the hydraulic disturbances that follow the trailing edge of the impeller blades and the fluid-dynamic interaction of the blades with the volute of the pump. This phenomenon can be an important source for hydraulic noise and vibration [2].

The magnitude of these flow fluctuations for a given pump is very dependent on the operating point [3]. Besides this flow rate dependence, there are geometrical features that affect flow fluctuations, not only within the pump, but also over the hydraulic circuit. One such feature is the radial gap between the exit of the impeller and the volute at the tongue region, [4,5]. The effect of the radial gap on the fluid-dynamic perturbations produced in the pump is particularly interesting, because pump manufacturers usually offer to equip each volute with several impellers of slightly different outlet diameter and thus different blade-tongue gap. This is so because these impellers can be conveniently obtained from a progressive cut-back of the blades, and manufacturers can offer a wide range of operating specifications without an important increment of production costs [6].

The main goal of this work was to evaluate the influence of the radial gap between the impeller exit and the volute tongue on the unsteady radial forces produced on the impeller of a centrifugal pump with volute casing. For such purpose, two different impellers were tested for one single volute, with outlet diameters of 190 and 200 mm, respectively (the former is a cut-back of the latter). The resulting radial gaps were 15.8% and 10% of the impeller radius and the respective specific speeds were ω_s=0.52, 0.53, for the smaller and bigger impellers, respectively.

Both experimental and numerical studies were performed. Measurements were carried out with pressure transducers installed on the shroud of the pump volute, at every 10 deg. Both static and fluctuating (blade-passing frequency) pressure values were obtained for both impellers over a wide range of flow rates. The experimental data were compared to the predictions from the numerical simulations of the flow using the commercial CFD code FLUENT. This comparison focused on both the steady and unsteady radial forces produced on the impeller of the pump due to the pressure distribution along the volute, as a preparatory step to the validation of the total radial forces predicted by the simulations.

Contributed by the Fluids Engineering Division of ASME for publication in the JOURNAL OF FLUIDS ENGINEERING. Manuscript received May 18, 2004; final manuscript received September 29, 2005. Review conducted by Joseph Katz.

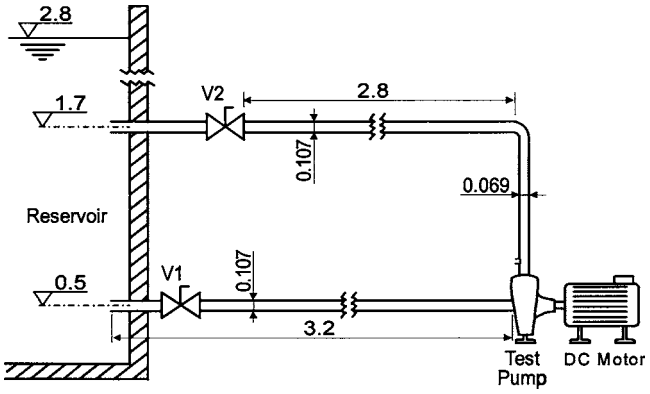

Fig. 1 Experimental setup for the pump measurements (dimensions in m)

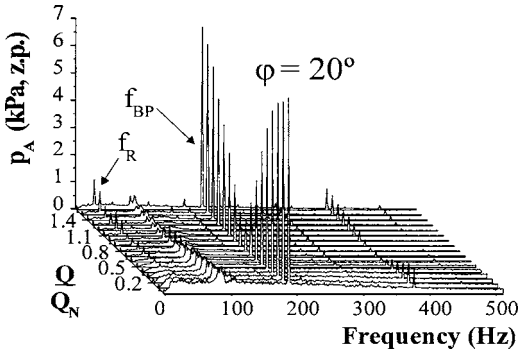

Fig. 3 Pressure spectrum as a function of flow rate (D_2 = 0.2 m). Position: 20 deg from volute tongue in the rotating direction.

Experimental Facility

In the hydraulic setup used for the experiments, water was pumped from and returned to a 100 m^3 reservoir (Fig. 1). The tested pump had a single axial suction duct and a vaneless spiral volute casing. This pump could be equipped with a shrouded seven-bladed impeller of either 190 or 200 mm outside diameter. The main parameters of this pump have been already described in previous studies [3,7,8]. The rotational speed was $\omega = 169.65$ rad/s and, therefore, the blade passing frequency is $f_{BP} = 189$ Hz. In this setup, measurement uncertainties were found to be less than ±2.5% for the flow rate and ±1.5% for the head.

For both impellers, 36 pressure taps were located, one at every 10 deg, on the volute shroud along a circumference with $R = 107$ mm (see Fig. 2). Fast-response pressure transducers Kistler 7031 were placed on these taps. After proper amplification, the resulting pressure signals and the signal from an optical tachometer were digitized and recorded in a PC equipped with a multichannel analog-to-digital conversion card. The signals were fast Fourier transform processed to obtain the pressure fluctuation data at the dominant frequencies, in particular the blade-passing frequency f_{BP}. Measurement uncertainty for the pressure fluctuations at f_{BP} was ±1.5%. A more detailed description of the test facility and the experimental procedure can be found elsewhere [3,7].

Tests were conducted at 17 flow rates, from 0% to 160% of the nominal flow rate, for both impellers. The result was the static pressure and the pressure fluctuation at the blade-passing frequency (amplitude and phase delay) for each of the 36 measurement positions, for each different operating condition. As an example, Fig. 3 shows the power spectra of the pressure at one position in the tongue region, 20 deg from the tongue edge, as a function of the flow rate for the impeller 200 mm in diameter. As expected, the unsteady content of the pressure is mostly associated with the blade-passing frequency. The amplitude is high for flow rates at the extremes, but at a minimum when the flow rate is near nominal. Further details on these results and discussion can be found in Ref. [3] or [8].

In this experimental facility, no velocity measurements were available. Therefore when studying the radial forces, only the pressure component of such forces could be calculated from the experimental data.

Numerical Model

The meshing details for the 3D model of the pump are discussed in Ref. [9]. The most relevant features of the model are the grid refinement in the volute tongue region and the sliding mesh technique, apart from the fully unsteady calculation with the blades changing relative positions for each time step. An example of the grid generated for one of the impellers is shown in Fig. 4.

The numerical code used (FLUENT) solves the fully 3D incompressible Navier-Stokes equations, including the centrifugal force source in the impeller and the unsteady terms. Turbulence was simulated with the standard k-ϵ model. Although the grid size used was not adequate to investigate local boundary layer variables, global values were well captured and the details of the flow near the tongue for the two impellers follow the usual trends

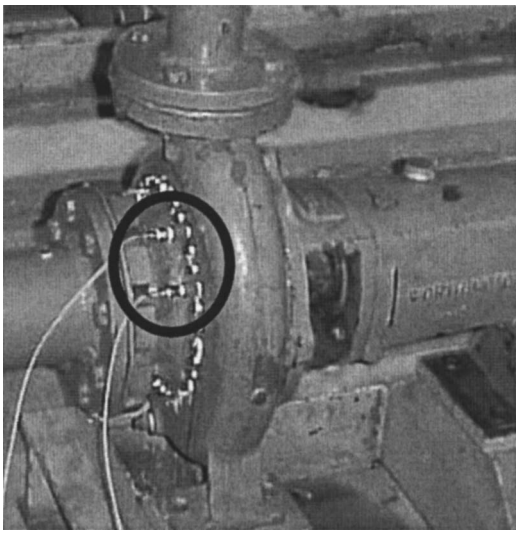

Fig. 2 View of the piezoelectric transducers mounted on the shroud side of the pump

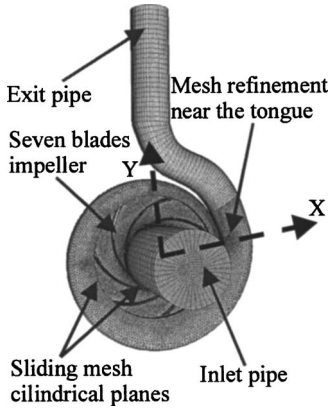

Fig. 4 Sketch of the pump unstructured mesh. (Inlet and outlet pipe portions are added).

found in the literature (for example, [1]). For such calculations, wall functions based on the logarithmic law were used. The time-dependent term scheme was second order and implicit. The pressure-velocity coupling was calculated by means of the SIMPLEC algorithm. Second order, upwind discretizations for the convection terms and central difference schemes for the diffusion terms were used.

The type of boundary conditions at both the inlet and outlet were selected based on convergence criteria and a good simulation of the flow feature through a real machine. In pumping systems, the flow rate can be controlled by modifying the circuit hydraulic resistance (for instance, by the opening or closing of a valve). This can be modeled by imposing a pressure drop at the exit as a function of the flow rate. On the other hand, a constant pressure level can be considered at the inlet side for all flow rates. Therefore, total pressure at the inlet and a pressure drop proportional to the kinetic energy at the outlet were imposed throughout the simulations. These boundary conditions avoid the definition of a uniform and constant velocity profile at the inlet or outlet, which, in general, would not be so realistic.

At the inlet and exit pipes, there is an unavoidable effect on the final flow solution as a result of the boundary conditions. A reasonable length must be added to the real machine geometry to avoid this effect as much as possible and to better simulate the pumping circuit influence. Previous models were developed with a similar technique and defined a preliminary approach to the problem, with less inlet and outlet lengths [10]. The comparison of results between the old and present models leads to the conclusion that the most recent model, presented here, provides assurance of a reasonable geometrical independence from the imposed boundary conditions.

A cluster with 12 Athlon-K7 nodes was used for the calculations. The time step used in the unsteady calculation was set to 2.94×10^{-4} s in order to get enough time resolution for the dynamic analysis. The Courant number was kept below 2, which assures very good time accuracy and numerical stability.

The number of iterations was adjusted to reduce the residuals below acceptable values in each time step. In particular, the ratio of the sum of the residuals and the sum of the fluxes for a given variable in all the cells was reduced down to the value of 10^{-5} (five orders of magnitude). After initializing the unsteady calculation with the steady solution, about five impeller revolutions were necessary to achieve the periodic unsteady solution convergence.

A final grid with about 335,000 cells was used in the present study. A comparison of the performance prediction curve for one of the impellers with this numerical model was previously presented [9]. The grid size dependence was studied through intensive tests for the bigger impeller [9]. As a conclusion, the overall performance of the pump was kept the same for the definitive grids, whose results are presented here. Particularly, even with less than half of the cells finally used for the computations, the variations observed in flow rate, head, and efficiency were kept under very reasonable values (always less than 1.2%). Besides these static value changes, a better and more detailed flow pattern, especially near the walls, could be observed with increasing cell numbers and this fact conditioned the selection of the finer grid as final, to proceed with the study.

The numerical accuracy of both steady and fluctuating results was estimated to be on the order of 2% and 1%, respectively. During the numerical study, the guidelines proposed in [11] were used and the numerical uncertainty was related to the change in certain reference values when different mesh refinements were considered. In other words, the values obtained for accuracy can be considered reasonable enough as to validate the numerical results.

The developed numerical model considers neither the leakage flows between the impeller and the casing walls nor the resulting disk friction. This would lead to an unavoidable growth in the number of cells, difficult to handle with existing calculation resources. Nevertheless, the influence of these physical volumes between the impeller shroud or hub and the exterior sidewalls on the unsteady radial forces can be assumed to be small. The effects of these volumes are mostly in a plane perpendicular to the rotational shaft, and then its major force would result in an axial direction. On the other hand, the magnitude of the flow rate circulating through these small volumes for commercial pumps with similar specific speed does not usually exceed 4% for the nominal flow rate [12].

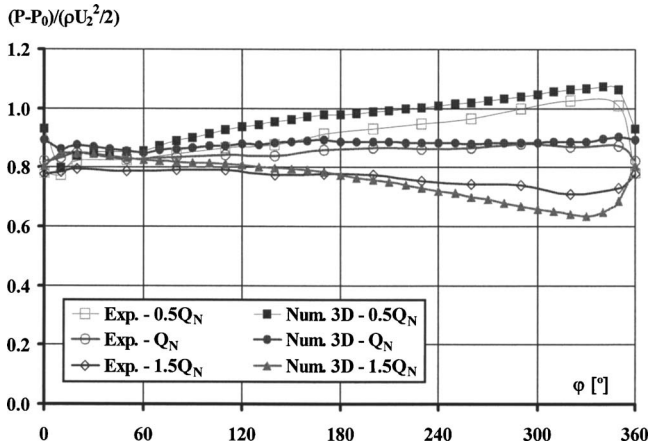

Fig. 5 Static pressure around the volute for three flow rates (comparison of the numerical and experimental results)

Steady Radial Forces for Both Impellers

The fluid dynamic interaction between the flow leaving the impeller and the static solid boundary that forms the casing of a centrifugal pump has been widely studied in the literature; see for example [6] for a general idea or [13] for a more specific problem. In particular, the effect of the radial gap was pointed out as an important parameter by many authors.

In order to show the static effect of the radial gap, first the static pressure fields on the shroud side around the volute were measured and calculated. Different flow rates were tested, ranging from 0% to 160% of the nominal flow rate, in steps of 10%. The experimental and numerical results for three of these flow rates are compared in Fig. 5 as a function of the angular position φ, which is measured from the line formed by the center of rotation and the position of the volute tongue edge.

For all the studied flow rates, the numerical results follow the trends of the experimental data, but some significant differences appear. At low flow rates, the predicted pressure values appear to be greater than the experimental ones. On the other hand, at high flow rates, at angular positions φ above 200 deg, the predicted values are smaller (Fig. 5). These differences can be attributed to not including the interstitial regions between the impeller hub and shroud and the corresponding lateral sides of the casing in the numerical model.

The effects of such interstitial regions are twofold. On one hand, some flow rate leakage circulates from the volute to the impeller inlet through the gap of the shroud side, so that the net flow rate through the impeller is greater than the external flow rate. According to the guidelines [12], the leakage flow at design operating conditions may be established at about 4% of the nominal flow rate, but its relative magnitude increases at lower flow rates. Consequently, for a given external flow rate, the predictions actually correspond to a somewhat smaller flow rate through the impeller than in the real pump, and, hence, the static pressure predictions can be expected to be greater than the experimental values. This is what can be observed in Fig. 5 for the low flow rate, or even for the high flow rate in the narrow zone of the volute ($\varphi<150$ deg).

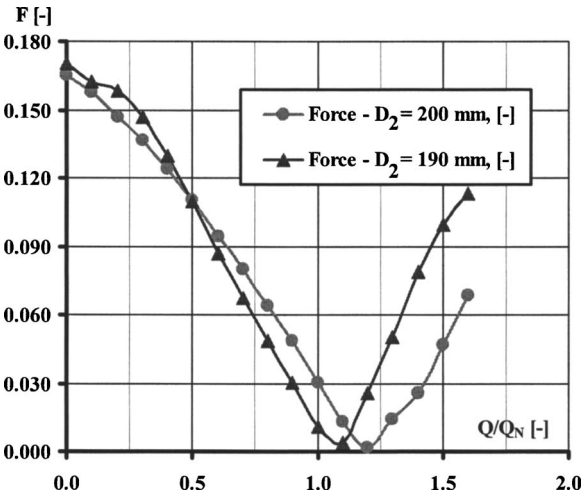

Fig. 6 Experimental comparison of the static pressure force for the two impellers

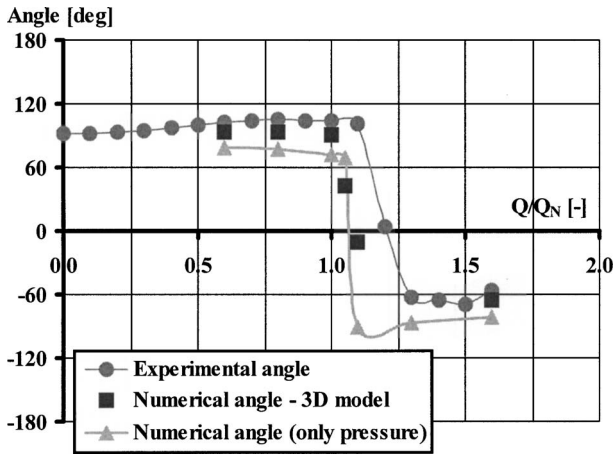

Fig. 7 Comparison of the static contribution for the force angle around the volute (angles referred to the rotation center to volute tongue direction). Impeller with D_2=200 mm.

On the other hand, the presence of the interstitial gaps between the impeller sides and the lateral walls of the casing means that the effective cross section of the volute in the real pump is somewhat greater than in the numerical model. This increment is particularly relevant at the tongue region, since it facilitates either the positive (for low flow rates) or negative (for high flow rates) flow exchange through the radial gap, i.e., it contributes to the attenuation of the static pressure difference across that tongue gap. For this reason, the experimental static pressure values for the high flow rate and angular position φ above 200 deg are greater than the corresponding numerical predictions.

From these results, and keeping in mind the existing differences, an integration to obtain the total force on the shaft was performed. For the numerical model a full integration over different axial positions is possible, whereas for the experimental measurements, only the pressure on the shroud is available. Therefore, for the experimental measurements a constant pressure distribution over the whole axial span was imposed. However, in the experimental data, the momentum due to the non-axisymmetric velocity field was not included because it was not measured.

The forces were calculated in the absolute coordinate system where the reference for the angle is the tongue position. The positive angular direction is the counter-rotating one (same reference as for the angle φ in Fig. 5).

In Fig. 6, the experimental results of the integration are shown for both impellers. An expected trend with a V shape was obtained, with a minimum force close to the nominal flow rate. If the similarity laws were applied, the same curve would be obtained because the plot is generated using nondimensional values. On the contrary, a shift of the minimum force value at higher flow rates for the bigger impeller was found. Similarity laws seem to be applicable for flow rates in the range of zero to $0.7Q_N$. Nevertheless, significant differences were found for higher flow rates. For the lowest flow range, 0 to $0.5Q_N$, the nondimensional static force is slightly higher for the smaller impeller. On the other hand, in its dimensional values and due to the bigger impeller diameter, the force is higher for the higher diameter up to the nominal flow rate. At higher flow rates, the static force is much higher for the smaller impeller, due to the lack of similarity and to the nominal flow rate shift. There is no data available to check possible differences for flow rates above $1.5Q_N$, but the trend indicates that this effect remains there and the smaller impeller produces higher static radial forces even in the nondimensional values.

Besides the difference in the calculation procedure, the numerical model captures satisfactorily the global trend for the angle of the obtained force, as shown in Fig. 7. A bigger difference in the value of the total radial force is obtained, but only for a reduced range of the flow rate, that is, for the highest flows (Fig. 8).

A shift in the minimum force position of about 10% of the nominal flow rate is seen when comparing numerical and experimental results. This could be a result of the disk friction forces induced by the leakage flows, which are not included in the numerical model yet exist in the real machine. The effect of such simplification on the calculated performance curves has been discussed in previous papers [9,14] with the conclusion that the efficiency at the nominal flow rate was overestimated. Nevertheless, the flow patterns numerically obtained were in agreement with the expected trends, for example, the location of the stagnation point in the volute tongue as a function of the flow rate, separation, and so forth.

Therefore, both static pressure and force are well captured for the bigger impeller and for the smaller one (produced as a cutback of the bigger one). These results show a minimum force at flow rates slightly higher than the nominal one for both impellers. The non-axisymmetric flow leaving the impeller has a very small influence on the static radial force at any flow rate.

Comparison of the Fluctuations in the Shroud Side Plane for Both Impellers

After the static values of the simulation were compared with the measurements for both impellers, the pressure fluctuations at the bladepassing frequency were examined. A circumferential integra-

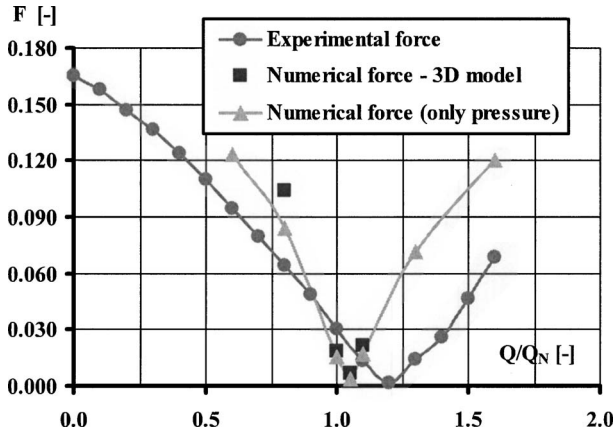

Fig. 8 Comparison of the static contribution for the force magnitude around the volute. Impeller with D_2=200 mm.

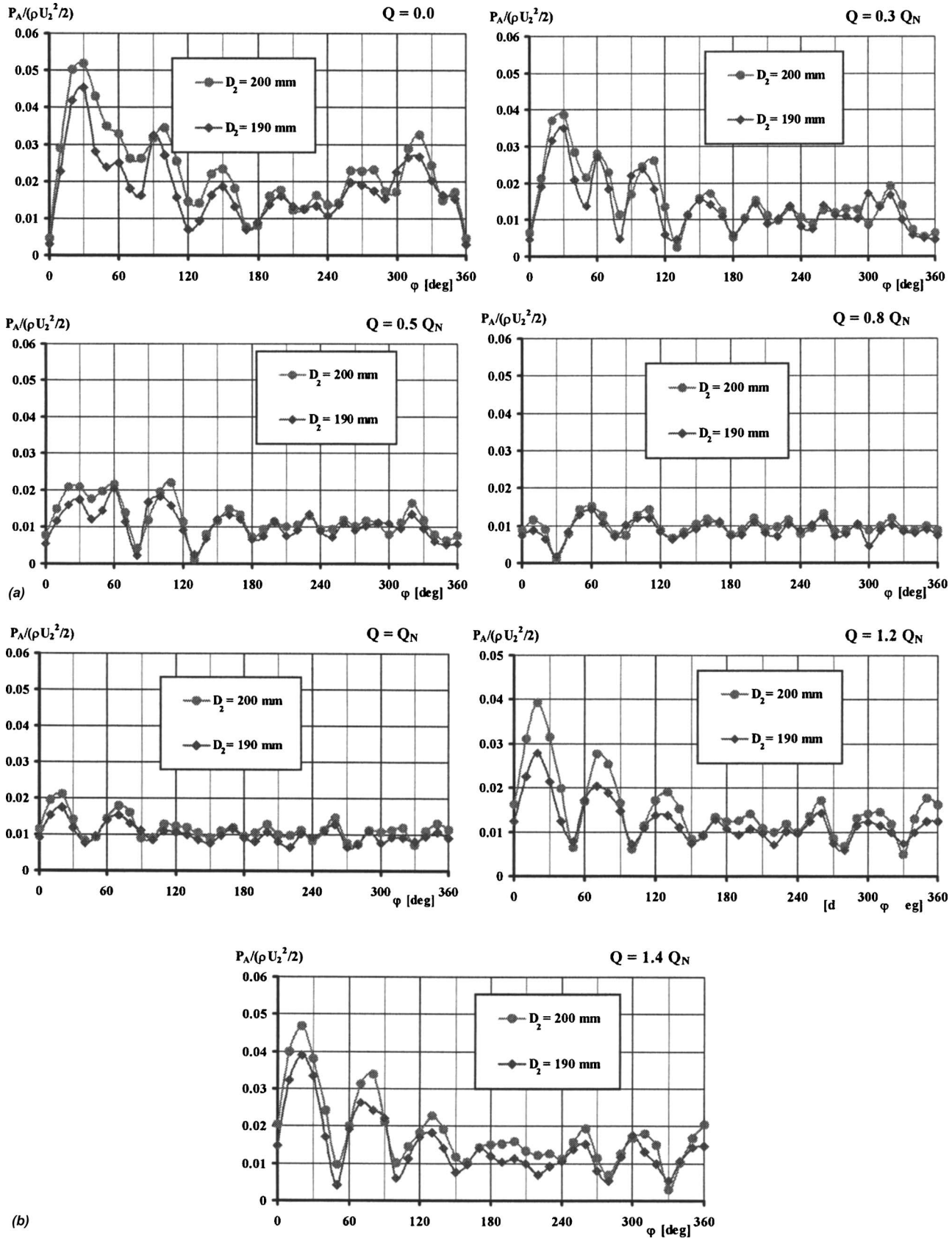

Fig. 9 (*a*) **Comparison of the pressure fluctuations at the blade-passing frequency for the two impellers $Q < Q_N$. Experimental measurements.** (*b*) **Comparison of the pressure fluctuations at the blade-passing frequency for the two impellers $Q \geq Q_N$. Experimental measurements.**

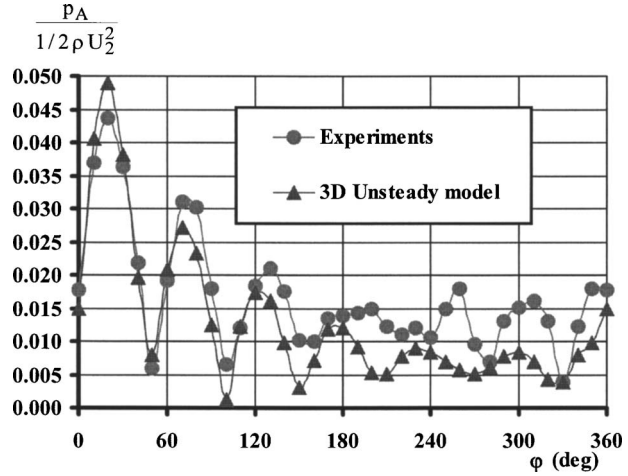

Fig. 10 Comparison of the pressure fluctuations at the blade-passing frequency for $Q=1.5Q_N$ on a shroud plane ($z=0.0$). Tongue at $\varphi=0$ deg and $D_2=200$ mm.

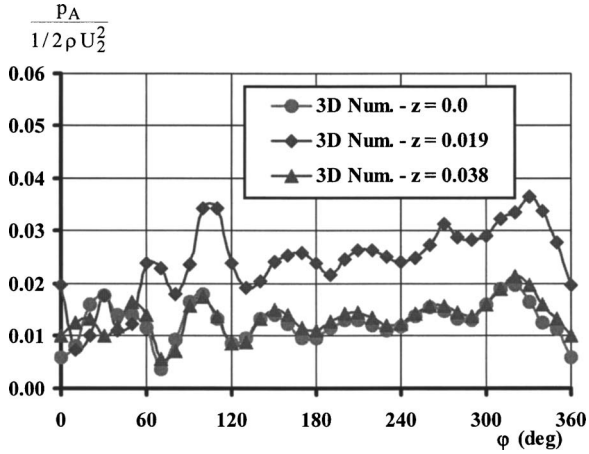

Fig. 11 Nondimensional pressure fluctuation at the blade-passing frequency for three axial positions at the volute (numerical values). The tongue is at $\varphi=0$ deg and $Q=0.5Q_N$.

tion of the pressure component at the blade-passing frequency was performed around the impeller exit position. This procedure is equivalent to performing a filtering of the pressure distribution on the volute at the blade-passing frequency for the different studied flow rates.

For this pump and under the selected operating conditions, no cavitation effects in the performance curve were found. The contribution of the dynamic effects, particularly the pressure values in the volute except at the blade-passing frequency, can be considered negligible (see Fig. 3, taken from the measurements). And this is also the case for any circumferential position. The previous statement does not mean that in other parts of the impeller or at the inlet or outlet pipes, other frequencies could show their effects. Therefore, the predominant effect is observed at the blade passing frequency. Before a full numerical to experimental comparison is performed, a comparison of the experimental results for the two impellers is analyzed (Fig. 9).

The experimental results for the two impellers are compared in Figs. 9(*a*) and 9(*b*), where six different flow rates are plotted. In these figures, the effect of the radial gap on the pressure distributions can be clearly seen.

For flow rates below the nominal (Fig. 9(*a*)), the differences in the amplitude of the pressure amplitude are quite small and limited to a region near and downstream of the volute tongue position, that is, angular positions with φ between 0 and 150 deg.

For flow rates higher than the nominal (Fig. 9(*b*)), the three different graphs show pressure amplitude differences for the two impellers are even higher and extend to all the circumferential positions.

These pressure fluctuations are also very well predicted for all flow rates by the numerical model for the bigger impeller. One example for 150% of the nominal flow rate is shown in Fig. 10. For the smaller impeller, similar conclusions can be drawn, although this study did not cover this case.

Radial Force Due to Blade-Passing-Frequency Effects

The numerically calculated pressure fluctuations at the blade-passing frequency can be used to compare different axial planes (not available in the experiments). Figure 11 shows how the unsteady pressure peak at the blade-passing frequency is not uniform over the whole axial span of the volute. This analysis for different planes was already mentioned in previous publications, but is shown and analyzed here for the sake of completeness [9].

For almost all the studied flows, a similar behavior was found. The values of the pressure fluctuations in both side planes (shroud and hub) are quite similar, but for the central plane a maximum value was obtained. This higher pressure in the center plane could be an explanation for the pair of counter-rotating vortices found in all circumferential positions, explained in more detail in [9].

In the figures that follow, the resulting radial force from the unsteady pressure fluctuations at the blade passing frequency are plotted. The horizontal component corresponds to the component of the unsteady radial force in the X direction (see Fig. 4). This direction is defined by two geometrical points: the rotational center and the volute tongue position. The vertical component (Y direction) is perpendicular in the counter-rotating direction. The results shown in the following figures trace an envelope for a force vector which rotates at the blade passing frequency. Therefore, the force completes Z rotations for each impeller one. In addition, for each force rotation, if the vector is placed in the origin of coordinates, the vector end evolves enclosed by the ellipse-like curves and would trace them. The rotation direction and the value of the nondimensionalization parameter are also added to these and following figures.

An integration procedure for the pressure fluctuations is defined taking into account the value and angular phase at the blade-passing frequency. Then, this integration will produce estimates of the radial forces at the blade-passing frequency. The integration was performed by assigning to each chosen measurement location a corresponding surface point in the impeller exit section. The spatial resolution is fixed by the 36 measurement positions. The value for the unsteady force is obtained following a procedure equivalent to that used for the static pressure, but takes into account the relative angle at this frequency for each flow rate and each impeller. Figures 12 and 13 show the results of the calculation for the two impellers based on the experimental values of the pressure fluctuations.

The integration procedure gives a force that resembles the total unsteady force, which rotates around the impeller with a complex and wide frequency range, at the blade-passing frequency. In other words, it is a calculation which filters the total unsteady force at such particular frequency. In other words, it corresponds to the component of the unsteady force at the blade passing frequency, which performs a rotation for each blade-passing period. When the force is aligned with the X axis, it would produce a radial force directed towards the volute tongue position.

For each blade-passing rotation ($2\pi/Z$ rad) the projected force for a given flow rate completes one of the elliptical shaped figures. The maximum force and angle vary with the flow rate for the smaller impeller, whereas the angle remains almost constant for the bigger impeller.

The comparison of Figs. 12 and 13 shows that the bigger impeller does not always produce a higher dynamic force. For low

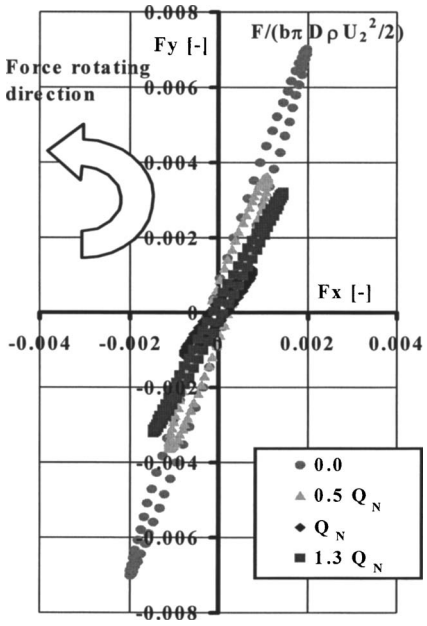

Fig. 12 Vector diagram of unsteady radial pressure force from experiments. A blade-passing period for D_2=190 mm.

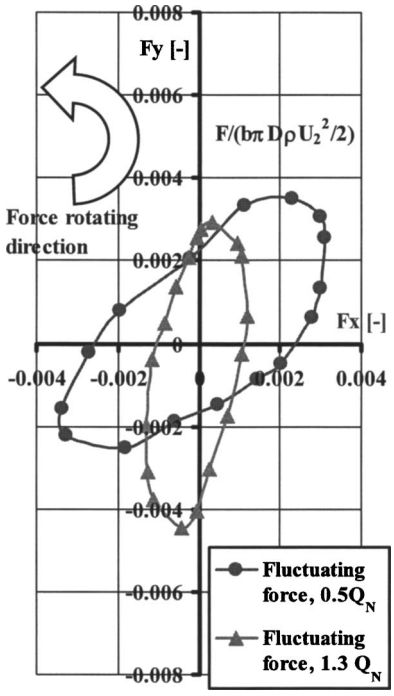

Fig. 14 Vector diagram of unsteady radial force numerically calculated during a blade passing period for D_2=200 mm

flow rates the trend was as expected (the bigger impeller gives rise to higher forces). For the higher flow rates, the opposite trend was found. From the available data, no absolute conclusion can be drawn about the origin of this difference. The extremely complex flow pattern appearing at flow rates higher than nominal could have different interactions with the external geometry and produce the measured behavior.

Using the developed numerical model, a full integration over the axial span is possible. The resulting unsteady forces for two off-design conditions of the bigger impeller are shown in Fig. 14.

Although the shape of the curve enclosing the vector forces is also elliptical, the minimum values and angles differ from the values experimentally observed. These differences can be attributed to the nonuniform axial distribution of the unsteady force at the blade-passing frequency, shown in Fig. 11.

Another effect on the force due to pressure fluctuations at the blade-passing frequency could be a result of momentum flux fluctuations. This effect might be important and has been reported in other existing studies [15]. Therefore, any comparison with the numerical results would be limited to the pressure component of such fluctuations.

If both axial span variations and velocity influence are discounted, and the calculated values are integrated following the same procedure as for the experimental results, different conclusions can be drawn. This integration was performed for the bigger impeller and the comparison between numerical and experimental results is shown in Figs. 15–17.

For all the flow rates tested, the agreement between model and experimental results is acceptable, both in value and angle. As can be observed in these three figures, the numerical model reproduces very precisely the pressure fluctuations at the blade-passing frequency, independent of the operating condition.

Therefore, when only the pressure fluctuations are considered, the numerical and experimental results describe almost the same force both in amplitude and phase. The effect of the axial span variations and the lack of uniform velocity around the volute are, thus, important when the unsteady forces are examined. This is opposite to the case of the steady forces.

Of course, when comparing the numerical results for the unsteady forces, the total force and the pressure force (which does not account for the momentum exchange) show relevant differences. A comparison of these forces is plotted in Fig. 18. At the low flow rate shown and as a general rule for the rates studied, the momentum components of the fluctuation force produce a significant increase of the envelope of the force and a slight turning of this envelope. In general, the effect of the other dynamic force components (apart from the pressure one) contributes to the unsteady radial forces damping their effects. In other words, the shape of the force envelope becomes more circular, thus decreasing the unbalanced force on the shaft.

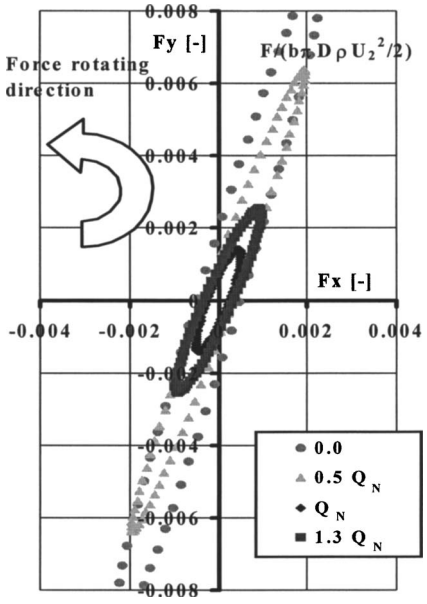

Fig. 13 Vector diagram of unsteady radial pressure force from experiments. A blade passing period for D_2=200 mm.

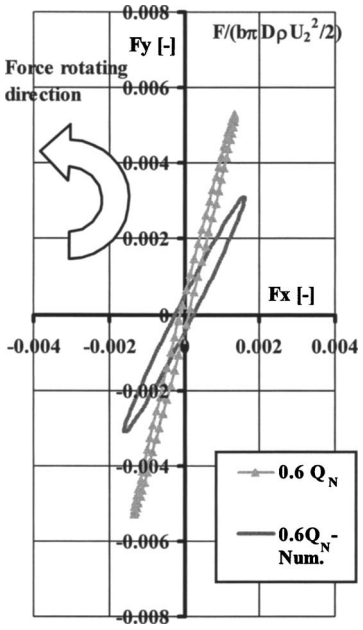

Fig. 15 Comparison of the vector diagram of unsteady radial force due to the pressure fluctuations during a blade-passing period for D_2=200 mm. Q=0.6Q_N.

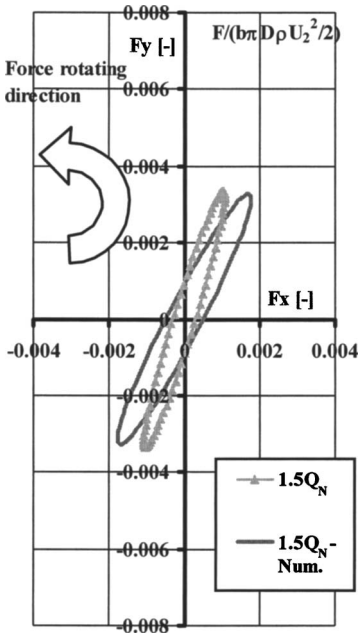

Fig. 17 Comparison of the vector diagram of unsteady radial force due to the pressure fluctuations during a blade-passing period for D_2=200 mm. Q=1.5Q_N.

Conclusions

The static and dynamic effects of the flow in a vaneless volute centrifugal pump with two different impellers were studied. The average pressure and pressure fluctuations in the shroud side of the volute have been used to obtain the resulting forces (average and at blade-passing frequency) both experimentally and numerically.

The experimental and numerical approaches used in the study have produced enough data to structure the study in two items, namely the static and unsteady effects of the flow passing through the pump (mainly pressure and radial forces). The unsteady or dynamic effects are more important at the blade-passing frequency and so this predominant frequency has been analyzed.

In spite of the difference in the average pressure at different axial planes, good agreement for the average force angle has been found. The experimental and numerical results are almost the same in the angle of the force, but differ in value for high flow rates.

However, a similar situation cannot be assumed for the blade-passing frequency. This could suggest that the general trend found

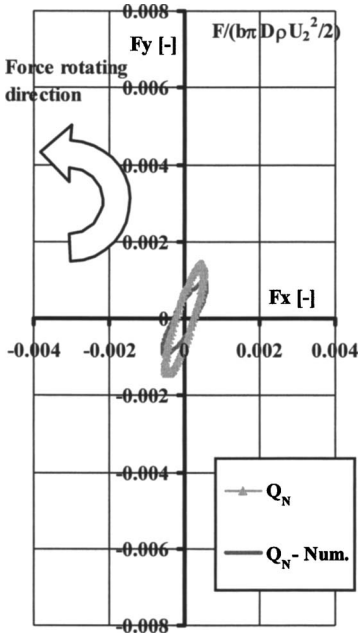

Fig. 16 Comparison of the vector diagram of unsteady radial force due to the pressure fluctuations during a blade-passing period for D_2=200 mm. Q=Q_N.

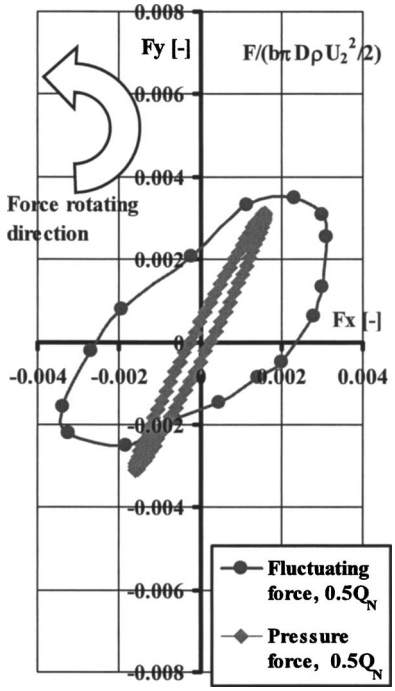

Fig. 18 Comparison of the vector diagram of unsteady radial force due to the pressure fluctuations and total force during a blade-passing period for D_2=200 mm. Q=0.5Q_N.

experimentally, considering only the pressure at the shroud side, is not a good estimate of the force at that particular frequency. In particular, the integration procedure for the unsteady forces can be used to filter the radial unsteady forces at the blade-passing frequency. The results, numerically obtained for the two impellers, have shown a lack of axial uniformity, which could be the origin of the differences observed. When the effect of the unsteady pressure pattern is isolated, the results of the numerical model and the experiments agree for all flow rates.

The difference in the radial gaps, from 15.8% to 10% of the impeller radius, does not produce a strong effect on the pressure fluctuations at any frequency and, in particular, at the blade-passing frequency. Nevertheless, an increase of 10% in the unsteady forces has been found for the bigger impeller. This could suggest that decreasing the impeller diameter in further steps would give rise to even higher forces. These dynamic effects should be considered together with the static force results, which indicated larger forces for the highest flow rates in the case of the smaller impeller.

Acknowledgment

The authors gratefully acknowledge the financial support from the Ministerio de Ciencia y Tecnologia (Spain) under Project Nos. MCT-01-DPI-2598, DPI2002-04266-C02-02, and DPI2003-09712.

Nomenclature

b_2 = impeller discharge width, m
D_2 = impeller discharge diameter, m
F = radial force due the unsteady pressure patterns in the absolute coordinate system, N
Fx, Fy = unsteady force components (horizontal and vertical) in the absolute coordinate system, N. Nondimensionalized with the product $\frac{1}{2}\pi\rho b D_2 U_2^2$
f_R, f_{BP} = rotating frequency, blade-passing frequency, Hz
k = turbulent kinetic energy, m^2/s^2
P, p_A = pressure, pressure amplitude at the blade-passing frequency, Pa. Nondimensionalized with the product $\frac{1}{2}\rho U_2^2$
P_0 = total pressure at inlet, Pa
Q, Q_N = flow rate, flow rate at nominal point, m^3/s
R = radial position, m
U_2 = peripheral velocity at impeller outlet, m/s
X, Y = main coordinates, m
Z = number of blades
z = axial position, m
ϵ = turbulent dissipation, m^2/s^3
ρ = density of the fluid (water), Kg/m^3
φ = angular position around impeller from the volute tongue location in the rotating direction, deg
ω = rotating speed, rad/s
ω_s = $\omega Q_N^{1/2}/(gH_N)^{3/4}$, specific speed

References

[1] Brennen, C. E., 1994, *Hydrodynamics of Pumps*, Oxford University Press and CETI Inc., Norwich, Vermont, USA.
[2] Chu, S., Dong, R., and Katz, J., 1995, "Relationship Between Unsteady Flow, Pressure Fluctuations, and Noise in a Centrifugal Pump-Part B: Effects of Blade-Tongue Interactions," ASME J. Fluids Eng., **117**, pp. 30–35.
[3] Parrondo, J. L., González, J., and Fernández, J., 2002, "The Effect of the Operating Point on the Pressure Fluctuations at the Blade Passage Frequency in the Volute of a Centrifugal Pump," ASME J. Fluids Eng., **124**, pp. 784–790.
[4] Dong, R., Chu, S., and Katz, J., 1997, "Effect of Modification to Tongue and Impeller Geometry on Unsteady Flow, Pressure Fluctuations, and Noise in a Centrifugal Pump," ASME J. Turbomach., **119**, pp. 506–515.
[5] Morgenroth, M., and Weaver, D. S., 1998, "Sound Generation by a Centrifugal Pump at Blade Passing Frequency," ASME J. Turbomach., **120**, pp. 736–743.
[6] Neumann, B., 1991, *The Interaction Between Geometry and Performance of a Centrifugal Pump*, MEP, London.
[7] González, J., 2000, "Modelización Numérica del Flujo no Estacionario en Bombas Centrífugas. Efectos Dinámicos de la Interacción entre Rodete y Voluta, Ph.D. thesis (in Spanish), Universidad de Oviedo, Spain.
[8] Parrondo, J. L., González, J., Pérez, J., and Fernández, J., 2002, "A Comparison Between the F_{bp} Pressure Fluctuation Data in the Volute of a Centrifugal Pump and the Predictions From a Simple Acoustic Model," *Proc. XXIst IAHR Symposium on Hydraulic Machinery and Systems*, EPFL, Lausanne, Switzerland.
[9] González, J., Fernández, J., Blanco, E., and Santolaria, C., 2002, "Numerical Simulation of the Dynamic Effects due to Impeller-Volute Interaction in a Centrifugal Pump," ASME J. Fluids Eng., **124**, pp. 348–355.
[10] Blanco, E., Fernández, J., González, J., and Santolaria, C, 2000, "Numerical Flow Simulation in a Centrifugal Pump With Impeller-Volute Interaction," ASME-FEDSM-200-11297.
[11] Freitas, C. J., 1993, "Journal of Fluids Engineering Editorial Policy Statement on the Control of Numerical Accuracy," ASME J. Fluids Eng., **115**, pp. 339–340.
[12] Karassik, I. G., Krutzsch, W. C., Fraser, W. H., and Messina, J. P., 1985, *Pump Handbook*, 2nd ed., McGraw-Hill, New York.
[13] Kaupert, K. A., and Staubli, T., 1999, "The Unsteady Pressure Field in a High Specific Speed Centrifugal Pump Impeller—Part I: Influence of the Volute," ASME J. Fluids Eng., **121**, pp. 621–626.
[14] González, J., Santolaria, C., Parrondo, J., Blanco, E., and Fernández, J., 2003, "Unsteady Radial Forces on the Impeller of a Centrifugal Pump With Radial Gap Variation," ASME-FEDSM-2003-45400.
[15] Tsukamoto, H., Uno, M., Hamafuku, N., and Okamura, T., 1995, "Pressure Fluctuation Downstream of a Diffuser Pump Impeller," FED (Am. Soc. Mech. Eng.), **216**, pp. 133–138.

Sayavur Bakhtiyarov[1]
Mechanical Engineering Department,
122 Weir Hall, 801 Leroy Place,
New Mexico Institute of Mining and Technology,
Socorro, NM 87801-4796

Mihai Dupac
103 Echlin Blvd,
Friction Products Division,
Haldex Brake Products,
Prattville, AL 36067

Ruel A. Overfelt
202 Ross Hall,
Mechanical Engineering Department,
Auburn University,
Auburn, AL 36849-5341

Shape Recovery of a Levitated Aspherical Droplet From 2D Image Information

This paper presents an image processing technique in order to predict the shape of a levitated aspherical droplet. The technique is of great importance to containerless materials processing. A majority of the electromagnetic levitation techniques utilizes two cameras at right angles to observe both transversal and frontal views. This allows obtaining two images of the droplet at instant time. In many cases, the portion of the frontal image is missing due to the heating coil. The newly developed technique allows restoration of the missing portion of the image information. The through image can be reconstructed by combining the recovered shapes. A special computer program is generated to simulate a normalized volume of the droplet. [DOI: 10.1115/1.2175157]

Keywords: electromagnetic levitation, thermophysical property measurement, image reconstruction, shape from shading

Introduction

The process of electromagnetic levitation (EML) is now a well-established technique in metallurgy. This technique consists of placing a piece of metal in a time-varying magnetic field produced by a coil carrying a high frequency electric current. The great advantage of EML process is that the levitation creates a containerless environment and prevents against the contamination of the sample with any impurities from the container walls when the metal is processed using the "traditional" melting method.

The EML process is used in metallurgical research, not only for its intrinsic theoretical value, but also for its various applications in engineering, such as thermophysical property measurement of materials. Conventional analysis for such a purpose, supposes to measure the frequencies of surface oscillation modes of the levitated droplet. Theoretical approaches for determining the oscillations of the droplet can be found in the studies by Bayazitoglu et al. [1], Bratz and Egry [2], Busse [3], and Cummings and Blackburn [4]. Chen and Overfelt [5] reported several measurements of surface tension using oscillating drop technique. The effect of static deformation on the oscillations of levitated droplets has been performed and the results are applied to demonstrate the possible improvements in surface tension measurement [6]. The complete review of theoretical and experimental works on EML is given by Bakhtiyarov and Overfelt [7].

Despite the fact that these conventional studies are very useful for a detailed description of materials properties, there are difficulties in computing the volume variations with respect to the temperature changes.

The objective of the present study is to perform a 3D reconstruction from 2D image information in order to compute the normalized volume of the aspherical droplet, and such as to predict thermophysical property of the levitated materials.

In the electromagnetic levitation experiments two cameras at right angles are usually used to take both transversal and frontal pictures of the levitated droplet. This allows obtaining two images of the droplet at instant time. In many cases, the frontal image of the levitated droplet is missing due to the blockage of the view by the heating coil.

The restoration process of a missing part from an object is known as "reverse engineering" technique. A reverse engineering typically starts with measuring an existing object so that a surface or a solid model can be deduced in order to analyze the shape errors between the parts and the model. The reverse engineering procedure covers three different fields: Electromechanical with the data capture, mathematical with the segmentation and surface-fitting tasks, and computer graphics/computational geometry for the solid model development.

In the mathematical field, several methods have been developed, such as a curvature-continuous surface technique based on the captured topological structure [8], B-spline surface fitting technique [9], quadratic surface fitting technique [10,11].

The process of image restoration can be considered as a surface fitting method, where the reconstructed surface needs to fit the initial surface. The newly developed technique called Convex Hull Cubic-Spline (CHCS) algorithm, allows restoration of the missing part of the image information.

Shape recovery is an inverse computer vision problem that transforms 2D images into 3D images. The methods, such as shape from shading (SFS), shape from texture and shape from motion are used for shape recovery. The SFS technique has been used for the first time by Horn [12] and can be regarded now as one of the classical problems in the computer vision.

A contour propagation method was used by Kimmel [13] in order to obtain both transversal and restored frontal views with different general light source estimations. The surface shape from image shading was obtained from each individual picture. The through image was reconstructed by combining the recovered shapes. A special computer program was generated to simulate the normalized volume of the droplet.

Electromagnetic Force and Surface Shape

In the process of electromagnetic levitation the applied magnetic field induces eddy currents in the metal. As a result of the interaction between the induced currents and the external magnetic field, a Lorentz force is produced and eddy currents heat or eventually melt the specimen due to the Joule effect.

The time-averaged Lorentz force density exerted on the droplet can be computed using $\mathbf{f}=\mathrm{Re}(\mathbf{j}\times\mathbf{B}^{*})$, where $\mathbf{J}$ is the induced eddy current density, $\mathbf{B}$ is the magnetic flux density, and Re(.) and * are the real part and the complex conjugate of the complex variable, respectively. If the applied current is strong enough, the electromagnetic forces can counterbalance the gravitational force to levitate the sample. The electromagnetically induced flow in the liquid metal may be turbulent, and it may affect the droplet shape.

[1]Corresponding author.

Contributed by the Fluids Engineering Division of ASME for publication in the JOURNAL OF FLUIDS ENGINEERING. Manuscript received June 17, 2004; final manuscript received September 23, 2005. Review conducted by Joseph Katz.

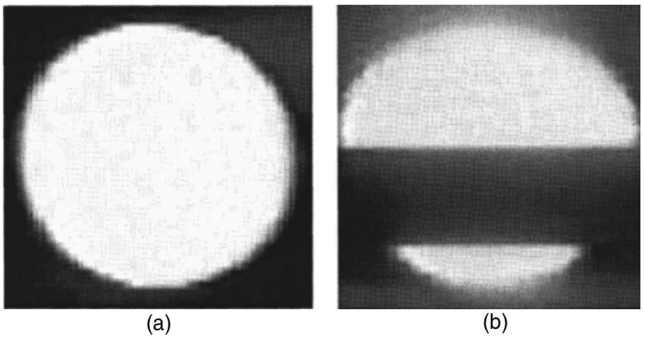

Fig. 1 Transversal (*a*) and frontal (*b*) views of the droplet in a levitation process

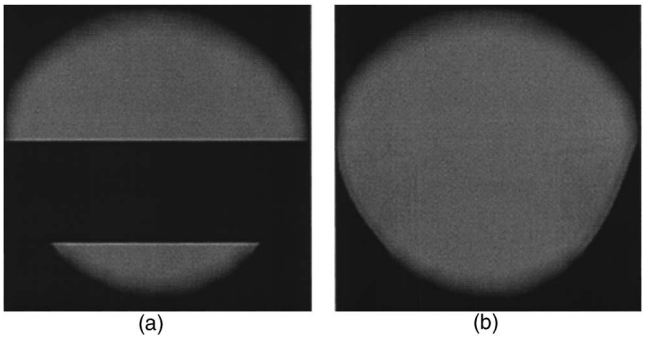

Fig. 2 Grayscale representation of frontal view of the droplet in a levitation process (*a*) and its recovered view (*b*)

Interacting with the external field, the suspended droplet can move, rotate or change the shape. The instability of the motion is produced (1) by the asymmetric distribution of the force field and (2) because of the effects of the interaction of the electromagnetic force with the molten metal. Surface oscillations, stirring and shape changes are the results of the motion instabilities.

The transversal and frontal views of the droplet in a levitation process are shown in Figs. 1(*a*) and 1(*b*), respectively.

Image Restoration

The process of image restoration can be regarded as a surface fitting method, where the reconstructed surface needs to fit trough the initial surface. In the restoration process the initial surface can be considered as an intensity information of the image.

For the restoration of the missing portion of the image, a newly developed technique based on a convex hull algorithm and cubic-spline functions is used. This new technique was used because of the local spherical property of the surface. The convex hull of a set of points is defined as the smallest convex set that includes the points. Computing a convex hull is one of the sophisticated computational geometry algorithms, and there are many variations of it. Both the Graham scan algorithm [14,15] and the "divide-and-conquer" algorithm [16] are used to determine the convex hull, but Graham scan has a low runtime constant in 2D and runs very fast there. There are numerous applications for convex hulls, and one of them is the shape analysis. For the restoration procedure we used a Graham scan algorithm. In order to complete the restoration procedure, a cubic-spline function was applied in order to interpolate the convex hull.

The function $S(x)$ is called an interpolating cubic-spline if

(1) it is a cubic polynomial

$$S(x) = S_i(x) = a_0^{(i)} + a_1^{(i)}(x - x_i) + a_2^{(i)}(x - x_i)^2 + a_3^{(i)}(x - x_i)^3 \tag{1}$$

on each interval $[x_i, x_{i+1}]$, $i = 0, 1, \ldots, m-1$

(2) it has the second continuous derivative on the segment $[a, b]$, e.g., the function is of the class $C^2[a, b]$

(3) it satisfies the condition

$$S(x_i) = y_i, \quad i = 0, 1, \ldots, m.$$

Such a spline function is a cubic polynomial on each interval $[x_i, x_{i+1}]$, $i = 0, 1, \ldots, m-1$, and hence it is defined by four coefficients.

Convex Hull Cubic-Spline algorithm:

Step 1. Apply Graham scan algorithm to determine the convex hull of the levitated droplet.

Step 2. Interpolate the point positions of the convex hull using a cubic-spline function, in order to restore the missing curve of the droplet.

Step 3. Interpolate the intensity information of the convex hull pixels using a cubic spline function in order to find the intensity information of the missing curve of the droplet.

Step 4. Store the new obtained information.

Step 5. Delete the convex hull obtained at Step 1.

Step 6. For the remaining part of the droplet repeat the algorithm.

Step 7. Put all the stored information together in order to obtain the recovered droplet.

Using the CHCS algorithm the missing part from the frontal view of the droplet in Fig. 2(*a*) was recovered as shown in Fig. 2(*b*). Figure 2(*a*) is a grayscale representation of Fig. 1(*b*).

An image of the perfect sphere (Fig. 3(*a*)) has been used to validate the restoration results. A portion of the image has been removed (Fig. 3(*b*)), in order to simulate the missing part due to blockage by the heating coil. The CHCS algorithm was applied in order to recover the missing part of the test specimen. The resulted image is shown in Fig. 3(*c*).

In order to evaluate the algorithm efficiency, the recovered image (Fig. 3(*c*)) was compared to the frontal original image (Fig. 3(*a*)) of the test specimen.

Surface Reconstruction

In order to reconstruct the image of the three-dimensional levitated droplet from the transversal and recovered frontal views, SFS algorithm was applied in this study. The SFS has been a research subject for over two decades, and it is considered as one of the classical problems of computer vision.

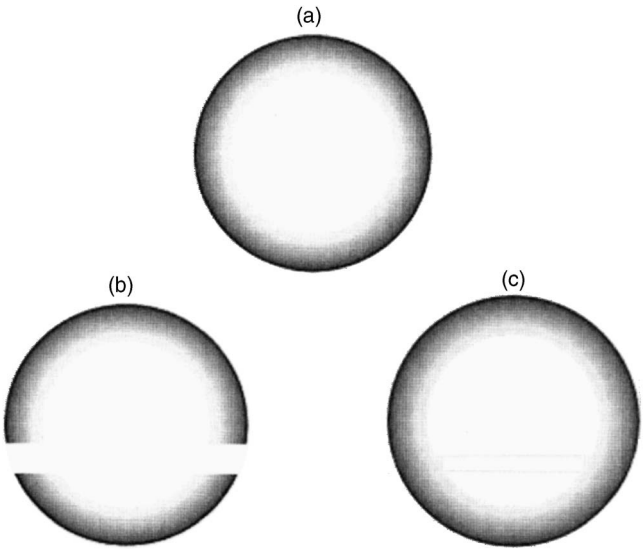

Fig. 3 A perfect sphere model to validate the restoration procedure

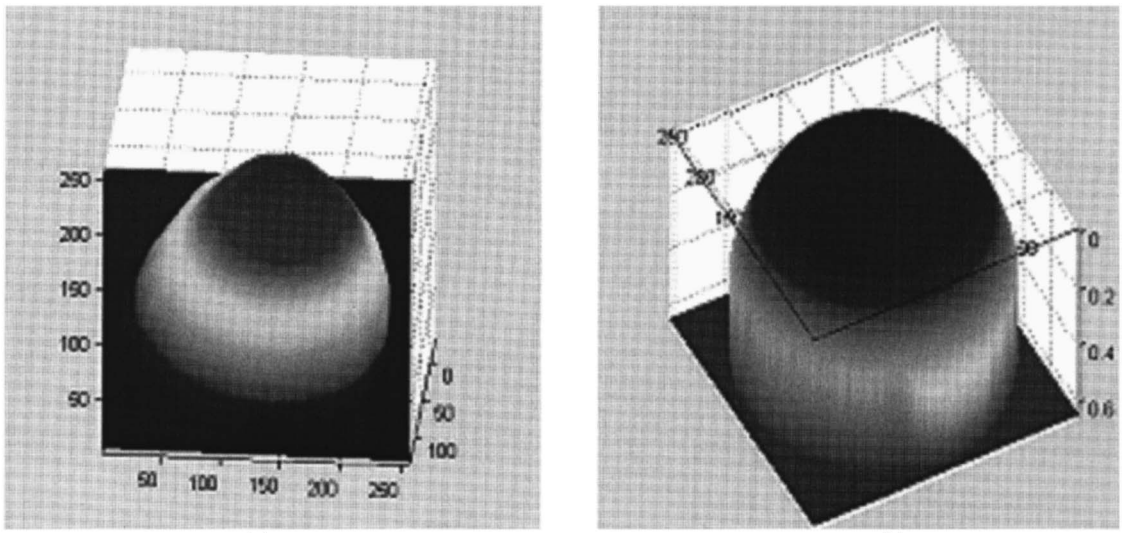

(a) (b)

Fig. 4 Reconstructed images of droplet (*a*) and perfect sphere (*b*)

In the SFS the main idea is that the local regions in an image $E(x,y)$ correspond to illuminated patches of a piecewise continuous surface whose height is represented by the function $z=f(x,y)$. The shaded image of the surface is defined as a brightness distribution $E(x,y)$. The brightness $E(x,y)$ can vary depending on the surface orientation, direction of illumination and material properties of the surface. The reflectance map $R(p,q)$, i.e., dependence between brightness and surface orientation, represents an explicit mapping between the surface normal and the brightness $E(x,y)=R(p,q)$, in terms of the surface gradient in the x and y directions, i.e., $p(x,y)=\partial z(x,y)/\partial x$ and $q(x,y)=\partial z(x,y)/\partial y$.

Shape from shading aims to recover the depth function $z(x,y)$ from the image $E(x,y)$ via a so-called shading rule or reflectance map. There are two main classes of integration techniques for finding surface height $z(x,y)$ from discrete gradients $p(x,y)$ and $q(x,y)$, local and global integration techniques. Local integration techniques perform well when the image is considered Lambertian and no noisy data are used. Here we consider Lambertian surface, with a constant radiance that is independent of the viewing direction. With respect to the definition of radiance, the radiant flux can be emitted, transmitted, and/or reflected by the surface. As a result, the brightness $E(x,y)$ is simply proportional to the orientation of the surface normal relative to the direction of the light source.

To solve the SFS, first we solved the normalized irradiance equation $E(x,y)=R(p,q)$, where the brightness $E(x,y)$ is the image of the object, and $R(p,q)$ is the reflectance of the surface patch with the local surface normal defined as $\mathbf{n}=(-p,-q,1)^T$.

Then, the surface unit normal can be written as

$$N=\frac{1}{\sqrt{1+p^2+q^2}}(-p,-q,1)^T. \tag{2}$$

For a light source at infinity, one can write the source direction as $\mathbf{i}=(-p_l,-q_l,1)^T$. Then, the unit light source direction can be written as

$$I=\frac{1}{\sqrt{1+p_l^2+q_l^2}}(-p_l,-q_l,1)^T. \tag{3}$$

Using the surface normal unit and light source direction unit for a Lambertian surface, the reflectance map was defined as $R(p,q)=I\cdot N$.

From image irradiance equation it is known that the image brightness is proportional to the radiance at the corresponding surface point. By normalizing both the reflectance map and the image intensity, the irradiance equation can be written as

$$E(x,y)=R(p,q)=I\cdot N=\frac{1+pp_l+qq_l}{\sqrt{1+p^2+q^2}\sqrt{1+p_l^2+q_l^2}}. \tag{4}$$

Solving the irradiance equation via the contour propagation method, and Eulerian formulation (for more details see Kimmel [6]) for a general light source direction, the droplet surface has been reconstructed. For the general light source direction estimation, the gradient was computed using a Sobel operator, where the average Fourier components in x and y directions were taken into the consideration.

Using the previous described method, the shape of the droplet and the shape of the perfect sphere were reconstructed as shown in Figs. 4(*a*) and 4(*b*), respectively.

The through images have been reconstructed by combining the recovered shapes. The shapes have been combined by identifying corresponding points of the images and precisely measuring the position of each point in the camera coordinates. The final reconstructed images of the droplet and the perfect sphere are shown in Figs. 5(*a*) and 5(*b*), respectively.

Volume Computation

The volume of the droplet was estimated by the following formula

$$V=\sum_{i=1}^{N} A_i\cdot h_i(P), \tag{5}$$

where A_i represents the area associated with the surface S_i, which was generated by each three adjoining points on the reconstructed droplet shape, $h_i(P)$ denotes the height from an interior point P to each surface S_i of the droplet, corrected for any scale changes in the image, and N represents the total number of surfaces generated from all disjoints of adjoining points, that clearly define the reconstructed shape.

Conclusions

The application of digital image processing to problems in materials science has grown rapidly in recent years. Digital images can be easily analyzed, using pixel counting, for example, to determine quantities such as volume and surface areas as well as the sizes and other stereological properties of individual particles or

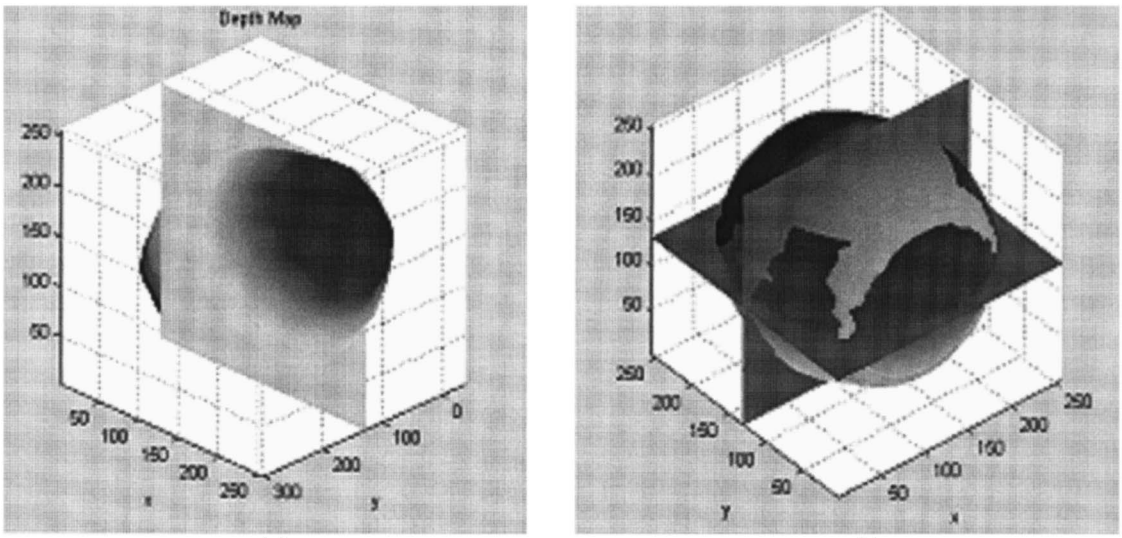

Fig. 5 Final reconstructed images of droplet (*a*) and perfect sphere (*b*)

thermophysical properties of materials. Such a technique was applied in this work in order to compute the volume of a levitated aspherical droplet.

The appropriateness of this approach has been illustrated through experiments, using a perfect sphere model and a real levitated droplet. Using a new technique (CHCS algorithm) based on correlating the computational geometry convex hull technique and the interpolation of a cubic-spline function, the missing portion of the frontal images was restored.

To validate the results an image of a perfect sphere model has been used. In order to evaluate the algorithm accuracy, the recovered image was compared to the original image of the perfect sphere. It appears that the differences between the original and recovered images (computed by subtracting the recovered image from the original one) are almost imperceptible. The algorithm performs the restoration with an accuracy of 99%.

To reconstruct the three-dimensional image of the levitated droplet from the transversal and recovered frontal views, a *shape from shading* algorithm was applied. The shapes of both the droplet and the perfect sphere were recovered. Then the shapes have been combined by identifying the corresponding points in the images and precisely measuring the position of each point in the camera coordinates. The true images have been obtained by combining the recovered shapes. A MATLAB computer program was generated to compute a normalized volume of the droplet.

Acknowledgment

The authors gratefully acknowledge the financial support received from NASA's Office of Biological and Physical Research through Marshall Space Flight Center under Cooperative Agreement No. NCC8-240.

Nomenclature

A_i = area
$\mathbf{B}$ = magnetic flux density
$E(x,y)$ = brightness
$\mathbf{f}$ = time-averaged Lorentz force density
f = frequency
h_i = height
I = light source direction unit
$\mathbf{J}$ = induced eddy current density
$\mathbf{n}$ = surface normal
N = surface normal unit
R = radius of the spherical specimen
$S(x)$ = interpolating cubic-spline
S_i = surface associated with the area A_i
V = volume of the droplet
P = interior point

References

[1] Bayazitoglu, Y., Sathuvalli, B., Suryanarayana, P. V. R., and Mitchell, G. F., 1996, "Determination of Surface Tension from the Shape Oscillations of an Electromagnetically Levitated Droplet," IEEE Trans. Magn., **8** (2), pp. 370–383.
[2] Bratz, A., and Egry, I., 1995, "Surface Oscillations of Electromagnetically Levitated Viscous Metal Droplet," J. Fluid Mech., **298**, pp. 341–359.
[3] Busse, F. H., 1984, "Oscillations of a Rotating Liquid Drop," J. Fluid Mech., **142**, pp. 1–8.
[4] Cummings, D. L., and Blackburn, D. A., 1989, "Oscillations of Magnetically Levitated Aspherical Droplets," J. Fluid Mech., **224**, pp. 395–416.
[5] Chen, S. F., and Overfelt, R. A., 1997, "Effects of Sample Size on Surface Tension Measurements of Nickel in Reduced Gravity Parabolic Flight," *Proceedings* 13th, *Symposium on Thermophysical Properties*, Boulder, CO, U.S.A.
[6] Suryanarayana, P. V. R., and Bayazitoglu, Y., 1990, "Effect of Static Deformation and External Forces on the Oscillations of Levitated Droplets," Phys. Fluids A, **5**, pp. 967–977.
[7] Bakhtiyarov, S. I., and Overfelt, R. A., 2003, "Electromagnetic Levitation: Theory, Experiments, Application," Recent Research Developments in Materials Science, **4**, pp. 81–123.
[8] Guo, B., 1997, "Surface Reconstruction: from Points to Splines," Comput.-Aided Des., **29** (4), pp. 269–277.
[9] Rogers, D. F., and Fog, N. G., 1989, "Constrained B-Spline Curve and Surface Fitting," Comput.-Aided Des., **21** (10), pp. 87–96.
[10] Chivate, P., and Jablokov, A. G., 1993, "Solid-Model Generation from Measured Point Data," Comput.-Aided Des., **25** (9), pp. 587–600.
[11] Bradley, C., Vickers, G. W., and Milroy, M., 1994, "Reverse Engineering of Quadratic Surfaces Employing Three-Dimensional Laser Scanning," Proc. Inst. Mech. Eng., **208**, pp. 21–28.
[12] Horn, B. K. P., 1987, "Obtaining shape from shading information," in *The Psychology of Computer Vision*, P. H. Winston, ed., McGraw-Hill, New York, pp. 115–155.
[13] Kimmel, R., 1995, "Tracking Level Sets by Level Sets: A Method for Solving the Shape from Shading Problem," Comput. Vis. Image Underst., **62** (2), pp. 47–58.
[14] Graham, R. L., 1972, "An Efficient Algorithm for Determining the Convex Hull of a Finite Planar Set," Information Processing Letters, **1**, pp. 132–133.
[15] Preparata, F. P., and Shamos, M. I., 1991, *Computational Geometry: An Introduction*, Springer Verlag, Berlin.
[16] Preparata, F. P., and Hong, S. J. S., 1977, "Convex Hulls of Finite Sets of Points in Two and Three Dimensions," CACM, **20** (2), pp. 87–93.

Numerical Simulation and Mixing Study of Pseudoplastic Fluids in an Industrial Helical Static Mixer

Ramin K. Rahmani
Research Assistant
e-mail: rkhrahmani@yahoo.com

Theo G. Keith
Distinguished University Professor
ASME Fellow
e-mail: tkeith@eng.utoledo.edu

Anahita Ayasoufi
Research Assistant
e-mail: aayasoufi@yahoo.com

Department of Mechanical, Industrial and Manufacturing Engineering,
The University of Toledo,
Toledo, OH 43606

Static mixers are increasingly being used to perform a variety of mixing tasks in industries, ranging from simple blending to complex multiphase reaction systems. Use of static mixers to process non-Newtonian fluids is quite common. Data on the pressure drop of non-Newtonian fluids in static mixers and the degree of mixing of materials through the mixer are very useful in the design and engineering application of these tools. This paper extends a previous study by the authors on an industrial helical static mixer and illustrates how static mixing processes of single-phase viscous liquids can be simulated numerically. A further aim is to provide an improved understanding of the flow pattern of pseudoplastic liquids through the mixer. A three-dimensional finite volume simulation is used to study the performance of the mixer. The flow velocities, pressure drops, etc., are calculated for various flow rates, using the Carreau and the power law models for non-Newtonian fluids. The numerical predictions by these two models are compared to existing experimental data. Also, a comparison of the mixer performance for both Newtonian and pseudoplastic fluids is presented. The effects of the Reynolds number of the flow and also properties of pseudoplastic fluids on the static mixer performance have been studied. It is shown that for the materials studied here, the fluid type is not effective on the degree of mixing. It is also shown that the fluid type has a major impact on the pressure drop across the mixer.
[DOI: 10.1115/1.2174058]

Keywords: static mixer, non-Newtonian fluid, Carreau law, power law, particles distribution uniformity

Introduction

Viscous liquids have to be homogenized in continuous operations in many branches of processing industries. Consequently, fluid mixing plays a critical role in the success or failure of many industrial processes. The use of static mixers has been utilized over a wide range of applications such as continuous mixing, blending, heat and mass transfer processes, chemical reactions, etc [1].

While mechanical agitators are commonly used for batch mixing, static mixers are often preferred for continuous mixing applications. Static mixers offer several advantages. They have low maintenance and operating costs, low space requirements, and no moving parts. One typical static mixer, the *helical static mixer*, consists of left- and right-twisting helical elements placed at a right angle to each other. The mixing elements, which are called segments, as one could imagine, appear to have been cut from a long periodic structure. Several of these segments are inserted in line at various locations, and housed in a pipe which squeezes the liquid through the resulting mixing element (Fig. 1). The helical insert causes a secondary flow in a plane perpendicular to the predominant axial flow. Despite wide spread usage, the way these mixers work is still not fully understood [2].

Due to the industrial importance of static mixers, many studies have been undertaken in attempts to characterize their performance. Pressure drop across a static mixer was studied experimentally for Newtonian and non-Newtonian fluids [3–7], since it is essential in order to correctly size the extruder or pump, feeding the static mixer. A set of consistency and power law indices, for a carboxymethyl cellulose (CMC) solution flow inside different static mixers, is given by Shah and Kale [3] and Chandra and Kale [4]; however Xu et al. [5], use specific values for the rheological properties of a CMC solution. Moreover, heat transfer [8], mass transfer [9], and also drop size distribution [10] in static mixers have been studied experimentally.

For a given application, besides experimentation, the modern approach to study the mixing processes is to use powerful CFD tools [11–18]. In recent years, significant progress has been made in the characterization of fluid-mechanical mixing using Lagrangian tracking techniques. The majority of the previous work on static mixers has focused on model flows that are two-dimensional in space and periodic in time. A smaller set of studies has considered simple, three-dimensional, spatially periodic flows [11,12] where a simplified, two-dimensional analytical approximation to the velocity field was obtained. Also, in spite of the fact that the majority of the working fluids in different industries are non-Newtonian, previous studies have considered mostly Newtonian fluids. A few studies considered non-Newtonian fluids for very low Reynolds numbers, e.g., [18].

A wide range of working fluids in industrial mixers are non-Newtonian, mostly pseudoplastic, fluids. These fluids are termed shear thinning since the viscosity decreases with increasing velocity gradient. Avalosse and Crochet studied the flow of a Newtonian fluid and a shear thinning non-Newtonian fluid through a Kenics mixer, using the finite-element method and periodic boundary conditions, that is, the mixer was assumed to contain an infinite number of segments. The flow Reynolds number was 0.01. [19]. They also used a Kenics device in order to mix two clays of different colors. The Reynolds number of the flow of the clays was on the order of 0.01. After the clays were flowed for some time, the system was stored in a freezer for four hours. Then, the mixture was cut into several parallel cross sections normal to the

Contributed by the Fluids Engineering Division of ASME for publication in the JOURNAL OF FLUIDS ENGINEERING. Manuscript received November 30, 2004; final manuscript received October 3, 2005. Assoc. Editor: Dennis Siginer. Paper presented at the 2004 ASME Heat Transfer/Fluids Engineering Summer Conference (HTFED2004), July 11–15, 2004, Charlotte, North Carolina, USA.

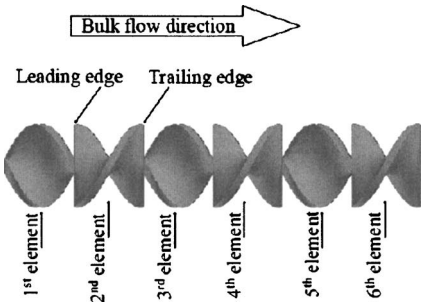

Fig. 1 A six-element static mixer

axis of mixer in order to set an experimental base to measure the accuracy of their numerical simulation. About 8000 fluid particles crossing the entry section were employed to study the mixing pattern by calculating the pathlines of particles, using the predicted velocity field as input. The number of lost particles (which is discussed later in this paper) was from 20% to 25% of the total particles released in the flow inlet. They concluded that the rheological properties of the working fluid have little influence on the obtained mixing pattern.

The non-Newtonian fluid studied here is carboxymethyl cellulose (CMC) in water. CMC is used in detergents as an antiredeposition agent, adhesives, latex paints and polishes, in foods, drugs, and cosmetics as a viscosifier, emulsion stabilizer, and thickener to improve texture, in textile warp sizing, and in paper processing. Several studies have been performed to investigate CMC properties or have reported making use of CMC properties, e.g., [20–23]. In this study, the CMC fluids are modeled by the Carreau law model for the shear stress, which provides an accurate representation of fluid behavior.

A high quality numerical solution of the velocity field can provide a suitable starting point to characterize mixing performance. This approach has allowed Lagrangian techniques to be applied to a fully three-dimensional flow in an industrial helical static mixer manufactured by the TAH, Inc. (Robbinsville, NJ). The mixer geometrical parameters are shown in Table 1. The solid material thickness of the mixer is about 22% of each segment length, which makes the zero thickness assumption of the mixer, as has been done in previous studies, questionable. Also, the ratio of the each segment length to the mixer diameter is about 0.846. In other words, the static mixer considered here is very compact; in a standard Kenics mixer, this ratio is 1.50–2.50.

In this paper, numerical techniques are applied to quantitatively evaluate the mixing performance of a static mixer for shear thinning non-Newtonian fluids. The range of modified Reynolds numbers is from $\mathrm{Re}'=0.01$ to $\mathrm{Re}'=1000$, where Re' is given by

$$\mathrm{Re}' = \frac{\rho U^{2-n} d^n}{\frac{k}{8}\left(\frac{6n+2}{n}\right)^n} \tag{1}$$

The following sections briefly present the governing equations and describe the numerical techniques used to obtain the velocity field and to characterize mixing at various Reynolds numbers, present and discuss the results, and summarize the outcomes of this work.

Table 1 Static mixer geometry

Diameter (d)	4.80 mm
Segment (element) length	4.06 mm
Thickness	0.89 mm
Entrance length	9.60 mm
Exit length	9.60 mm

Table 2 Rheological properties of CMC solutions

Concentration (ppm)	n	κ (Pa s^{n-1})	μ_0 (Pa s)	λ (s)
50	0.8118	0.00561	0.0042	0.214
500	0.7900	0.02629	0.0190	0.213
5000	0.7900	0.32839	0.3100	0.760

Analysis

Flow across a helical static mixer is a fully three-dimensional chaotic flow [24]. For steady incompressible flow, the mass conservation and the momentum equations can be written as

$$\frac{\partial u_i}{\partial x_i} = 0 \tag{2}$$

$$\rho\frac{\partial (u_i u_j)}{\partial x_j} + \frac{\partial p}{\partial x_i} = \frac{\partial \tau_{ij}}{\partial x_j} + \rho g_i + F_i \tag{3}$$

In the absence of a gravitational body force and any external body force, the two last terms on the right side of Eq. (3) are zero. The stress tensor τ_{ij} in Eq. (3) is given by

$$\tau_{ij} = \mu\left(\frac{\partial u_i}{\partial x_j} + \frac{\partial u_j}{\partial x_i}\right) - \frac{2}{3}\mu\frac{\partial u_k}{\partial x_k}\delta_{ij} \tag{4}$$

where μ is the molecular viscosity. It is mentioned that for an incompressible steady flow the last term of Eq. (4) is zero. For Newtonian fluids, μ is independent of the strain rate of the flow. For non-Newtonian fluids, viscosity becomes a function of the strain rate. Details about different models for non-Newtonian viscosity can be found in the literature, e.g., [25–27]. In this study, two models are considered: the power law model, and the Carreau model. The power law model for the shear stress uses the following equation for the viscosity:

$$\mu = \kappa e^{T/T_0}\dot{\gamma}^{n-1} \tag{5}$$

The Carreau model attempts to describe a wide range of fluids by the establishment of a curve fit to piece together functions for both Newtonian and shear-thinning non-Newtonian laws. The Carreau model uses the following equation for the viscosity:

$$\mu = \mu_\infty + (\mu_0 - \mu_\infty)[1 + (\lambda e^{T/T_0}\dot{\gamma})^2]^{(n-1)/2} \tag{6}$$

Values of μ_0, λ, κ, and n used in Eqs. (5) and (6) for this study can be found in Table 2; these values are based on the data given in [20–22]. μ_∞ is assumed to be zero. The reference temperature (T_0) is 25°C, which is also the working temperature in this study. It may be worth mentioning that the temperature has a significant effect on the rheological parameters of CMC [28].

The power law model predicts infinite viscosity when the shear rate goes to zero. The difference between values of viscosity predicted by the power law and the Carreau models is significant when the shear rate is small. Figure 2 shows the difference between the viscosities predicted by these two models for different shear rate values. This difference is non-dimensionalized by dividing by the viscosity value predicted by the Carreau model.

Numerical Simulation

The numerical simulation of the flow and mixing in the helical static mixer has been performed via a two-step procedure. In the first step, the flow velocity (and pressure) is computed. The velocity values are then used as input to the second step that consists of the calculation of the particle trajectories within the computed flow fields and also the residence time distribution of the fluid in the static mixer.

Mesh Generation. Effective numerical processes for computational fluid dynamics (CFD) problems depend on the geometric

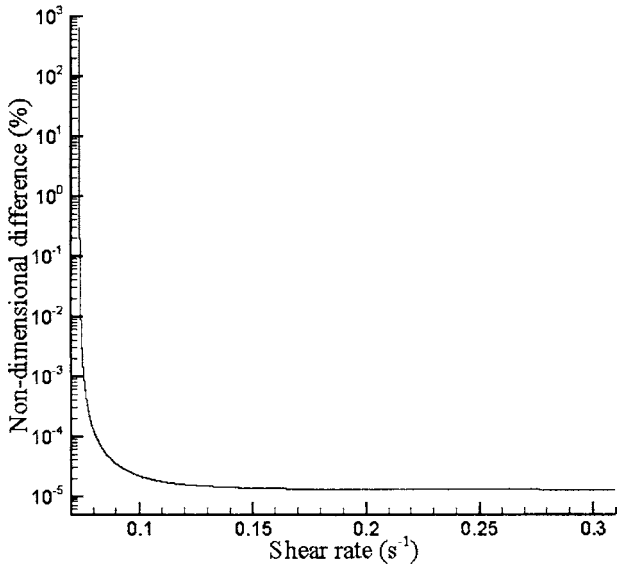

Fig. 2 Nondimensionalized difference between the viscosities predicted by the power law and the Carreau models

modeling as well as the grid generation and grid quality. An unstructured hexagonal mesh (which compares to a tetrahedral mesh is more suitable for problems involving shear flow) was generated to model the static mixer inside a pipe; the geometry was modeled completely, with no simplifications. To achieve the most accurate results from the solver all efforts have been made to maximize the quality of the mesh. Instead of the traditional approach of three-dimensional unstructured mesh generation, in which the solid and boundary surfaces grids are generated prior to the volume meshing, here a novel technique is used. The flow-field geometry is cut by a large number of parallel planes perpendicular to the pipe centerline. These parallel planes are distributed uniformly with the same distance to each other. The cross section of each plane is meshed with an interval size equal to the distance between each two planes. The next step is to mesh the flow-field volume using these cross-sectional surface meshes. This technique leads to a high quality grid, which, in turn, improves the rate of convergence of the flow solver. It also makes the particle tracking calculations much faster and easier. Different mesh quality tests were performed on the generated mesh, and validated the very high quality of the grid [29].

Flow Computation. The solver used in this study for the flow computation is a commercial code (FLUENT[1]). This code uses the Eulerian approach to solve the equations on a computational mesh, based on a cell-centered finite volume discretization. The solver is a segregated, implicit, second-order upwind [30]. All calculations were performed in double precision. To obtain second-order accuracy, quantities at the cell faces are computed using a multidimensional linear reconstruction approach [30,31]. Pressure-velocity coupling is achieved by using the SIMPLEC (SIMPLE-Consistent) algorithm [32].

Particle Tracking. To determine the efficiency of a mixer, it is necessary to establish means by which the fluid mixing can be gauged both qualitatively and quantitatively. In the present study, this was achieved by calculating the trajectories of fluid particles in the flow-field of the mixer. This method avoids the problem of excessive numerical diffusion that is observed if the species continuity equations are solved [15].

For a steady flow, the fluid particles trajectories correspond to streamlines. Therefore, trajectories are tracked by integrating the vector equation of motion, using the numerically computed velocity field as input.

$$\frac{dx_i}{dt} = u_i \tag{7}$$

Some care must be taken in integrating the Eq. (7) that describes particle motion in order to retain a sufficient degree of accuracy. To obtain an accurate global evaluation of the mixing, the study of the trajectories of a large number of particles has been undertaken.

Preliminary tests have indicated that while lower-order schemes appear to provide acceptable results, they accentuate the problem of *lost particles*, that is, particles that are trapped near a solid wall, where the local velocity is zero, or leave the computational domain. For the results presented in this paper, a fourth-order Runge-Kutta integration algorithm with adaptive step-size control was employed. To avoid problems near stagnation points, the numerical integration of the streamline equation was performed using a fixed spatial increment rather than a fixed time step. Figure 3 shows the trajectory of one particle through the mixer. By this method, the particle locations within the cross sections of the flow-field can be obtained. With these considerations, the number of lost particles was minimized. The number of lost particles is the most for the case of $\mathrm{Re}' = 1000$ and CMC concentration of 500 ppm, which is 7.14% of the particles that entered the flow-field. No attempt was made to replace lost particles by reinjection into the flow field, since this may unduly perturb the mixing analysis.

Fig. 3 Path line of one particle through the mixer

At the entry of the inlet pipe section, a large number of zero-volume and zero-mass fluid particles are distributed uniformly and trajectories of these particles are calculated by integrating Eq. (7) for each one individually. For a wide range of Reynolds numbers, the velocity field shows a periodicity matching that of the helical static mixer geometry [13], the particle tracking can take advantage of this periodicity to extend the simulation results from a six-element base-case mixer to devices of greater length. The six-element base case is divided into an entrance section (inlet tube and first two helical elements), a central periodic section (two helical elements), and an exit section (outlet tube and last two helical elements). Within the numerical method of the particle tracker, the central section can be repeated as a spatially periodic unit to extend the tracking to a mixer of any length.

Residence Time Distribution. The *Residence time distribution* (RTD) is used to characterize the uniformity of the history of fluid elements in the static mixer. A similar history for all fluid elements in the flow is a desirable feature in order to provide the uniformity of the product quality. This can be achieved by a narrow distribution of the residence times for chemical reactors. RTD for flows in a static mixer has been studied experimentally [33] and numerically [34,35]. Here, the RTD for a shear thinning, non-Newtonian, fluid in a helical static mixer was calculated by tracking about

[1]FLUENT is a registered trademark of Fluent Inc., Lebanon, NH.

30,000 uniformly spaced, zero-mass, zero-volume, particles initially located in the top half of the flowfield inlet. The trajectories of these particles were tracked through the flow via integration of Eq. (8). The residence time of each particle was measured from the point when the particle passed the cross-sectional plane of the leading edge of the first mixing element to the point when the particle crossed the cross section of the trailing edge of the last mixing element. The measured residence time is nondimensionalized by the residence time of a fluid particle traveling at the bulk flow velocity in a pipe with no mixer. Given the value of the nondimensionalized residence time (t^*) for all fluid particles which have passed the cross-sectional plane, the fraction of the volumetric flow which has a residence time between t^* and $t^* + dt^*$ can be calculated. This parameter is known as the *distribution function* $f(t^*)$.

Particles Distribution Uniformity. A perfect result of mixing of two fluids can be defined as a uniform distribution of each fluid particles in the flow-field cross section. Based on this idea, assume that the cross section of the flow is divided to very small identical in shape and size plane sectors. If N_s is the total number of plane sectors, and $N_{(i)}$ is the number of particles placed in the ith sector, then the *particle distribution function of the first kind* for the ith sector is given by

$$pd_1(i) = \frac{\left| \frac{N_p}{N_s} - N_{(i)} \right|}{N_p} \tag{8}$$

Now assume the flow-field cross section is divided into equal angles by a large number, say N_l, of symmetry lines. If the number of particles on the left side of the ith symmetry line is $N_{\text{Left}}(i)$, and the particles on the right side of this line is $N_{\text{Right}}(i)$, then the *particle distribution function of the second kind* for the ith symmetry line is given by

$$pd_2(i) = \frac{|N_{\text{Left}}(i) - N_{\text{Right}}(i)|}{N_p} \tag{9}$$

Using the particle distribution functions of the first and second kind, the *particles distribution uniformity* (PDU) can be defined as

$$\text{PDU} = \left(1 - \frac{1}{2\left(1 - \frac{1}{N_s}\right)} \sum_{i=1}^{N_s \to \infty} pd_1(i) \right) \left(1 - \frac{1}{N_l} \sum_{i=1}^{N_l \to \infty} pd_2(i) \right) \tag{10}$$

This function varies between zero (the poorest distribution of particles) and one (a totally uniform distribution of particles). It is worthwhile noticing that to obtain a meaningful value for PDU, N_s should be smaller or equal to N_p and N_l should be smaller or equal to $1/2N_p$; also each of the N_s and N_l should be greater than or equal to 2.

In this study, 501,740 zero-volume and zero-mass particles were distributed uniformly in the half circular plane of the inlet surface at the entry of the inlet pipe section. This can be viewed as a simplified model for the diametrical feeding of the mixer with two component fluids. Particle trajectories corresponding to only one of the fluids are calculated.

Structure Radius. As a quantitative measure of the fluid mixing, the size of flow structures at different flow cross sections is considered. The two-dimensional structure radius at a given axial location (r_s) normalized to the pipe radius, has been defined to correspond to the radius of the largest circle that can be drawn around a particle of one of the fluid components that does not contain any particles of the other fluid component [36]. This structure radius corresponds to the striation thickness generally measured experimentally [16].

Intensity of Segregation. In early 1950s, Danckwerts introduced the *intensity of segregation* [37]. The intensity of segregation is defined as the ratio of the variance of the concentration values over the variance of the segregated system. Toor investigated this parameter in details [38]. Dispersive mixing, as well as distributive mixing, can be characterized by the intensity of segregation [39,40]. Details about intensity of segregation can be found in the literature, e.g., [41,42]. The heterogeneity of the mixture can be represented in terms of the variance s^2 of such measurements, defined as

$$s^2 = \frac{1}{\tilde{n} - 1} \sum_{i=1}^{\tilde{n}} (c_i - \bar{c})^2 \tag{11}$$

where c_i is the concentration of traced particles and $\bar{c}$ is its average. If c_i is the same everywhere, then s^2 is zero. If the system has two immiscible phases, i.e., when all fluid elements are segregated, so that c_i at every point is either zero or one, the variance has, then, its maximum value

$$s^2_{\max} = \bar{c}(1 - \bar{c}) \tag{12}$$

The normalization of the variance to its maximum value is called intensity of segregation

$$I = \frac{s^2}{s^2_{\max}} \tag{13}$$

Intensity of segregation is a measure of the deviations of concentration within dissimilar regions of a mixture. When transposed in a CFD context, it represents a statistical measure of concentration of tracer positions over a given cross section, called a Poincaré section, for instance at the exit of the mixer [43]. It varies between zero and one. When the intensity of segregation is zero, an ideal distributive mixing is obtained. A value of one represents total segregation. In practice, however, the values of intensity of segregation, even for a very poor mixture, lie much closer to zero than to one [44].

It is also mentioned that the *coefficient of variation* (COV) can be used to measure the intensity of segregation [45]. COV is given by

$$\text{COV} = \frac{1}{c} \sqrt{\frac{\sum_{i=1}^{\tilde{n}} (c_i - \bar{c})^2}{\tilde{n} - 1}} \tag{14}$$

where c_i is the concentration of particles per unit of area in the ith computational cell, $\bar{c}$ is the average concentration, and $\tilde{n}$ is the number of cells in the grid in the given cross-section.

At the entry of the inlet pipe section, two sets of 501,740 zero-volume and zero-mass particles were distributed uniformly in each of the half circular planes of the inlet surface. Again, this can be viewed as a simplified model for the diametrical feeding of the mixer with two component fluids. To compute the value of COV, particle trajectories corresponding to both of the fluids are calculated.

G value. About 60 years ago, Camp and Stein [46] developed the root-mean-squared G value to characterize mixing in flocculation basins by analogy with the shear rate in a simple, one-dimensional, laminar shear flow (Couette flow). Although it has been demonstrated that the original derivation of the G value was flawed for three-dimensional flows and could not be universally applied to different types of mixers or different size mixers, nonetheless, the G value remains entrenched in the engineering literature and continues to be used [29]. Because of that, it is not entirely futile to use the obtained numerical results to calculate the G value and explore it. For any in-line mixer, the G value is calculated based on the energy losses that occur in the mixer as follows:

$$\text{G value} = \left(\frac{Q\Delta p}{\mu V_m}\right)^{1/2} \tag{15}$$

Numerical Solution Accuracy. It is important that the accuracy of the numerical solutions be analyzed before confidence in the predictive ability of the numerical techniques can be justified. For the present study of mixing under noncreeping flow conditions, there is unfortunately an absence of sufficiently detailed and accurate experimental data to undertake a complete validation of the numerical results. A detailed mesh convergence study has indicated that the computational mesh employed in the present study is sufficiently refined to provide good numerical resolution. The length of each computational cell is about 5.8% of the smallest edge of the geometry; and 1,691,199 computational cells were used to numerically determine the flow-field. Moreover, a study conducted using different numbers of particles for the mixing analysis, has shown that the results are independent of the number of particles. The use of an inadequate number of particles to analyze mixing gives the impression that a high level of mixing has been achieved using less number of mixing elements. As the N_p is increasing, the presence of the striations associated with the mixing process is more and more evident [29].

For the Carreau model, comparison with certain experimental values of the pressure drop across the mixer measured for the standard element twist angle shows very good agreement over a range of flow conditions $0.01 \leqslant \mathrm{Re}' \leqslant 1000$.

Results and Discussion

Using the numerical method described above, the flow in a six-element static mixer has been analyzed for a number of different flow conditions. In each case the initial conditions are set so that the axial velocity (u_1) is equal to bulk velocity and $u_2 = u_3 = 0$. The number of iterations required to obtain a converged solution was found to be a function of the flow regime. For a mesh containing 1,691,199 cells, from 830 iterations (for creeping flow) to 2320 iterations (for laminar flow) were necessary (with convergence defined as achieving a residual less than 10^{-5}, defined as the L2 norm) for the power law model. The number of iterations needed for the Carreau model ranged from 830 to 2280. The effect of the model, used for the viscosity non-Newtonian fluid, on the number of iterations needed to obtain a converged solution is not significant. For flows with the same Reynolds number and different levels of CMC concentration, the number of iterations needed to obtain a converged solution is almost the same as above.

Figure 4 shows the pressure drop through a six-element static mixer predicted by the Carreau model and the existing experimental data for a CMC concentration of 50 ppm, 500 ppm, and 5000 ppm, respectively, from top to bottom. The pressure drop values across the mixer for different Reynolds numbers predicted by the Carreau model are in excellent agreement with existing experimental data [5]. It should be mentioned that the CMC concentration level has a significant impact on the pressure drop values across the static mixer. For the same Reynolds number, the pressure drop for the case of a CMC concentration level of 500 ppm is of the order of 10^{-2} of the pressure drop for the case of a concentration level of 5000 ppm, and for the case of a concentration level of 50 ppm, it is of the order of 10^{-1} of the pressure drop, as that of a concentration level of 500 ppm. Therefore, the concentration level of a CMC solution has a major impact on the required energy to maintain the flow through the helical static mixer.

The power law model's results do not agree well with the experimental data, especially when the Reynolds number is small. Also, it was found that for a prescribed Reynolds number, the pressure drop predicted by the power law model is less accurate when the CMC concentration is higher, as it can be seen in Table 3. The values shown by the ΔP^* symbol are the predicted pressure drop by the power law model, divided by the pressure drop predicted by the Carreau model.

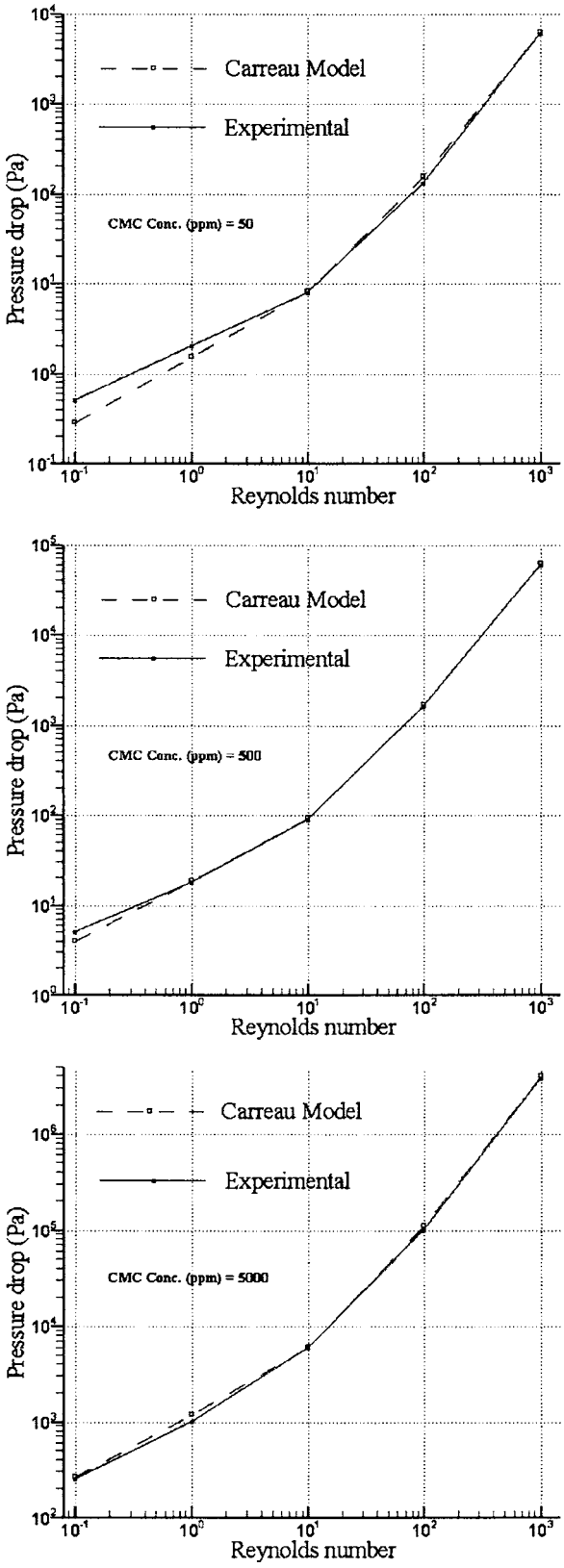

Fig. 4 Pressure drop through the six-element mixer

When the shear rates encountered in a static mixer are fairly low, variation of the viscosity value from its zero shear viscosity

Table 3 Pressure drop prediction for different Reynolds number and different CMC concentrations

Re′	CMC Conc. (ppm)	ΔP^*
0.1	50	1.034
0.1	500	1.203
0.1	5000	2.369
1	50	1.309
1	500	1.745
1	5000	3.299
10	50	1.741
10	500	2.360
10	5000	3.010
100	50	1.229
100	500	1.280
100	5000	1.282
1000	50	1.105
1000	500	1.106
1000	5000	1.106

is small. In such cases the working fluid exhibits a behavior very close to that of a Newtonian fluid; and the power law model predicts much higher values for viscosity leading to significantly higher skin friction and pressure drop across the flow-field. For the case of $\mathrm{Re}'=1$ and a CMC concentration of 50 ppm (5000 ppm), the ratio of predicted viscosity to zero shear viscosity (μ/μ_0) ranges from 0.56 to 1.00 (0.20 to 0.92); the shear rate is about zero for a large portion of the flow field and therefore the power law model is inaccurate. On the other hand for the case of a Reynolds number of 1000 and a CMC concentration of 5000 ppm, μ/μ_0 ranges from 0.05 to 0.46 and fluid behavior can be modeled with acceptable accuracy by the power law model.

The trajectories of particles injected into the mixer from the top half of the flow inlet have been calculated. Figure 5 illustrates the redistribution of particles at the end of even numbered mixing element for $\mathrm{Re}'=0.01$ and different concentration levels of CMC. The results obtained are in very good agreement with experimental data of [19]. For the case of CMC concentration of 5000 ppm, using the Carreau model, the plots of the particle positions at the end of the second, fourth, and sixth elements, respectively, from left to right (shown in Fig. 6) illustrate the redistribution of the released particles via the combined effects of flow division and reversal, resulting in stretching and folding of the observed structures. Islands of separated flow (large areas of the flow cross section which are completely occupied by only one fluid component) are distinguishable after the flow passes the second mixing element. Increasing the Reynolds number results in these few large islands breaking into several smaller islands. The islands, observed after the second elements in low Reynolds number flows, divide to narrow line shaped regions when flow passes the fourth element, and can still be recognized after the sixth element for lower Reynolds number. Again, increasing the Reynolds number results in the separated areas breaking and therefore increases the mixing of fluid particles in the same cross-section.

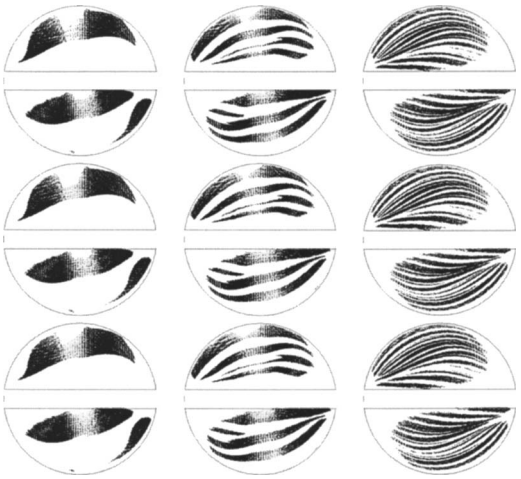

Fig. 5 Particles locations at second, fourth, and sixth element, respectively, from left to right. (CMC concentration level from top to bottom: 50 ppm, 500 ppm, and 5000 ppm)

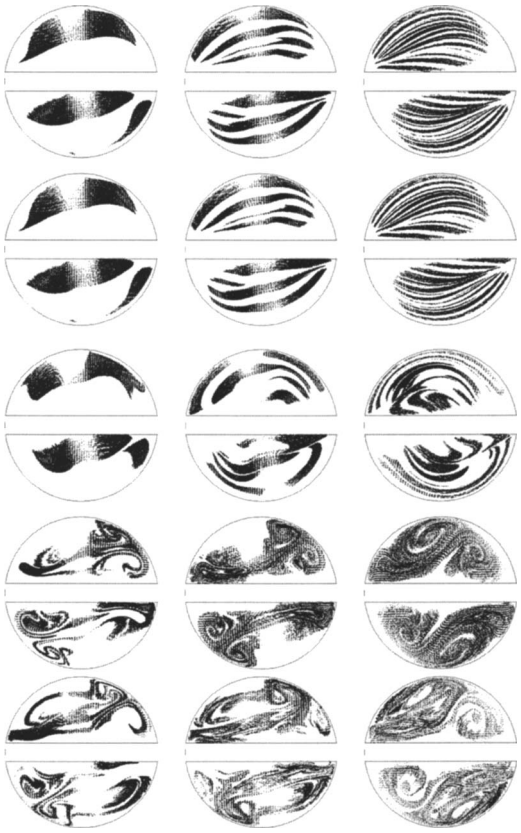

Fig. 6 Particles locations at second, fourth, and sixth element. From top to bottom $\mathrm{Re}'=0.1$, 1, 10, 100, and 1000

Comparing the obtained particle distributions for the cases of $\mathrm{Re}'=0.01$ (Fig. 5), $\mathrm{Re}'=0.1$, and $\mathrm{Re}'=1$ shows no difference between the patterns, leading to the conclusion that for very low Reynolds numbers, fluid mixing is virtually the same. The particles distribution pattern is still similar to those patterns when the Reynolds number increases to 10; however, the patterns observed for $\mathrm{Re}'=100$ and $\mathrm{Re}'=1000$ are different. Spiral motion and areas of swirling flow are distinguishable for higher Reynolds numbers. For low Reynolds numbers the particle distribution pattern is antisymmetric. This pattern can be observed after the second mixing element for higher Reynolds numbers; however, as the flow passes through the mixer the particle distribution changes into a more symmetric pattern for higher Reynolds numbers.

By observing particle distributions at different flow cross section and for different flow Reynolds numbers, it can be easily recognized that the concentration level of the non-Newtonian fluid has no impact on the fluid elements redistribution in the flow field; and therefore, structure radius in a given flow cross section is not a function of the fluid concentration [47]. Figure 7 presents structure radii at different flow cross sections for a CMC solution with a concentration level of 5000 ppm for $\mathrm{Re}'=1$. At the flow inlet $r_s=0.5$, and at the end of the first mixing element $r_s\approx 0.2$. At the end of the second element $r_s\approx 0.1$. As the flow passes through the mixer, the structure radius decreases, and the rate of decrease of the structure radius also decreases. Structure radius has virtually

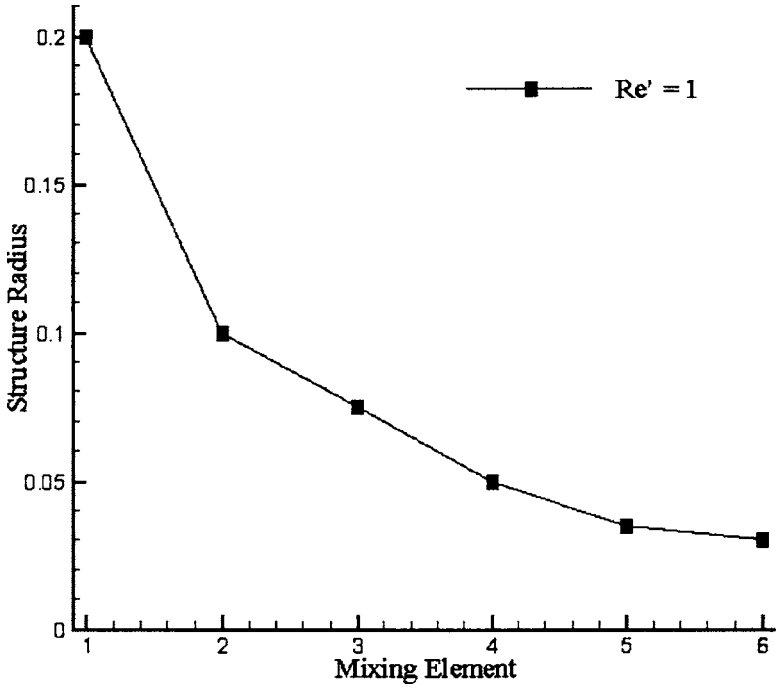

Fig. 7 Structure radii for Re′=1 (CMC concentration level: 5000 ppm)

the same pattern and virtually the same magnitudes for both Newtonian (Fig. 8) and non-Newtonian working fluids, when the flow Reynolds number is one. Figure 9 presents structure radii at the end of the last mixing element for Re′=0.1, 1, 10, 100, and 1000. The general pattern is that by increasing the Reynolds number, the structure radius should decrease. However, for Re′=10, the radius structure at the last mixing element is higher compared to the radius structure at the same flow cross-section, when Re′=1 or less. It suggests that working fluids are less mixed at this Reynolds number, compare to the case of Re′=1. Comparing the results obtained for Newtonian working fluid (Fig. 10), it is observed that the structure radius follows the same pattern. However, for Reynolds numbers equal to or greater than 10, the structure radius values are slightly different. For a flow Reynolds number of 10, r_s is about 20% larger for the non-Newtonian fluid, which suggests that the helical static mixer has a better performance when the working fluid is Newtonian; although, the overall performance of a helical static mixer is low at a Reynolds number of 10 for both Newtonian and non-Newtonian fluids.

The PDU values after the second, fourth, and sixth mixing el-

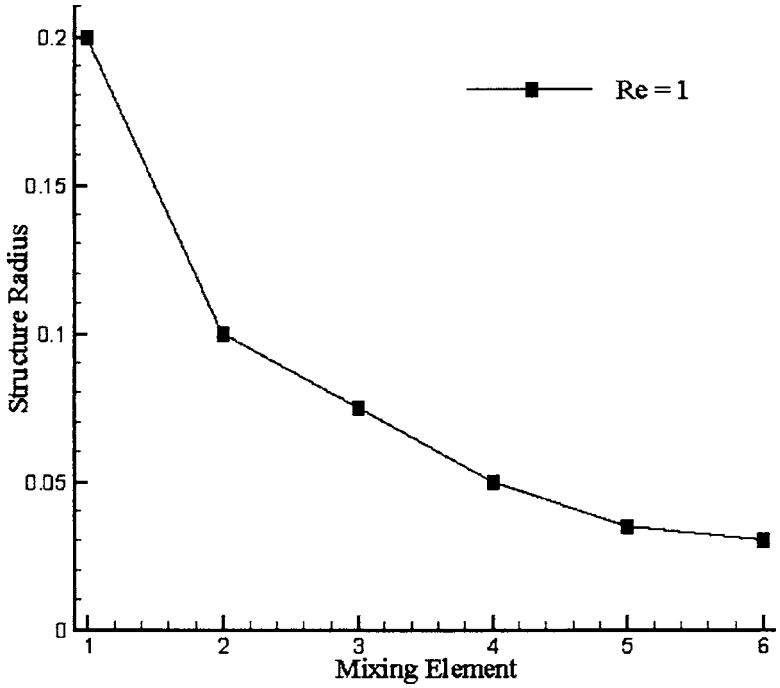

Fig. 8 Structure radii at the end of each mixing element when Re=1 (Newtonian fluid)

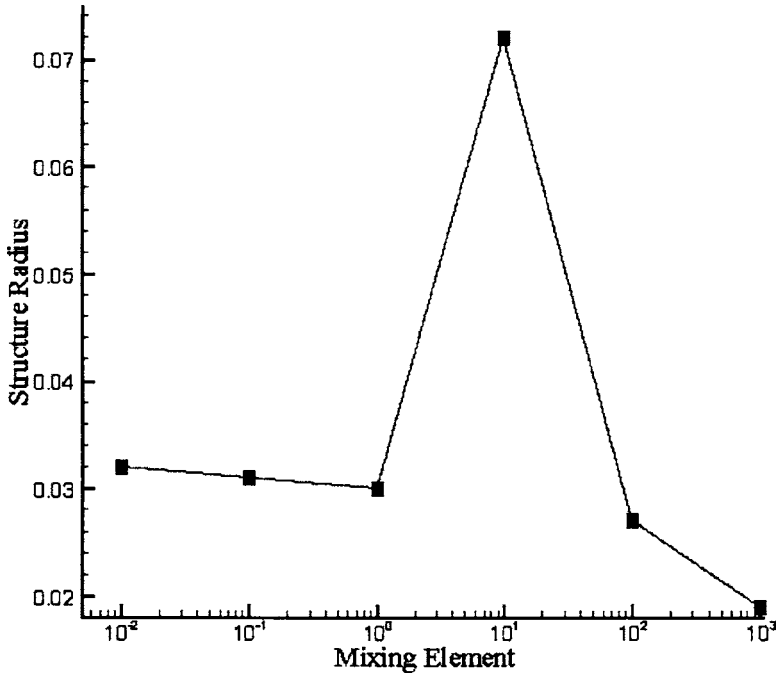

Fig. 9 Structure radii at the end of the last mixing element (CMC concentration level: 5000 ppm)

ements are shown in Fig. 11, for a CMC concentration level of 5000 ppm. These values are calculated based on the velocity fields predicted by the Carreau model. The PDU values for $Re' = 0.01$ and $Re' = 0.1$ are very close and almost the same as those shown in the figures for the case of Reynolds number equal to one. Increasing the Reynolds number increases the PDU values. A significant increase in the PDU values can be seen when the Reynolds number increases to 100; by increasing the Reynolds number from 100 to 1000, again the PDU values increase at the second mixing element, and also at the other mixing elements. For low Reynolds number flows, the PDU increases at the last mixing element, however, for higher Reynolds number flows, the PDU drops at the end of the helical static mixer. It can be explained by the fact that the flow enters the pipe with no mixer after this point and laminar flow in an empty pipe boundary conditions are applied to the flow, tending to the reduction of mixing process.

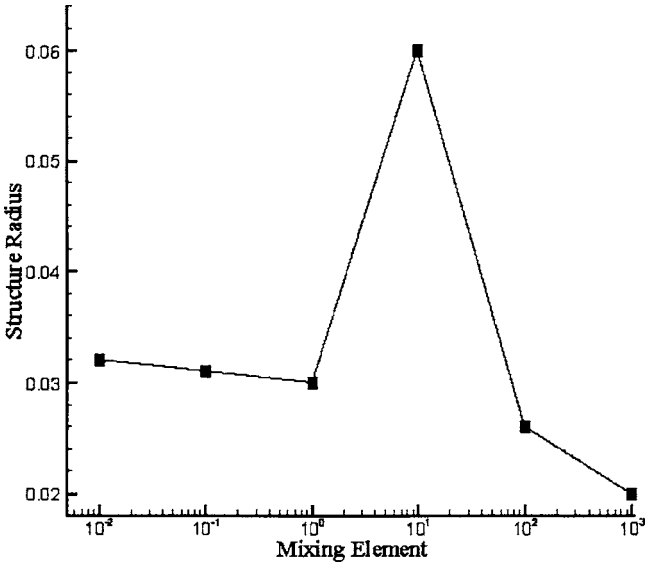

Fig. 10 Structure radii at the end of the last mixing element (Newtonian fluid)

The PDU values, for different levels of a CMC solution, are presented in Table 4. As might be expected, the PDU values for different CMC concentrations (50 ppm, 500 ppm, and 5000 ppm) are very close. The largest difference between the PDU values occurs when Reynolds number is 1000, between CMC solutions with concentration levels of 50 ppm and 5000 ppm, which is about 4%.

To quantify the performance of the helical static mixer, studied here, the obtained PDU values at the sixth mixing element for a Newtonian fluid and for a CMC solution are compared in Table 4. It is observed that, for the low Reynolds numbers flow condition, the PDU values are nearly the same for both Newtonian and shear thinning, non-Newtonian, fluids. The PDU value increases more for a CMC solution by increasing the Reynolds number to 100. For a Reynolds number of 1000, the helical static mixer manifests slightly higher performance when the working fluid is Newtonian. It should be mentioned that the difference between PDU values for a Newtonian fluid and for the non-Newtonian fluid flows studied in this particular mixer is not more than 7%. Also, as can be seen, the static mixer performance is low at a Reynolds number of 10 for both Newtonian and shear thinning, non-Newtonian, fluids.

Table 4 *PDU* values at the sixth mixing element

Reynolds number	*PDU* Newtonian	*PDU* CMC solution 50 ppm	*PDU* CMC solution 500 ppm	*PDU* CMC solution 5000 ppm
0.1	0.721	0.725	0.722	0.730
1	0.716	0.721	0.722	0.723
10	0.665	0.660	0.666	0.666
100	0.736	0.793	0.774	0.775
1000	0.776	0.800	0.770	0.767

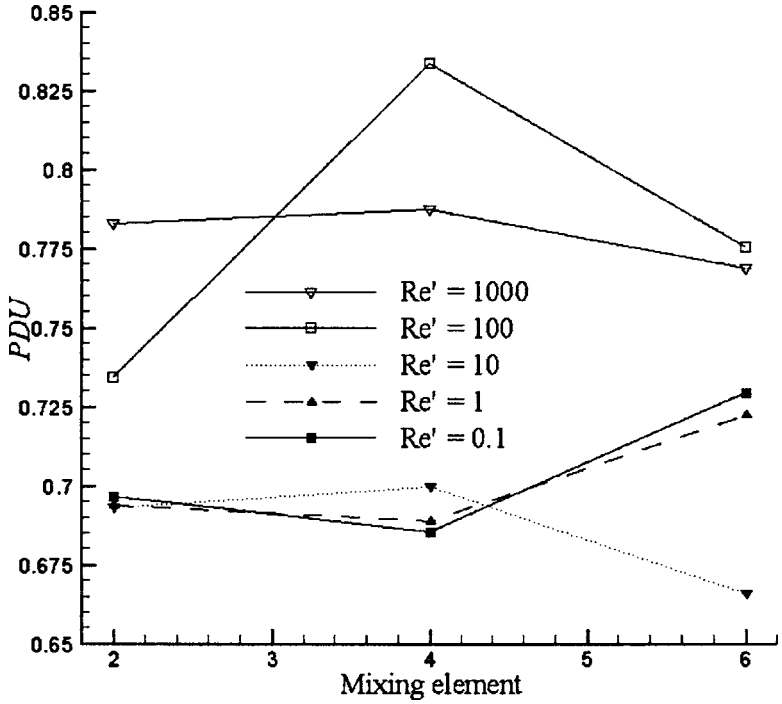

Fig. 11 *PDU* values for a CMC solution

Figure 12 shows the computed values of the intensity of segregation at the end of the last mixing element for different flow Reynolds numbers (for CMC concentrations of 5000 ppm). It follows the same pattern as PDU values; for Reynolds numbers 0.1 and 1 it has the same value, it increases at Reynolds number of 10 (indicating less mixing), it decreases significantly at Reynolds number of 100, and for $Re' = 1000$, it slightly reduces. Similarly, for laminar flow of a Newtonian fluid, it has been observed that a helical static mixer creates a better mixture around Reynolds number 100 and a poorer mixture around Reynolds number 10 [36]. Considering the methodology of determination of values of PDU and COV, it is evident that the computational time needed to determine the intensity of segregation is about two times the computational time which is needed to calculate the value of PDU for each case.

To study the RTD for different CMC concentrations in the static mixer, the distribution function for CMC concentration levels of 50 ppm, 500 ppm, and 5000 ppm were calculated and are shown

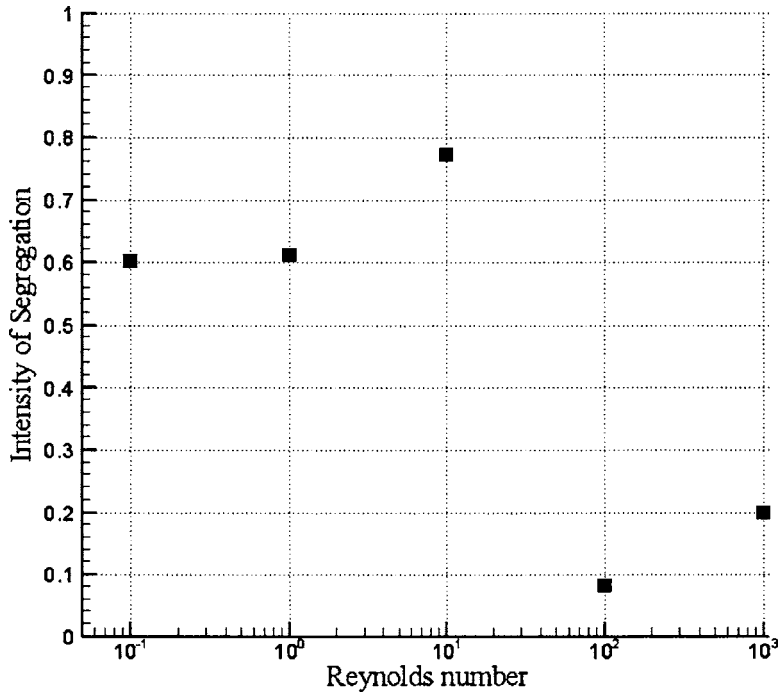

Fig. 12 Intensity of segregation at the sixth element

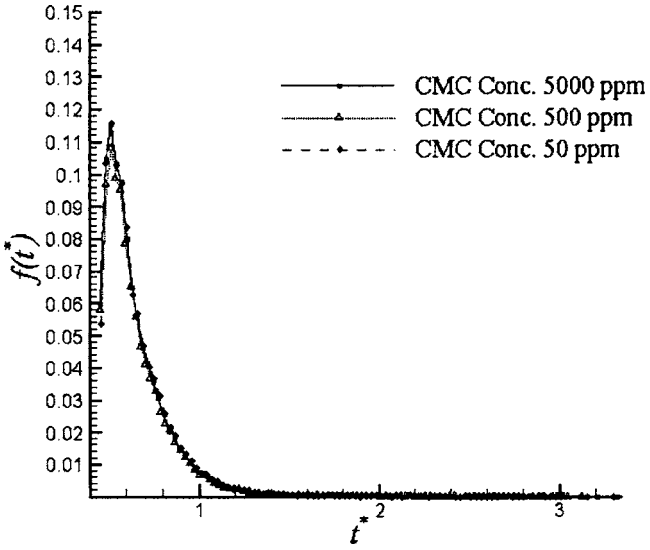

Fig. 13 Distribution function for CMC solutions flow in the six-element static mixer ($Re' = 1, dt^* = 0.01$)

in Fig. 13. As can be seen, $f(t^*)$ is almost the same for t^* values less than one.

Figure 14 shows the distribution function for a CMC concentration level of 5000 ppm, calculated for $Re' = 1$, 10, and 100. For the case of $Re' = 100$, the distribution function is more symmetric and for this case the maximum t^* is 2.4, while for $Re' = 1$, 10 the maximum t^* is about 3.2. However, for $Re' = 1$, 10 the distribution function has a higher peak value.

The *standard deviations* of the distribution function for different flow conditions are shown in Table 5. For the case of $Re' = 1$, the difference between values of the standard deviations for flows with different levels of CMC concentration are very close, indicating that the distribution function is not influenced by the rheological properties of the fluid. For the case of a CMC concentration level of 5000 ppm, as can be seen, the values of the standard deviation of the distribution function for various Reynolds numbers are significantly different. The standard deviation of the distribution function for the case of $Re' = 100$ is 22% smaller than the standard deviation of the distribution function for the case of

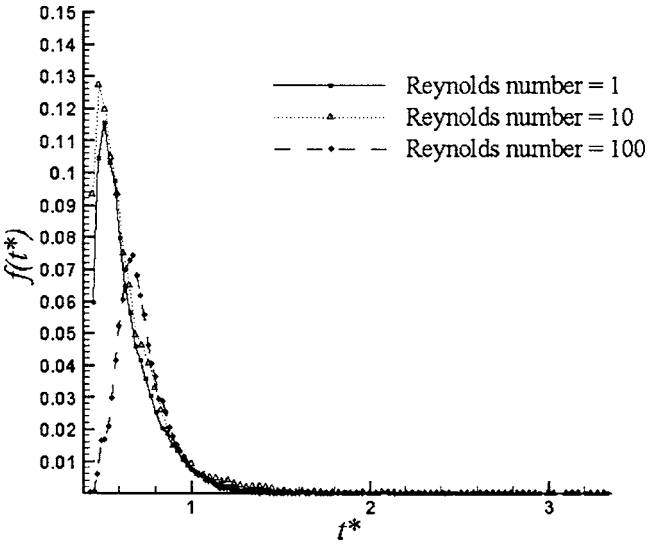

Fig. 14 Distribution function for flow in a six-element static mixer ($dt^* = 0.01$)

Table 5 Standard deviation of the distribution function

Re′	CMC Conc. ppm	Standard deviation
1	50	2.453E-002
1	500	2.373E-002
1	5000	2.460E-002
10	5000	2.622E-002
100	5000	1.919E-002
1000	5000	1.310E-002

$Re' = 1$ and it is 27% smaller than the standard deviation of the distribution function for the case of $Re' = 10$. For the case of $Re' = 1000$, the standard deviation of the distribution function is about 70% of the standard deviation of the distribution function for the case of $Re' = 100$. This indicates that the static mixer has a better residence time distribution for the flows with a higher Reynolds number.

It is important to compare the performance of the static mixer with Newtonian fluids against that with shear thinning non-Newtonian fluids. Comparison of the pressure drops across the helical static mixer using Newtonian and non-Newtonian fluids shows a significant increase in pressure drop for the case of non-Newtonian fluid, as shown in Table 6. The values denoted by the ΔP^* symbol represent the pressure drop for a Newtonian fluid (water), divided by the pressure drop for a CMC solution in water (with a concentration of 50 ppm). Adding CMC to water leads to more energy required to maintain the flow through a static mixer inside of a pipe or channel; also increasing the concentration level of CMC increases the required energy significantly.

Figure 15 shows plots of the particle positions at the end of the second, fourth, and sixth mixing elements, respectively, from left to right for a Newtonian fluid, for Re=0.1, 10, 100, and 1000. The distribution of particles for the case of Re=1, is the same as the distribution of particles for the case of Re=0.1 and therefore are not shown here. As can be seen, the locations of particles for the case of Re=10 is similar to that for the case of Re=0.1 for a Newtonian fluid. Comparing Fig. 6 to Fig. 15 shows that in the low Reynolds number flow regime, the mixing patterns are almost the same for both Newtonian and non-Newtonian fluids. Fluid mixing increases more for non-Newtonian fluids by increasing the Reynolds number to 100. For a Reynolds number of 1000, the distributions of particles for a Newtonian fluid and for a, shear thinning, non-Newtonian fluid appear almost the same.

The vorticity magnitudes at the end of the second, fourth, and sixth mixing elements are presented in Table 7 for a CMC solution (with a concentration of 5000 ppm) and in Table 8 for a Newtonian fluid (water). As may be expected, the mean and the maximum vorticity magnitudes are increased by increasing the Reynolds number. Also, it is observed that the vorticity magnitude is overall smaller at the end of the last mixing element compared to the vorticity magnitude at the other elements; the flow after the last mixing element gradually merges to that of the flow in a pipe with no mixer. For the last mixing element, the mean vorticity magnitude is much smaller than the maximum vorticity magnitude; although by increasing the Reynolds number the contrast between the mean and maximum values of vorticity at the last mixing element and the other mixing elements is less pronounced. As can

Table 6 Pressure drop comparison

Reynolds number	ΔP^*
1	0.060
10	0.116
100	0.170
1000	0.349

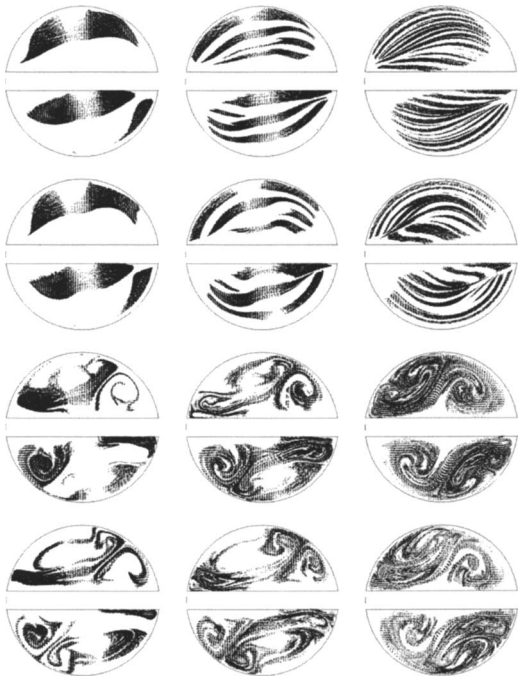

Fig. 15 Particle distributions for a Newtonian fluid at the end of the second, fourth, and sixth mixing elements (from top to bottom Re=0.1, 10, 100, and 1000)

be seen, the order of magnitude of the vorticity for a Newtonian fluid is 10^{-2} times the order of magnitude of the vorticity for a CMC solution; however both follow nearly the same pattern. Considering the given PDU values in Table 4, it is seen that the order of magnitude of vorticity has no direct bearing on mixing.

Figure 16 shows the distribution function for water. The distribution function is more similar for different Reynolds numbers for cases involving Newtonian fluids. Also, at a certain Reynolds number it has a smaller value for higher t^*, for Newtonian fluid; however, the non-Newtonian fluid manifests a more uniform pattern of distribution function.

Figures 17–19 show the calculated G values for different CMC concentration levels. All three logarithmic diagrams are slightly nonlinear, suggesting that for a given material, the G value in the static mixer studied here is proportional to the flow Reynolds number. G value increases significantly when the concentration level of CMC solution is increased, indicating that more energy is required to maintain the flow in the pipe.

To determine the mixer efficiency, a combination of pressure drop across the static mixer and the resulted mixing can be used. The mixer efficiency can be defined by using PDU value as [46]

$$\text{eff} = \frac{\text{PDU}}{\Delta \hat{P}} \tag{16}$$

Table 7 Vorticity magnitude at second, fourth, and sixth mixing element (CMC solution)

	Mean vorticity 1/s			Maximum vorticity 1/s		
Re	2nd	4th	6th	2nd	4th	6th
1	3.74E2	3.67E2	1.51E2	1.83E3	1.77E3	2.70E3
10	2.34E3	2.30E3	9.76E2	1.21E4	1.21E4	1.36E4
100	3.15E4	2.94E4	1.01E4	1.35E5	1.13E5	6.91E4
1000	2.72E5	2.52E5	1.18E5	1.30E6	1.23E6	9.31E5

Table 8 Vorticity magnitude at second, fourth, and sixth mixing element (Newtonian fluid)

	Mean vorticity 1/s			Maximum vorticity 1/s		
Re	2nd	4th	6th	2nd	4th	6th
1	2.42E0	2.40E0	9.30E-1	1.18E1	1.18E1	1.13E1
10	2.29E1	2.28E1	9.07E0	1.19E2	1.18E2	9.07E1
100	3.09E2	3.03E2	1.16E2	1.33E3	1.29E3	6.94E2
1000	5.19E3	4.78E3	2.19E3	2.20E4	2.05E4	1.16E4

The PDU value at the end of the last mixing element is used in Eq. (16). $\Delta \hat{P}$ is nondimensional pressure and is defined as

$$\Delta \hat{P} = \frac{\text{Pressure drop in a pipe with static mixer}}{\text{Pressure drop in a pipe without static mixer}} \tag{17}$$

Table 9 presents the six-element static mixer efficiency for different CMC solutions and water as a Newtonian fluid. The CMC solution concentration level has almost no impact on the mixer efficiency. Mixer efficiency is almost the same for different concentration levels, when the flow Reynolds number is the same. Helical static mixer has a higher efficiency for non-Newtonian fluids. For low Reynolds number flows, when the working fluid is non-Newtonian, static mixer efficiency is more than two times of the mixer efficiency, when the working fluid is Newtonian. For higher Reynolds numbers, the superiority of the static mixer with non-Newtonian fluids to the mixer with Newtonian fluids is less pronounced; for a Reynolds number of 1000, the helical static mixer efficiency with a non-Newtonian fluid is about 15% more than the static mixer efficiency with a Newtonian fluid.

CMC solution is a pseudoplastic or shear thinning fluid. Other kinds of non-Newtonian fluids (such as dilatant or Bingham fluids) have different rheological properties, which might lead to different static mixer performance. Also a much thicker CMC solution might lead to different static mixer performance, when the variation of the real viscosity from the apparent viscosity (zero shear viscosity) is significantly high.

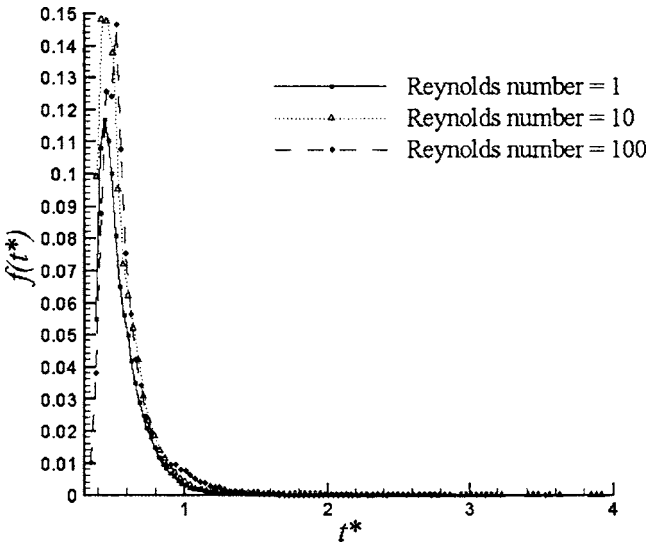

Fig. 16 Distribution function for Newtonian fluid in a six-element static mixer ($dt^*=0.01$)

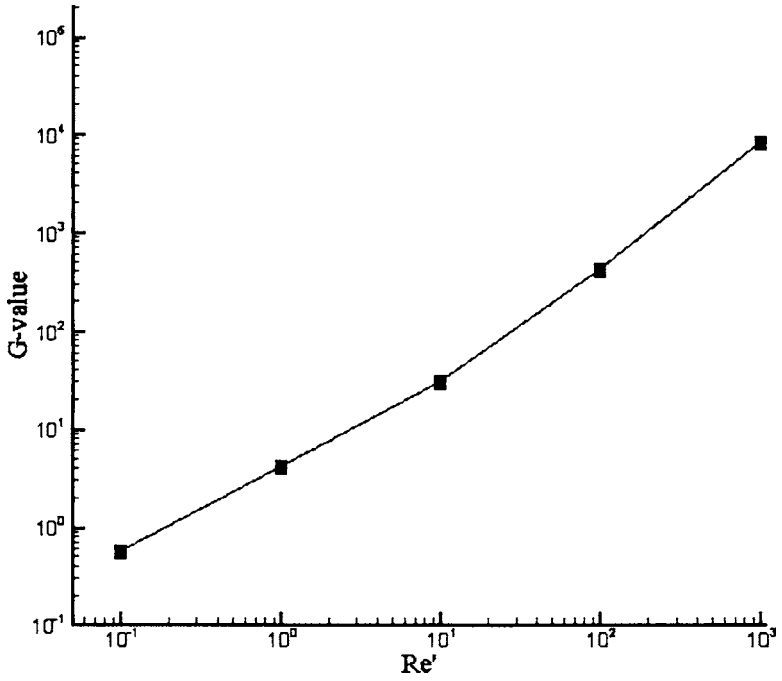

Fig. 17 G values for a six-element mixer (1/s). CMC concentration level: 50 ppm.

Conclusions

Performance of an industrial helical static mixer using pseudoplastic fluids was efficiently studied on a personal computer (PC). It was observed that the power law model can lead to unrealistic results in the study of static mixer performance.

The Reynolds number has a major impact on the performance of a static mixer. For low Reynolds number flows most of the fluid particles are separated; however, in the creeping flow regime (Reynolds numbers up to one) the mixing pattern does not vary much with the flow Reynolds number. There is a transition in the flow at higher Reynolds numbers. By increasing the Reynolds number, mixing of fluid particles is increased; however, when the Reynolds number is ten the obtained mixing is relatively poor. The rheological properties of the shear thinning material, studied here, do not affect mixing in the static mixer. It also was shown that for the same flow Reynolds number, the helical static mixer has different efficiencies for Newtonian and pseudoplastic fluids. The pressure drop across the static mixer is affected by the con-

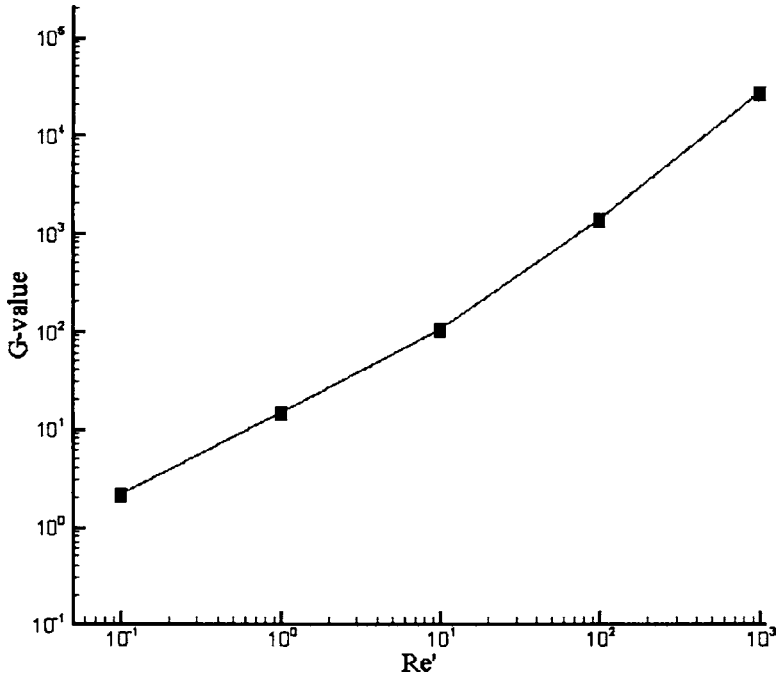

Fig. 18 G values for a six-element mixer (1/s). CMC concentration level: 500 ppm.

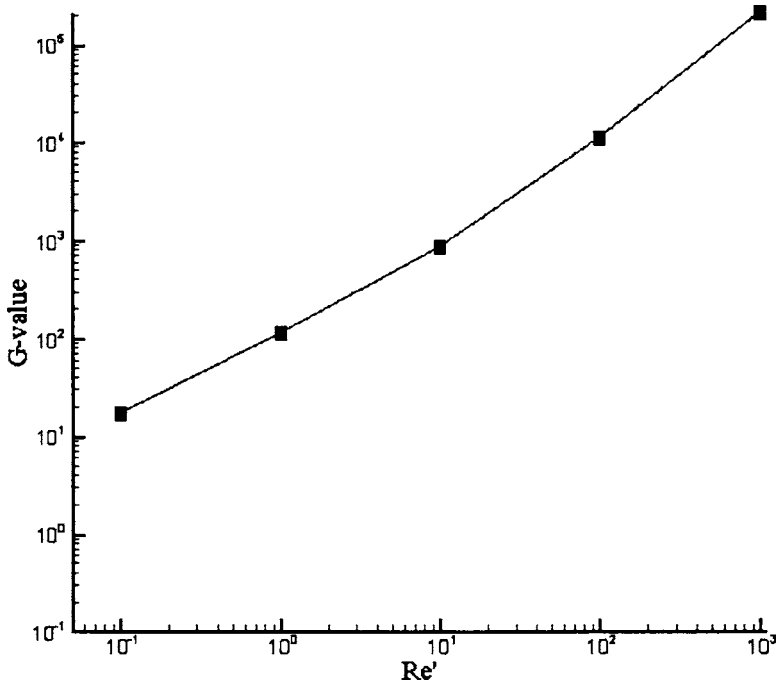

Fig. 19 G values for a six-element mixer (1/s). CMC concentration level: 5000 ppm

Table 9 Helical static mixer efficiency

Reynolds number	Efficiency (water)	Efficiency (50 ppm)	Efficiency (500 ppm)	Efficiency (5000 ppm)
0.1	0.047	0.101	0.102	0.118
1	0.047	0.090	0.093	0.117
10	0.043	0.095	0.098	0.098
100	0.025	0.037	0.036	0.037
1000	0.009	0.011	0.011	0.011

centration level. Dilute CMC solutions leads to very low pressure drops. The pressure drop increases significantly with increasing concentration level. The mixed fluid pattern, however, is not affected by the concentration level of the CMC solution.

Acknowledgment

This research was sponsored by Illinois Tool Works, Inc.

Nomenclature

$\bar{c}$ = average concentration
c_i = concentration of particles per unit of area in a cell
d = pipe diameter
E = total energy
F_i = external force vector ($i=1,2,3$)
g = acceleration due to gravity
I = intensity of segregation
K = thermal conductivity
n = power law index
p = pressure
Q = volumetric flow rate
N_p = particles released at the flowfield inlet
$pd_1(i)$ = particle distribution function of the first kind ($i=1,\ldots,N_s$)
$pd_2(i)$ = particle distribution function of the second kind ($i=1,\ldots,N_l$)
Re' = Reynolds number of non-Newtonian fluid
r_s = structure radius
t^* = nondimensionalized residence time
T = temperature
T_0 = reference temperature
U = bulk velocity
u_i = velocity vector ($i=1,2,3$)
V_m = mixer volume
x_i = Position vector ($i=1,2,3$)
$\dot{\gamma}$ = shear rate
δ_{ij} = Kronecker delta (=1 if $i=j$, =0 if $i\neq j$)
κ = consistency index
λ = time constant in the Carreau law
μ = molecular viscosity
ρ = density
τ_{ij} = stress tensor ($i,j=1,2,3$)

References

[1] Baker, J. R., 1991, "Motionless Mixers Stir Up New Uses," Chem. Eng. Prog., **87**(6), pp. 32–38.
[2] Hobbs, D. M., 1998, "Characterization of a Kenics Static Mixer Under Laminar Flow Conditions," PhD thesis, Rutgers, The State University of New Jersey, New Jersey.
[3] Shah, N. F., and Kale, D. D., 1991, "Pressure Drop for Laminar Flow of Non-Newtonian Fluids in Static Mixers," Chem. Eng. Sci., **46**, pp. 2159–2161.
[4] Chandra, K. G., and Kale, D. D., 1992, "Pressure Drop for Laminar Flow of Viscoelastic Fluids in Static Mixers," Chem. Eng. Sci., **47**, pp. 2097–2100.
[5] Xu, G., Feng, L., Li, Y., and Wang, K., 1997, "Pressure Drop of Pseudo-Plastic Fluids in Static Mixers," Chin. J. Chem. Eng., **5**(1), pp. 93–96.
[6] Pahl, M. H., and Muschlknautz, E., 1982, "Static Mixers and Their Applications," Int. Chem. Eng., **22**, pp. 197–205.
[7] Boss, J., and Czastkiewicz, W., 1982, "Principles of Scale-Up for Laminar Mixing Process of Newtonian Fluids in Fluids in Static Mixer," Int. Chem. Eng., **22**(2), pp. 362–367.
[8] Morris, W. D., and Proctor, R., 1977, "The Effect of Twist Ration on Forced Convection in the Kenics Static Mixer," Ind. Eng. Chem. Process Des. Dev., **16**, pp. 406–412.
[9] Morris, W. D., and Misson, P., 1974, "An Experimental Investigation of Mass Transfer and Flow Resistance in the Kenics Static Mixer," Ind. Eng. Chem. Process Des. Dev., **13**, pp. 270–279.
[10] Middleman, S., 1974, "Drop Size Distributions Produced by Turbulent Pipe Flow of Immiscible Fluids Through a Static Mixer," Ind. Eng. Chem. Process

Des. Dev., **13**, pp. 78–83.
[11] Khakhar, D. V., Franjione, J. G., and Ottino, J. M., 1987, "A Case Study of Chaotic Mixing in Deterministic Flows: The Partitioned-Pipe Mixer," Chem. Eng. Sci., **42**(12), pp. 2909–2926.
[12] Kusch, H. A., and Ottino, J. M., 1992, "Experiments on Mixing in Continuous Chaotic Flows," J. Fluid Mech., **236**, pp. 319–348.
[13] Hobbs, D. M., and Muzzio, F. J., 1998, "Reynolds Number Effects on Laminar Mixing in the Kenics Static Mixer," Chem. Eng. J., **70**, pp. 93–104.
[14] Jones, S. C., Sotiropoulos, F., and Amirtharajah, A., 2002, "Numerical Modeling of Helical Static Mixer for Water Treatment," J. Environ. Eng., **128**, pp. 431–440.
[15] Byrde, O., and Sawley, M. L., 1999, "Optimization of a Kenics Static Mixer for Non-Creeping Flow Conditions," Chem. Eng. J., **72**, pp. 163–169.
[16] Byrde, O., and Sawley, M. L., 1999, "Parallel Computation and Analysis of the in a Static Mixer," Comput. Fluids, **28**, pp. 1–18.
[17] Shintre, S. N., and Ulbrecht, J. J., 1983, "A Model of Mixing in Motionless Mixer," Chem. Eng. Commun., **24**, pp. 115–138.
[18] Shintre, S. N., 1988, "Mixing of Non-Newtonian (Pseudo-plastic) Fluids in Motionless Mixer," *Proc. Sixth European Conference on Mixing*, Pavia, Italy, Air Science Company, Gloucestershire, UK, pp. 551–556.
[19] Avalosse, T., and Crochet, M. J., 1997, "Finite-Element Simulation of Mixing: 2. Three-Dimensional Flow Through a Kenics Mixer," AIChE J., **43**(3), pp. 588–597.
[20] Tam, K. C., and Tiu, C., 1989, "Steady and Dynamic Shear Properties of Aqueous Polymer Solution," J. Rheol., **33**(2), pp. 257–280.
[21] Matijašić, G., and Glasnović, A., 2001, "Measurement and Evaluation of Drag Coefficient for Settling of Spherical Particles in Pseudoplastic Fluid," Chem. Biochem. Eng. Q., **15**(1), pp. 21–24.
[22] Femin, R. J., Kumaresan, G., and Velan, M., 1998, "Bed Expansion and Pressure Drop Studies in a Liquid-Solid Inverse Fluidized Bed Reactor," Bioprocess Eng., **19**, pp. 137–142.
[23] Lin, C. X., and Ko, S. Y., 1995, "Effects of Temperature and Concentration on the Steady Shear Properties of Aqueous Solutions of Carbopol and CMC," Int. Commun. Heat Mass Transfer, **22**(2), pp. 157–166.
[24] Hobbs, D. M., and Muzzio, F. J., 1997, "The Kenics Static Mixer: A Three-Dimensional Chaotic Flow," Chem. Eng. J., **67**, pp. 153–166.
[25] Tanner, R. I., 2000, *Engineering Rheology*, Oxford University Press.
[26] Wilkinson, W. L., 1960, *Non-Newtonian Fluids: Fluid Mechanics, Mixing and Heat Transfer*, Pergamon Press, London, UK.
[27] Owens, R. G., and Phillips, T. N., 2002, *Computational Rheology*, Imperial College Press, London, UK.
[28] Abdelrahim, K. A., and Ramaswamy, H. S., 1995, "High Temperature/Pressure Rheology of Carboxymethyl Cellulose (CMC)," Food Res. Int., **28**(3), pp. 285–290.
[29] Rahmani, R. K., Keith, T. G., and Ayasoufi, A., 2005, "Three-Dimensional Numerical Simulation and Performance Study of an Industrial Helical Static Mixer," ASME J. Fluids Eng., **127**(3), pp. 467–483.
[30] Warming, R. F., and Beam, R. M., 1976, "Upwind Second-Order Difference Schemes and Applications in Unsteady Aerodynamic Flows," AIAA J., **14**(9), pp. 1241–1249.
[31] Barth, T. J., and Jespersen, D., 1989, "The Design and Application of Upwind Schemes on Unstructured Meshes," Technical Report AIAA-89-0366, AIAA 27th Aerospace Sciences Meeting, Reno, Nevada.
[32] Vandoormaal, J. P., and Raithby, G. D., 1984, "Enhancements of the SIMPLE Method for Predicting Incompressible Fluid Flows," Numer. Heat Transfer, **7**, pp. 147–163.
[33] Tung, T. T., 1976, "Low Reynolds Number Entrance Flows: A Study of a Motionless Mixer," Ph.D. thesis, University of Massachusetts, MA.
[34] Kemblowski, Z., and Pustelnik, P., 1988, "Residence Time Distribution of a Power-law Fluid in Kenics Static Mixers," Chem. Eng. Sci., **43**(3), pp. 473–478.
[35] Nauman, E. B., 1991, "On Residence Time and Trajectory Calculations in Motionless Mixers," Chem. Eng. J., **47**, pp. 141–148.
[36] Byrde, O., 1997, "Massively Parallel Flow Computation With Application to Fluid Mixing," PhD thesis, Ecole Polytechnique Federale de Lausanne.
[37] Danckwerts, P. V., 1952, "The Definition and Measurement of Some Characteristics of Mixtures," Appl. Sci. Res., Sect. A, **3**, pp. 279–296.
[38] Toor, H. L., 1997, "Intensity of Segregation Revisited," AIChE J., **43**(1), pp. 263–264.
[39] Mickaily-Huber, E. S., Bertrand, F., Tanguy, P., Meyer, T., Renken, A., Rys, F. S., and Wehrli, M., 1996, "Numerical Simulations of Mixing in an SMRX Static Mixer," Chem. Eng. J., **63**, pp. 117–126.
[40] Lawal, A., and Kalyon, D. M., 1995, "Simulation of Intensity of Segregation Distributions Using Three-Dimensional FEM Analysis: Application to Corotating Twin Screw Extrusion Processing," J. Appl. Polym. Sci., **58**, pp. 1501–1507.
[41] Middleman, S., 1977, *Fundamentals of Polymer Processings*, McGraw-Hill, New York.
[42] Baird, D. G., and Collias, D. I., 1998, *Polymer Processing Principles and Design*, Wiley, New York.
[43] Heniche, M., Tanguy, P. A., Reeder, M. F., and Fasano, J. B., 2005, "Numerical Investigation of Blade Shape in Static Mixing," AIChE J., **51**(1), pp. 44–58.
[44] Onwulata, C., 2005, *Encapsulated and Powdered Foods*, Taylor & Francis, CRC Press, Boca Raton, FL.
[45] Rauline, D., Le Blevec, J. M., Bousquet, J., and Tanguy, P. A., 2000, "A Comparative Assessment of the Performance of the Kenics and SMX Static Mixers," Trans. Inst. Chem. Eng., Part A, **78**, pp. 389–395.
[46] Camp, T. R., and Stein, P. C., 1943, "Velocity Gradients and Internal Work in Fluid Friction," J. Boston Soc. Civ. Eng., **30**(4), pp. 219–237.
[47] Rahmani, R. K., 2004, "Three-Dimensional Numerical Simulation and Performance Study of an Industrial Helical Static Mixer," PhD thesis, The University of Toledo, Toledo, OH.

Numerical Analysis of Unsteady Viscous Flow Through a Weis-Fogh-Type Ship Propulsion Mechanism Using the Advanced Vortex Method

Kideok Ro[1]
School of Mechanical and Aerospace
Institute of Marine Industry,
Gyeongsang National University,
Korea
e-mail: rokid@gaechuk.gsnu.ac.kr

Baoshan Zhu
Department of Thermal Engineering,
Tsinghua University,
China

Hokeun Kang
School of Mechanical and Aerospace
Institute of Marine Industry,
Gyeongsang National University,
Korea

The velocity and pressure field of a ship's Weis-Fogh-type propulsion mechanism are studied in this paper using an advanced vortex method. The wing (NACA0010 airfoil) and channel are approximated by source and vortex panels, and free vortices are introduced away from the body surfaces. The viscous diffusion of fluid is represented using the core-spreading model to the discrete vortices. The velocity is calculated on the basis of the generalized Biot-Savart law and the pressure field is calculated from an integral, based on the instantaneous velocity and vorticity distributions in the flow field. Two-dimensional unsteady viscous flow calculations of this propulsion mechanism are shown, and the calculated results agree qualitatively with the measured thrust and drag due to unmodeled large fluctuations in the measured data. [DOI: 10.1115/1.2174059]

Keywords: computational fluid dynamics, vortex method, propulsion mechanism, unsteady flow

Introduction

The Weis-Fogh mechanism, discovered through the analysis of wing motion in the hovering flight of a small bee called Encarsia Formosa, is a novel and very efficient mechanism for lift generation [1,2]. In the flight of this tiny bee, the beating rate of the wings is about 400 Hz, and the Reynolds number R_e, defined by the wing chord and mean velocity of the leading edge, is approximately 30. The lift coefficient (C_L) is approximately 3–4 for the bee's wing, which is much higher than the lift coefficient that would be calculated for this wing in steady flow. This means that the insect efficiently generates lift using unsteady wing motion.

Tsutahara and Kimura [3] and Tsutahara et al. [4] tested a model propulsion unit, which used a two-dimensional representation of the Weis-Fogh mechanism. The model was installed in a water channel, and the tests showed that this propulsive device operates very effectively. Ro [5] simulated the unsteady flow fields around the wing by applying the conventional discrete vortex method while the propulsive mechanism was being operated, and also verified the time variation of the thrust and the drag on the wing. Because the simulation was modeled as a potential flow (no viscosity), and the wing was approximated as a plate without thickness, these numerical predictions have limitations compared with the experimental results.

This paper clearly verifies the velocity and pressure fields in the Weis-Fogh-type ship propulsion mechanism using the advanced vortex method [6], and contributes to its practical application as a propulsion system. The vortex methods [6,7] consist of a simple algorithm based on the physics of flow, and provide easy-to-handle and completely grid-free Lagrangian calculations of unsteady and vortical flows without the use of any Reynold's averaged Navier-Stokes (RANS) type turbulence models. The methods are also utilized to devise an advanced scheme of simulating the unsteady viscous flow through a Weis-Fogh-type ship propulsion mechanism.

Numerical Method

A Model of a Propulsion Device. Figure 1 shows the analytical model of a Weis-Fogh-type ship propulsion mechanism. The figure shows the upper part of the model; the wing in the water channel oscillates up and down, and the hydrodynamic forces on the wing pull it to the left (the direction toward which the ship is progressing). This model is identical to the Tsutahara and Kimura model [3], and so a brief synopsis of it will be sufficient.

A wing is installed in a square channel. When the point p corresponding to the center axis of the wing is oscillated back and forth along the y axis, the wing first opens at point p from the lower surface (opening stage). Then, maintaining an open angle α, the wing moves upward (translating stage), and finally rotates and closes on the upper surface (closing stage) through the reciprocal motion of point p. It then executes an opening stage at the upper surface once more, moves downward, and repeats the closing stage at the lower surface.

Originally, in the Weis-Fogh mechanism, circulation in the opposite direction is formed at each wing, as a pair of flat-plate wings open while their trailing edges touch. Through the principle of mirror images, the combination of channel walls and a single wing represents the same flow.

Introduction of a Nascent Vortex Elements. The model of the Weis-Fogh-type propulsion mechanism utilizes the driving system shown in Fig. 1. Comparing it with the results of Ro's experiment [5], the numerical model is set up to duplicate the experimental conditions, and the shape of the wing is also set at NACA0010, as given in the reference. By calculating the velocity and the pressure fields of this propulsion unit during the movement of the wing shown in Figs. 1(a) and 1(b) for every time step, we can predict the thrust and drag of the unit. The movement of the wing at the opening and closing stages is easily represented by combin-

[1]Corresponding author.

Contributed by the Fluids Engineering Division of ASME for publication in the JOURNAL OF FLUIDS ENGINEERING. Manuscript received January 5, 2005; final manuscript received December 12, 2005. Assoc. Editor: Yu-Tai Lee.

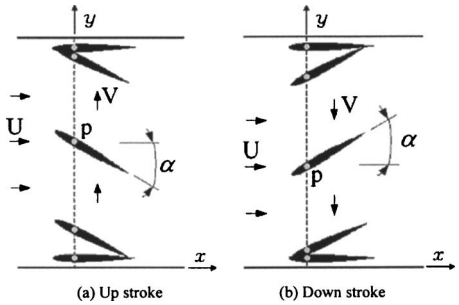

Fig. 1 A model of propulsion mechanism

ing the translating and rotating motions. Two kinds of panels, source panels and vortex panels, are distributed on the surfaces of each object. A vortex panel resembles a vortex sheet with the vorticity distributed along the solid boundary of the object. At this time, the unknowns that should be determined at each time step are the source strength on the panel for M pieces and the circulation around the wing and two walls of the water channel. These unknowns are obtained using the Neumann condition in Eq. (1) at the center of the source panel for M pieces ($i=1,2,3,\ldots,M$), and the theorem of Kelvin in Eq. (2) for the circulation of each object perimeter, $\Gamma_b=\gamma_{\mathrm{bs}}\cdot S_b$.

$$\left\{\sum_{j=1}^{M}(\boldsymbol{u}^{\mathrm{sp}}+\boldsymbol{u}^{\mathrm{vp}})_{ij}+\sum_{k=1}^{N}\boldsymbol{u}_{ik}^{\mathrm{vo}}+\mathrm{U}\right\}\boldsymbol{n}_i=\boldsymbol{u}_i\cdot\boldsymbol{n}_i \tag{1}$$

$$\Gamma_b+\sum_{k=1}^{N_b}\Gamma_{bk}^{\mathrm{vo}}=0 \tag{2}$$

Here $\boldsymbol{u}^{\mathrm{sp}}$, $\boldsymbol{u}^{\mathrm{vp}}$, and $\boldsymbol{u}^{\mathrm{vo}}$ are the induced velocities deduced from the source panels, the vortex panels, and the vortex elements introduced into the flow field; U and $\boldsymbol{u}_i$ are the uniform flow and the velocity of the i-th control point; $\boldsymbol{n}_i$ is the unit normal vector at the i-th point; γ_{bs} represents the circulation per unit length for each object along the perimeter S_b and $\Gamma_{bk}^{\mathrm{vo}}$ is the circulation of the vortex element that is emitted by each object. Here, assuming that γ_{bs} is uniformly distributed around the object, it can be obtained from $\gamma_{\mathrm{bs}}=\Gamma_b/S_b$, then $\boldsymbol{u}^{\mathrm{vp}}$ is calculated by γ_{bs}. In the case of the conventional vortex method, this situation was found to be numerically unstable. In this paper, however, by considering a double fold of the source and vortex panels, the above unstable numreical problem could be eliminated.

Figure 2 illustrates the schematic of the thin vorticity layer and the introduction of the nascent vortex elements. The vorticity field near the solid surface is represented by the proper distribution of the vorticity layers and the discrete vortex elements to satisfy the nonslip condition on the body surface. A thin vorticity layer with thickness h_i is considered along the body surface, and the solid body is discretized using source panels, as shown in Fig. 2. Assuming that the flow is two dimensional and that there is a linear distribution of the velocity in the thin vorticity layer, and for the simplicity of illustration, suppose the body is stationary, the normal convective velocity V_c on the outer boundary of the vorticity layer can be expressed using the relation of continuity of flow and the no-slip condition on the body surface for the element of the vorticity layer [abcd] as

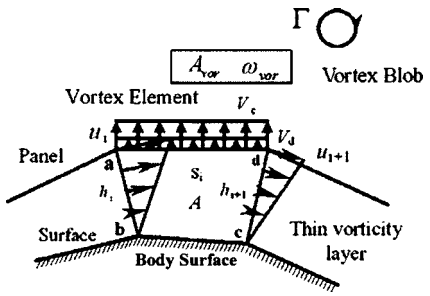

Fig. 2 Thin vorticity layer and nascent vortex element

$$V_c=\frac{1}{s_i}\left\{\frac{h_iu_i}{2}-\frac{h_{i+1}u_{i+1}}{2}\right\} \tag{3}$$

in which s_i, h_i, and u_i represent the panel length, the thickness of the vorticity layer, and the tangential velocity at the panel edge. As the body is movable, Eq. (3) is still valid when u_i, is a velocity relative to the moving body.

On the other hand, the vorticity of the thin shear layer diffuses through the panel into the flow field. In order to account for this vorticity diffusion, a diffusion velocity was employed in the same manner as the vorticity layer spreading method proposed by Kamemoto [6]. The vorticity layer spreading method is based on the viscous diffusion of the vorticity in the shear layer developing over a suddenly accelerated plate wall. In this case, the displacement thickness of the vorticity layer (δ) diffuses over time as $\delta=1.136(\nu t)^{0.5}$ from the solid surface at time t. Differentiating δ by t and substituting the thickness of the vorticity layer h_i into δ, we obtain the diffusion velocity V_d at the outer boundary of the vorticity layer as

$$V_d=\frac{1.136^2\nu}{h_i+h_{i+1}} \tag{4}$$

Here, ν is the kinematic viscosity of the fluid. If the value of (V_c+V_d) becomes positive, a nascent vortex element is introduced in the flow field, where the thickness h_{vor} and the vorticity ω_{vor} of the vortex element are obtained as follows:

$$h_{\mathrm{vor}}=(V_c+V_d)dt \tag{5}$$

and

$$\omega_{\mathrm{vor}}=\frac{\Gamma}{A+A_{\mathrm{vor}}} \tag{6}$$

Here, Γ is the circulation originally involved in the element of the vorticity layer [abcd] calculated according to Eqs. (1) and (2), and A and A_{vor} are the areas of the vorticity layer element and the nascent vortex element. A vortex blob at fixed height is substituted for the square-type vortex element generated during each time step. Moreover, as a linear distribution of velocity is assumed in the thin vorticity layer, the shearing stress on the wall surface τ_w is approximated from the following equation, as long as the thickness of the vorticity layer is sufficiently thin:

$$\tau_w=\mu\frac{\partial u}{\partial y}=-\mu\omega \tag{7}$$

Calculation of the Velocity Field. A trajectory of the vortex shedding element over the time step dt is approximated by applying the Adams-Bashforth method as

$$\boldsymbol{r}(t+dt)=\boldsymbol{r}(t)+\{1.5\boldsymbol{u}(t)-0.5\boldsymbol{u}(t-dt)\}dt \tag{8}$$

in which the motion $\boldsymbol{u}$ of the vortex element can be derived from the following Biot-Savart law Eq. (9) that includes source panels, vortex sheet panels, and all vortex elements existing in the flow field.

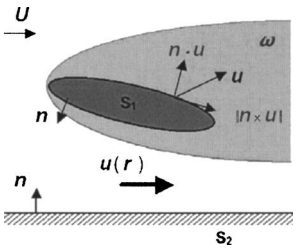

Fig. 3 Flow field involving vorticity region

$$\boldsymbol{u}(\boldsymbol{r}) = \frac{1}{2\pi}\int \frac{\omega \times \boldsymbol{R}}{R^2} dV - \frac{1}{2\pi} \times \int_{S_0} \left[\frac{(\boldsymbol{n}_0 \cdot \boldsymbol{u}_0)\cdot \boldsymbol{R}_0}{R_0^2} - \frac{(\boldsymbol{n}_0 \times \boldsymbol{u}_0)\times \boldsymbol{R}_0}{R_0^2} \right] dS_0 \quad (9)$$

$\boldsymbol{R}_0$ of the second term on the RHS of Eq. (9) represents $\boldsymbol{R}_0 = \boldsymbol{r} - \boldsymbol{r}_0$ and $R_0 = |\boldsymbol{R}_0|$. Moreover, the dot product $\boldsymbol{n}_0 \times \boldsymbol{u}_0$ and the cross product $\boldsymbol{n}_0 \cdot \boldsymbol{u}_0$ show the velocity components of the normal and tangential directions on the boundary surface, respectively, and they coincide with the source and the vortex distributions on the surface. Accordingly, as shown in Eq. (9) and Fig. 3, a velocity field of the viscous and incompressible flows corresponds to the field integration relating to the vorticity distributions in the flow field, the surface integration concerning the source, and the vortex distribution around the boundary surface.

The Lagrangian expression for the vorticity transport equation is expressed as

$$\frac{d\boldsymbol{\omega}}{dt} = (\boldsymbol{\omega} \cdot grad)\boldsymbol{u} + \nu \nabla^2 \omega \quad (10)$$

The first term of the RHS disappears for a two-dimensional case. The second term or the viscous diffusion term is approximated using the core spreading method.

$$\epsilon_k(t + dt) = \epsilon_k(t) + \frac{2.242^2 \nu}{2\epsilon_k(t)} dt \quad (11)$$

Greengard [8] objected to the core spreading method based on a lack of convergence in the limit of infinitesimal parameters, but Rossi [9] showed that the core expansion with splitting was convergent. However splitting leads to an excessive number of computational particles. According to the work of Nakajima and Kida [10], although the error order for the convection term is $(dt)^2$ when the core spreading model is used, the dissipation rate of the vorticity is $e = (4dt/R_e)^{0.5}$. If $e \ll 1$, the error order is e^2 for the vorticity. Therefore, if dt is small enough, after the introduction of discrete vortices, the core spreading model is valid at an initial stage. In this study, we use Eq. (11) to account for the viscous effects to reduce the computing time.

For the flow fields of the current propulsion system, the vortex distribution, time lines, streak lines, and velocity field are predicted at each time step using Eq. (9), and the streamline and equivorticity contours are plotted from the vector field.

Calculation of the Pressure Field. If the divergence is applied to the Navier-Stokes equation, the pressure Poisson equation becomes

$$\nabla^2 p = -\rho \, \mathrm{div}(\boldsymbol{u} \cdot \mathrm{grad}\, \boldsymbol{u}) \quad (12)$$

In general, the pressure field is obtained by calculating the Poisson equation using the finite difference method. However, in the process some lattices must be generated in the flow field which negates the advantages of the vortex method, i.e., no need for grid. Therefore, in this research, instead of using the finite difference method of the Poisson equation, the pressure in the flow field is obtained from the integration equation formulated by Uhlman [11] as follows,

$$\beta H + \int_{S_0} H \frac{\partial G}{\partial \boldsymbol{n}} dS_0 = -\int \nabla(\boldsymbol{u} \times \boldsymbol{\omega}) dV - \int_{S_0} \left\{ G \cdot \boldsymbol{n} \cdot \frac{\partial \boldsymbol{u}}{\partial t} + \nu \cdot \boldsymbol{n} \cdot (\nabla G \times \boldsymbol{\omega}) \right\} dS_0 \quad (13)$$

Here, $\beta = 1$ inside the flow volume V and $\beta = 1/2$ on the boundary surface S_0. G is the fundamental solution of the scalar Laplace equation with the delta function expressed as

$$G = \frac{1}{2\pi} \log\left(\frac{1}{R}\right) \quad (14)$$

and H is the Bernoulli-type variable, defined as follows:

$$H_i = \frac{p_i}{\rho} + \frac{u_i^2}{2} \quad (15)$$

The pressure field of the propulsion mechanism is calculated from the pressure distribution on the body surfaces using Eqs. (13) and (15) during each time step, and with this information, isobaric lines of the entire flow field are computed. By integrating the normal component of the pressure and the tangential component of the shear stress around the wing surface, the hydrodynamic force F acting on the wing is obtained using

$$\boldsymbol{F} = iF_x + jF_y = \oint_{S_0} \{(-p \cdot \boldsymbol{n}) + \tau_w \cdot \mathbf{t}\} dS_0 \quad (16)$$

in which F_x and F_y represent the components of force in the x and y directions, taken as the negative thrust $-T$, and the negative drag force $-D$, respectively.

The Calculation Conditions. The experimental conditions of Ro [5] is used for the simulation, i.e., the wing chord is set as $C = 1$, uniform flow is $U = 1$, velocity of the wing axis is $V = 1$, the attack angle of the wing is $\alpha = 30$ deg, the distance from the trailing edge to the wing axis r_p is $r_p = 0.75C$, and the length, width, and thickness of the water channel are $l = 5.75C$, $h = 2.5$C, and 0.02C, respectively. Tsutahara and Kimura [3] showed experimentally a high thrust efficiency at the velocity ratio $V/U = 1.0$ with the angle of attack $\alpha = 30$ deg. As expressed in the previous section, it is assumed that two flat plates and a wing in the flow field are installed, the surfaces of each object are represented with double panels, i.e., with a finite number (M_b pieces) of source and vortex panels, where the panels of each object are $M_b = 80$. In the present calculation, the time step size dt is set at $dt = 0.015$ during the translating stage and as $dt_o = dt \times r_p/C$ and $dt_c = dt \times (1 - r_p/C)$ during the opening and closing stages. The results of the above procedure reveal the values for the time steps where the distances moved by the leading or trailing edges are all equal during the entire stroke.

Numerical Tests of the Present Method. In order to show the accuracy and discuss the influence of the panel number and time step size, we consider the case of flow past a circular cylinder. A panel number $M = 80$ and 160 for time step size $dt = 0.02$ and 0.01 were considered for flow at a Reynolds number of 3000. A comparison of the streamline patterns at nondimensional time $t = 5$ was made between the present results and the flow visualization results of Bouard and Coutanceau [12] as shown in Fig. 4. It should be noted from the results shown in Fig. 4 that when the number M of panels increases from 80 to 160, and the time step size dt decreases from 0.02 to 0.01, the calculated streamline pattern agrees

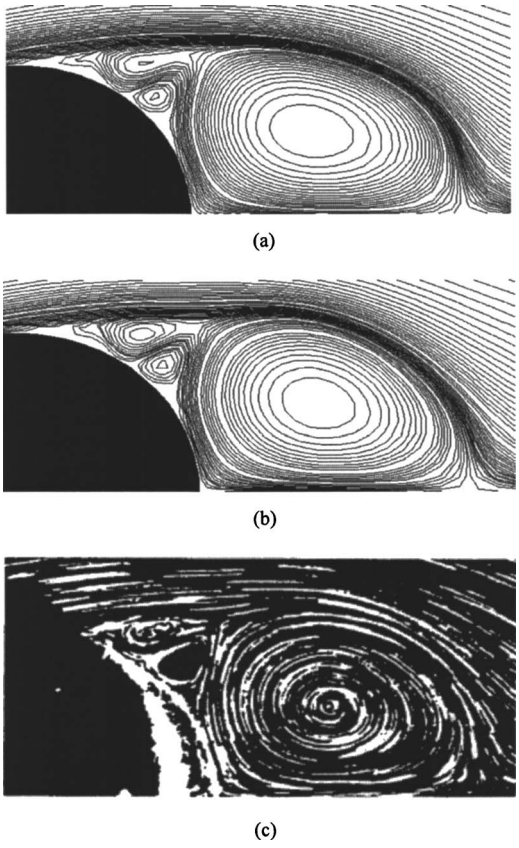

Fig. 4 Comparison of streamlines for Re=3000 at *t*=5.0, (*a*) present method, panel number 80, *dt*=0.02; (*b*) present method, panel number 160, *dt*=0.01; (*c*) flow visualization by Bouard and Coutanceau [9]

better with the experimental results [9]. Panel number $M=80$ and time step size $dt=0.02$ is satisfactory in the comparison of global streamline patterns, though the secondary vortices are slightly larger for the bigger panel number $M=160$ and smaller time step size $dt=0.01$.

Figure 5 shows the vorticity distribution at the surface of the circular cylinder with the time corresponding to Fig. 4. When the number of the panels increases from $M=80$ to 160 and the time step size decreases from $dt=0.02$ to 0.01, the improvement in peak values of the boundary surface is obvious. Figure 6 shows the pressure distribution on the boundary surface corresponding to Fig. 5. The improvement in pressure distribution is less than that

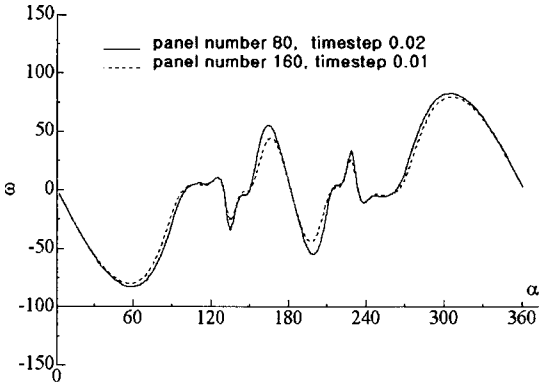

Fig. 5 Surface vorticity distribution for different number of panels and time step size: Re=3000, *t*=5.0

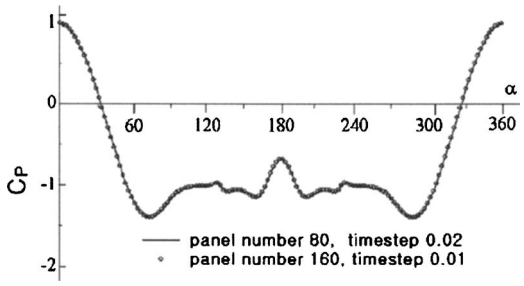

Fig. 6 Surface pressure distribution for different number of panels and time step size: Re=3000, *t*=5.0

in the vorticity distribution, which is expected. If the vorticity is known to be of acceptable accuracy, the pressure will be very accurate because it is one order higher in accuracy than that of the vorticity.

The longer time evolution of the flow at a Reynolds number of 1000 is presented. The panel number used for the simulation is $M=80$ and the time step size is $dt=0.02$. The time histories of the drag and lift coefficients are given in Fig. 7. In the present study, no artificial perturbation was applied to the flow to initiate the alternate vortex shedding; rather, it is triggered solely by the numerical diffusion during the calculation. After an extended time evolution, i.e., $t>90$, the vortex shedding process finally settles down, forming the regular vortex pattern in its wake. From Fig. 7, it can be calculated that the average C_D value after $t>90$ is about 1.37, and the Strouhal number St, is about 0.24. At Re=1000, the values of an average of C_D and S_t obtained by Roshko [13] in his experiment, are about 1.20 and 0.21, respectively. Both results are a little higher than the results obtained from the experiment due to the effects of a two-dimensional calculation.

Results and Discussion

Figure 8 shows the continuous flow pattern around the wing (NACA0010) during one stroke for Re=5900, which is defined based on the wing chord and uniform flow speed. Figure 8(*a*) refers to the numerical results of the streak lines and Fig. 8(*b*) represents the visualization photograph observed in the hydrogen bubble technique by Ro [5] under the same conditions as in Fig. 8(*a*). In Fig. (8), 1 represents the opening stage; 2 to 4, the translating stage; and 5, the closing stage. The discontinuity of the streak lines seen in the vicinity of the trailing edge is due to the effects of the vortices generated at the trailing edge. Overall, the simulation results of the entire stroke agree with the visualizations.

Figure 9 shows the streamlines (*a*) and the velocity vectors (*b*) around the wing during one stroke, under the same conditions as in Fig. 8. Here, considering the streamlines that pass the wing, we

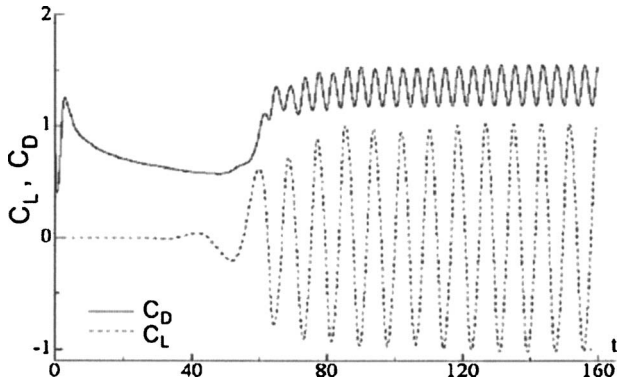

Fig. 7 Time variations in lift and drag coefficients: Re=1000

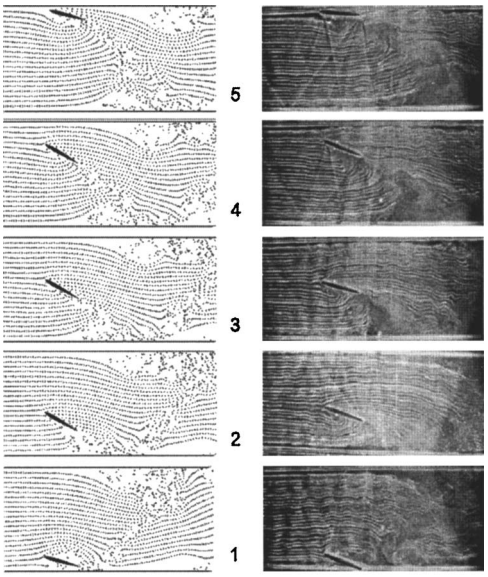

Fig. 8 Streak lines for one stroke of the wing (C=1, h=2.5C, V/U=1.0, r_p=0.75C, and α=30 deg)

know that the flow goes around the wing, because streamlines bend to the moving direction of the wing at all stages and move together with the wing. The streamlines on the closed curve near both sides of the water channel are the effect of the vortex due to the occurrence of the reciprocating motion in the wing. As shown in the velocity vectors (b), the clockwise vortex exists at around the lower part of the wall, while the counterclockwise vortex appears near the upper part of the wall.

Figure 10 shows the results of the vortex distributions, the equi-vorticity contours and the isobaric lines when the wing reaches the center of the water channel from its start at the bottom wall. In Fig. 10(a), the vortices shed from the wall surfaces of the water channel flow downstream along the wall surface due to the effect of the uniform flow. Furthermore, in the vortex distribution around the wing, the vortex shedding on the wing surface was

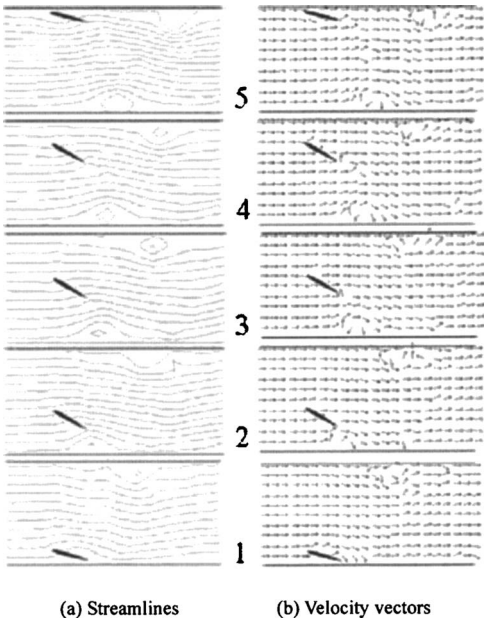

Fig. 9 Flow pattern for one stroke of the wing

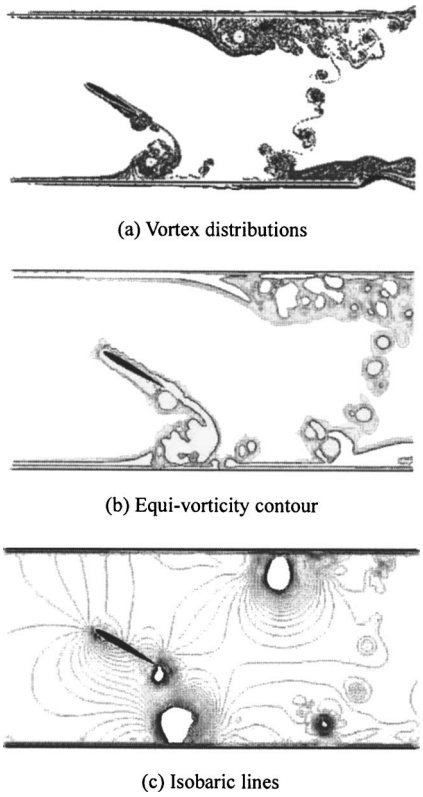

Fig. 10 Various flowfields at the point 3 of Fig. 8

separated at the trailing edge of the wing after it flows along the surface of the wing. The separated vortex is mixed with the vortex shedding at the wall surface creating a complicated flow field as is also shown in Fig. 10(b).

Figure 11 shows the distribution of the pressure coefficient C_p on the surface of the wing. In Fig. 11(a)–11(c) represent the opening, translating, and closing stages, respectively. These correspond to positions 1, 3, and 5 in Figs. 8 and 9. Moreover, the 0.0 point on the horizontal axis for each figure corresponds to the p point in Fig. 1 and to the distance r_p=0.75C from the trailing edge to the p point. The arrows correspond to the locations of the wing surface, which show in a counterclockwise direction starting from the trailing edge of the wing. Looking at the pressure distribution at the opening stage in Fig. 11(a), the pressure coefficient in the leeward side has a negative value from the trailing edge to the p point (the 0.0 point), while the pressure on the windward side indicates almost a positive value except in the vicinity of the trailing edge. Contrarily, the pressure on the leeward side has an almost negative value from the p point to the leading edge but shows a positive value on the windward side. Considering the pressure distribution around the wing at the translating stage in Fig. 11(b), the pressure coefficient in the leeward side was almost positive, while the pressure on the windward side shows a negative value. More significantly, it is also proven that the pressure has a large difference between the windward side and the leeward side in the vicinity of the leading edge. Considering the pressure distribution at the closing stage in Fig. 11(c), the pressure coefficient in the leeward side has a positive value similar to that in the translating stage, while the pressure on the windward side had a negative value even as the pressure difference between the windward side and the leeward side is not significant at the vicinity of the leading edge.

Figure 12 shows the time history of the thrust coefficient C_T at α=30 deg and V/U=1.0. The horizontal axis represents the vertical traveling distance of the wing axis normalized by the channel width. This value means the number of strokes. In Fig. 12, the

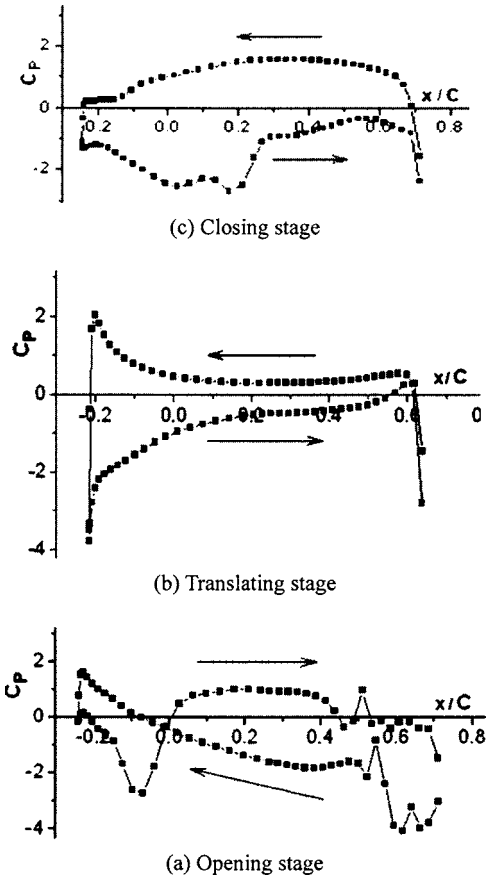

Fig. 11 Pressure distribution around the wing ((*a*), (*b*), and (*c*) in the figure correspond to 1, 3, and 5 points in Fig. 8)

solid lines represent the numerical results using the present calculating method while the dashed line is from the experimental results measured by Ro [5] using the same conditions. The experimental large fluctuations are due to the surface wave generated by the wing movement. The particularly large fluctuations occurred in the early stage of each stroke is due to the inertial force of the wing and the flow around the wing. In the opening stage, the thrust coefficient C_T shows negative values from both numerical and experimental results. In the translating stage, the numerical results show an increase in thrust, but the trend of the experimental data is not clear due to severe fluctuations.

Figure 13 shows the numerical and experimental results of the drag coefficient C_D taken at the same conditions as in Fig. 12. The drag coefficient C_D also shows a fairly good match in the qualitative trend between the calculated and measured results. The drag coefficient C_D also gradually increases as the wing approaches the opposite wall from which it started. However, the experimental

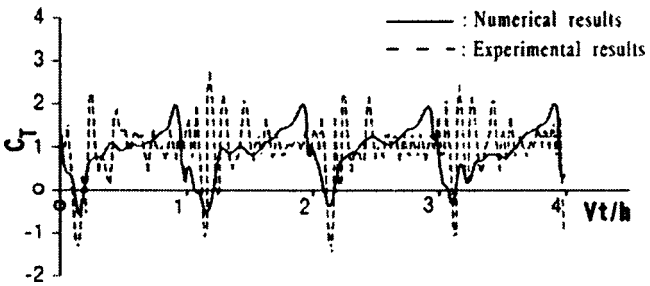

Fig. 12 Time variations for thrust coefficients

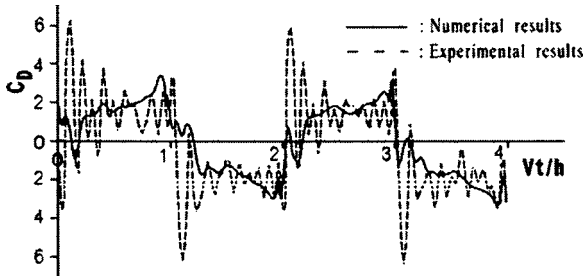

Fig. 13 Time variations for drag coefficients

trend is unclear due to the large fluctuations. The mean values of thrust coefficient and the drag coefficient were approximately 1.0 and 2.0, respectively, at both solid and dashed lines of Figs. 12 and 13, and the numerical results are also quantitatively comparable with the experimental results.

In Figs. 12 and 13, the discrepancy between the numerical results (solid lines) and the experimental results (dashed lines) is also due to the use of the analytical model shown in Fig. 1, which the flow surrounding the wing is assumed to be two dimensional. In the experiment, however, the free surface exists above the wing and affects the flow around the wing.

Conclusions

This research simulates the velocity and pressure fields of a Weis-Fogh-type ship propulsion mechanism using an advanced vortex method. The wing and water channel are represented by a finite number of source and vortex panels, and the vortex shedding is taken from the entire surface of each object. Both the velocity and the pressure fields are predicted with integral equations. The results are summarized as follows:

(1) The vortices which rotated in opposite directions near the two walls of the water channel are generated by the reciprocating motion of the wing.
(2) The pressure distribution on the wing surface is shown to have entirely different characteristics during the opening stage, the translating stage, and the closing stage.
(3) The coefficients of thrust (C_T) and drag (C_D) gradually increased as the wing approaches the opposite wall from which it started.

This research simulates only the velocity ratio $V/U=1.0$ with an angle of attack of $\alpha=30$ deg, which shows a high thrust efficiency. To precisely evaluate the characteristics of this propulsion mechanism, however, a more detailed calculation of the various parameters such as the width of the water channel, the velocity ratio V/U, the distance r_p from the trailing edge to the p point, and the angle of attack α should be studied.

Nomenclature

A = area of vorticity layer element
A_{vor} = area of nascent vortex element
C = chord length of wing
C_D = drag coefficient
C_L = lift coefficient
C_T = thrust coefficient
D = drag acting on wing
dt = time step size
F_x = x component of force acting on wing
F_y = y component of force acting on wing
G = fundamental solution of scalar Laplace equation
H = Bernoulli-type variable

h = width of water channel
h_i = thickness of vorticity layer at i node of panel
h_{vor} = thickness of nascent vortex element
l = length of water channel
M = number of panels
M_b = number of panels for each object
N = number of vortex elements
N_b = number of vortex elements from each object
n_0 = unit normal vector of a point on boundary surface
n_i = unit normal vector of i-th control point
p = center axis of the wing or pressure
Re = Reynolds number
r = position vector of vortex elements
r_0 = position vector of a point on boundary surface
$\mathbf{r}_p$ = distance from trailing edge of wing to wing axis
S_0 = boundary surface
S_b = length of each object perimeter
s_i = panel length at i-node panel
St = Strouhal number
T = thrust acting on wing
t = time or nondimensional time
t = unit tangential vector
U = uniform flow
u = $|\mathrm{u}|$
u_i = tangential velocity at i node of a panel
u_i = induced velocity at i-th control point
u^{sp} = induced velocities by source panels
u^{vo} = induced velocities by vortex elements
u^{vp} = induced velocities by vortex panels
V = movement velocity of wing axis or region inside flow
V_c = normal convective velocity
V_d = diffusion velocity at out boundary of vorticity layer

Greek Letters

α = maximum opening angle
Γ = circulation involved in vorticity layer element
Γ_b = circulation of each object circumference
Γ_b^{vo} = circulation of the vortex element from each object
γ_{bs} = circulation of unit length for each object circumference
δ = displacement thickness of vorticity layer
ϵ_k = core radio for k-th vortex element
μ = viscosity coefficient of fluid
υ = kinematic viscosity of fluid
ρ = density of fluid
τ_w = shearing stress on wall surface
$\boldsymbol{\omega}$ = vorticity
ω_{vor} = vorticity of nascent vortex element

Subscripts

0 = boundary surface
b = object
bs = object surface
c = convective
D = drag
d = diffusion
L = lift
p = point
T = thrust
vor = nascent vortex
w = wall surface
x = x component
y = y component

Superscripts

sp = source panels
vo = vortex elements
vp = vortex panels

Acknowledgment

This work was supported by the Korea Research Foundation Grant (KRF-2003-041-D00639) and the NURI Project, in which the main calculations were performed by using the supercomputing resources of the Korea Institute of Science and Technology Information (KISTI). The authors wish to thank Professor Kyoji Kamemoto, Yokohama National University, for his valuable comments.

References

[1] Weis-Fogh, T., 1973, "Quick Estimates of Flight Fitness in Hovering Animals, Including Novel Mechanism for Lift Production," J. Exp. Biol., **59**, pp. 169–230.
[2] Lighthill, M. J., 1973, "On the Weis-Fogh Mechanism of Lift Generation," J. Fluid Mech., **60**, pp. 1–17.
[3] Tsutahara, M., and Kimura, T., 1987, "An Application of the Weis-Fogh Mechanism to Ship Propulsion," ASME J. Fluids Eng., **109**, pp. 107–113.
[4] Tsutahara, M., Kimura, T., and Ro, K. D., 1989, "Ship Propulsion Using the Weis-Fogh Mechanism," Bull. Mar. Eng. Soc. in Japan, **17**(2), pp. 49–55.
[5] Ro, K. D., 2000, "Calculation of Thrust and Drag Characteristics for Ship's Propulsion Mechanism of Weis-Fogh Type," KSME Int. J., **14**(11), pp. 1249–1258.
[6] Kamemoto, K., 1995, "On Attractive Features of the Vortex Methods," *Computational Fluid Dynamics Review* M. Hafez and K. Oshima, eds., Wiley, New York, pp. 334–353.
[7] Leonard, A., 1980, "Vortex Methods for Flow Simulations," J. Comput. Phys., **37**, pp. 289–335.
[8] Greengard, C., 1985, "The Core Spreading Vortex Method Approximated the Wrong Equation," J. Comput. Phys., **61**, pp. 345–347.
[9] Rossi, L. F., 1996, "Resurrecting Core Spreading Vortex Methods: A New Scheme that is Both Deterministic and Convergent," SIAM J. Sci. Comput. (USA), **17**, pp. 370–397.
[10] Nakajima, T., and Kida, T., 1990, "A Remark of Discrete Vortex Method (Derivation from Navier-Stokes Equation)," Trans. Jpn. Soc. Mech. Eng., Ser. B, **56-531**, pp. 3284–3291 (in Japanese)
[11] Uhlman, J. S., 1992, "An Integral Equation Formulation of the Equation of Motion of an Incompressible Fluid," Naval Undersea Warfare Center T.R. 10-086.
[12] Bouard, R., and Coutancea, M., 1980, "The Early Stage Development of the Wake Behind an Impulsively Started Cylinder for $40 < \mathrm{Re} < 10^4$," J. Fluid Mech., **101**, pp. 583–606.
[13] Roshko, A., 1954, "On the Development of Turbulent Wakes from Vortex Sheets, NACA Reports 1191.

Experimental Investigation of Unstably Stratified Buoyant Wakes

Wayne N. Kraft

Malcolm J. Andrews[1]
e-mail: mandrews@tamu.edu

Department of Mechanical Engineering,
Texas A&M University,
College Station, TX 77843

A water channel has been used as a statistically steady experiment to investigate the development of a buoyant plane wake. Parallel streams of hot and cold water are initially separated by a splitter plate and are oriented to create an unstable stratification. At the end of the splitter plate, the two streams are allowed to mix and a buoyancy-driven mixing layer develops. The continuous, unstable stratification inside the developing mixing layer provides the necessary environment to study the buoyant wake. Downstream a cylinder was placed at the center of the mixing layer. As a result the dynamic flows of the plane wake and buoyancy-driven mixing layer interact. Particle image velocimetry and a high-resolution thermocouple system have been used to measure the response of the plane wake to buoyancy driven turbulence. Velocity and density measurements are used as a basis from which we describe the transition, and return to equilibrium, of the buoyancy-driven mixing layer. Visual observation of the wake does not show the usual vortex street associated with a cylinder wake, but the effect of the wake is apparent in the measured vertical velocity fluctuations. An expected peak in velocity fluctuations in the wake is found, however the decay of vertical velocity fluctuations occurs at a reduced rate due to vertical momentum transport into the wake region from buoyancy-driven turbulence. Therefore for wakes where buoyancy is driving the motion, a remarkably fast recovery of a buoyancy-driven Rayleigh-Taylor mixing in the wake region is found.
[DOI: 10.1115/1.2174060]

Introduction

Exploration of turbulent wakes in a stratified flow offers a unique opportunity to study the chaotic nature of turbulence. Rather than selectively studying the mechanisms of shear or buoyancy, the investigation of a buoyant wake allows study of the complex dynamics associated with their interaction. In the present work the wake is generated by turbulent, unstably stratified flow moving past a cylindrical obstruction as shown in Fig. 1. A buoyancy-driven mixing layer flows past the cylindrical obstruction forming a buoyant plane wake. We have examined the development of the wake and the subsequent recovery to buoyancy-dominated turbulence.

Our motivation for this research was to provide insight into the nonequilibrium development of turbulent mixing which occurs when momentum (the wake) is injected into a buoyancy-driven mixing layer. Indeed, such a situation is closely related to the interaction between shock waves and Rayleigh-Taylor-driven mixing that occurs during the implosion phase of inertial confinement fusion, as buoyancy-driven mixing limits the energy yield of the overall thermonuclear process [1]. In particular, during ICF shockwaves pass through the turbulent mix, depositing momentum in the direction of the density gradients and disturbing the equilibrium growth of buoyancy-driven mixing. Interaction of the Rayleigh-Taylor instability and the passing shockwave is not well understood. Although the detailed dynamics that occur in the ICF process cannot be replicated in the current experiment, a similar interaction of the Rayleigh-Taylor instability with a disturbance which redistributes momentum has been examined. By locating a cylinder inside the developing mixing layer, the equilibrium of the turbulent mix is disturbed. Like a shockwave, the cylinder wake redistributes momentum in the vertical direction (i.e., the direction of the density gradient) [2]. Although the mechanism for depositing momentum in the current experiment is different than a shockwave, the result on the buoyancy-driven turbulence once the shockwave has passed is similar. Therefore the current experiment allows observation of relaxation back to an equilibrium state dominated by the Rayleigh-Taylor instability. A consequence of this experimental arrangement is the ability to study nonequilibrium turbulence and also to investigate the buoyant wake.

Background

The Rayleigh-Taylor fluid instability arises when a pressure gradient is imposed on a density gradient along the interface of two fluids with $\nabla p \cdot \nabla \rho < 0$ [3]. Just such conditions arise when a heavy fluid is situated above a light fluid under gravity. Subsequent growth of buoyancy-driven Rayleigh-Taylor instability proceeds through linear instability, nonlinear instability, and finally to a self-similar equilibrium [4]. The governing parameter for buoyancy driven instability is the Atwood number, $A=(\rho_1-\rho_2)/(\rho_1+\rho_2)$, where ρ_1 and ρ_2 are the heavy and light fluid densities, respectively [4]. For the present experiment the Atwood number range is $5\times10^{-4}\leqslant A\leqslant 7.5\times10^{-4}$.

When a wake is introduced to the buoyancy driven mix, it disturbs the equilibrium of the Rayleigh-Taylor mixing region. This can be seen in Fig. 1. Shear layers shed from the cylinder surface roll-up into vortices in a periodic manner behind the cylinder, and viscous effects dissipate the subsequent turbulent motion. Buoyancy, however, serves as a source of turbulent kinetic energy inside the wake. In particular, potential energy, stored in the mean flow through unstable density gradients, is converted to turbulent kinetic energy as the fluids overturn. At a downstream point a balance occurs between the wake dissipation and turbulent energy production from buoyancy, thereafter buoyancy-driven turbulence recovers to dominate the flow dynamics.

A Reynolds number for the wake is conventionally defined as $\mathrm{Re}=UD/\nu$. Above the critical Reynolds number range, $140\leqslant \mathrm{Re}$

[1]Corresponding author.

Contributed by the Fluids Engineering Division of ASME for publication in the JOURNAL OF FLUIDS ENGINEERING. Manuscript received December 15, 2004; final manuscript received November 1, 2005. Assoc. Editor: James A. Liburdy. Paper presented at the 2004 ASME Heat Transfer/Fluids Engineering Summer Conference (HT-FED2004), July 11, 2004–July 15, 2004, Charlotte, North Carolina, USA.

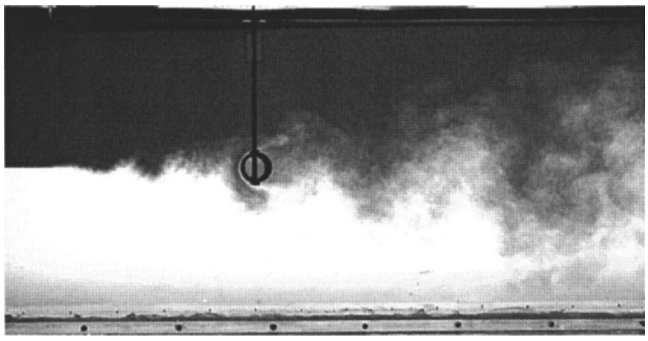

Fig. 1 Buoyant wake formed from a cylinder placed at the centerline of a buoyancy-driven mixing layer

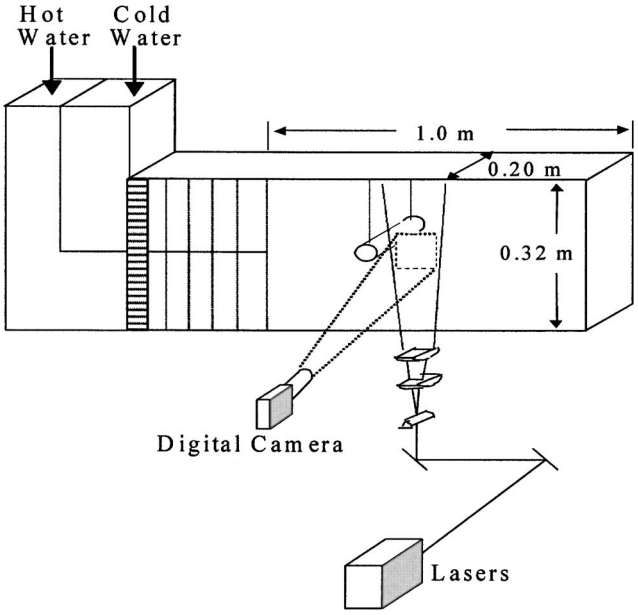

Fig. 2 Schematic of experimental apparatus

$\leqslant 190$, the wake becomes turbulent [5]. The results presented here are at a Re range of $640 \leqslant \mathrm{Re} \leqslant 720$ and are expected to be turbulent. Effects of stratification in the wake are usually included in the characteristic buoyancy frequency, N, where $N^2 = -g/\rho_0(\partial\rho/\partial z)$ [2,6–8]. To evaluate N the density gradient, $\partial\rho/\partial z$, is approximated as $(\rho_1 - \rho_2)/D$ for the turbulent mixing layer around the cylinder. It is also useful to determine the ratio of inertial forces to buoyancy forces, as given by the internal Froude number, $\mathrm{Fi} = U/ND$. This nondimensional parameter is a function of the free stream velocity, the diameter of the cylinder, and the characteristic buoyancy frequency. As $\mathrm{Fi} \to 0$ the effects of stratification become dominant. The internal Froude number has been utilized extensively when describing the stably stratified wake [2,6–8], however, as we describe next, it cannot accurately describe the physical nature of the current work. The characteristic buoyancy frequency utilized in Fi is associated with internal waves generated by the restoring force of stabilizing buoyancy. For unstable stratification, and buoyancy-driven turbulence specifically, such restoring forces do not occur. However, it is useful to calculate Fi to illustrate the difference in flow regimes between the current work and previous research in stratified wakes. Since the magnitude of Fi provides a direct comparison between the ratio of inertial forces to buoyancy forces in stably stratified wakes, the negative value of $\partial\rho/\partial z$ that occurs for unstably stratified flow suggests the use of Fi^2 for a meaningful comparison to be made. So, we assign flows with unstable density gradients as a $(-)\mathrm{Fi}^2$, and those with stable density gradients as a $(+)\mathrm{Fi}^2$. The internal Froude number examined in the present work is approximately $\mathrm{Fi}^2 = \pm 7$.

Early investigations of wakes focused primarily on the near wake structure and excluded buoyancy effects as illustrated in the comprehensive review by Williamson [5]. Recently researchers have sought to understand the effects of buoyancy in the turbulent wake, but this has been limited to the inclusion of stabilizing buoyancy. The first investigations of stably stratified wakes were performed by Pao [9], where a stratified, turbulent wake was created by towing a cylinder or grid through a tank with stably stratified salt water. Pao reported spectra of turbulent velocity and density measurements in the wake region. Recent experiments in stratified wakes were performed by Xu et al. [6], Speeding [2,7], and Bonnier and Eiff [8]. Xu et al. investigated the turbulent wake behind a cylinder in a stably stratified flow and compared stratified measurements with results from turbulence models. Speeding [2,7] and Bonnier and Eiff [8] described the structure and decay of a turbulent axisymmetric wake subjected to stabilizing buoyancy, and in particular identified and described regions of the wake collapse. All these studies are for stabilizing buoyancy; we could find none for the instance of destabilizing buoyancy, which is the subject of the present paper.

Experimental Apparatus

The experimental apparatus is shown schematically in Fig. 2 and is comprised of a Plexiglas flow channel with an inlet and exit plenum at either end. This unstably stratified water channel has been extensively described previously [10–12], so here we present the key elements and modifications we made to incorporate a cylinder that generates a wake. The flow channel is 241 cm in length, 32 cm deep, and has a width of 20 cm. Water is supplied to the flow channel via the inlet plenum from two 500 gal supply tanks. Two parallel streams of water enter the inlet plenum and are separated by a horizontal splitter plate. Prior to the test section, a series of flow straighteners and wire meshes are utilized to minimize the free stream turbulence [10]. The splitter plate is 0.32 cm thick and the end has a knife-edge with an included angle of 2.5 deg. At the end of the splitter plate the two streams are allowed to mix. To reduce the momentum deficit created by the knife-edge, a fine wire mesh, 35×35 grids/in.^{2}, is placed at the end of the splitter plate. The mean flow rate is adjusted using calibrated rotameters and the desired stratification in the test section is achieved by adjusting the temperatures of the two supply tanks. Temperature differences between the two inlet streams range from 5 °C to 7 °C. These temperature differences are related to density through an equation of state which is given in the following section. For unstable stratification, cold (heavy) water enters the test section above hot (light) water.

In the presence of a small perturbation and unstable stratification, a buoyancy-driven mixing layer develops downstream from the splitter plate. As shown in Fig. 3 a cylinder placed at the

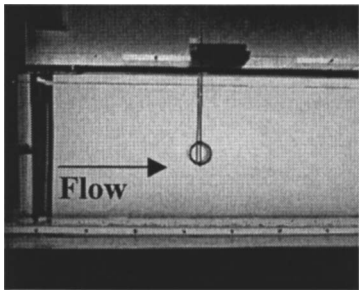

Fig. 3 Flow channel test section with cylindrical obstruction

Table 1 Experimental parameters

Mean velocity	U (cm/s)	4 - 4.5
Cylinder diameter	D (cm)	1.6
Kinematic viscosity	ν (cm/s^2)	0.01
Reynolds number	Re	640-720
Internal Froude number	Fi^2	-7
Atwood number	A	5.0 x 10^{-4}

centerline of the mixing layer disrupts the buoyancy-driven turbulence downstream. The cylinder is located 30 cm downstream of the splitter plate at the centerline of the mixing layer and is oriented horizontally and perpendicular to the stream wise direction. The cylinder was constructed from a section of hollow PVC pipe that was suspended from the top of the flow channel. Table 1 lists the parameter range for the experiments performed using this apparatus.

Measurement Diagnostics

The dynamics of a buoyant wake are investigated through velocity and density measurements at the centerline of the wake. These measurements were taken using particle image velocimetry (PIV) and a high-resolution thermocouple system (details are given below). In addition, qualitative observations were made through visualization techniques using Nigrosene dye.

PIV was used to obtain velocity measurements in the wake of the cylinder. The PIV system consisted of two 120 mJ Nd-Yag pulse lasers that each fire at a rate of 15 Hz. By alternating the pulse of each laser an effective sampling rate of 30 Hz was achieved. Neutrally buoyant hollow, silvered glass spheres, 10 μm in diameter, were seeded in each stream at a concentration of 5–7.5 ml per 500 gal of water. A series of cylindrical lenses formed a laser sheet of approximately 1 mm thickness, which projected through the water channel vertically. Images of seed particles were captured using a KODAK Megaplus digital camera. The physical window size captured by the digital camera was a region 6 cm$\times$4.5 cm. A data acquisition system records 1200 successive digital images at 640$\times$480 pixels. MatPIV cross-correlation software was used to obtain velocity measurements [13]. Successive images were compared in sequence, resulting in 1199 measured velocity fields. Each set of images processed was separated by a time interval of 0.033 s which with the physical window size is more than adequate to resolve the low flow velocities ($<$5 cm/s). Statistical convergence of velocity measurements using these measurement parameters was verified by evaluating the uncertainty in rms vertical velocities. Statistical convergence was evaluated at a point 15D downstream of the cylinder where the vertical velocity fluctuations exhibited a large variance. An uncertainty for the rms vertical velocity fluctuations is determined via an estimate for its variance as described by Benedict and Gould [14] in Eq. (1),

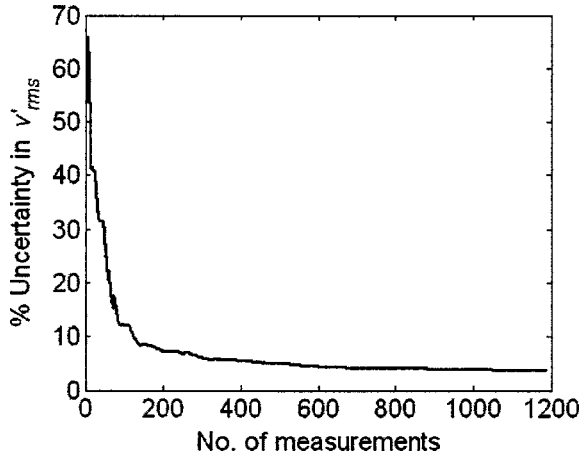

Fig. 4 Percent uncertainty in the rms of vertical velocity fluctuations

$$\mathrm{var}(v'_{\mathrm{rms}}) = [\overline{v'^4} - (\overline{v'^2})^2]/4N\overline{v'^2}, \tag{1}$$

where N is the number of measurements. The percent uncertainty in the rms of vertical velocity fluctuations found from this analysis is shown in Fig. 4. As can be seen in Fig. 4, the measurement method and quantity of measurements does show statistical convergence for a typical rms vertical velocity fluctuation with an uncertainty of ±3.6%. A more detailed description of the PIV techniques employed can be found in [12], and the issue of light refraction has been previously addressed and found negligible at the small density differences being used [15].

Density measurements were acquired through a high-resolution thermocouple system. An E-type thermocouple was suspended in the flow using a vertical rake. The thermocouple was sampled at 50,000 Hz using a 16-bit data acquisition board for a total sample time of ~120 s. To reduce noise, a local average of 100 samples was used to obtain an effective sampling rate of 500 Hz. The diameter of the thermocouple is 0.16 mm with a thermal response time of 0.016 s. Limited by the thermal response time, the thermocouple resolves frequencies up to ~60 Hz, insufficient to fully resolve the expected Bachelor scales for this flow [11]. However, the majority of energy contained in the density fluctuations is in structures significantly larger than this lower limit [11]. Temperature measurements at the centerline of the mixing layer were converted to densities using an equation of state found in [16],

$$\rho = \frac{999.8396 + 18.2249T - 0.007922T^2 - 55.448 \times 10^{-6}T^3 + 149.756 \times 10^{-9}T^4 - 393.295 \times 10^{-12}T^5}{1 + 18.159 \times 10^{-3}T} \tag{2}$$

The centerline of the mixing layer was determined by traversing the thermocouple through the mixing layer. A displacement coefficient, ϕ, is used to determine the location of the centerline of the mixing layer, where ϕ=0.5 at the centerline. The displacement coefficient, $\phi=(T_2-T_{\mathrm{avg}})/(T_2-T_1)$, is defined in terms of the cold water stream temperature, T_1, and hot water stream temperature, T_2.

Visualization of the interaction between the plane wake and the buoyancy-driven mixing layer was performed by marking the cold fluid with blue Nigrosene dye, 15 ml/500 gal. This allows the mixing of the hot and cold fluids to be visualized as light and dark regions. Photographs of the experiment using Nigrosene dye were taken using a Sony Mavica 1.2 megapixel digital camera.

Qualitative Observations

Figure 5 shows photographs taken from three separate experiments with Nigrosene dye added to the cold (top) water stream.

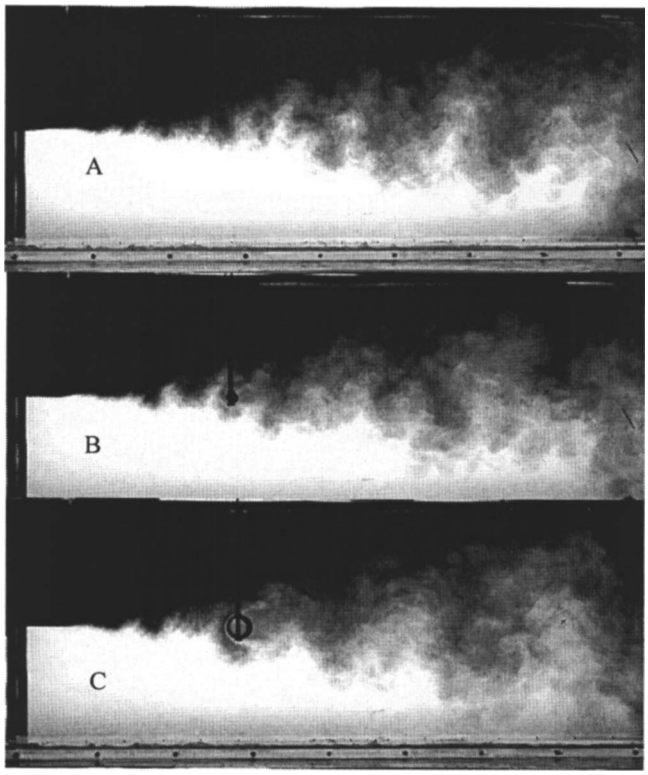

Fig. 5 Visualization of wake- and buoyancy-dominated turbulence using Nigrosene dye. (*a*) Rayleigh-Taylor-driven mixing layer, (*b*) Rayleigh-Taylor-driven mixing layer with a cylinder wake, *D*=1.6 cm, and (*c*) Rayleigh-Taylor-driven mixing layer with a cylinder wake, *D*=3.25 cm.

Figure 5(*a*) shows a pure Rayleigh-Taylor-driven mix; Fig. 5(*b*) shows the development of the same Rayleigh-Taylor-driven mixing layer as Fig. 5(*a*) but with a 1.6 cm diameter cylinder that introduces a wake; and Fig. 5(*c*) is similar to Fig. 5(*b*) but uses a 3.25 cm diameter cylinder. In addition to visualizing the buoyant wake, comparison of the three experiments illustrates the effect the cylinder has on the developing buoyancy-driven mixing layer. Comparison of Fig. 5(*c*) with Fig. 5(*a*) reveals that the cylinder has introduced a dominant wake wavelength into the turbulent mixing layer behind the cylinder. The same effect is also present in Fig. 5(*b*) but is not as clearly defined. This dominant wavelength disturbance corresponds to the shedding frequency associated with the cylinder wake. Inspection of Figs. 5(*b*) and 5(*c*) and comparison with Fig. 5(*a*), just upstream of the cylinder, reveal that that the cylinder is redirecting the flow approximately one cylinder diameter upstream. In particular, Fig. 5(*c*) shows a large structure flowing around and off the bottom of the cylinder, associated with an induced wake flow. Furthermore, comparison of Figs. 5(*a*) and 5(*b*) shows that the wake from the small diameter cylinder has added little effect on the overall mix width, as judged by the depth of penetration by the dye. However, comparison of Fig. 5(*a*) with Fig. 5(*c*) shows that large wake disturbances have considerably enhanced the overall width, and thus the growth rate of the mix region. Turning now to the flow structures behind the cylinder, it is striking in Figs. 5(*b*) and 5(*c*) that the usual wake structures of alternating regions of opposite sign vortices associated with a vortex street are not readily apparent. A well-defined vortex sheet is usually expected for the present cylinder Reynolds numbers from 640 to 720 [4]. A visualization of the wake without buoyancy taken from the present apparatus is shown in Fig. 6, clearly demonstrating the vortex street (again Nigrosene dye is used to mark the top water stream). The periodic nature of the wake in Fig. 6 is clearly visible as stems of the vortex pairs are

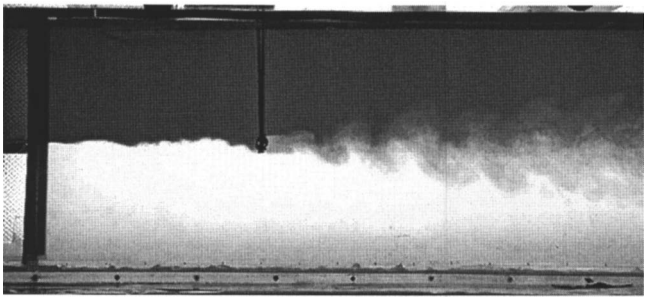

Fig. 6 Visualization of the wake behind a cylinder with no buoyancy for a cylinder diameter of 1.6 cm and free steam velocity of 4 cm/s

present at regular intervals. The turbulent nature of the shedding vortices of Fig. 6 results in a three-dimensional behavior, most noticeably as the wake develops further downstream. In contrast the periodic shedding of vortices for the wake with unstable buoyancy in Figs. 5(*b*) and 5(*c*) is not seen, due to buoyancy-driven turbulence in the mixing layer that quickly dominates the flow.

The similarity of Figs. 5(*b*) and 5(*c*) with the pure buoyancy case of Fig. 5(*a*) suggests that the small scale structures are either being driven by buoyancy or retained from the buoyancy-driven mix upstream of the cylinder or perhaps both. It is evident in Figs. 5(*b*) and 5(*c*) that downstream, on the right side of the photographs ($x/D>15$), the structures appear very similar to the Rayleigh-Taylor plumes seen on the right of Fig. 5(*a*). These observations indicate that buoyancy has quickly resumed a dominate role downstream of the cylinder.

Results

Quantitative measurements of the rms vertical velocity fluctuations have been taken using the PIV technique described previously. Figure 7 shows the measured vertical velocity fluctuations, taken at the centerline for a wake induced by a 1.6 cm diameter cylinder, for the cases of no buoyancy (circles), stable buoyancy (triangles), and, unstable buoyancy (squares). The flow conditions for each case are given in Table 2. Inspection of Fig. 7 reveals several interesting and immediate observations for $x/D>6$. In particular, comparison of the unstable buoyancy case (squares) with the no-buoyancy case (circles) shows a smaller rate of dissi-

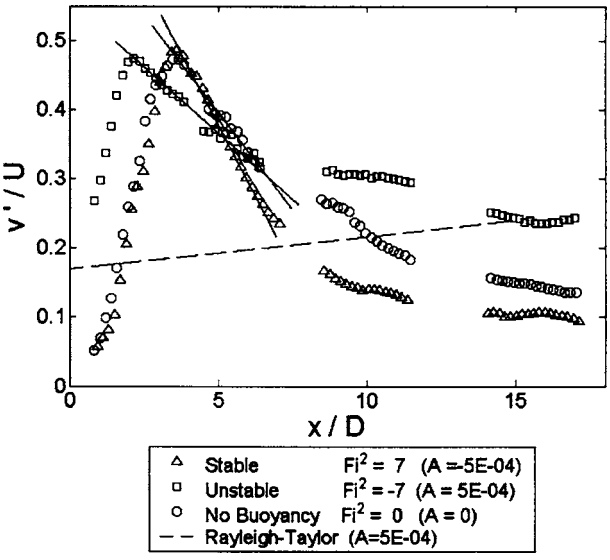

Fig. 7 Centerline rms vertical velocity fluctuations in the cylinder wake with *D*=1.6 cm

Table 2 Decay rates of vertical velocity fluctuations

Stratification	Fi^2	A	dv'/dx (U/D)
None	∞	0	-0.054
Stable	7	-5.0×10^{-4}	-0.077
Stable	10	-7.5×10^{-4}	-0.085
Unstable	-7	5.0×10^{-4}	-0.038

pation of v' for $x/D > 3$, associated with a buoyancy feed of potential energy into the vertical velocity fluctuations that competes with dissipation associated with the wake. In contrast, velocity fluctuations (triangles) in the stabilizing buoyancy case are suppressed by buoyancy and as a result decay faster in the region behind the cylinder. Figure 7 also shows the growth of vertical velocity fluctuations for a plain Rayleigh-Taylor mix (dashed line). Experimental results showing the linear increase of vertical velocity fluctuations for the plain Rayleigh-Taylor mixing layer are obtained from [12]. A linear fit has been applied to these results and is shown in Fig. 7 as the dashed line. Comparison of the vertical velocity fluctuations of the plain Rayleigh-Taylor mixing layer (dashed line) with the unstably buoyant wake (squares) reveals that the buoyant wake results are converging towards the behavior of the Rayleigh-Taylor mix very rapidly downstream of the cylinder, $x/D > 12$. This would seem to indicate a return to dominance of the buoyancy-driven turbulence and the Rayleigh-Taylor instability. The dynamical implications of these results are still being considered, but it is apparent that strong wake dissipation, evident in Fig. 7 for the no-buoyancy case, is quickly overcome in the unstable buoyancy case. Indeed, inspection of Fig. 7 suggests the wake length scales increase, which in turn provides an accelerating release of potential energy. This competition between dissipation and potential energy release is seemingly balanced at about 6 cylinder diameters downstream where v' is approximately equal for all three wake flows. However, it is likely that this fixed point is a result of the equal and opposite flow parameters of $Fi^2 = \pm 7$ and corresponding $A = \pm 5 \times 10^{-4}$.

The near-field results for $x/D < 6$ are shown in Fig. 8. The vertical velocity fluctuation data seen in Fig. 8 are the same as that of Fig. 7, but with an expanded view. The left side of the plot shows that the unstable buoyancy case (squares) starts with an initially higher level of vertical velocity fluctuation; we attribute this to the Rayleigh-Taylor mix formed upstream of the cylinder. The peak vertical velocity for the no-buoyancy and stable buoyancy cases occur at approximately the same location, $x/D \sim 3.5$, as might be expected because the wake dominates in the near cylinder region. However, for the unstably stratified buoyant case the peak vertical velocity fluctuation, v', occurs at $x/D \sim 2$. This apparent shift may be caused by high momentum transport near the cylinder due to the upstream turbulence associated with the Rayleigh-Taylor mix. Higher levels of turbulence prior to the cylinder result in an increase in momentum transport behind the cylinder, thereby increasing the entrainment of fluid into the recirculation vortex, causing it to shed closer to the cylinder. Similar peak values of v' for the three cases is a reflection of similar wake dynamics, however the shift of the peak, which we associate with upstream turbulence due to Rayleigh-Taylor mixing, implies that small scale mixing can significantly affect the overall development.

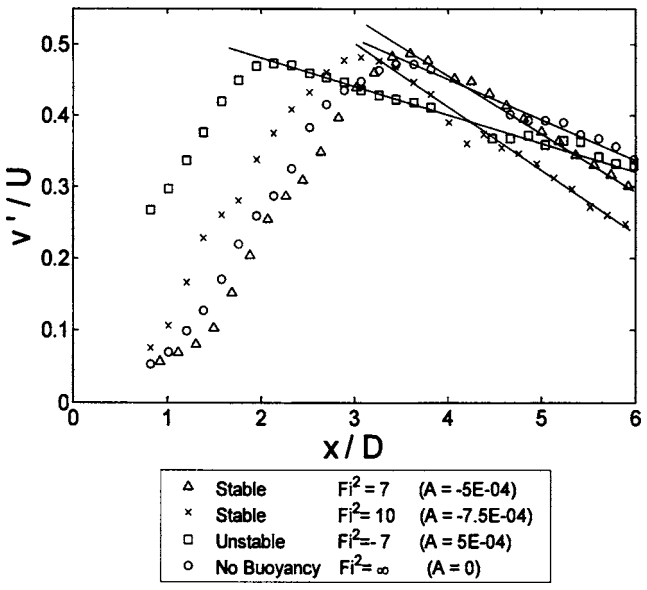

Fig. 8 Decay of near wake centerline rms vertical velocity fluctuations

Figure 8 also shows a decay of v' in the vicinity immediately after the peak velocity. An approximately linear decay for each case is apparent but with different slopes. The steepest slope, and hence the greatest decay, is for the stable buoyancy case and is readily attributed to the stabilizing effect of the density statification. The lowest slope is for the unstable buoyancy case and again is attributed to the release of potential energy from the unstable density stratification feeding into the kinetic energy of the flow, and thus the vertical velocity fluctuations. For reference the slopes have been measured and are reported in Table 2. The gradients in Table 2 have been nondimensionalized with the wake shedding frequency U/D.

In addition to the described velocity measurements, rms density fluctuations were recorded at the centerline of the wake. The density fluctuations have been used to evaluate the extent of molecular mixing inside the wake. The following parameters are defined to evaluate molecular mix [11]:

$$f_1 = \lim_{T \to \infty} \frac{1}{T} \int_0^T \frac{\rho - \rho_2}{\rho_1 - \rho_2} dt \tag{3}$$

$$f_2 = 1 - f_1 \tag{4}$$

$$B_0 = \lim_{T \to \infty} \frac{1}{T} \int_0^T (\rho - \bar{\rho})^2 dt / \Delta\rho^2 \tag{5}$$

$$B_2 = f_1 f_2 \tag{6}$$

$$\theta = 1 - \frac{B_0}{B_2} \tag{7}$$

The volume fractions of the cold and hot fluids inside the wake are given by f_1 and f_2. The volume fraction of f_1, for example, represents the ratio of fluid 1 at a desired location in the flow to the total volume of fluid passing through that location over a given time. B_0 is the intensity of the turbulent density fluctuations and B_2 is the same measure but as if the two streams were completely immiscible. The level of molecular mixing (fluid segregation) is evaluated through the molecular mix parameter, θ. For two completely molecular mixed fluids θ is equal to 1 and for two immiscible fluids θ is 0 [17].

Figure 9 shows the molecular mix parameter, θ, behind the cylinder for the unstable (squares) and stable (circles) wakes with stratifications of $A = 5 \times 10^{-4}$, -5×10^{-4} respectively, together with the levels of molecular mix found in a plain Rayleigh-Taylor mix (diamonds) [12]. Directly behind the cylinder it is readily seen that θ is very close to 1 for both the stable and unstable stratifications. This is due to the recirculation region immediately behind the cylinder that provides long residence times and fine scale mixing. The length of this region is the formation length for the shedding vortices, shown as the vertical dashed lines in Fig. 9.

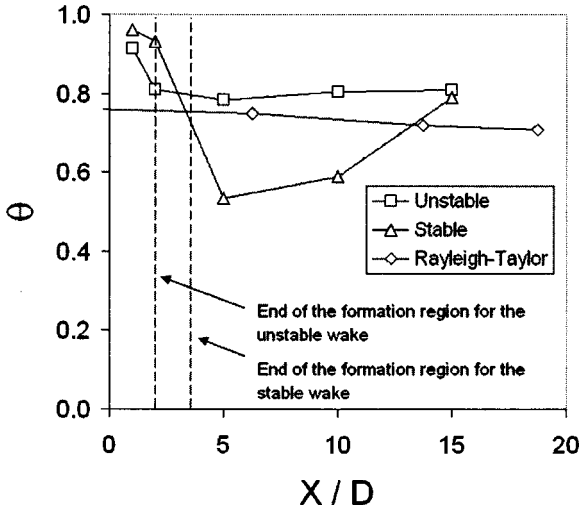

Fig. 9 Molecular mix parameter measured at the centerline in the wake of a cylinder. Data for the Rayleigh-Taylor mixing layer obtained from Ramaprabhu and Andrews [12].

The formation length is marked by the location of the peak centerline velocity fluctuation [4]. In both instances the level of molecular mixing decreases rapidly outside the recirculation region. However, the unstable case quickly approaches an approximately constant value of $\theta=0.8$, a result close to the plain Rayleigh-Taylor mixing layer [12]. In contrast, the stable case continues to decrease to a minimum of $\theta=0.54$ at $x/D=5$, indicating a remarkable amount of *demixing* (i.e., a tendency toward a segregated two-fluid configuration). However, far downstream of the cylinder at $x/D=15$, both the stable and unstably stratified wakes approach similar levels of molecular mixing. Thermal diffusion, enhanced by the dynamics of the turbulent wake, results in an increase of the mixing in the stably stratified wake. A comparison can also be made between the plain Rayleigh-Taylor mixing layer (diamonds) and the instance when a wake is introduced (squares); similar behavior and magnitudes of molecular mix are seen in Fig. 9, further demonstrating the relaxation of the disturbed flow towards a Rayleigh-Taylor mixing layer. The larger value of θ for unstably stratified wake is indicative that the cylinder and the subsequent wake appear to improve the molecular mixing inside the buoyancy-driven mixing layer.

Conclusions

Recent work to characterize a buoyant wake has been presented and discussed. A cylinder was placed at the center of a developing buoyancy-driven mix, and subsequent interaction between the wake and buoyancy was studied. From visual observations of the wake, the cylinder has a distinct effect on the buoyancy-driven turbulence. In particular, a dominant wavelength associated with the wake shedding frequency is apparent in the photographs of the experiment. Also an increase in the growth rate of the mixing layer can be seen for larger cylinder diameters. However, the characteristic vortex street does not appear as would be expected for a typical wake at the current range of Reynolds numbers, $640 \leqslant \mathrm{Re} \leqslant 720$. The dynamics of the wake are also evident in the measured vertical velocity fluctuations, with the peak of vertical velocity fluctuation being associated with the wake dynamics. Similar vertical velocity fluctuation peaks are found for the wake with unstable stratification, stable stratification, and no stratification. However, the effect of buoyancy can be seen in the initial decay of the rms vertical velocity fluctuations. The steepest rms vertical velocity fluctuation gradient is found for stabilizing buoyancy and the shallowest for unstable buoyancy. For unstable buoyancy, the shallow rms velocity collapse behind the cylinder is caused by the transport of energy to the wake from potential energy stored via unstable density gradients, and ultimately results in a remarkably rapid return to the characteristic behavior of the Rayleigh-Taylor mix. Measurements of density fluctuations inside the mixing layer yield insight into the molecular mixing that occurs. At the centerline of the unstably stratified wake, the molecular mix parameter returns rapidly to an approximately constant value, similar to the measured behavior for a Rayleigh-Taylor mix. However, the recirculation zone of the wake results in an increased molecular mix when compared with a plain Rayleigh-Taylor case. Clearly the present results indicate the complexity that arises when two competing equilibria resolve their individual dynamics into a single observable flow.

Acknowledgment

This research was sponsored by the National Nuclear Security Administration under the Stewardship Science Academic Alliances program through DOE Research Grant No. DE-FG03-99DP00276/A000.

Nomenclature

$A=(\rho_1-\rho_2)/(\rho_1+\rho_2)$ = Atwood number
$\mathrm{Fi}=U/ND$ = internal Froude number
D = cylinder diameter, cm
N = characteristic buoyancy frequency, l/s
$\mathrm{Re}=UD/\nu$ = Reynolds number
U = mean velocity, cm/s
ν = kinematic viscosity cm^2/s
ρ = density, g/cm^3
θ = molecular mix fraction

References

[1] Lindl, J. D., 1998, *Inertial Confinement Fusion: The Quest for Ignition and Energy Gain Using Indirect Drive*, Springer-Verlag, New York.
[2] Spedding, G. R., 1997, "The Evolution of Initially Turbulent Bluff-Body Wakes at High Internal Froude Number," J. Fluid Mech., **337**, pp. 283–301.
[3] Chandrasekhar, S., 1961, *Hydrodynamic and Hydromagnetic Stability*, Clarendon, Oxford.
[4] Youngs, D. L., 1984, "Numerical Simulation of Turbulent Mixing by Rayleigh-Taylor Instability," Physica D, **12**, pp. 32–44.
[5] Williamson, C. H. K., 1996, "Vortex Dynamics in the Cylinder Wake," Annu. Rev. Fluid Mech., **28**, pp. 477–534.
[6] Xu, Y., Fernando, J. S., and Boyer, D. L., 1995, "Turbulent Wakes of Stratified Flow Past a Cylinder," Phys. Fluids, **7**(9), pp. 2243–2255.
[7] Spedding, G. R., 2002, "Vertical Structure in Stratified Wakes with High Initial Froude Number," J. Fluid Mech., **454**, pp. 71–112.
[8] Bonnier, M., and Eiff, O., 2002, "Experimental Investigation of a Turbulent Wake in a Stably Stratified Fluid," Phys. Fluids, **14**(2), pp. 791–801.
[9] Pao, Y., 1973, "Measurements of Internal Waves and Turbulence in Two-Dimensional Stratified Shear Flows," Boundary-Layer Meteorol., **5**, pp. 177–193.
[10] Snider, D. M., and Andrews, M. J., 1994, "Rayleigh-Taylor and Shear Driven Mixing With an Unstable Stratification," Phys. Fluids, **6**(10), pp. 3324–3334.
[11] Wilson, P. N., and Andrews, M. J., 2002, "Spectral Measurements of Rayleigh-Taylor Mixing at Small Atwood Number," Phys. Fluids, **14**(3), pp. 938–945.
[12] Ramaprabhu, P., and Andrews, M. J., 2004, "Experimental Investigation of Rayleigh-Taylor Mixing at Small Atwood Numbers," J. Fluid Mech., **502**, pp. 233–271.
[13] Grue, J., Jensen, A., Rusas, P., and Sveen, J. K., 2000, "Breaking and Broadening of Internal Solitary Waves," J. Fluid Mech., **413**, pp. 181–217.
[14] Benedict, L. H., and Gould, R. D., 1996, "Towards Better Estimates for Turbulence Statistics," Exp. Fluids, **22**, pp. 129–136.
[15] Ramaprabhu, P., and Andrews, M. J., 2003, "Simultaneous Measurements of Velocity and Density in Buoyancy-Driven Mixing," Exp. Fluids, **34**, pp. 98–106.
[16] Kukulka, D. J., 1981, "Thermodynamic and Transport Properties of Pure and Saline Water," M.S. dissertation, State University of New York at Buffalo.
[17] Youngs, D. L., 1990, "Three-Dimensional Numerical Simulation of Turbulent Mixing by Rayleigh-Taylor Instability," Phys. Fluids A, **3**(5), pp. 1312–1320.

Venkata Nori
Graduate Research Assistant

Nelson Lerma
Undergraduate Research Assistant

Jonas Gustavsson
Postdoctral Associate

Corin Segal
Associate Professor

Department of Mechanical and Aerospace Engineering,
University of Florida,
Gainesville, Florida 32611

Rene Fernandez
Aerospace Engineer
NASA Glenn Research Center,
Cleveland, Ohio 44135

Forced Oscillations in a Mixed-Compression Inlet at Mach 3.5 for Pulse Detonation Engine Systems

The effects of oscillatory backpressure on the air induction system for pulse detonation engines were examined for a two-dimensional, mixed-compression configuration at a freestream Mach number of 3.5. The pressure perturbations at the diffuser exit were produced by injecting air through four ports located at the corners of the exit cross section. The frequency, coupling of the ports and airflow rates through the ports were varied, simulating the operation of detonation tubes. A terminal normal shock in the diffuser oscillated in the excited inlet, causing large pressure fluctuation amplitudes at some locations. Large injection mass flows resulted in inlet flow oscillations throughout the inlet, increased the spillage, yet did not cause inlet unstart.
[DOI: 10.1115/1.2174061]

Introduction

The pulse detonation engine (PDE) will be an attractive alternative to gas-turbine and rocket engines if the predicted high efficiency, simple design, and low weight materialize. Based on ideal-cycle analysis, up to 33% higher cycle efficiency can be achieved compared to a Brayton cycle [1–4]. To achieve high specific impulse, high operational frequencies in the 50–200 Hz range, which appears feasible within current technology limits, are required. With a suitable air intake system, a PDE is expected to operate over a wide velocity range from zero to supersonic speeds. The thrust may be controlled through changing the firing frequency or the detonation tube filling [6].

There are several challenges in the design of a viable PDE, particularly in the area of detonation initiation. Deflagration-to-detonation transition (DDT) in detonation tubes with practical propellants would require significant tube length, whereas direct initiation (DI) requires substantial initiation energies [5–8]. A recent review of relevant PDE related theoretical and practical issues was presented by Kailasanath [9].

Efficient operation of the PDE also presents inlet design challenges: (i) the external air flow needs to be decelerated from supersonic freestream conditions to a low Mach number, typically about 0.2, at the detonation tube entrance, without large losses in stagnation pressure; (ii) the opening and closing of the detonation tube valves at the back of the inlet should not affect the sensitive boundary layers in the inlet and cause an inlet unstart [10–12].

PDE tubes combined into batteries with a common inlet have two advantages compared to single-tube inlets: smoother thrust and weaker excitations of the inlet's flow as the blocked mass flow in front of one tube may spill into the adjacent detonation tube. An earlier theoretical study [6] indicated that during transient flow at the inlet exit produced by the valving system of a stack of detonation tubes, the time available for the air transfer between adjacent tubes is O(10 μs), which is significantly shorter than the time required to form a hammershock, O(10 ms). Thus, the concept of a plenum inlet supplying air to multiple tubes has the potential to become a practical solution for the inlet of a PDE.

Contributed by the Fluids Engineering Division of ASME for publication in the JOURNAL OF FLUIDS ENGINEERING. Manuscript received March 31, 2004; final manuscript received October 21, 2005. Review conducted by Joseph Katz.

Studies on forcibly excited transonic and low supersonic inlets [10–15] indicate that the shock displacement amplitudes decrease with increasing backpressure excitation frequency in the subresonance regime. Previous studies also indicate that large-amplitude or low-frequency oscillations tend to move the mean shock position upstream of the diffuser eventually leading to an inlet unstart. At higher excitation frequencies, the shock train was predicted to be stable. The strength of the terminal shock in the inlet also plays an important role in deciding the inlet flow stability to externally imposed pressure perturbations. The separation zone produced by the shock-boundary layer interaction may act as an effective medium for propagating shock-generated disturbances.

Previous experiments [15–17] of two-dimensional and axisymmetric inlets, using mechanical blockage simulating PDE tubes out of phase with respect to one another, indicated that the pressure oscillations were moderate and within 3% of the freestream stagnation pressure without flow instability noted near the inlet capture. Higher amplitudes have been recorded with lower excitation frequencies and higher cross flow blockage.

The present investigation is a continuation of these studies with a two-dimensional inlet operating at a higher freestream Mach number of 3.5 and having a mixed-compression configuration. This inlet employed a fluidic rather than mechanical blockage, which was used in previous studies. Several different injection geometric patterns were tested and injection frequencies of 5 and 10 Hz were tested. While these frequencies are an order of magnitude or more lower than those required to make a PDE produce sufficient thrust to be a viable propulsion alternative, previous studies have shown that in the low-frequency range, the induced amplitude tends to fall with increasing frequency [10–15]. Bleed regions on the cowl and ramp were incorporated to reduce the effects of boundary layer separation. Separation zones and complex wave patterns were observed due to substantial boundary layer growth and shock-induced separation. The stagnation pressure recovery at the exit was 0.3, similar to findings of previous work with a similar configuration but a larger-scale, unblocked inlet [18]. This study focused on the effects of (i) injection geometry configurations, (ii) mass injected into the inlet, and (iii) frequency of air injection on the inlet performance and flow stability. Described below is the extent of these effects and the upstream interactions in the inlet duct in terms of amplitude, rms, and spatial extent of the flow perturbations.

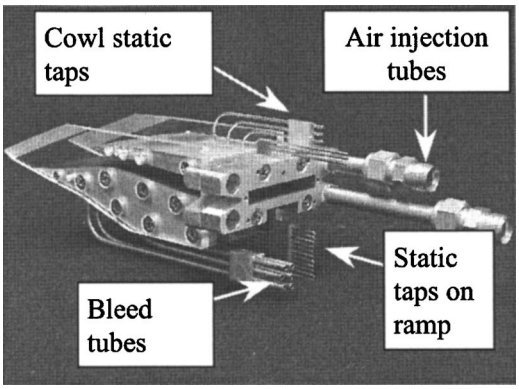

Fig. 1 PDE inlet with injection block mounted at the back. Rear side view of the inlet showing its main components.

Experimental Setup

Geometric Configuration. The present inlet was derived from a previous configuration [18] with the leading edge modified to operate with shock-on-lip at Mach 3.5. Figure 1 shows the inlet model with the four air injection ports at the exit, two of which have had the injection tubes removed for clarity. The two-dimensional compression system consisted of two 5 deg wedges on the ramp, and the cowl. The cowl is inclined at a constant, −4 deg relative to the horizontal and has a leading edge at $X/L=0.355$ with a full angle of 16 deg. The geometric throat with a height of 6.2 mm was located at $X/L=0.567$. The exit plane of the inlet was a 9×50 mm^2 rectangle. Figure 2 illustrates the inlet's shock system as calculated from the oblique shock relations, and gives the total ramp length $L=135$ mm and exit height $h=9$ mm used for normalizing the axial coordinate X and the vertical coordinate y, respectively. Due to viscous effects, a separation region was observed between $X/L=0.226$ and $X/L=0.396$, resulting in increased spillage at the inlet entrance. To reduce the extent of this separated region, 6% of the inlet capture was bled out equally from two locations, at $0.264<X/L<0.287$ and $0.418<X/L<0.441$, respectively, as shown in Fig. 3. The bleed plenums were connected to a vacuum line outside the wind tunnel. Each of the two shaded areas shown in Fig. 3(*b*) contained 60 evenly distributed 0.25-mm diameter holes, giving a total bleed surface area of 6 mm^2. Wall static pressures were measured at 11 different streamwise locations as shown in Fig. 3, along a common axis offset by 10 mm in the spanwise direction from the inlet centerline. Static pressures were measured at four locations aft of the terminal shock both on the cowl and the ramp simultaneously in selected experiments. Stagnation pressure measurements were taken at the exit of the inlet with a vertical stagnation pressure rake having three probes embedded in the exit injection block, as shown in Fig. 4. The equidistantly spaced probes measured the stagnation pressure at $Y^*=y/h=0.145$, 0.500, and 0.855 at the exit section.

Air Injection System. The injection block located at the inlet exit housed the air injection ports, which were located at the four corners of the exit cross section of the inlet as shown in Fig. 5(*a*). The 7.9 mm diameter circular jets were perpendicular to the streamwise direction at $X/L=1.045$ and had an angle of 13.4 deg to the horizontal plane. In a given run, all ports were operated at the same frequency—either 5 Hz or 10 Hz depending on the test conditions. Figure 5(*b*) shows a schematic of the external jet ex-

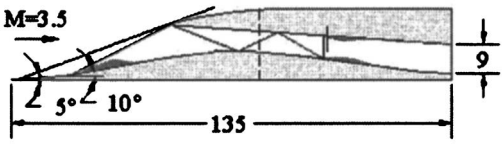

Fig. 2 Shock structure as calculated from oblique shock relations with terminal normal shock. Estimated regions of separated flow are shaded. All dimensions are in mm.

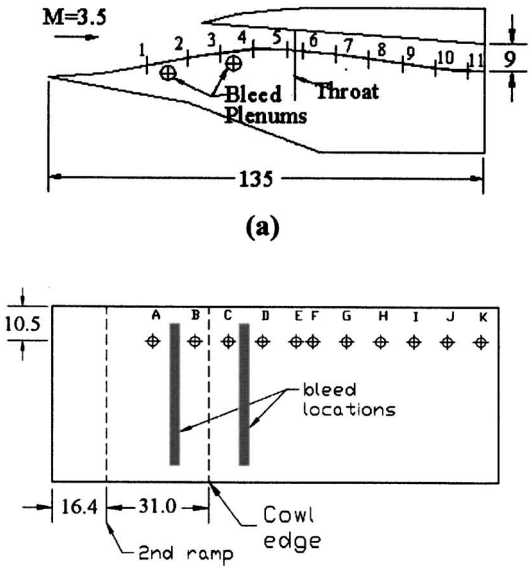

tap	X/L	tap	X/L
A	0.226	G	0.659
B	0.320	H	0.734
C	0.395	I	0.809
D	0.470	J	0.884
E	0.546	K	0.960
F	0.583		

(c)

Fig. 3 (*a*) Inlet schematic showing the location of wall static pressure taps and bleed plenums along with the definitions of $L=135$ mm and $h=9$ mm used for axial and vertical normalization, respectively. (*b*) Top view schematic of the inlet ramp showing static tap and boundary layer bleed locations. (*c*) Static tap streamwise locations. All dimensions are in millimeters.

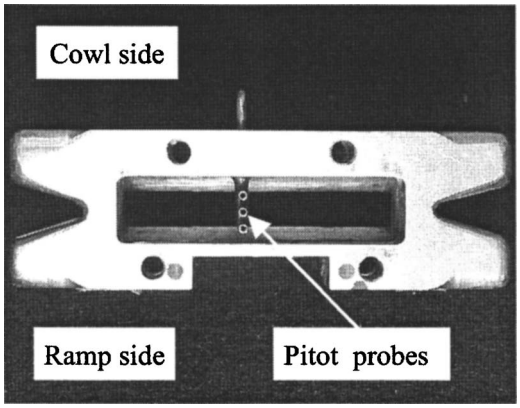

Fig. 4 Front view of the exit injection block with the stagnation pressure rake embedded in it with the probe designations. Flow is into the page.

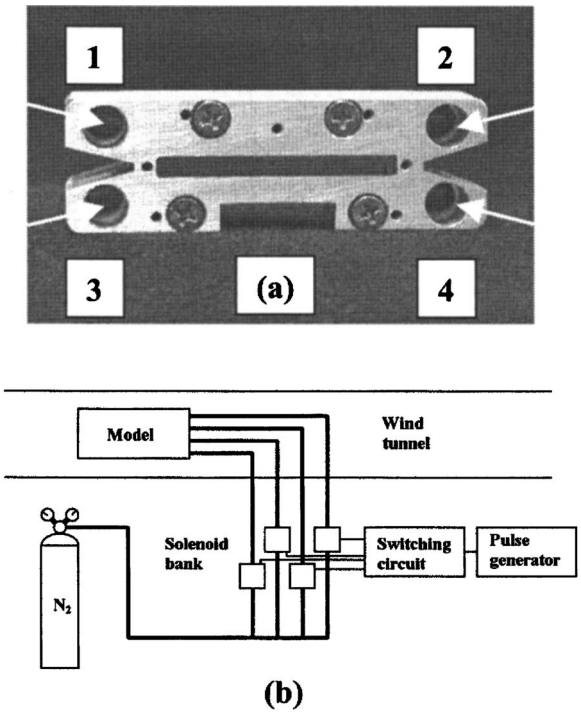

Fig. 5 (*a*) **Rear view of the exit injection block with the port designations and the injection configurations below. Flow is out of the page. 1. Cowl coupling: Ports (1,2) inject air. 2. Ramp coupling: Ports (3,4) inject air. 3. Side coupling: Ports (1,3) inject air. 4. Cowl-ramp coupling: Ports (1,2) and (3,4) inject air, 180 deg out of phase. 5. Side-side coupling: Ports (1,3) and (2,4) inject air, 180 deg out of phase. 6. Ninety degree phase coupling: Each port injects air at 90 deg out of phase with the neighboring ports.** (*b*) **Air injection system schematic.**

(a)

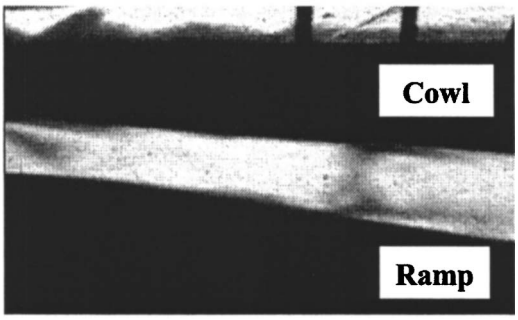

(b)

Fig. 7 Schlieren images. (*a*) **Entire flow field in the inlet without injection. The shocks generated by the two wedges are visible along with the separation bubble on the second wedge, which produces the expansion associated with reattachment.** (*b*) **Close-up view of the terminal shock structure and the separation induced both on the cowl and the ramp.**

citation system. Air was supplied through four 4.9 mm inner diameter pipes passed through the wind tunnel wall downstream of the model and connected to a bank of four solenoid valves. A custom-built transistor-transistor logic (TTL) circuit controlled the frequency and the coupling of the injection solenoid valves. The circuit takes a 50% duty cycle square wave signal from a Leader LFG-1300S function generator and produces four 25% duty cycle, square wave output signals whose phase relation can be changed allowing one, two, or four valves to be synchronized in different configurations.

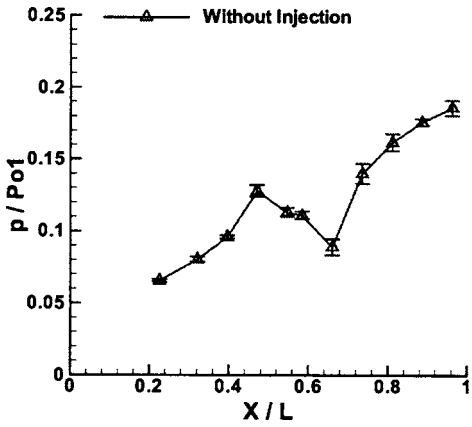

Fig. 6 Mean wall static pressures normalized by the wind tunnel stagnation pressure with no air injection

Pressure Data and Image Acquisition System. The static pressures and stagnation pressures were measured using a PSI® 9010 scanner and three Omega® PX-303 transducers. Two Omega® transducers measured the upstream and downstream pressures across a solenoid valve. The Omega® transducers were read along with the tunnel stagnation and static pressures at 1 kHz sampling frequency using a 12-bit NI® AT-MIO-16E-2 DAQ board on a personal computer (PC), while the pressure scanner was read at 25 Hz. The Omega® and PSI® 9010 transducers used in this model had stable calibrations giving slope differences of $<0.5\%$ between calibrations carried out at different times. Constant offsets were corrected for through adjusting the transducer calibrations at atmospheric conditions prior to each run. The uncertainty at a representative tunnel stagnation pressure of 7.8 atm was 0.3% of P_{01} for the pressure measurements. The dynamic response of the transducer-tubing system was evaluated in a previous tests where it was found that 0.8 m tubing with 1.5 mm inner diameter connected to between pressure taps and the PX-303 transducers produced a response in the 5–100 Hz interval that was well approximated by a first-order system with a time constant of 22 ms. This suggested that the amplitude of a sinusoidal pressure signal at 5 Hz and 10 Hz will be underestimated by 3.5% and 12%, respectively.

Using a 150 mm diameter schlieren system, the shock system in the inlet model was observed throughout the test to ensure that no unstart or major shift in the external flow field occurred during the experiment. The schlieren images projected onto a screen were captured using a camcorder.

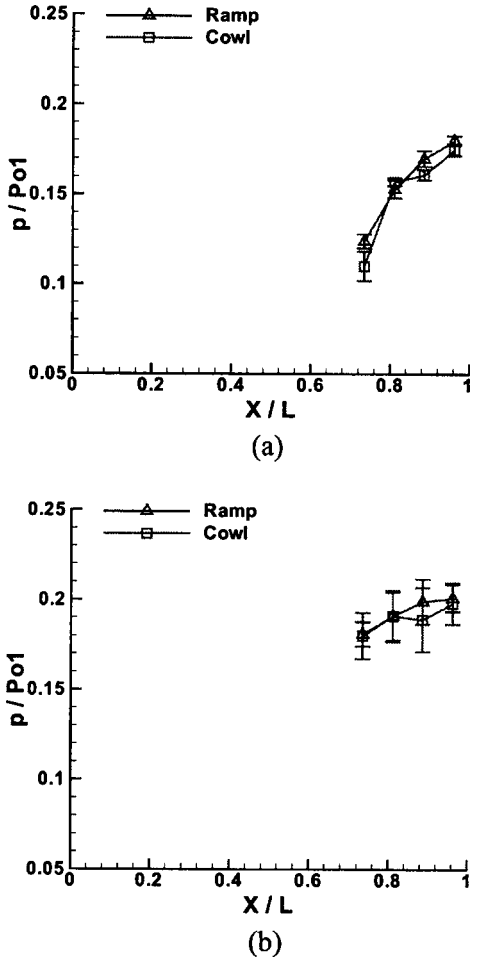

Fig. 8 Comparison between the ramp and the cowl mean normalized static pressures. (*a*) Noninjection case. (*b*) Injection case.

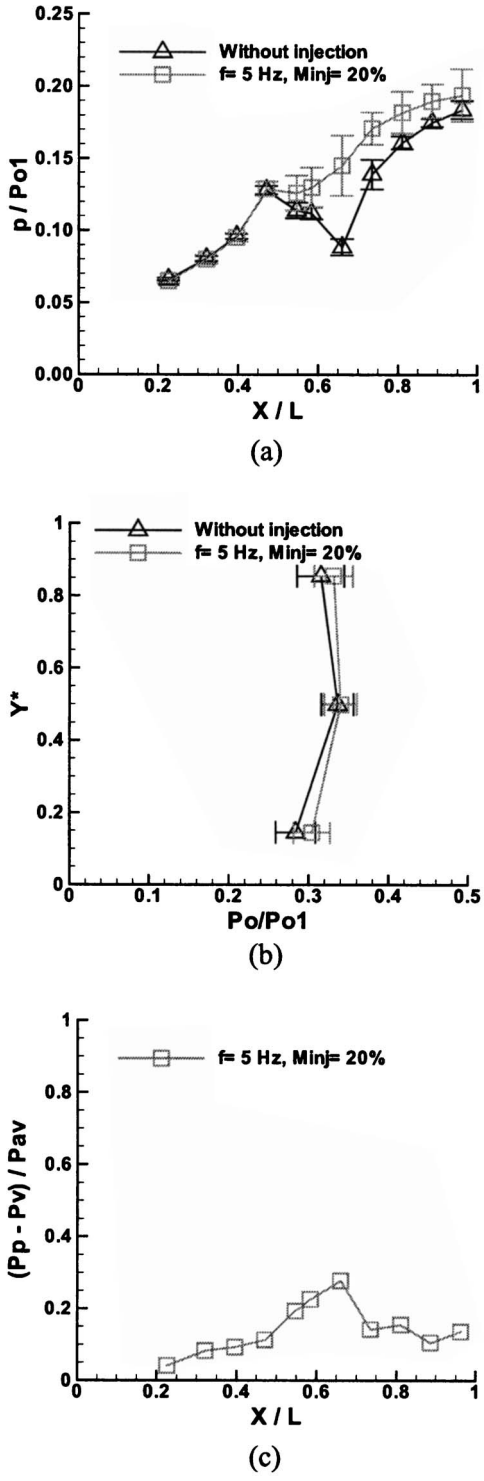

Fig. 9 Plots for comparing the excited and the unexcited inlet, for M_{inj}=20% and f=5 Hz for the 90 deg phase coupling case. (*a*) Mean normalized wall static pressure. The error bars show the ±×RMS fluctuation amplitude. (*b*) Normalized exit stagnation pressure. (*c*) Normalized wall static pressure fluctuation.

Test Conditions. The (MAE) department wind tunnel used for the present investigation is a continuously variable Mach 1.5-4 blowdown tunnel with a 150×150 mm^2 test section cross section. The 14 atm storage tank pressure allowed runs in excess of 30 s duration to be achieved at the Mach 3.5 test condition. Examination of the temporal flow quality in the wind tunnel using a centrally mounted Pitot probe indicated a near-Gaussian pressure distribution with 1% P_{01} rms. Fourier transform analysis revealed no significant peaks in the frequency spectrum. During the runs, dry air at 300 K stagnation temperature was maintained while the tunnel stagnation pressure dropped from 13 atm to 7 atm. The high initial stagnation pressure was necessary to start the tunnel and was followed by a plateau during the latter half of the run where the stagnation pressure dropped from 0.55 atm to 0.48 atm. During the 3 s time when the solenoid valves were operated and data acquired during this phase, the tunnel stagnation pressure drop was $<$0.25 atm. Despite the large drop in stagnation pressure during the course of a run, the variation of all steady-state inlet stagnation and static pressures remained stable within ±1.5% of P_{01} throughout a run, when normalized by the tunnel stagnation pressure. This also meant that the local Mach numbers were constant, and hence there was no fluctuation in speed of sound, flow speeds, or Reynolds number during the runs as long as heat conduction effects near the model surface are neglected.

Experiments were carried out with

- Six different injection configurations: intermittent on a side, cowl, ramp, alternating side-side, cowl-ramp, and circulating around the injection block in 90 deg phase coupling.
- Two different nominal injection mass flows: 20% and 40% of inlet capture.
- Two different frequencies: 5 Hz and 10 Hz.

The unexcited inlet capture mass flow was 195 g/s when the

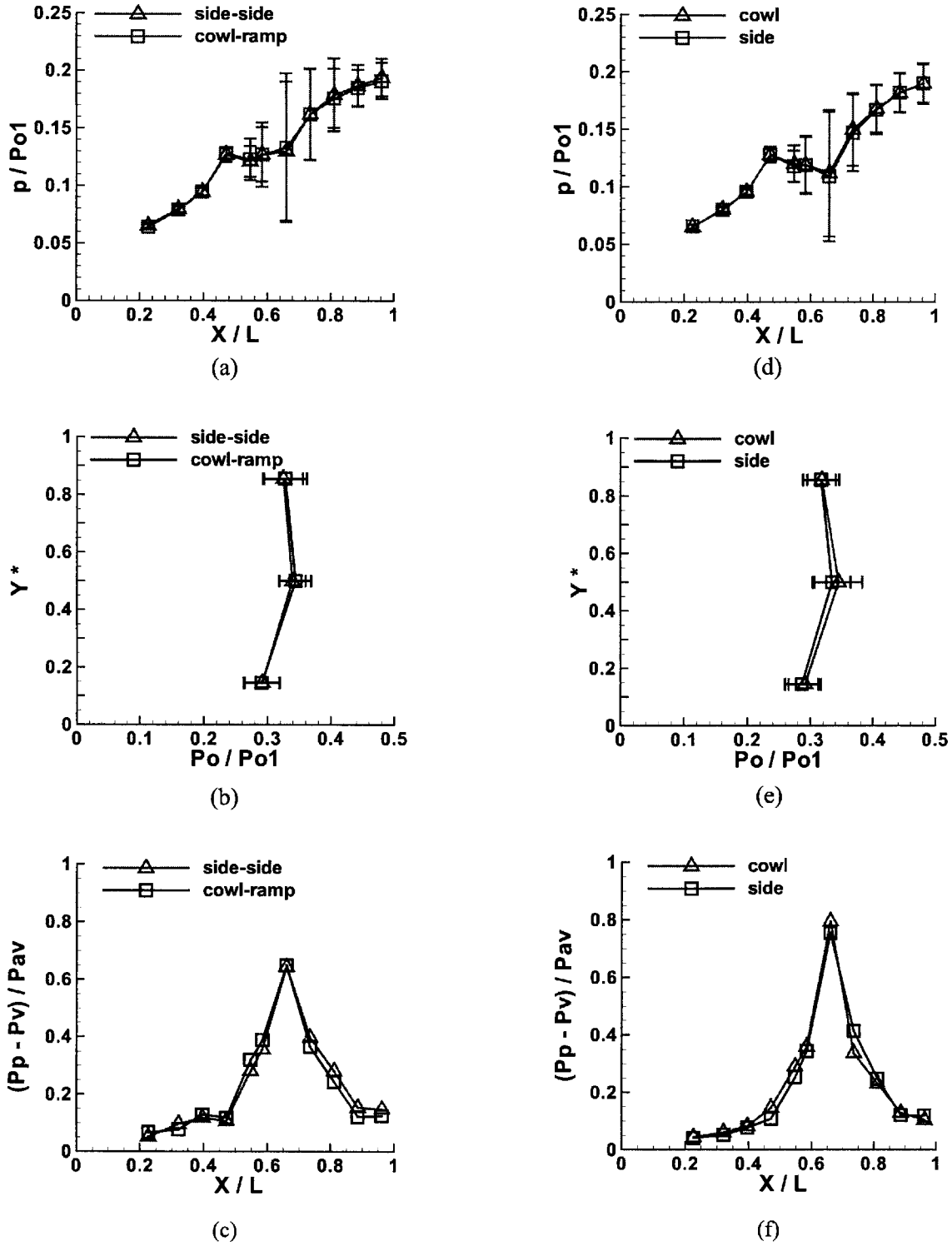

Fig. 10 Configuration effects: side-side versus cowl-ramp ((*a*), (*b*), and (*c*)); cowl versus side ((*d*), (*e*), and (*f*)); cowl versus ramp ((*g*), (*h*), and (*i*)); side-side versus side ((*j*), (*k*), and (*l*)); 90 deg phase versus cowl ramp ((*m*), (*n*), and (*o*)); 90 deg phase versus, side ((*p*), (*q*), and (*r*)). • (*a*), (*d*), (*g*), (*j*), (*m*), and (*p*): Mean normalized wall static pressure. The error bars show the ±2×RMS fluctuation amplitude. • (*b*), (*e*), (*h*), (*k*), (*n*), and (*q*): Normalized exit stagnation pressure. • (*c*), (*f*), (*i*), (*l*), (*o*), and (*r*): Normalized wall static pressure fluctuation.

tunnel stagnation pressure was 7.8 atm. The mass injected into the inlet was estimated from the flow coefficient of the solenoid valve using the measured upstream and downstream pressures at the solenoid valve. The mass injected into the inlet is given as a percentage of the unexcited inlet capture mass flow. The relative uncertainty in the mass flow measurements is estimated at ±10%.

Results and Discussion

Flow Field in the Inlet. Static pressure distribution for the unexcited inlet is shown in Fig. 6. The error bars in this figure show ±2 standard deviations. The schlieren images as shown in Figs. 7(*a*) and 7(*b*) confirm the existence of the normal shock at

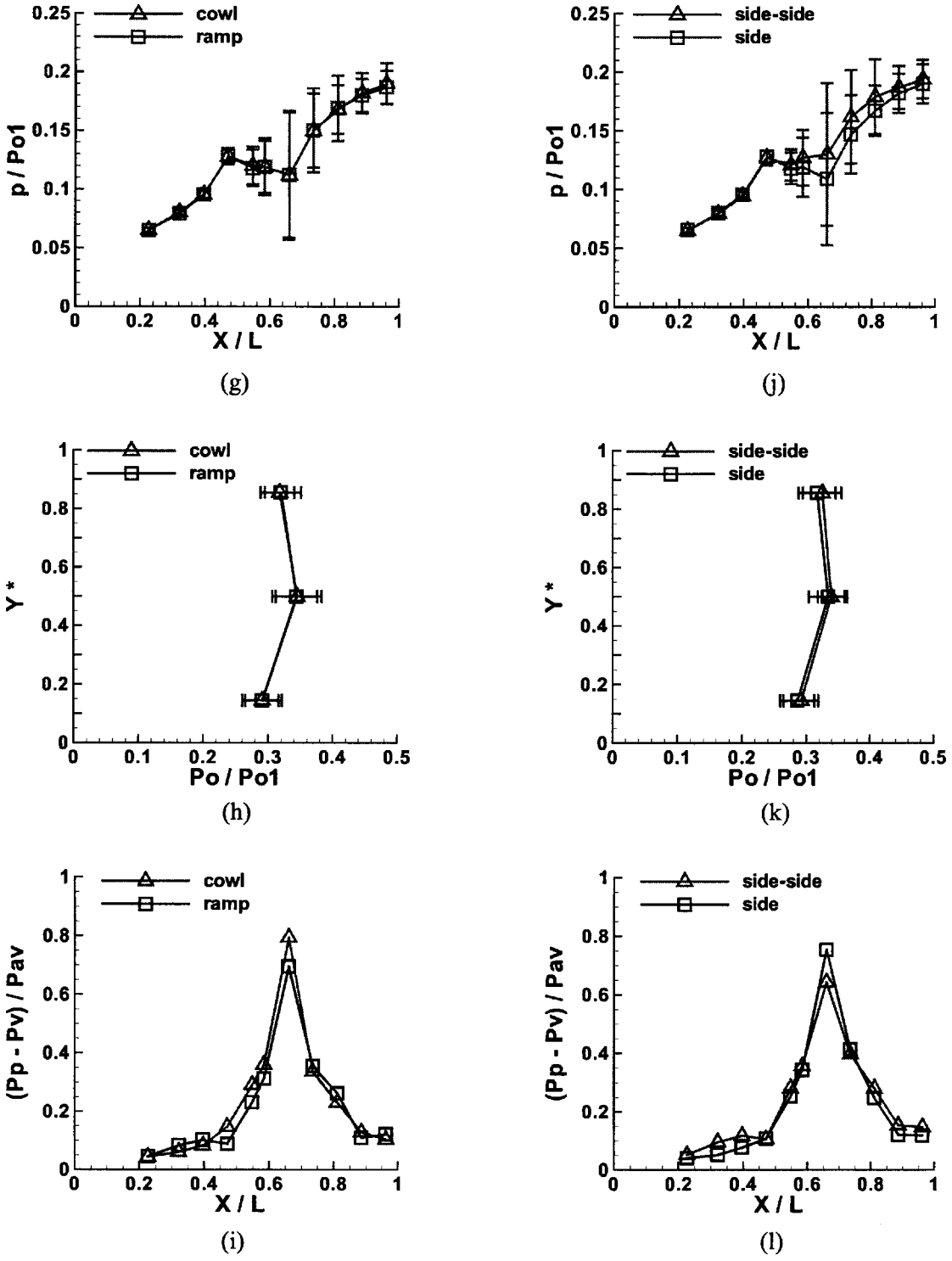

Fig. 10 (*Continued*).

the location $X/L \sim 0.73$, which explains the sudden jump in the static pressure at tap 7. Figure 7(*a*) shows the entire inlet flow field with the complex wave system at the inlet capture. The shocks generated by the two wedges are visible along with the separation bubble on the second wedge, which produces a secondary shock associated with reattachment. The dark band seen in Fig. 7(*a*) emerging from the ramp downstream of the separation bubble and extending close to the cowl is not related to the flow features. Rather, it is an optical effect caused by stresses in the side Plexiglas® plate. Shocks reflect from the inlet's wall upstream of the terminal normal shock. Figure 7(*b*) shows the terminal shock with the thick boundary layers on both cowl and ramp along with its three dimensionality giving it a less sharply defined schlieren image. The separated regions produced by the terminal shock are also shown as shaded areas in Fig. 2. Therefore, the pressure rise across the shock is 50% of the value calculated for a normal shock that occupies the entire cross section. The overall static pressure rise in the inlet is 13% of P_{01}.

Comparison of Ramp and Cowl Static Pressures. Static pressure measurements were taken on both the cowl and the ramp surfaces at the locations immediately downstream of the shock to

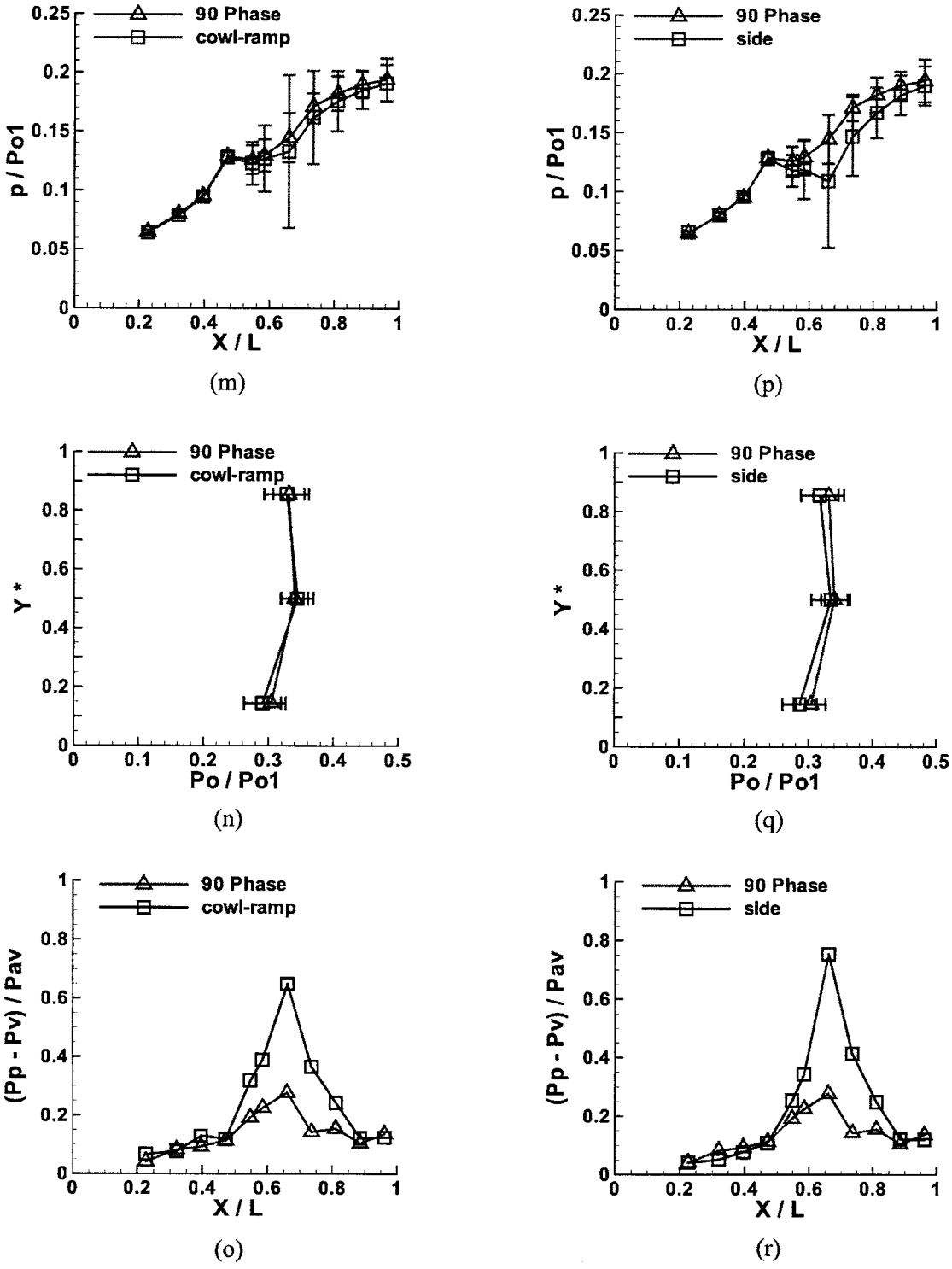

Fig. 10 (*Continued*).

check if there were any differences between the two static pressure profiles due to the shock-induced separation region. Figures 8(*a*) and 8(*b*) compares the mean normalized static pressures measured on the ramp and the cowl for both the noninjection and the injection case. In the injection case, a flow rate equal to 40% of the inlet capture flow was injected at a pulse frequency of 5 Hz and using 90 deg phase offset coupling. It can be seen that the static pressure measurements on the cowl and the ramp agree, but with variation at $X/L=0.89$.

Effects of Injection Configuration. The 20% mass injection and 5 Hz backpressure excitation frequency case was considered to evaluate the effects of injection configurations. The labeling of exit injection block ports, injection configurations, and their abbreviations are given in Fig. 5. Ninety degree phase coupling is considered for comparing the unexcited inlet with that of the excited inlet and the plots shown in Fig. 9. Figure 9(*a*), indicates that the mean levels of static pressures downstream of the throat in the excited inlet are higher than the corresponding ones of the unex-

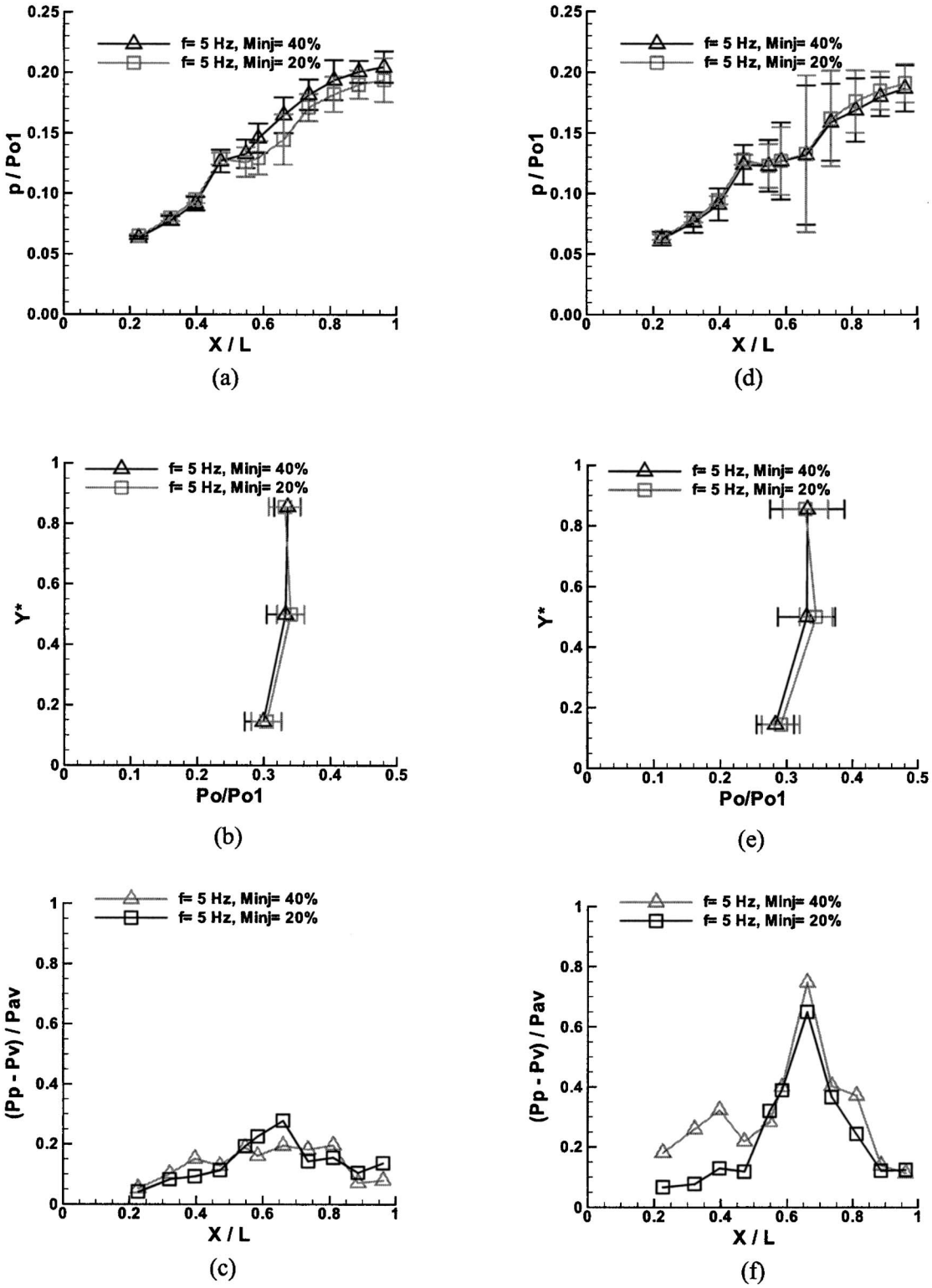

Fig. 11 Mass injection effects: 90 deg phase configuration ((*a*), (*b*), and (*c*)); side-side configuration ((*d*), (*e*), and (*f*)); cowl-ramp configuration ((*g*), (*h*), and (*i*)); side configuration ((*j*), (*k*), and (*l*)); cowl configuration ((*m*), (*n*), and (*o*)); ramp configuration, ((*p*), (*q*), and (*r*)). • (*a*), (*d*), (*g*), (*j*), (*m*), and (*p*): Mean normalized wall static pressure. The error bars show the ±2×rms fluctuation amplitude. • (*b*), (*e*), (*h*), (*k*), (*n*), and (*q*): Normalized exit stagnation pressure. • (*c*), (*f*), (*i*), (*l*), (*o*), and (*r*): Normalized wall static pressure fluctuation.

cited inlet. The same trend is observed with the pressure oscillations produced in the inlet. The stagnation pressure at the exit also changed because of the terminal shock oscillations. The exit stagnation pressures follow the typical trend in that the pressure values are lower near both the cowl and ramp walls and increasing from the walls to the center section, as observed in Fig. 9(*b*). It is also observed that the ramp side stagnation pressure is always lower than the cowl side measured stagnation pressure because of the greater degree of separation on the ramp side. All these phenomena can be attributed to the large-scale terminal shock oscil-

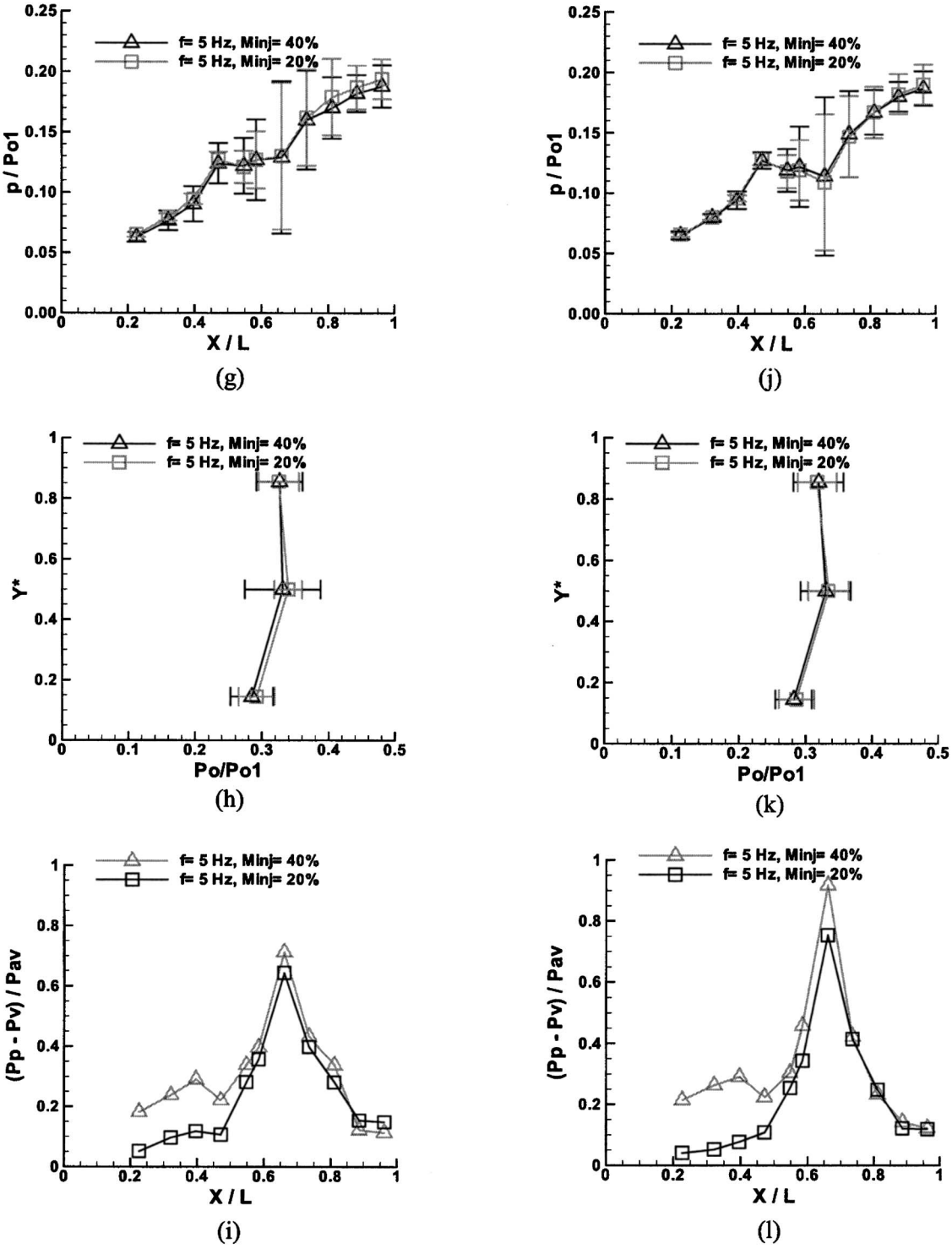

Fig. 11 (***Continued***).

lations generated in the excited inlet. Figure 9(*c*) shows that the largest pressure fluctuations were found near the location of the terminal shock rather than at the injection ports. The average normalized pressure fluctuation of the six most downstream ports was 0.17 at 5 Hz injection to be compared to 0.05 without injection, illustrating that the fluctuations were primarily due to pulsating injection rather than the inherent instability of the separated region.

Figure 10 shows the effect of injection configuration on the static and stagnation pressure measured at the inlet exit. From Figs. 10(*a*)–10(*c*) it can be observed that the cowl-ramp and the side-side injection configurations produce almost identical levels of static pressure, stagnation pressure at the exit, and their associated oscillations during injection. The same is true with the cowl, ramp, and side injection configurations as can be deduced from Figs. 10(*d*)–10(*i*). The cowl-ramp and side-side configurations generated slightly larger mean static and exit stagnation pressures, while the corresponding fluctuations were smaller than for the side, cowl, or ramp couplings, as shown in Fig. 10. It should be noted, however, that the differences in the fluctuation

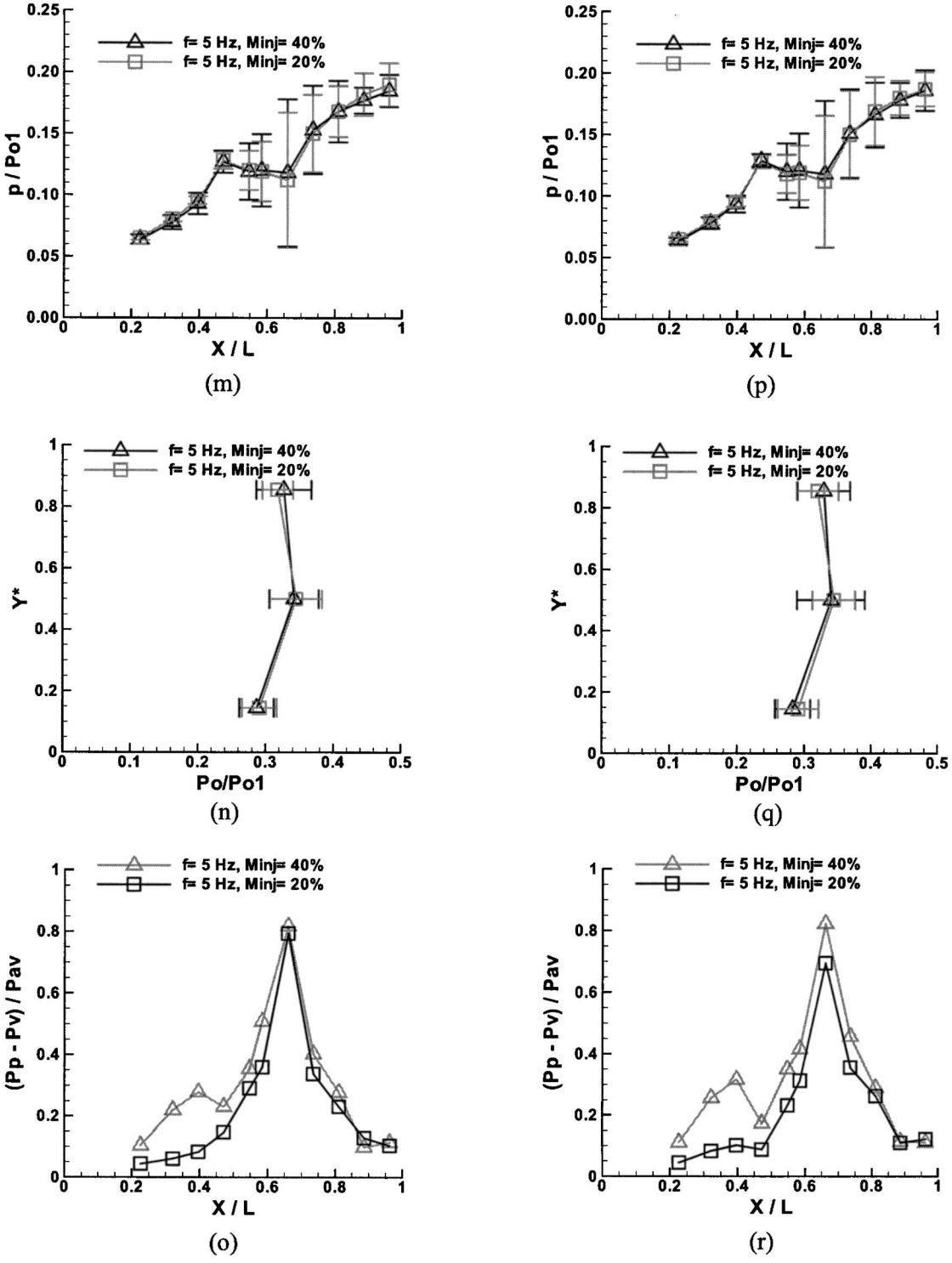

Fig. 11 (***Continued***).

for the side-side coupling and side coupling, as shown in Fig. 10(*l*) can be attributed to the differences in the mean pressure levels attained in the respective injection configuration. The cowl-ramp and the side-side configurations produced shock oscillations whose effects propagated farther upstream than those of the cowl, ramp, or side couplings, as illustrated by Fig. 10(*j*). The differences may be due to the fact that in the cowl-ramp and the side-side coupling configurations, air is injected from all the ports in the exit injection block, which may have caused a larger degree of shock displacement, and thus the observed effects. From Fig. 10(*m*), it can be inferred that among all injection configurations, the 90 deg phase configuration produced the largest levels of mean static pressure in the inlet. Also note that the 90 deg phase coupling produced the lowest levels of shock oscillations and, therefore pressure oscillations. For example, considering Fig. 10(*p*), the rms intensities reached to a maximum of 7% of the local mean static pressure in the case of 90 deg phase coupling while a maximum of 25% was attained in the case of side-side and ramp-cowl coupling. This maximum occurs at tap 7, about which the shock is oscillating. As shown in the plots, static pressure taps 6, 7, and 8 at $X/L=0.584$, 0.660, and 0.735 are affected by the

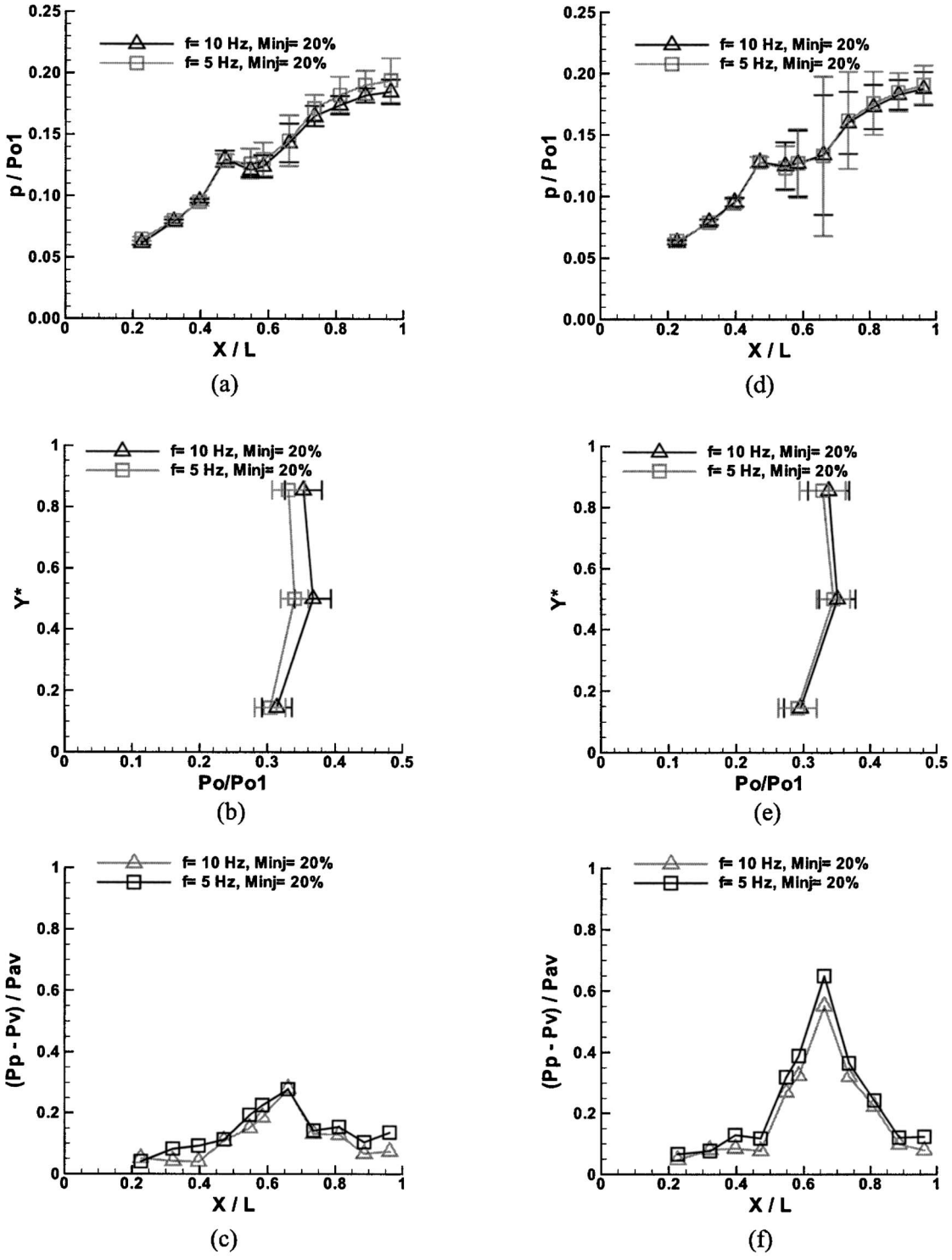

Fig. 12 Frequency effects: 90 deg phase configuration ((*a*), (*b*), and (*c*)); cowl-ramp configuration ((*d*), (*e*), and (*f*)); side-side configuration ((*g*), (*h*), and (*i*)). • (*a*), (*d*), and (*g*): Mean normalized wall static pressure. The error bars show the ±2× rms fluctuation amplitude. • (*b*), (*e*), and (*h*): Normalized exit stagnation pressure. • (*d*), (*f*), and (*i*): Normalized wall static pressure fluctuation.

shock oscillations. The recorded rms variations in the wall pressures were <12% of the corresponding mean static pressures.

Effect of Mass Injection. Effecfs of injection mass flows of 20% and 40% of the inlet capture flow were compared for all six injection configurations at a backpressure excitation frequency of 5 Hz, with the results presented in Fig. 11. In Figs. 11(*a*)–11(*c*) for the 90 deg phase coupling, increased mass injection led to an increase in the mean static pressure downstream of the throat of up to 0.02 P_{01}. It is noteworthy that the oscillations produced in the 40% case are either equal or smaller than those produced in the 20% case. Interestingly, for the other injection configurations, as in Figs. 11(*d*)–11(*r*), the mean levels of the static pressure are

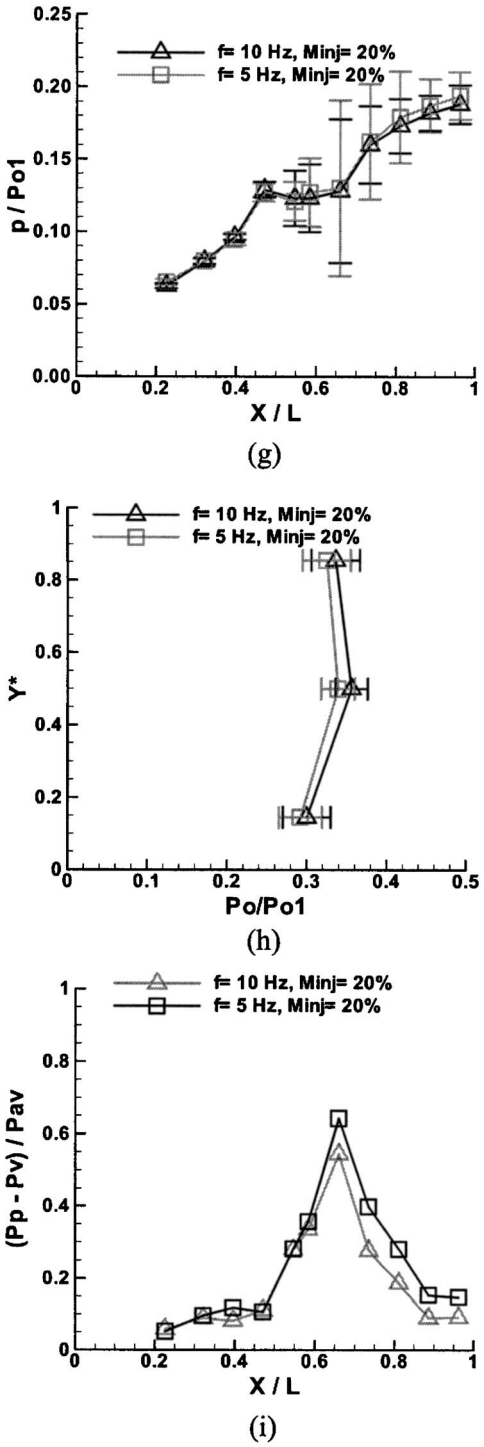

Fig. 12 (***Continued***).

almost identical for both the injection flow cases. Nevertheless, for the 40% case, large pressure oscillations are generated and the effect is clearly felt in the static taps upstream of the throat for all configurations, except 90 deg phase coupling. For example, in the side-side configuration rms intensities for tap 3 ($X/L=0.396$) were 3% and 8% of the mean static pressure, for the 20% and 40% injection cases, respectively. Thus, in general, the 20% injection case produced pressure oscillations, which were confined to the downstream of the throat, whereas the 40% injection case produced oscillations, affecting the static pressure all the way up to the capture. This can be clearly seen by comparing the static pressure fluctuation for the different cases as shown in Figs. 11(*c*), 11(*f*), 11(*i*), and 11(*l*). In the 40% case a small drop in pressure could be observed in the first three static taps during injection. This was due to the increased spillage in the 40% injection case and the accompanied weakening of the leading edge wave system.

Frequency Effects. Tests were conducted with the same injection mass flow, i.e., 20% of the inlet capture, but with different excitation frequency for three representative injection configurations, namely, the 90 deg phase coupling, cowl-ramp, and side-side coupling.

Figures 12(*a*)–12(*i*) compare the effects produced by the excitation frequencies 5 Hz and 10 Hz the inlet flowfield. In all the injection configurations considered here, the 5 Hz excitation case produced larger pressure oscillations than the 10 Hz case as can be seen in the fluctuation versus X/L plots of Fig. 12. The rms intensities in the 5 Hz case were 1.05–1.5 times higher than those of the 10 Hz case, to be compared to 10% damping expected due to the response of the tubing/transducer system. The change in frequency did not have any significant effect on the mean pressure levels on the cowl-ramp and side-side configurations considered, but the higher injection mass flow in the 5 Hz case produced slightly higher mean static pressure levels for the 90 deg phase coupling.

The mean exit stagnation pressures in the 10 Hz case were $0-0.03\ P_{01}$ higher than in the 5 Hz case for all injection configurations, as shown in Figs. 12(*b*), 12(*e*), and 12(*h*).

Summary

A two-dimensional, mixed compression PDE inlet was tested in Mach 3.5 air flow with oscillations produced by air injection at the exit cross section simulating the operation of PDE detonation tubes. The upstream effect of the backpressure oscillation on the inlet flow and on the inlet pressure recovery were measured. The results indicated the following:

- Shock-induced separations are found both on the second external ramp and behind the terminal shock in the diffuser.
- A separation bubble was noted on the second wedge, which disrupts the flow and caused a complex shock and expansion wave system.
- In general, mean upstream shock migration as well as terminal shock oscillations were produced by the pulsed air injection and the mean levels of static pressure downstream of the throat increased during injection.
- Large-amplitude pressure oscillations were observed with rms intensities as high as 25% of the local mean static pressure in all the injection configurations at 5 Hz and 20% mass flow except the 90 deg phase coupling, where it reached 7%.
- Even when a substantial amount of the inlet capture mass was injected, i.e., 40% of capture, the inlet remained started, though with increased spillage.
- For a given injection mass flow and excitation frequency, the 90 deg phase coupling produced the lowest levels of pressure oscillations, but also produced the highest mean static pressure downstream of the throat compared to the other coupling configurations.
- For a given injection mass flow and excitation frequency, the side-side and cowl-ramp injection configurations produced similar mean levels of static pressure throughout the inlet during injection. The same was true with the cowl, ramp, and side couplings, but the mean static pressure produced in these cases was slightly lower than those produced by the cowl-ramp and the side-side couplings.
- For a given injection mass flow and excitation frequency, the cowl-ramp and side configurations produced shock

oscillations whose effects propagated farther upstream than those of the cowl, ramp, and side couplings.

- While the 20% injection case resulted in pressure oscillations confined to the downstream of the throat, the higher mass flow case produced pressure oscillations propagating all the way up to the inlet capture.
- The mean static pressure downstream of the throat was not affected significantly by the injectant mass flow, except for the 90 deg phase injection configuration, where the higher mass flow case led to increases of up to 0.02 P_{01} downstream of the throat.
- The stagnation pressure at the exit was not affected significantly by mass injection. Mean observed total pressure recovery of 0.3 and 0.33 were produced in the unexcited and the excited inlet, respectively. The low pressure recovery was a result of both shock system losses and presence of separated regions in the inlet
- The static pressure rise in the inlet was 13% of P_{01}. The backpressure ratio, defined as the ratio between the exit static pressure to the freestream stagnation pressure, was 0.2.
- For a given injection mass flow and an injection configuration, lower backpressure excitation frequency produced larger pressure oscillations.

Acknowlegdment

This work has been supported by a grant from NASA Glenn Research Center with Dr. Rene Fernandez as the technical monitor.

Nomenclature

f = excitation frequency, Hz
h = inlet height at the exit cross section, mm
L = inlet length, leading edge of the ramp exit, mm
M_{lnj} = mass injected, as a portion of the unexcited inlet capture mass flow
P_v = lowest static pressure during valve operation at a particular tap, atm
P_p = peak static pressure during valve operation at a particular tap, atm
P_{av} = mean static pressure during valve operation at a particular tap, atm
$(P_p-P_v)/P_{\mathrm{av}}$ = normalized pressure fluctuation
p = static pressure, atm
P_{rms} = rms of static pressure, atm
P_0 = stagnation pressure at the exit, atm
P_{01} = tunnel free-stream stagnation pressure, atm
X = streamwise coordinate measured from the leading edge of the ramp, mm
X/L = nondimensional streamwise coordinate
y = Ordinate measured from the ramp, at the exit cross section, mm
$Y^*=y/h$ = nondimensional vertical coordinate

References

[1] Heiser, W. H., and Pratt, D. T., 2002, "Thermodynamic Cycle Analysis of Pulse Detonation Engines," J. Propul. Power, **18**(1), pp. 68–76.
[2] Santoro, R. J., Conrad, C., Lee, S. Y., and Pal, S., 2001, "Fundamental Multi-Cycle Studies of the Performance of Pulse Detonation Engines," *Proceedings of the ISABE 2001 Conference*, Bangalore, India, September.
[3] Wu, Y. H., Ma, F. H., and Yang, V., 2002, "System Performance and Thermodynamic Cycle Analysis of Air-Breathing Pulse Detonation Engines," AIAA Paper 2002-0473, *40th AIAA Aerospace Sciences Meeting and Exhibit*, Reno, NV, January.
[4] Povinelli, L. A., 2001, "Comparison of Pulse Detonation Engine Performance with Thermodynamic Cycle Analysis," AIAA 2001-1212, *Proceedings of the ISABE 2001 Conference*, Bangalore, India, September.
[5] Bussing, T., and Pappas, G., 1996, "Pulse Detonation Engine Theory and Concepts," Developments in High-Speed-Vehicle Propulsion Systems, Prog. Astronaut. Aeronaut., **165**, pp. 421–472.
[6] Pegg, R. J., Couch, B. D., and Hunter, L. G., 1996, "Pulse Detonation Engine Air Induction System Analysis," AIAA Paper 96-2918, *32nd Joint Propulsion Conference*, Lake Buenavista, FL, July.
[7] Schultz, E., Wintenberger, E., and Shepherd, J. E., 1999, "Investigation of deflagration detonation transition for application to pulse detonation engine ignition systems," *Proceedings of the 16th JANNAF Propulsion Symposium*, pp. 175–202.
[8] Li, S. C., Varatharajan, B., and Williams, F. A., 2001, "The Chemistry of JP-10 Ignition," AIAA 2001-1074, *39th Aerospace Sciences Meeting and Exhibit*, Reno, NV, January.
[9] Kailasanath, K., 2002, "Recent Developments in the Research on Pulse Detonation Engines," AIAA 2002-0470, *40th AIAA Aerospace Sciences Meeting & Exhibit*, Reno, NV, January.
[10] Sajben, M., Bogar, T. J., and Kroutil, J. C., 1984, "Forced Oscillations in Supercritical Diffuser Flows," AIAA J., **22**(4), pp. 465–474.
[11] Bogar, T. J., 1986, "Structure of Self-Excited Oscillations in Transonic Diffuser Flows," AIAA J., **24**(1), pp. 54–61.
[12] Biedron, B. T., and Adamson, T. C., 1988, "Unsteady Flow in a Supercritical Supersonic Diffuser," AIAA J., **26**(11), pp. 1336–1345.
[13] Bogar, T. J., Sajben, M., and Kroutil, J. C., 1985, "Response of a Supersonic Inlet to Downstream Perturbations," J. Propul. Power, **1**(2), pp. 118–125.
[14] Ott, P., Bölcs, A., and Fransson, T. H., 1993, "Experimental and Numerical Study of the Time-Dependent Pressure Response of a Shock Wave Oscillating in a Nozzle," Paper 93-GT-139, *ASME Turbo-Expo, Land, Sea and Air*, Cincinnati, OH, May 24–27.
[15] Gustavsson, J., Nori, V., and Segal, C., 2003, "Inlet/Engine Interactions in an Axisymmetric Pulse Detonation Engine System," J. Propul. Power, **19**(2), pp. 282–285.
[16] Mullagiri, S., Gustavsson, J. P. R., and Segal, C., 2001, "Modeling of Air Intake and Engine Interaction in Pulse Detonation Engine Systems," AIAA 2001-1211, *Proceedings of the ISABE 2001 Conference*, Bangalore, India, September.
[17] Mullagiri, S., Gustavsson, J., Segal, C., 2001, "Modelling of Air Intake and Engine Interactions in Pulse Detonation Engine Systems," *Proceedings of the 13th ONR Propulsion Meeting*, pp. 155–160.
[18] Fernandez, R., and Nenni, J., 2002, "Pulsed Detonation Engine Inlet Experimental and CFD Results," NASA TM 2002-211581.

Investigation of Microbubble Boundary Layer Using Particle Tracking Velocimetry

Javier Ortiz-Villafuerte[1]

Yassin A Hassan[2]
e-mail: y-hassan@tamu.edu

Department of Nuclear Engineering,
Texas A&M University,
College Station, TX 77843-3133

Particle tracking velocimetry has been used to measure the velocity fields of both continuous phase and dispersed microbubble phase, in a turbulent boundary layer, of a channel flow. Hydrogen and oxygen microbubbles were generated by electrolysis. The average size of the microbubbles was 15 μm in radius. Drag reductions up to 40% were obtained, when the accumulation of microbubbles took place in a critical zone within the buffer layer. It is confirmed that a combination of concentration and distribution of microbubbles in the boundary layer can achieve high drag reduction values. Microbubble distribution across the boundary layer and their influence on the profile of the components of the liquid mean velocity vector are presented. The spanwise component of the mean vorticity field was inferred from the measured velocity fields. A decrease in the magnitude of the vorticity is found, leading to an increase of the viscous sublayer thickness. This behavior is similar to the observation of drag reduction by polymer and surfactant injection into liquid flows. The results obtained indicate that drag reduction by microbubble injection is not a simple consequence of density effects, but is an active and dynamic interaction between the turbulence structure in the buffer zone and the distribution of the microbubbles. [DOI: 10.1115/1.2174062]

Keywords: drag reduction, microbubbles, PIV, PTV

1 Introduction

A renewed interest for drag reduction technologies and research has been noticed during the last few years. Much research has been performed with polymer and surfactants injection in duct and boundary layer flows. Alternatively, drag reduction due to microbubble injection in turbulent boundary layers has also gained attention, because of its environmental friendship. This type of drag reduction is particularly important for maritime transportation applications, since 80% of the total drag in a large ship is due to skin friction [1]. Minimizing the drag encountered by vehicles moving in air or water and the fluid resistance in gas, water, or oil pipelines leads to saving in fuel consumption. When higher rates of mass, momentum, or heat transfer are desired, it is imperative that the concomitant drag penalty be kept to a minimum. Reducing drag saves enormous resources spent to overcome it and is clearly advantageous to the environment, the economy, and the overall industrial competitiveness [2].

McCormick and Bhattacharyya [3] showed a significant reduction of frictional resistance can be achieved using microbubbles, at low void fractions. In their work, hydrogen microbubbles generated by electrolysis produced up to 30% drag reduction over a body of revolution with less than 1% void fraction. They also showed that as the Reynolds number of the liquid increased, the effectiveness of microbubbles in reducing drag diminished with the same gas injection rate. This is also obtained at high Reynolds numbers of 10^8 that was reported in a recent experiment over a flat plate [4]. Moreover, the drag reduction degree of persistence was greater at lower speeds with a given gas injection rate, and the drag reduction increased with the increase of gas injection rate.

As in polymer drag reduction, microbubbles have been shown the capability of achieving drag reductions as high as 80% on flat plate boundary layers [5]. By combining polymers and microbubbles, Fontaine et al. [6] achieved drag reductions greater than 80%. They suggested that polymer drag reduction was independent of the mechanism responsible for the microbubble skin friction reduction. Takahashi et al. [7] reported skin friction reduction up to 32% on a 50 m long ship model.

Despite many studies on microbubble drag reduction, there is no complete agreement on the microbubble physical phenomena leading to drag reduction. Issues such as microbubble size and distribution in the boundary layer have been recognized as key parameters in achieving important gains in drag reduction, but the role of such parameters is not yet fully understood. Microbubble generation is another important issue, since the net energy saving in a system must account for the energy required to produce the microbubbles. Generally, large amounts of gas are required to reach high levels of drag reduction. Experimental studies have shown, however, that microbubbles with size of the same order of the length scale of the liquid phase turbulence perform better in achieving drag reduction, and lower gas injection rates are required [8].

Among the main factors considered responsible for the microbubble drag reduction phenomena are the decrease of density, the increase of effective viscosity, and the liquid turbulence-microbubble interactions. Buoyancy effects in microbubble drag reduction have been reported by Madavant et al. [5] and Sanders et al. [4]. In a flat plate boundary layer, Madavan et al. achieved higher drag reduction in their plate-on-top experiment than in the plate-on-bottom case. Sanders et al. reached almost 100% drag reduction when the injected gas formed a layer underneath the flat plate. The increase of the void fraction increases the local effective viscosity and reduces the turbulent momentum transfer [9,10]. Turbulence modification of the liquid boundary layer has been measured by Kitagawa et al. [11]. They measured an increase of both nondimensional streamwise and normal turbulence intensities, and a decrease of the Reynolds stress, with void fraction increase.

Numerical simulations have been used also as a means to in-

[1]Currently at Department of Nuclear Systems, National Institute for Nuclear Research, Ocoyoacac, Mexico 52045.

[2]Corresponding author.

Contributed by the Fluids Engineering Division of ASME for publication in the JOURNAL OF FLUIDS ENGINEERING. Manuscript received March 31, 2004; final manuscript received October 11, 2005. Review conducted by Joseph Katz.

vestigate the underlying mechanism of microbubble drag reduction. Madavan et al. [12] determined that microbubble size and distribution in the boundary layer were major issues in the microbubble drag reduction phenomena. Similar results were found by Xu et al. [13] with a direct numerical simulation (DNS) of a fully developed turbulent channel flow using a force-coupling method (FCM). Their results indicate that the initial seeding of microbubbles has an important effect on the pressure gradient and viscous drag force. Furthermore, smaller microbubbles gave a sustained reduction in drag, while larger bubbles only exhibited transient drag reduction. A reduction in mean drag of 6.2% was achieved at a void fraction of 4.24%. The microbubbles were seeded from a location having a distance from the wall of $y^+ = 20$. Recently, Ferrante and Elghobashi [14] performed a DNS on a spatially developing turbulent boundary layer over a flat plate with microbubbles injection. They obtained a maximum drag reduction of 20.2% at a void fraction of 2%. They concluded that the drag reduction was caused by a velocity divergence effect, associated with the void fraction. The presence of microbubbles generates a local positive divergence of the fluid velocity, creating a positive mean normal velocity at a farther distance from the wall. This reduces the mean streamwise velocity and displaces the quasistreamwise longitudinal vortical structures away from the wall due to the presence of bubbles. This displacement increases the spanwise gaps between the wall streaks associated with the sweep events and reduces the streamwise velocity of these streaks.

Although DNS of microbubble turbulent boundary layers provides insight into the physical phenomena responsible for the drag reduction, it is not currently feasible to use it for practical designs of maritime and other transportation means that could take advantage of the drag reduction phenomenon. Thus, multiphase Reynolds averaged Navier-Stokes (RANS) methods are being developed for simulations of three-dimensional geometries at relevant high Reynolds numbers [15,16].

In this paper, particle tracking velocimetry (PTV) is used to obtain velocity components of both continuous and microbubble dispersed particle image velocimetry (PIV) images. It is shown that microbubbles with an average radius of 15 μm flowing in the buffer layer can produce drag reductions of about 40%. This confirms the necessity of a specific concentration of microbubbles in the buffer zone of the boundary layer to achieve high drag reductions. The modification of the components of the liquid mean velocity distributions across the boundary layer is presented for different drag reductions. Further, the vorticity modification due to the presence of microbubbles in a channel turbulent boundary layer was investigated. Vorticity fields of the two phase flow at different drag reductions are presented and compared.

Experimental Setup

A flow facility was constructed to study the turbulent boundary layer in a channel flow. A schematic of the flow system used in this experiment is illustrated in Fig. 1. One of the supply tanks is located 2.85 m above the channel level. In normal operation, the pumped water into the upper tank exceeds the flow that can be delivered to the channel through a 2.54 cm diameter hose; thus, it ensures a constant pressure head. When it is full, it provides a constant water column of 3.65 m. Its capacity is 0.21 m^3. This tank is also used as a phase separator, to avoid air flowing into the channel, and to assure a single-phase water flow. The other tank is about 1 m below the channel level. Its capacity is 0.35 m^3. This tank receives the overflow from the upper tank, and it is also used to mix the seed tracer particles with the flow. The chanel is made of 12.7 mm thick Plexiglas. Its length is 3.05 m, and the cross-sectional area A is 15 cm $\times$ 8.81 cm. The center of the measurement area was located at 205.62 cm from the inlet nozzle and 45.88 cm from the exit nozzle. The inlet nozzle has plastic screens and flow straighteners to ensure a uniform flow. Two water filters with several filter layers prevented any particles larger than 10 μm to flow into the channel. Prior to each test, the water is continuously run through the filter, to ensure that only the seed tracers will be flowing during the measurements. The flow was seeded with 6 μm polystyrene tracer particles. Their density is 1050 kg/m^3. A volumetric flow rate Q of 1.02×10^{-3} m^3/s was used, and the obtained averaged cross-sectional velocity $u_m = Q/A$ was 7.72×10^{-2} m/s.

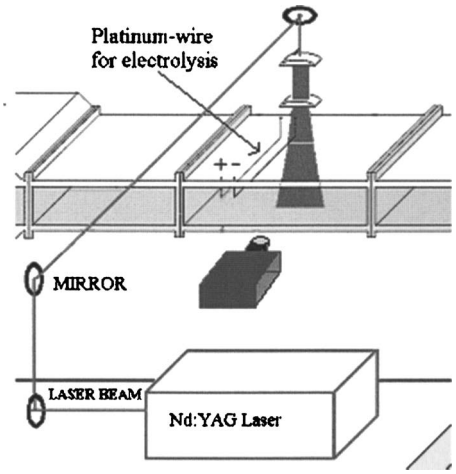

Fig. 1 Sketch of the PIV setup

Two platinum (Pt) wires each with a diameter of 76 μm was located about 1 cm from the channel upper wall. These wires serve as cathode and anode for microbubble generation via electrolysis. The first wire was located at a distance of 35.56 cm, while the second wire, the anode, was at 11.43 cm along the streamwise direction from the measurement area. When the power supply delivers its current, hydrogen bubbles are produced on the anode, while oxygen bubbles are generated on the cathode. The anode produces a higher bubble density than the cathode, and the bubbles are smaller. The influence of the Pt wires on the flow is negligible, since the Reynolds number based on the wire diameter is less than 10, and the wire is located at more than 1500 wire diameters from the measurement zone.

The PIV system consisted of a high power laser, a high resolution charge coupled device (CCD) camera, a pulse generator, and acquisition boards and software. The illumination source for the PIV system was a dual oscillator Nd:YAG laser. Since the frequency of the laser oscillators is fixed at 30 Hz each, a pulse generator is utilized to fire each lamp at the desired time, and with the required time separation between pulses. The maximum power is rated at 400 mJ per pulse, for the 532 nm wavelength (corresponding to green light), but the actual maximum output power achievable range is from 300 mJ to 350 mJ per pulse. The pulse width is about 7 ns. A sketch of the PIV and optical setup is shown in Fig. 1. This figure also shows the location of the Pt wires.

PIV images are acquired by a high resolution CCD camera. A typical image from a PIV measurement of the two phase boundary layer is shown in Fig. 2. The camera resolution is 10 bits, 1016 $\times$ 1016 pixels, and it runs at 30 Hz. This camera has a 1-in. CCD array format, and the pixel size is 9 μm. The CCD camera also has the trigger double exposure capability, which allows for acquiring two successive frames every 30th of a second. In order to do so, the data acquired during the first CCD array exposure is moved to a transfer array in about 5 μs, and then the CCD array is ready again to acquire new data. The data in the transfer array is sent out to the imaging board. Therefore, correct synchronization must be performed between the CCD camera and the laser system light pulsing. A high accuracy pulse generator performs the synchronization.

The exposure time for the first frame is only 0.128 ms, but for the second frame the CCD array is exposed for 32.4 ms. Thus, the

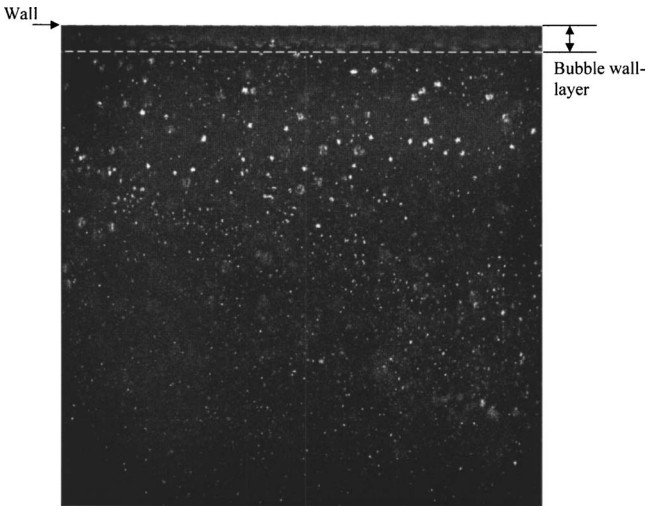

Fig. 2 Typical image from a two phase boundary layer measurement

first laser oscillator must be fired during the first frame exposure, but the second laser light pulse can be fired anytime during the 32.4 ms that the CCD array is again exposed, so that the time interval between two consecutive frames can be set as desired. Clearly, this feature allows studying highly turbulent flows with a high spatial resolution. In this work, the time separation between images used was 1 ms, the view area was set to 1.05 cm^2, and the resolution of the camera was set to 8 bits, 1008×1012 pixels. The velocity field acquisition rate, i.e. two successive frames with a time separation of 1 ms was 30 Hz.

Data Processing

In this study, particle tracking routines based on the cross correlation algorithm were employed. Two different programs were used for particle extraction and tracking process. The resulting velocity vectors from each application were then compared and combined. This hybrid tracking technique greatly increased the total number of velocity vectors used for the flow field analysis. The first software allowed for online image processing and tracking of the particle fluid tracers. Thus, the image threshold and tracking parameters can be easily and correctly set for a whole data set. The particle extraction algorithm is based on the template matching. The template is a one-dimensional pattern with three points, which accelerates the particle detection [17]. The tracking process is a binary correlation method [18]. Label matching and median filter checking are used in a post-processing step to reduce particle mismatching during the tracking process. This program is considered robust and reliable for particle centroid determination and tracking, as proven during the First International PIV Challenge [19]. Recently, this software has been improved. The recent version of the software was tested at our lab with six different synthetic image pairs of a strong vortex with different seeding concentrations. These cases were obtained from the First International PIV Challenge.[3] The number of vectors found with this improved version increased and the root-mean-square (rms) error in pixels was reduced from 0.433 to 0.362 which is about 16.2% reduction in the error. This error reduction was obtained in five out of the six benchmarked cases.

The second particle extraction and tracking program is a home-developed routine by Hassan et al. [20], and it has been improved over the years. The particle centroid determination algorithm uses a two-dimensional mask to determine the area of the particle image, and then a center-of-mass calculation yields the particle image centroid. The border of the spots is determined from the computation of the average gray scale intensities on windows of given dimensions. The influence of the average intensity of the surrounding windows is also taken into account in the calculations. Then, all those pixels with intensities higher than the average plus a standard deviation are kept for the calculations. This allows separating the different particle spot images in each window. The obtained particles are then binarized and labeled for the cross-correlation tracking step. Next, the pixels that belong to the same spot are used for the computation of the centroid. This software was also tested with the same image pairs mentioned above, yielding a lower number of vectors, but similar results to those of the first software with comparable rms error. Another advantage of this software is that the search region can be predetermined. This is particularly important in areas where the particle displacements are small, as in the regions close to the wall. A consistency filter is used to ensure vector quality.

In the tracking process, the flow field PIV images for single- and two-phase flows were divided into multiregions parallel to the channel wall, to resolve the high velocity gradient of the boundary layer. Each image was divided into four strips normal to the y direction with an optimum thickness for the tracking process. Determining the optimum thickness is to have a lesser number of regions to accelerate the tracking process, while ensuring that the magnitude and direction of the velocity vectors are consistent within the region. Figure 3 shows a vector velocity field composed of 40 instantaneous, consecutive, velocity fields. This figure also shows the four regions used for the particle tracking, and the velocity profile obtained once the whole data processing was complete. The region thicknesses for this case were chosen to be $\Delta y = 1.1$ mm, 2.1 mm, 5.7 mm, and 1.6 mm, for regions 1, 2, 3, and 4, respectively.

Once the velocity vectors are obtained from both particle tracking algorithms, they undergo a filtering process. The filters are applied independently to the vector data sets from each tracking process. The first filter is related to a specified cross correlation value. In our case, to achieve high accuracy in velocity vectors, only those vectors with a cross correlation coefficient value higher than the average value of a whole vector data set are considered in the flow field analysis. During this step usually about 50% of the total vectors are removed. Next, neighbor and consistency filters were applied. Some of the vectors can easily be determined as erroneous vectors. These vectors were with direction and/or magnitude far deviated from the neighbors. The filters' function is to remove vectors that are not within the average +/− a standard deviation value of the magnitude and direction of the representative velocity vector in a small window. This step ensured that velocity gradients were continuous along the x and y directions. Then, those vectors close to the image boundaries are also removed. In this step about 10% of the vectors are removed. In total, only about 40% of the initially tracked vectors were kept for the flow analysis after the filtering process. The remaining vectors from each process are combined to one single file, where they are compared to remove repeated vectors.

Once the velocity vectors from the hybrid-tracking scheme are filtered, all the instantaneous velocity fields $\mathbf{U}=\mathbf{U}(U,V)$ are added in a single data file. Then, mean velocity $\bar{\mathbf{U}}=\bar{\mathbf{U}}(\bar{U},\bar{V})$ and fluctuating velocity $\mathbf{u}=\mathbf{u}(u,v)$ fields are calculated. The Reynolds decomposition relation was used here to obtain the fluctuating velocity field, i.e.; $\mathbf{u}=\mathbf{U}-\bar{\mathbf{U}}$.

Finally, the velocity vector accurate positions from the wall are determined. This y coordinate, from the wall, is important in the computation of the wall friction velocity.

Single-Phase Boundary Layer Measurements

In this study, the single-phase measurements consisted of ten image data sets. Each set was composed of 100 consecutive 1008×1012 pixel, 8-bit images. Thus, a total of 500 velocity

[3] www.pivchallenge.org

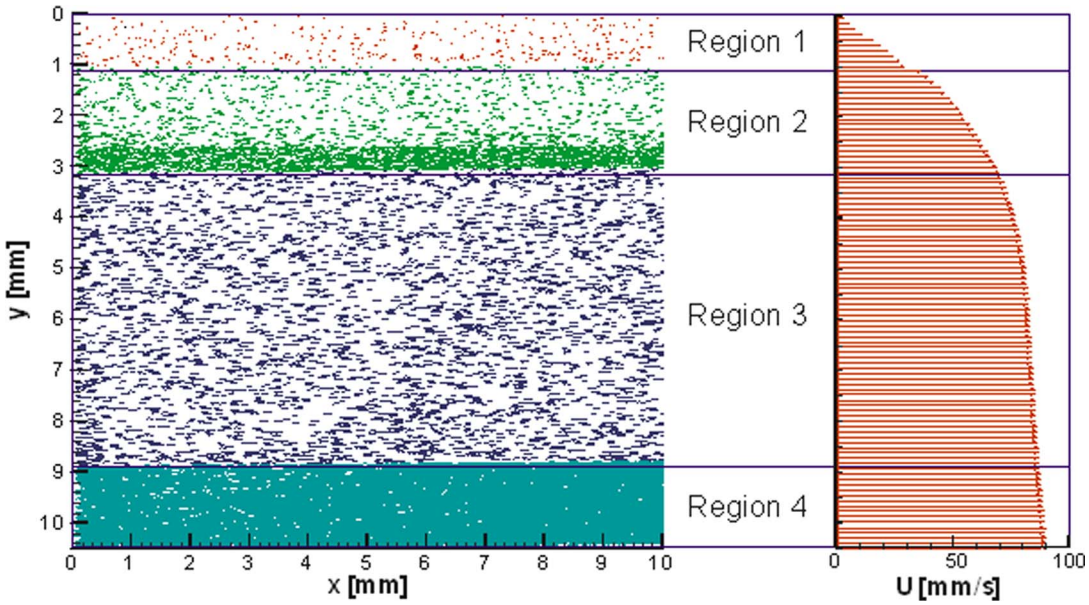

Fig. 3 Overlay of the velocity vectors from 40 consecutive instantaneous fields, and final velocity profile after dividing the velocity field into multiregions for optimum tracking

fields were obtained. However, because not all the images satisfied the minimum quality necessary for image processing, about 450 velocity fields were used for the final data analysis. The mean cross-sectional velocity was 7.72 cm/s. The Reynolds number Re based on the half height of the channel H is 3400. Based on the hydraulic diameter, Re was 8570. The measurement zone was located at $L/2H=23.34$.

Single-phase velocity vectors, of an average of 59,434 vectors per data set, were used to calculate the mean velocity profile along the y direction, within the measurement zone. Each point on the velocity profile was computed by averaging all the velocity vectors that fall in region sheets of 1008×20 pixels, with 50% overlapping. Two main issues are related to choosing the suitable grid size for the ensemble average. First, it has enough data points on the mean velocity profile to compute the friction velocity. Second, the total number of vectors, used for the calculation of the average velocity vector at each point of the velocity profile should be at least the required minimum samples for achieving reliable statistics. Regarding the number of vectors required for the ensemble average, it was considered that about a 1000 velocity vectors per strip is appropriate for the averaging process. This was, however, not achievable for some of the microbubble laden flow data sets; particularly, high void fraction sets. Taking into consideration that not all of the strips could have the minimum vector quantity required, it was determined that at least 20 data points were required to satisfactorily compute the friction velocity from the mean velocity profile. For the reasons just discussed, it was concluded that region sheets of 1008×20 pixels sizes were appropriate.

From the average of the ten mean velocity profiles, one from each data set, it was determined that the boundary layer size δ was about 7.5 mm. This is based on the premise that at such a position the mean velocity reached 99% of the velocity outside the boundary layer, i.e.; $\delta_{99}\approx7.5$ mm. The external velocity was considered to be the mean cross-sectional velocity. Point statistics for the mean and turbulence quantities were calculated with the total number of instantaneous velocity vectors, which was 594,344 vectors, assuming homogeneous flow in the streamwise direction.

Wall Friction Velocity

Friction drag reduction measurements require that the wall shear stress τ_w is either directly measured or calculated from the pressure drop. Once τ_w is known, the skin friction coefficient C_f for the cases of drag reduction and without drag reduction can be compared. C_f is calculated from

$$C_f=\frac{\tau_w}{\frac{1}{2}\rho u_m^2} \tag{1}$$

which is equivalent to

$$C_f=2\left(\frac{u_\tau}{u_m}\right)^2 \tag{2}$$

where ρ is the liquid density, and u_τ is the wall friction velocity. For low Re, the pressure drop in a short distance requires very high accuracy differential pressure transducers, which are not easily commercially available and are expensive. Moreover, the uncertainty of such differential pressure transducers is of the same order of the required measurements. The use of hot film probes or hot wires is common for the measurement of wall shear stress, but they may induce disturbances to the flow, especially close to the wall. Another problem related to the use of pressure transducers, hot wires, or hot films is that the presence of high voltages contaminates the actual sensor signal. In our particular case, these kinds of sensors could not be employed because of the high voltage used for the electrolysis process, which introduced high intensity noise. Thus, it was not possible to discriminate noise from the actual signal of the pressure transducers. The height of the water column at different streamwise positions showed no reliable measurable difference either.

The PIV technique, and its derivative PTV in our case, allows measuring the velocity field at regions close to the wall. From these measurements u_τ can be determined, since in the viscous sublayer $u^+=y^+$. Here u^+ and y^+ are the velocity and the normal distance from the wall normalized with near-wall scales. However, it is necessary to determine the limit of the viscous sublayer ($y^+=5$) region, which is the distance from the wall, in physical coordinates, that transition from the viscous layer to the buffer zone occurs. Therefore, a rough estimation of u_τ needs to be obtained, and then, the data points that fall in the viscous sublayer can be used to determine the best estimate of u_τ value.

In this study, three approaches are performed to evaluate u_τ value: namely, from the Blasius equation, power law, and Durst et al. method.

For flow in conducts, the Blasius equation for the friction factor can be used to calculate u_τ as a first approximation, since C_f is a function of Re. For channel flow, the relationship between C_f and Re is given by

$$C_f = 0.073 \mathrm{Re}_m^{-1/4} \tag{3}$$

where Re_m is the Reynolds number based on the mean flow, that is,

$$\mathrm{Re}_m = \frac{2Hu_m}{\nu} \tag{4}$$

where ν is the kinematic viscosity of the liquid.

Another option to approximate the trial of u_τ is to use the power law form for the mean velocity distribution, instead of the traditional Law of the Wall, of a turbulent boundary layer

$$u^+ = Cy^{+\alpha} \tag{5}$$

In this case, for channel or pipe flow, u_τ can be computed from [21]

$$u_\tau \frac{d}{\nu} = \left[\frac{\mathrm{Re}_m 2^\alpha \alpha(1+\alpha)(2+\alpha)}{\sqrt{3}+5\alpha} \right]^{1/(1+\alpha)} \tag{6}$$

where

$$\alpha = \frac{3}{2 \ln \mathrm{Re}_m} \tag{7}$$

and d is the pipe diameter or the channel height. The value of C in Eq. (5) is calculated from

$$C = \frac{\sqrt{3}+5\alpha}{2\alpha} \tag{8}$$

The main problem in calculating u_τ from velocity measurements in the viscous sublayer is that very few data points can be obtained, and the measurement uncertainty can be high, due to closeness to the wall. To avoid this problem, Durst et al. [22] have proposed an alternative method to estimate u_τ. This method allows using points up to a distance $y^+=12$ and therefore more data points can be used to determine u_τ. This method consists of expanding the fluctuating components of the velocity vectors in a Taylor series to approximate the Reynolds stress in the near wall region. This approximation is substituted into the momentum equation. Then, u_τ and the distance to the wall correction y_0 are computed from the solution to the polynomial using least-squares fitting (Eq. (9)).

$$\bar{U} = \frac{u_\tau^2}{\nu}(y-y_0) - \frac{u_\tau^2}{2R\nu}(y-y_0)^2 + D(y-y_0)^4 + E(y-y_0)^5 \tag{9}$$

In Eq. (9), R is the pipe diameter or the channel half height H. The parameters D and E have insignificant contribution, so they can be either included or ignored in the computations of u_τ. Our experience indicates that these two parameters slightly improve the final result of u_τ. If they are not considered in the computations, it will generally require more iterations to reach the same final value of u_τ. The wall correction y_0, on the other hand, can be used as free parameter to accelerate the calculations and improve results. The y_0 parameter can be obtained with high accuracy during the image calibration where the channel wall can be accurately determined, either before or after the experiments. Since y_0 is considered already known, and D and E can be ignored, consequently, Eq. (9) reduces to

$$\bar{U} = \frac{u_\tau^2}{\nu} y - \frac{u_\tau^2}{2R\nu} y^2 \tag{10}$$

which is equivalent to

$$\bar{U}^+ = y^+ - \frac{1}{2R^+} y^{+2} \tag{11}$$

where

$$R^+ = \frac{Ru_\tau}{\nu} \tag{12}$$

is the dimensionless pipe radius, and is replaced by nondimensional channel half height H^+ for channel flows.

To achieve a first approximation of u_τ, the Blasius equation or the power Law can be used. Iterations for each point that satisfies $y^+ \leqslant 12$ are performed using Eqs. (11) and (12), until u_τ converges. Finally, an average value of u_τ can be calculated. Figure 4 shows a comparison of the nondimensional velocity profile, obtained from the average of all ten single phase data sets, using u_τ from each of the methods described above. It also includes the Law of the Wall and the power law profiles. In this figure, Durst, Blasius, and power, refer to the u_τ value used for the calculation of the wall variables, computed from each respective method. Clearly, the Durst et al. method shows the best agreement with both the Law of the Wall and the power law in the log region. Therefore, we selected the Durst et al. method for the calculation of u_τ. The Law of the Wall is given here by Schlichting and Gersten [23]

$$u^+ = y^+ \quad 0 \leqslant y^+ < 5 \tag{13}$$

for the pure viscous sublayer

$$u^+ = \frac{1}{\Lambda}\left[\frac{1}{3} \ln\left(\frac{\Lambda y^+ + 1}{\sqrt{(\Lambda y^+)^2 - \Lambda y^+ + 1}} \right) + \frac{1}{\sqrt{3}}\left(\arctan\left(\frac{2\Lambda y^+ - 1}{\sqrt{3}} \right) + \frac{\pi}{6} \right) \right] + \frac{1}{4\kappa} \ln(1 + \kappa B y^{+4}) \quad 5 < y^+ < 70 \tag{14}$$

where $\kappa=0.41$, $A=6.1\times10^{-4}$, $B=1.43\times10^{-3}$, $\Lambda=(A+B)^{1/3}=0.127$ for the buffer layer; and finally for the overlap or logarithmic layer

$$u^+ = \frac{1}{\kappa} \ln(y^+) + C^+ \quad y^+ > 70 \tag{15}$$

where

$$C^+ = \frac{2\pi}{3\sqrt{3}\Lambda} + \frac{1}{4\kappa} \ln(\kappa B) = 5.0 \tag{16}$$

In our case, we did not reach the overlap layer in any of our measurements. In this case, the power law is given by

$$u^+ = 7.60 y^{+0.170} \tag{17}$$

The Law of the Wall approach better described our measurement data within the boundary layer. It is known that the power law is not valid in the region $y^+ \leqslant 30$, as also confirmed in Fig. 4. It has also been argued that the Law of the Wall is not valid in the same region; however, our data show a reasonable agreement.

Two-Phase Boundary Layer Measurements

The microbubbles were generated at a distance of 1 cm from the top wall. The measurement zone was about 35 cm from the Pt wire position. Prior to the PIV measurements, images of the bubbles generated via the electrolysis process were taken. From these images, and using the Pt wire diameter (76 μm) size as reference, the microbubble diameter was determined, at different liquid flow rates. About 60% of the generated microbubbles had a diameter less or equal to 40 μm at a liquid velocity of 10 mm/s, with two main peaks at 26.6 μm and 30.4 μm, as shown in Fig. 5. This study involved a higher flow rate. Consequently, the expected microbubble size generated by electrolysis had a peak less

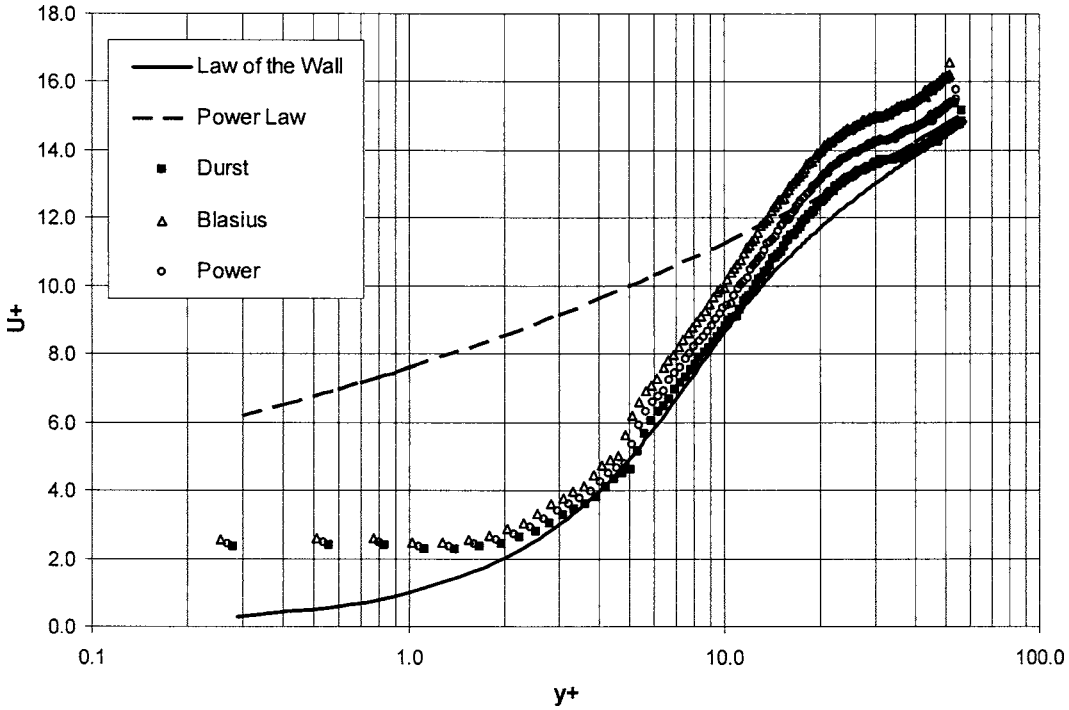

Fig. 4 Comparison of the mean velocity profile in the single phase boundary layer, using the three different methods shown to compute the wall friction velocity

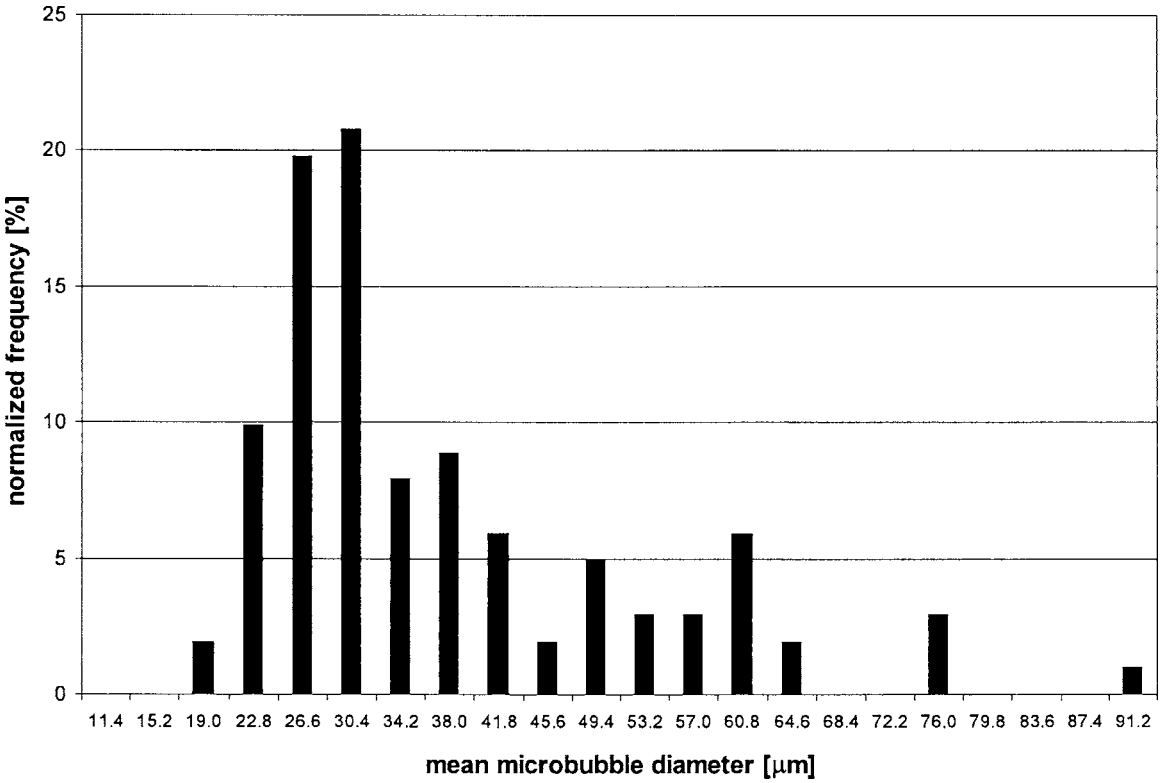

Fig. 5 Microbubble size distribution at a liquid velocity of 10 mm/s

than 30 μm. Ten image data sets of the microbubble laden flow were acquired at the same liquid flow rate in the single-phase flow test case. Due to the buoyancy, microbubble accumulation occurred at the top wall. This can be seen at the upper part of the image in Fig. 2, and thus resulting in an increase of the void fraction in the measurement volume. An average of 45 velocity fields (90 frames) were obtained from each data set. The average number of vectors per data set was above 70,000.

In several experimental studies, it is indicated that the drag reduction increases as volumetric bubble concentration, β increases, until a maximum value of the drag reduction is reached [1,5,6]. No increase in the drag reduction was observed beyond

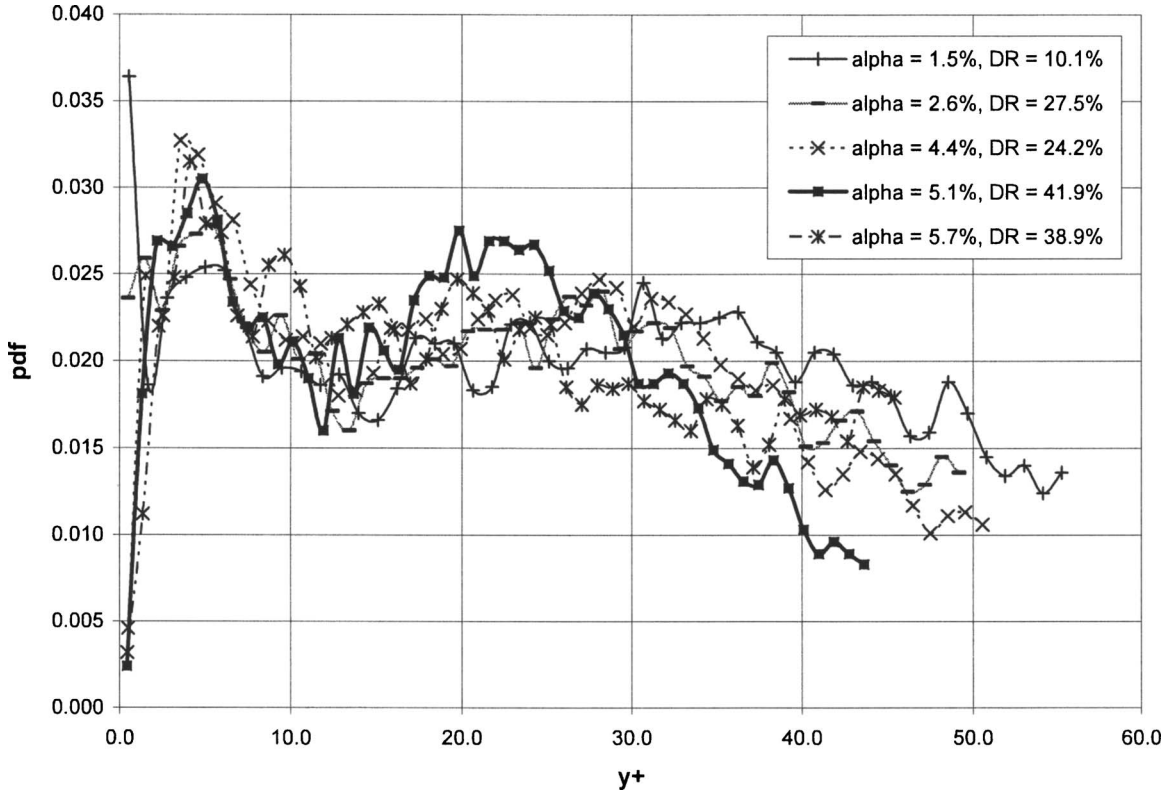

Fig. 6 Distribution of the freely moving microbubbles in the boundary layer, for five different drag reduction values

this value during the increase in β. Drag reductions as high as 80% were achieved with a value of $\beta=25\%$, reported by Fontaine et al. [6]. However, β was about 40% in the study of Madavan et al. [5] for the same 80% drag reduction gain. Note that two different geometries were employed in the mentioned studies, but similar definitions for the volumetric liquid flow rate Q_l were used. However, since void fraction α is not necessarily equal to β, a correlation between α and drag reduction is not clear at present time.

In principle, both size and spatial distribution of the microbubbles are obtained from PIV data. The distinction between particle fluid tracers and microbubble images was performed using both the area and brightness of the image spots. Microbubble images have larger area and higher gray level than the tracer images. In this study, low local void fractions were produced, i.e., less than 5%. Such low void fractions allow the use of the PTV technique for the velocity field measurements of both dispersed and continuous phases. Although the microbubble production rate was kept constant during all the measurements, there was microbubble accumulation at the channel top wall. The thickness of this bubble layer at the top wall depends on the liquid velocity for each different test. In this study, the total void fraction in the measurement volume was calculated by adding the contribution of the top wall bubble layer plus the freely flowing microbubbles within the viewing volume, that is

$$\alpha = \alpha_{\mathrm{bl}} + \alpha_{\mathrm{fb}} \tag{18}$$

where α_{bl} is the void fraction of the layer of accumulated microbubbles at the channel top wall (wall-bubble layer), and α_{fb} is the void fraction due to microbubbles that transport with the flow (free bubble). The first part of α was computed assuming that the bubble layer occupied volume of a rectangular box V_{bl}, that is,

$$V_{\mathrm{bl}} = l \times b \times h, \tag{19}$$

where l is the image size along the x direction (1008 pixel $=10.54$ mm), b is the laser light sheet width ($\sim$1 mm), and h is the bubble layer thickness which accumulated at the top wall. This parameter h varied from 15 to 63 pixels, and thus, α_{bl} varied from 1.5% to 6.2%. Particularly, the second contribution α_{fb} did not change, in practice, during the experiment under same flow condition. A maximum of 300 microbubbles was found on the images representing the contribution of α_{fb}. Therefore, the value of α is close to the value of α_{bl}. However, the distribution of the freely moving microbubbles in the boundary layer (α_{fb} distribution) was proved to be a key parameter in achieving the drag reduction. In this study, it is found that the local distribution and profile of α_{fb} in the boundary layer have paramount influence on the drag reduction.

Figure 6 shows the α_{fb} distribution versus y, the normal distance from the wall, for five different two phase microbubble/water data sets. The void fraction values shown in the figure are for the total value of α within the viewing volume. It can be noted that the different data sets do not have a common initial point. This reflects the thickness of the microbubble layer at the top of the channel wall. Also, these profiles do not start at a value of zero; however, the number of microbubbles at the initial point is small. In these data sets, the distribution clearly indicates two peaks. The first peak appears just after the bubble layer ($y^+\sim5$), and the second peak at about the middle of the measurement area ($y^+\sim25$). The first peak is quite narrow compared to the second one, in which a gradual increase and decrease can be seen. It is also noted that the maximum value of α of 5.7% does not corre-

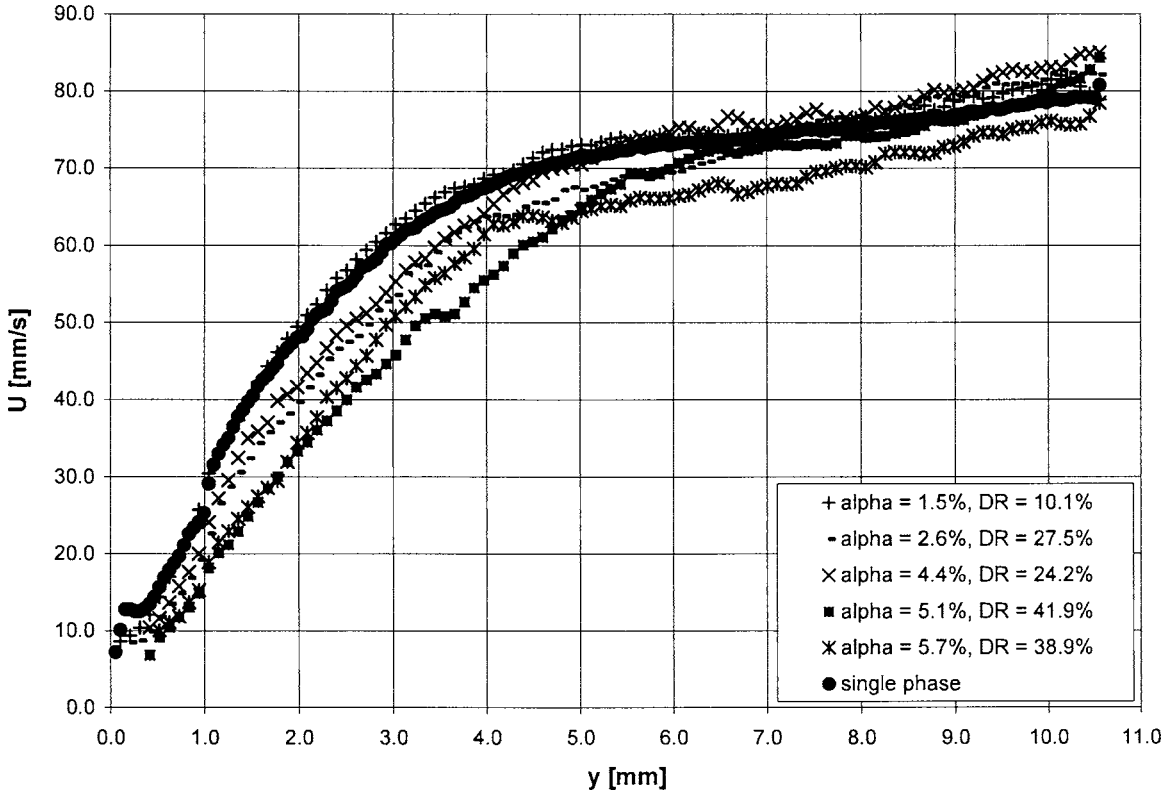

Fig. 7 Modification of the profiles of the streamwise component of the liquid mean velocity vector across the two phase boundary layer, for five different drag reductions, in physical coordinates

spond to the highest peaks at $y^+ \sim 25$. Beyond a distance of about 10 mm from the wall, the bubble distribution rapidly falls towards zero.

Drag Reduction Results

In this study, the drag reduction was calculated based on the measurements of the wall friction velocity u_τ. To calculate the drag reduction (DR) we use the ratio of the skin friction coefficient of the microbubble laden turbulent boundary layer C_f to the skin friction coefficient of the liquid single-phase turbulent boundary layer C_{f0}. This ratio is equal to the ratio of the wall shear stress of the microbubble/water flow τ_w to the wall shear stress of the single liquid flow τ_{w0} case. Thus, using Eq. (2), the percent drag reduction was calculated from

$$\mathrm{DR} = 100 \times \left[1 - \left(\frac{u_\tau}{u_{\tau 0}} \right)^2 \right] \tag{20}$$

It is known that an increase in the void fraction in the boundary layer leads to an increase in drag reduction, until a maximum value is reached. In this study, the magnitude of local microbubble void fraction in the buffer zone is found to be the key parameter in drag reduction. The stagnant bubble layer at the top of the channel wall has practically insignificant effect on the drag reduction. Figure 6 shows that the first peak of the microbubble PDF, which is located in the viscous sublayer, does not play an important role in the drag reduction phenomenon. In addition, Fig. 6 indicates that although the void fraction profiles are similar, those profiles with microbubble accumulations within the zone from $y^+ \approx 15$ to 30 achieve higher drag reductions. For example, the case of $\alpha = 5.1\%$ yields higher drag reduction than the case of $\alpha = 5.7\%$. This is due to a higher local void fraction within this critical zone ($y^+ \approx 15$ to 30) for the case of $\alpha = 5.1\%$. By injecting more microbubbles, the probability of obtaining more bubbles in the buffer zone increases. This is the first time, to our knowledge, that present experimental local information confirms that high percentage drag reductions can be achieved with very low local void fractions, once they are within the critical zone.

Figure 7 shows the effect of the void fraction on the streamwise component U of the liquid mean velocity distribution across the normal distance from the wall. With larger values of the microbubble void fraction in the critical zone (see Fig. 6), smaller velocity gradients near the wall are obtained. This figure clearly shows a decrease of the slope dU/dy as drag reduction reaches higher values. It is an indication of the thickening of the viscous layer. It is interesting to note the close similarity of velocity profile, and drag reduction, produced with two quite different values of void fraction, $\alpha = 2.6\%$ and $\alpha = 4.4\%$. However, the microbubble accumulation within the critical zone, $y^+ \approx 15$ to 30, has practically the same values, as shown in Fig. 6. This again confirms that the α_{fb} distribution is a paramount parameter in the drag reduction phenomenon by microbubble injection in the boundary layer.

The velocity profiles shown in Fig. 7, normalized by the wall friction velocity, are presented in Fig. 8. Note in this figure that the viscous sublayer grows up to a distance of $y^+ \approx 12$ (compared to the limit $y^+ = 5$ for single phase) for the higher drag reduction cases. The log-law region is retained, but it is displaced upward and parallel to the single-phase case. A similar behavior is obtained with surfactants and polymers [24,25]. Increasing the local void fractions within the critical zone deviates more from the single phase flow law of the wall in the buffer and logarithmic regions, as clearly shown in Fig. 8. The figure further indicates that the data, for the obtained different drag reduction cases, follow closely the curve $u^+ = y^+$ up to $y^+ \approx 12$. Then, they tend to preserve a profile closer to linear, in the log scale, than the single phase case up to $y^+ \approx 20$, where the log-law profile starts becoming apparent. It is clear that the transition from the modified buffer to log-law regions is not as smooth as it usually develops for the single phase flow cases.

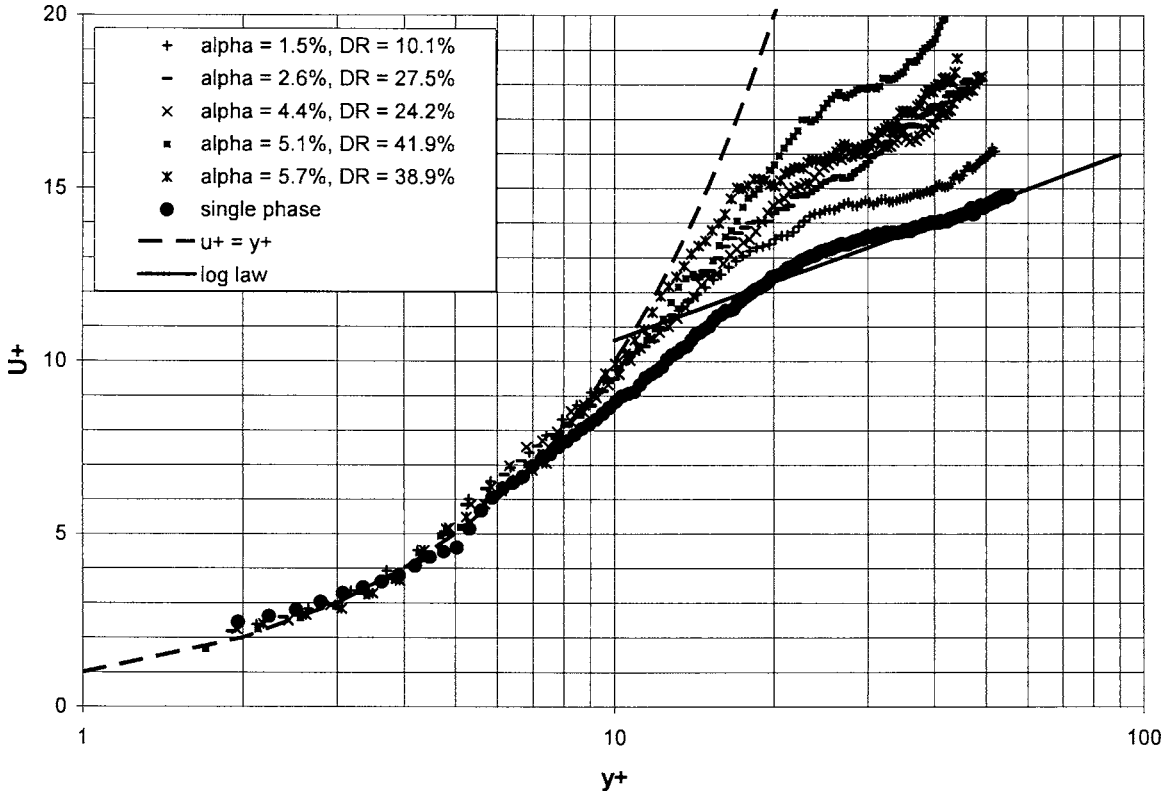

Fig. 8 Modification of the profiles of the streamwise component of the liquid mean velocity vector across the two phase boundary layer, for five different drag reductions, in wall coordinates

To explain the drag reduction phenomenon, Xu et al. [3], from their numerical simulation results, suggested three mechanisms involved: the initial seeding location of microbubbles, density effects, and specific correlations between microbubbles and liquid turbulence. The increase of drag reduction with increasing void fraction has been reported, and the modification of the turbulence in the boundary layer was also measured. In this work, it is also shown that the location of the microbubbles is a key parameter in the description of the phenomenon. One way to address the buoyancy influence in the microbubble drag reduction is to determine the modification of the normal component of the liquid mean velocity vector V across the boundary layer with various drag reductions and/or the void fraction magnitudes. Figure 9 demonstrates this effect. It is clear that for the high drag reduction case (41.9%), V is moving away from the wall (positive direction). On the contrary, the lowest drag reduction case shows a tendency to move toward the wall. The rest of the cases are not shown to avoid overcrowding the figure. However, similar trends are obtained, i.e., normal velocity components of liquid phase are positive (away from the wall) with high drag reduction, and moving toward the wall for low drag reduction (DR $<$ 20%). It should be mentioned that the bulk velocity in this experiment was low. Figure 9 indicates that the buoyancy effect only cannot explain completely the drag reduction phenomenon. Ferrante and Elghobashi [14] concluded, from their numerical simulation results, that the drag reduction was caused almost entirely by a velocity divergence effect, associated with the void fraction, since the presence of microbubbles generated a local positive divergence of the fluid velocity, creating a positive mean velocity normal (and away from) the wall.

All the cases investigated by Ferrante and Elghobashi show the positive divergence of the fluid velocity. However, the data, in Fig. 9, for the case of lowest drag reduction (10.1%) shows V going toward the wall (negative direction), while in the 27.5% and 24.2% cases (not shown in the figure) the data points spread noticeably between the trend lines. Although this could be a consequence of the high uncertainty of this velocity component, considering its small magnitude, it also indicates that a threshold value for the void fraction is required, for the velocity gradient effect to occur. Figure 9 can also be used to estimate the error of the normal velocity component. This can be deduced from the average normal velocity profile for single liquid phase flow test. The mean error value was −0.24 mm/s, with a standard deviation of 0.23 mm/s. It is clear from the figure that the error reduces as moving farther from the wall. If the error for each of the four tracking segmented regions as illustrated in Fig. 3 is considered, the rms error of the normal velocity component is 0.42 mm/s, 0.30 mm/s, 0.11 mm/s, and 0.08 mm/s, for regions 1, 2, 3, and 4, respectively. The first two values of the rms error are higher than those computed from the error propagation formula, as it will be shown in the measurement uncertainty section. It is clear that better resolution of the normal velocity components near-wall region is required.

Vorticity fields were derived from the measured velocity fields for the single- and two-phase flow cases. The spanwise z component of the mean vorticity field was computed with central finite differences, from the measured velocity fields of the continuous phase. In this calculation, the velocity fields were divided into regions of 60×60 pixels, with 50% overlapping. The vorticity results showed a similar finding of drag reduction by polymer and surfactant injection [25,26]. Regions of high vorticity decrease as drag reductions increase. Figures 10–12 show the z component of the mean vorticity field for three different drag reduction cases of 10%, 27.5%, and 41.9%, respectively. The single-phase vorticity field is about the same as the case of 10% drag reduction. The reduction of vorticity magnitude occurs close to the wall as the drag reductions increases. It indicates that microbubble/turbulence interactions occur in the buffer zone, leading to a destruction of vorticity structures within the transition region from viscous to the buffer zone. These results plus the findings related to the modifi-

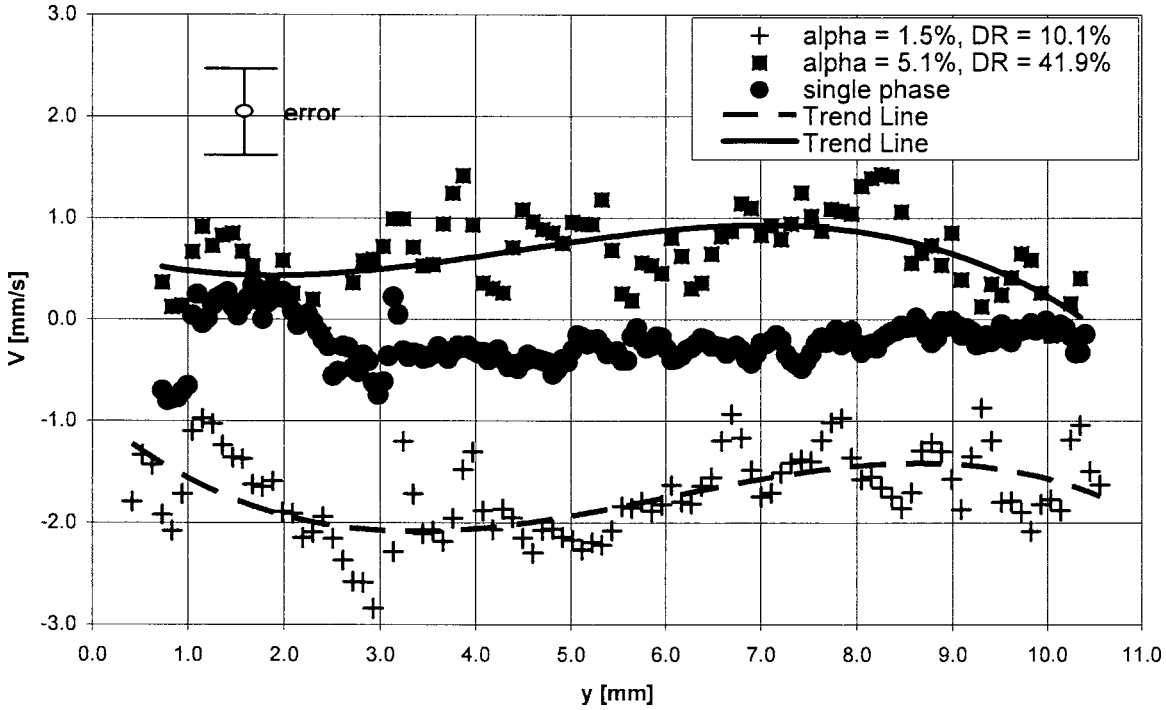

Fig. 9 Modification of the profiles of the normal component of the liquid mean velocity vector across the two phase boundary layer, for the highest and lowest cases of drag reduction, in physical coordinates

cation of the components of the mean velocity vector infer that drag reduction by microbubble injection is not a simple consequence of density effects only.

Measurement Uncertainty

The uncertainty in the velocity measurements obtained using PTV is a direct consequence of a combination of errors from two main sources. These are the localization of the centroid of the seed particle and microbubble images and their displacements in the two-dimensional (2D) images, and the uncertainty of how well the tracer particles follow the actual fluid motion. This last uncertainty can be determined utilizing the particle Stokes number, which is calculated as the ratio of the relaxation time of the seed particle to the characteristic time of the flow. The particle relaxation time τ_p, also known as the momentum or velocity response time, is the time needed by a seed particle to reach the value $e^{-1}U$, if the particle was initially at rest. Here U is the fluid velocity. The time τ_p can be computed from

$$\tau_p = \frac{(2\rho_p + \rho_f)d_p^2}{36\mu_f} \tag{21}$$

where ρ is the density, d the seed tracer diameter, μ the viscosity, and the subscripts p refers to particle properties, and f to the fluid properties. In this experiment, $\rho_p = 1050$ kg/m^3, $\rho_f = 1000$ kg/m^3, $d_p = 6 \times 10^{-6}$ m, and $\mu_f = 1002 \times 10^{-6}$ kg/(m s). Thus, the relaxation time of the seed was calculated to be 3.0 μs.

The fluid time scale τ_f is the time needed by the fluid to be advected within a characteristic length L, at a velocity U, that is

$$\tau_f = \frac{L}{U} \tag{22}$$

To compute the characteristic time of the flow, the seed tracer mean diameter and the average cross-sectional velocity of the liquid were used. The resultant fluid time scale is 77.7 μs. Then, the resulting Stokes number τ_p/τ_f is 3.9×10^{-2}. Therefore, the 6 μm seed particles closely followed the fluid motion changes, and therefore did not significantly contribute to the total error.

The major source of error in this experimental investigation is the uncertainty in determining the centroid of the spot images of both the tracer particles and microbubbles. The error in locating the centroid displacements depends on the optical parameters of the camera, lenses, laser, and the algorithm for finding the particle-image centroid. As mentioned before, two different software applications were used for spot centroid finding and particle tracking. In both cases, the centroid is computed using the center-of-mass location method, by weighing every pixel with the value of its intensity, that is, if $I(x,y)$ is the gray scale pixel intensity at the position (x,y) on an tracer seed particle or microbubble spot image, the center-of-mass location is given by

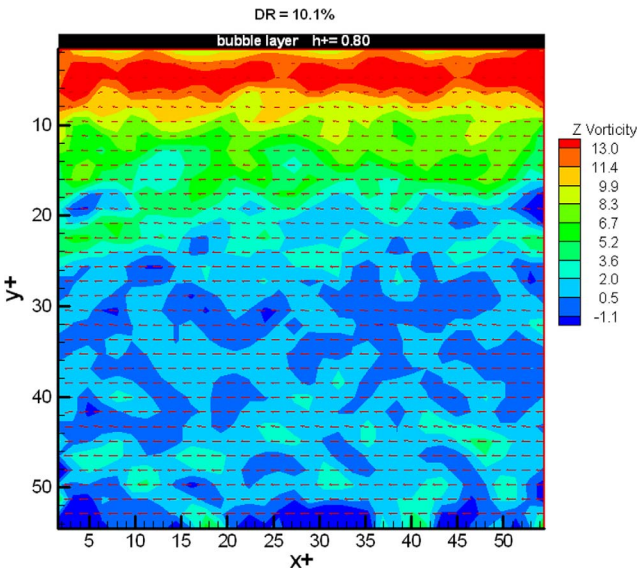

Fig. 10 *z* component of the mean vorticity field for the drag reduction of 10.1% case

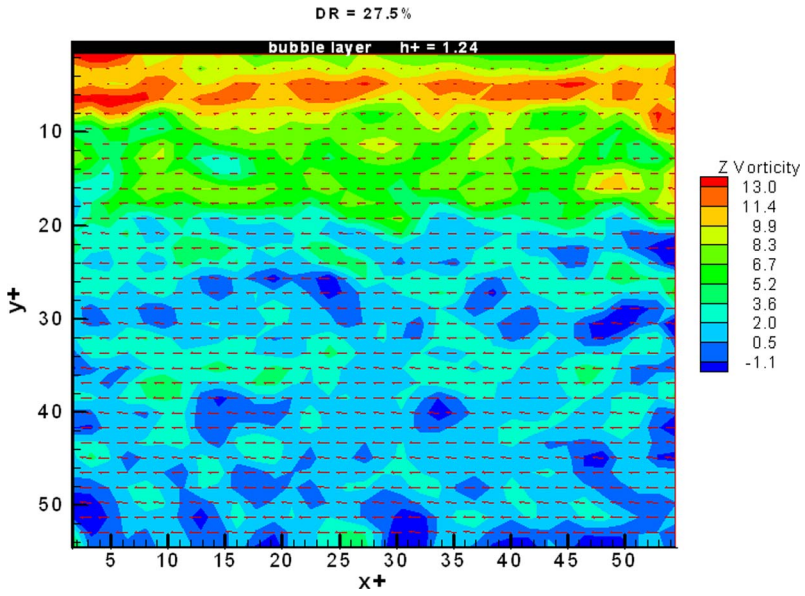

Fig. 11 ***z*** **component of the mean vorticity field for the drag reduction of 27.5% case**

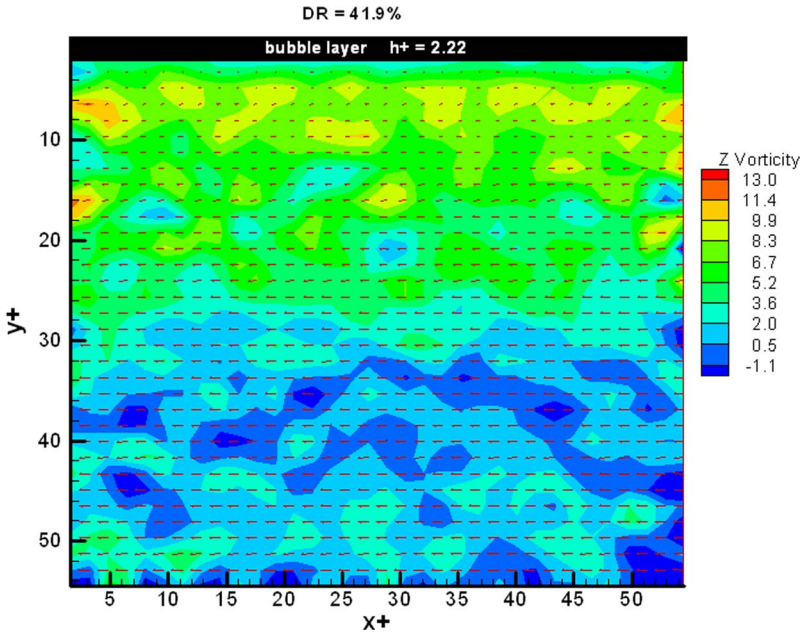

Fig. 12 ***z*** **component of the mean vorticity field for the drag reduction of 41.9% case**

$$(x_0,y_0)_{\text{center-of-mass}} = \frac{\sum_{\text{spot area}} (x,y) \times I(x,y)}{\sum_{\text{spot area}} I(x,y)}. \quad (23)$$

The centroid in this case is called the first-order moment. This algorithm requires a precise determination of the spot image border. This kind of algorithm has typical errors smaller than 0.01 pixel for simulated ideal particle images [27]. However, the error increases as the noise increases and the spot image size decreases. By applying image calibration, a rms error of 0.1 pixel in calculating the particle image centroids was determined. Using the tests of the PIV Challenge [19], it was found a rms error of 0.4 pixel for the displacement on two consecutive frames, for the homemade software application. This error was assumed as the overall error of the measurements, although the other algorithm had a small rms error of 0.25 pixel.

The uncertainty of the components of the velocity vector can be computed through the error propagation formula. This relationship assumes that if the errors associated to a measurement are small

and symmetric around zero, the uncertainty associated to any quantity σ_s derived from, for example, three measurements is given by

$$\sigma_s^2 = \left(\frac{\partial s}{\partial r_1}\right)^2 \sigma_{r1}^2 + \left(\frac{\partial s}{\partial r_2}\right)^2 \sigma_{r2}^{2'} + \left(\frac{\partial s}{\partial r_3}\right)^2 \sigma_{r3}^{2'} \tag{24}$$

where r_1, r_2, and r_3 are the values of the measurements, and σ_{r1}, σ_{r2}, and σ_{r3}, are their respective associated errors. Thus, to calculate the uncertainty of the components of the instantaneous velocity vectors $\mathbf{U}=\mathbf{U}(U,V)$, we first note that the velocity components are calculated from the subtraction of the coordinates of the position vector $\mathbf{X}=\mathbf{X}(x,y)$ divided by the time interval between laser pulses Δt. Thus, using Eq. (24), the rms error value of 0.4 pixel implies an error of 0.28 pixel in the calculation of the particle image centroids for the two particle images needed in calculating the displacement. In terms of velocity units, the rms error is then 4.18 mm/s for each velocity component. This value is determined considering negligible error in the time separation between frames (1 ms), and the 0.4 pixel error of the particle image displacement. Although 4.18 mm/s seems a high value, only the first two or three grid points along the y direction had velocity values lower than 10 mm/s. The percentage rms value with respect to the average velocity in the channel is about 5.4%.

The friction velocity u_τ was computed from the average value of the U component at each different y position. Therefore, the uncertainty of u_τ relates to that of $\bar{U}$, which, in turn, comes from the error of the instantaneous values of U. The uncertainty σ associated to the components of the mean velocity vector $\bar{\mathbf{U}}=\bar{\mathbf{U}}(\bar{U},\bar{V})$ can be calculated, using again Eq. (24), from

$$\sigma_{\bar{U},\bar{V}} = \frac{\sigma_{U,V}}{\sqrt{n}} \tag{25}$$

where n is the total number of samples employed in the average calculation. The value of n was 1000, except for about the first four or five grid points, out of at least 21 grid points used in the computation of u_τ, as previously indicated. Thus, $\sigma_{\bar{U},\bar{V}}=0.13$ mm/s. This is a top value for the uncertainty in the calculation of u_τ. Finally, the maximum calculated error of the drag reduction is about 6.9%, i.e., $\sigma_{\mathrm{DR}}=6.9\%$.

For the vorticity uncertainty, using again the error propagation formula, it can be shown that $\sigma_{\omega z}=\sigma_{\bar{U}}/\Delta x$. Now, since there were at least 100 velocity vectors in each grid point, $\sigma_{\bar{U},\bar{V}}=0.42$ mm/s and $\Delta x=0.63$ mm, $\sigma_{\omega z}=0.67$ Hz.

The total void fraction was considered to have contributions of a bubble layer formed at the top wall of the channel, plus the microbubbles freely flowing in the view volume. Practically $\alpha=\alpha_{\mathrm{bl}}$ as is estimated from Eq. (18). Thus, it is considered that the uncertainty in the calculation of α_{fb}, σ_{fb}, can be neglected in the calculation of the total error associated with α. To determine the value of α_{bl}, the images were enhanced and expanded, so the boundary of the bubble layer could be accurately obtained. Therefore uncertainty associated to α is considered to be 2 pixels (0.021 mm).

Conclusions

The presence of microbubbles within the critical zone of the buffer layer yields a drag reduction similar to the results obtained from drag reduction due to the addition of surfactants and polymers. The thickening of the viscous zone and upward shifts of the logarithmic region are observed. It was also shown that the microbubble layer formed at the channel top wall has no major role in drag reduction. The present data suggest that the most important aspect in achieving high drag reductions is the accumulation of microbubbles in a critical zone in the buffer layer, from $y^+ \approx 15$ to $y^+ \approx 30$. It indicates that there is a minimum critical microbubble void fraction necessary to achieve drag reductions of about 20% or higher. It is the first time, to our knowledge, that high percentage drag reductions can be achieved with low local void fractions.

The vorticity fields also show similarities to drag reduction characteristics by polymer and surfactant injection. The reduction of vorticity magnitude occurs close to the wall as the drag reductions increases. The modification of the normal and streamwise components of the mean velocity vector across the two-phase boundary layer has been presented and discussed. It is shown that for the high drag reduction cases the normal velocity component shifts away from the wall indicating a positive value of the normal velocity component. This phenomenon is not clear yet for the low drag reduction cases, where measurement uncertainty could be an important issue. The results obtained so far lead to the conclusion that drag reduction by microbubble injection is not a simple consequence of density effects, but is an active and dynamic interaction between the turbulence structure in the buffer zone and the microbubbles concentration in this region.

Acknowledgment

Acknowledgement is due to the reviewers of this paper, for their valuable comments and suggestions.

References

[1] Kodama, Y., Kakugawa, A., Takahashi, T., and Kawashima, H., 2000, "Experimental Study on Microbubbles and Their Applicability to Ship for Skin Friction Reduction," Int. J. Heat Fluid Flow, **21**, pp. 582–588.
[2] Gad-el-Hak, M., 2000, *Flow Control: Passive, Active and Reactive Flow Management*, Cambridge University Press, Cambridge, England.
[3] McCormick, M. E., and Bhattacharyya, R., 1973, "Drag Reduction on a Submersible Hull by Electrolysis," Nav. Eng. J., **85**, pp. 11–16.
[4] Sanders, W. C., Ivy, E. M., Ceccio, S. L., Dowling, D. R., and Perlin, M., 2003, "Microbubble Drag Reduction at High Reynolds Number," *4th ASME JSME Joint Fluids Engineering Conference*, Honolulu, HI, Paper No. FEDSM2003-45649.
[5] Madavan, N. K., Deutsch, S., and Merkle, C. L., 1984, "Reduction of Turbulent Skin Friction by Microbubbles," Phys. Fluids, **27**, pp. 356–363.
[6] Fontaine, A., Deutsch, S., Brungart, T. A., Petrie, H. L., and Fenstermacker, M., 1999, "Drag Reduction by Coupled Systems: Microbubble Injection with Homogeneous Polymer and Surfactant Solutions," Exp. Fluids, **26**, pp. 397–403.
[7] Takahashi, T., Kakugawa, A., Kodama, Y., and Makino, M., 2001, "Experimental Study on Drag Reduction by Microbubbles Using a 50m-Long Flat Plate Ship," *Second International Symposium on Turbulence and Shear Flow Phenomena*, 1, Stockholm, Sweden, pp. 175–180.
[8] Kawamura, T., Moriguchi, Y., Kato, H., Kakugawa, A., and Kodama, Y., 2003, "Effect of Bubble Size on the Microbubble Drag Reduction of a Turbulent Boundary Layer," *4th ASME JSME Joint Fluids Engineering Conference*, Honolulu, HI, Paper No. FEDSM2003-45645.
[9] Madavan, N. K., Deutsch, S., and Merkle, C. L., 1985, "Measurements of Local Skin Friction in a Reynolds Bubble-Modified Turbulent Boundary Layer." J. Fluid Mech., **156**, pp. 237–256.
[10] Legner, H. H., 1984, "A Simple Model for Gas Bubble Drag Reduction," Phys. Fluids, **27**, pp. 2788–2790.
[11] Kitagawa, A., Sugiyama, K., Ashihara, M., Hishida, K., and Kodama, Y., 2003, "Measurement of Turbulence Modification by Microbubbles Causing Frictional Drag Reduction," *4th ASME JSME Joint Fluids Engineering Conference*, Honolulu, HI, Paper No. FEDSM2003-45648.
[12] Madavan, N. K., Merkle, C. L., and Deutsch, S., 1985b, "Numerical Investigations into the Mechanisms of Microbubble Drag Reduction," ASME J. Fluids Eng., **107**, pp. 370–377.
[13] Xu, J., Maxey, M. R., and Karniadakis, G., 2002, "Numerical Simulation of Turbulent Drag Reduction Using Micro-Bubbles," J. Fluid Mech., **468**, pp. 271–281.
[14] Ferrante, A., and Elghobashi, S., 2004, "On the Physical Mechanisms of Drag Reduction in a Spatially Developing Turbulent Boundary Layer Laden with Microbubbles," J. Fluid Mech., **503**, pp. 345–355.
[15] Arakawa, K., Toda, K., and Yamamoto, M., 2003, "Modeling and Computational Study on Microbubble Two-Phase Turbulent Flow," *4th ASME JSME Joint Fluids Engineering Conference*, Honolulu, HI, Paper No. FEDSM2003-45760.
[16] Kunz, R. F., Deutsch, S., and Lindau, J. W., 2003, "Two Fluid Modeling of Microbubble Turbulent Drag Reduction," *4th ASME JSME Joint Fluids Engineering Conference*, Honolulu, HI, Paper No. FEDSM2003-45640.
[17] Yamamoto, Y., Gobara, R., and Uemura, T., 2001, "High-Efficiency Particle Detection Method Using 1D-correlation," *3rd Pacific Symposium on Flow Visualization and Image Processing*, Maui, HI, Paper No. F3130.
[18] Uemura, T., Yamamoto, F., and Ohmi, K., 1991, "Mixing Flow in a Cylindrical Vessel Agitated by a Bubbling Jet," *Application of Laser Techniques to Fluid Mechanics*, Springer-Verlag, Berlin, pp. 512–536.

[19] Stalisnas, M., Okamoto, K., and Kähler, C., 2003, "Main Results of the First International PIV Challenge," Meas. Sci. Technol., **14**, pp. R63–R89.
[20] Hassan, Y. A., Blanchat, T. K., Seeley, Jr.C. H., and Canaan, R. E., 1992, "Simultaneous Velocity Measurements of Both Components of a Two-Phase Flow Using Particle Image Velocimetry," Int. J. Multiphase Flow, **18**, pp. 371–395.
[21] Djenidi, L., Dubief, Y., and Antonia, R. A., 1997, Advantages of Using a Power Law in a Low R_θ Turbulent Boundary Layer," Exp. Fluids, **22**, pp. 348–350.
[22] Durst, F., Kikura, H., Lekakis, I., Jovanovic, J., and Ye, Q., 1996, "Wall Shear Stress Determination from Near-Wall Mean Velocity Data in Turbulent Pipe and Channel Flows," Exp. Fluids, **20**, pp. 417–428.
[23] Schlichting, H., and Gersten, K., 2000, *Boundary Layer Theory*, 8th ed., Springer, New York.
[24] Warholic, M. D., Massah, H., and Hanratty, T. J., 1999, "Influence of Drag-Reducing Polymers on Turbulence: Effects of Reynolds Number, Concentration and Mixing," Exp. Fluids, **27**, pp. 461–472.
[25] White, C. M., Somandepalli, V. S. R., and Mungal, M. G., 2004, "The Turbulence Structure of Drag-Reduced Boundary Layer Flow," Exp. Fluids, **36**, pp. 62–69.
[26] Dubief, Y., White, C. M., Terrapon, V. E., Shaqfeh, E. S. G., Lele, S. K., and Moin, P., 2003, "Numerical Simulation of High Drag Reduction Regime in Polymer Solutions," *4th ASME JSME Joint Fluids Engineering Conference*, Honolulu, HI, Paper No. FEDSM2003-45652.
[27] Udrea, D. D., Bryanston-Cross, P. J., Moroni, M., and Querzoli, G., 2000, "Particle Tracking Velocimetry Techniques," *Particle Image Velocimtery. Progress towards Industrial Application*, Kluwer Academic, Dordrecht, The Netherlands, pp. 279–304.

A Computational Study of the Flow Around an Isolated Wheel in Contact With the Ground

James McManus

Xin Zhang
e-mail: XZhang@soton.ac.uk

Aerospace Engineering,
School of Engineering Sciences,
University of Southampton,
Southampton SO17 1BJ, UK

The flow around an isolated wheel in contact with the ground is computed by the Unsteady Reynolds-Averaged Navier-Stokes (URANS) method. Two cases are considered, a stationary wheel on a stationary ground and a rotating wheel on a moving ground. The computed wheel geometry is a detailed and accurate representation of the geometry used in the experiments of Fackrell and Harvey. The time-averaged computed flow is examined to reveal both new flow structures and new details of flow structures known from previous experiments. The mechanisms of formation of the flow structures are explained. A general schematic picture of the flow is presented. Surface pressures and pressure lift and drag forces are computed and compared to experimental results and show good agreement. The grid sensitivity of the computations is examined and shown to be small. The results have application to the design of road vehicles. [DOI: 10.1115/1.2175158]

1 Introduction

The flow around a wheel in contact with the ground is of importance in the field of road vehicle design and aerodynamics. Wheels can have a significant influence on the flow around road vehicles. This is particularly so for open-wheeled racing cars where the wheels contribute some 40% [1] of the total drag and introduce considerable complexity to the flow around other elements of the car. Wheels are also a major contributor to the noise generated by ordinary road vehicles [2] such as cars and trucks. Despite the obvious practical importance of the flow that remains poorly understood. The current understanding, based on assumption and limited experiment, falls short of the detailed understanding of similar bluff body flows such as that around a cube [3] or a simplified vehicle body [4]. A factor in this is undoubtedly the difficulties that arise when one tries to measure the forces and pressures acting upon a wheel rotating in contact with the ground. Computational approaches may offer a means to study the flow that avoids some of these difficulties.

A number of attempts have been made to measure the aerodynamic forces acting upon a wheel in contact with the ground. These attempts have met with varying levels of success. Two basic methods have been tried and they are described in this paper by the terms direct and indirect. The direct method is to measure the aerodynamic forces using a wind tunnel balance or, more recently, a load cell. The problem with this method is the interference of unknown and variable contact forces acting between the wheel and the ground. This is principally a problem for the lift force measurement since the contact forces act parallel to the lift force. The indirect method is to measure the surface pressure, using an electronic system inside the wheel, and integrate over the surface to derive the aerodynamic forces. Although this avoids the problem of contact forces it brings with it the considerable problem of putting sensitive electronics inside a rapidly rotating wheel.

Morelli [5,6], Stapleford and Carr [7], and Cogotti [8] made aerodynamic force measurements using the direct method. In each case a fixed ground plane was used and a small gap left between the wheel and the ground to allow rotation by a motor. In one set of experiments, Stapleford and Carr [7] also used a moving ground and left a small gap to avoid the interference of contact forces. For the experiments with a fixed ground, Stapleford and Carr [7], and Cogotti [8] sealed the gap with strips of paper and foam rubber, respectively. The results indicated that the stationary and rotating wheels both produced positive lift when the gap was sealed. If the gap was left unsealed, for the rotating wheel only, negative lift was produced. The rotating wheel, with the gap sealed, produced less lift and less drag than the stationary wheel. These results demonstrated that a wheel must be in actual or effective contact with the ground for a correct experimental simulation.

Most studies of road vehicles, particularly those that operate in ground effect, are conducted with a moving ground to eliminate the ground boundary layer beneath the vehicle. As such actual ground contact for wheels is the only practical option and direct lift force measurements have long been unfeasible, although direct drag force measurements have been possible with wheel drag load cells for some time. Recent advances in load cell and moving ground technology have made it possible to make direct lift force measurements with the wheel in contact with the ground. Rather than suspending the wheel from a wind tunnel balance the wheel rests on a load cell beneath the moving ground belt. Waschle et al. [9] used this approach and reported results in qualitative agreement with the earlier work of Stapleford and Carr [7], and Cogotti [8].

Fackrell and Harvey [10–12] made the first, and probably best known, aerodynamic force and pressure measurements with the indirect method. A moving ground was used and the wheel could be configured with a range of tread widths and sidewall profiles. The results confirmed the lift and drag force characteristics observed in the earlier work of Stapleford and Carr [7], and Cogotti [8]. For the rotating wheel, they predicted and observed a sharp positive pressure peak, at roughly $C_P=2$, immediately upstream of the line of contact between the wheel and ground. It was proposed that the pressure peak was the result of a "pumping" effect that occurs as the boundary layers on the moving wheel and ground surfaces are forced towards the line of contact before emerging in a jet at the edges of the wheel. They regarded this as a unique feature of the rotating wheel flow and one that had an important influence on the surrounding flowfield. Based on the same considerations a negative pressure peak, downstream of the line of contact, was predicted but not observed.

Recently, Hinson [13], Whitbread [14], Skea et al. [15], and Mears et al. [16–18] have also made aerodynamic force and pressure measurements by the indirect method. A quantitative comparison of these results and Fackrell and Harvey's [10–12] results is not meaningful since a different wheel geometry was used in

Contributed by the Fluids Engineering Division for ASME for publication in the JOURNAL OF FLUIDS ENGINEERING. Manuscript received July 14, 2005; final manuscript received October 12, 2005. Assoc. Editor: Surya P Vanka.

each study. On a qualitative basis the comparison of rotating wheel surface pressures is good all around but near the line of contact it is poor. Hinson [13], Whitbread [14], and Mears et al. [16–18] observed a positive pressure peak followed by a negative peak and a series of large amplitude negative pressure oscillations. Skea et al. [15] observed neither peak. The pressure oscillations have a frequency that is independent of velocity and closely similar to the natural frequency of the pressure sensors. The nonaerodynamic character of these pressure oscillations leads us to suggest that their origin is in the resonant response of the pressure measurement systems. A pressure measurement system inside a rotating wheel is exposed to a very rapidly changing pressure distribution. The influence of response characteristics and resonances within the system, from the pressure sensor, tubing, and electronic components is likely to be critical.

The flow around a wheel, and in particular the wake, has been the subject of a number of studies. Fackrell and Harvey [10–12] measured the total pressure in the wake. They observed that the wake of the rotating wheel was taller and narrower than that of the stationary wheel. The taller wake was indicative of earlier separation and this was confirmed by the surface pressure measurements. The narrowing of the wake with wheel rotation was unexpected since the proposed jetting behavior at the line of contact should logically have caused the wake near the ground to widen. The observation was attributed to the existence of a horseshoe vortex upstream of the stationary wheel, which was not present for the rotating wheel, however, no experimental confirmation was made.

Cogotti [8] proposed a model to describe the flow around a wheel. In this model, the wake consisted of three pairs of counterrotating vortices, one each from the top and bottom of the wheel and one from the hub cavity. Later, a similar model was proposed by Mercker et al. [19] though the sense of rotation of the vortices was different. Both of these models were based on theoretical assumptions and had no basis in experiment. Bearman et al. [20] made measurements of total pressure and vorticity in the wake of Fackrell and Harvey's [10–12] wheel. They observed a counterrotating vortex pair on the ground with the sense of rotation, as viewed from behind, being clockwise and anti-clockwise for the left and right vortices, respectively. The vortices behind the rotating wheel were weaker than those behind the stationary wheel. No other vortices were observed although this may have been due to the measurement plane being two and half wheel diameters downstream. Further measurements by Mears et al. [17,18] and Waschle et al. [9] confirm the existence of the ground vortices but again no other vortices were observed.

Axon et al. [21,22] made the first computational study of the flow around a wheel. The Steady Reynolds-Averaged Navier-Stokes (SRANS) method, with the two-layer RNG $k-\epsilon$ turbulence model, was used to calculate the flow around the wheel referred to as "B2" in the experiments of Fackrell and Harvey [10–12]. The complex hub and sidewall profile of the experimental wheel were reduced to a flat sided cylinder with radiused edges for the computations. Computed results for forces, pressures and wake total pressure were reported to be in qualitative agreement with the experimental results. For the rotating wheel, the computed surface pressure formed a positive peak of $C_P=1.8$ upstream of the line of contact. A negative peak was not observed. The computed point of separation was 30 deg downstream of the experimentally observed position of 280 deg. Computed lift and drag coefficients were $C_L=0.476$ and $C_D=0.602$, an overprediction of 8.2% and 3.8%, respectively. A number of similar studies have been made by Skea et al. [15,23], Kellar et al. [24] and Knowles et al. [25]. A single URANS study was made by Basara et al. [26]. Unfortunately, disparate wheel geometries and limited results make these studies of limited use in assessing the accuracy of the computational methods when applied to the wheel flow.

Waschle et al. [9] computed, using SRANS and Lattice-Boltzmann methods, the flow around an accurately modelled representation of their experimental wheel geometry. Quantitative comparisons of forces and wake velocities showed that SRANS, with the two-layer standard $k-\epsilon$ turbulence model, gave the best overall results for the rotating wheel. Computed force coefficients were $C_L=0.341$ and $C_D=0.531$. Compared to the directly measured experimental force coefficients, of $C_L=0.315$ and $C_D=0.566$, the errors were 8.3% and −6.2% for lift and drag respectively. Computed velocities in the wake had an average error, depending on the plane examined, of 6–10%. SRANS, with the log-law standard $k-\epsilon$ turbulence model, and Lattice-Boltzmann methods showed similar, though inferior, levels of accuracy. The main experimentally observed feature of the wake, a pair of ground vortices, was captured by all computations.

Mears et al. [18] used the same computational approach to calculate the forces acting on their experimental wheel. A quantitative comparison with experimental forces, indirectly measured with their pressure measurement system, showed significant differences of −31% and 8.9% for lift and drag, respectively. The computed force coefficients of $C_L=0.29$ and $C_D=0.61$ were similar to the values reported by Waschle et al. [9] for their similar wheel geometry. A point made by Mears et al. [18]. Two alternative measurements of drag, from a drag load cell and from the integration of wake momentum deficit, both put the drag at $C_D=0.63$, a figure that agrees better with the computed drag. The results raise the question of the accuracy of force measurements, particularly of lift, made with the indirect method. The problems, noted earlier, with surface pressure measurements would primarily affect the accuracy of the lift force measurement, as is seen to be the case here.

This paper has three aims: First, to present a URANS computation of the flow around the exact wheel geometry studied by Fackrell and Harvey [10–12], and to compare this to their experimental results. Their study is the most detailed and often referenced work on the flow. We acknowledge that the highly separated three dimensional flow around the wheel is far removed from the thin shear layers used for RANS turbulence model calibration. However, RANS is the method of choice for vehicle aerodynamic simulations. A situation that will not change for the foreseeable future because of the prohibitive computational expense of alternative approaches. As others have demonstrated, and we demonstrate here, the RANS method is capable of capturing the mean flow structures with good accuracy. Second, to gain an understanding of the mean flow, its constituent structures and their mechanisms of formation. Based on this a general schematic picture of the flow is presented. Third, the study will hopefully clarify the understanding of the flow and resolve some of the uncertainties arising from previous studies.

The paper is organized as follows. Section 2 describes the computational approach, including numerical methods, turbulence modeling, and boundary conditions. Section 3 examines the computational results for flow structures, surface pressures, and forces. Computational results are compared to experimental results. Grid sensitivity and turbulence modeling are examined. The paper concludes with a discussion in Sec. 4.

2 Description of Computations

2.1 Wheel Geometry and Flow Conditions. The computations model the experimental configuration used by Fackrell and Harvey [10–12]. A range of tread widths and sidewall profiles were used in their experiments. We chose to study a single wheel geometry, described in their nomenclature as "A2," for which the most detailed rotating results were reported. A set of coordinates describing the wheel profile was determined by scanning and carefully measuring Figs. 2-1 and 2-2 in [11]. The wheel has a diameter of 0.416 m and a breadth of 0.191 m. Further details of the wheel dimensions are shown in Fig. 1.

The experiments were conducted at a Reynolds number, based on wheel diameter, of 5.3×10^5. This corresponds to a flow veloc-

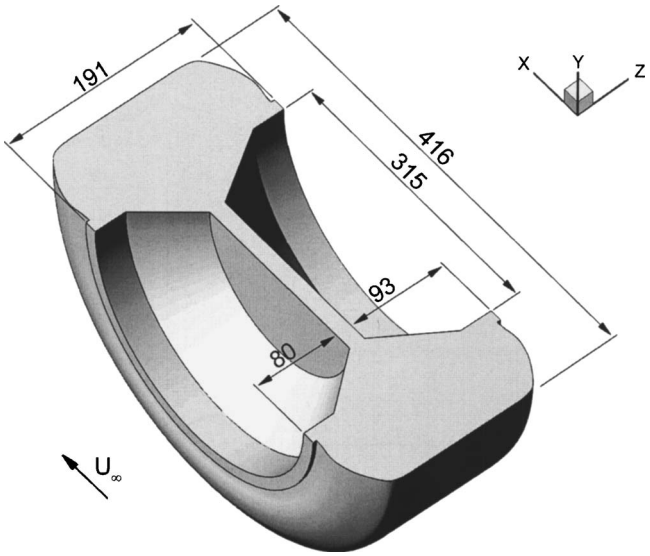

Fig. 1 Section view of wheel showing dimensions (in mm)

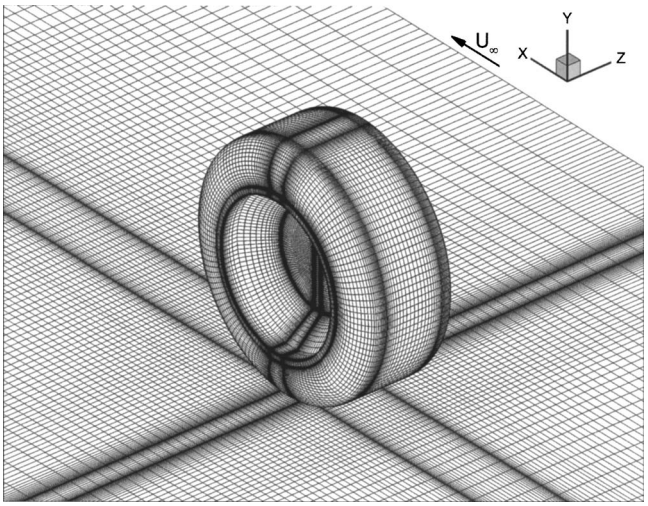

Fig. 2 Computational grid on the wheel and road surfaces (fine, 2.94 million cells)

ity of 18.6 m/s. The freestream turbulence was stated to be "about 0.2%." The computational analysis was conducted at the same Reynolds number and turbulence level. The flow was modeled as incompressible because of the low Mach number (approximately 0.05).

2.2 Governing Equations. The governing equations are the incompressible RANS equations for continuity and momentum [27]:

$$\frac{\partial \bar{u}_i}{\partial x_i} = 0 \tag{1}$$

$$\frac{\partial \bar{u}_i}{\partial t} + \bar{u}_j \frac{\partial \bar{u}_i}{\partial x_j} = -\frac{1}{\rho}\frac{\partial \bar{p}}{\partial x_i} + \nu \frac{\partial^2 \bar{u}_i}{\partial x_j^2} - \frac{\partial}{\partial x_j}(\overline{u_i' u_j'}) \tag{2}$$

where ρ is the air density, p is the air pressure, ν is the kinematic viscosity, u_i is the velocity in the ith direction (i.e.: $i=1,2,3=u,v,w$) and similarly u_j is the velocity in the jth direction (i.e.: $j=1,2,3=u,v,w$). The directional tensors, x_i and x_j, are defined for the ith and jth directions (i.e.: $i=1,2,3=x,y,z$ and $j=1,2,3=x,y,z$). Mean and fluctuating quantities are indicated by the overbar and the prime, respectively. The turbulent, or Reynolds, stresses, $\rho \overline{u_i' u_j'}$, are not known analytically and must determined with a statistical turbulence model.

2.3 Turbulence Modeling. Two turbulence models were employed to calculate the turbulent stresses, the one-equation Spalart-Allmaras (S-A) model [28] and the two equation Realizable $k-\epsilon$ (RKE) model [29]. The S-A model was chosen because of its common application in industrial flow computation, including road vehicle flows. The S-A model has a reputation for economy and robustness. The RKE model represents a more advanced class of two-equation turbulence model. It was chosen because it has been shown by its authors [29] to perform well for flows involving rotation and large-scale separation. Both of these features are prominent in the flow around a rotating wheel.

2.4 Numerical Method. The incompressible RANS equations are solved using an implicit, segregated, three-dimensional finite volume method. A second-order accurate, upwind discretization scheme is used for the convective and viscous terms of the RANS equations. Pressure-velocity coupling is implemented with the SIMPLEC algorithm. Temporal discretization is done using an implicit, second-order scheme. A multigrid scheme is used to accelerate the rate of convergence. Additional details of the numerical method can be found in [27].

2.5 Computational Grid. The computational grid (Fig. 2) is closely modeled on the experimental configuration, with the same width and height as the test section, and the same wheel position within the test section. The geometry of the computational grid is shown in Fig. 3. All of the geometric quantities are nondimensionalized with the wheel diameter, d, equal to 0.416 m. The domain is $z_1/d=3.66$ in width and $y_1/d=2.93$ in height. The inflow boundary was placed a distance $x_1/d=5$ upstream of the wheel and the outflow boundary a distance $x_3/d=15$ downstream of the wheel. These upstream and downstream distances were chosen, after preliminary SRANS simulations, to be large enough to minimize the influence of the boundaries on the final solution and small enough to minimize the number of grid cells. Similar values have been found sufficient in simulations of comparable bluff

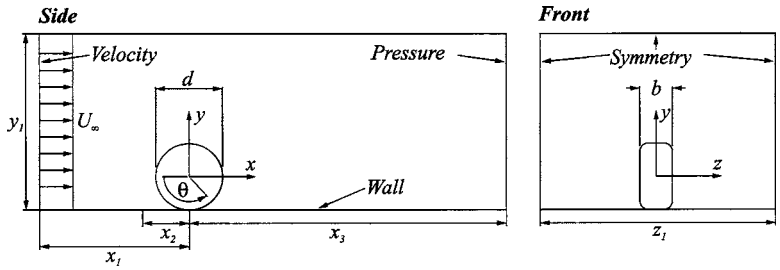

Fig. 3 Geometry of the wheel and computational domain

bodies, including wall mounted cubes [30], bus-shaped bodies [31] and landing gear [32]. As a simplification the suspension system for the wheel is not included in the computational grid.

The computational grid is made of 113 structured blocks, of these 46 blocks are arranged on the surface of the wheel with the remainder of the blocks filling the computational domain. An upper limit of 3 million grid cells was placed on the mesh to keep the computational requirements to a manageable level. This grid resolution is comparable to recent studies by Knowles et al. [25] (0.96 million), Mears et al. [18] (3.1 million) and Waschle [9] (6.7 million) and substantially more than the only other unsteady study by Basara et al. [26] (0.4 million). The large number of blocks was necessary to achieve the required placement and density of grid cells, without exceeding the self-imposed limit on the number of grid cells. Care was taken to wrap the majority of the surface blocks around the wheel, thereby minimizing the number of grid lines, at boundary layer density, propagated into the computational domain. The total number of cells was 2.94, 1.86, and 1.23 million in the fine, medium and coarse grids, respectively. Cells were clustered towards the walls to resolve the near-wall boundary layer with an average fine grid $y^+ \approx 2.5$ and a stretching ratio of 1.2 or less.

2.6 Boundary Conditions. A velocity inlet boundary condition prescribed a uniform velocity profile at 18.6 m/s with turbulence intensity of 0.2% and a hydraulic diameter of 1.35 m. Hydraulic diameter was calculated in the standard way from the width and height of the test section. At the outflow boundary, a pressure outlet boundary condition specified a gauge pressure of zero. A slip boundary condition (symmetry) was specified on the tunnel walls to avoid the need to resolve the boundary layer on these surfaces. The action of the boundary layer scoop was simulated by specifying a slip boundary condition on the ground from the inlet boundary to a position $x_2/d=1.68$ upstream from the center of the wheel. A no-slip boundary condition was specified on the wheel and ground. Velocities on these boundaries were set appropriately to simulate the two experimental cases considered, a stationary wheel on a stationary ground and a rotating wheel on a moving ground. For the stationary case, the velocity of the wheel and road was set to zero. For the rotating case, the angular velocity of the wheel was set to 89.44 rad/s. This equated to a peripheral velocity, at the line of contact with the ground, equal to the velocity of the ground which was set to the freestream velocity of 18.6 m/s.

2.7 Running Procedure. A steady simulation was commenced with the computational domain initialized everywhere to the freestream conditions at the inflow boundary. The steady simulation was continued until residuals had converged by three orders of magnitude and leveled off. A more rigorous standard of convergence is not achievable since the steady solution for this flow is not stable. This is a known problem with steady simulations of similar bluff body flows [32,33]. The steady simulation was used to initialize the computational domain for the unsteady simulation. Initializing the unsteady simulation in this way reduced the amount of computation required to reach the developed flow. A time step of 0.01, nondimensionalized by wheel diameter and freestream velocity, was used. At each time step the residuals were required to converge by three orders of magnitude. Some 20 to 40 sub-iterations were required to achieve this. The flow was allowed to develop for 10 nondimensional time units before taking samples for time-averaging. Time-averaging was performed for a further 35 nondimensional time units which corresponds to approximately four periods of the lowest frequency oscillation observed in the flow.

3 Results

3.1 Flow Features. In this section, structures are identified in the time-averaged flow around the stationary and rotating wheels.

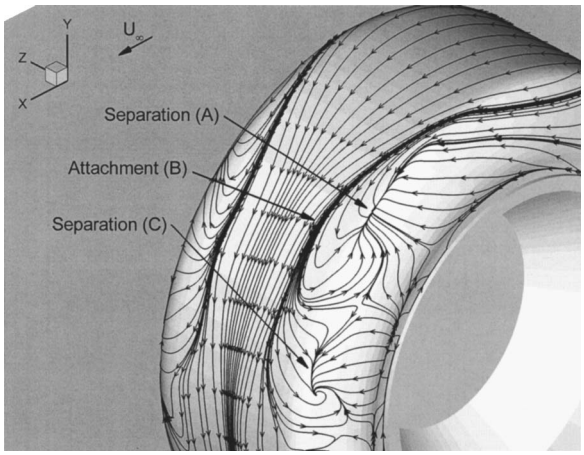

Fig. 4 Surface flow lines on the stationary wheel

Differences in these structures between the stationary and rotating wheels are examined and related to the experimentally observed changes in the character of the flow. The results are from computations on the fine grid with the RKE turbulence model.

3.1.1 Upper Near Wake Stationary. The flow over the upper surfaces of the wheel separates (A in Fig. 4) on the rear part of the circumferential small radius corner formed between the tread and side surfaces. A reattachment in the flow occurs (B in Fig. 4) on the central rear tread surface as flow around the sides of the wheel is entrained into the flow over the central upper and rear surfaces (D in Fig. 5). The decelerating flow on the rear surface of the wheel is energized by the entrained main streamwise flow around the sides. This promotes a central region of attached flow that is directed down the rear face of the wheel and toward the ground. A peak downward velocity of approximately 0.5 U_∞ is observed. The experiments [10–12] also indicated that there was a region of attached flow that was swept down the rear face of the wheel.

A similar flow physics occurs on the base of a vehicle body with a slanted rear upper surface [4]. The flow, coming off the sharp slant side edge, rolls up to form a trailing vortex if the base slant angle is in the range 10–30 deg from the horizontal. The vortices entrain flow over the slanted base and maintain an attached flow. Vortices are not observed to form on the rear face of

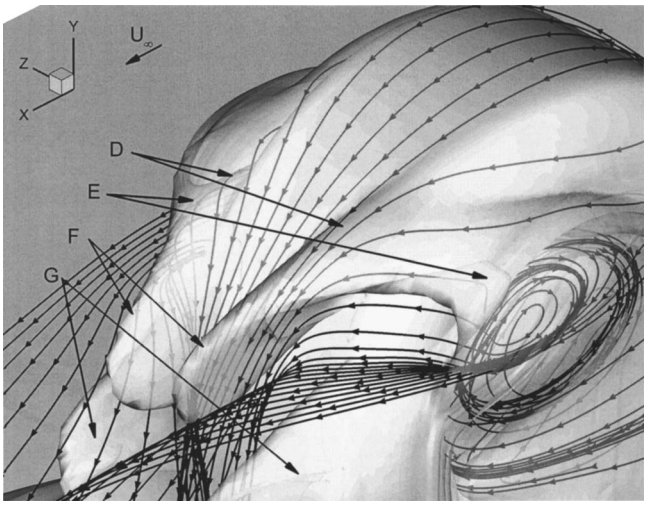

Fig. 5 Isosurface of vorticity magnitude $\Omega d/U_\infty=3.5$ and streamlines in the upper near wake of the stationary wheel

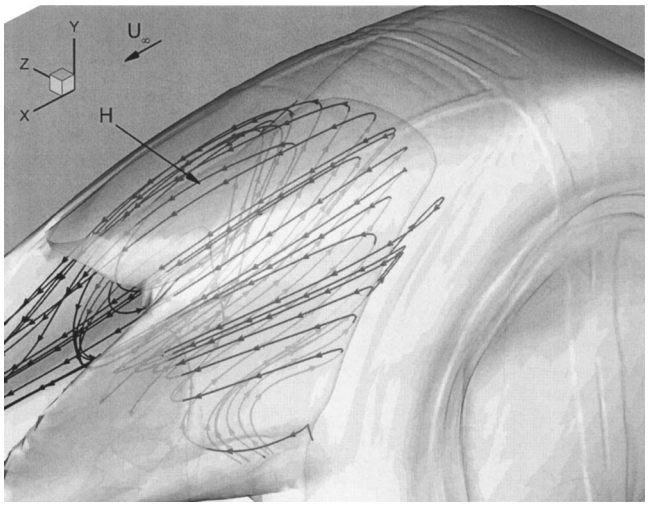

Fig. 6 Isosurface of vorticity magnitude $\Omega d/U_\infty = 3.5$ and streamlines in the upper near wake of the rotating wheel

the wheel, perhaps because the rounded side edge or the constantly varying rear face angle suppress their formation. However, the interacting flows appear to have the same effect on flow attachment.

A low velocity flow exists from the top of each hub cavity and interacts with the main streamwise flow around the sides of the wheel. The regions of interaction are delineated by arch shaped separated shear layers (E in Fig. 5) that extend from the hub cavity shear layers, around the upper sides of the wheel and into the wake. The shear layers, surrounding main streamwise flow, and hub cavity flows are all entrained into the downward flow at the rear of the wheel in two regions, indicated by high vorticity magnitude, that extend into the wake (F in Fig. 5). Another separated region is formed on the rearmost side edges (G in Fig. 5). The rotation in the associated surface flow (C in Fig. 4) indicates a small circulation in the separated region that is imparted by the flow into and down the rear face of the wheel.

Rotating. The flow separates on the upper surfaces of the wheel and forms an arch shaped vortex (H in Fig. 6). In agreement with the experiments [10–12] the separated region is formed near the top of the wheel and has a width and a height that is approximately the same as the projected outline of the wheel. Similar vortex structures are observed in the wake of other bluff bodies, an arch shaped vortex in the wake of a wall mounted cube [34] and a ring vortex in the wake of a vehicle body [4].

3.1.2 Lower Separation Region Stationary. A large separated region is formed on the ground and lower side surfaces on each side of the wheel (K in Fig. 7). The flow above the ground in front of the wheel (I in Fig. 7) is accelerated by the contracting space between the ground and wheel tread surfaces. It emerges in a high velocity sideward directed flow in front of the line of contact (J in Fig. 7), rapidly decelerates in the expanding space, and is deflected downstream by the main streamwise flow.

Rotating. The flow (Fig. 8) is essentially identical to that for the stationary wheel. In agreement with the experiments [10–12] the separated region is smaller compared to the same region for the stationary wheel. Fackrell and Harvey [10–12] were surprised by the result. They expected that the positive pressure peak on the rotating wheel would increase the velocity of the sideward directed flow emerging from under the front of the wheel. Logically the separated region would then be enlarged. To explain the anomaly they proposed, but did not observe, that the boundary layer in front of the stationary wheel was separating and rolling up to form a horseshoe vortex around the wheel. We find no evidence of a horseshoe vortex, or any other type of vortex, in this region of the flow and propose an alternative explanation. We propose that the real cause of the anomaly is the difference in the oncoming flow conditions. The stationary wheel sits in a boundary layer, approximately 16 mm thick, built up on the stationary ground surface. The flow emerging from under the front of the stationary wheel is deflected by the low velocity boundary layer flow. In contrast, the flow emerging from under the front of the rotating wheel is deflected by flow with the full freestream velocity. Consequently, the separation region formed around the stationary wheel is deflected less and, therefore, grows larger than is the case for the rotating wheel.

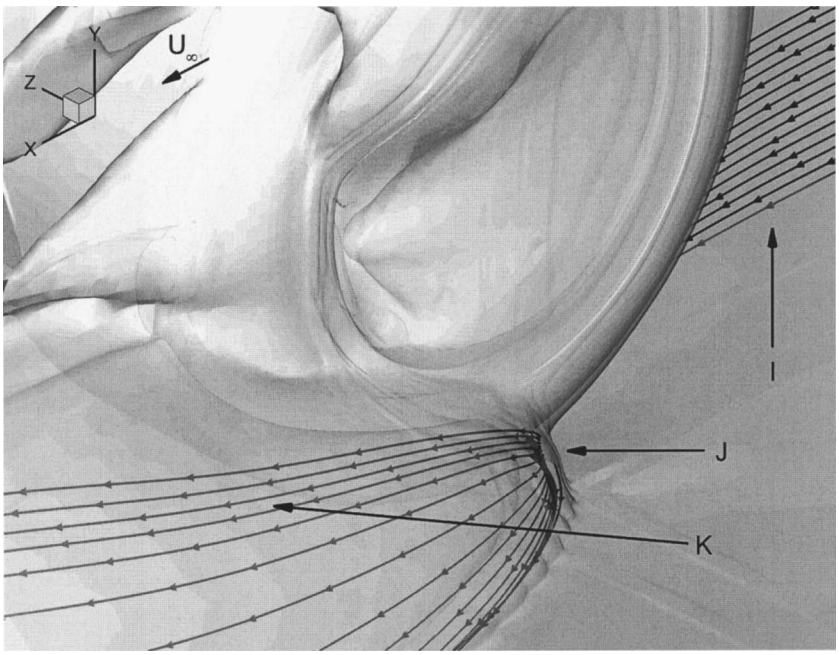

Fig. 7 Isosurface of vorticity magnitude $\Omega d/U_\infty = 3.5$ and streamlines in the lower separation region of the stationary wheels

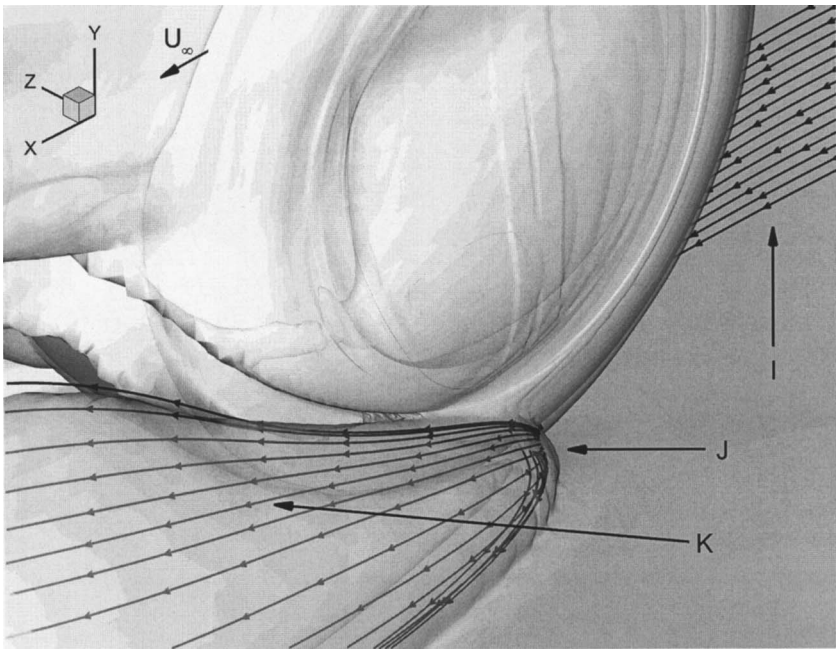

Fig. 8 Isosurface of vorticity magnitude $\Omega d/U_\infty = 3.5$ and streamlines in the lower separation region of the rotating wheel

3.1.3 Lower Near Wake Stationary. A pair of counterrotating longitudinal vortices (L in Fig. 9) are formed in the lower near wake of the wheel in agreement with experiment [20]. These vortices are created when the flow down the rear face of the wheel (M in Fig. 9) encounters the ground and rolls up. The flow down the rear face of the wheel originates, by a process described earlier, in the upper near wake. The rotation of the left and right vortices, as viewed from behind, is clockwise and anti-clockwise, respectively. The Vortices fill the near wake region, extending upstream to the rear face of the wheel and extending laterally to the shear layer from the lower separation region. Downstream the vortices spread laterally and weaken but remain discernable to the limit of the domain as regions of low momentum and low vorticity.

Rotating. In common with the stationary wheel, a pair of counterrotating longitudinal vortices (N in Fig. 10) are formed in the lower near wake of the wheel. Evident differences exist in their mechanism of formation. Whereas the stationary wheel vortices are formed when the flow down the rear face of the wheel rolls up

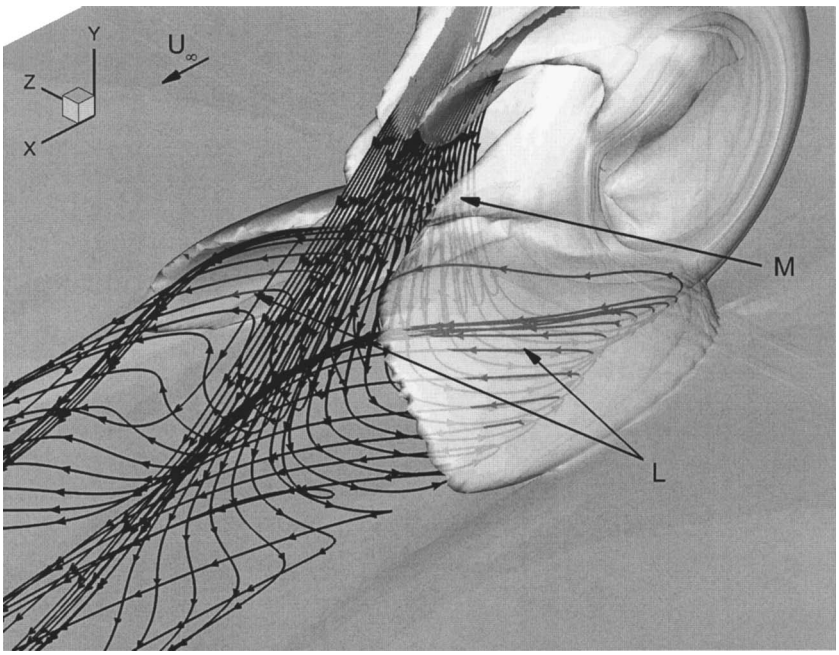

Fig. 9 Isosurface of vorticity magnitude $\Omega d/U_\infty = 3.5$ and streamlines in the lower near wake of the stationary wheel

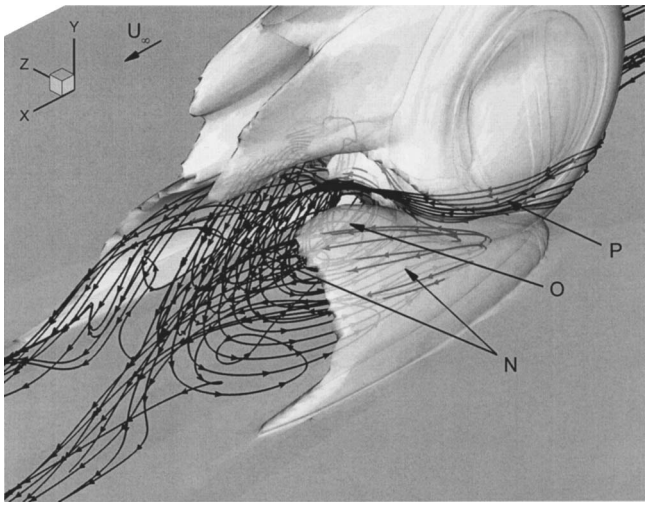

Fig. 10 Isosurface of vorticity magnitude $\Omega d/U_\infty=3.5$ and streamlines in the lower near wake of the rotating wheel

on the ground, the rotating wheel vortices can be best described as areas of recirculation formed in the wake of the lower separation region. The rotation of the wheel also appears to induce a small vortex in the $z/d=0$ plane behind the wheel (O in Fig. 10). This vortex and the entrainment of flow around the sides of the wheel (P in Fig 10) probably act to enhance the circulation of the longitudinal vortices. The differing mechanisms of formation are reflected in the strength of the vortices. In agreement with experiment [20] the vortices (Fig. 11) are noticeably weaker, and spread less laterally, than those behind the stationary wheel. Otherwise, despite the differing mechanisms of formation, they are similar overall.

3.2 Surface Pressure. The time-averaged surface pressure on the stationary and rotating wheels was computed. The centerline surface pressure is shown in Fig. 12 compared to Fackrell and Harvey's [10–12] experimental measurements. Unfortunately, the

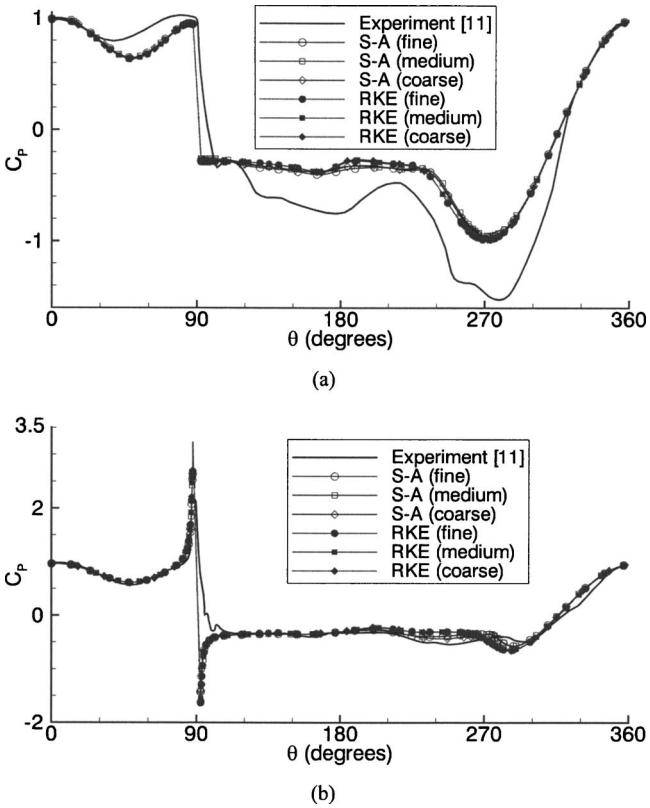

Fig. 12 Surface pressure distribution on the centreline of the wheel. (*a*) Stationary. (*b*) Rotating. Note that the experimental and computational wheel geometry is different for the stationary wheel.

authors chose to use a 33% wider wheel for the stationary measurements. As such those results are included for qualitative comparison only. The computed results referred to are from the fine grid.

Stationary. The flow stagnates at a point, slightly below the front of the wheel, predicted as $\theta=4.5$ deg by the S-A and RKE

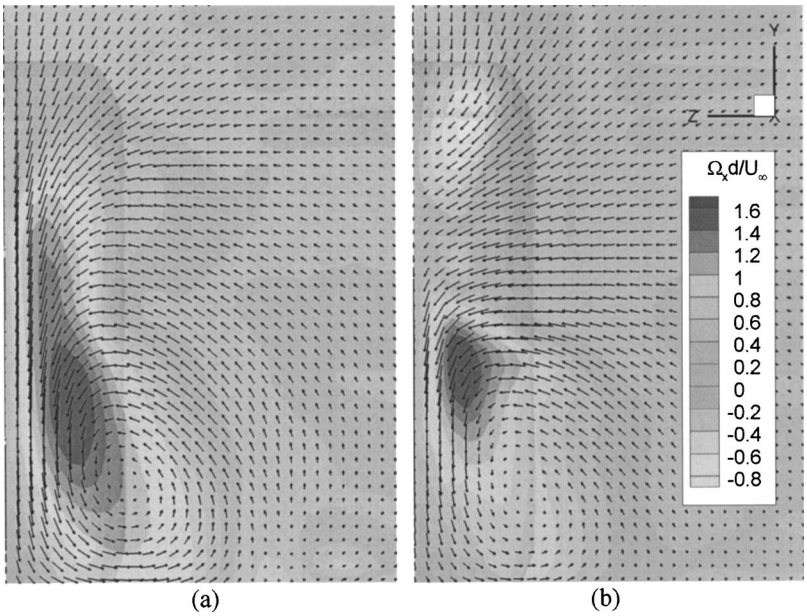

Fig. 11 Vorticity and velocity vectors in the $x/d=1$ plane showing a longitudinal vortex in the lower near wake of the wheel. (*a*) Stationary. (*b*) Rotating.

computations. The pressure then falls as the ground is approached before rising to a stagnation at the upstream side of the line of contact. The flow downstream from the front stagnation point, over the upper surfaces, is rapidly accelerated by the curvature of the wheel. A recovery in the pressure continues until separation appears to occur. Consistent with [10–12] separation is taken as the point where pressure recovery ceases. The S-A computation predicts separation at $\theta=232$ deg and the RKE computation slightly further downstream at $\theta=225$ deg. Separation was observed at $\theta=210$ deg in the experiments on the wider wheel. The surface flow (Fig. 4) earlier indicated that the separation is not across the full width of the wheel and the central region remains attached. After separation a base region is formed with a fairly constant pressure of approximately $C_P=-0.35$.

Rotating. The experimental measurement shows that the flow stagnates, slightly below the front of the wheel, at $\theta=5.6$ deg compared to $\theta=4.2$ deg for the S-A and RKE computations. The pressure falls as the ground is approached before sharply rising in a positive pressure peak at the line of contact. This pressure peak is the result of a "pumping" effect that occurs as the boundary layers on the moving wheel and ground surfaces are forced towards the line of contact. The computed pressure peaks are essentially identical, $C_P=3.22$ (S-A) and $C_P=3.24$ (RKE), and are 36% higher than the experimental pressure peak of $C_P=2.36$. After the line of contact the pressure falls to a negative pressure peak caused by the same "pumping" effect in reverse. The negative peak was not captured in the experiments. The predicted values of the negative peak are $C_P=-1.49$ (S-A) and $C_P=-1.69$ (RKE). Separation occurs in the experiment at $\theta=280$ deg, 10 deg in front of the top of the wheel. Both computations predict separation further downstream at 270 deg (S-A) and 255 deg (RKE). The base region of the flow has a fairly similar and constant pressure of about $C_P=-0.3$. The base pressures differ slightly immediately after separation, being −0.39 (experiment), −0.34 (S-A), and −0.31 (RKE), reflecting the increasing downstream position of the separation.

The agreement between the experimental measurements and the computations for the stationary wheel is as good as could be expected considering the 33% difference in width. As one would expect the wider wheel used in the experiments is able to maintain a lower pressure on the top and base surfaces. Importantly the qualitative appearance agrees well and this confirms that the computations have at least captured the basic physics of the stationary wheel flow. For the rotating wheel, the agreement between the experimental measurements and both the S-A and RKE predictions is good overall. The S-A computation predicts the separation and base pressure better that the RKE computation, but both perform surprisingly well given the well known theoretical unsuitability of RANS to highly separated flows.

A region of significant disagreement between experiment and computation occurs near the line of contact of the rotating wheel. The computations predict both a positive and negative pressure peak in agreement with Fackrell and Harvey's [10–12] theoretical prediction. In their experiments the pressure rises to a lower positive pressure peak before falling to the base pressure over a distance of 25 deg and missing the negative pressure peak entirely. To explain this behavior it was argued that the moving ground was lifting and touching the wheel in the low pressure region behind the wheel. Although this may have been the case, it also seems likely that the transient response of the pressure sensor, tubing, electronics, etc. plays a part in distorting the rapidly changing pressure signal of the rotating wheel. We are inclined towards the latter explanation in the light of the similar qualitative disagreement among subsequent experimental results [13–18] for this region of the flow. Whatever the explanation the experimental pressure near the line of contact of the rotating wheel is not reliable. The computation possibly represents a better, at least qualitatively accurate, picture of the pressure in this region.

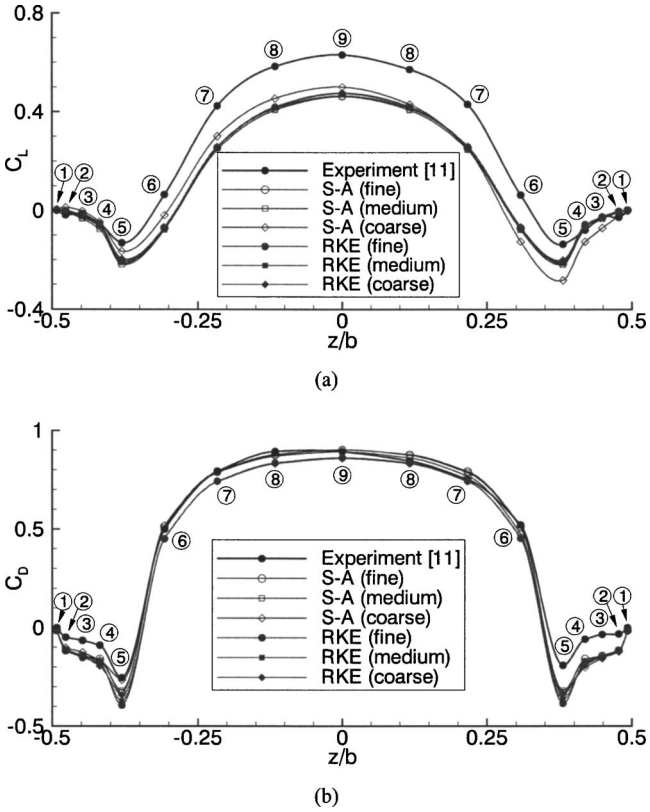

Fig. 13 Sectional pressure force coefficients across the width of the rotating wheel. (*a*) Lift. (*b*) Drag. Circled numbers identify pressure tappings.

3.3 Pressure Lift and Drag Forces. The time-averaged surface pressures were integrated over the surface of the wheel to obtain the section (Fig. 13) and total (Table 1) pressure lift and drag coefficients. The results are compared to Fackrell and Harvey's [10–12] experimental results. The integration procedure used in the experiments was exactly followed and the surface pressures taken from the same position as the 17 spanwise pressure tappings covering the tread and side surfaces. The numbering of the tappings follows the convention used in the experiments. Computed results are from the fine grid.

The section lift and drag coefficients for the rotating wheel are shown in Fig. 13. The difference between the experimental and computed section lift coefficients is significant. For example, at the center of the wheel (Tapping 9, Fig. 13(*a*)) the experimental section lift is $C_L=0.64$ compared to the computed section lift of $C_L=-0.46$ (S-A) and $C_L=0.47$ (RKE). The other pressure tappings on the tread surface (Tappings 5–9) are similarly affected. The section lift discrepancy is a result of the error in the surface pressure measurements around the line of contact, specifically the

Table 1 Time-averaged pressure lift and drag force coefficients

Case	Stationary		Rotating	
	C_L	C_D	C_L	C_D
S-A (Fine)	0.349	0.523	0.152	0.475
S-A (Medium)	0.342	0.513	0.146	0.473
S-A (Coarse)	0.346	0.520	0.164	0.467
RKE (Fine)	0.357	0.482	0.156	0.434
RKE (Medium)	0.356	0.483	0.156	0.436
RKE (Coarse)	0.356	0.483	0.160	0.437
Experiment [11]	n/a	n/a	0.28	0.51

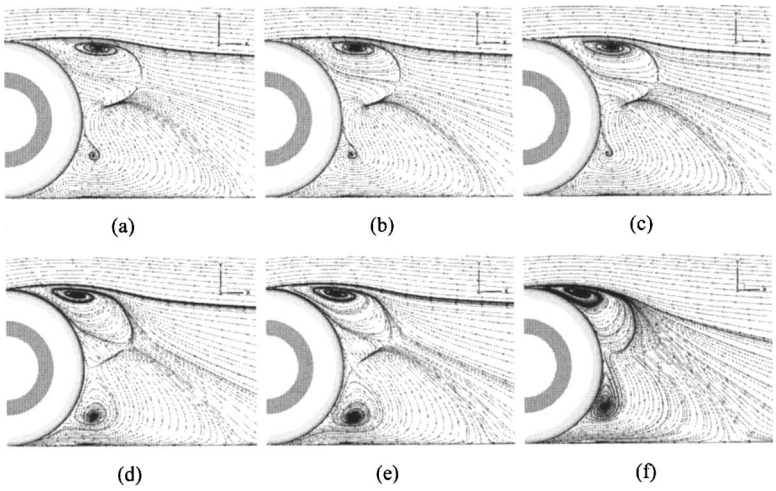

Fig. 14 Streamlines in the $z/d=0$ plane of the rotating wheel. (*a*) RKE, fine. (*b*) RKE, medium. (*c*) RKE, coarse. (*d*) S-A, fine. (*e*) S-A, medium. (*f*) S-A, coarse.

exaggerated width of the positive pressure peak and the absence of the negative pressure peak. Although the misprediction of separation on the top of the wheel has an effect its net effect on lift is small in comparison. Agreement between experimental and computed section drag coefficients (Fig. 13(*b*)) is good overall. On the sides of the wheel (Tappings 1–4, Fig. 13(*b*)) the agreement worsens. Inspection of the pressure for these tappings indicate that the computations overpredict the negative pressure, and hence the acceleration of the flow, on the forward part of the sides. A small asymmetry in the section drag coefficients is caused by the supporting strut on the +z side of the wheel in the experiment.

The pressure lift and drag coefficients are presented in Table 1. In agreement with experiment [10–12] the forces on the rotating wheel are less than the forces on the stationary wheel. The S-A and RKE computations give similar results for the forces on the stationary wheel. Experimental forces were not reported for the stationary wheel so we cannot comment on the accuracy of these results. The large difference between the experimental, $C_L=0.28$, and computed lift forces, $C_L=0.152$ (S-A) and $C_L=0.156$ (RKE), for the rotating wheel reflect the differences noted in the section lift coefficient. Better agreement is found between the experimental drag force, $C_D=0.51$, and the computed drag forces, $C_L=0.47$ (S-A) and $C_L=0.43$ (RKE).

The agreement between the computed and experimental pressure lift and drag forces is mixed. The discrepancy in section and total lift coefficients is large and was found to be the result of differences in the surface pressure occurring near the line of contact of the rotating wheel. Differences that we believe are caused by errors in the experimental measurement of surface pressure. The S-A and RKE computations predict a similar value for the lift coefficient. The computed section and total drag coefficients agree well with experiment, with the S-A results being slightly better than the RKE results.

3.4 Grid Sensitivity. The influence of grid resolution on the computations is examined with a grid sensitivity study. The computed pressure forces (Table 1) show a small dependence on the three different grid resolutions. The grid dependence of the S-A computations is noticeably larger than for the RKE computations and is not monotonic with the grid resolution. Some insight into the grid dependence of the S-A computations comes from examining the variation in section lift and drag forces (Fig. 13) across the width of the wheel. The differences between the three grids, particularly the coarse grid, suggest a dependence of the flowfield on the grid resolution that doesn't occur in the RKE computations.

To further examine the dependence of the flowfield on the grid resolution the streamlines on the $z/d=0$ plane of the rotating wheel are plotted in Fig. 14. All of the computations predict the same basic flow structures, including the separation from the top of the wheel and the vortex behind the wheel on the ground. The S-A computations show an evident dependence on the grid resolution. Most obviously in the differing size and position of the flow structures in the coarse grid computation compared to the same structures in the fine and medium grid computations. The RKE computations show no obvious dependence on the grid resolution.

4 Discussion

A computational study of the flow around an isolated wheel in contact with the ground was performed using the unsteady Reynolds-averaged Navier-Stokes method. The computational results were compared with the time-averaged surface pressure and pressure force measurements made by Fackrell and Harvey [10–12]. The time-averaged computed flowfield was examined to reveal new flow structures and new details of known flow structures.

We present for the first time a detailed and general schematic picture (Fig. 15) of the flow structures around an isolated wheel in contact with the ground. In the upper near wake of the stationary wheel, there is a region of interaction between the flow over the top of the wheel and the main flow around the sides of the wheel. This entrains the energetic main flow and promotes a central region of attached high velocity flow down the rear face of the wheel. For the rotating wheel, the flow separates near the top of the wheel and forms an arch shaped vortex. A trailing vortex pair in the upper wake of both the stationary and rotating wheel, proposed on the basis of theoretical considerations by Cogotti [8] and Mercker et al. [19], is not observed. A separated region is formed on the ground from the flow emerging from under the front of the wheel. In agreement with experiment [10–12] this region is smaller for the rotating wheel compared to the same region for the stationary wheel. We did not observe the horseshoe vortex in front of the stationary wheel proposed by Fackrell and Harvey [10–12] to explain this. Instead, we suggest that the boundary layer built up on the stationary ground tends to deflect the flow emerging from under the front of the wheel less than is the case for the moving ground. A pair of counterrotating longitudinal vortices are formed in the lower near wake of the wheel. In agreement with experiment [20], the vortices behind the rotating wheel are weaker

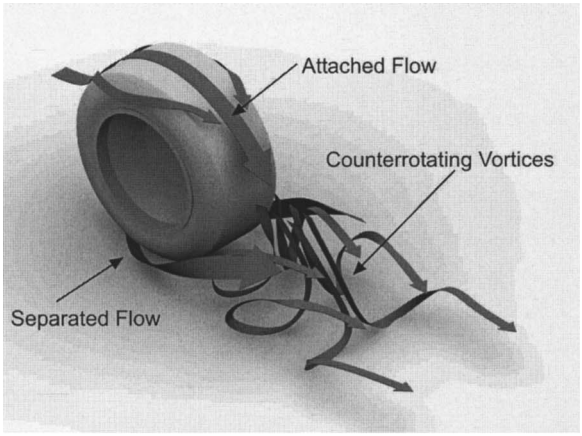

(a)

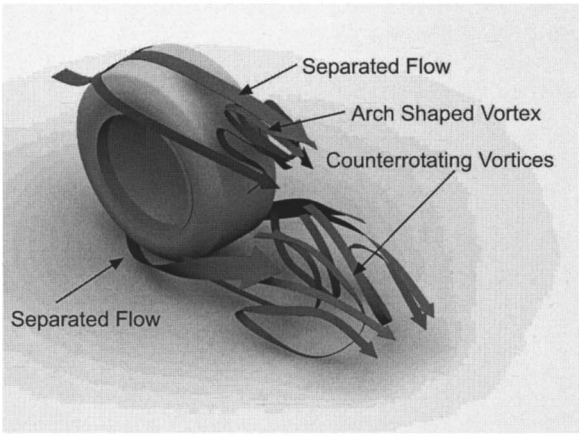

(b)

Fig. 15 Schematic diagrams of the general isolated wheel flow. (*a*) Stationary. (*b*) Rotating.

than those behind the stationary wheel. We have identified differences in the mechanisms of formation to explain this observation.

Comparison to experiment [10–12] shows that the computations predict the surface pressures and pressure lift and drag forces with good accuracy overall. Although, for the rotating wheel, the agreement on surface pressure near to the line of contact is poor. We have argued that this is due errors in the surface pressure measurements and not a shortcoming in the computations. More generally these errors seem to be a shortcoming common to all pressure measurement systems [13–18]. The agreement on lift reflects the agreement on surface pressure for the rotating wheel. Drag is relatively insensitive to the pressure near the line of contact and as such the agreement on drag is much better. The computations with both the S-A and RKE turbulence models predict similar results, but the S-A computations were better at predicting surface pressures, separation position and pressure forces. Although the S-A computations showed a greater degree of sensitivity, especially in the flowfield, to the grid resolution than did the RKE computations. In conclusion, the good quantitative and qualitative agreement with the experimental results shows that computations have successfully captured the mean structures in the flow around an isolated wheel in contact with the ground.

Acknowledgment

The authors wish to thank BAR Honda Fl, especially Willem Toet and Jonathan Zerihan, for their assistance during the course of this work.

Nomenclature

A = wheel frontal area, m^2
b = wheel breadth, m
C_D = drag coefficient, $D/(q_\infty A)$
C_L = lift coefficient, $L/(q_\infty A)$
C_P = pressure coefficient, $(p-p_\infty)/q_\infty$
d = wheel diameter, (m)
D = drag, N
L = lift, N
Ω = vorticity magnitude, s^{-1}
p = static pressure, N/m^2
p_∞ = freestream static pressure, N/m^2
q_∞ = freestream dynamic pressure, $\rho_\infty U_\infty^2/2$, N/m^2
Re = Reynolds Number, $\rho_\infty U_\infty d/\mu$
U_∞ = freestream velocity, m/s
u,v,w = velocity components in x,y,z directions, m/s
x,y,z = cartesian right handed coordinates, $x+ve$ downstream, $y+ve$ up, $z+ve$ to port, (m)

Greek Symbols

μ = dynamic viscosity, kg/(m·s)
θ = angular position of wheel, $+ve$ in the direction of rotation, deg
ρ_∞ = freestream density, kg/m^3

References

[1] Agathangelou, B., and Gascoyne, M., 1998, "Aerodynamic Design Considerations of a Formula 1 Racing Car," SAE International Congress and Exposition, Detroit, Michigan, U.S.A., 23–26 February, SAE Paper No. 980399.
[2] Nelson, P. M., and Phillips, S. M., 1997, "Quieter Road Surfaces," Transport Research Laboratory Annual Review 1997, Transport Research Laboratory, Crowthorne, U.K.
[3] Hussein, H. J., and Martinuzzi, R. J., 1996, "Energy Balance for the Turbulent Flow Around a Surface Mounted Cube Placed in a Channel," Phys. Fluids, **8**, pp. 764–780.
[4] Ahmed, S. R., Ramm, G., and Faltin, G., 1984, "Some Salient Features of the Time-Averaged Ground Vehicle Wake," SAE Paper No. 840300.
[5] Morelli, A., 1969, "Aerodynamic Effects on an Automobile Wheel," Technical Report Translation 47/69, MIRA. Translated from (in Italian) Morelli, A., 1969, "Aerodynamic Effects on the Car Wheel," ATA Review, **22**(6), pp. 281–288, June.
[6] Morelli, A., 1970, "Aerodynamic Actions on an Automobile Wheel," Paper 5, In Scibor-Rylski, A. J., editor, *Road Vehicle Aerodynamics Proceedings of the First Symposium on Road Vehicle Aerodynamics*, City University, London, U.K.
[7] Stapleford, W. R., and Carr, G. W., 1970, "Aerodynamic Characteristics of Exposed Rotating Whecls," Technical Report No. 1970/2, MIRA, Nuneaton, U.K.
[8] Cogotti, A., 1983, "Aerodynamic Characteristics of Car Wheels," International Journal of Vehicle Design, Technological Advances In Vehicle Design Series, Special Publication SP3, Impact of Aerodynamics on Vehicle Design, pp. 173–196.
[9] Waschle, A., Cyr, S., Kuthada, T., and Wiedemann, J., 2004, "Flow Around an Isolated Wheel — Experimental and Numerical Comparison of Two CFD Codes," SAE Motorsports Engineering Conference and Exhibition, Dearborn, Michigan, U.S.A., 30 November–3 December, SAE Paper No. 2004-01-0445.
[10] Fackrell, J. E., and Harvey, J. K., 1973, "The Flowfield and Pressure Distribution of an Isolated Road Wheel," in *Advances in Road Vehicle Aerodynamics*, Stephens, H. S., ed., BHRA Fluid Engineering, pp. 155–165.
[11] Fackrell, J. E., 1974, "The Aerodynamics of an Isolated Wheel Rotating in Contact With the Ground," Ph.D. thesis, University of London, London, U.K.
[12] Fackrell, J. E., and Harvey, J. K., 1975, "The Aerodynamics of an Isolated Road Wheel," in Pershing, B., editor, *Proceedings of the Second AIAA Symposium of Aerodynamics of Sports and Competition Automobiles*, Los Angeles, California, U.S.A., 11 May, pp. 119–125.
[13] Hinson, M., 1999, "Measurement of the Lift Produced by an Isolated, Rotating Formula One Wheel Using a New Pressure Measurement System," M.Sc. thesis, Cranfield University, U.K.
[14] Whitbread, L., 2000, "Measurement of the Lift Distribution on a Rotating Wheel," M.Sc. thesis, Cranfield University, U.K.
[15] Skea, A. F., Bullen, P. R., and Qiao, J., 2000, "CFD Simulations and Experimental Measurements of the Flow Over a Rotating Wheel in a Wheel Arch," SAE 2000 World Congress, Detroit, Michigan, U.S.A., 6–9 March, SAE Paper No. 2000-01-0487.
[16] Mears, A. P., Dominy, R. G., and Sims-Williams, D. B., 2002, "The Flow About an Isolated Rotating Wheel — Effects of Yaw on Lift, Drag and Flow Structure," 4th MIRA International Vehicle Aerodynamics Conference, Warwick, U.K., 16–17 October.

[17] Mears, A. P., Dominy, R. G., and Sims-Williams, D. B., 2002, "The Air Flow About an Exposed Racing Wheel," SAE Motorsports Engineering Conference and Exhibition, Indianapolis, Indiana, U.S.A., 2–5 December, SAE Paper No. 2002-01-3290.
[18] Mears, A. P., Crossland, S. C., and Dominy, R. G., 2004, "An Investigation Into the Flow-Field About an Exposed Racing Wheel," SAE Motorsports Engineering Conference and Exhibition, Dearborn, Michigan, U.S.A., 30 November–3 December, SAE Paper No. 2004-01-0446.
[19] Mercker, E., Breuer, N., Berneburg, H., and Emmelmann, H. J., 1991, "On the Aerodynamic Interference Due to the Rolling Wheels of Passenger Cars," SAE Publication No. 910311.
[20] Bearman, P. W., De Beer, D., Hamidy, E., and Harvey, J. K., 1988, "The Effect of a Moving Floor on Wind-Tunnel Simulation of Road Vehicles," SAE Paper No. 880245.
[21] Axon, L., Garry, K., and Howell, J., 1998, "An Evaluation of CFD for Modelling the Flow Around Stationary and Rotating Wheels," SAE Paper No. 980032.
[22] Axon, L., 1999, "The Aerodynamic Characteristics of Automobile Wheels - CFD Prediction and Wind Tunnel Experiment," Ph.D. thesis, Cranfield University, U.K.
[23] Skea, A. F., Bullen, P. R., and Qiao, J., 1998, "The Use of CFD to Predict the Air Flow Around a Rotating Wheel," 2nd MIRA International Conference on Vehicle Aerodynamics, Coventry, U.K., 20–21 October.
[24] Kellar, W. P., Pearse, S. R. G., and Savill, A. M., 1999, "Formula 1 Car Wheel Aerodynamics," Sports Engineering, **2**, pp. 203–212.
[25] Knowles, R., Saddington, A., and Knowles, K., 2002, "Simulation and Experiments on an Isolated Racecar Wheel Rotating in Ground Contact," 4th MIRA International Vehicle Aerodynamics Conference, Warwick, U.K., 16–17 October.
[26] Basara, B., Beader, D., and Przulj, V., 2000, "Numerical Simulation of the Air Flow Around a Rotating Wheel," 3rd MIRA International Vehicle Aerodynamics Conference, Rugby, U.K., 18–19 October.
[27] Fluent Incorporated, 2001, "FLUENT 6.0 *User's Guide*," Fluent Incorporated, Lebanon, New Hampshire, U.S.A.
[28] Spalart, P. R., and Allmaras, S. R., 1992, "A One-Equation Turbulence Model for Aerodynamic Flows," 30th AIAA Aerospace Sciences Meeting and Exhibit, Reno, Nevada, U.S.A., 6–9 January, AIAA Paper No. 92-0439.
[29] Shih, T. H., Liou, W. W., Shabbir, A., Yang, Z., and Zhu, J., 1995, "A New k-ϵ Eddy Viscosity Model for High Reynolds Number Turbulent Flows," Comput. Fluids, **24**(3), pp. 227–238.
[30] Krajnovic, S., and Davidson, L., 2002, "Large-Eddy Simulation of the Flow Around a Bluff Body," AIAA J., **40**(5), pp. 927–936.
[31] Krajnovic, S., and Davidson, L., 2003, "Numerical Study of the Flow Around a Bus-Shaped Body," ASME J. Fluids Eng., **125**(3), pp. 500–509.
[32] Hedges, L. S., Travin, A. K., and Spalart, P. R., 2002, "Detached-Eddy Simulations Over a Simplified Landing Gear," ASME J. Fluids Eng., **124**(2), pp. 413–423.
[33] Han, T., 1989, "Computational Analysis of Three-Dimensional Turbulent Flow Around a Bluff Body in Ground Proximity," AIAA J., **27**(9), pp. 1213–1219.
[34] Martinuzzi, R., and Tropea, C., 1993, "The Flow Around Surface-Mounted Prismatic Obstacles Placed in a Fully Developed Channel Flow," ASME J. Fluids Eng., **115**(1), pp. 85–91.

B. Podvin

Y. Fraigneau

F. Lusseyran

P. Gougat
e-mail: podvin@limsi.fr

LIMSI-CNRS UPR3251,
Université Paris-Sud,
91403 Orsay Cedex,
France

A Reconstruction Method for the Flow Past an Open Cavity

In this paper we propose a method to reconstruct the flow at a given time over a region of space using partial instantaneous measurements and full-space proper orthogonal decomposition (POD) statistical information. The procedure is tested for the flow past an open cavity. 3D and 2D POD analysis are used to characterize the physics of the flow. We show that the full 3D flow can be estimated from a 2D section at an instant in time provided that some 3D statistical information—i.e., the largest POD modes of the flow—is made available. [DOI: 10.1115/1.2175159]

1 Introduction

The development of numerical simulation—whether direct or large-eddy simulation— over the past decades has led to the generation of ever-increasing amounts of data [1]. Technological advances—such as PIV [2]—have also entailed substantial increases of experimental data. Exploitation and post-treatment of these large databases can be a daunting task. In this context data reduction techniques such as the POD—proper orthogonal decomposition—have enjoyed a wide popularity. For instance, Bonnet et al. [3] have recently reviewed the application of POD techniques to turbulent shear flows. Proper orthogonal decomposition was introduced by Lumley in turbulence [4] in order to extract the most energetic structures of the flow. Classical POD requires the computation of the spatial velocity autocorrelation tensor and provides a basis of three-dimensional space functions or structures which best represent in the energetic sense the organized motions of the flow. To determine how the amplitudes of the POD structures evolve over time one needs to project the full velocity field onto those structures. In practice, owing to experimental constraints or computer memory limitations, these straightforward operations may be difficult or even impossible to carry out.

Various versions of POD have been elaborated over the years. In particular the idea of using POD for better sensing and control has given rise to many developments [5–7]. Picard and Delville [6], Taylor and Glauser [8] have combined the POD analysis with a LSE (linear stochastic estimation) technique to estimate the remote velocity field from pressure signals at the wall or at the free boundary of a round jet. Since a crucial mechanism may not be energetically dominant in the flow, Maurel et al. [9] have introduced the concept of extended POD modes. A POD analysis is first performed on a signal that consists of flow realizations defined on some subdomain of the flow—for instance, it could be the velocity field restricted to some spatial subdomain or the pressure field. POD spatial modes and temporal coefficients are computed and stored. Extended modes can then be obtained for the flow on a different subdomain by projecting the corresponding flow realizations on the POD coefficients of the first signal. Boree [7] shows that these extended modes are able to extract the only part in the second signal that is correlated with the corresponding eigenmodes of the first signal. The method was used to study the jet/vortex interaction in a flow model for an internal combustion engine. The initial subdomain— centered on the vortex motion—represented only 3% of the total kinetic energy.

Many approaches focus on simplified versions of POD in which for instance only one component of the velocity field or only a portion of the space is considered. As Rempfer [10] has pointed out, the potential pitfall of these approaches is to miss some essential physics of the flow. In contrast here we will use the fully three-dimensional information associated with the empirical eigenfunctions, while relying on partial instantaneous measurements to reconstruct the flow.

The motivation for this stems from a numerical/experimental comparison for the flow past an open cavity. [11]. The flow past an open cavity can be a useful representation for industrial applications such as the car industry, where control of aeroacoustic disturbances within the vehicle could improve the performance of the car and the comfort of the motorist. Another type of application is the dispersion of pollutants in canyon-like streets with cross-wind. The POD has been applied to a number of flows within cavities [12,13]. Understanding the dynamics of these complex flows is not a trivial task, and requires extensive simulation and modelling. Despite constant advances in computer power, it does not make sense to expect to represent realistic configurations at very high Reynolds numbers with direct numerical simulation. An alternative would be to use LES, but the small-scale model they rely on needs to be validated against experimental data.

Generally speaking, simulation runs are long and costly, but give access to the entire velocity field, while experiments provide only localized measurements. The idea is then to use the numerical flow as a surrogate on which extensive statistical analysis can be performed. In particular, the 3D POD modes can be computed. Using these modes, it becomes possible to recover the instantaneous 3D flow from 2D sections of the flow—such as those available using PIV in an experiment. One could in particular obtain long time-series of the 3D flow, which are very costly to simulate numerically.

The paper is organized as follows: Section 2 presents the reconstruction method. The numerical simulation is detailed on Sec. 3. POD analysis results of the flow in the cavity are given in Sec. 4. Tests of the reconstruction method are made in Sec. 5. A conclusion is given in Sec. 6.

2 The POD-Based Reconstruction

2.1 The Proper Orthogonal Decomposition. The proper orthogonal decomposition is a statistical technique that is widely used in various fields under different names (such as Karhunen-Loève decomposition or Principal Component Analysis). It was first introduced in Fluid Mechanics by Lumley [14] for turbulence. The reader is referred to Berkooz et al. [15], or to the book by Holmes, Lumley, and Berkooz [16] for a complete introduction to the proper orthogonal decomposition.

The basic idea is to expand the velocity field $\underline{u}(\underline{x},t)$ as the superposition of signal-dependent, "energetically optimal" spatial structures $\underline{\phi}(x)$ with time-varying amplitude $a(t)$:

Contributed by the Fluids Engineering Division of ASME for publication in the JOURNAL OF FLUIDS ENGINEERING. Manuscript received July 14, 2005; final manuscript received October 26, 2005. Review conducted by Joseph Katz.

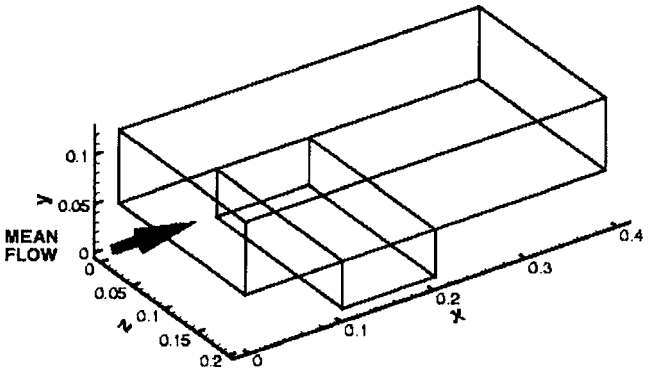

Fig. 1 Box configuration

$$\underline{u}(\underline{x},t) = \sum_{n=1}^{\infty} a^n(t)\underline{\phi}^n(\underline{x}) \tag{1}$$

for $\underline{x} \in \Omega$ where Ω is a subset of $\mathcal{R}^3$ The empirical functions $\underline{\phi}^n$ are defined to be such that the average difference between the signal and its representation truncated at any level n is minimal. In other words

$$M = \langle \| \underline{u}(\underline{x},t) - \sum_{i=1}^{n} a^i(t)\underline{\phi}^i(x) \|^2 \rangle \tag{2}$$

is minimal. One can then show that the empirical functions are solutions of the eigenproblem

$$\int \langle \underline{u}(\underline{x},t)\underline{u}(\underline{x}',t) \rangle \cdot \underline{\phi}^i(\underline{x}')d\underline{x}' = \lambda^i \underline{\phi}^i(x) \tag{3}$$

where $\langle \underline{u}(\underline{x},t)\underline{u}(\underline{x}',t) \rangle$ is the spatial autocorrelation tensor at zero-time lag obtained using temporal average over N various fields at different times t_n. The eigenvalue λ^i represents the energy of the velocity field associated with the mode i.

By construction, the empirical functions are orthogonal. We choose to make them orthonormal:

$$\int \underline{\phi}^n(\underline{x}) \cdot \underline{\phi}^m(\underline{x})dx = \delta_{nm} \tag{4}$$

Once empirical functions are known, the temporal coefficients $a^n(t)$ can be obtained by projection

$$a^n(t) = \int \underline{u}(\underline{x},t) \cdot \underline{\phi}^n(\underline{x})d\underline{x} \tag{5}$$

The $a^n(t)$ have zero mean, are uncorrelated and their variance is equal to λ^n. Note that a^n represents the evolution of the full-space structure, and therefore, requires the knowledge of the full velocity field.

If we denote $\underline{u}^n(\underline{x}) = \underline{u}(\underline{x},t_n)$ then

$$\langle \underline{u}(\underline{x},t)\underline{u}(\underline{x}',t) \rangle = \frac{1}{N}\sum_{n=1}^{N} \underline{u}^n(\underline{x})\underline{u}^n(\underline{x}') \tag{6}$$

Sirovich [17] has shown that the problem (3) is equivalent to the following eigenproblem:

$$\left[\frac{1}{N} \int < \underline{u}^i(\underline{x}) \cdot \underline{u}^j(\underline{x}) > d\underline{x} \right] A^j = \lambda A^i \tag{7}$$

and

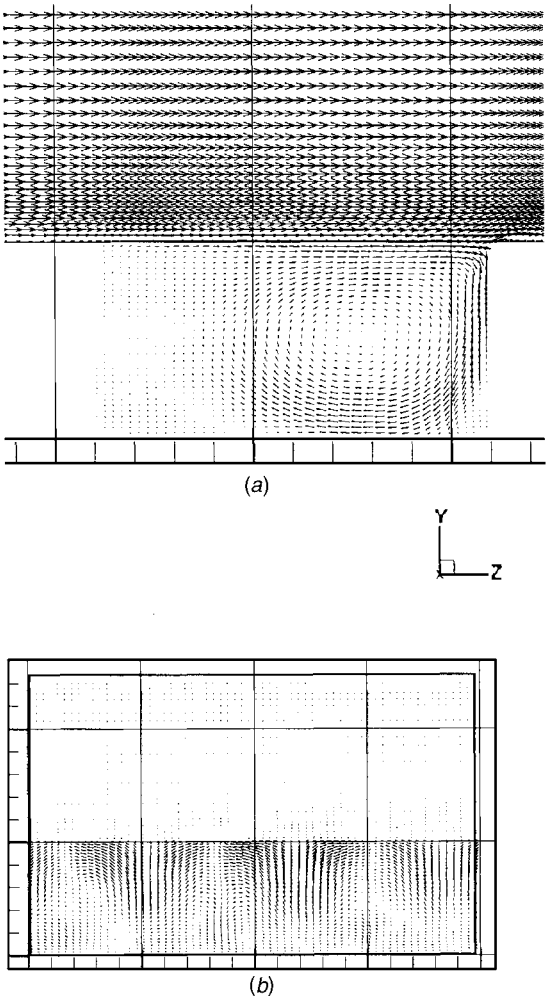

Fig. 2 (*a*) Mean flow in the *x*–*y* plane at *z*=100 mm. (*b*) Mean flow in the *y*–*z* plane at *x*=120 mm (scale is six times in part (*a*)).

$$\underline{\phi}(\underline{x}) = \sum_{j=1}^{N} A^j \underline{u}^j(\underline{x}) \tag{8}$$

The advantage of this formulation is that the dimension of the problem is given by the number of instantaneous fields or *snapshots* available, whereas in the original formulation, the problem depends on the size of the physical grid times the number of components of the signal.

In all that follows the POD based on the method of snapshots will be applied to the time-varying fluctuating part of the velocity field.

3 Reconstruction Method

Let us write the POD decomposition of the velocity field

$$\underline{u}(x,y,z,t) = \sum_{n=1}^{\infty} a^n(t)\underline{\phi}^n(x,y,z) \tag{9}$$

where

$$a^n(t) = \int \underline{u}(x,y,z,t) \cdot \underline{\phi}^n(x,y,z)dxdydz \tag{10}$$

In practice, the decomposition is limited to N POD modes (N being large enough so that the flow is well represented):

$$\underline{u}(x,y,z,t) \sim \sum_{n=1}^{N} a^n(t)\underline{\phi}^n(x,y,z) \tag{11}$$

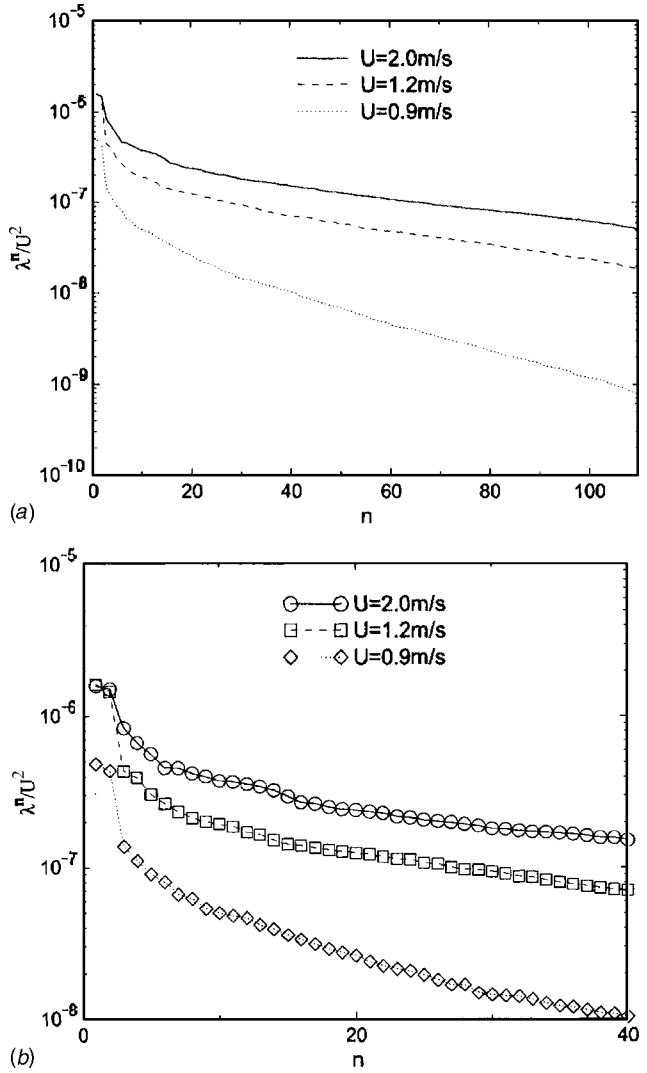

Fig. 3 (*a*) **POD spectrum at** $U=0.9,1.2,2.0$ **m/s;** (*b*) **blow-up**

Let us now assume that only some components of the velocity field can be measured on a continuous subset D of Ω. Without any loss of generality let us assume that D is the plane $z=Z$, where Z is a constant and that only the first two components of the velocity field u and v are known. This corresponds in our case to the experimental PIV data obtained by Lusseyran et al. [11] In the plane of measurements $z=Z$, one has

$$\underline{u}(x,y,Z,t) = \sum_{n=1}^{N} a^n(t)\underline{\phi}^n(x,y,Z) \tag{12}$$

If we project the velocity field in Eq. (12) onto the 2D restriction of the 3D POD structure to the plane $z=Z$, this yields in tensor notation

$$U_m = M_{mn}a^n \tag{13}$$

where

$$U_m = \int (u(x,y,Z,t)\phi_u^m(x,y,Z) + v(x,y,Z,t)\phi_v^m(x,y,Z))dxdy \tag{14}$$

and

$$M_{nm} = \int (\phi_u^n(x,y,Z)\phi_u^m(x,y,Z) + \phi_v^n(x,y,Z)\phi_v^m(x,y,Z))dxdy \tag{15}$$

M is a positive, symmetric matrix of size N, which characterizes the restricted scalar product of the eigen functions on the subdomain. If $D=\Omega$ and the three components of u could be measured, M would be the identity matrix. It is therefore reasonable to expect that for a choice of a sufficiently large domain D, M will be well-conditioned. As U_m is known, the idea is to solve the linear system (13) for a^n and then substitute the solution in the POD decomposition of u in (11).

The terms we wish to neglect in Eq. (11) are

$$T_p = \sum_{n>N} a^n \int (\phi_u^n(x,y,Z) \times \phi_u^p(x,y,Z)\phi_v^n(x,y,Z)\phi_v^p(x,y,Z))dxdy \tag{16}$$

By definition, since the velocity field has finite energy, we know that

$$\lim_{N\to\infty} \sum_{n>N} a^n = 0 \tag{17}$$

We also know that the scalar product

$$M_{np} = \int (\phi_u^n(x,y,Z)\phi_u^p(x,y,Z) + \phi_v^n(x,y,Z)\phi_v^p(x,y,Z))dxdy \tag{18}$$

is smaller than 1 in absolute value (Cauchy-Schwartz inequality). Moreover, we expect higher POD modes to be associated with smaller scales—it has even been shown that under certain conditions POD modes converge towards Fourier modes [16]—so that we can assume

$$\lim_{N\to\infty} M_{np} = 0 \quad \forall\, n>N, p>N, n\neq p \tag{19}$$

We can, therefore, expect the terms T_N to be small, for large N.

4 The Numerical Simulation

4.1 Equations of Motion. We will use $\cdot$ to represent the scalar product of two vectors. The equations of motion considered here are the Navier-Stokes equations for incompressible flow:

- Mass equation

$$\nabla \cdot \boldsymbol{V} = 0$$

- Momentum equations

$$\frac{\partial \boldsymbol{V}}{\partial t} + \nabla \cdot \boldsymbol{V}^t\boldsymbol{V} = -\frac{1}{\rho_0}\nabla P + \nabla \cdot \nu \nabla \boldsymbol{V}$$

where t is the time, ρ_0 the uniform and constant density, P the pressure, and ν the kinematic viscosity (constant).

We describe briefly the numerical method used, which is similar to this used by Gadouin and Le Quéré [18]. Momentum equations are discretized following a finite volume approach on a staggered structured grid with a second order approximation in time and space. Scalar variables are defined at cell centers whereas vector variables are defined at cells boundaries. Advection fluxes are calculated with a QUICK scheme—Quadratic Upstream Interpolation for Convective Kinematics [19]—and the viscous terms are defined with a standard second-order centered scheme. The time discretization is approximated by a second-order Backward Euler scheme. An implicit discretization is carried out on the viscous terms to increase stability and the advection fluxes are esti-

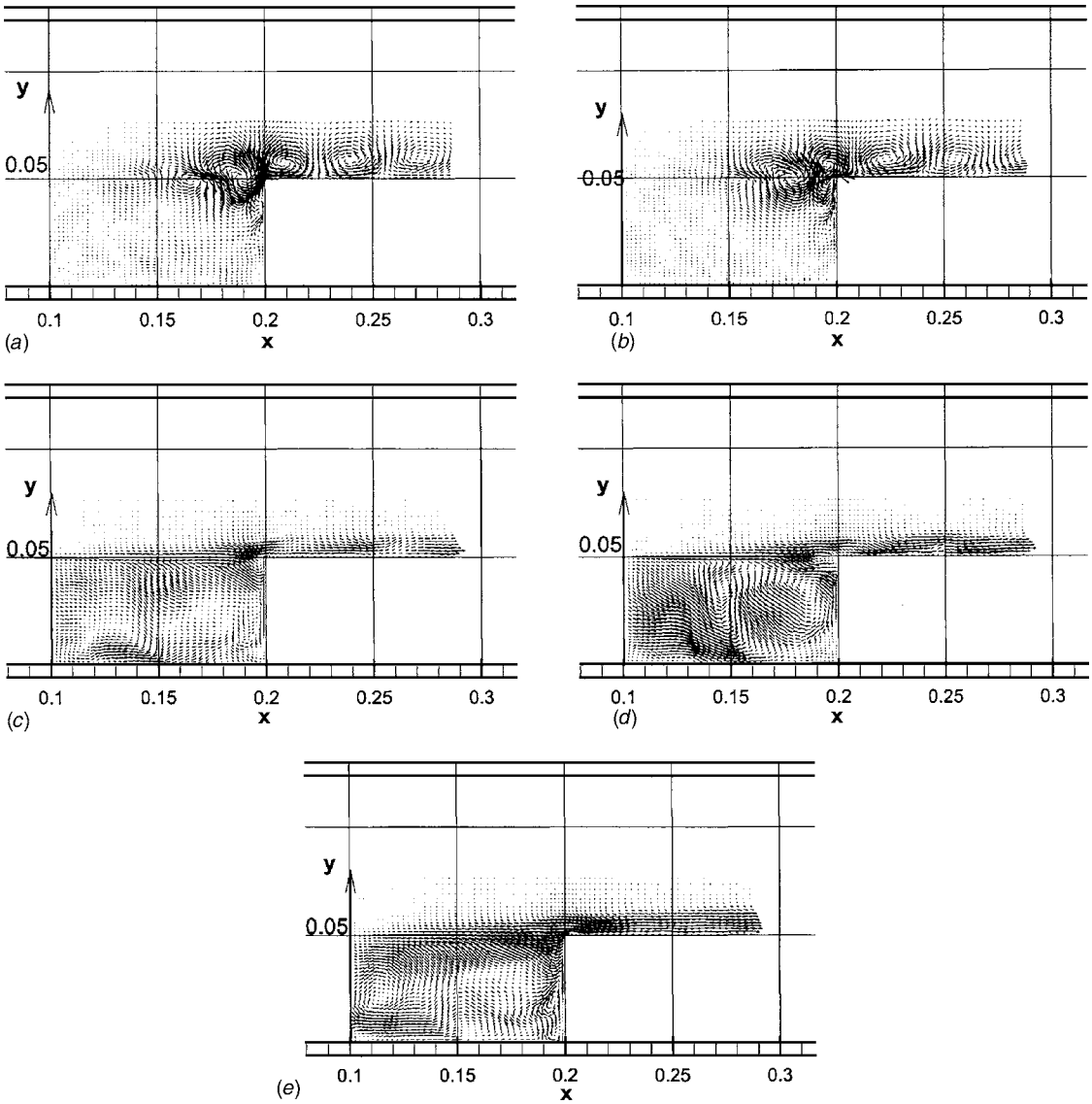

Fig. 4 Longitudinal section of the *n*th 3D POD structure at *z*=100 mm; (*a*) *n*=1; (*b*) *n*=2; (*c*) *n*=3; (*d*) *n*=4; (*e*) *n*=5

mated at time $(n+1)\delta t$ using an Adams-Bashforth's extrapolation from results at time $n\delta t$ and $(n-1)\delta t$. The pressure gradient is written explicitly.

The momentum equation for each velocity component is written as an Helmoltz's equation:

$$\left(I - \nu\frac{2\delta t}{3}\nabla^2\right)V^* = -\nabla P^n + S^{n,n-1}$$

V^* is the velocity field estimated at time $(n+1)\delta t$. P^n is the pressure field at time $n\delta t$. $S^{n,n-1}$ contains all terms defined at time $n\delta t$ and $(n-1)\delta t$ which represent time derivatives and advection fluxes.

Equations are integrated using an ADI (alternating direction implicit) method [20]. To ensure the zero divergence of velocity field, we use a projection method to determine the correction to apply to the velocity field obtained from Helmoltz's equations and to update the pressure field. One solves the Poisson's equation

$$\Delta\Phi = \rho\frac{\nabla V^*}{\Delta t}$$

for Φ where $\Phi = P^{n+1} - P^n$ and V^* is the nonzero divergence velocity field integrated from the Helmoltz's equation. At each time-step, the equation is solved with an iterative method (Gauss-Seidel with relaxation) coupled with a multigrid approach. When Φ is known, we update the pressure field P^{n+1} and correct the velocity field using:

$$V = V^* - \Delta t\frac{\nabla V^*}{\rho}$$

4.2 The Numerical Domain. The numerical domain is shown in Fig. 1. In all that follows, we will respectively denote x, y, z, the longitudinal, vertical, and transverse directions of the flow, and u, v, w, the corresponding velocity components. The cavity is 100 mm long and 50 mm high. The total height of the domain is 125 mm. These dimensions are the same as in the experiment of Lusseyran. The main difference between the numerical and the experimental configurations is that periodic conditions were used in the simulation, since it is assumed that end effects are unlikely to be felt in the mid-cavity plane, where experimental measurements are made. A spanwise periodic length of 200 mm was used in the simulation. The numerical laminar profile was obtained from a 2D channel flow simulation and found to match closely that of the experiment. The numerical upstream length was then

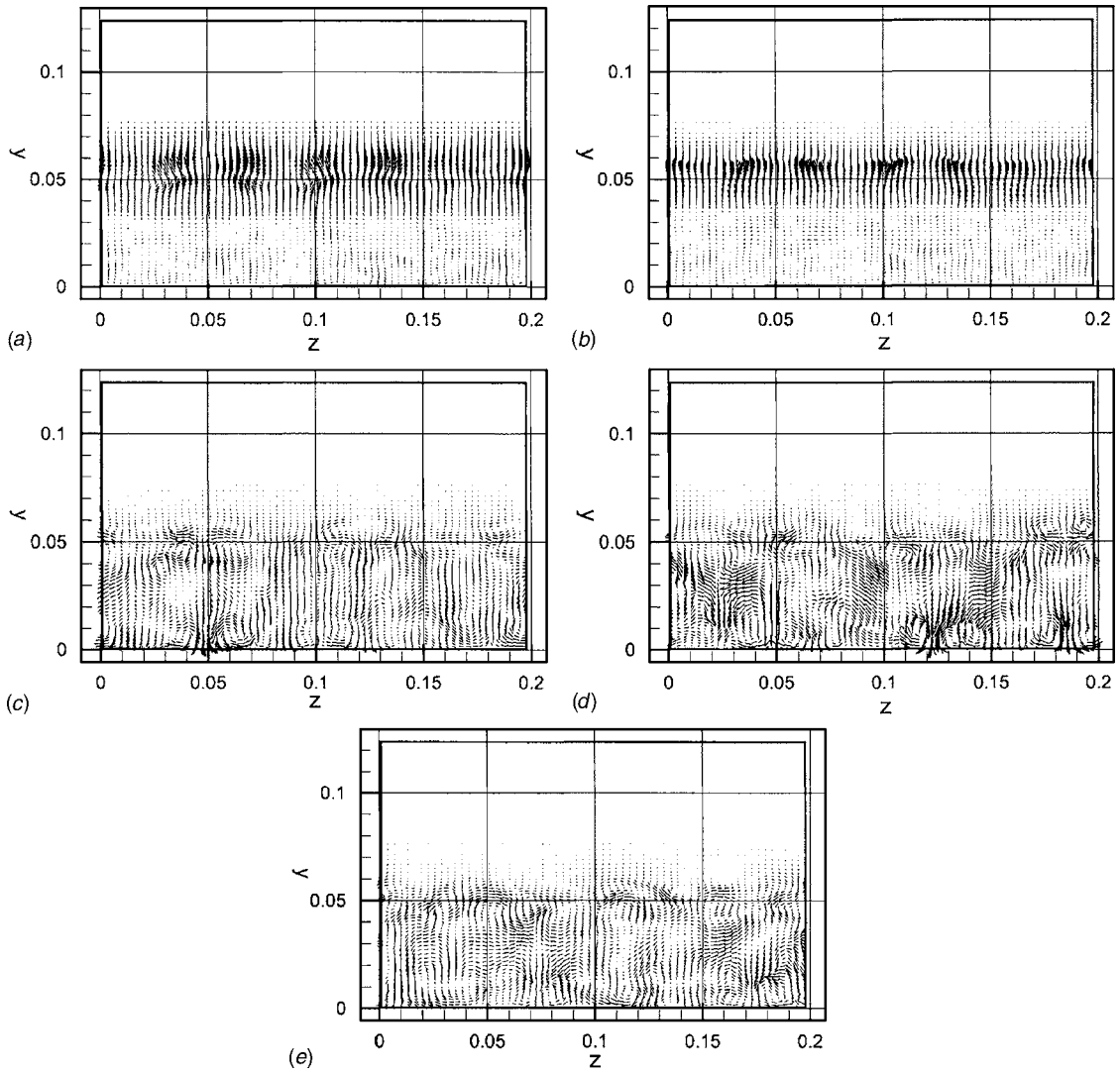

Fig. 5 Cross section of the *n*th 3D POD structure at $x=190$ mm; (*a*) $n=1$, (*b*) $n=2$, (*c*) $n=3$, (*d*) $n=4$, (*e*) $n=5$

110 mm from the inlet boundary condition so that the numerical cavity extended from $x=110$ mm up to $x=210$ mm The total length of the domain was 410 mm.

For the boundary conditions at the outlet,the longitudinal velocity component was computed using mass conservation over the domain. The gradient of the other two velocity components was set to zero. No-slip conditions were used at the walls. We used 256 cells in the longitudinal direction, and 128 in the spanwise and normal directions. The mesh was refined near the walls and over the cavity in order to obtain a fine resolution concerning the upstream laminar boundary layer, the stress layer and eddy structures generated by instabilities. To minimize numerical inaccuracy, the greatest size variation between successive cells was 5% (3% over the cavity) and the dimensional ratio for one cell was of the order of unity.

5 POD Analysis

The POD was applied to the three-dimensional domain spanned by the numerical simulation for different incoming flow velocities $U=0.9$ m/s, $U=1.2$ m/s, $U=2.0$ m/s. As we did not find significant changes in the other cases, we chose to focus on the case $U=1.2$ m/s. The corresponding Reynolds number based on the incoming flow speed and cavity height is 4000.

Figure 2(*a*) shows that the mean motion essentially consists of (i) a shear layer impinging on the downstream corner of the cavity and (ii) a vortex motion whose axis is parallel to the transverse direction z. A cross section of the mean flow at $x=120$ mm in the upstream part of the cavity—see Fig. 2(*b*)—shows the presence of a spanwise modulation of the flow over the cavity height. The motion can be characterized by a spanwise wavenumber of $k_z=3$—which corresponds to a periodic dimension of about 70 mm. This agrees with previous experimental observations [21] showing that the spanwise dimension of the structures is about the same as the streamwise dimension. This modulation of the flow persists throughout the cavity and the downstream boundary layer. We cannot determine at this point how this particular wavenumber was selected, and whether the selection process is an artefact of the numerical simulation (since there is no wall in the spanwise direction).

The POD modes were initially computed on the entire physical domain. We then found that if the domain was restricted to the cavity and the bottom half-channel above and downstream of it, the POD modes corresponding to that subdomain were identical to the restriction of the POD modes defined on the full domain. We therefore chose to limit our study to that subdomain. Over a 140 samples were used to extract the POD modes. As is now well known, the POD spectrum provides two different types of information: Its rate of decay is a measure of the complexity of the flow, and the presence of multiple eigenvalues can help us detect spatio-temporal symetries in the flow. As Fig. 3 shows, the POD

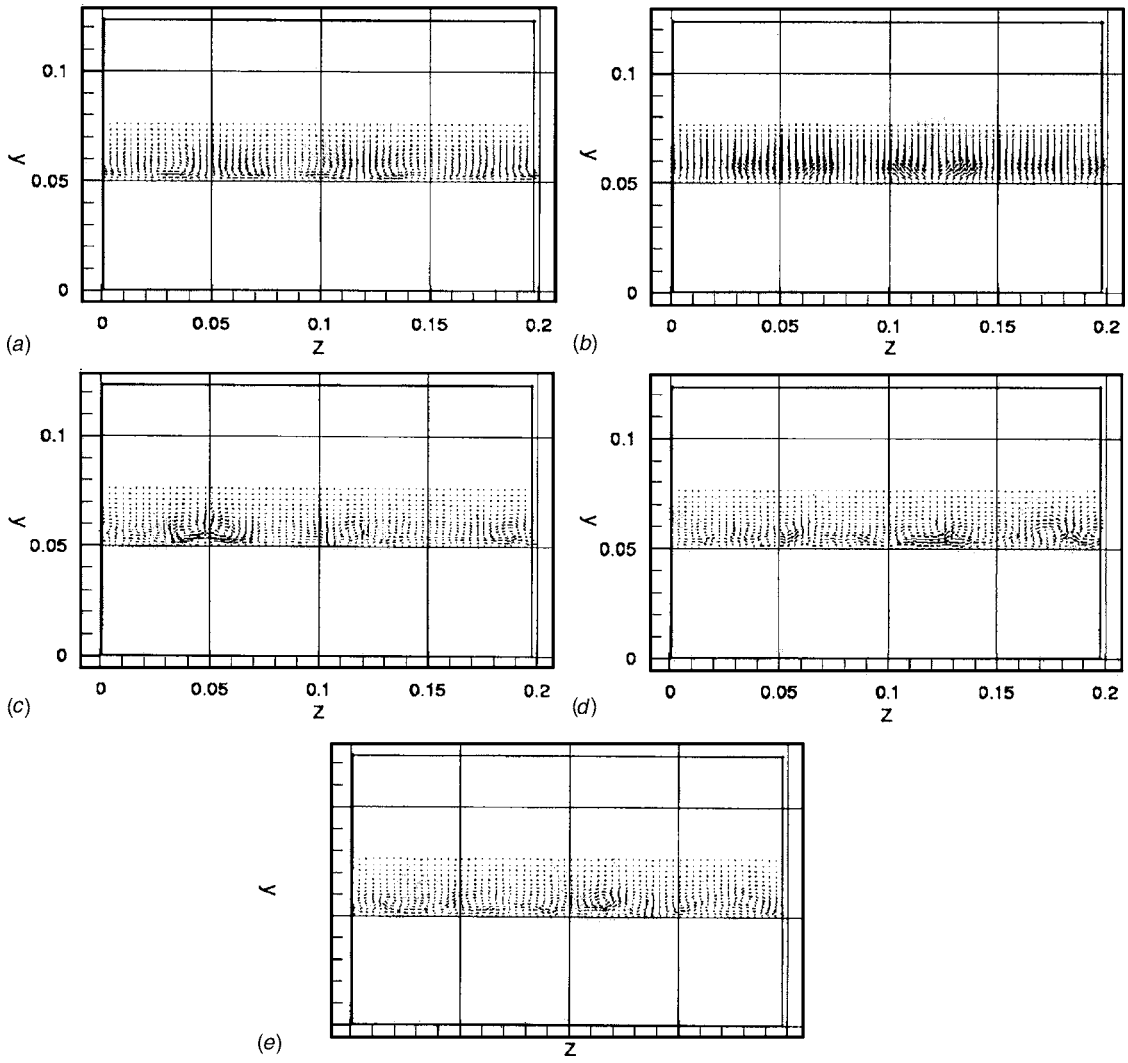

Fig. 6 Cross section of the *n*th 3D POD structure at $x=250$ mm; (*a*) n=1, (*b*) n=2, (*c*) n=3, (*d*) n=4, (*e*) n=5

spectrum is essentially the same for all three incoming speeds, but the flow becomes slightly more complex with the incoming flow speed as the tail of the spectrum flattens. Figures 4–7 show the characteristics of the first fivePOD eigenmodes.

The first two eigenvalues of the spectrum are almost equal, and appear to correspond to a spatially growing structure of the Kelvin-Helmholtz type that impinges on the donwstream corner of the cavity (Fig. 4). A cross view section in the $y-z$ plane (Figs. 5(*a*), 5(*b*), 6(*a*), and 6(*b*)) shows a spanwise modulation of the structures with a dominant wavenumber $kz=3$. This modulation appears to correspond to a secondary instability of the Kelvin-Helmholtz rolls. The amplitude of this instability remains moderate, even in the downstream boundary layer (see Fig. 7).

The next-order structures—see Figs. 4(*c*) to 4(*e*)—show fluctuating vortex motions within the cavity, associated with local accelerations and decelerations of the flow in the downstream boundary layer. This representation agrees with visual experimental observations made of a "pulsating vortex" inside the cavity. A cross section of the flows shows the presence of counter-rotating streamwise vortices, both in the cavity, where they appear roughly aligned with the mean vortex, and in the downstream boundary layer (see Figs. 5(*c*) to 5(*e*) and 6(*c*) to 6(*e*)). The streamwise vorticity pattern (see Figs. 7(*c*) and 7(*d*)) indicates that the position of these Taylor-Gortler-like vortices is related to the spanwise modulation of the mean flow and the shear layer modes, but the nature of the coupling between these different structures remains unclear.

The temporal evolution of the first five POD eigenmodes is reported in Fig. 8. A remarkable fact is that the modes appear to be naturally separated in the frequency domain. For $U=1.2$ m/s the shear layer modes are characterized by a single high frequency of 13.5 Hz—corresponding to the experimental mode 2 reported by Lusseyran et al. [22]. This frequency is in agreement with Rockwell's theoretical model for fluid-dynamic instabilities [23]. In contrast, the higher-order modes are dominated by very low frequencies—less than 1 Hz.

We then performed 2D POD analysis for both u and v components in a domain which consisted of the cavity and a strip of 3 cm high above it. We arbitrarily picked the plane $Z=100$ mm and checked that what was observed there was typical of other planes $Z=cst$. About over 100 snapshots were used. The numerical 2D eigenfunctions are shown in Fig. 9 for the plane $Z=100$ mm. The most striking feature of these modes is that they appear to be a mixture of the shear-layer and cavity modes which make up the 3D POD modes. This mixture of physical structures corresponds to a mixture of temporal frequencies, as can be seen in Fig. 10.

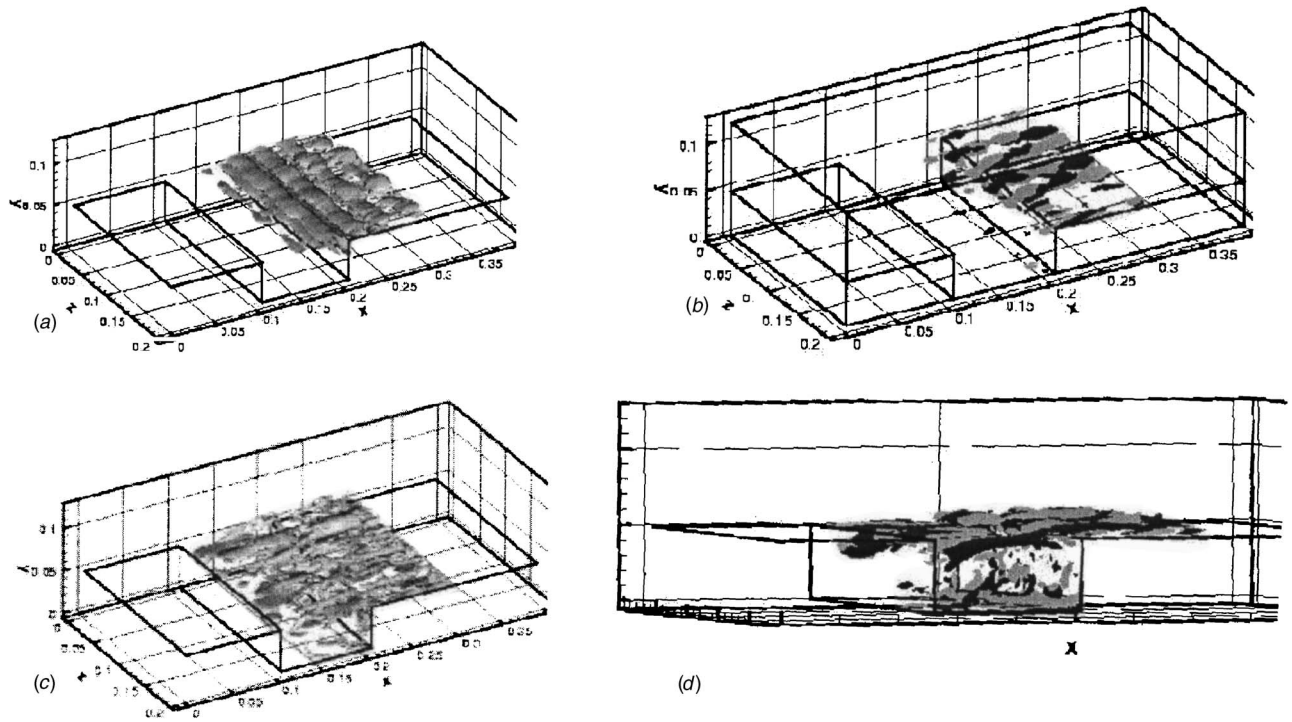

Fig. 7 (*a*) **Total vorticity in first eigenfunction** $\|\nabla\times\underline{\phi}^1\| = |\Omega| = 15\ \mathrm{s}^{-1}$. (*b*) **Streamwise vorticity in first eigenfunction** $\|(\nabla\times\underline{\phi}^1)_u\| = |\omega_x| = 8\ \mathrm{s}^{-1}$ **(dark colors mean positive values, and light colors negative ones).** (*c*) **Total vorticity in third eigenfunction** $\|\nabla\times\underline{\phi}^3\| = |\Omega| = 15\ \mathrm{s}^{-1}$. (*d*) **Streamwise vorticity in third eigenfunction** $\|(\nabla\times\underline{\phi}^3)_u\| = |\omega_x| = 8\ \mathrm{s}^{-1}$ **(dark colors mean positive values, and light colors negative ones).**

To find out if this effect was due to the exclusion of the channel flow in the analysis, we performed the POD on a 2D domain which included the channel lower-half as well (the 2D restriction of the 3D domain used in Sec. 5). The POD modes again turned out to be a mixture of cavity modes and shear-layer structures. This coupling therefore appears as a consequence of the loss of three-dimensionality in the flow.

6 3D reconstruction from 2D data

The reconstruction method described in Sec. 2 was tested on the numerical simulation of the flow over the cavity. The inlet velocity was $U=1.2$ m/s. The 3D reconstruction was performed on the domain used in Sec. 3—i.e., limited to the cavity and the half-channel immediately above and donwstream of it. Periodic boundary conditions were used in the transverse direction.

The matrix M is represented in Fig. 11. As could be expected, it is essentially diagonal dominant, particularly for the higher-order modes $n \geqslant 30$. To test the robustness of the procedure, we examined two different, relatively low values of N, which is the number of POD modes used to build the linear system and to reconstruct the full 3D flow. Figure 12 shows how much of the flow can be reconstructed for a given number of POD modes when the true and the estimated POD coefficients are used. One can see that with $N=80$ modes—which represent 88% of the energy—we were able to produce an estimate that could capture up to 72% of the flow energy—that is 28% less. With a system of 60 modes—less than twice the total number of POD modes— we found that up to 60% of the energy could be obtained with the estimation, while the true flow reconstruction represented 80% of the energy. Clearly, the performance of the procedure deteriorates as less modes are included, but relatively slowly, which indicates that the procedure has some robustness. Once again, this success probably capitalizes on the fact that neglected high-order, low-energy POD modes are essentially small-scale motions which are not very well correlated with the larger scales, so that their contribution to the

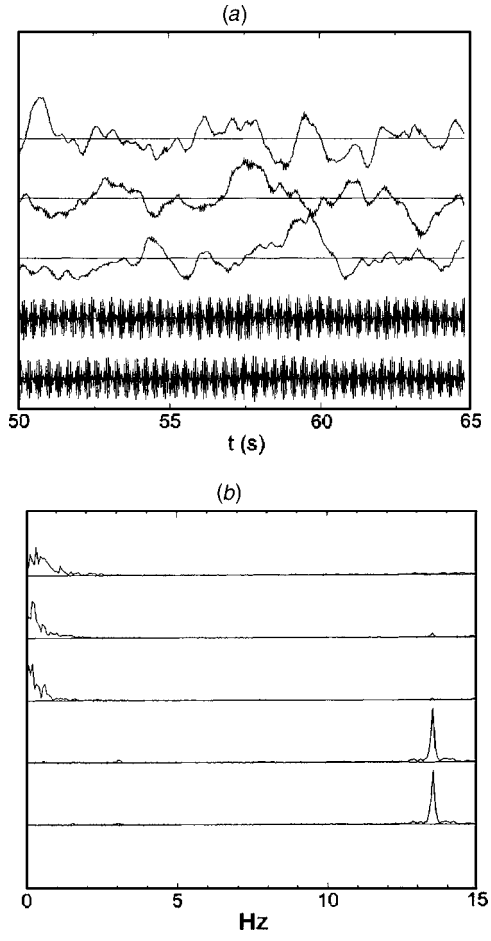

Fig. 8 POD coefficients $a^n(t)$ **for** $n=1$ **to 5 from bottom to top:** (*a*) $a^n(t)$, (*b*) **time spectra** $|\hat{a}^n(f)|$

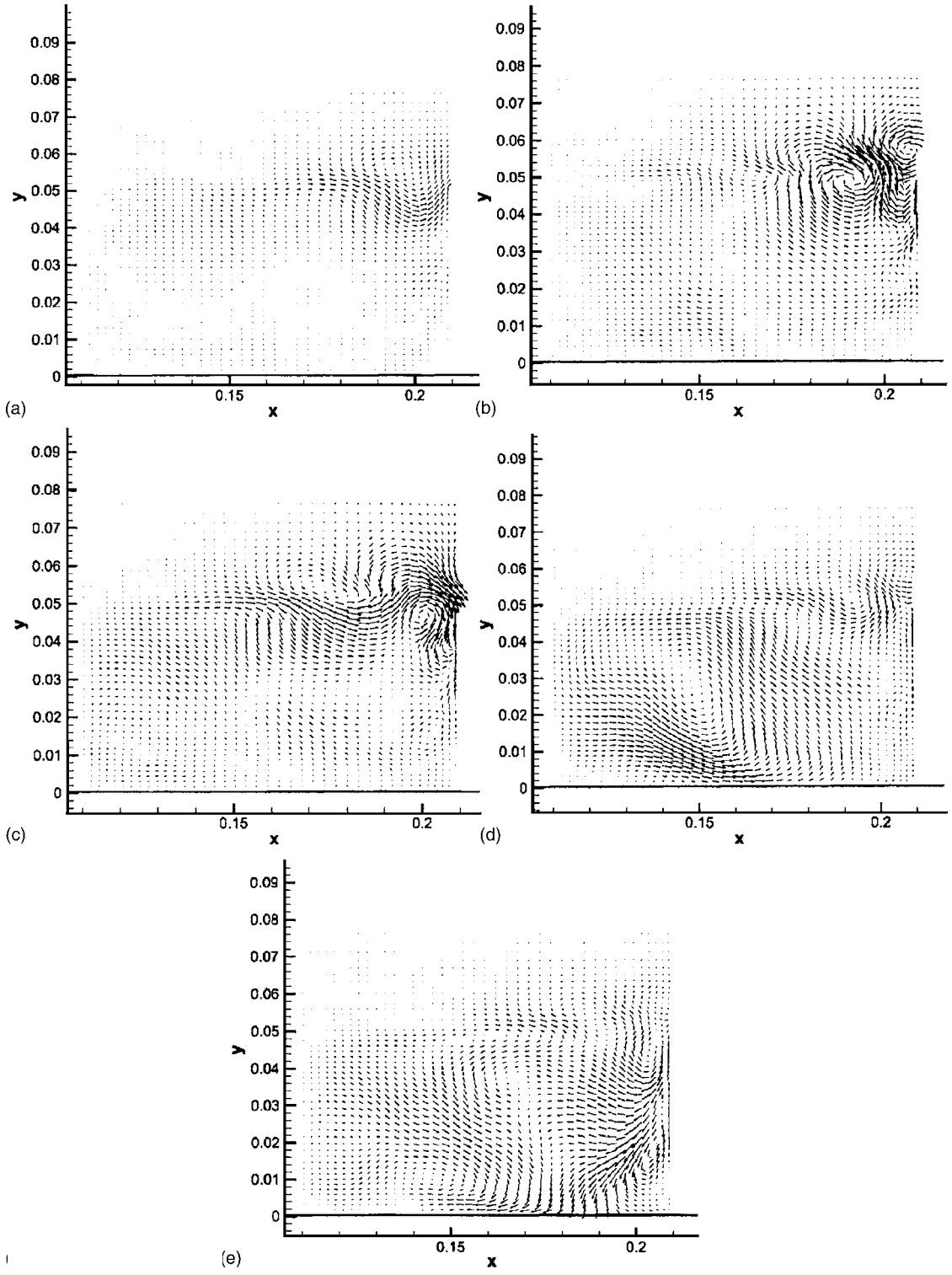

Fig. 9 Numerical *n*th 2D POD structure; (*a*) *n*=1, (*b*) *n*=2, (*c*) *n*=3, (*d*) *n*=4, (*e*) *n*=5

linear equations for the large scales is likely to be very small. This ensures that the poorly determined the small scales does not alter too much the estimation of the large scales.

The first few modes are indeed well estimated in both cases, as is evidenced in Fig. 13, which compares the real POD coefficients for the first five modes with the ones obtained from the reconstruction procedure. As expected, the error increases as the number of modes decreases. We note that no attempt was made to filter out the estimate, whereas it is clear that even a simple moving average would substantially improve the procedure. We have used here extensive, fine-scale 2D measurements. Since only flow integrals are used, it is likely that using a coarse grid of measurements would not affect the results too much.

One limiting factor of the procedure seems to be that three-dimensional data is always required to construct the POD eigenfunctions. For higher Reynolds numbers, and/or more complex flow geometries, the limits of numerical simulation will be reached. It is however important to realize that POD eigenfunc-

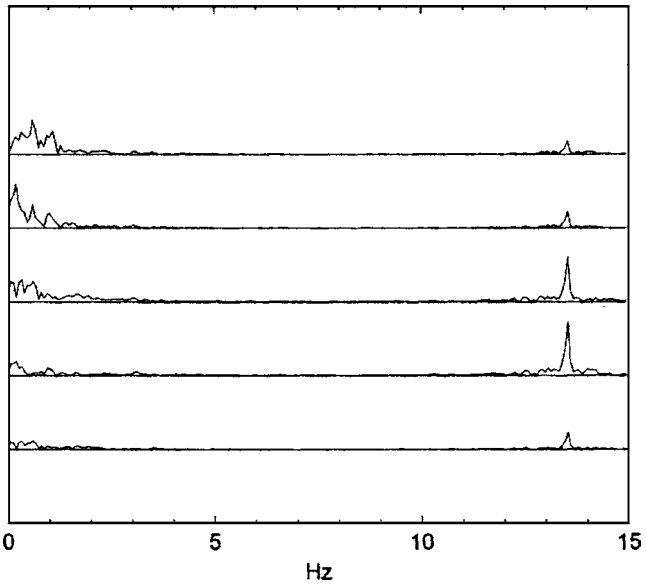

Fig. 10 2D POD coefficients time spectra—the sampling rate is 30 Hz: $|\hat{a}^n(f)|$ with n=1 to 5 from bottom to top

tions are not only an efficient way of storing 3D velocity data, but that they also contain structural information about the flow, an information which can be inferred and extrapolated in some cases by theoretical means. Moreover, if we try to represent the flow of interest by a simpler, surrogate simulation, one way to evaluate the adequacy of the representation is to perform a POD analysis on the subset of space where information is available for both flows. By comparing the restricted eigenfunctions there, one could infer modifications for the full-space eigenfunctions. It would then be interesting to compare the real flow with its reconstruction based on the surrogate. We leave this to be investigated in future study.

7 Conclusion

In this paper we have described a method to reconstruct the flow using partial measurements. This method was tested on the flow past an open cavity. POD analysis showed that the 3D POD modes of that flow are able to separate physical motions occuring

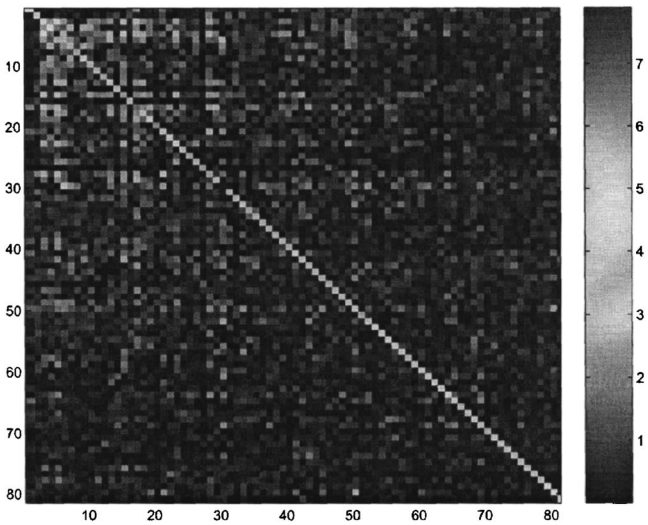

Fig. 11 Matrix coefficients (in absolute value). Lighter colors correspond to higher values.

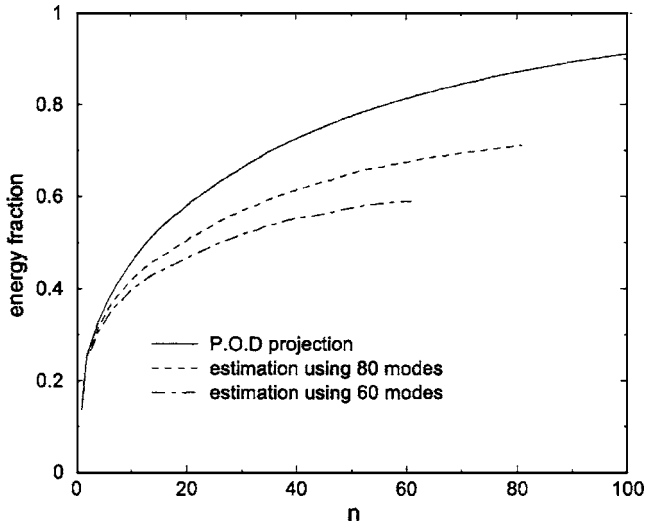

Fig. 12 Amount of flow energy captured by the exact and the estimated reconstructions; solid line: $|\Sigma_n a^n \underline{\phi}^n(\underline{x})|^2 / \int |\underline{u}(\underline{x})|^2 d\underline{x}$ where a^n is the true POD coefficient; dashed line $|\Sigma_n a^n_{est} \underline{\phi}^n(\underline{x})|^2 / \int |\underline{u}(\underline{x})|^2 d\underline{x}$ where a^n_{est} was estimated from a linear system with 80 modes; dot-dashed line: $|\Sigma_n a^n_{est} \underline{\phi}^n(\underline{x})|^2 / \int |\underline{u}(\underline{x})|^2 d\underline{x}$ where a^n_{est} was estimated from a linear system with 60 modes

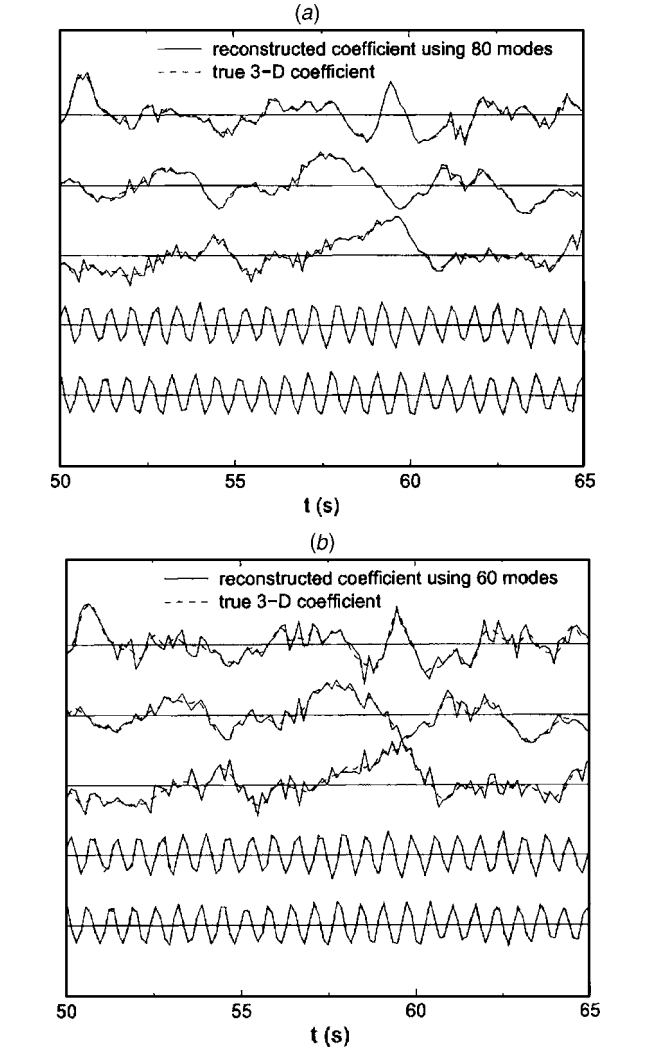

Fig. 13 Extract and estimated 3D POD coefficients $a^n(t)$, with n=1 to 5 from bottom to top: (*a*) using 80 modes in the estimation, (*b*) using 60 modes in the estimation

at distinct time scales, a property that was not shared by 2D POD modes. We built a 3D approximation for the flow using a subset of the 3D POD modes and 2D, two-component velocity measurements. Results suggest that a reliable flow estimator can be obtained by combining flow spatial (POD) second-order statistics with localized partial measurements.

References

[1] Moin, P., and Mahesh, K., 1998, "Direct Numerical Simulation: A Tool in Turbulence Research T.R. Bewley and D.S. Henningson," Annu. Rev. Fluid Mech., **30**, pp. 539–578.

[2] Bonnet, J. P., and Delville, J., 2001, "Review of Coherent Structures in Turbulent Free Shear Flows and Their Possible Influence on Computational Methods," Appl. Sci. Res., **66**(4), pp. 333–353.

[3] Bonnet, J. P., and Delville, J., 2001, "Review of Coherent Structures in Turbulent Free Shear Flows and Their Possible Influence on Computational Methods," Flow, Turbul. Combust., **66**, pp. 333–353.

[4] Lumley, J. L., 1967, *The Structure of Inhomogeneous Turbulent Flows in Atmospheric Turbulence and Wave Propagation*, A. M. Yaglom and V. I. Tatarski, eds., Nauka, Moscow, pp. 166–178.

[5] Murray, N., and Ukeiley, L., 2002, "Estimating the Shear Layer Velocity Field Above an Open Cavity From Surface Pressure Measurements," AIAA Paper No. 2002–2866.

[6] Picard, C., and Delville, J., 2000, "Pressure Velocity Coupling in a Subsonic Round Jet," Int. J. Heat Fluid Flow, **21**, pp. 359–364.

[7] Boree, J., 2003, "Extended Proper Orthogonal Decomposition: A Tool to Analyze Correlated Events in Turbulent Flows," Exp. Fluids, **35**(2), pp. 188–192.

[8] Taylor, J., and Glauser, M., 2002, "Toward Practical Flow Sensing and Control Via POD and lse-based low-dimensional tools," *ASME 2002 Fluids Engineering Division Summer Meeting, Montreal, Quebec, 14–18 July.*

[9] Maurel, S., Boree, J., and Lumley, J. L., 2001, "Extended Proper Orthogonal Decomposition: Application to Jet/Vortex Interaction," Flow, Turbul. Combust., **67**, pp. 125–136.

[10] Rempfer, D., 2000, "On low-dimensional Galerkin Models for Fluid Flow," Theor. Comput. Fluid Dyn., **14**, pp. 75–88.

[11] Lusseyran, F., Faure, T., Eschenbrenner, C., and Fraigneau, Y., 2004, "Shear Layer Instability and Frequency Modes Inside an Open Cavity," *Proceedings ICTAM 2004*, Varsaw, Poland, 15–21 Aug.

[12] Williams, D. R., Rowley, C. W., Fabris, D., Colonius, T., and Murray, R. M., 2002, "Model-Based Control of Cavity Oscillations, Part I: Experiments," in *Proceedings 40th AIAA Aerospace Meeting*, AIAA.

[13] Podvin, B., 2001, "Low-Order P.O.D-Based Models for the Flow in a Differentially Heated Cavity," Phys. Fluids, **13**(11), pp. 3204–3214.

[14] Lumley, J. L., 1967, "The Structure of Inhomogeneous Turbulent Flows," in *Atmospheric Turbulence and Radio Wave Propagation*, A. M Iaglom and V. I. Tatarski, eds., Nauka, Moscow, pp. 221–227.

[15] Berkooz, G., Holmes, P., and Lumley, J. L., 1993, "The Proper Orthogonal Decomposition in the Analysis of Turbulent Flows," Annu. Rev. Fluid Mech., **25**, pp. 539–575.

[16] Holmes, P., Lumley, J. L., and Berkooz, G., 1996, *Turbulence, Coherent Structures, Dynamical Systems and Symmetry*, Cambridge University Press, Cambridge, MA.

[17] Sirovich, L., 1987, "Turbulence and the Dynamics of Coherent Structures Part I: Coherent Structures," Q. Appl. Math., **45**(3), pp. 561–571.

[18] Gadouin, E., Le Quéré, P., and Daube, O., 2001, "A General Methodology for Investigating Flow Instability in Complex Geometries: Application to Natural Convection in Enclosures," Int. J. Numer. Methods Fluids, **37**(2), pp. 175–208.

[19] Leonard, B. P., 1979, "A Stable and Accurate Convective Modelling Procedure Based on Quadratic Upstream interpolation," Comput. Methods Appl. Mech. Eng., **19**, pp. 59–98.

[20] Hirsch, C., 1987, *Numerical Computation of Internal and External Flows*, Wiley, New York.

[21] Rockwell, D., and Naudascher, E., 1979, "Self-Sustained Oscillations of Impinging Free Shear Layers," Annu. Rev. Fluid Mech., **11**, pp. 67–94.

[22] Lusseyran, F., Rambert, A., Gougat, P., Fraigneau, Y., Elcafsi, A., and Quénot, G., 2002, "Relationship Between Fourier-Modes and Spatial Structures in a Cavity—Boundary Layer Interaction at Moderate Reynolds Numbers," in *Proceedings 11th Int. Symp. on Applications of Laser Techniques to Fluid Mechanics*, Lisboa.

[23] Rockwell, D., 1977, "Prediction of Oscillation Frequencies for Unstable Flow Past Cavities," ASME J. Fluids Eng., **99**, pp. 294–300.

Numerical Simulations and Experimental Study of Liquid Metal Flow Around Sand Core

Sayavur I. Bakhtiyarov
Associate Professor
New Mexico Institute of Mining and Technology,
Mechanical Engineering Department,
122 Weir Hall,
801 Leroy Place,
Socorro, NM 87801-4796

This paper presents the results of experimental and numerical studies of the hot distortion phenomenon in the phenolic urethane cold box systems used in metal casting. Dual Pushrod Dilatometry has been used to measure a thermal expansion/contraction of phenolic urethane cold box sand core specimens at temperatures ranging from 20°C *to* 600°C. *High temperature tensile tests showed that the tensile strength of the phenolic urethane cold box sand cores is significantly affected by the bench life, temperature and binders level. High temperature hot distortion furnace tests on cylindrical cores showed that some coatings increase the temperature limit when distortion starts, but application of coating cannot prevent distortion. The hot distortion test during metal casting showed that regardless of the application of coating, the type of coating, and anti-veining additives, all cores with density greater than the density of the molten metal (magnesium alloy) were significantly distorted. Numerical simulations of the liquid metal flow around the cylindrical sand core and analysis of dynamic forces acting on the core during the fill process showed that a buoyancy force is the major contributor to the hot distortion. It is concluded that the one of the solutions in preventing the hot distortion of sand cores is optimizing their weight, which will balance the buoyancy force and will bring the resultant force to the minimum. The hot distortion test castings using optimized sand cores with density almost equal to the density of the molten magnesium proved our predictions, and hot distortion has been prevented.* [DOI: 10.1115/1.2175160]

Introduction

The phenolic urethane (PU) cold box process offered many advantages since being introduced to the metalcasting industry in 1968. However, the lower hot strength of this molds, and consequently, the highly pronounced hot distortion phenomenon has been a major disadvantage of the process. The low hot strength can result in an increased frequency of casting defects. The hot distortion is considered to be a consequence of thermal expansion and resin breakdown at high temperatures. The distortion characteristics become more important when castings require thin cores.

In 1966 the British Cast Iron Research Association (BCIRA) developed a hot distortion test (HDT) apparatus to determine the high temperature characteristics of bonding agents and sand mixtures [1,2]. It is considered one of the major tests for evaluation of various sand/resin systems. The hot distortion test was based on the observation that a thin strip of rigidly bonded sand when heated on one face will curl away from the source of heat due to differential thermal expansion between the hot and opposite cold face. It is assumed that the amount of curl is proportional to the coefficient of thermal expansion of the bonded sand. In other words, the distortion curve rise characterizes the thermal rigidity, and the length of the time axis until the core breaks roughly describes the thermal stability [3]. Later, the original apparatus was re-designed in order to eliminate a number of shortcomings [4]. In the new equipment a gas burner was used to heat the test specimen, which has cantilever loading.

Laitar and Johnson [5] described a new phenolic urethane cold box system, which demonstrated improved hot strength over conventional systems. The hot distortion properties were estimated by analyzing both dilatometer collapsibility and BCIRA hot distortion curves. Investigation of the effect of changes in the part 1/part 2 ratio showed that the highest hot strength can be obtained in the 55/45 to 60/40 range.

Fountaine and Horton [6] compared different cold box resin systems (amine cured phenolic urethane, sulfur dioxide cured FRC acrylic epoxy, methylformate ester-cured phenolic) under laboratory test casting conditions with BCIRA results for the same systems. The test casting was designed to reproduce hot distortion during pouring and solidification. The results of this study showed that phenolic urethane resins performed better in respect to core distortion than the other systems. Comparison of distortion characteristics of the various coremaking processes is presented in another work of Fountaine and Horton [7]. The general dimensional properties for phenolic hot box and shell, as well as the cold box coremaking binders under laboratory conditions were studied. The coldbox systems were the amine-cured phenolic urethane and SO_2-cured FRC acrylic-epoxy. The effect of the red iron oxide addition was investigated. It is mentioned that the distortion is affected by many factors, such as gate placement, cope height, metal temperature, pouring time, and gating ratios.

Summarizing the prior works on hot distortion, it is necessary to mention that the existing methods are limited in selection to a particular binders system to correspond the application regarding the core distortion phenomenon. The hot distortion curves well represent resin characteristics, but not necessarily under casting conditions. Almost all efforts in prior researches were directed toward optimization of resin system characteristics via manipulating the coremaking process, amount of binders, part 1/part 2 ratio, using additives, applying coating, etc. Test castings were based on a "best guess" approach. Fluid dynamics aspects of the liquid metal flow around the cores were ignored. However, without fundamental understanding of thermo-kinetics and fluid dynamics of liquid metal—sand core interactions, it is difficult to make decisions in preventing defects such as hot distortion, core breakage, etc.

Recently, Bakhtiyarov et al. [8,9] presented the results of experimental and numerical studies of hot distortion phenomenon in

Contributed by the Fluids Engineering Division of ASME for publication in the JOURNAL OF FLUIDS ENGINEERING. Manuscript received February 11, 2005; final manuscript received October 25, 2005. Assoc. Editor: Dennis Siginer. Paper presented at the 2004 ASME Heat Transfer/Fluids Engineering Summer Conference (HTFED2004), July 11, 2004–July 15, 2004, Charlotte, North Carolina, USA.

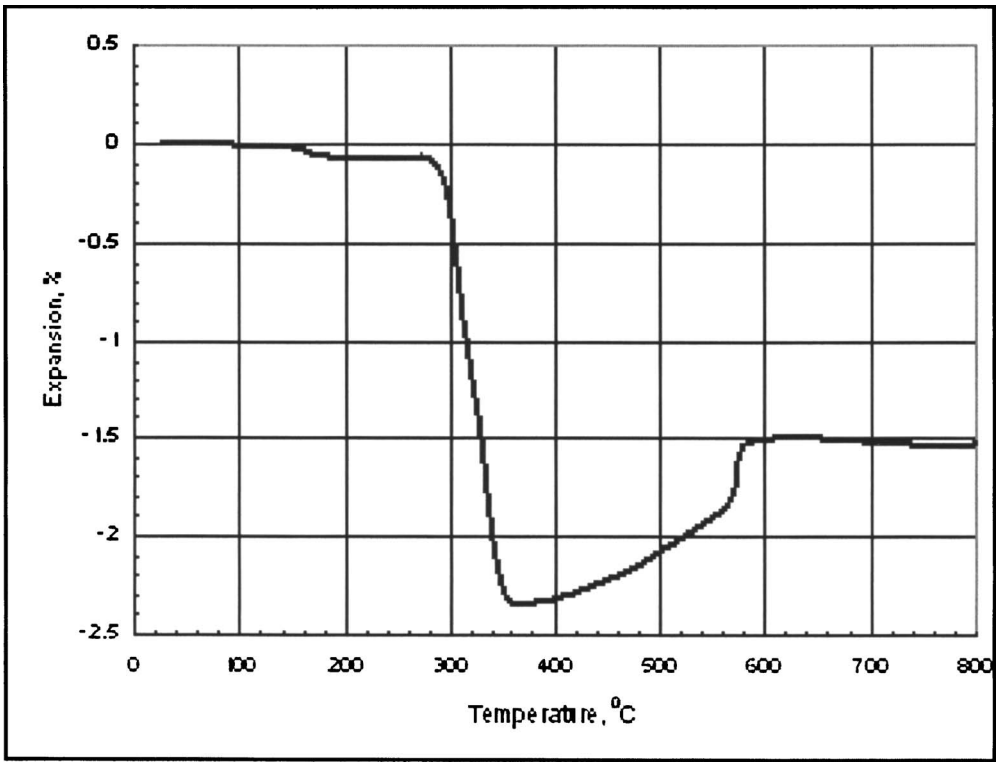

Fig. 1 Variation of thermal expansion/contraction of sand core specimens with temperature

aluminum casting. The high temperature tensile tests showed that the tensile strength of the phenolic urethane cold box silica sand cores is significantly affected by the bench life, temperature and binders level. High temperature hot distortion furnace tests on cylindrical cores showed that some aluminum coatings increase the temperature limit when distortion starts, but cannot prevent it. The hot distortion test aluminum castings showed that regardless of the application of coating, the type of coating, and anti-veining additives, all cores (silica sand) with density less than the density of the molten metal (aluminum alloy) were significantly distorted. Numerical simulations of the liquid metal flow around the cylindrical sand core and analysis of dynamic forces acting on the core during fill process showed that a buoyancy force is the major contributor to the hot distortion. It is concluded that the one of the solutions in preventing the hot distortion of sand cores is increasing their weigh, which will balance the buoyancy force and will bring the resultant force to the minimum. The hot distortion test castings using zircon sand cores (both coated and noncoated) with density almost equal to the density of the molten aluminum proved our predictions, and hot distortion has been prevented.

In this paper we present the results of systematic experimental and numerical studies of hot distortion in phenolic urethane cold box systems during magnesium casting. CFD simulations of the nature and significance of the forces exerted on the core during mold filling process allowed to develop the measures for preventing the hot distortion in casting.

Thermophysical and Mechanical Properties of Test Core Material

In this work we studied a hot distortion phenomenon in the phenolic urethane cold box system. The resin system evaluated was an amine cured two-part phenolic urethane: A phenolic resin (ISOCURE® Part I LF-305) and polymeric isocyanate (ISOCURE® Part II 52-904 GR). The sand cores were made out of silica sand and zircon sand. Recently, synthetic iron oxides (SIO) have been used extensively for reducing nitrogen and veining defects. Therefore, in some cores we used SIO (Spherox®) as an additive (1%) to the silica sand. A scanning electron microscope has been used for chemical analysis of sand particulate. EDS data analysis was conducted using ISIS LINK® Software (Oxford Instruments, Inc.). The results of the analysis showed that the silica sand contains a significant amount (1.23%) of aluminum oxide. The amount of other components is insignificant, except ferric oxide (0.3%) and calcium oxide (0.1%).

To determine the thermal expansion/contraction of sand cores, we produced cylindrical core specimens of 25 mm long and 10 mm diameter. The sands were bonded with 1.5% phenolic resin at a 55/45 part 1 to part 2 ratio using a commercial core shooter. Dual Pushrod Dilatometry has been used to measure a thermal expansion/contraction of sand core specimens in the temperature range from 25°C to 800°C. The heating rate was 20°C per minute.

The results of thermal expansion/contraction analyses for the silica sand core are presented in Fig. 1. As seen from these data, at temperatures up to 300°C the test sand cores don't show any significant changes in volume. Although up to 0.1% contraction can be observed at temperatures up to 300°C. At temperatures above 300°C a dramatic contraction for sand core samples was observed. The test sand cores contract about 1.75%. At temperature 360°C the contraction process ends and cores begin expanding. Expansion process stops at temperature 580°C, and no further changes in density were observed with temperature increasing up to 800°C. The observed phenomena have the following explanation. At temperatures up to 300°C, due to combined effect of expansion and contraction of sand and resin binder, there are no significant changes in specimen's volume. At temperatures 300°C and above, the resin binders start melting and then burning off. Therefore, the core specimens will contract. When the resin binders completely burned off (T=360°C), the contraction process stops, then sand grains, free of resin binders start expanding. This process continues up to 580°C, and then the expansion process stops due to a possible displacive phase transition in silica, and a

slight contraction is observed above 580°C. The visual observations of the sand cores after the tests confirmed this explanation. As expected, after the tests the specimens lost the mass about 1.5%, which was the mass of resin binders in the sand cores.

Next, we determined the effect of Part 1 to Part 2 ratio, bench life (BL), and temperature on tensile strength of the test sand cores with 1.5% resin binders. Sand core test specimens used to evaluate test material were prepared of a size and shape defined by standard test methods. In this task we prepared standard "dog-bone" sand core specimens in order to conduct tension testing. The core shooter has been used to prepare dog-bones of 13 mm thick. The following process parameters were targeted: 350 kPa blow pressure, 1.0 s blow time, 2.0 s gassing time, 70 kPa gassing pressure, 105 kPa purge pressure, 6.0 s purge time. Tension tests were conducted using computer controlled testing machine equipped with a heating furnace. This machine allowed conducting tension tests at temperatures up to 2000°C. Special grips were used to hold the dog-bone core samples during the tests.

The test results showed that the tensile strength of sand cores made of silica sand is significantly affected by bench life. After 1 h of the bench life the tensile strength decreases ~15%. Test temperature more dramatically affects the tensile strength. At 204°C the tensile strength decreases ~20%, at 247°C it decreases ~50%. Part 1 to Part 2 ratio also affects the tensile strength. Decreasing the percentage of Part 1 from 55% to 50% results in ~10% decrease of tensile strength.

High Temperature Hot Distortion Tests of Sand Core Specimens

High temperature hot distortion tests were conducted using 300 mm long and 19 mm diameter half-cylindrical cores. These specimens were prepared using a commercial core shooter. Both coated and noncoated silica sand, zircon sand, and silica sand +1% Spherox® cores were tested in these studies. Tests were conducted for cores with 1.5% (55/45) binders level. Two furnaces have been used for high temperature hot distortion tests, which allowed conducting the tests at temperatures up to 500°C. At temperature ~300°C, all core specimens were distorted. High temperature hot distortion furnace tests on cylindrical cores showed that the coating increases the temperature limit when distortion starts, but application of coating cannot prevent distortion.

Numerical Simulation of Molten Metal Flow around Semicircular Cylinder

As mentioned above, most efforts in prior research works were directed toward optimization of resin system characteristics via manipulating the coremaking process type, the binder level, using different additives, coating application, etc. However, the fluid dynamic aspects of the molten metal flow around the cores were completely ignored. One would assume that without fundamental understanding of thermo-kinetics and fluid dynamics of liquid metal—sand core interaction, it is impossible to make right decisions in preventing defects such as hot distortion, core breakage, etc.

Before the liquid metal reaches the sand cores, only gravitational forces act on each cylindrical core. When the liquid front reaches the bottom of the cores, the buoyancy forces act in the direction opposite to the forces of gravity. The buoyancy forces increase as more of the cylinder becomes submerged in the liquid, and reach their maximum when liquid surface reaches the top surface of the cylinder. The further upward propagation of the liquid level generates the liquid head pressure on the core cylinders. It is important to mention, that the forces mentioned above are the resultants of the rather complex distribution of forces over the cross section of the core cylinder at a built-in or fixed support. A built-in or fixed support is capable of supporting an axial force a transverse force (shear force), and a couple (bending moment) to prevent rotation. Obviously, in this process the fluid flow effect must be taken into the consideration. Flow around bluff bodies has been a topic of practical importance for many decades. Cylinders with circular and the square cross-sections are the most adopted geometries for fundamental understanding of the flow dynamics. The present part of this work is aimed at the numerical simulation of the viscous fluid (molten metal) flow past a semicircle cylinder (sand core) for low Reynolds numbers (Fig. 2). The simulation is intended to clarify the significance of the external and viscous forces exerted on the cylinder. The steady state, two-dimensional Navier-Stokes equations along with the incompressibility constraint have been numerically solved in the present study. The partial differential equations for continuity and momentum may be expressed as:

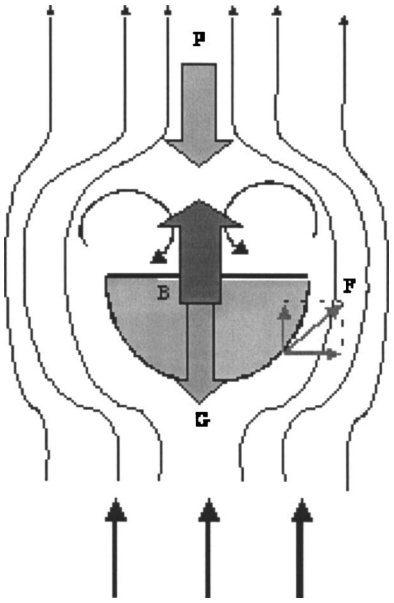

Fig. 2 CFD model of molten metal flow past a semicircle cylinder

$$(u \cdot \nabla)u = \frac{1}{\rho} \nabla p + F_{\text{ext}} + F_{\text{vis}}, \tag{1}$$

$$\nabla \cdot u = 0, \tag{2}$$

where ρ denoted the constant fluid density, p indicated the scalar pressure field, $\boldsymbol{F}_{\text{ext}}$ are the external forces acting on the fluid, such gravity, $\boldsymbol{F}_{\text{vis}}$ are the shear forces between fluid particles. Equation (2) expresses the law of conservation of mass. For every fixed volume inside the flow domain, the influx of fluid must equal the efflux of fluid in each infinitesimal time step. For all the solid surfaces in the obstacle, the no-slip boundary condition has been used: $\boldsymbol{u}=0$. Due to the low Reynolds numbers, the wake (separation flow) formation behind the cylinder was neglected in present work (Fig. 2). The data obtained on thermal expansion were incorporated into the CFD simulations. The mold filling patterns obtained by using FLOW-3D software are shown in Fig. 3. The figure represents variation of the velocity vector and pressure inside the mold cavity with time. According to these simulations, it takes 5 s to fill the mold, which is in good agreement with the experimental data.

The numerical simulations of the hydrostatic equilibrium conditions of the sand core cylinder in the liquid metal, and the flow dynamics around the cylinder revealed that for the materials considered in the real castings the buoyancy and gravity forces are the major contributors to the core distortion. Figure 4 represents the variation of the resultant force applied on the zircon sand core with the liquid height in the mold. As seen from this figure, until the liquid metal front touches the bottom of the core, only gravity

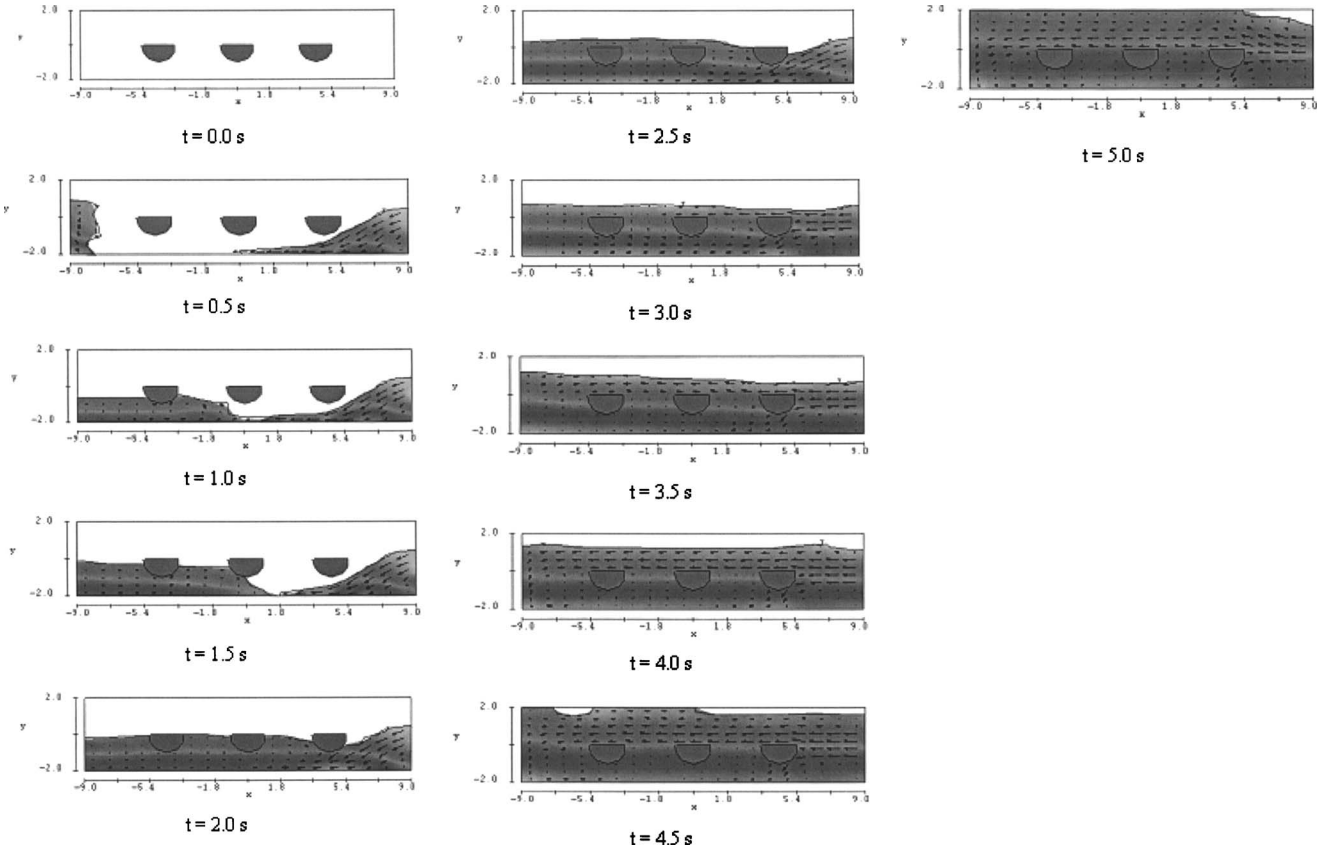

Fig. 3 Mold filling patterns simulated by FLOW-3D software

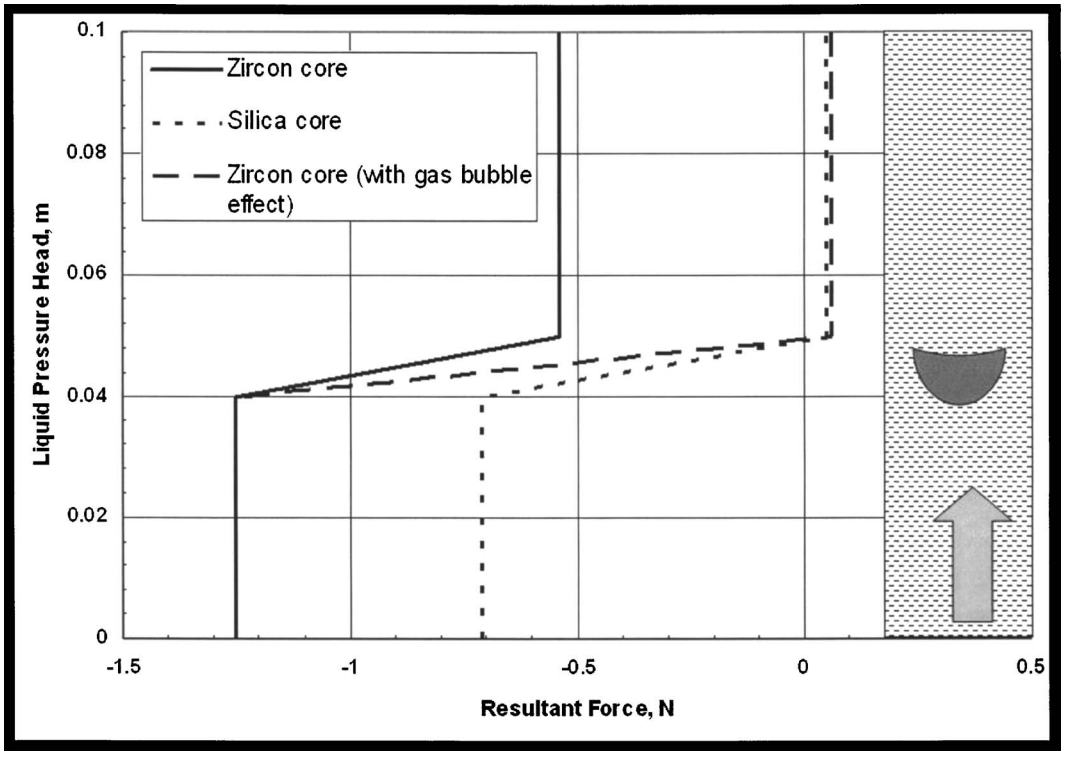

Fig. 4 Variation of the resultant force exerted on the core with liquid metal head

Table 1 Density characteristics of core specimens

Core specimen	Mass, g	ρ_s, g/cm^3	ρ_s/ρ_{Mg}
Zircon	126.8	2.930	1.831
Silica+1%SIO	73.1	1.689	1.056
Silica	66.5	1.537	0.961

force acts on the sand core cylinder (−1.25 N). As soon as the liquid magnesium submerges the cylindrical core, the buoyancy force starts acting on the cylinder in the direction opposite to the gravity force. When the core cylinder is completely submerged into the molten metal, the buoyancy force achieves its maximum value (0.71 N), and hence the resultant force (−0.54 N) is acting downward. The high temperature tensile strength and hot distortion furnace tests demonstrated that at temperatures even far below the melting point of the magnesium alloys, the phenolic urethane system sand cores are loosing their rigidity and exhibit same plasticity. Therefore, at molten metal temperatures under the applied resultant force, one would expect that the fixed-supported cylindrical heavy core would distort downward. In contrast to the zircon core, the silica sand core has almost the same density as the molten magnesium alloy. Hence, the resultant force at the end of the mold filling process is equal to zero. In fact, that is exactly what we observed in our hot distortion test castings with zircon and silica sand cores described in the next section. From these simulations and the experimental results, we concluded that the one of the solutions in preventing the hot distortion of the sand cores is the optimizing their weigh, which will balance the buoyancy force, and will bring the resultant force to the minimum (or to zero). Therefore, the next hot distortion test castings were performed using sand cores with different densities.

Hot Distortion Test Castings

The hot distortion test castings were done to study the distortion phenomenon during pouring and solidification of the molten magnesium alloy. The test specimens for hot distortion test castings were produced with parameters identical to those of the oven heating tests (silica sand, zircon sand, and silica sand +1% SIO additive). The density characteristics of sand core specimens are presented in Table 1. The V-process technique has been used to cast magnesium AZ91E alloy in order to estimate the hot distortion and the degradation of sand core specimens. The casting procedure was identical to that described previously [10,11]. The test cores were placed on the drag side of the mold as shown in Fig. 5. About 50 mm space was allowed on the top and bottom of the core to be surrounded by cast metal. To eliminate metal flow over the cores during pouring, we used the side gating system. Two ingates (19 mm × 19 mm) provided the molten alloy into the mold. An open riser has been used in order to prevent any shrinkage and air entrapment inside the casting. The temperature variations during the pouring and solidification were monitored inside the sprue and riser. The casting trials were held at Auburn University, AL. Twenty pounds of AZ91E alloy were melted using standard magnesium melting practices and CO_2+1%SF_6 cover gas for melt protection. Hexachloroethane tablets were added to the metal as a degassing agent and grain refiner. The pouring temperature was 760°C. After pouring, shakeout and surface cleaning, the casting was transversally cut (Fig. 6), and the cores were examined dimensionally for distortion. Figures 7–9 show transversally cut castings with zircon, silica+1%SIO, and silica sand cores, respectively. An examination of the transversally

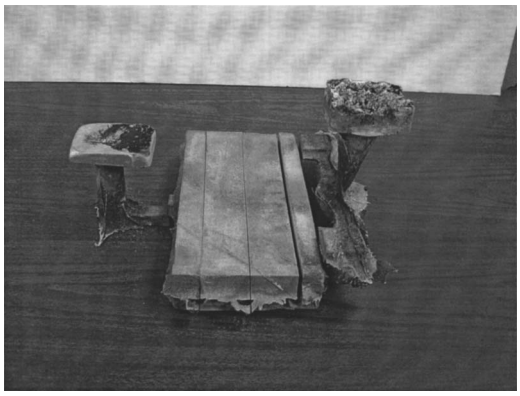

Fig. 6 Magnesium hot distortion test casting

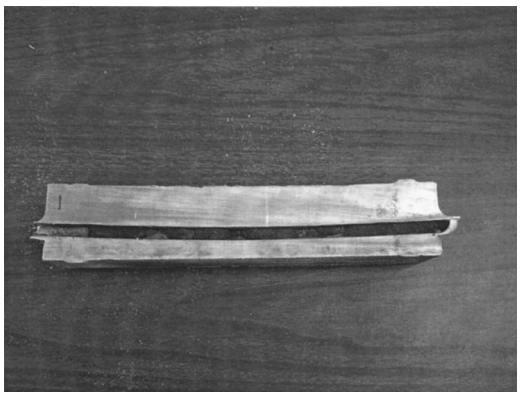

Fig. 7 Hot distortion test casting with zircon sand cores

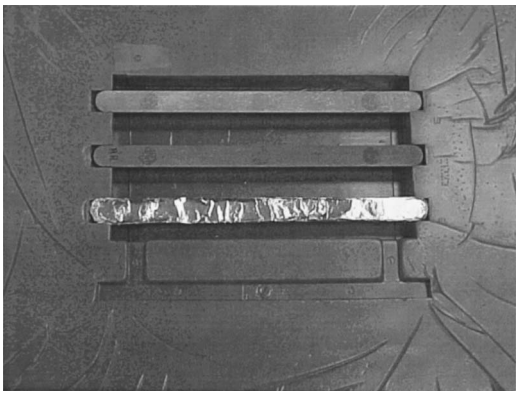

Fig. 5 Sand core specimens in the mold for hot distortion tests

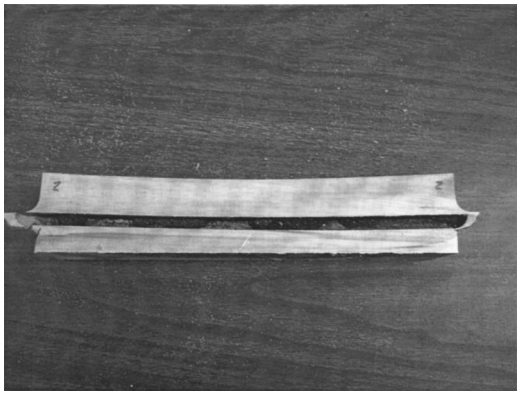

Fig. 8 Hot distortion test casting with silica+1%SIO sand cores

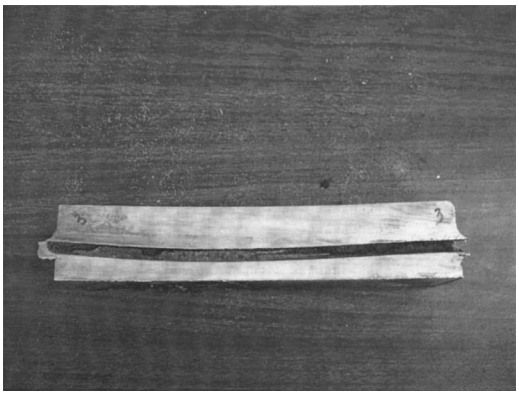

Fig. 9 Hot distortion test casting with silica sand cores

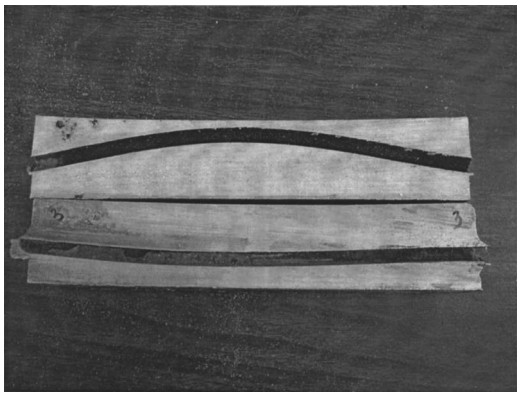

Fig. 11 Hot distortion test casting with silica sand cores in aluminum (above) and magnesium (below) castings

sliced casting showed that zircon and silica cores are slightly distorted downward. The test casting results did not reveal hot distortion for silica+1% SIO cores, which have densities close to the density of the molten alloy (Table 1).

One would assume that the zircon core must be distorted significantly due to its higher (1.8 times) density than the molten magnesium alloy, and hence the higher buoyancy force. The effect of the buoyancy force on core distortion was analyzed in our previous works [8,9]. However, in magnesium casting there was not a significant difference between the distortion of heavier (zircon) and lighter (silica) cores. Our magnesium casting practices using phenolic urethane cold box system showed a significant amount of decomposed gases evolved from the cores [10,11]. One would assume that the gases evolved from the core reduce the liquid pressure head above the core, and the buoyancy force increases (Fig. 10). The increase in buoyancy force decreases the downward distortion of the core. If we suggest that the volume of the gases evolved from the core is 10% of the volume of the core, we will have 0.06 N resultant force acting on the core at the end of the mold filling process (Fig. 4). However, this assumption requires further investigations.

Figure 11 presents the comparison of core distortion between aluminum [8,9] and magnesium (present work) castings.

Conclusions

Dual Pushrod Dilatometry has been used to measure a thermal expansion/contraction of phenolic urethane cold box sand core specimens in the temperature range from 25°C to 800°C at a heating rate of 20° per minute. At temperatures up to 300°C, due to combined effect of expansion and contraction of sand and resin binder, no significant changes in specimen's volume were observed. At temperatures 300°C and above, the resin binders start melting and then burning off. Therefore, the core specimens contracted. When the resin binders completely burned off (T =360°C), the contraction process stops, then sand grains, free of resin binders start expanding. This process continues up to 560°C, and then the expansion process stops. During the tests the specimens lost mass (~1.5%) equal to the mass of resin binders in the sand cores.

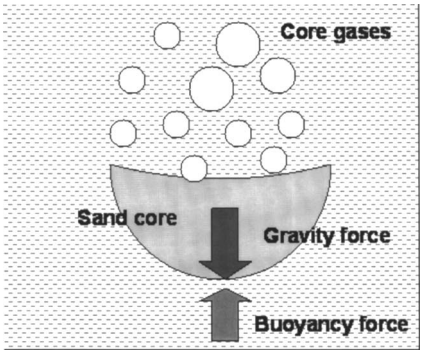

Fig. 10 Effect of core gases on force balance

The high temperature tensile tests showed that the tensile strength of the phenolic urethane cold box sand cores is significantly affected by the bench life. After 1 h of the bench life the tensile strength of silica sand cores decreases ~15%. Test temperature more dramatically affects the tensile strength. At 200°C the tensile strength of silica sand cores decreases ~20%, at 250°C it decreases ~50%. Part 1 to Part 2 ratio also affects the tensile strength. For example, decreasing the percentage of Part 1 from 55% to 50% in silica sand core results in 10% decrease of the tensile strength.

High temperature hot distortion furnace tests were conducted using 300 mm long and 19 mm diameter half-cylindrical phenolic urethane cold box cores at temperatures up to 500°C. At temperature ~300°C, all cores were distorted.

Numerical simulations of the liquid metal flow around the cylindrical sand core and analysis of dynamic forces acting on the core during fill process showed that buoyancy and gravity forces are the major contributors to the hot distortion phenomenon. It is concluded that the one of the solutions in preventing the hot distortion of sand cores is optimizing their density, which will balance the buoyancy force and will bring the resultant force to the minimum.

The hot distortion test castings were done to study distortion in phenolic urethane cold box cores during pouring and solidification of the molten magnesium alloy AZ91E. An examination of the transversally sliced casting showed that zircon and silica cores are slightly distorted downward. The test casting results did not reveal hot distortion for silica+1% SIO cores, which have densities close to the density of the molten alloy. We assume that the gases evolved from the core reduce the liquid pressure head above the core, and the buoyancy force increases. The increase in buoyancy force decreases the downward distortion even the heavier cores such as zircon sand core.

Acknowledgment

The author gratefully acknowledges the financial support received from NASA's Space Product Development at Marshall Space Flight Center under Cooperative Agreement No. NCC8-240. The technical assistance of the staff of Flow Science, Inc. is acknowledged.

References

[1] Morgan, A. D., 1967, "A Hot Distortion Test (HDT) Apparatus," British Cast Iron Research Association Journal, **15**, pp. 228–242.

[2] Morgan, A. D., 1969, "A Hot Distortion Test Apparatus," Australian Convention of Foundry Institutes, Paper No. 13, Auckland, New Zealand, p. 55.
[3] Gardziella, A., Kwasniok, A., and Cobos, L., 1996, "Recent Studies Comparing Coremaking Processes," Mod. Cast., **3**, pp. 39–42.
[4] Morgan, A. D., and Fasham, E. W., 1973, "A Hot Distortion Test Apparatus with Gas Burner," British Cast Iron Research Association Journal, **21**, pp. 516–520.
[5] Laitar, R., and Johnson, C. K., 1986, "High Hot Strength Phenolic Urethane Cold Box System," AFS Transactions, **94**, pp. 187–194.
[6] Fountaine, G. C., and Horton, K. B., 1990, "Hot Distortion of Cold Box System," AFS Transactions, **98**, pp. 9–16.
[7] Bakhtiyarov, S. I., Sherwin, C., and Overfelt, R. A., 2004, "Hot Distortion Studies in Phenolic Urethane Cold Box System," AFS Transactions, **112**, pp. 555–573.
[8] Fountaine, G. C., and Horton, K. B., 1993, "Comparison of Core Distortion Using Various Binder Systems," AFS Transactions, **101**, pp. 721–724.
[9] Bakhtiyarov, S. I., Suryawanshi, A., Capps, J., and Overfelt, R. A., 2004, "Numerical Simulations and Experimental Study of Hot Core Distortion Phenomenon in Aluminum Casting," *Proceedings of the ASME Heat Transfer/Fluids Engineering Summer Conference*, D. A. Siginer, ed., Charlotte, NC.
[10] Bakhtiyarov, S. I., and Overfelt, R. A., 2004, "First V-Process Casting of Magnesium," AFS Transactions, **112**, pp. 959–970.
[11] Bakhtiyarov, S. I., and Overfelt, R. A., 2004, "First Magnesium V-Process Casting," in *Magnesium Technology 2004*, A. A. Luo, ed., TMS Publications, pp. 187–192.

Power Law Turbulent Velocity Profile in Transitional Rough Pipes

Noor Afzal

Abu Seena

Department of Mechanical Engineering,
Aligarh University,
Aligarh 202 002, India

Afzal Bushra

Department of Civil and Environment Engineering,
University of Windsor,
Windsor, Ontario N9B 3P4, Canada

Alternate power law velocity profile $u_+=A\zeta^\alpha$ in transitional rough pipe fully turbulent flow, has been proposed, in terms of new appropriate inner rough wall variables ($\zeta=Z_+/\phi$, $u_\phi=u/\phi$), and new parameters $R_\phi=R_\tau/\phi$ termed as the roughness friction Reynolds number, $\mathrm{Re}_\phi=\mathrm{Re}/\phi$ termed as the roughness Reynolds number and ϕ termed as roughness scale (along with normal wall coordinate $Z=y+\epsilon_r$ where ϵ_r is the shift of the origin of boundary layer due to the rough wall, $Z_+=Zu_\tau/\nu$ and $u_+=u/u_\tau$). The envelope of the power law shows that the power law constants α and A depend on the parameter R_ϕ (i.e., $\alpha=\alpha(R_\phi)$ and $A=A(R_\phi)$) but explicitly independent of the wall roughness parameter h/δ (roughness height h in pipe of radius δ). The roughness scale ϕ has been related to the roughness function ΔU_+ of Clauser representing the velocity shift caused by wall roughness. The present results of the velocity profile, just slightly above the wall roughness level h, remain valid for all types of wall roughness. The data of Nikuradse for sand-grain roughness, in transitional and fully rough pipes, has been considered, which provides good support to the predictions of an alternate power law velocity profile, based on single parameter R_ϕ, the roughness friction Reynolds number.
[DOI: 10.1115/1.2175161]

1 Introduction

The power law velocity profile in wall bounded turbulent shear flow on smooth wall is

$$u_+ = Cy_+^\gamma, \tag{1a}$$

$$u_+ = \frac{u}{u_\tau}, \tag{1b}$$

$$y_+ = \frac{yu_\tau}{\nu} \tag{1c}$$

Here u is the velocity in stream wise x-direction, y is coordinate and for smooth wall. Further, $u_\tau=\sqrt{\tau_w/\rho}$ is the friction velocity, τ_w is the skin friction, ρ is the fluid density, ν is the molecular kinematic viscosity of fluid and $\lambda=8(u_\tau/U_b)^2$ is the friction factor. Nikuradse [1] analyzed his smooth pipes data in terms of the power law (1*a*) and estimated the power law constants γ and C which have been the function of Reynolds numbers $\mathrm{Re}=U_bd/\nu$ based on bulk velocity U_b and pipe diameter $d=2\delta$ and $\delta=a$ is the pipe radius. Barenblatt et al. [2,3] proposed the power law constants γ and C, supported by the data of Nikuradse [1] for smooth pipe, as given by the expressions

$$\gamma = \frac{3}{2\ln \mathrm{Re}}, \tag{2a}$$

$$C = \frac{1}{\sqrt{3}}\ln \mathrm{Re} + \frac{5}{2} \tag{2b}$$

Alternate expressions have also been presented by Kailasnath [4], Zagarola et al. [5], and Afzal [6] for fully developed turbulent pipe flow and George and Castillo [7], Afzal [8–10] and Panton [11] for the turbulent boundary layers. A good review of data for the power law velocity profile is given by Yaglom [12].

The proposal of Barenblatt [2] is reviving an issue raised already in Prandtl [13] about the connection between the power law and log law velocity profile. The way in which Prandtl and Barenblatt had been looking at similar issues, where the exponent in the power law are Reynolds number dependent whereas the constants in log law are not. Buschmann and Gad-el-Hak [14] analyzed the extensive experimental data for velocity distribution in the turbulent boundary layer with no pressure gradient, and proposed that the existing data covering a wide range of Reynolds numbers supports the log law and power law with equal measure throughout most of the overlap region. Further, Buschmann and Gad-el-Hak [15] observed that Afzal [6,9] rigorously demonstrated the equivalence of the power and log laws at very high Reynolds numbers. The power law in turbulent boundary layer flows was also considered in the "Second International Workshop on Wall-Bounded Turbulent Flows," and in the summary report Eaton and Nagib [16] have pointed out that Afzal highlighted a number of limitations in the asymptotic analysis leading to the power law for the boundary layer theory by George and Castillo [7]. In particular the last of terms shown here is ignored by them and leads to inappropriate limits:

$$\frac{u}{U_\infty} = 1 + G(Y) - \frac{u_\tau}{U_\infty}U_1(Y) \tag{3}$$

He also highlighted the relation between power law and log law which has been discussed in several of his papers [6,9], i.e., "representing the power law in terms of log law and other way around." It is shown above the envelop of the power law gives log law and vice versa (Afzal [10,17]). This means that in fully developed turbulent pipe or channel flow the log law exists, then power law also exists there (Afzal [6] and Wosnik et al. [18]).

In transitional roughness the roughness parameter $h_+=hu_\tau/\nu$ also becomes significant, where h is the hydraulic roughness, and an additional variable becomes significant. Further, in fully rough wall case, the dependence on ν, the molecular kinematic viscosity, through Reynolds number Re is not appropriate, where wall hydraulic roughness h is very much larger than viscous scale ν/u_τ. The normal coordinate in transitional rough pipes is $Z=y+\epsilon_r$, where ϵ_r is the shift of origin of the normal coordinate in the

Contributed by the Fluids Engineering Division of ASME for publication in the JOURNAL OF FLUIDS ENGINEERING. Manuscript received February 14, 2005; final manuscript received October 2, 2005. Assoc. Editor: Ugo Piomelli.

boundary layer, caused by irregular protrusions on the rough wall. The types of roughness commonly considered may be the sand-grain roughness, the commercial technical roughness, the *k*-type roughness, the *d*-type roughness in the engineering applications along with wide variety of the atmospheric roughness. Consequently, the sole effect of roughness is the shift of the velocity profile in the overlap region of the rough wall with respect to the smooth wall values. The roughness function may be determined by three methods described in Schultz and Myers [19]. The classical log law theory for rough pipes, along with the limiting cases of fully smooth and fully rough pipes, have been first proposed by Millikan [20] and have been extensively reviewed (Schlichting [21], Raupach, Antonia, and Rajagopalan [22], Piquet [23], and Jimenez [24]), and some basic relations are described in the Appendix.

The present work considers the power law velocity profile in transitional roughness in the pipes. Nikuradse [25] for his sand-grain data, estimated the power law index γ in relation (1*a*), which in addition to Re also depends on hydraulic roughness h_+. The power law constants γ and C in relation (1), from sand-grain roughness data of Nikuradse, have been estimated by Porporato and Sordo [26], as displayed in Fig. 1 of their paper, whose analytical representation $\gamma=\gamma(\mathrm{Re},h/a)$ and $C=C(\mathrm{Re},h/a)$ would be a complex issue and no correlations were proposed.

In a turbulent boundary layer on a rough wall, Balachandar et al. [27,28] modified the power law velocity profie (1*a*) for roughness effects as

$$u_+ = Cy_+^{\gamma} - \Delta U_+ \tag{4}$$

Here ΔU_+ is the roughness parameter, representing a shift of velocity profile curve downwards when compared with smooth wall power law, in analogy with Clauser [29] and Hama [30] described by log law (A1), given in the Appendix . In case of smooth wall, the power index $\gamma=\gamma(\mathrm{Re})$ and prefactor $C=C(\mathrm{Re})$, but by adopting $C=7.957$ and $\gamma=0.1551$ for smooth wall, the shift ΔU_+ was estimated as a function of hydraulic roughness h_+, but no correlation was proposed. For a rough surface, Seo [31] and Seo and Castillo [32], extended the work of George and Castillo [7] for smooth surface with shift in origin as $y_+ + j_+$. The power law velocity profile on the rough wall, in the outer and inner layers, become

$$\frac{u}{u_\tau} = C_i E_i (y_+ + j_+)^{\gamma_S+\gamma_R}, \tag{5a}$$

$$\frac{u}{U_\infty} = C_0 E_0 (Y + j)^{\gamma_S+\gamma_R}, \tag{5b}$$

$$\frac{U_\infty}{u_\tau} = \frac{C_i E_i}{C_0 E_0} R_\tau^{\gamma_S+\gamma_R} \tag{5c}$$

Here γ_S the power law index and C_i and C_0 the prefactors in inner and outer layers are constants of smooth wall theory and γ_R the power law index and E_i and E_0 the prefactors in inner and outer layers are due to the wall roughness effects. From data of zero pressure gradient boundary layer $j_+=jR_\tau=-16$ was adopted, and power law constants for smooth wall become

$$\gamma_S = 0.0362 + 1.334(\ln R_\tau)^{-1.46}, \tag{6a}$$

$$C_i = 55C_0 \exp[-4.234/(\ln R_\tau)^{0.46}], \tag{6b}$$

$$C_0 = 1 + 0.283 \exp(-0.005898R_\tau) \tag{6c}$$

Earlier, for turbulent boundary layer on rough wall, Kotey et al. [33] proposed power law relation (5*a*) with $j_+=-16$, and for various roughness the parameters γ_R and E_i were tabulated in Table II of their paper, but no correlation was proposed. Seo [31] and Seo and Castillo [32] from rough wall data proposed the following correlations

$$\gamma_R = 0.0065h_+^{0.60126}, \tag{7a}$$

$$E_i = [1 + 0.03551h_+^{0.88647}]^{-1}, \tag{7b}$$

$$E_0 = 1 + 0.00576h_+^{0.517} \tag{7c}$$

Seo [31] and Seo and Castillo [32] outer layer relations (5*b*) and (7*c*) depend on roughness parameter h_+, which is not in accordance with Townsend's similarity hypothesis on rough wall (see Flack et al. [34]). Further, let the outer layer slip velocity at the surface is represented as $u(x,Y=0)=U_S(x)$. The earlier work of George, Castillo, and Knecht [35] corresponds to $j=0$, where outer relation (5*b*) at $Y=0$ demands $U_S=0$. Consequently, the boundary condition of no slip at the wall $u(Y=0)=U_S=0$ is satisfied by outer layer in the overlap region, the inner wall layer is not needed, and in particular the inner relation (5*a*) becomes redundant. George and Castillo [7], Seo [31], and Seo and Castillo [32] adopted $j=-16/R_\tau$ and the outer relation (5*b*) predicts the slip velocity at the surface $U_S=C_0E_0(-16/R_\tau)^\alpha$, a complex relation for fully smooth, transitional and fully rough surfaces. It also implies that outer relation (5*b*) scaling is not appropriate (see also Afzal [10,17]). According to the work of Wosnik, Castillo, and George [18] the power law velocity profile does not exist for fully developed turbulent pipe flow, and the log law does not exist for turbulent boundary layer. On the other hand, the present work adds to the power law theory a new and rational approach of scaling for transitional pipe roughness effects as described below.

The appropriate rough wall new variables, that strain classical smooth wall variables by roughness scale ϕ, are given below

$$\zeta = \frac{Zu_{\tau\phi}}{\nu} = \frac{Z_+}{\phi}, \quad Z_+ = \frac{Zu_\tau}{\nu}, \quad Z = y + \epsilon_r \tag{8}$$

$$u_\phi = \frac{u}{\phi}, \quad u_{\tau\phi} = \frac{u_\tau}{\phi}, \quad u_+ = \frac{u_\phi}{u_{\tau\phi}} = \frac{u}{u_\tau} \tag{9}$$

where ϵ_r is the virtual origin located below the top of the roughness element, ϕ is the roughness scale, connected with roughness function ΔU_+, as

$$\Delta U_+ = \frac{1}{k}\ln \phi \tag{10}$$

where $h_+=0$, $\Delta U_+=0$, and $\phi=1$ for fully smooth wall and $h_+ \to \infty$, $\Delta U_+ \to \infty$, and $\phi \to \infty$ for fully rough wall. The two appropriate new parameters are R_ϕ, the roughness friction Reynolds number

$$R_\phi = \frac{\delta u_{\tau\phi}}{\nu} = \frac{R_\tau}{\phi}, \quad R_r = \frac{\delta U_\tau}{\nu} \tag{11}$$

and Re_ϕ, the roughness Reynolds number

$$\mathrm{Re}_\phi = \frac{2\delta U_{b\phi}}{\nu} = \frac{\mathrm{Re}}{\phi}, \quad \mathrm{Re} = \frac{2\delta U_b}{\nu} \tag{12}$$

where $U_{b\phi}=U_b/\phi$, U_b is average velocity in a pipe of radius δ, R_τ is the friction Reynolds number and Re is the Reynolds number based on average velocity and pipe diameter.

The aim of the present work is to extend the classical power law velocity profile (1) in terms of generalized wall variables (8)–(12) for transitional rough pipes. It is shown that in the generalized power laws proposed here, the power law constants depend on roughness friction Reynolds number R_ϕ. The findings have been supported by the extensive experimental data.

2 Power Law Velocity Profile on Transitional Rough Wall

The present work, dealing with transitional roughness in pipes, considered the a new inner wall variable ζ, which gives the power

laws for velocity profile and friction factor of a transitional rough wall. The power law turbulent velocity profile u_+ may be expressed as

$$u_+ = A\zeta^\alpha \tag{13}$$

The appropriate partially rough wall variable ζ or R_ϕ is related to the smooth wall variable Z_+ or R_τ strained by power law roughness scale ϕ, which entirely describes the transitional rough wall effects in the mean turbulent shear flow. The crucial issue is the definition of the roughness scale ϕ, which is adopted from relation (10) in terms of roughness function ΔU_+. In case of fully smooth wall $\phi=1$, the proposed alternate power law relation (13) reduces to the classical power law (1) implying $\alpha=\gamma$ and $A=C$. In outer variables (13) may also be expressed as

$$u_+ = A_1 Y^\alpha, \tag{14a}$$

$$Y = \frac{Z}{\delta}, \tag{14b}$$

$$A_1 = AR_\phi^\alpha \tag{14c}$$

It is well known that in the fully developed turbulent pipe flow, the velocity profile exhibits a weak defect layer which may be neglected ($E=0$) and the entire flow is described by the single wall layer, which is called the "main body of flow," approximation. An implication on the relation (13) where flow velocity is U_c at the pipe or channel axis gives

$$U_{c+} = AR_\phi^\alpha + E, \quad U_{c+} = \frac{U_c}{u_\tau} \tag{15}$$

the skin friction power law for a transitional rough wall. The power law relations (14*a*) and (15) upon subtraction give

$$\frac{U_c - u}{u_\tau} = A_1(1 - Y^\alpha) + E \tag{16}$$

The second implication of the "main body of flow" approximation, is that the power law velocity (13) may be integrated over entire cross section (say a pipe of radius δ) to obtain the bulk averaged velocity

$$U_b = \frac{2}{\delta^2}\int_0^\delta (\delta - y)u(y)dy = u_\tau R_\phi^\alpha \frac{2A}{(1+\alpha)(2+\alpha)} \tag{17}$$

The relations (14) and (15) connecting the average velocity U_b with characteristic velocity U_c at the pipe axis is

$$\frac{U_b}{U_c} = \frac{2}{(1+\alpha)(2+\alpha)}, \tag{18a}$$

$$\frac{U_c - U_b}{u_\tau} = AR_\phi^\alpha \frac{\alpha(3+\alpha)}{(1+\alpha)(2+\alpha)} \tag{18b}$$

The friction factor λ based on power law expression (18*a*) becomes

$$\lambda = 8\left[\frac{1}{2A}(1+\alpha)(2+\alpha)R_\phi^{-\alpha}\right]^2 \tag{19}$$

which may also be expressed as

$$\lambda = 8\left[\frac{2^{\alpha-1}}{A}(1+\alpha)(2+\alpha)\mathrm{Re}_\phi^{-\alpha}\right]^{2/(1+\alpha)} \tag{20}$$

Here R_ϕ, the roughness Reynolds number defined by relation (12*a*) for fully smooth pipe yields $\phi=1$, $\mathrm{Re}_\phi=\mathrm{Re}$.

3 Envelop of Power Law Friction Factor

Barenblatt [2,3] for smooth pipe walls considered the envelope of the power law velocity profile (1), subjected to the power law constants (2*a*) and (2*b*), which gives the log law velocity profile. In the present work, the power law friction factor (15) has been analyzed for its envelope. The large Reynolds numbers $R_\phi \to \infty$ implies $u_\tau/U_c \to 0$ and the relation (15) implies $\alpha \to 0$ and $A \to \infty$. Consequently, the power law prefactor A may be expressed in terms of power index α, through simple approximation

$$A = \frac{a}{\alpha} + b + \cdots \tag{21}$$

where a and b are constants to be determined for the transitional rough pipes. This relation in functional form has also been supported by smooth pipe work of Barenblatt [2] and Kailasnath [4]. The friction factor power law (15), based on relation (21) may also be expressed as

$$U_{c+} = \left(\frac{a}{\alpha} + b\right)\exp(\alpha \ln R_\phi) + E \tag{22}$$

which forms a family of curves in $(U_{c+}, \ln R_\phi)$-plane, where α is the parameter of the family. The family has an envelope which satisfies both Eq. (22) and equation $\partial U_{c+}/\partial\alpha=0$ giving

$$\left(1 + \frac{b}{a}\alpha\right)\alpha \ln R_\phi = 1 \tag{23}$$

The solution may also be expressed as

$$\alpha \ln R_\phi = \beta, \tag{24a}$$

$$\beta = \frac{a}{2b}\ln R_\phi\left[\left(1 + \frac{4b}{a \ln R_\phi}\right)^{1/2} - 1\right] \tag{24b}$$

In the skin friction power law (15), the constant A and power index α may be eliminated from relation (23) to obtain skin friction log law

$$\frac{U_c}{u_\tau} = \frac{1}{k}\ln R_\phi + B + E, \tag{25a}$$

$$\frac{U_c}{u_\tau} = \frac{1}{k}\ln R_\tau + B + E - \frac{1}{k}\ln \phi, \tag{25b}$$

$$k^{-1} = \frac{a}{\beta}\exp(\beta), \tag{26a}$$

$$B = b\exp(\beta) \tag{26b}$$

where k is the Karman constant and B is the intercept of log law. The results shows that the envelop of the skin friction power law (15) is given by log law (25*a*).

4 Analysis of the Results

The power law constant A from relation (21) may also be expressed in two other forms, firstly eliminating constants a and b through relations (26*a*) and (26*b*) and secondly using (23) and (24*b*), respectively give

$$A = \left(\frac{\beta}{k\alpha} + B\right)\exp(-\beta), \tag{27a}$$

$$A = \left(\frac{1}{k}\ln R_\phi + B\right)\exp(-\beta) \tag{27b}$$

The expression (24*b*) may be simplified from relation (24*a*) to get

$$\beta = \left(1 + \frac{kB}{\ln R_\phi}\right)^{-1} \tag{28}$$

The friction factor λ relation (20), after elimination of constant A from (27*a*), yields

$$\lambda = 2\left[\frac{k\alpha(1+\alpha)(2+\alpha)}{\beta + kB\alpha}\right]^2 \tag{29}$$

which may further be simplified by using relation (28) to obtain

$$\lambda = 2[k\alpha(1+\alpha)(2+\alpha)]^2 \tag{30a}$$

The relation (30*a*) in view of average velocity (18*a*) simplifies the friction factor as

$$\lambda = 8[k\alpha U_c/U_b]^2 \tag{30b}$$

For large Reynolds numbers the asymptotic expansions for relations (24*a*), (27*b*), and (28) for power law constants become

$$\alpha = \frac{1}{\ln R_\phi}\left[1 - \frac{kB}{\ln R_\phi} + \cdots\right], \tag{31a}$$

$$A = \frac{1}{k}\left[\ln R_\phi + kB - \frac{A_2}{\ln R_\phi} + \cdots\right]\exp(-1), \tag{31b}$$

$$\beta = 1 - \frac{kB}{\ln R_\phi} + \left(\frac{kB}{\ln R_\phi}\right)^2 + \cdots \tag{32}$$

Alternate form of the power law constants α and A may also be expressed in terms of the friction velocity. The $\ln R_\phi$ term in relation (24*a*) of power index α and relation (27*b*) for prefactor A may be eliminated from relation (25*a*) to obtain

$$\alpha = k^{-1}\epsilon, \tag{33a}$$

$$A = \frac{1}{\epsilon}\exp(-\beta), \tag{33b}$$

$$\epsilon = \frac{u_\tau}{U_c} \tag{33c}$$

and relation (28) for β is simplified as

$$\beta = 1 - B\epsilon \tag{34}$$

where ϵ is the nondimensional friction velocity with respect to U_c the velocity at pipe or channel axis. The relations (33*a*) and (33*b*) for α and A, may also be expressed in terms of average velocity U_b instead of the axis velocity U_c. The relation (18*b*) may be expressed as

$$\frac{U_c - U_b}{u_\tau} = -D_b\frac{2k(3k+\epsilon)}{3(k+\epsilon)(2k+\epsilon)}, \tag{35a}$$

$$D_b = -\frac{3}{2k} \tag{35b}$$

and large Reynolds number asymptotic expansion as $\epsilon \to 0$ gives

$$U_c = U_b[1 - D_b J + O(J^2)], \tag{36a}$$

$$J = \frac{u_\tau}{U_b} = \sqrt{\frac{\lambda}{8}} \tag{36b}$$

The power law constants (33*a*), (33*b*), and (34) based on relations (36*a*) become

$$\alpha = \frac{k^{-1}J}{1 - D_b J + O(J^2)}, \tag{37a}$$

$$A = \left(\frac{1}{J} - D_b + O(J)\right)\exp(-\beta), \tag{37b}$$

$$\beta = 1 - \frac{BJ}{1 - D_b J} \tag{37c}$$

The power-law index α and prefactor A from relations depend explicitly on R_ϕ or ϵ, which in turn depends on h_+ and h/a. The asymptotic expansion of power law friction factor (25*a*) based on relation (36*a*) for $R_\phi \to \infty$ becomes

$$\sqrt{\frac{8}{\lambda}} = k^{-1}\ln R_\phi + B + D_b + O\left(\frac{1}{\ln R_\phi}\right) \tag{38}$$

which may be compared to this order with relation (A11) of log law theory (Appendix).

5 Results and Discussion

The alternate power law velocity profiles (13) and (14) and power law constants (24*a*), (27*b*), and (28) are summarized below

$$u_+ = A\zeta^\alpha, \tag{39a}$$

$$u_+ = A_1 Y^\alpha, \tag{39b}$$

$$A_1 = AR_\phi^\alpha, \tag{39c}$$

$$\alpha = \frac{\beta}{\ln R_\phi}, \tag{40a}$$

$$A = \left(\frac{1}{k}\ln R_\phi + B\right)\exp(-\beta), \tag{40b}$$

$$\beta = \left(1 + \frac{kB}{\ln R_\phi}\right)^{-1} \tag{40c}$$

along with friction factor power law

$$\frac{U_c}{u_\tau} = AR_\phi^\alpha + E \tag{41}$$

The power law velocity profile theory presented in this paper holds for any kind of transitional roughness, including the limiting cases of fully rough and fully smooth walls as asymptotic cases. The type of roughness enters through the roughness scale ϕ, and its method of determination is described now. The envelop of the skin friction power law (22) is the log law (25*b*) which in the light of relation (10) for roughness scale ϕ becomes

$$\phi = \exp(k\Delta U_+) \tag{42}$$

and the relation (25*b*) yields

$$\frac{U_c}{u_\tau} = \frac{1}{k}\ln R_\tau + B + E - \Delta U_+ \tag{43}$$

The relation (43) may also be expressed in terms of δ/h as

$$\frac{U_c}{u_\tau} = \frac{1}{k}\ln\frac{\delta}{h} + B_T + E \tag{44}$$

where the roughness function ΔU_+ and roughness scale ϕ become

$$\Delta U_+ = \frac{1}{k}\ln h_+ + B - B_T, \tag{45a}$$

$$\phi = \exp(k\Delta U_+) = h_+\exp[k(B - B_T)] \tag{45b}$$

Here B and $B_T(h_+)$ are the intercepts of log laws in fully smooth wall and transitional rough wall flows. In case of fully rough wall, as shown later, $B_T = B_F$. It may be noted that the envelope of power law is log law, whose further analysis leads to expression (45*a*) for the roughness function ΔU_+, which turns out same as expression (A4) of classical roughness function from log law theory described in the Appendix .

Based on ϕ value, the new proposed variables $\zeta = Z_+/\phi$ and $R_\phi = R_\tau/\phi$ may be estimated. The alternate power law velocity profile (39*a*), and the power law constants (40*a*)–(40*c*) and (41) may also be expressed as

$$u_+ = A[Z_+\exp(-k\Delta U_+)]^\alpha, \tag{46a}$$

$$\frac{U_c}{u_\tau} = [R_\tau \exp(-k\Delta U_+)]^\alpha + E, \tag{46b}$$

$$\alpha = \frac{\beta}{\ln R_\tau - k\Delta U_+}, \tag{47a}$$

$$A = \left(\frac{1}{k}\ln R_\tau + B - \Delta U_+\right)\exp(-\beta), \tag{47b}$$

$$\beta = \left(1 + \frac{kB}{\ln R_\tau - k\Delta U_+}\right)^{-1} \tag{47c}$$

The hydraulic roughness function ΔU_+ or ϕ given by relations (47*a*) and (47*b*) like friction factor λ, is a function of the hydraulic wall roughness subjected to the oncoming stream, and not a function of power law or log law theory. The uncertainty associated in the estimation of roughness function ΔU_+ may be of same order as the uncertainty associated in estimation of friction factor λ. Moreover, the roughness function ΔU_+ is not a universal function for all roughness types. Nikuradse's [25] pipe flow experiments with closely packed, uniformly sand grain indicated that this roughness type is a universal function with h simply being the diameter of individual sand grains. However, the roughness function for most naturally occuring surfaces do not behave like closely packed, uniform sand grain. Colebrook [36] demonstrated this in a study of the irregular surface roughness in pipes resulting from the manufacturing process, where proper roughness scale h in terms of given roughness geometry is difficult to specify (Hama [30]). More than one roughness scale may be required to adequately represent an arbitrary roughness caused by irregular protrusions of rough surface. The types of roughness commonly considered may be the sand-grain roughness, the commercial technical roughness, the k-type roughness, the h-type roughness in the engineering applications along with wide variety of the atmospheric surfaces, etc., for which the roughness functions ΔU_+or the roughness scale ϕ is needed.

Colebrook [36] for commercial technical monotonic roughness, simplified the transitional roughness scale (45*a*) and (45*b*) and fortuitously proposed the roughness scale ϕ as simple composite sum of contribution from fully smooth wall $\phi=1$ and fully rough wall $\phi=h_+\exp[k(B-B_F)]$, which may be stated as

$$\phi = 1 + \chi h_+, \tag{48a}$$

$$\Delta U_+ = \frac{1}{k}\ln(1 + \chi h_+) \tag{48b}$$

and the roughness friction Reynolds number R_ϕ may be estimated as

$$R_\phi = \frac{R_\tau}{1 + \chi h_+}, \tag{49a}$$

$$\chi = \exp[k(B - B_F)] \tag{49b}$$

where $B=5.5$, $B_T=B_F=8.5$, and $\chi=0.306$. On the basis of relations (48) and (49), the power law profiles (46) and (47) for commercial technical roughness become

$$u_+ = A\left(\frac{Z_+}{1 + \chi h_+}\right)^\alpha, \tag{50a}$$

$$\frac{U_c}{u_\tau} = A\left(\frac{R_\tau}{1 + \chi h_+}\right)^\alpha + E, \tag{50b}$$

$$\frac{u}{U_c} = \left(\frac{Z}{\delta}\right)^\alpha,\ E = 0, \tag{50c}$$

$$\alpha = \frac{\beta}{\ln[R_\tau/(1 + \chi h_+)]}, \tag{51a}$$

$$A = \left[\frac{1}{k}\ln\left(\frac{R_\tau}{1 + \chi h_+}\right) + \beta\right]\exp(-\beta), \tag{51b}$$

$$\beta = \left(1 + \frac{kB}{\ln[R_\tau/(1 + \chi h_+)]}\right)^{-1} \tag{51c}$$

For inflectional roughness, the relations (48*a*)–(49*a*) and (50*a*)–(51*c*) would also remain valid provided χ is replaced by $\chi\exp(-j/h_+)$ according to relation (A20). In the present work the application of the power law theory has been applied to the sand-grain rough pipe data of Nikuradse [25]. These measurements of rough pipes, rightly celebrated for their care and completeness, have become a sort of crucial test for the experimental verification of any proposed law for velocity profile. The homogeneous roughness was obtained by gluing sand grain with various assigned diameters h to the walls of steel pipes with different diameters. The measurements were conducted using a series of tiny Pitot probes (internal diameter ranging from 0.21 and 0.3 mm and length 30 mm) placed in a Section 1 to 2 mm downstream end of the pipe, and obtained detailed and careful measurements up to the near wall proximity, for various values of roughness δ/h and Reynolds number Re.

The velocity profile data of Nikuradse's [25] sand-grain roughness for roughness parameters $\delta/h=60$ and $8 \leqslant h_+ \leqslant 369.8$ are shown in Figs. 1(*a*)–1(*d*). The classical power law velocity distribution, in the smooth wall variables (Z_+, u_+) and classical smooth wall power law relation, in terms of log-log plot, has been shown in Fig. 1(*a*). The velocity profiles, in the overlap region, represented by a line $u_+=CZ_+^\alpha$ are also shown in Fig. 1(*a*), which shift the locations, as the value of h_+ changes, and power law index γ and prefactor C may be estimated. The velocity distribution shifted by roughness function $u_+ + \Delta U_+$ against traditional smooth wall variable Z_+ is shown in Fig. 1(*b*) on log-log plot, and the profile $u_+ + \Delta U_+ = CZ_+^\alpha$ does not depend on wall roughness. The velocity profile u_+ alternate power law (38*a*) in terms of transitional roughness variable ζ versus u_+, is shown in Fig. 1(*c*) in log-log plot, for the same data of Nikuradse [25], do not explicitly depends on surface roughness, and the data collapse in the close neighborhood of relation $u_+=A\zeta^\alpha$. The power law index α and prefactor A as a function of roughness friction Reynolds number R_ϕ have been estimated. The power law velocity profile (36*b*), in the outer variables $u_+=A_1Y^\alpha$, $Y=Z/\delta$, is shown as log-log plots in Figs. 1(*d*), which reveals the similarity of the data analogous to that observed in Fig. 1(*d*). Another velocity profile data of Nikuradse [25] for $\delta/h=15$ and $31 \leqslant h_+ \leqslant 1250.3$ are also shown in the Figs. 2(*a*)–2(*d*), whose behaviour is analogous to Figs. 1(*a*)–1(*d*), and no additional comment is needed.

The power law velocity profile (39*a*) and skin friction power law (41), for the bulk of the flow approximation, give a remarkably simple relation for power law velocity distribution

$$\frac{u}{U_c} = A_0\left(\frac{Z}{\delta}\right)^\alpha, \tag{52a}$$

$$A_0 \sim 1 \tag{52b}$$

The Nikuradse [25] velocity profile data in terms of variables u/U_c versus Z/δ is shown in Fig. 3 as log-log plot, which predicts $A_0=1$ in second place of decimal. This shows the order to which the bulk flow approximation relations (52*a*) and (52*b*) holds good. The velocity profiles linear region in Fig. 4, shows that the power index α depends on roughness friction Reynolds number R_ϕ. The velocity profile for $h_+=64.4$ (middle one out of seven velocity profiles in $\delta/h=60$ data of Nikuradse [25]) show little departure from the prediction, in the overlap region. A careful inspection of Fig. 1(*a*) shows that the line fitted to the data for $h_+=64.4$ em-

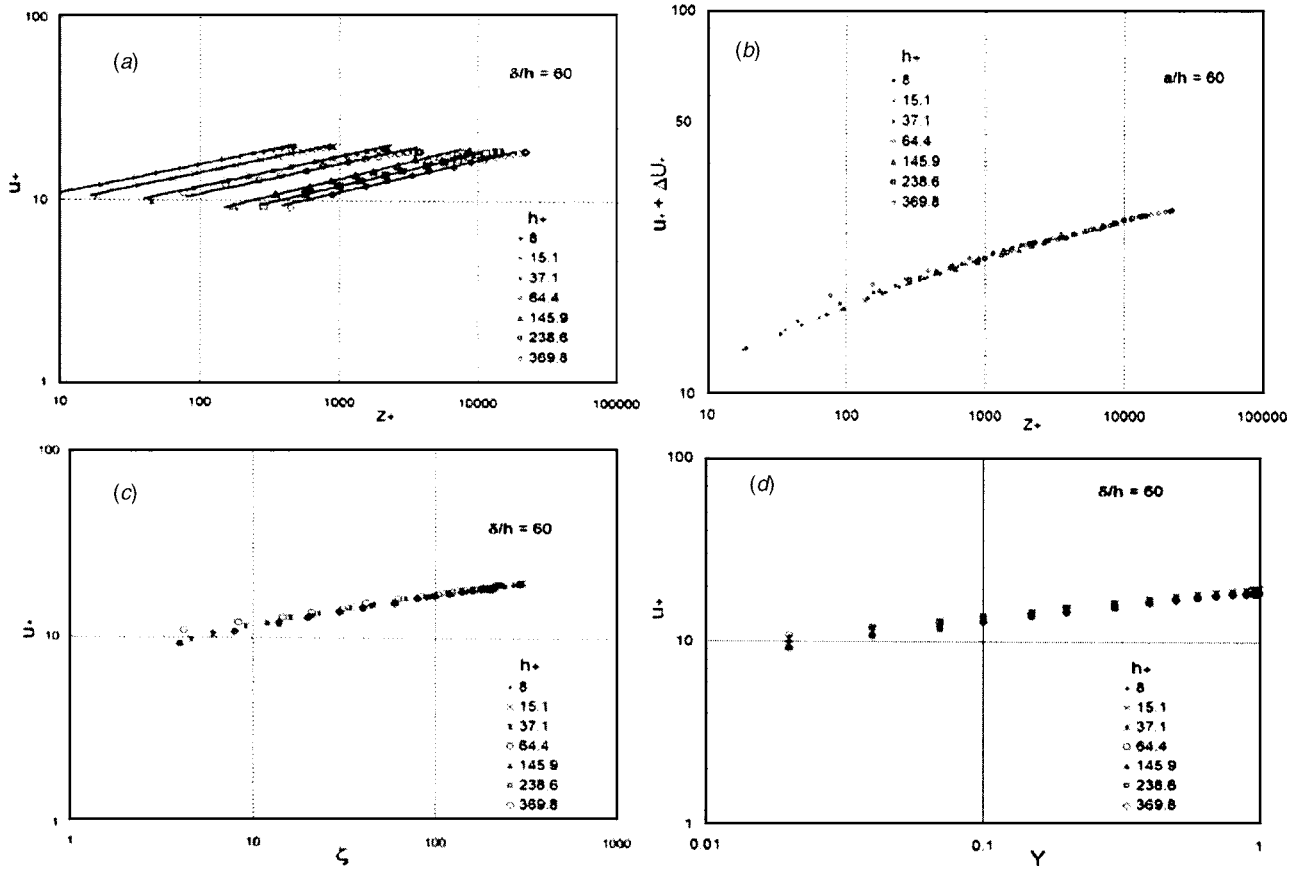

Fig. 1 The power law velocity distribution in log-log plots for sand-grain rough pipe data of Nikuradse for various values of h_+ with $\delta/h=60$: (*a*) Traditional inner power law velocity profile $u_+=CZ_+^\alpha$, in smooth wall variables (u_+, Z_+). (*b*) Velocity profile shifted by the roughness function $u_+ + \Delta U_+$ against traditional smooth wall variable Z_+ according to the power law relation $u_+ + \Delta U_+ = CZ_+^\alpha$. (*c*) Proposed inner transitionally rough wall variable ζ for velocity profile u_+, based on proposed inner power law velocity profile $u_+=A\zeta^\alpha$. (*d*) Proposed outer power law velocity profile $u_+=A_1 Y^\alpha$, in outer variables (u_+, Y).

braces few data points in the overlap region, that may also be observed in other Figs. 2 and 3.

The velocity profiles were measured by Nikuradse [25] in the sand-grain roughness for $\delta/h=15$, 30.6, 60, 126, 212, and 507. Nikuradse [25] displayed the data in his Fig. 18, in terms of power law velocity profile (1*a*) as log-log plots, and estimated the power law index α, as a function of roughness parameter δ/h, but computation of prefactor C was ignored, that has been estimated in present work. In alternate power law profile (39*a*), the behavior of power law constants α and A determined from experimental data of Nikuradse [25], may be analysed in terms of parameter $R_\phi = R_\tau/\phi$, the roughness friction Reynolds number, in order to observe the support provided by the experimental data to present predictions $\alpha=\alpha(R_\phi)$ and $A=A(R_\phi)$ in transitional rough pipes.

In order to check self-consistency, of each power law velocity profile data, A against α^{-1} have been shown in Fig. 4, from data for various values on δ/h, which supports the universality of the proposed relation $A=A(\alpha)$ with no appreciable scatter in the data. The present prediction (37*b*) represented by relation $A=0.92/\alpha+2.2$ compares very well with the experimental sand-grain roughness data. The power law index α for various values on δ/h have been shown in Fig. 5 against roughness friction Reynolds number R_ϕ. In the same figure, the prediction $\alpha=1/\ln R_\phi$ from relation (40*a*) with $\beta=1$ for large Reynolds number R_ϕ is also shown, which for lower values of the Reynolds numbers R_ϕ represents the upper limit of the data scatter. The higher order effect, in power index α, in the relation (40*a*) may be employed, by estimating β for description of little departure of data observed in Fig. 5. However, the fully rough pipe data has been in agreement with large Reynolds numbers line $\alpha=1/\ln R_\phi$. This implies that the data scatter, in flows other than fully rough pipe, may be due to the uncertainities associated with estimation of friction velocity u_τ and roughness scale ϕ associated with parameter R_ϕ, the roughness friction Reynolds numbers. The power law constant A has been shown in Fig. 6 against roughness friction Reynolds number R_ϕ. In the same figure, best linear fit line $A=0.8\ln R_\phi+3.25$ is also shown. However, the data would not be inconsistent with slope 0.92 instead of 0.8. The fully rough pipe data has been again very close to the best line, implying that scatter in the data for other data, may be associated with uncertainities in the estimation of friction velocity u_τ and roughness scale ϕ associated with parameter R_ϕ.

Next step is to consider, the power law constants α and A, predictions in terms of friction factor λ. The experimental data of Nikuradse [25], provided support to the present proposed relations $\alpha=\alpha(\lambda)$ and $A=A(\lambda)$ in a transitional rough pipes. The power law index α data for various values on δ/h, have been shown in Fig. 7 against friction factor λ. The relation α verus λ, represented as $\alpha=\alpha(\lambda)$, with some data scatter compares well with the leading order relation (37*a*) given by relation $\alpha=0.88\sqrt{\lambda}$. The results for power law constant A against λ have been shown in Fig. 8, which due to data scatter has been also shown the best linear fit $A=0.92/\sqrt{\lambda}+2.6$ to the data. Further, the relation (37*b*) giving $A=1.04/\sqrt{\lambda}+1.38$, however, may not be inconsistent within in the data scatter region. The fully rough pipe data has been very close and almost to the best line, also implying that the scatter in the other data, may be due to uncertainities associated with determi-

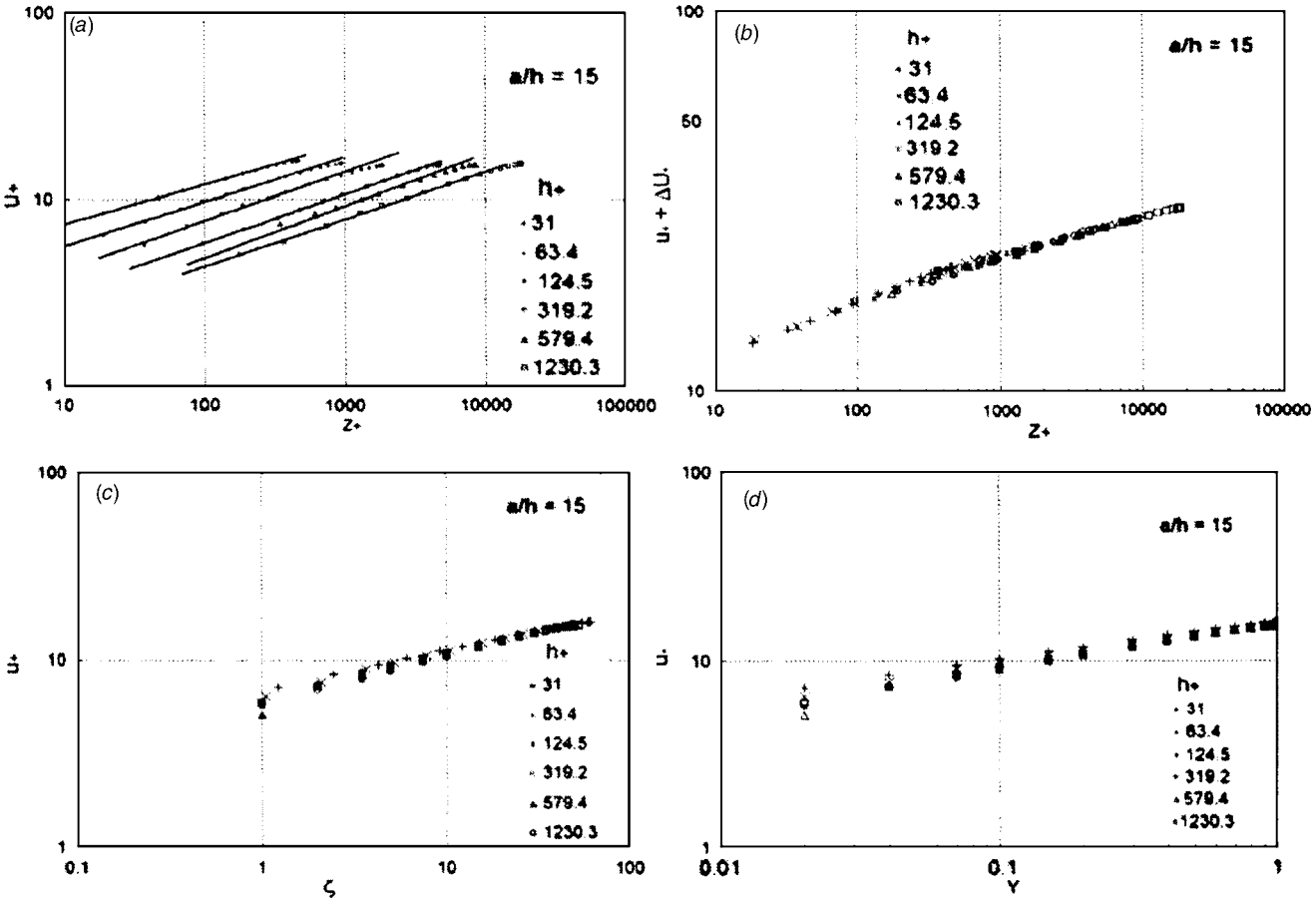

Fig. 2 The power law velocity distribution in log-log plots for sand-grain rough pipe data of Nikuradse for various values of h_+ with $\delta/h=15$: (*a*) Traditional inner power law velocity profile $u_+=CZ_+^{\alpha}$, in smooth wall variables (u_+, Z_+). (*b*) Velocity profile shifted by the roughness function $u_+ + \Delta U_+$ against traditional smooth wall variable Z_+ according to the power law relation $u_+ + \Delta U_+ = CZ_+^{\alpha}$. (*c*) Proposed inner transitionally rough wall variable ζ for velocity profile u_+, based on proposed inner power law velocity profile $u_+ = A\zeta^{\alpha}$. (*d*) Proposed outer power law velocity profile $u_+ = A_1 Y^{\alpha}$, in outer variables (u_+, Y).

nation of the friction velocity u_τ and roughness scale ϕ associated with parameter R_ϕ. Further, the higher order effects in relations (36*a*) and (36*b*) and the effects of the outer layer, neglected under the bulk of the flow approximation, would require further work, apart from uncertainities associated with estimation of friction velocity u_τ. The friction factor λ relation (30) based on α from relations (40*a*) and (40*c*) with parameter $kB=2$ has been computed. The ratio λ_e/λ of the experimental data λ_e to the predicted values λ of the friction factors have been shown in Fig. 9.The line $\lambda_e/\lambda=1$ shown in the same figure compares well, in a remarkably good manner, with the experimental data of Nikuradse for transi-

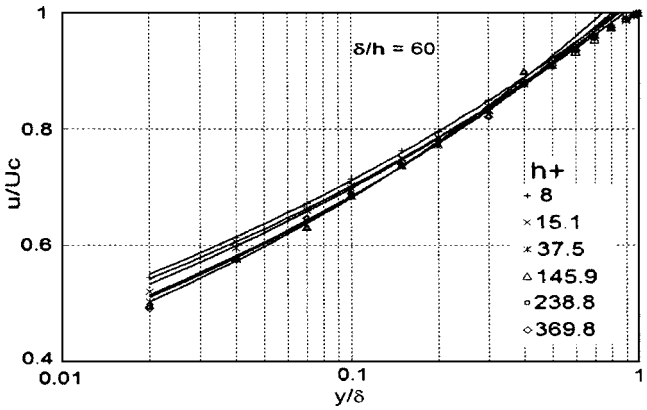

Fig. 3 The power law velocity distribution $u/Uc=Y^{\alpha}$ from relations (52*a*) and (52*b*) in the sand-grain rough pipe data of Nikuradse for various values of h_+ with $\delta/h=60$

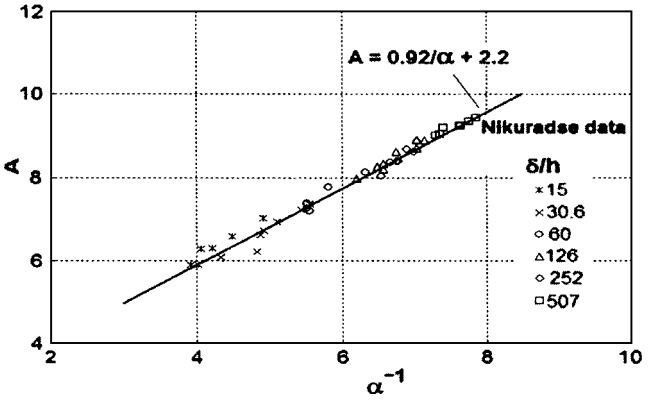

Fig. 4 Comparison of power law constant A relation (27*a*) against inverse of the power law index α with the experimental data of fully developed turbulent flow in transitional rough pipe data of Nikuradse for various values of δ/h in pipes. Proposed relation——$A=0.92/\alpha+2.2$.

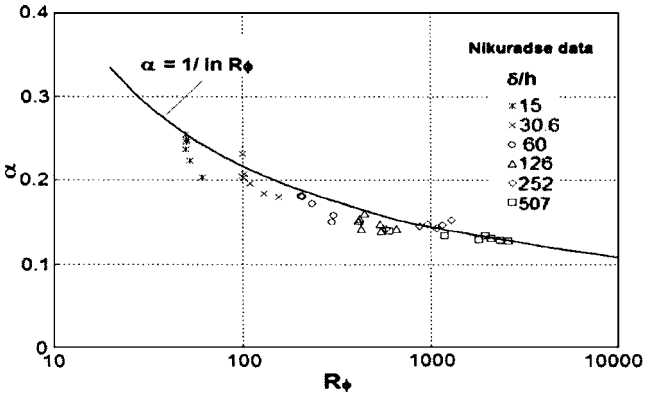

Fig. 5 Comparison of the power law index α relation (40*a*) against roughness friction Reynolds number R_ϕ with the experimental data of the fully developed turbulent flow in transitional rough pipe of Nikuradse for various values of δ/h in pipes. Proposed relation—— $\alpha=1/\ln R_\phi$.

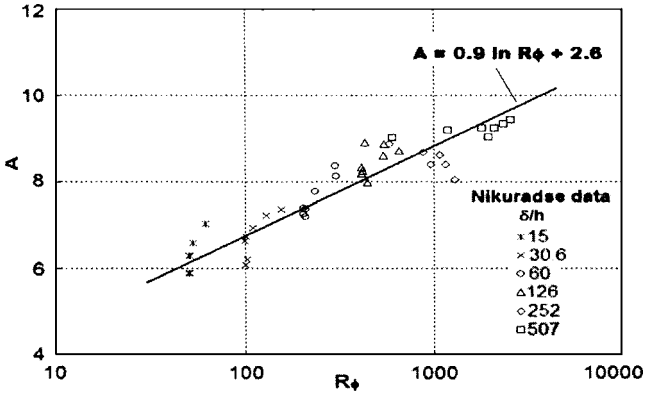

Fig. 6 Comparison of the power law constant A relation (40*b*) against roughness friction Reynolds number R_ϕ with the experimental data of the transitional rough pipe data of Nikuradse for various values of δ/h. values in pipes) for Nikuradse data. Proposed relation——$A=0.9\ln R_\phi+2.6$.

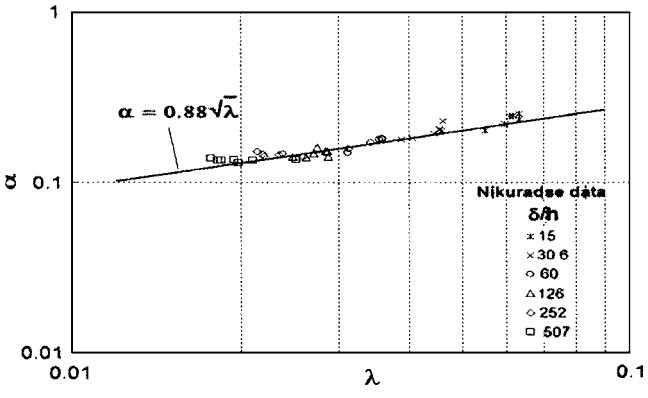

Fig. 7 Comparison of the power law index α against friction factor λ based on relation (37*a*) with fully developed turbulent flow in transitional rough pipe data of Nikuradse for various values of δ/h in pipes. Proposed relation——$\alpha=0.88\sqrt{\lambda}$.

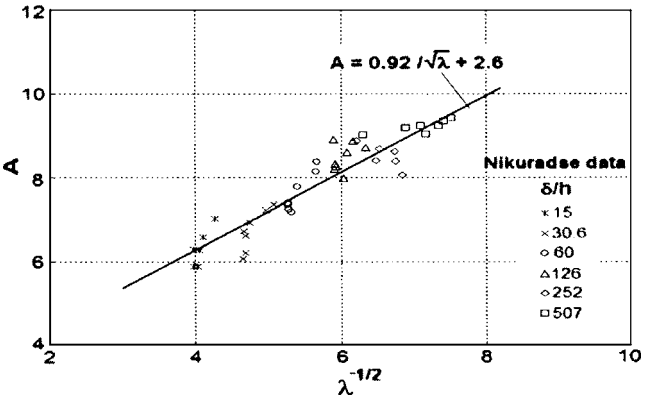

Fig. 8 Comparison of power law constant A against parameter $\lambda^{-1/2}$ based on inverse nondimensional friction factor relation (37*b*) with for fully developed turbulent flow in transitional rough pipe data of Nikuradse for varios values of δ/h in pipes. Proposed relation——$A=0.92/\sqrt{\lambda}+2.6$.

tional roughness in pipes. The skin friction power law (15) has an envelope as log law (41), which for large Reynolds number R_ϕ, with $k=0.4$ and $B=5.5$, gives

$$\frac{1}{\sqrt{\lambda}} = 2.03\log_{10}(\mathrm{Re}_\phi\sqrt{\lambda}) - 0.91 + O\left(\frac{1}{\ln \mathrm{Re}_\phi}\right). \tag{53}$$

where $\mathrm{Re}_\phi=\mathrm{Re}/\phi$ is the roughness Reynolds number, and adjusting the constants slightly (following Prandtl [13], see Schlichting [21]) yields

$$\frac{1}{\sqrt{\lambda}} = 2\log_{10}(\mathrm{Re}_\phi\sqrt{\lambda}) - 0.8 + O\left(\frac{1}{\ln \mathrm{Re}_\phi\sqrt{\lambda}}\right) \tag{54}$$

The relation (54) may also be expressed in terms of R_ϕ roughness friction Reynolds number as

$$\frac{1}{\sqrt{\lambda}} = 2\log_{10}(\mathrm{Re}_\phi\sqrt{32}) - 0.8 + O\left(\frac{1}{\ln \mathrm{R}_\phi}\right) \tag{55}$$

The friction factor λ relation (54) or (55) in terms of parameter Re_ϕ or R_ϕ, remains same for all types of the wall roughness, may be the sand-grain infectional roughness, the Colebrook monotonic roughness, bar type roughness, atmospheric ground roughness, etc. For example, in traditional variables, Nikuradse [1,25] in his Fig. 9 (or Schlichting [21], Fig. 20.18, p. 521) for a given value of

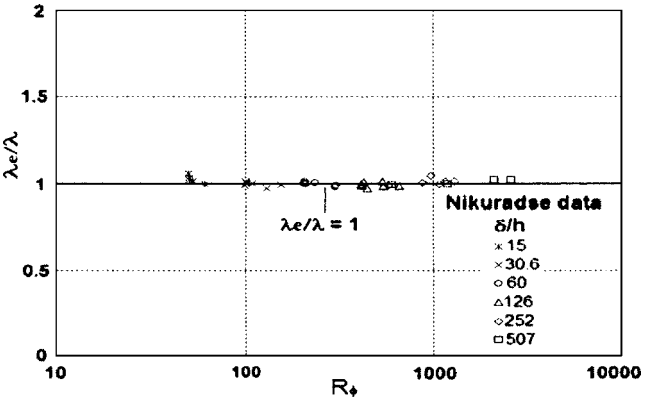

Fig. 9 Comparision of λ_e/λ, the ratio of the experimental to predicted values of friction factors against the roughness friction Reynolds number R_ϕ with fully developed turbulent flow in transitional rough pipe data of Nikuradse for various values of δ/h in pipes. Proposed relation—— $\lambda_e/\lambda=1$.

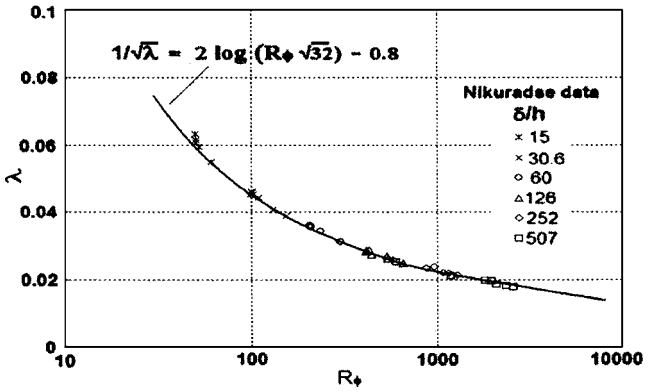

Fig. 10 Comparison of the friction factor λ against the roughness friction Reynolds number $R_\phi = R_\tau/\phi$ from prediction (55) with data of Nikuradse for various values of δ/h for fully developed turbulent flow in transitional rough pipes. Proposed relation——$1/\sqrt{\lambda} = 2\log_{10}(R_\phi\sqrt{32}) - 0.8$.

δ/h has shown that the friction factor is a distinct line, which shifts with change in the values of roughness δ/h, where as in present alternate variable R_ϕ the friction factor for all types of roughness is universal collapsing on a single line predicted by relation (55). Likewise, friction factor for Colebrook commercial monotonic roughness, is shown by Moody [37] plots, where each value δ/h distinct line is obtained, where as in the present alternate variable R_ϕ all the data collapse on a single line relation (55).

The lowest order friction factor relation (55), based on the power law envelope, has been the same as relation (A18) from the log law theory, described in the Appendix. In fact for smooth flow $\phi=1$, $\mathrm{Re}_\phi=\mathrm{Re}$ the relation (54) becomes same as Prandtl's universal friction factor relation (A19). The friction factor data has been shown in Fig. 10 against roughness friction Reynolds number R_ϕ, where transitional rough pipes data of Nikuradse [25] collapse on a single line represented by prediction (52). The numerical values $a=0.92$ and $b=2.02$ power law constants corresponds to the log law universal constants $k=0.4$ and $B=5.5$ (Schlichting [21]). The predictions, displayed in various figures, with power law constant $a=0.92$ compare with the data. It is well known, that Prandtl [13] (see also Schlichting [21]) slightly adjusted $B+D_b$ while proposing the relation (A14) for smooth pipe data, and the same have been adopted here in the transitional rough pipes predictions (55) from power law or (A13) from log law. Likewise, the constant b (or B) in Figs. 7 and 9 and constant D_b in Fig. 9 have been slightly adjusted for data comparison. Barenblatt [2,3] and Zagarola et al. [5,38] proposed changes in the classical values of k, the Karman constant and B, the log law intercept based on power law theory. Moreover, several proposals based on classical log law theory also widely vary where $k=0.461$ and $B=7.13$ (Smith and Walker [39]) and $k=0.37$ and $B=3.7$ (Zanoun et al. [40]).

The present work considered sand-grain roughness data. For any other type of roughness, the roughness scale ϕ may be estimated from data, but the power law constants α and A in power law velocity profile (13), in terms of the parameters $R_\phi=R_\tau/\phi$ and $\mathrm{Re}_\phi=\mathrm{Re}/\phi$, would remain the same, as proposed in present work. Further, the power law solution considered here has been equivalent with classical log law solution for very large Reynolds numbers R_ϕ in the overlap domain. This is not surprising as we are dealing with the open functional equation of the turbulent motion, without any closure hypothesis. The higher order effects in power law theory is of order $(\ln R_\phi)^{-1}$ and in log law theory is of order R_ϕ^{-1}. Consequently, the power law solution and log law solution are not equivalent for lower Reynolds numbers (Afzal [10,17]).

6 Conclusions

(1) Two new parameters $R_\phi=R_\tau/\phi$, the roughness friction Reynolds number and $\mathrm{Re}_\phi=\mathrm{Re}/\phi$, the roughness Reynolds number have been proposed. An alternate power law velocity profile $u_+=A\zeta^\alpha$ in new inner wall variable $\zeta=Z_+/\phi$ have also been proposed for transitionally rough pipes. Here ϕ is the roughness scale connected with the roughness function ΔU_+.

(2) The power law constants α and A for transitionally rough pipes, remain same as in smooth pipe case, provided R_τ and Re in smooth wall relations are replaced by corresponding roughness Reynolds numbers R_ϕ and Re_ϕ as appropriate.

(3) The theory shows power law constants $\alpha=\alpha(R_\phi)=\alpha(\lambda)$ and $A=A(R_\phi)=A(\lambda)$, remain same for transitional roughness as well as smooth pipes.

(4) In traditional variables, the velocity profile in terms of inner variable Z_+, and the friction factor λ in terms of friction Reynolds number Re_τ or Reynolds number Re, depend on pipes roughness. Further, the power law constants $\alpha=\alpha(\mathrm{Re},h_+)$ and $A=A(\mathrm{Re},h_+)$ in addition to Reynolds number Re shall also depend on transitional roughness of the pipes.

(5) The velocity profile (13) in terms of alternate inner variable ζ, and the friction factor relations (19) or (20) in terms of parameter Re_ϕ or R_ϕ, proposed in the present work, remains same for all types of the wall roughness, i.e., these are explicitly independent of pipes roughness. But the roughness is implicitly presents due to involvement of the roughness scale ϕ in definitions of the inner variable ζ, the roughness friction Reynolds number $R_\phi=R_\tau/\phi$ and roughness Reynolds number $\mathrm{Re}_\phi=\mathrm{Re}/\phi$. For smooth pipes $\phi=1$ and friction factor relation yield the Prandtl universal friction factor of smooth pipes.

Appendix: Logarithmic Velocity Profile

The log law theories in fully developed, turbulent flow, in fully smooth pipe or channel, have been studied by Millikan [20], Tennekes [41], Afzal and Yajnik [42], Afzal [43], Wosnik, Castillo, and George [18], and Buschmann and Gad-el-Hak [15]. Millikan [20] also proposed the log law theory for transitionally rough pipes and limiting case of fully rough pipes. The turbulent flow on transitionally rough wall has been extensively reviewed (Schlichting [21], Raupach, Antonia, and Rajagopalan [22], Piquet [23], and Jimenez [24]). It is well known that in the fully developed turbulent pipe flow, the velocity profile exhibits a very weak defect layer (wake parameter II small), which may be neglected and the entire flow is described by the single wall layer and it is called the "main body of flow," approximation. The log law velocity profile for transitionally rough wall becomes (Schlichting [21], Raupach, Antonia, and Rajagopalan [22], Piquet [23], Jimenez [24], and Antonia and Krogstad [44])

$$\frac{u}{u_\tau} = \frac{1}{k}\ln Z_+ + B - \Delta U_+ \tag{A1}$$

and skin friction log law becomes

$$\frac{U_c}{u_\tau} = \frac{1}{k}\ln R_\tau + B + D - \Delta U_+ \tag{A2}$$

The log law of the rough wall (A1) has been represented as the sum of smooth wall log law (in classical inner wall variable Z_+, with Karman constant k and wall intercept B as universal constants on a smooth wall) and the effects of the wall roughness have been incorporated through roughness function ΔU_+ defined by Clauser [29] and Hama [30] as an additional term. Likewise, the skin friction log law for a rough wall (A2), under the bulk of flow approximation, also contains the Clauser roughness function

ΔU_+ as an additive term. For various types of roughness the data on roughness function ΔU_+ may be found in the reviews by Schlichting [21], Raupach, Antonia, and Rajagopalan [22], Piquet [23], and Jimenez [24]. The roughness function ΔU_+ may be determined by three methods described in Schultz and Myers [19].

The velocity profile (A1) in terms of fully rough wall variable Z/h may be expressed as

$$\frac{u}{u_\tau} = \frac{1}{k} \ln \frac{Z}{h} + B_T \tag{A3}$$

provided B_T is expressed in terms of roughness function $\Delta U+$ as given below

$$\Delta U_+ = \frac{1}{k} \ln h_+ + B - B_T \tag{A4}$$

Here B and B_T are the intercepts of log laws in fully smooth and transitional roughness. For $B=5$ is smooth wall constant and for the fully rough wall $B_T=B_F=8.5$.

Let us consider alternate inner variable ζ, Reynolds numbers R_ϕ, and Re_ϕ and the roughness scale ϕ, defined by relations (6)–(9), for ready reference are stated below

$$\zeta = \frac{Z_+}{\phi}, \tag{A5a}$$

$$R_\phi = \frac{R_\tau}{\phi}, \tag{A5b}$$

$$\mathrm{Re}_\phi = \frac{\mathrm{Re}}{\phi}, \tag{A5c}$$

$$\Delta U_+ = \frac{1}{k} \ln \phi \tag{A5d}$$

The roughness scale $\phi(h_+)$ from relations (A4) and (A5*d*) becomes

$$\phi = \exp(k\Delta U_+) = h_+ \exp[k(B - B_T)] \tag{A6}$$

Introduction of the new variables (A6) and (A7), in the velocity profile (A1) becomes

$$\frac{u}{u_\tau} = \frac{1}{k} \ln \zeta + B \tag{A7}$$

and the skin friction log law (A2) becomes

$$\frac{U_c}{u_\tau} = \frac{1}{k} \ln R_\phi + B + D \tag{A8}$$

The log law velocity profile (A7) and skin friction (A8) are the universal functions, and roughness properties have been inherited in the alternate wall variable ζ and Reynolds number R_ϕ through relations (A5). The log law velocity profile (A7), subjected to the "main body of flow" approximation ($D=E=0$), may be integrated over entire cross section (say, pipe radius δ) to obtain the bulk averaged velocity

$$U_b = \frac{2}{\delta^2} \int_0^\delta (\delta - y) u(y) dy = u_\tau \left(\frac{1}{k} \ln R_\phi + B - \frac{3}{2k} \right) \tag{A9}$$

The relations (A9) and (A8) connect the average velocity U_b with characteristic outer velocity U_c by the relation

$$U_b = U_c + D_b u_\tau \quad D_b = -\frac{3}{2k} \tag{A10}$$

The friction factor $\lambda = 8(u_\tau/U_b)^2$, from relations (A8) and (A10), becomes

$$\sqrt{\frac{8}{\lambda}} = k^{-1} \ln R_\phi + B + D_b \tag{A11}$$

and numerical values $k=0.4$, $D_b=-3.75$, and $B=5.5$ yield $1/(k\sqrt{8})=2.03$ and $(B+D_b)/\sqrt{8}=0.091$ and further the constants are slightly adjusted (following Prandtl [13,21]) to obtain

$$\frac{1}{\sqrt{\lambda}} = 2 \log_{10}(\mathrm{Re}_\phi \sqrt{\lambda}) - 0.8 \tag{A12}$$

The relation (A12) may also be expressed in terms of R_ϕ to obtain

$$\frac{1}{\sqrt{\lambda}} = 2 \log_{10}(R_\phi \sqrt{32}) - 0.8 \tag{A13}$$

For smooth flow $\phi=1$, $\mathrm{Re}_\phi=\mathrm{Re}$ and relation (A13) gives Prandtl universal relation

$$\frac{1}{\sqrt{\lambda}} = 2 \log_{10}(\mathrm{Re}\sqrt{\lambda}) - 0.8 \tag{A14}$$

Commercial Technical Roughness. Colebrook [36] in commercial technical roughness, fortuitously proposed that roughness scale ϕ in transitional rough wall is simple sum of ϕ for fully smooth wall $\phi=1$ where $B_T=B$ and fully rough wall $\phi=\chi h_+$ where $B_T=B_F$ and $\chi=\exp[k(B-B_F)]=0.306$ for $B=5.5$ and $B_F=8.5$. The composite relation becomes $\phi=1+\chi h_+$ which gives

$$\Delta U_+ = \frac{1}{k} \ln(1 + \chi h_+), \quad R_\phi = \frac{R_\tau}{1 + \chi h_+}, \quad \chi = \exp[k(B - B_F) = 0.306 \tag{A15}$$

In terms of parameter R_ϕ given by relation (A6) all the data for the commercial technical roughness in Colebrook [36]) shall also collapse on a single line (A12). Further, in the classical Moody [37] plot (see p. 528, Fig. 20.25 Schlichting [21]) in which for each value of roughness parameter a/h there is a represented line, where as in the present work all the lines of the Moody plot collapse on a single relation (A12) in terms of parameter R_ϕ predicted here. Further, based on relations (A15) the friction factor relation (A2) becomes

$$\frac{1}{\sqrt{\lambda}} = 2 \log_{10}\left(\frac{\mathrm{Re}\sqrt{\lambda}}{1 + \chi h_+} \right) - 0.8 \tag{A16}$$

which may also be expressed in standard [36] form as

$$\frac{1}{\sqrt{\lambda}} = -2 \log_{10}\left(\frac{2.51}{\mathrm{Re}\sqrt{\lambda}} + \frac{\chi}{1.12} \frac{h}{d} \right) \tag{A17}$$

Likewise, the power law velocity profile data for Colebrook technical roughness, the roughness scale ϕ may be estimated from relations (A15). The power law constants ϕ and A data for commercial technical roughness may be displayed in terms of R_ϕ, which would follow the same relations as shown in various figures, which holds for all types of roughness including the smooth wall.

Sand Grain Roughness. The roughness function ΔU_+ relation (A4) in terms B_T the log law constant for transitionally rough wall, was used by Nikuradse [25] for tabulation of B_T from his sand-grain roughness pipe data as a function of roughness parameter h_+. Guo [46] expressed B_T data of Nikuradse [25] by the relation

$$B_T = 8.5 + \frac{5.75 \log_{10} h_+ - 3.25}{\exp[\log_{10}^3(1 + h_+^{0.88})]} \tag{A18}$$

The roughness function ΔU_+ correlation, from Nikuradse data, proposed by Loselevich and Pilipenko (see Cebeci [47]) is

$$\Delta U_+ = (B - 8.5 + k^{-1} \ln h_+) \times \sin[0.4258(\ln h_+ - 0.811)] = \frac{1}{k} \ln \phi \tag{A19}$$

for $2.25 \leqslant h_+ < 90$ with $B=5.2$ and $k=0.42$.

The roughness scale ϕ for infectional roughness of Nikuradse is obtained by Afzal [45], from modification of Colebrook [36] monotonic relation (A15) of transitional roughness domain, by introducing an exponential function that approaches unity for $h_+ \to \infty$, as stated below

$$\phi = 1 + \chi h_+ \exp\left(-\frac{j}{h_+}\right), \quad \chi = \exp[k(B - B_F)] \tag{A20}$$

$$\Delta U_+ = \frac{1}{k} \ln\left[1 + \chi h_+ \exp\left(-\frac{j}{h_+}\right)\right] \tag{A21}$$

where $j=0$ for Colebrook [36] monotonic roughness and $j=11$ for infectional roughness of Nikuradse [25]. The predictions are described in Afzal [48,49].

References

[1] Nikuradse, J., 1932, "Laws of Turbulent Flow in Smooth Pipes," *VDI, Forchungsheft N-356* (English translation NACA TTF-10, p. 359)

[2] Barenblatt, G. I., 1993, "Scaling Laws for Fully Developed Turbulent Shear Flows, Part I: Basic Hypothesis and Analysis," J. Fluid Mech., **248**, pp. 513–520.

[3] Barenblatt, G. I., Chorin, A. J., and Prostokishin, V. M., 1997, "Scaling Laws for Fully Developed Turbulent Flow in Pipes," Appl. Mech. Rev., **90**, pp. 413–429.

[4] Kailasnath, P., 1993, "Reynolds Number Effect and The Momentum Flux in Turbulent Boundary Layer," Ph.D. thesis, Mason Lab., Yale University.

[5] Zagarola, M. V., Perry, A. E., and Smits, A. J., 1997, "Log Laws or Power Laws: The Scaling in the Overlap Region," Phys. Fluids, **9**, pp. 2094–2100.

[6] Afzal, N., 2001, "Power Law and Log Law Velocity Profiles in Fully Developed Turbulent Pipe Flow: Equivalent Relations at Large Reynolds Numbers," Acta Mech., **151**, pp. 171–183.

[7] George, W., and Castillo, L., 1997, "Zero Pressure Gradient Turbulent Boundary Layer," Appl. Mech. Rev., **50**, pp. 689–729.

[8] Afzal, N., 1997, "Power Law in Wall and Wake Layers of a Turbulent Boundary Layer," *Proceedings Seventh Asian Congress of Fluid Mechanics*, Allied Publishers Limited, New Delhi, pp. 805–808.

[9] Afzal, N., 2001, "Power Law and Log Law Velocity Profiles in Turbulent Boundary Layer: Equivalent Relations at Large Reynolds Numbers," Acta Mech., **151**, pp. 195–216.

[10] Afzal, N., 2005, "Scaling of Power Law Velocity Profile in Wall-Bounded Turbulent Shear Flows.," *AIAA-2005-0109, 43rd AIAA Aerospace Sciences Meeting and Exhibit*, 10–13 Jan., Reno, Nevada.

[11] Panton, R. L., 2002, "Evaluation of the Barenblatt-Chorin-Prostokishin Power Law for Turbulent Boundary Layers," Phys. Fluids, **14**, pp. 1806–1808.

[12] Yaglom, A. M., 2001, "The Century of Turbulence Theory: The Main Achievements and Unsolved Problems," *New Trends in Turbulence: Nouveaux Aspects*, M. Lesieur, A. Yaglom, and F. David, eds., Les Houches: EPT, Springer-Verlag, Berlin, Vol. 74.

[13] Prandtl, L., 1934, "The Mechanics of Viscous Fluids," in *Aerodynamics Theory, Vol. 3*, W. F. Durand, ed., California Institute of Technology, Pasadena, California, pp. 34–208.

[14] Buschmann, M. H., and Gad-el-Hak, K., 2003, "The Debate Concerning the Mean Velocity Profile of a Turbulent Boundary Layer," AIAA J., **41**(4), pp. 565–572.

[15] Buschmann, M. H., and Gad-el-Hak, K., 2003, "Generalized Logarithmic Law and its Consequences," AIAA J., **41**(1), pp. 40–48.

[16] Eaton, J. K., and Nagib, H. M., 2004, "Report: 'Second International Workshop on Wall-Bounded Turbulent Flows,' by H. Nagib and A. J. Smits," from 2–5 November, the Abdus Salem International Center for Theoretical Physics, Trieste, Italy.

[17] Afzal, N., 2005, "Analysis of Power Law and Log Law Velocity Profiles in Overlap Region of a Turbulent Wall Jet," Proc. R. Soc. London, Ser. A, **461**, pp. 1889–1910.

[18] Wosnik, M., Castillo, L., and George, W. K., 2000, "A Theory for Turbulent Pipe and Channel Flows," J. Fluid Mech., **421**, pp. 115–145.

[19] Schultz, M. P., and Myers, A., 2003, "Comparison of Three Roughness Function Determination Methods," Exp. Fluids, **35**(4), pp. 372–379.

[20] Millikan, C. B., 1938, "A Critical Discussion of Turbulent Flow in Channels and Circular tubes," *Proc. Fifth. International Congress of Applied Mechaics*, J. P. Den Hartog and H. Peters, eds., Wiley, New York, pp. 386–392.

[21] Schlichting, H., 1968, *Boundary Layer Theory*, McGraw-Hill, New York.

[22] Raupach, M. R., Antonia, R. A., and Rajagopalan, S., 1991, "Rough-Wall Turbulent Boundary Layer," Adv. Appl. Mech., **44**, pp. 1–25.

[23] Piquet, J., 1999, *Turbulent Flow*, Springer-Verlag, Berlin.

[24] Jimenez, J., 2004, "Turbulent Flow Over Rough Walls," Annu. Rev. Fluid Mech., **36**, pp. 173–196.

[25] Nikuradse, J., 1933, "Laws of Flow in Rough Pipe," *VDI*, *Forchungsheft N-361* (English translation NACA TM 1292, 1950).

[26] Porporato, A., and Sordo, S., 2001, "On the Incomplete Similarity for Turbulent Velocity Profiles in Rough Pipes," Phys. Fluids, **13**(9), pp. 2596–2601.

[27] Balachandar, R., Hagel, K., and Blakely, D., 2002, "Velocity Distribution in Decelerating Flow Over Rough Surface", Can. J. Civ. Eng., **29**, 211–221.

[28] Balachandar, R., Blackely, D., and Bugg, J., 2002, "Friction Factor and the Power Law Velocity Profile in Smooth and Rough Shallow Open Channel Flow Can. J. Civ. Eng., **29**, pp. 256–266.

[29] Clauser, F. H., 1954, "Turbulent Boundary Layers in Adverse Pressure Gradients," J. Aeronaut. Sci., **4**, 91–108.

[30] Hama, F. R., 1954, "Boundary Layer Characteristics for Smooth and Rough Surfaces," Soc. Nav. Archit. Mar. Eng., Trans., **63**, pp. 353–358.

[31] Seo, J., 2003, "Investigation of the Upstream Conditions and Surface Roughness in Turbulent Boundary Layer," Ph.D. thesis, Rensselaer Polytechnic Institute, New York.

[32] Seo, J., and Castillo, L., 2004, "Rough Surface Turbulent Boundary Layer: The Composite Profiles," *AIAA 2004-1287*, *42nd AIAA Aerospace Sciences Meeting and Exhibit*, 5–8 Jan., Reno, Nevada.

[33] Kotey, N. A., Bergstrom, D. J., and Tachie, T. F., 2003, "Power Law for Rough Wall Turbulent Boundary Layer," Phys. Fluids, **15**, 1396–1404.

[34] Flack, K. A, Schultz, M. P., and Shapiro, T. A., 2005, "Experimental Support for Townsend's Reynolds Number Similarity Hypothesis on Rough Walls," Phys. Fluids, **17**, p. 035102.

[35] George, W., Castillo, L., and Knecht, P., 1996, "The Zero Pressure Gradient Turbulent Boundary Layer," *Technical Report TRL-153* Turbulence Research Lab., State University of New York at Buffalo.

[36] Colebrook, C. F., 1939, "Turbulent Flow in Pipes With particular Reference to the Transition Region Between the Smooth and Rough Pipe Laws," Proc. Inst. of Civ. Eng. (UK), **11**, pp. 133–156.

[37] Moody, L. F., 1944, "Friction Factor for Pipe Flow," Trans. ASME, **66**, pp. 676–684.

[38] Zagarola, M. V., and Smits, A. J., 1998, "Mean Flow Scaling in Turbulent Pipe Flow," J. Fluid Mech., **373**, 33–79.

[39] Smith, D. W., and Walker, J. H., 1958, "Skin Friction Measurements in Incompressible Flow," *NACA TN* 4231.

[40] Zanoun, E. S., Durst, F., and Nagib, H., 2003, "Evaluating the Law of the Wall in Two Dimensional Fully Developed Turbulent Channel Flow," Phys. Fluids, **15**, pp. 3079–3089.

[41] Tennekes, H., 1968, "Outline of a Second Order Theory of Turbulent Pipe Flow," AIAA J., **6**, pp. 1735–1740.

[42] Afzal, N., and Yajnik, K., 1973, "Analysis of Turbulent Pipe and Channel Flow at Moderately large Reynolds number," J. Fluid Mech., **61**, pp. 23–31.

[43] Afzal, N., 1976, "Millikan's Argument at Moderately Large Reynolds Numbers," Phys. Fluids, **19**, pp. 600–602.

[44] Antonia, R. A., and Krogstad, P.-A., 2001, "Turbulence Structure in Boundary Layer Over Different types of Surface Roughness," Fluid Dyn. Res., **28**, pp. 139–157.

[45] Afzal, N., 2005, "Power Law Velocity Profile in a Turbulent Boundary Layer on Transitional Rough Walls," in preparation.

[46] Guo, J., 2001, "Discussion on 'A Simple Method of Measuring Shear Stress on Rough Boundaries,'" J. Hydraul. Res., **39**, pp. 445–226.

[47] Cebeci, T., 2004, *Analysis of Turbulent Flows*, Elsevier, New York.

[48] Afzal, N., and Seena, A., 2005, "Alternate Scales for Turbulent Flow in Transitional Rough Pipes: Universal Log laws," in prepartion.

[49] Afzal, N., 2005, "Alternate Scales for Turbulent Boundary Layers on Transitional Rough Walls: Universal Log Laws," in preparation.

Anisotropy-Invariant Mapping of Turbulence in a Flow Past an Unswept Airfoil at High Angle of Attack

N. Jovičić

M. Breuer[1]

J. Jovanović

e-mail: breuer@lstm.uni-erlangen.de

Institute of Fluid Mechanics,
University of Erlangen-Nürnberg,
D-91058 Erlangen, Germany

Turbulence investigations of the flow past an unswept wing at a high angle of attack are reported. Detailed predictions were carried out using large-eddy simulations (LES) with very fine grids in the vicinity of the wall in order to resolve the near-wall structures. Since only a well-resolved LES ensures reliable results and hence allows a detailed analysis of turbulence, the Reynolds number investigated was restricted to $\mathrm{Re}_c = 10^5$ *based on the chord length c. Admittedly, under real flight conditions* Re_c *is considerably higher (about* $(35-40)\cdot 10^6$*). However, in combination with the inclination angle of attack* $\alpha = 18$ *deg this* Re_c *value guarantees a practically relevant flow behavior, i.e., the flow exhibits a trailing-edge separation including some interesting flow phenomena such as a thin separation bubble, transition, separation of the turbulent boundary layer, and large-scale vortical structures in the wake. Due to the fine grid resolution applied, the aforementioned flow features are predicted in detail. Thus, reliable results are obtained which form the basis for advanced turbulence analysis. In order to provide a deeper insight into the nature of turbulence, the flow was analyzed using the invariant theory of turbulence by Lumley and Newman (J. Fluid Mech.,* ***82****, 161–178, 1977). Therefore, the anisotropy of various portions of the flow was extracted and displayed in the invariant map. This allowed us to examine the state of turbulence in distinct regions and provided an improved illustration of what happens in the turbulent flow. Thus, turbulence itself and the way in which it develops were extensively investigated, leading to an improved understanding of the physical mechanisms involved, not restricted to a standard test case such as channel flow but for a realistic, practically relevant flow problem at a moderate Reynolds number.* [DOI: 10.1115/1.2175162]

1 Introduction

Turbulence is one of rare unsolved problems in fluid mechanics. Despite major efforts put into its investigation, we are still far from understanding the full mechanisms involved. This includes in particular the way in which turbulence evolves from initial disturbances in laminar flows, which commonly is denoted the transition process. Applying novel experimental techniques, numerical simulations or theoretical considerations, numerous contributions have been made to shed more light on the transition process and the structure of turbulence in general. It is universally accepted that the transition in a boundary layer starts with the amplification of initially two-dimensional instability waves called *Tollmien-Schlichting* (TS) waves. Then, by the development of three-dimensional structures, streamwise vortical structures are formed from which strong shear layers arise. Finally, turbulent spots originate and subsequently they merge into a fully developed turbulent region [1]. Transition observed in laminar separation bubbles basically follows the scenario described above. However, initial disturbances leading to instabilities in the separated shear layer are more strongly amplified than the corresponding ones in a boundary layer. Hence, in such a case the transitional region is considerably shorter. In addition, the transition process in a separation bubble is influenced by *feedback interactions*, i.e., the flow in the reattachment region has an impact on the upstream portions of the pre-separated flow [2]. In recent years, extensive direct numerical simulations (DNS) of the transition process in the boundary layer for the flow over a flat plate both with and without separation bubbles have been performed, e.g., by Meyer et al. [3], Kloker and Stemmer [4] and Lang et al. [5]. In these simulations, controlled two-dimensional disturbances (TS waves) were introduced which triggered the transition process. Hence this procedure allowed the analysis of the transition scenario starting from well-defined initial conditions. Furthermore, several studies (see, e.g., Ducros et al. [6] or Huai et al. [7]) have confirmed that accurate predictions of transition to turbulence are also possible based on the large-eddy simulation (LES) technique. Assuming that an appropriate subgrid scale model such as a dynamic model or a filtered-structure-function model is applied, the same flow physics can be captured at a significant fraction of the DNS cost. However, these LES predictions [6,7] have in common with the DNS cases mentioned above, that some kind of upstream forcing is applied to trigger the transition process.

The present paper is concerned with a different strategy. Transition to turbulence under a strong adverse pressure gradient is allowed to happen naturally, i.e., without applying any forcing. For the flow past a highly inclined airfoil (without leading-edge stall), transition normally occurs in combination with a separation bubble. Thus, by adequately resolving the bubble using the LES technique, the transition process for this practically relevant flow can be observed and analyzed. Furthermore, the present investigations were aimed at improving the understanding of various types of turbulence states appearing in different regions of the flow. These include the attached turbulent boundary layer, the free shear layer, the recirculation region and the wake. On the one hand, the available computing power for numerical investigations is ever increasing, providing a solid basis for scientific work. On

[1]Corresponding author.

Contributed by the Fluids Engineering Division of ASME for publication in the JOURNAL OF FLUIDS ENGINEERING. Manuscript received February 17, 2005; final manuscript received October 21, 2005. Assoc. Editor: Ugo Piomelli.

the other hand, theoretical methods have existed for a fairly long time which have barely been exploited to their full extent. One example is the anisotropy-invariant theory which was developed by Lumley and Newman [8] and Lumley [9] in the 1970s. By looking at the anisotropy of a turbulent flow, different states of turbulence can be distinguished. At the same time, this permits a different view at turbulence, revealing additional information which cannot be observed in real (or physical) space.

In the recent literature, there are some contributions on the application of anisotropy-invariant theory to extend the knowledge of turbulent flows. Antonia et al. [10] have provided for the first time detailed evaluations of anisotropic properties of the small-scale structure of turbulence by plotting trajectories of invariants across the anisotropy invariant map using the databases of direct numerical simulations of turbulent channel flows. Seidl [11] evaluated the anisotropy tensor for the flow past a sphere to quantify the deviation from isotropy. He demonstrated that completely different scenarios exist through the map even for small separations in physical space. Krogstad and Torbergsen [12] analyzed the anisotropy invariants in a turbulent pipe flow. They found that the turbulence in the core region of the pipe flow was close to the axisymmetric state and that it asymptotically approaches the two-component state in close proximity to the wall, i.e., turbulence was found to develop along the boundaries of the anisotropy map. Analyzing turbulent channel flows with respect to the anisotropy in the flow, Fischer et al. [13] have gained improved insights into the dynamics of turbulence in the near-wall region. Schenck and Jovanović [14] investigated the state of turbulence in plane and axisymmetric wake flows. In both wakes, turbulence was close to isotropy and deviated only moderately from the axisymmetric state. With the intention of treating the transition process in a flat plate boundary layer using statistical tools, Jovanović and Pashtrapanska [15] applied the invariant theory to obtain closure for the transport equations of the disturbances and derived the criterion for the onset of transition valid for two-component disturbances.

Applying the anisotropy-invariant theory to well-resolved LES allows us to study the mechanisms of turbulence for a realistic flow problem of practical interest in more detail. Understanding the *mechanisms* of turbulence is the first step towards *controlling* them. Knowing *why* transition takes place provides us with information about what can be done to *avoid* it. Thus, exploiting both the increased possibilities of numerical simulation and advanced theories can lead to improvements in numerous applications.

2 Anisotropy-Invariant Theory

Lumley and Newman [8] and Lumley [9] found that the state of turbulence can be characterized by the amount of anisotropy that prevails in the flow. The anisotropy of a flow can be derived from the Reynolds stresses $\tau_{ij}=-\rho\overline{u_i u_j}$ by subtracting the isotropic part from τ_{ij} and normalizing with $\tau_{ss}=-\rho\overline{u_s u_s}$. This leads to the nondimensional anisotropy tensor

$$a_{ij}=\frac{\overline{u_i u_j}}{2k}-\frac{1}{3}\delta_{ij}, \tag{1}$$

with turbulent kinetic energy $k=\frac{1}{2}\overline{u_s u_s}$ and Kronecker delta δ_{ij}. The tensor a_{ij} has three scalar invariants:

$$a_{ii}=0, \quad \mathrm{II}_a=a_{ij}a_{ji}, \quad \mathrm{III}_a=a_{ij}a_{jk}a_{ki}. \tag{2}$$

By cross-plotting II_a and III_a, the state of turbulence in a flow can be displayed with respect to its anisotropy. If the scalar invariants II_a and III_a are evaluated for the case of a two-component turbulence (one component of the velocity fluctuations is negligibly small compared with the other two), this leads to

$$\mathrm{II}_a=\tfrac{2}{9}+2\mathrm{III}_a. \tag{3}$$

Doing the same for the axisymmetric turbulence (two components are equal in magnitude) yields

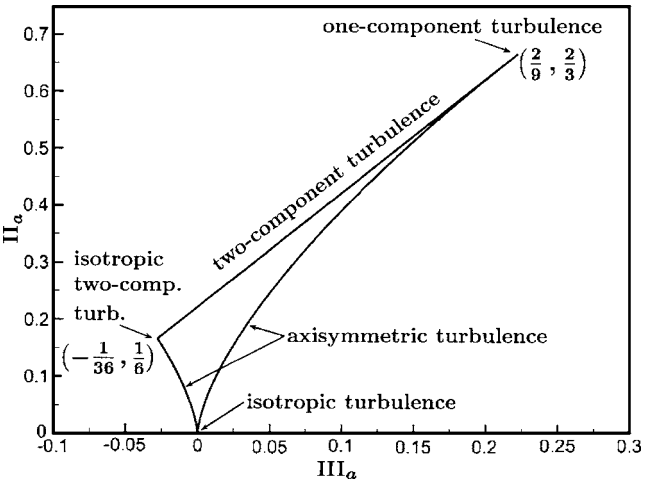

Fig. 1 Invariant map according to Lumley and Newman [8]

$$\mathrm{II}_a=\tfrac{3}{2}\left(\tfrac{4}{3}|\mathrm{III}_a|\right)^{2/3}. \tag{4}$$

Hence if relations (3) and (4) are cross-plotted, as is done in Fig. 1, they define a narrow region called the *anisotropy-invariant map*. It can be shown that all physically realizable turbulence has to lie within this small region [9]. However, different states of turbulence are represented by different parts of the map.

The boundaries of the invariant map describe the limiting states of turbulence. Isotropic turbulence is found at the lower corner point of the map (the origin in Fig. 1) where $\mathrm{II}_a=\mathrm{III}_a=0$, hence the anisotropy is zero. The left branch of the map ($\mathrm{III}_a<0$) describes axisymmetric turbulence in which one component of the velocity fluctuations is smaller than the other two. In the literature, this is sometimes referred to as "pancake" type of turbulence. The simplest example of this type is the passage of grid turbulence through axisymmetric contraction. In contrast, the axisymmetric turbulence on the right side ($\mathrm{III}_a>0$) is characterized by one fluctuating component which dominates over the other two. This, for example, holds for grid turbulence through axisymmetric expansion and is called "cigar"-like turbulence. The remaining boundary line on top of the map is the limiting case of a two-component turbulence (see Eq. (3)) as it can be found in the direct vicinity of walls (viscous sublayer). Here, the wall-normal component of the velocity fluctuations is tending towards zero, leaving only the wall-parallel components. The corner point on the left-hand side of the anisotropy-invariant map represents a turbulence state in which only two fluctuating components of equal intensity exist. This state is called two-component isotropic turbulence. Finally, the top end of the map describes one-component turbulence, which consists merely of one fluctuating component.

Hence the bounding states of turbulence of the invariant map are well defined. Based on the results of numerical simulations and experimental investigations on such kinds of turbulent flows following the bounds of the map, Jovanović [16] was able to formulate complete turbulence closure for all unknown correlations in the transport equations of the turbulent stresses and for all limiting states of turbulence.

3 Flow Configuration and Results

3.1 Configuration. The flow configuration considered is according to the experimental setup of Lerche and Dallmann [17] in which an unswept airfoil based on a NACA-4415 profile is mounted inside a plane channel of height 3 c (c= chord length). In Fig. 2(a) the configuration investigated ($\alpha=18$ deg; $\mathrm{Re}_c=u_\infty\cdot c/\nu=10^5$) is shown schematically. Upstream and downstream of the airfoil the channel has a length of $2c$ and $3c$, respectively. In order to exclude the unknown effect of any wall function, no-slip and

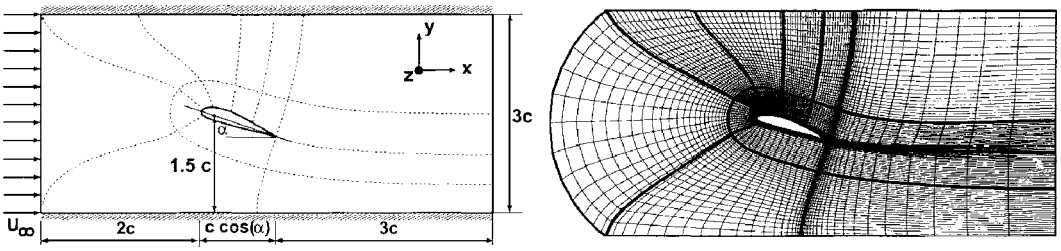

Fig. 2 (a) Two-dimensional sketch of the geometric configuration including block boundaries (thick lines) and (b) *x–y* plane of the grid (only every 5th grid line of the coarser grid is shown)

impermeability conditions are employed at the surface of the airfoil. To save grid points, the channel walls are approximated by slip conditions. The experimental setup was designed to yield a flow field whose statistical quantities are independent of the spanwise coordinate. Therefore, periodicity in the spanwise direction is assumed and a spanwise computational domain of depth $z_{\max}=1.0c$ is chosen based on a detailed investigation for the flow around an inclined flat plate [18]. At the inlet of the computational domain a constant velocity u_∞ is prescribed, whereas at the outlet of the computational domain a convective boundary condition is applied [19,20].

The numerical simulations were carried out based on the large-eddy simulation approach. The LES code *LESOCC* is based on a 3D finite-volume method for arbitrary nonorthogonal and non-staggered grids [19–21]. It is highly vectorized and additionally parallelized. The simulations were carried out on a Hitachi SR8000-F1 SMP system with a sustained performance of about 40.9 GFlops on 16 SMP nodes. The spatial discretization of all fluxes is based on central differences of second-order accuracy. As shown in Ferziger and Perić [22] the order of accuracy of this scheme is retained on nonuniformly distributed grids for mild expansion factors (e.g., $\Delta x_{i+1}/\Delta x_i \lesssim 1.05$) as used in the present study. A low-storage, multi-stage Runge-Kutta method (second-order accurate) was applied for time-marching. For modeling the nonresolvable subgrid scales the dynamic approach of Germano et al. [23] and Lilly [24] was taken into account. Hence the subgrid scales are modeled by a Smagorinsky model [25] where the Smagorinsky value is computed dynamically as a function of space and time based on the resolved flow field. In order to stabilize the dynamic model, averaging of the numerator and the denominator in the relation for the determination of the Smagorinsky value [23,24] was carried out in the spanwise homogeneous direction and also in time using a recursive digital low-pass filter [19–21].

The simulations were performed using a block-structured C-type grid consisting of 16 blocks with about 16.23 million control volumes (CVs) in total, whereas 100 CVs were taken along the spanwise direction. At the wing profile 490 CVs were used in tangential direction, of which 360 CVs are located at the upper side of the airfoil. A vertical cross section through the grid together with the block boundaries is displayed in Fig. 2(*b*). Large efforts were made to ensure a high grid quality, e.g., mild expansion factors as mentioned above and high grid orthogonality and smoothness. The grid points are clustered in the vicinity of the airfoil and at the leading and trailing edges. The height of the first layer of CVs along the airfoil surface was about $\Delta y/c=0.0005$. This corresponds to $y^+\approx 1.5$ in the region close to the airfoil nose at the upper side of the airfoil and at the entire lower side. The remaining part of the upper side yields $y^+<1$. In the direction parallel to the airfoil surface the grid resolution yields $x^+\approx 15$ and $x^+\approx 90$ on the upper and lower side of the airfoil, respectively.

A dimensionless time step $\Delta t=8\cdot 10^{-5}$ was chosen where the time is normalized by the ratio of the chord length and the free-stream velocity, c/u_∞. The time-averaged results are based on averaging intervals of at least 80 dimensionless time units and additional averaging in the spanwise direction. A careful validation procedure was carried out for the computational results, including a direct comparison with airfoil predictions of another group applying a completely different numerical approach and grid [26]. Very good agreement was found for that case, providing confidence in the present results.

Furthermore, to justify the present grid resolution, it is compared with previous LES predictions. In [27] the flow around a circular cylinder at $\mathrm{Re}=140,000$ was studied in detail. Two grids were applied, i.e., with $165\times 165\times 64$ and $325\times 325\times 64$ nodes leading to a resolution in the 2D plane of about 27,000 and 105,000 grid points, respectively. Hence although the Reynolds number was a factor of 1.4 higher than in the present case, even the fine grid applied less grid points in the 2D plane (and also in the spanwise direction) than used in the present case. Additionally, the height of the first layer of CVs along the surface was $\Delta y/c=4\times 10^{-4}$ whereas in the present case a comparable size was used on the grid with 16.23 million CVs. In the case of the cylinder flow even the coarser grid delivered reliable results in close agreement to the experimental measurements.

In [28] the flow around an airfoil close to stall was studied by LES at $\mathrm{Re}=2\times 10^6$. Although the Reynolds number is a factor of 20 larger than in the present investigation, a cross-sectional resolution of about 176,000 nodes was used which is of comparable size as the present one tackling $\mathrm{Re}=10^5$. Nevertheless, the authors [28] claim that the transition mechanism has been captured. Based on the results of these studies an additional justification of the present resolution is achieved.

Finally, it should be noted that enormously high resolution are not required for the interpretation of the results of interest; qualitative but not quantitative insights are important at first place. Grid refinement and especially high resolution near the wall are important in a part of the domain where a fully developed turbulent state is expected; in the transitional region the spatial resolution requirements are less critical.

3.2 Flow Results. Under the conditions considered, the flow past the airfoil yields a trailing-edge stall including some interesting flow features. As can be seen from the time-averaged flow field in Fig. 3, the oncoming flow hits the airfoil and initially a very thin laminar boundary layer evolves. At the airfoil nose the flow is strongly accelerated (see C_p distribution in Fig. 4). Shortly after, the boundary layer separates owing to the strong adverse pressure gradient followed by an immediate transition to turbulence in the shear layer close to the wall. Thus, the turbulent flow reattaches and a closed (short) separation bubble is formed (see [5]). Despite the still existing adverse pressure gradient, the turbulent boundary layer remains attached until at approximately 65% of the chord length c a recirculation region emerges rotating in a clockwise direction.

In order to validate the results of the present investigation, they were compared both with results obtained on a refined grid with about $23\cdot 10^6$ CVs (132 in spanwise direction) and experimental data at the same flow conditions [29]. For the refined grid the

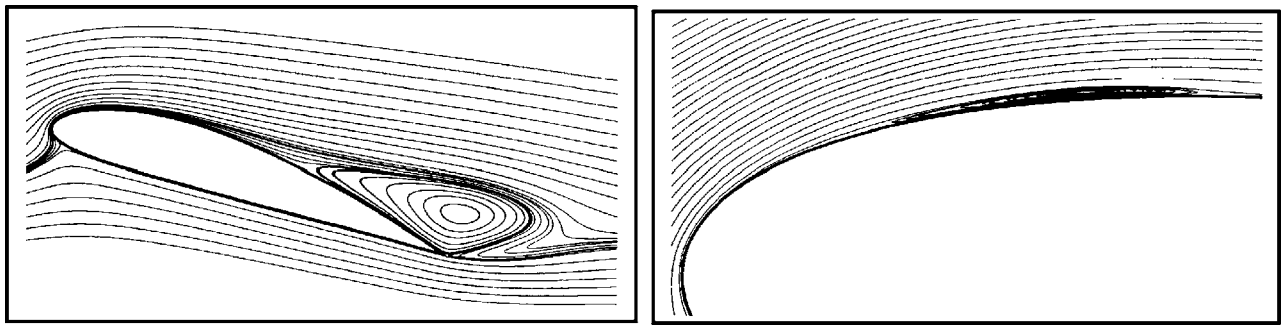

Fig. 3 Streamlines of the time-averaged flow field (left) and a zoomed airfoil nose region (right); $Re_c=10^5$, $\alpha=18$ deg, $16.23\cdot10^6$ CVs

height of the first layer of CVs along the airfoil surface was about $\Delta y/c=0.00025$, i.e., it was halved compared to the grid with about 16.23 million CVs. As can be seen from Fig. 5 in comparison with Fig. 3, similar findings are observed in all three cases. However, from the experimental data the recirculation zone at the trailing edge is slightly more elongated compared to that of the predicted results.

Furthermore, to provide a quantitative comparison of the simulated results and the experimental measurements, profiles of the tangential velocity at three positions along the airfoil and one in the wake, respectively, are presented in Fig. 6. The velocities are normalized by the undisturbed velocity u_∞ and the coordinates by the chord length c, respectively. Overall, the results are in very good agreement, although minor deviations exist. From the profiles at the locations $x'/c=0.6$ and $x'/c=0.8$ (The coordinate x' is aligned with the chord starting at the nose.) it is obvious that the flow separation on the refined grid is slightly shifted upstream compared with the results of the present investigation. The largest discrepancy between the predicted results and the experiment is found in the wake of the airfoil. However, since both predictions agree quite well, this strengthens the confidence in the simulated results.

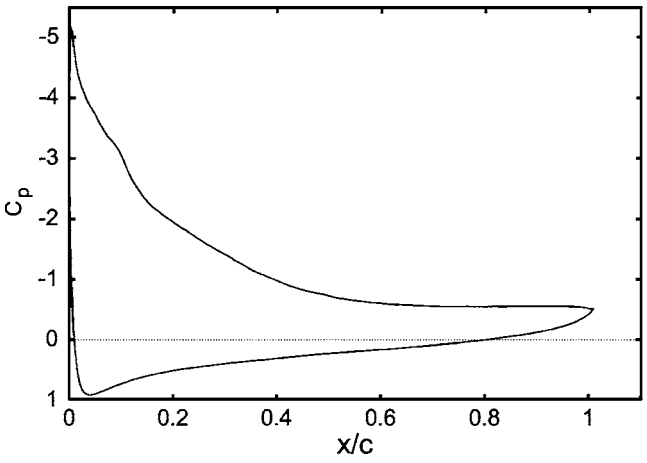

Fig. 4 Distribution of the pressure coefficient $C_p=(p-p_\infty)/(0.5\rho_\infty u_\infty^2)$ of the time-averaged flow; $Re_c=10^5$, $\alpha=18$ deg

In contrast to a previously computed case at $Re_c=20,000$ [26,30], in the present case no dominating trailing-edge vortices and no asymmetric shedding motion including a corresponding Strouhal number could be observed. The boundary layer at the leeward side remains attached along a large portion of the chord and consequently the flow field does not show typical flow features observed in bluff-body configurations.

The leading-edge separation bubble shown in Fig. 3 is an extremely shallow feature. However, it is strongly connected to the transition process. Naturally, instabilities in the separated shear layer which originates at the airfoil nose are strongly amplified, leading to a laminar flow breakdown. As a result, a transitional region occurs in the shear layer still close to the wall. The turbulent flow reattaches and traps some fluid into a small recirculation region (separation bubble).

This kind of transition to turbulence in separation bubbles is often observed in flows past airfoils. However, owing to the extremely small extensions of such bubbles, they are difficult to investigate both numerically and experimentally. Hence, in order to allow accurate predictions and analysis, the near-wall region has to be resolved well by a large number of control volumes. In the present predictions, the bubble itself with a thickness of about $\Delta y/c=0.00323$ was covered by at least six or twelve control volumes on the grids with about 16 and 23 million CVs, respectively, which obviously was enough to capture this feature.

Consequently, the present simulation results allow one to investigate the transition process (without any forcing) for a flow configuration of practical interest. Since the transition itself is not yet fully understood, it is also not clear whether the forcing mecha-

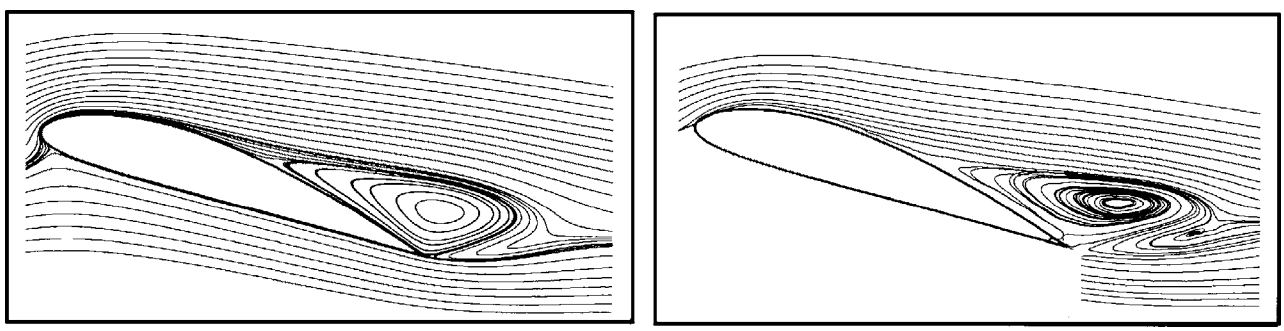

Fig. 5 Streamlines of the time-averaged flow field obtained on a refined grid with about $23\cdot10^6$ control volumes (left) and from experimental investigations [29] (right), $Re_c=10^5$, $\alpha=18$ deg

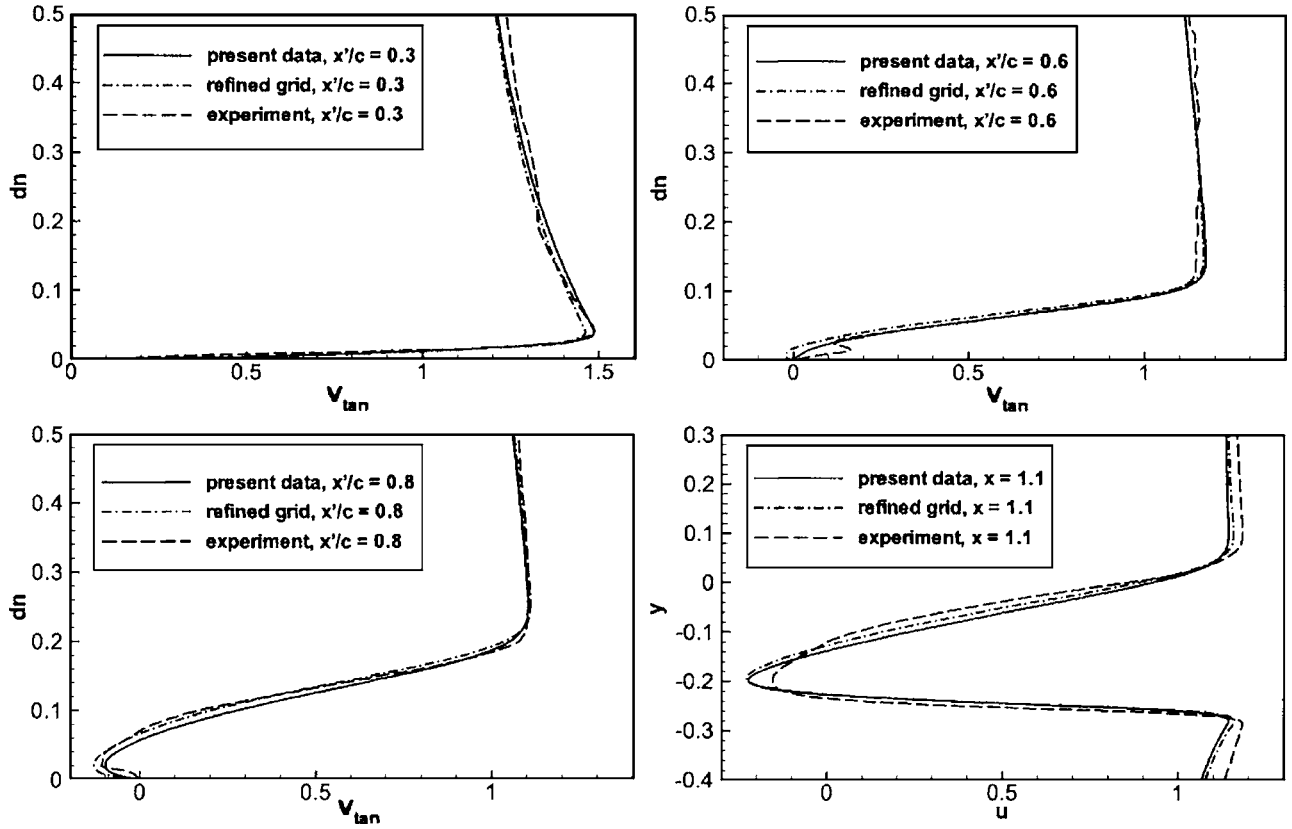

Fig. 6 Profiles of the tangential velocity at three different locations along the airfoil and one in the wake, present data, refined grid simulation and experimental data [29], $Re_c=10^5$, $\alpha=18$ deg (x' is aligned with the chord starting at the nose. *dn* denotes the wall-normal distance from the airfoil. The velocities are normalized by the undisturbed velocity u_∞ and the coordinates by the chord length *c*, respectively.).

nisms often applied in transition research influence this process. Although in the present simulation the flow is well resolved in wall-normal and mean-flow directions, admittedly this might not sufficiently be the case in the spanwise direction ($z^+ \approx 20-60$). However, owing to the high inclination angle in the present study, an adequate lateral domain size is also important to allow unconstrained development and movement of the largest structures in the flow. Hence, a compromise between spanwise resolution and domain size had to be found [18]. Nevertheless, the present results yield some interesting insights into the transition process which help to improve the physical understanding.

The relative importance of the airfoil nose region also becomes evident in the distribution of the turbulent kinetic energy k normalized by u_∞^2 which is depicted in Fig. 7. Additionally, in Fig. 8 the distribution of the most important Reynolds stress components $\overline{u'u'}$, $\overline{v'v'}$, $\overline{w'w'}$, and $\overline{u'v'}$(again normalized by u_∞^2) are shown in order to provide information about the magnitude of these components. The highest values of k are found in the region where transition takes place and the separation bubble appears. This indicates that turbulence is heavily generated there. This observation is strongly supported by animations of the flow field in the vicinity of the nose region. Furthermore, increased values of the turbulent kinetic energy exist in the turbulent boundary layer downstream of the bubble, in the free shear layer of the separated turbulent boundary layer and in the wake of the airfoil. Since turbulence plays a significant role in these regions, it is important to improve the understanding of its physical mechanisms. Therefore, the turbulence states in various parts of the flow were analyzed and are interpreted in the following section.

4 Anisotropy-Invariant Mapping of the Flow Field

In order to investigate the turbulent flow in more detail, the results were analyzed according to the invariant theory. Based on the resolved Reynolds stresses, the invariants II_a and III_a of the anisotropy tensor a_{ij} were evaluated. This was done for the com-

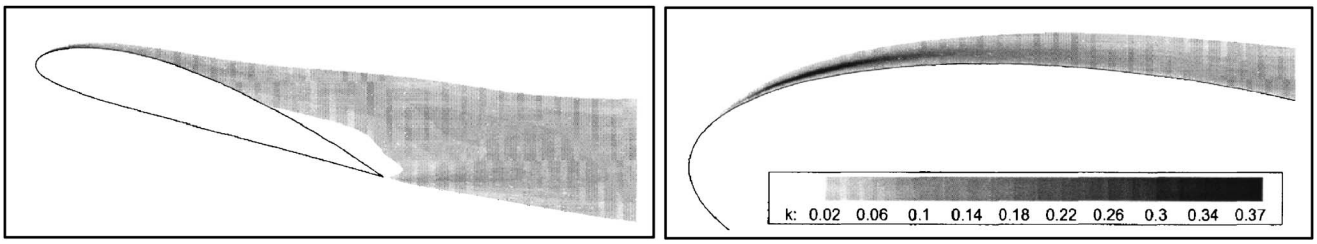

Fig. 7 Distribution of the resolved (nondimensional) turbulent kinetic energy *k*; $Re_c=10^5$, $\alpha=18$ deg. *k* is normalized by the square of the undisturbed velocity u_∞.

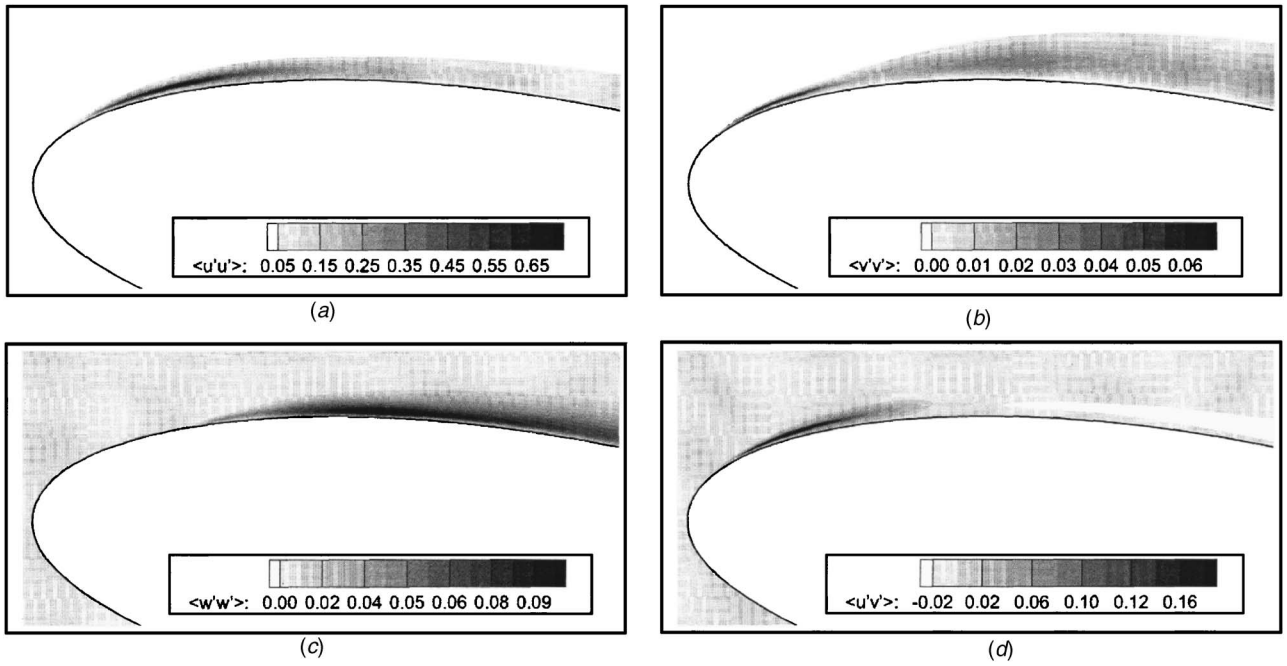

Fig. 8 Distribution of the resolved Reynolds stresses (a) $\overline{u'u'}$ (b) $\overline{v'v'}$ (c) $\overline{w'w'}$ and (d) $\overline{u'v'}$, Re_c=100,000 and α=18 deg. The stresses are normalized by the square of the undisturbed velocity u_∞.

plete flow field, thus allowing the analysis of the development of the anisotropy of turbulence across the anisotropy-invariant map.

In Fig. 9 a large region enclosing the airfoil including the entire flow field of interest is plotted into the invariant map. As can be seen, almost the entire map is covered. This demonstrates the complexity of the investigated flow and also indicates that nearly all possible states of turbulence occur. At the same time, this explains why most of the turbulence models used in the Reynolds-averaged Navier-Stokes approach (RANS), such as the standard k-ϵ model, fail to predict complex separated flows. The majority of these statistical models were developed to function for nearly isotropic turbulence and can handle anisotropic flows, e.g., close to walls, only by either the use of wall functions or special low-Re variants. Thus, a flow such as that investigated here with huge variations of the anisotropy of turbulence shown in Fig. 9 cannot be predicted well based on simplified statistical models.

Since in wall-bounded flows turbulence is generated close to the walls, this flow region is of particular interest. Therefore, a thin layer away from the airfoil surface (up to $y^+ \approx 40$), shown in Fig. 10, was examined in more detail. After the flow attaches the airfoil, first a thin accelerated laminar boundary layer develops in the region marked A. The anisotropy in this portion of the flow corresponds to the upper part of the invariant map, as can be seen from Fig. 10(*A*). However, as visible in Fig. 8 the Reynolds stresses are extremely small in the vicinity of the stagnation point and thus the scalar invariants predicted have to be dealt with great care. Nevertheless, a closer examination of the instantaneous flow field reveals that the velocity fluctuations leading to anisotropies covering this particular part of the anisotropy map do not give rise to any transition or breakdown to turbulence. Analyzing region B where the separation bubble is observed and transition takes place, leads to the trace in the anisotropy-invariant map shown in Fig. 10(*B*). Large parts of the invariant map are covered, reaching from the one-component limit at the right-hand corner of the map to the two-component isotropic turbulence located at the left-hand corner. In the accelerated flow region covering the front part of the separation bubble, the turbulence state is highly anisotropic and corresponds to the portion of the map close to the one-component limit. Further downstream within region B, the decelerated flow separates and forms a free shear layer in which instabilities are observed. Owing to these instabilities, the flow undergoes transition to turbulence and subsequently reattaches to the airfoil sur-

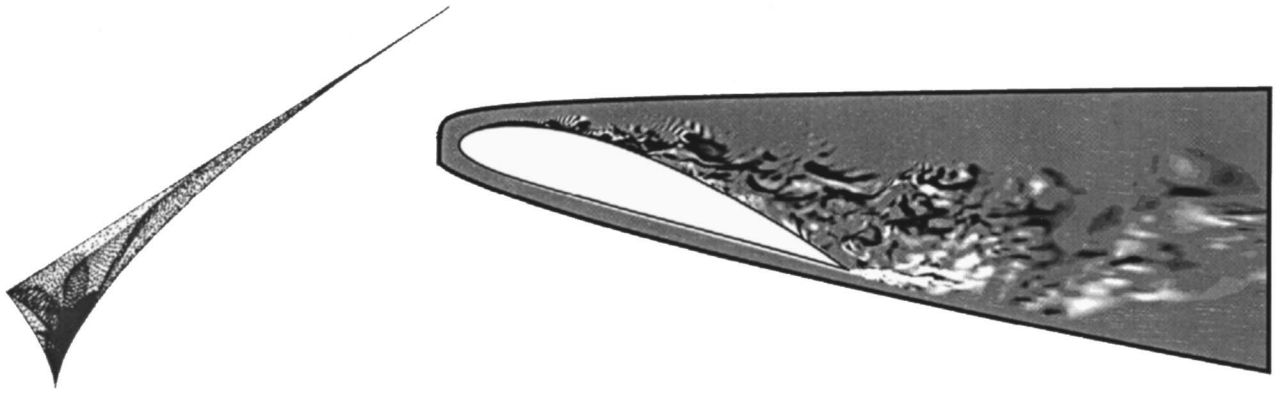

Fig. 9 Anisotropy-invariant map of the whole flow region of interest

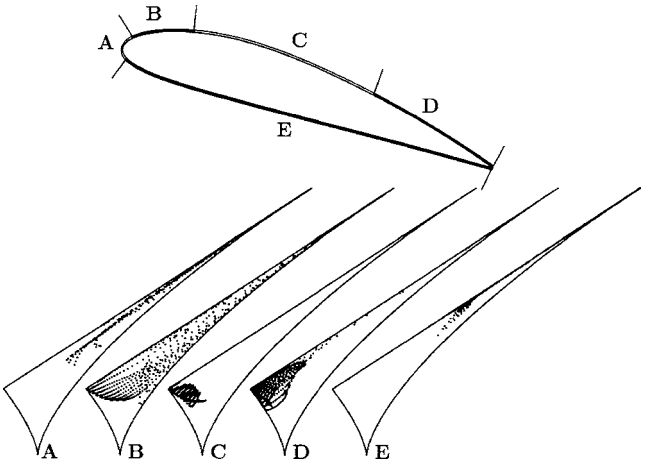

Fig. 10 Anisotropy-invariant mapping of turbulence in the near-wall region of the flow past an airfoil at high angle of attack

face. In the invariant map, this flow behavior is rendered by anisotropies moving away from the one-component turbulence and reaching the region close to its left corner point. This part of the map represents a state which is highly unstable and tends to produce turbulence very rapidly. Hence the trajectory of the invariants in the map which corresponds to the flow region designated (B) spans from the region in the map where no generation of turbulence was detected to highly unstable regions where transition and breakdown to turbulence occurred. Hence, between the one-component turbulence and the two-component isotropic turbulence there must be a threshold value which quantifies the transition process from the stable laminar state towards the unstable turbulent state. In the authors' opinion, each transitional flow will exhibit an invariant-map behavior such as that shown in Fig. 10(*B*) with large variation of anisotropy. Moreover, it is remarkable how strongly the nature of turbulence can differ, even for a very restricted portion of the flow. This clearly demonstrates the difficulties in predicting transitional flows.

Downstream of the separation bubble an attached turbulent boundary layer is formed. Plotting the invariants II_a and III_a corresponding to the region C into the invariant map yields the distribution of anisotropies displayed in Fig. 10(*C*). Although a relatively large physical region is represented, only a comparably small part close to the isotropic two-component limit of the map is covered. This is contrary to the previously analyzed region of the separation bubble. It may indicate some sort of self-similarity in the turbulent boundary layer with respect to the anisotropy.

The near-wall region close to the trailing edge of the airfoil, where a flow recirculation region exists, comprises the anisotropies depicted in Fig. 10(*D*). This flow region occupies the part of the map close to the isotropic two-component turbulence, whereas most of the anisotropies lie very close to the boundaries of the map.

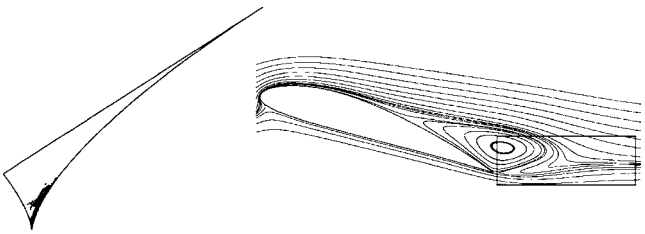

Fig. 11 Anisotropy-invariant mapping of the near-wake region close to the trailing edge of the airfoil

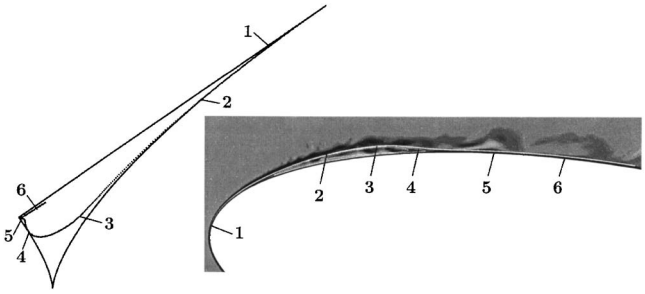

Fig. 12 Anisotropy-invariant mapping of the transitional flow region at the airfoil nose where the separation bubble is formed: Certain locations along the streamline (thick white line) are marked together with their corresponding positions in the invariant map (grid: 23 million CVs)

At the pressure side of the airfoil shown in Fig. 10(*E*), an accelerated laminar boundary layer exists with some fluctuations of low amplitude. Owing to the flow acceleration, these fluctuations are highly anisotropic and cover upper portions of the invariant map (Fig. 10(*E*)). These fluctuations cannot be amplified and the flow at the pressure side of the airfoil remains laminar.

Apart from the near-wall region, the wake region is also of great interest. Therefore, the region enclosed by the rectangle in Fig. 11 was evaluated in terms of anisotropy and traced across the map. The flow in this region is slightly anisotropic. In some parts of the rectangle where the flow from above the airfoil and that from below interact, the flow is even perfectly isotropic. Turbulence at locations in the rectangular region which deviates from the isotropic state tends to be of axisymmetric type belonging to the right branch of the map where one fluctuating component dominates over the other two. Similar findings were reported by Schenck and Jovanović [14], who experimentally investigated the turbulence in the plane wake behind a cylinder. They observed that turbulence in the centerline region of a plane wake deviates marginally from the axisymmetric state with $III_a > 0$.

In order to understand more precisely the dynamics of turbulence for this flow field, the results were also analyzed by animating states of turbulence in the anisotropy-invariant map. Therefore, animations were created, displaying the development of turbulence in various regions of the flow field.[2] The most interesting flow feature was the transition to turbulence occurring in the region of the separation bubble close to the airfoil nose. Hence this portion of the flow was animated in such a way that streamwise positions in the physical space were subsequently transferred into the invariant space defined by the anisotropy map. Thus, the different states of turbulence which are observed along the streamwise direction in the transitional flow region can be followed in the map. This provides a hint into the *dynamic* process associated with transition and leads to an alternative scenario which can contribute to an improved understanding of its mechanisms.

Figures 12 and 13 show the states of anisotropy in the transitional flow region close to the airfoil nose evaluated along a streamline of the averaged flow, which is located approximately in the center of the shear layer. Figure 12 is based on the results obtained on the finer grid (23 million CVs) whereas Fig. 13 depicts the corresponding analysis using the results obtained on the coarser grid (16 million CVs). This is done in order to demonstrate, that qualitatively the same behavior in the development of the anisotropy states is observed for both grids. Additionally (for the fine-grid results only), in Fig. 14 the rms values of all fluctuating velocity components along the same streamline are provided

[2]On the web page www.lstm.uni-erlangen.de/~njovicic some of these animations representing the flow in the anisotropy-invariant map can be found.

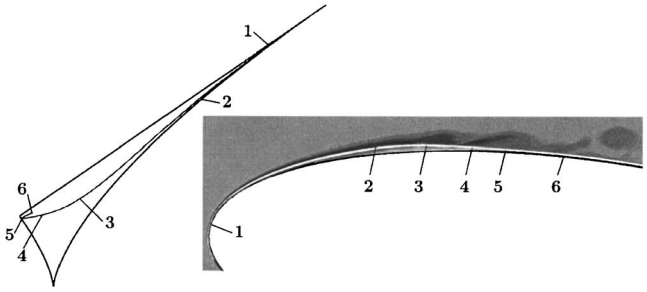

Fig. 13 Same as in Fig. 12, however, obtained on a coarser grid with approx. 16 million CVs

in order to support the explanations below. In a statistical sense the flow along this streamline represents the complete transition process, since regions of *laminar*, *transitional*, and *fully turbulent* flow are covered by it. As described earlier, the flow right after the leading edge of the airfoil is laminar. Fluctuations within this flow region (marked (1) in Figs. 12 and 13) appear at the upper part of the anisotropy-invariant map close the one-component limit which is the point of maximum anisotropy. Passing the airfoil nose, the flow soon separates forming a shear layer while it still remains laminar. Within the shear layer (2), the fluctuations are rapidly increasing. The corresponding states of anisotropy closely follow the right branch of the invariant map, which describes axisymmetric type of anisotropy, where one fluctuating velocity component is larger than the other two ($u'_{\mathrm{rms}} > v'_{\mathrm{rms}} \approx w'_{\mathrm{rms}}$, see Fig. 14).

Further downstream within the shear layer at the position denoted (3), the spanwise component w'_{rms} is particularly increased towards the level of u'_{rms} fluctuations. This is due to the development of three-dimensional disturbances in the shear layer. As a consequence, the anisotropy in the flow along this streamline is decreasing and thus moving towards the lower corner point of the invariant map. At position (3) the flow is highly unstable, however, not yet fully turbulent. At the same time, the anisotropy in the flow starts to deviate from the right border line of the map, since the constraints of axisymmetry are not longer valid. Instead of that, a situation arises where the individual fluctuating components are contributing to the turbulence production with different, however, considerable intensities ($u'_{\mathrm{rms}} > w'_{\mathrm{rms}} > v'_{\mathrm{rms}}$). At position (4), where the averaged flow reattaches to the airfoil surface, the flow is obviously turbulent, otherwise it would not have reattached at all. As can be seen from Fig. 14, the w'_{rms} fluctuation intensity has reached the level of u'_{rms} as it is usually observed in transitional flows. In the invariant map, the corresponding states

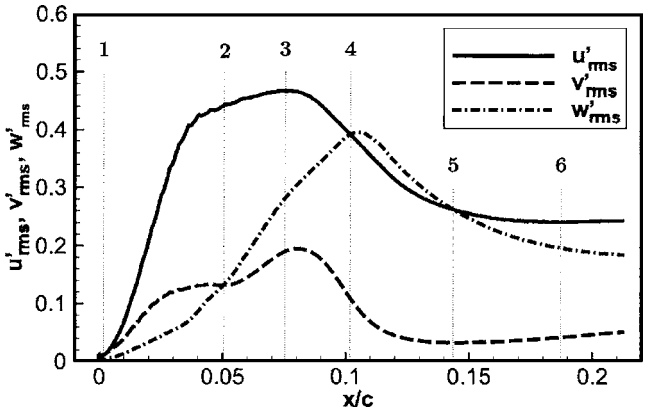

Fig. 14 Distribution of u'_{rms}, v'_{rms}, and w'_{rms} (normalized by the undisturbed velocity u_∞) as a function of streamwise position along the streamline shown in Fig. 12

of anisotropy are located very close to the left border of the map which describes an axisymmetrical type of turbulence where two fluctuating components are equal and the third one is smaller ($u'_{\mathrm{rms}} \approx w'_{\mathrm{rms}} > v'_{\mathrm{rms}}$). Since the flow is turbulent at (4) whereas it is not at (3), consequently transition to turbulence is observed in the anisotropy-invariant map somewhere between these two locations. Thus, the transition process is clearly connected to a strong decrease of anisotropy below a certain threshold value in the anisotropy-invariant map. It is of course difficult to specify an exact "line of transition" in the map for such a complex flow. However, Jovanović and Pashtrapanska [15] deduced a transition criterion for wall-bounded flows based on boundary layer and channel flow results.

Downstream of the reattachment point a turbulent boundary layer flow develops. The streamline along which the anisotropy is evaluated reaches rather close to the airfoil surface where the wall-normal component is small compared to the other two (see Fig. 14). Therefore, the anisotropy in the flow at the positions (5) and (6) is of two-component type of turbulence following closely the upper bound of the map.

The traces of anisotropy in the invariant maps depicted in Figs. 12 and 13, respectively, do obviously deviate. However, one has to bear in mind, that the evaluation of anisotropy in a turbulent flow is based on higher-order statistics, which are very sensitive with respect to many issues. This includes a possible grid dependency as well as differences in the exact positions of the streamtraces in the center of the respective shear layer. The most striking point is the way the anisotropy *develops* from a highly anisotropic state close to the one-component limit towards the left branch of the map. It is strongly believed that a similar behavior can be observed in other cases of transitional flows, too.

Thus, the process of laminar to turbulent transition can be analyzed by studying different states of turbulence in the anisotropy-invariant map. This provides a supplementary view of how to study these very complicated processes and how to support further investigations of this flow phenomenon.

5 Conclusions

The concept of LES strongly supports that the dynamics of the most important flow structures are captured accurately. This allowed advanced interpretation of transition and breakdown to turbulence using the tools of invariant theory. When applied to wall-bounded flows as in the present case the methodology requires to resolve all scales which are vitally contributing to the turbulent kinetic energy budget. Because in wall turbulence the important scales become relatively small compared with those in the outer layer, LES predictions have to rely on a very fine DNS-like grid in the vicinity of the wall to capture all these scales appropriately. However, overall the grid sizes used for LES are smaller than for DNS and thus the LES technique allows one to go beyond the limit of previous DNS studies.

In this study, a complex turbulent flow of practical relevance, namely the separated flow past an unswept wing, was tackled. At a Reynolds number $\mathrm{Re}_c = 10^5$ and angle of attack $\alpha = 18$ deg, a trailing-edge stall is observed. Consequently, the flow in the nose region is laminar only along a short distance. Thereafter, a tiny laminar separation bubble is formed which triggers the transition to turbulence. The turbulent boundary layer is able to resist the adverse pressure gradient over a long distance but finally separates, leading to a recirculation region in the vicinity of the trailing edge. Owing to the very fine grid applied, highly reliable results are obtained. The near-wall region was well resolved, thus allowing us to analyze the turbulence mechanisms there in more detail.

Turbulence in a flow can be characterized by the level of anisotropy. Various states of turbulence with a specific behavior exist in a flow and correspond to different parts of the anisotropy-invariant map. Hence, depending on the position in the map, a turbulent flow behaves differently. A very interesting insight into the transition phenomenon was found in this study by the repre-

sentation of the transition region in the invariant map. The transition process, when projected into the anisotropy-invariant map, starts initially from the one-component state and develops subsequently by decreasing the anisotropy in the velocity fluctuations as the flow approaches the fully developed turbulent state. In final stages of the transition process, the anisotropy settles near the isotropic two-component state of turbulence.

Using the tools of invariant theory allows insights into turbulence which are not easy to access in physical space. This enables an improved understanding of transition and breakdown to turbulence. Knowledge of the mechanisms responsible for the origin of turbulence is necessary in order to develop techniques capable of controlling it.

Acknowledgment

The project was financially supported by the *Deutsche Forschungsgemeinschaft* (German Research Foundation) within the *Verbundschwerpunktprogramm Transition*, *TK V* (BR 1847/2 and DU 101/53-3). The computations were carried out on the German Federal Top-Level Computer Hitachi SR 8000-F1 at HLRB Munich. All kinds of support are gratefully acknowledged.

References

[1] Boiko, A. V., Grek, G. R., Dovgal, A. V., and Kozlov, V. V., 2002, *The Origin of Turbulence in Near-Wall Flows*, Springer, Berlin, Heidelberg.

[2] Dovgal, A. V., Kozlov, V. V., and Michalke, A., 1994, "Laminar Boundary Layer Separation: Instability and Associated Phenomena," Prog. Aerosp. Sci., **30**, pp. 61–94.

[3] Meyer, D. G. W., Rist, U., and Wagner, S., 2003, "Direct Numerical Simulation of the Development of Asymmetric Perturbations at Very Late Stages of the Transition Process," in *Recent Results in Laminar-Turbulent Transition, Notes on Numer. Fluid Mech. and Multidisc. Design*, Springer, New York, Vol. 86, pp. 63–74.

[4] Kloker, M., and Stemmer, C., 2003, "Three-dimensional Steady Disturbance Modes in the Blasius Boundary Layer – A DNS Study," in *Recent Results in Laminar-Turbulent Transition, Notes on Numer. Fluid Mech. and Multidisc. Design*, Springer, New York, Vol. 86, pp. 91–110.

[5] Lang, M., Marxen, O., Rist, U., and Wagner, S., 2003, "A Combined Numerical and Experimental Investigation of Transition in a Laminar Separation Bubble," in *Recent Results in Laminar-Turbulent Transition. Notes on Numer. Fluid Mech. and Multidisc. Design*, Springer, New York, Vol. 86, pp. 149–164.

[6] Ducros, F., Comte, P., and Lesieur, M., 1996, "Large-Eddy Simulation of Transition to Turbulence in a Boundary Layer Developing Spatially Over a Flat Plate," J. Fluid Mech., **326**, pp. 1–36.

[7] Huai, X., Joslin, R. D., and Piomelli, U., 1997, "Large-Eddy Simulation of Transition to Turbulence in Boundary Layers," Theor. Comput. Fluid Dyn., **9**, pp. 149–163.

[8] Lumley, J. L., and Newman, G., 1977, "The Return to Isotropy of Homogeneous Turbulence," J. Fluid Mech., **82**, pp. 161–178.

[9] Lumley, J. L., 1978, "Computational Modeling of Turbulent Flows," Adv. Appl. Mech., **18**, pp. 123–176.

[10] Antonia, R. A., Kim, J., and Browne, L. W. B., 1991, "Some Characteristics of Small-Scale Turbulence in a Turbulent Duct Flow," J. Fluid Mech., **233**, pp. 369–388.

[11] Seidl, V., 1997, "Entwicklung und Anwendung eines parallelen Finite-Volumen-Verfahrens zur Strömungssimulation auf unstrukturierten Gittern mit lokaler Verfeinerung," Dissertation, Institut für Schiffbau, Universität Hamburg, Bericht Nr. 585.

[12] Krogstad, P., and Torbergsen, L. E., 2000, "Invariant Analysis of Turbulent Pipe Flow," Flow, Turbul. Combust., **64**, pp. 161–181.

[13] Fischer, M., Jovanović, J., and Durst, F., 2001, "Reynolds Number Effects in the Near-Wall Region of Turbulent Channel Flows," Phys. Fluids, **13** (6), pp. 1755–1767.

[14] Schenck, T., and Jovanović, J., 2002, "Measurement of the Instantaneous Velocity Gradients in Plane and Axisymmetric Turbulent Wake Flows," ASME J. Fluids Eng., **124**, pp. 143–153.

[15] Jovanović, J., and Pashtrapanska, M., 2004, "On the Criterion for the Determination Transition Onset and Breakdown to Turbulence in Wall-Bounded Flows," ASME J. Fluids Eng., **126**, pp. 626–633.

[16] Jovanović, J., 2004, *Statistical Dynamics of Turbulence*, Springer, Berlin, Heidelberg.

[17] Lerche, Th., and Dallmann, U. Ch., 1999, "Das Prinzipexperiment COSTWING I: Dokument. der Aufbauphase," Institut für Strömungsmechanik, DLR Göttingen, IB 223–99 A04.

[18] Breuer, M., and Jovičić, N., 2001, "Separated Flow Around a Flat Plate at High Incidence: An LES Investigation," J. Turbul., **2**, pp. 1–15.

[19] Breuer, M., 1998, "Large-Eddy Simulation of the Sub-Critical Flow Past a Circular Cylinder: Numerical and Modeling Aspects," Int. J. Numer. Methods Fluids, **28**, pp. 1281–1302.

[20] Breuer, M., 2002, "Direkte Numerische Simulation und Large-Eddy Simulation turbulenter Strömungen auf Hochleistungsrechnern," Habilitationsschrift, Univ. Erlangen-Nürnberg, Berichte a. d. Strömungstech., ISBN 3-8265-9958-6, Shaker.

[21] Breuer, M., and Rodi, W., 1996, "Large- Eddy Simulation of Complex Turbulent Flows of Practical Interest," in *Flow Simulation with High-Performance Computers II, Notes on Numer. Fluid Mech.*, Vieweg, Braunschweig, Vol. 52, pp. 258–274.

[22] Ferziger, J. H., and Perić, M., 1999, *Computational Methods for Fluid Dynamics*, Springer, New York.

[23] Germano, M., Piomelli, U., Moin, P., and Cabot, W. H., 1991, "A Dynamic Subgrid Scale Eddy Viscosity Model," Phys. Fluids A, **3**(7), pp. 1760–1765.

[24] Lilly, D. K., 1992, "A Proposed Modification of the Germano Subgrid Scale Closure Method," Phys. Fluids A, **4**(3), pp. 633–635.

[25] Smagorinsky, J., 1963, "General Circulation Experiments with the Primitive Equations, I, The Basic Experiment," Mon. Weather Rev., **91**, pp. 99–165.

[26] Jovičić, N., Evans, G., Breuer, M., and Friedrich, R., 2003, "Comparison of Two Large-Eddy Simulations for a Stalled Airfoil Flow Using Different Finite-Volume Formulations," Notes on Numer. Fluid Mech. and Multidisc. Design, **86**, pp. 293–306.

[27] Breuer, M., 2000, "A Challenging Test Case for Large Eddy Simulation: High Reynolds Number Circular Cylinder Flow," Int. J. Heat Fluid Flow, **21**(5), pp. 648–654, Elsevier Science B. V., Amsterdam.

[28] Dahlström, S., and Davidson, L., 2003, "Large Eddy Simulation Applied to a High-Reynolds Flow Around an Airfoil Close to Stall," AIAA Paper No. 2003–0776, Reno, NV.

[29] Kindler, K., Kreplin, H.-P., and Ronneberger, D., 2003, "Experimentelle Untersuchung kohärenter Strukturen in kritischen Tragflügelströmungen," Interner Bericht, IB 224 - 2003 A 11, Inst. f. Aerodynamik und Strömungstechnik, DLR Göttingen.

[30] Jovičić, N., and Breuer, M., 2004, "Separated Flow Past an Airfoil at High Angle of Attack: LES Predictions and Analysis," *Proceedings of the Fifth Int. ERCOFTAC Workshop on DNS and LES: DLES-5*, Munich University of Technology, Germany, Aug. 27–29, 2003, ERCOFTAC Series, 9, pp. 611–618, Direct and Large–Eddy Simulation V, R. Friedrich, B. J. Geurts, and O. Métais, eds. Kluwer Academic Publishers, Dordrecht.

Qiang Zhang
Research Assistant Professor

Matt Goodro
Undergraduate Research Assistant

Phillip M. Ligrani[1]
Professor
ASME Fellow

Convective Heat Transfer Laboratory,
Department of Mechanical Engineering,
University of Utah,
Salt Lake City, Utah 84112-9208

Ricardo Trindade
Staff Engineer
Turbine Durability,
United Technologies,
Pratt and Whitney Corp.,
400 Main Street, M/S 169-29,
East Hartford, CT 06108

Sri Sreekanth
Principle Engineer
Turbine Cooling and Static Structures,
Pratt and Whitney – Canada Corp. 22MC1,
1801 Courtney Park Drive East,
Mississauga, Ontario L5T1J3, Canada

Influence of Surface Roughness on the Aerodynamic Losses of a Turbine Vane

The effects of surface roughness on the aerodynamic performance of a turbine vane are investigated for three Mach number distributions, one of which results in transonic flow. Four turbine vanes, each with the same shape and exterior dimensions, are employed with different rough surfaces. The nonuniform, irregular, three-dimensional roughness on the tested vanes is employed to match the roughness which exists on operating turbine vanes subject to extended operating times with significant particulate deposition on the surfaces. Wake profiles are measured for two different positions downstream the vane trailing edge. The contributions of varying surface roughness to aerodynamic losses, Mach number profiles, normalized kinetic energy profiles, Integrated Aerodynamics Losses (IAL), area-averaged loss coefficients, and mass-averaged loss coefficients are quantified. Total pressure losses, Mach number deficits, and deficits of kinetic energy all increase at each profile location within the wake as the size of equivalent sandgrain roughness increases, provided the roughness on the surfaces is uniform. Corresponding Integrated Aerodynamic Loss IAL magnitudes increase either as Mach numbers along the airfoil are higher, or as the size of surface roughness increases. Data are also provided which illustrate the larger loss magnitudes which are present with flow turning and cambered airfoils, than with symmetric airfoils. Also described are wake broadening, profile asymmetry, and effects of increased turbulent diffusion, variable surface roughness, and streamwise development.
[DOI: 10.1115/1.2175163]

1 Introduction

Turbomachinery efficiency and operational behavior are influenced in important ways by the surface roughness of the turbine vanes and blades. This paper presents experimental results which illustrate the effects of roughness on the aerodynamic losses produced by cambered turbine vanes, both with and without different types of surface roughness, operating over a range of flow conditions which match those used in industrial applications.

The influence of surface roughness on adjacent flow behavior has been of interest for researchers for almost 100 years. The use of equivalent sandgrain roughness size k_s to characterize and quantify rough surfaces was first proposed and utilized by Nikuradse [1] and Schlichting [2]. This quantity represents the size of sand grains which give the same skin friction coefficients in internal passages as the roughness being evaluated. This measure of roughness size continues to be used widely in empirical correlation equations (which are based on experimental data) to represent rough surface behavior, and for closure models employed in a variety of numerical prediction codes. Later re-evaluation and additional advances in the use of equivalent sandgrain roughness are made by many researchers, including Coleman et al. [3], Sigal and Danberg [4,5], Van Rij et al. [6] and Zhang et al. [7].

In a paper published in 1975, Bammert and Sandstede [8] describe the influences of different manufacturing tolerances and turbine airfoil surface roughness characteristics on the overall performance of turbines. Particular attention is devoted to the effects of these parameters on efficiency, relative mass flow, enthalpy drop, and outlet flow angle. Later work by the same authors [9] considers the effects of the surface roughness on the boundary layer development along blades arranged in a stationary cascade. Momentum thicknesses are as much as three times values measured on smooth airfoils in regions of decelerating flow. Kind et al. [10] investigate the effects of partial roughness coverage of blade surfaces by measuring pressure distributions, profile losses, and the flow deviations produced by a planar turbine cascade. Different roughness heights, and different roughness element spacings are considered. According to the authors, the largest profile loss increases are produced by roughness located on the suction surface. Bogard et al. [11] analyze the surface roughness characteristics of turbine vanes that have undergone a significant number of hours of operation. Flat plate surfaces with cone shaped elements are used to simulate the roughness which is present on these vane surfaces. According to the authors, the effects of surface roughness and high free-stream turbulence are additive along flat plates, and can produce heat transfer rate increases that are as much as 100% greater than smooth surface values. Abuaf et al. [12] quantify heat transfer and aerodynamics performance characteristics of turbine airfoils with different surface finish treatments. Experimental results show that tumbling and polishing reduce the average roughness size and improve overall performance. The authors also employ a Reynolds analogy to determine skin friction coefficients, drag forces, and aerodynamic efficiencies from airfoil surface heat transfer data. Leipold et al. [13] employ a compressor cascade to investigate the influences of surface roughness at different inlet flow angles and Reynolds numbers. The investigators indicate that surface roughness has no effect upon the presence or location of laminar separation, and that the roughness alters turbulent boundary layer separation at high Reynolds numbers.

[1]Corresponding author.

Contributed by the Fluids Engineering Division of ASME for publication in the JOURNAL OF FLUIDS ENGINEERING. Manuscript received February 3, 2005; final manuscript received October 16, 2005. Review conducted by Joseph Katz. Paper presented at the TURBO EXPO 2005 in Reno.

The investigation by Sitaram et al. [14] attempts to reduce losses by reducing the laminar separation bubble on the suction surface of a turbine rotor blade by means of a two-dimensional roughness element. Experimental data on wake pressure defects, velocity, flow angle, and wake decay characteristics are obtained. They conclude that blade static pressure distributions are little altered by surface roughness on suction surfaces. Combined effects of surface roughness, freestream turbulence and Reynolds number on heat transfer and laminar-turbulent transition are investigated by Stripf et al. [15]. Their results show a strong influence of roughness on the onset of transition even for the smallest roughness Reynolds numbers. Roberts and Yaras [16] also present experimental results showing that transition inception location remains sensitive to surface roughness with increasing freestream turbulence.

Boyle and Senyitko [17] compare total pressure losses for smooth and rough vanes over a range of Reynolds and Mach numbers for three turbulence levels. Their work concentrates on loss differences between the rough and smooth vanes, and on approaches to predicting surface roughness effects. They indicate that, at high Reynolds numbers, roughness nearly doubles loss levels compared to ones which exist for the lowest Reynolds number employed. The effects of surface roughness on the aerodynamic performance of symmetric airfoils are investigated by Zhang et al. [18] with different inlet turbulence intensity levels. Their results show that effects of changing the size of surface roughness on the Integrated Aerodynamic Losses (IAL) are substantial, whereas the effects of different inlet turbulence intensity levels are generally relatively small. In another study, Zhang et al. [19] present experimental data on wake turbulence structure also measured downstream of symmetric airfoils with different surface roughness and inlet turbulence intensity levels. These authors indicate that all wake profile quantities broaden and vortex shedding frequencies decrease as either the level of surface roughness or the turbulence intensity increases. Note that significant flow turning from a cambered airfoil is not present in these two investigations by Zhang et al. [18,19].

The present investigation is different from the investigations of Zhang et al. [7,18,19] because a cambered turbine vane is used which produces substantial flow turning, and matches a vane configuration employed in an industrial application. Considered are the effects of surface roughness on aerodynamic losses downstream of the vane for three different Mach number distributions, one of which results in transonic flow (and matches flow conditions in an industrial application). One smooth vane is employed, along with two other vanes with three-dimensional roughness distributed uniformly over entire vane surfaces. A fourth vane is also employed with roughness of different sizes distributed over the vane surface (i.e., a variable rough surface) whose arrangement is based on observations of roughened turbine vanes from industrial applications. All four turbine vanes have the same shape and exterior dimensions. These aspects of the present approach make the present investigation unique and different from other investigations of turbine airfoil aerodynamic losses. As such, the data provide useful information to designers of turbomachinery components for evaluation of turbine efficiency, and to individuals developing models for CFD predictions. Wake profile data are presented for two different locations downstream the vane trailing edge, which illustrate the influences of varying surface roughness and vane Mach number on local aerodynamic losses, local Mach numbers, local kinetic energy, Integrated Aerodynamics Losses (IAL), area-averaged loss coefficients, and mass-averaged loss coefficients. Included are comparisons with results from several other recent investigations [10,17,20–22].

2 Experimental Apparatus and Procedures

2.1 Transonic Wind Tunnel (TWT). The University of Utah Transonic Wind Tunnel (TWT) is used for the study because it produces Mach numbers, pressure variations, Reynolds numbers, passage mass flow rates, and scaled physical dimensions which match values along airfoils in operating aero-engines and in gas turbines used for utility power generation. The TWT blow-down type facility consists of two main parts: (i) compressor and storage tanks, and (ii) wind tunnel. The wind tunnel consists of five major sub-sections: (i) flow rate and pressure level management apparatus, (ii) plenum tank, (iii) inlet ducting and test section, (iv) plenum, exit ducting, and ejector, and (v) control panel. Detailed descriptions are provided by Jackson et al. [23] and Furukawa and Ligrani [24].

Table 1 Operating conditions

Exit Mach number M_{ex}	0.35	0.50	0.71
Exit Reynolds number*	0.5×10^6	0.7×10^6	0.95×10^6
Inlet Reynolds number*	0.2×10^6	0.3×10^6	0.4×10^6
Inlet Mach number	0.15	0.19	0.23
Inlet Total Pressure (kPa)	94	98	106
Inlet Turbulence Intensity	1.6%	1.2%	1.1%
Inlet Relative humidity	15-20%	15-20%	15-20%

A Gardner-Denver Co. model RL-1155-CB compressor is used to pressurize the array of eight tanks whose total capacity volume is 11.9 m^3. A VanAir VAS93039 model D16-5 Deliquescent desiccant dryer, a Pall Corp. 5EHG-4882-207 oil filter, and two Permanent Filter Corp. No. 13846 particulate filters are located just downstream of the compressor to remove particulates and moisture from the air. A Fisher pressure regulator with a 6×4 EWT design sliding gate valve, a Fisher type 667 diaphragm actuator, a 3582 series valve positioner, and a Powers 535 1/4 DIN process controller are used to regulate the pressure in the test section as the storage tanks discharge. A plenum tank, a 30.48 cm inner diameter pipe, a circular-to-square transition duct, a nozzle, and the test section then follow. The test section is connected to a large 92.71 cm by 91.44 cm by 91.44 cm plenum with a square plastic flange at its outlet. The plenum diffuses high speed air from the test section exit into a reservoir of low velocity air. This plenum is then connected to two ducts which are subsequently connected to the atmosphere.

Experimental parameters for the three different operating conditions employed in this study are tabulated in Table 1.

2.2 Test Section. The present test section is designed to match Reynolds numbers, Mach numbers, pressure gradients, passage mass flow rates, boundary layer development, streamline curvature, airfoil camber, and physical dimensions of turbine vanes in operating industrial engines. A schematic diagram of the test section with the cambered vane is shown in Fig. 1, along with the *x*-*y* coordinate system used for wake profile measurements. The inlet of the test section is 12.70 cm by 12.70 cm. The side and bottom walls of the test section are made of steel, and top wall is made up of acrylic. As shown in Fig. 1, two zinc-selenide windows are also placed on both of the sidewalls, so that the entire airfoil surface is accessible to optical, surface temperature measurement schemes such as infrared thermography.

Appropriate cascade flow conditions are maintained, in part, by a pair of adjustable bleed ducts which are located on the two side walls, as shown in Fig. 1. The flow rate of each bleed duct is regulated using an adjustable ball valve. Following these, the test section walls have the same pressure side and suction side contours as the test vane. The exit area and exit flow direction from the cascade test section can be altered by changing the angles of the two exit tailboards, which are also shown in Fig. 1. Thus, (i)

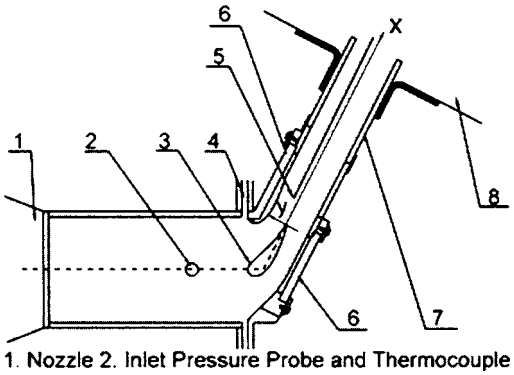

Fig. 1 Schematic diagram of the test section, including wake coordinate system

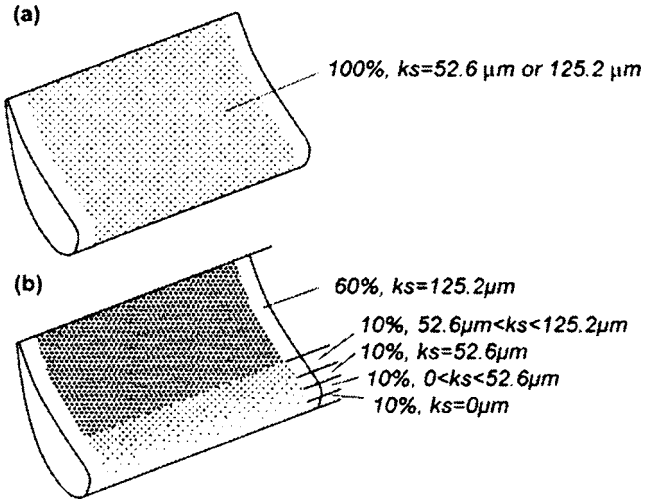

Fig. 2 Test section vanes with rough surfaces. (*a*) Vane with uniform roughness. (*b*) Vane with variable roughness on pressure side.

changing the total pressure at the test section inlet using the pressure regulator/sliding gate valve arrangement; (ii) changing the angular positions of the two tailboards; and (iii) adjusting the ball valves of the bleeding system are employed to alter the Mach number distribution along the vane in the test section, for a particular vane and test section configuration. By adjusting these items, appropriate Mach number distributions along the test vane are obtained, which are discussed later in the paper.

2.3 Test Vanes and Surface Roughness. Table 2 gives geometric parameters of the test vanes. The coordinates of this test vane profile were provided by personnel at Pratt and Whitney Canada Corporation, along with appropriate operating conditions which are used in industrial environments.

Four different vanes, all with the same exterior dimensions but with different surface roughness characteristics, are used. One vane has a smooth surface, two other vanes have uniform rough surfaces, and one vane has variable roughness on the pressure side. The roughness applied simulates the actual roughness which develops on operating turbine airfoils, over long operating times, due to particulate deposition and to spallation of thermal barrier coatings (TBCs). The roughness is applied by bonding nickel particles, manufactured by Praxair Surface Technologies, Inc., to the test vane surfaces. The bonding is implemented using a layer of Cotronics Corp. Duralco 132 aluminum-filled, high thermoconductivity epoxy. This epoxy and the roughness particles are applied to an indented region located across the central span of each airfoil. This approach is used to give the same exterior dimensions to the surfaces of all four test vanes, regardless of whether their surfaces are smooth or rough.

A schematic diagram of test turbine vane with uniform rough surfaces is shown in Fig. 2(*a*). The vane with the uniform smaller-sized roughness elements has Praxair T1166F particles, which range in size from 20 to 53 μm. The vane with the uniform larger-sized roughness elements has Praxair NI-914 particles, which range in size from 88 to 149 μm. The vane with variable roughness is shown in Fig. 2(*b*). Four types of different Nickel based powders are used on the pressure side of a test vane, while the suction side is left smooth. Detailed information regarding the nickel powders and surface coverage for the variable rough vane is given in Table 3.

The arrangement of variable rough surface is based on observations of roughened turbine vanes from industrial applications. From these observations, the suction side is more or less uniform in roughness, and remains at or very close to the "as-cast" condition, even after very long operating times. Pressure side roughness, on the other hand, is more variable. Local roughness magnitudes are often the same as on suction side roughness at the leading edge. Local roughness sizes then vary linearly to the full roughness size, which are typically reached at about 40% of the distance along the pressure surface. Thus, differences in surface roughness characteristics between the suction and the pressured sides can be very significant due to the different flow and operating conditions encountered. There is also a considerable scatter in the roughness patterns both in qualitative and quantitative terms that are present on vanes and blades from operating engines. The configuration of variable roughness investigated is one typical configuration, as shown by the data presented in Fig. 2(*b*) and in Table 3.

Table 2 Test vane geometric parameters

True Chord *c*	7.27cm
Axial Chord *cx*	4.85 cm
Pitch *p*	6.35 cm
Span	12.7 cm
Flow turning angle	62.75°

Table 3 Nickel based powders used on the test vane with variable surface roughness on the pressure side

Percentage of the surface distance on the PS Side (starting from LE)	Powder Name	Size (μm)
0 - 10%		0
10% - 20%	NI-105	5-45
20% - 30%	T1166F	20-53
30% - 40%	NI-107	45-106
40% - 100%	NI-914	88-149

2.4 Pressure and Temperature Measurements. As tests are conducted, Validyne Model DP15-46 pressure transducers (with diaphragms rated at 13.8, 34.5, or 344.7 kPa), and calibrated copper-constantan thermocouples are used to sense pressures and temperatures at different locations throughout the facility. A United Sensor PLC-8-KL pitot-static probe with an attached, calibrated Watlow standard type-K copper-constantan thermocouple, and a four-hole conical-tipped pressure probe also with a similar thermocouple are used to sense total pressure, static pressure, and recovery temperature at the inlet and exit of the test section, respectively, during each blow down. Mach numbers, sonic velocities, total temperatures, and static temperatures are determined from these data. The four-hole probe has a tip which is 1.27 mm in diameter, and a stem which is 3.18 mm in diameter. Each port has a diameter of 0.25 mm. The overall response time of the pressure measuring system is about 0.2 s. The conical probe is aligned using two yaw ports placed on either side of the probe. The probe is located downstream of the vane. The position in the streamwise direction is adjustable. As a blow down is underway, it is traversed across a full pitch using a two-axis traversing sled with two Superior Electric synchronous stepper motors, connected to a Superior Electric programmable motion controller and a Superior Electric driver. Commands for the operation of the motion controller are provided by LABVIEW 7.0 software and pass though a serial port after they originate in a Dell Precision 530 PC workstation. Each profile is measured through the wake from minus y/cx locations to positive y/cx locations, and then repeated as the probe is traversed in the opposite direction. The resulting data are subsequently averaged at each wake measurement location.

Voltages from the carrier demodulators and thermocouples are read sequentially using Hewlett-Packard HP44222T and HP44222A relay multiplexer card assemblies, installed in a Hewlett-Packard HP3497A low-speed Data Acquisition/ Control Unit. This system provides thermocouple compensation electronically such that voltages for type T thermocouples are given relative to 0 °C. The voltage outputs from this unit are acquired by the Dell Precision 530 PC workstation through its USB port, using LABVIEW 7.0 software and a GPIB-USB-B adaptor made by National Instruments.

2.5 Longitudinal Turbulence Intensity Measurements. A single, horizontal-type platinum-plated tungsten hot-wire sensor, with a diameter of 12.7 μm and a length of 2.54 mm, is employed to measure the time varying longitudinal component of velocity at the inlet of the test section. The time-averaged longitudinal velocity, and longitudinal turbulence intensity are then determined from these measurements. The measurement location is one axial chord length upstream of the vane leading edge. The hot-wire probe is driven by a Disa 55M10 constant-temperature hot-wire anemometer bridge with an overheat ratio of 1.6. The analog signal from this bridge is then processed using a Dantec 56N20 signal conditioner with a low-pass, anti-aliasing filter set to 100 kHz. The time-varying output voltage signal is then sampled at a 200 kHz rate using a DATEL PCI441D I/O board installed in the Dell Precision 530 PC workstation. During each measurement, 2,000,000 voltage values are sampled over a time period of 10 s. Data are acquired using LABVIEW 7.0 software and then processed further using MATLAB 6.1 software. The entire measurement system, including the hot-wire sensor, is calibrated in the free-stream of the TWT. A Kiel type pressure probe, wall static taps, and a copper-constantan thermocouple are used to measure and determine the total pressure, static pressure, recovery temperature, and velocity at the inlet of the test section as the calibration is conducted.

2.6 Experimental Uncertainties. Uncertainty estimates are based on 95% confidence levels, and determined using procedures described by Kline and McClintock [25] and by Moffat [26]. Mach number uncertainty is 0.002. Uncertainty of temperatures is 0.15 °C. Pressure uncertainty is 0.25 kPa. Uncertainties of $C_p, M_e/M_{e\infty}$, and KE are 0.0013 (0.07), 0.0023 (0.96), and 0.03(0.90), respectively, where typical nominal values of these quantities are given in parenthesis. IAL uncertainty is 0.04 N/cm(0.800 N/cm). Magnitudes of IAL, determined from replicate runs, are always within IAL uncertainty ranges.

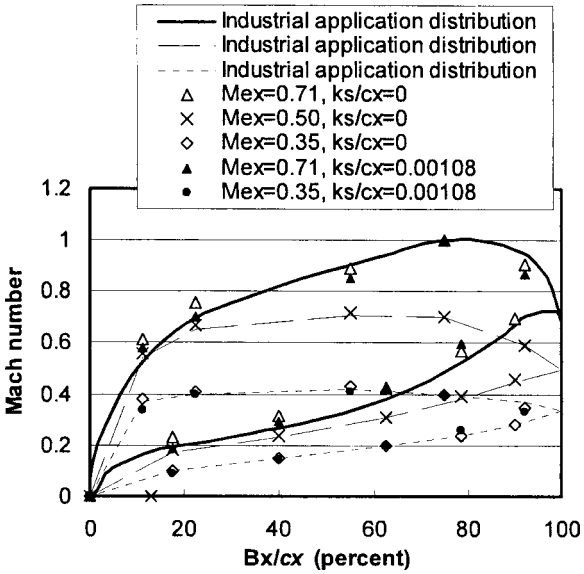

Fig. 3 Mach number distributions along the test vane

3 Experimental Results and Discussion

3.1 Test Section Flow Characteristics and Mach Number Distributions. During each blow-down test, the total pressure, Reynolds number, and turbulence level at the test section inlet are maintained in a continuous and steady fashion for 45 s long time intervals. Such characteristics are not only due to the TWT design, but also to the excellent performance characteristics of the TWT mainstream air pressure regulator and its controller. The total pressure and static pressure show excellent spatial uniformity at the inlet of the test section. Here, total pressure and static pressure values vary by less than 0.5% of mean values as measurements are made at five different pitchwise locations. Magnitudes of inlet turbulence intensity, based on longitudinal velocity fluctuations, are 1.1% for $M_{ex}=0.71$, 1.2% for $M_{ex}=0.50$, and 1.6% for $M_{ex}=0.35$. The measurement location for these values is one chord length upstream of the vane leading edge.

Table 1 gives experimental conditions for the three different operating conditions which are employed in this study. Figure 3 shows the Mach number distributions along the turbine vane pressure side and along the vane suction side for each of these three operating conditions. Each different operating condition is produced by setting a different stagnation pressure at the test section inlet using the TWT mainstream air pressure regulator. Note that the exact same positions of the tailboards and the same flow settings on the bleeding system (shown in Fig. 1) are used for each flow condition. The data shown in Fig. 3 are based upon measurements of total pressure at the test section inlet, and vane mid-span static pressures. These are measured using two different airfoils which are constructed especially for this task: (i) A smooth vane ($k_s/cx=0$), and (ii) a vane with uniform roughness ($k_s/cx=0.00108$). Each of these vanes has five pressure taps on the pressure side, and five pressure taps on the suction side, as well as one pressure tap located on the leading edge at the vane midspan. As shown in Fig. 3, one Mach number distribution employed in this study is transonic on the vane suction side and subsonic on the pressure side, and the other two operating conditions are completely subsonic. Note that a strong adverse pressure gradient is

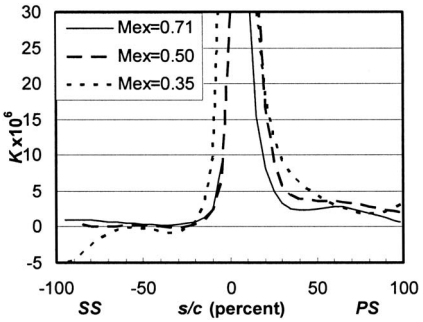

Fig. 4 Distributions of acceleration parameter *K*

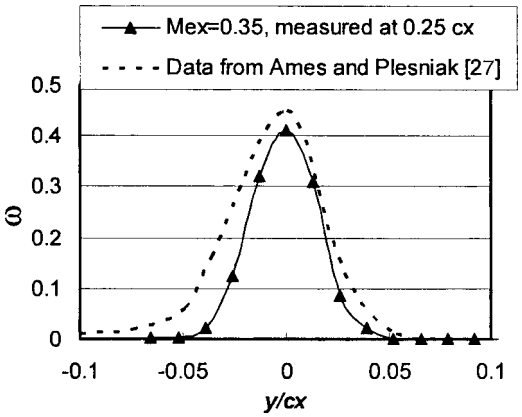

Fig. 5 Comparison of smooth vane wake total pressure loss coefficient profile with similar data from Ames and Plesniak [27]

present on the suction side of the vane when $Bx/cx>0.80$ for $M_{ex}=0.71$. Figure 3 also shows that the Mach number distributions on pressure and suction sides for all three exit Mach numbers are in excellent agreement with data from operating gas turbine engine environments.

Figure 3 also shows that the Mach number distributions for the roughened vane with $k_s/cx=0.00108$ and the smooth vane are in excellent agreement for two of the experimental conditions corresponding to $M_{ex}=0.71$ and $M_{ex}=0.35$. This means that: (i) the roughness has little effect on the airfoil Mach number and surface static pressure distributions, and (ii) the contour shapes of the smooth vane and uniformly roughened vane with $k_s/cx=0.00108$ are the same. This first result is consistent with data from Bammert and Sandstede [9] and Kind et al. [10], who also show that roughness has only small effects on the turbine airfoil pressure distributions. Note that the trailing edge area is not accessible for measurement because static pressure tap tubes cannot be installed in the portion of the vane with such a small trailing edge diameter. However, numerical predictions by Zhang et al. [7] show that static pressures are only slightly different near the trailing edges of symmetric airfoils with smooth and uniformly roughened surfaces.

Figure 4 presents distributions of acceleration parameter K. For each flow condition, considerably higher acceleration parameters are present on the pressure side ($K>2\times10^{-6}$). The resulting acceleration is expected to produce thinning of the turbulent boundary layers accompanied by a suppression of boundary layer turbulence.

3.2 Comparison With Results From Ames and Plesniak. To verify experimental data obtained and procedures employed, a comparison is made with results from Ames and Plesniak [27]. To do this, a total loss coefficient ω is determined, which is defined using

$$\omega=\frac{P_{oi}-P_{oe}}{P_{oi}-P_{se}} \tag{1}$$

The Ames and Plesniak data are taken approximately 0.3 axial chord lengths downstream of a smooth vane with $M_{ex}=0.27$. The vane used by Ames and Plesniak is two times the size of vanes from present study, and has an exit angle of 72.4 deg, compared to an exit angle of 62.75 deg for the present investigation. The present data used for comparison are obtained for $M_{ex}=0.35$ at a measurement location of 0.25 axial chord length downstream of the trailing edge of a smooth vane. Figure 5 shows that the two sets of data have similar magnitudes and similar qualitative distributions. The small quantitative differences are due to slightly different vane configurations, flow conditions, and measurement locations relative to the vane trailing edges. Overall, the agreement between the two data sets provides verification of procedures and results from the present study. Note that no significant freestream losses are present in either study at these experimental conditions because they entail the use of low inlet turbulence intensities and relatively low subsonic Mach numbers.

3.3 Rough Surfaces Measurement and Characterization. Magnitudes of equivalent sandgrain roughness are determined for all surfaces under investigation using procedures described by Van Rij et al. [6]. The first step in this process is determination of detailed surface contour coordinates using a Wyko high-resolution Optical Surface Profilometer. Figure 6(*a*) shows an enlarged image of a portion of the test rough surface which is comprised of nickel powder T1166F, obtained from such optical profilometry data. The image of a rough surface from the pressure side of a turbine vane from a utility power engine is shown in Fig. 6(*b*). This particular sample is obtained from a location on the surface which is located close to the trailing edge area, which is roughened due to surface particulate deposition. The qualitative and quantitative similarity of the two images is apparent, including the distributions, irregularity, nonuniformity, and three-dimensional nature of the roughness elements. Equivalent sand grain roughness size of this real turbine vane surface is about 62.3 μm, which is close to 52.59 μm, the size for the test surface with Nickel powder T1166F. Table 4 also shows the similarity of other surface roughness statistics from the utility power engine turbine vane to test surfaces comprised of Nickel powders T1166F and NI-914.

The second step in the procedure is numerical determination of a modified version of the Sigal and Danberg roughness parameter Λ_s [4–6]. According to van Rij et al. [6], the modified version of Λ_s is defined using

$$\Lambda_s=\left(\frac{S}{S_f}\right)\left(\frac{S_f}{S_s}\right)^{-1.6} \tag{2}$$

where S is the reference area, or the area of the smooth base surface before adding on the roughness, S_f is the total frontal area over the rough surface, and S_s is the windward wetted surface area of all of the roughness elements on the surface. S/S_f is then a roughness density parameter, and S/S_s is a roughness shape parameter.

In the third part of the procedure, with Λ_s known, the ratio of equivalent sandgrain roughness size to mean roughness height, k_s/k, is determined using a correlation for three-dimensional, irregular roughness with irregular geometry and arrangement. According to van Rij et al. [6], k_s/k is given by

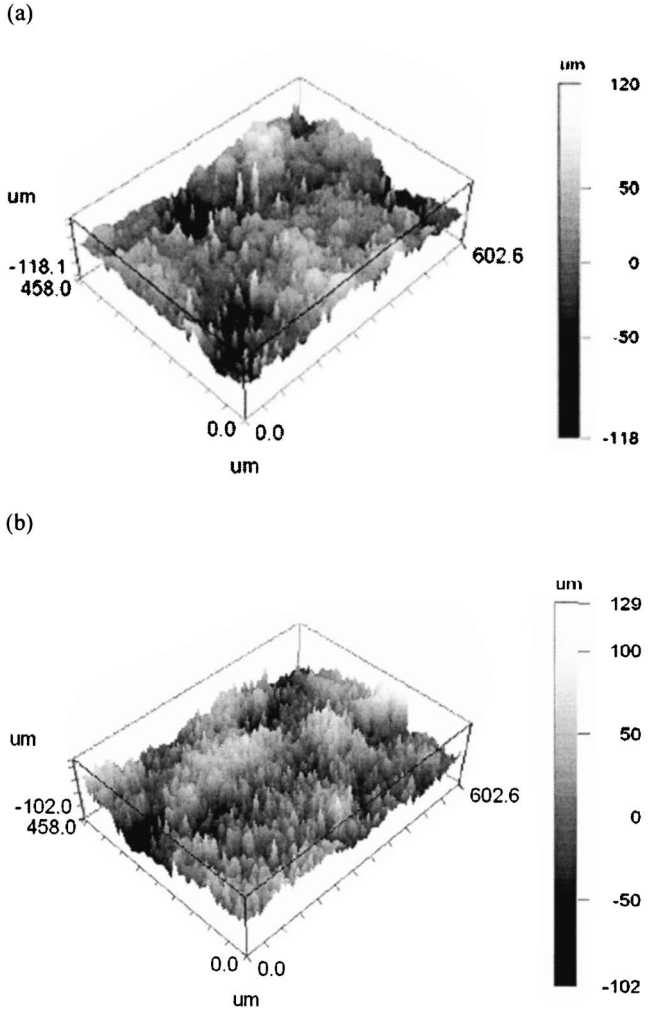

Fig. 6 Three-dimensional Wyko profilometry traces of portions of the rough surfaces. (*a*) Simulated rough surface with small-sized roughness elements. (*b*) Rough surface from the pressure side of a turbine vane with particulate deposition from a utility power engine.

$$\frac{k_s}{k} = \begin{cases} 1.584 \times 10^{-5} \Lambda_S^{5.683} & \Lambda_S \leqslant 7.842 \\ 1.802 \Lambda_S^{0.0304} & 7.842 \leqslant \Lambda_S \leqslant 28.12 \\ 255.5 \Lambda_S^{-1.454} & 28.12 \leqslant \Lambda_S \end{cases} \quad (3)$$

The mean roughness height k is estimated as the distance between the maximum point of the ensemble-average of all of the roughness peaks in any roughness sample, and a base height. Determination of this base location is based on analytic procedures which are also given by Van Rij et al. [6].

With this approach, magnitudes of equivalent sand grain roughness size for the three-dimensional, irregular roughness of the present study are determined. Resulting values are given in Table 4, where each is based on an average of measurements from eight separate profilometry scans of each surface.

3.4 Local Aerodynamic Performance. Here, the effects of surface roughness and exit Mach number on the local wake profiles are presented and discussed. To provide an appropriate standard of comparison, each profile is measured over one complete exit pitch spacing (or one complete exit vane spacing). In addition, the inlet total pressure is always kept constant as different vanes are employed for the same operating condition.

Figures 7 and 8 show the effects of surface roughness on normalized local total pressure losses C_p, normalized local Mach numbers $M_e/M_{e,\infty}$ and normalized local kinetic energy KE for $M_{ex}=0.71$. These data are measured in the wake at 0.25 chord lengths and one axial chord length downstream of vanes, respectively. The different profiles provide information on local wake deficits of total pressure, Mach number, and kinetic energy. Data are given for a smooth vane, and vanes with uniform small-sized roughness ($k_s/cx=0.00108$), uniform large-sized roughness ($k_s/cx=0.00258$), and variable roughness. The inlet total pressure is kept constant at 106 kPa to maintain the same operating condition.

The wake profiles shown in Figs. 7 and 8 are asymmetric. Suction side wakes (at negative y/cx) are thicker than the pressure side wakes (at positive y/cx). The asymmetry in the wake is due to loading on the vane surface, and the past history of the flow. In addition, the growth and development of boundary layers on the suction and pressure sides are different. On the suction side, where local freestream velocities are higher, the boundary layers continue to become thicker up to the trailing edge. The thicker boundary layers then separate from the suction surface of the vane, which affects wake behavior immediately downstream of the trailing edge. In contrast, on the pressure side, boundary layers decrease in thickness in the back section of the vane contour as a result of locally higher flow acceleration. Bammert and Sandstede [9] report data showing the boundary layer on the suction side is considerably thicker than on the pressure side. According to them, wake profile losses are determined more by suction side events by a factor about 2.5–3.5 times compared to events originating near the pressure side.

Figure 7 shows that total pressure losses, Mach number deficits, and deficits of kinetic energy all increase at each y/cx location within the wake as k_s/cx increases, provided the roughness on the surfaces is uniform. The boundary layers along the vane surfaces are thickened as k_s/cx increases, which is accompanied by higher magnitudes of Reynolds stress tensor components, higher magnitudes of local turbulent transport, and higher surface skin friction coefficients. The broader wakes with increased roughness size in Fig. 7 are then the result of: (i) different boundary layer development with various roughness, (earlier laminar-turbulent transition might be caused by surface roughness, as discussed by Stripf et al. [15] and Roberts and Yaras [16].); (ii) augmentations mixing and turbulent transport in the boundary layers which develop along the

Table 4 Characteristics of rough surfaces investigated

Surface	Λ_s	k_s/k	$k(\mu m)$	$k_s(\mu m)$	k_s/cx
Smooth	3020.7	.0026	3.50	.0094	0
Rough Surface with Nickel Powder T1166F	20.1	1.889	27.92	52.59	.00108
Rough Surface with Nickel Powder NI-914	15.4	1.959	64.03	125.19	.00258
Variable Rough Surface				See Fig. 2b	
Turbine vane from a utility power engine	43.5	1.641	40.82	62.30	.00129

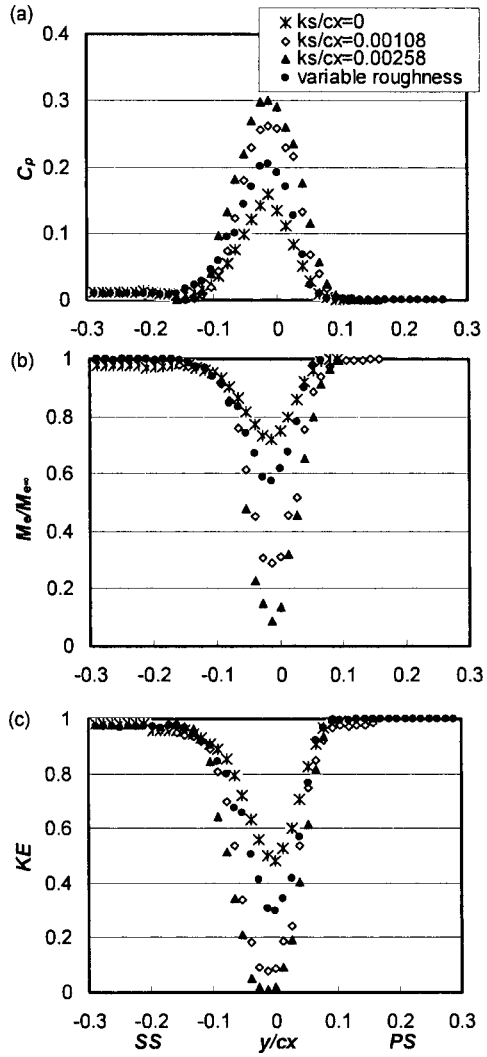

Fig. 7 Profiles measured at 0.25 axial chord length downstream of the test vane for M_{ex}=0.71. (*a*) Normalized local total pressure losses. (*b*) Normalized local Mach numbers. (*c*) Normalized local kinetic energy.

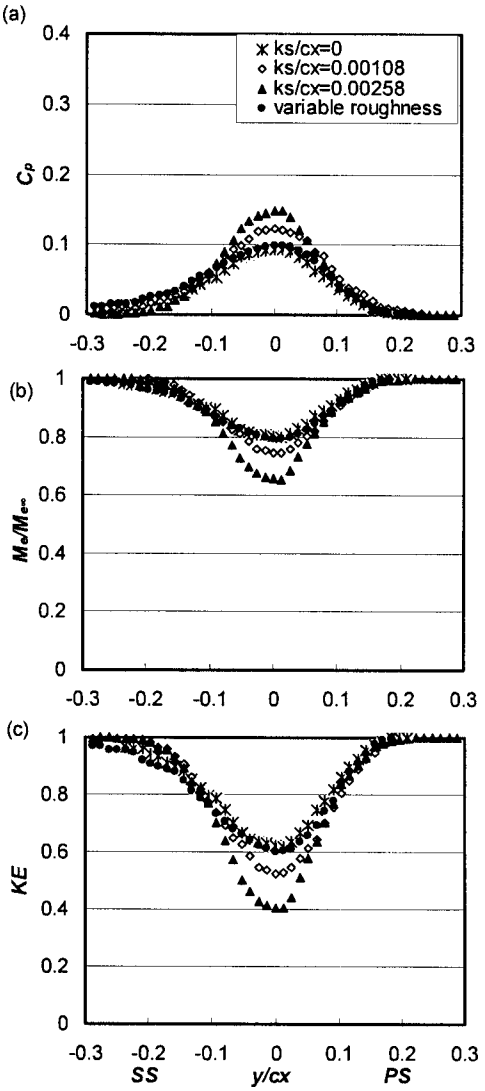

Fig. 8 Profiles measured at one axial chord length downstream of the test vane for M_{ex}=0.71. (*a*) Normalized local total pressure losses. (*b*) Normalized local Mach numbers. (*c*) Normalized local kinetic energy.

roughened vanes; (iii) thicker boundary layers at the trailing edges of the roughened vanes; and (iv) increased turbulent diffusion in the transverse direction within the wake as it advects downstream.

Compared with the results in Fig. 7, the profiles in Fig. 8 (measured one chord length downstream of the vane) are broader (i.e., spread over a wider range of y/cx), with lower peak values. This is mostly a result of transverse turbulent diffusion of streamwise momentum as the wake advects from 0.25 to one axial chord length downstream. Figures 7 and 8 additionally show that increased thickening of the wake is especially apparent as surface roughness size becomes larger. This is especially apparent and more substantial within the wake at negative y/cx values, or downstream of the suction sides of the vanes. In contrast, the effects of surface roughness are much less apparent for positive y/cx values, or downstream of the pressure sides of the vanes. This is especially evident in Fig. 8 since profiles for all three k_s/cx values (0, 0.00108, 0.00258), as well as for the variable roughness vane, are similar for $y/cx > 0.05$. This is partially due to the different growth of boundary layers on the pressure and suction sides for different amounts of surface roughness.

Figures 7 and 8 also include measurements made downstream of the vane with variable roughness shown in Fig. 2(*b*). In most cases, variable surface roughness profile points in Figs. 7 and 8 lie between the profiles measured with $k_s/cx=0$, and $k_s/cx=0.00108$ for $y/cx > -0.1$. This is partially due to different rates of boundary layer development as different levels of roughness are encountered along the vane pressure surface. This gives different magnitudes of boundary layer mixing and losses, and a different wake initial condition near the vane trailing edge, compared to vanes with uniformly roughened surfaces. These changes produced on the vane pressure side appear to have some influence on initial wake behavior downstream of the vane suction side. As a result, suction side wake profiles at $y/cx < 0$ downstream of the vane with a variable rough surface are widened. Thus, suction side wake profiles in Figs. 7 and 8 are also widened somewhat for the vane with variable roughness, even though this vane has a smooth suction side. Overall, the wakes are pushed toward smaller y/cx values as they are advected downstream (i.e., towards the vane suction side), regardless of the level, uniformity, or variability of the roughness along the surfaces of the vanes.

Figures 9 and 10 show the effects of surface roughness on C_p profiles in the wake which are measured one axial chord length downstream of test vanes at M_{ex}=0.50 and 0.35, respectively. From these two figures, the asymmetry, widening and broadening wake with roughness are quite similar to results which are given

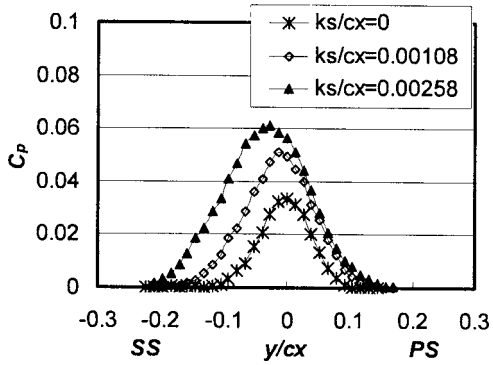

Fig. 9 Normalized local total pressure loss profiles measured at one axial chord length downstream of the test vane for M_{ex} =0.50

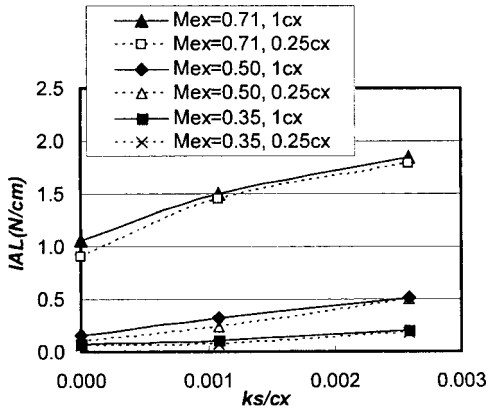

Fig. 11 Comparison of normalized integrated aerodynamic loss as dependent upon the normalized equivalent sand grain roughness size

in Fig. 8(*a*). For example, as the level of surface roughness increases, losses increase substantially at negative y/cx values (i.e., downstream of vane suction sides), whereas smaller variations with changing surface roughness are evident at positive y/cx values (i.e., downstream of vane pressure sides). Comparing results in Figs. 10, 9, and 8(*a*) shows that peak values of total pressure loss coefficients increase dramatically as M_{ex} increases. For example, peak values are approximately 0.03 at M_{ex}=0.35, 0.06 at M_{ex}=0.50, and 0.15 at M_{ex}=0.71. The wakes also become wider as M_{ex} increases. Wider C_p profiles are a result of higher advection speeds, as well as increased diffusion within the wake. The change of the Mach number distribution along the vane for different M_{ex} also affects the pressure gradient imposed on the boundary layer. At higher exit Mach numbers, greater losses are created due to higher rates of turbulence mixing with higher stain rates. Compressibility, which becomes more important at higher exit Mach numbers, also produces additional alterations to the character and development of boundary layers.

Figures 9 and 10 also show wake shifting towards more negative y/cx values with streamwise development. This becomes more substantial as the level of surface roughness increases, or as the exit Mach number decreases. For example, the data in Fig. 9 for M_{ex}=0.50 indicate that the roughened vanes with k_s/cx =0.00108 and k_s/cx=0.00258 have flow deviation angles estimated to be 0.7 and 1.5 deg, respectively. Figure 10 for M_{ex} =0.35 shows that roughness produces even larger deviation angles of approximately 1.3 and 2.9 deg for k_s/cx=0.00108 and k_s/cx =0.00258, respectively. Deviation angles thus appear to increase as M_{ex} decreases or as k_s/cx increases. Larger flow deviations are more apparent at lower exit Mach numbers probably because of earlier flow separation near the suction side trailing edge.

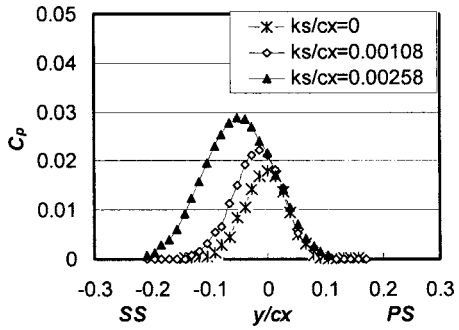

Fig. 10 Normalized local total pressure loss profiles measured at one axial chord length downstream of the test vane for M_{ex} =0.35

3.5 Integrated Aerodynamic Losses. Dimensional magnitudes of Integrated Aerodynamic Loss, IAL, are determined by integrating profiles of $(P_{oi}-P_{oe})$ with respect to y in the transverse flow direction across the wake for one single vane spacing, from $-p/2$ to $p/2$.

$$\mathrm{IAL} = \int_{-p/2}^{p/2} (P_{oi} - P_{oe})dy \tag{4}$$

In the present study, IAL magnitudes are mostly the result of two phenomena. These are: (i) the losses resulting from formation of the boundary layers along the vane surfaces, and (ii) the flow separation, recirculation zone, and wake mixing losses that are initially present just downstream of the vanes.

IAL magnitudes are determined from profiles that are measured 25% of one axial chord length, and one axial chord length downstream of the turbine vane. Such IAL magnitudes are presented in Fig. 11 as dependent upon the normalized equivalent sandgrain roughness size for three exit Mach numbers. The overall trends of the data in this figure illustrate the dominating influences, first, of the Mach number distribution along the airfoil (as designated by exit Mach number), and second, of the surface roughness (as characterized by normalized equivalent sandgrain roughness size). For each value of k_s/cx, dramatic and important IAL magnitude increases are present as higher Mach numbers are present along the airfoil. This is mostly due to higher advection speeds, increased diffusion, and probably earlier laminar to turbulent boundary layer transition of the boundary layers at higher Mach numbers, noting that Reynolds numbers and Mach numbers are not independent in the present study. IAL magnitudes also increase almost linearly as k_s/cx increases for each profile measurement location and for each value of exit Mach number. The IAL differences obtained at each M_{ex} for $1cx$ and $0.25cx$ are relatively small compared to overall IAL loss magnitudes. This is a result of how momentum and turbulence kinetic energy are conserved through the wake. Near the vane trailing edge, most turbulence in the wake is initially produced in the separated and recirculating flow zones, which give the initial condition for wake profile development, as well as initial values of turbulence at the beginning of the wake. As the wake continues to develop downstream, turbulence decays with streamwise distance because turbulence production is less than diffusion and advection. As a result, the shape of momentum deficit changes mostly due to the transverse diffusion of momentum. Overall magnitudes of total pressure deficits and momentum deficits then do not change greatly as the wake is advected in the streamwise direction because not much mean streamwise momentum is converted into turbulence by local shear and turbulence production. Such trends in the present data are consistent with results presented by Mee et al. [28], who suggest that most en-

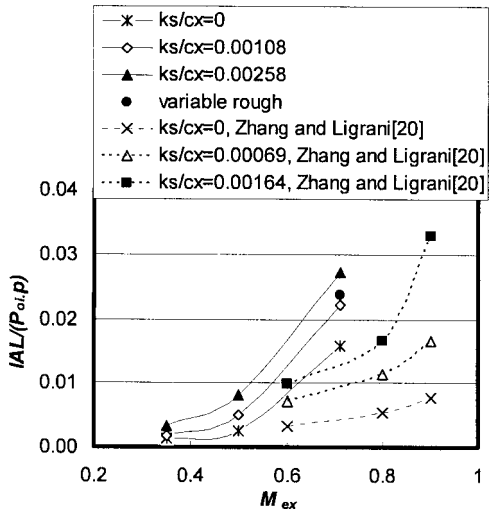

Fig. 12 Comparison of normalized integrated aerodynamic loss magnitudes as dependent upon exit Mach number, and measured one chord length downstream of the airfoils

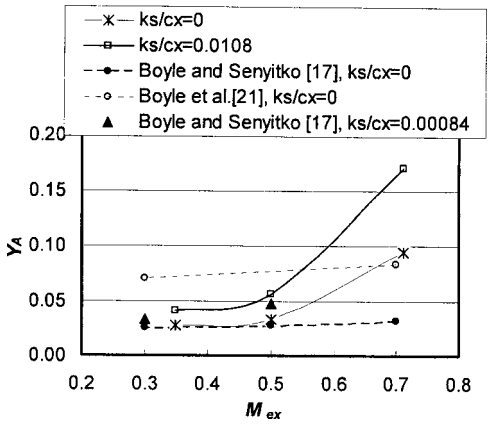

Fig. 13 Comparison of area averaged loss coefficient with Boyle and Senyitko [17], and Boyle et al. [21]

tropy increases take places close to the trailing edge of the airfoils. Additional mixing losses are then only a small fraction of overall loss magnitudes.

IAL data are normalized using the test section passage pitch p and test section inlet stagnation pressure P_{oi} in Fig. 12, which shows how *IAL* data vary with exit Mach number for different values of k_s/cx. IAL values increase as the exit Mach number increases for each value of k_s/cx. Note that dramatic increases in IAL magnitudes are observed as the exit Mach number increases from 0.50 to 0.71. This is due in part to the flow diffusion zone which is present for $Bx/cx > 0.80$ on the suction side of the $M_{ex} = 0.71$ vane. The overall data trend is consistent with results from Zhang and Ligrani [20], whose data for a symmetric airfoil are included in Fig. 12 and show similar qualitative trends. When compared at the same exit Mach number, the present normalized IAL data for cambered test vanes are then much higher than data obtained downstream of straight symmetric airfoils without flow turning. This is due to different flow diffusion-separation zones, and different flow development over the symmetric and cambered airfoils from different pressure gradients and different amounts of streamline curvature which are imposed on airfoil boundary layers. Such imposed pressure gradients are a result of airfoil shape, the imposed Mach number distribution, and streamline curvature and flow turning in the flow outside of the boundary layers. Overall, these results show that greater losses are present with flow turning and cambered airfoils.

One data point is included in Fig. 12 for the vane with variable roughness. As mentioned, different wake behavior is tied to different rates of boundary layer development (especially on the vane pressure side), different magnitudes of boundary layer mixing and losses, and a different wake initial condition near the vane trailing edge (on both pressure and suction sides), compared to vanes with uniformly roughened surfaces. As a result, the corresponding normalized IAL value in Fig. 12 is between values for the $k_s/cx = 0.00108$ and $k_s/cx = 0.00258$ uniformly roughened vanes for an exit Mach number of 0.71.

3.6 Comparisons With Loss Data From Other Research Groups. Different loss coefficient definitions are generally employed by different research groups. Of these, Boyle and Senyiko [17] and Boyle et al. [21] employ an area averaged loss coefficient, Y_A, in their analysis, which is defined using an equation of the form

$$Y_A = \frac{P_{oi} - P_{oe,A}}{P_{oi} - P_{se,A}} \tag{5}$$

Here, $P_{oe,A}$ and $P_{se,A}$ are area averaged exit total pressure and static pressure, respectively. These are determined using equations given by

$$P_{oe,A} = \int_{-p/2}^{p/2} P_{oe} d(y/p) \tag{6}$$

and

$$P_{se,A} = \int_{-p/2}^{p/2} P_{se} d(y/p) \tag{7}$$

respectively. Boyle and Senyiko [17] employ vanes with 5.18 cm axial chord length and 75 deg flow turning angle. Their data are based on measurements made 0.35 of an axial chord length downstream of their vane. In the same experimental facility, Boyle et al. [21] employ vanes with 4.445 cm axial chord length and approximately 80 deg flow turning angle in their investigation. Figure 13 shows comparisons of their data with results from the present study over a range of exit Mach numbers and different k_s/cx values. These data indicate that higher Y_A losses are generally observed as either exit Mach number or surface roughness increases. Of particular interest is the dramatic increase in present Y_A magnitudes that occurs as the exit Mach number increases from 0.5 to 0.7 for the airfoils with k_s/cx magnitudes of 0 and 0.0108. Note that Y_A magnitudes from smooth vanes from Boyle and Senyiko [17] and Boyle et al. [21] are somewhat different from each other because of different vane configurations and different operating conditions in the two investigations. Such differences also partially account for some of the differences between these data and results from the present investigation. In other cases, the present results show agreement with some of the results from Refs. [17,21].

Kind et al. [10] employ a mass averaged loss coefficient, Y_p in their turbine cascade investigation, which is defined using

$$Y_p = \frac{P_{oi} - P_{oe,m}}{q_{e,m}} \tag{8}$$

where $p_{oe,m}$ and $q_{e,m}$ are mass-averaged exit total pressure, and mass-averaged dynamic pressure, respectively. These two parameters are defined with equations that are given by

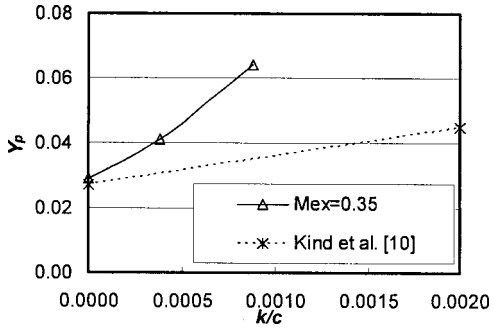

Fig. 14 Comparison of mass averaged loss coefficients with similar results from Kind et al. [10]

$$P_{oe,m} = \frac{\int_{-p/2}^{p/2} \rho u P_{oe} dy}{\rho_\infty u_\infty p} \tag{9}$$

and

$$q_{e,m} = \frac{\int_{-p/2}^{p/2} \rho u q_e dy}{\rho_\infty u_\infty p} \tag{10}$$

respectively. Data from Kind et al. [10] are presented and compared with some data from the present investigation in Fig. 14. Their data are measured 0.4 of an axial chord length downstream of their airfoil. In Fig. 14, Y_p loss coefficient data are given as they vary with normalized mean roughness height k/c since sandgrain roughness height, k_s, is not available from Kind et al. [10]. Y_p loss coefficient results from the present study as well as from Kind et al. [10] increase as the normalized mean roughness height becomes larger. Similar magnitudes of Y_p for the two studies are evident for $k/c=0$ (i.e., smooth vane surfaces). However, differences are evident between the two data sets when $k/c>0$, which are most likely due to different surface roughness characteristics. For example, the Kind et al. [10] roughness with k/c of 0.002, may be comprised of roughness elements with different density compared to ones employed in the present study. Such roughness could thus give different Y_p loss coefficient magnitudes even though mean roughness heights may be comparable.

4 Summary and Conclusions

The effects of surface roughness on the aerodynamic performance of a turbine vane are investigated for three Mach number distributions, one of which results in transonic flow. All three Mach number distributions and the vane configuration match arrangements employed in industrial applications. One smooth vane is employed, along with two other vanes with three-dimensional roughness distributed uniformly over entire vane surfaces. A fourth vane is also employed with roughness of different sizes distributed over the vane surface (i.e., a variable rough surface) whose arrangement is based on observations of roughened turbine vanes from industrial applications. All four turbine vanes have the same shape and exterior dimensions. This is verified for the smooth vane and the vane with uniform $k_s/cx=0.00108$ roughness since the same Mach number distribution is present with each.

The nonuniform, irregular, three-dimensional roughness on the tested vanes is employed to match the roughness which exists on operating turbine vanes and blades subject to extended operating times with significant particulate deposition on the surfaces. This is verified by detailed three-dimensional optical profilometry traces and rough surface statistics (such as equivalent sandgrain roughness size) which are similar for the roughness from a power engine turbine blade and the test surfaces employed in this study.

Total pressure losses, Mach number deficits, and deficits of kinetic energy all increase at each y/cx location within the wake as k_s/cx increases, regardless of the level, uniformity, or variability of the roughness along the surfaces of the vanes. The wakes also become broader with increased roughness size or with increased exit Mach number M_{ex} due to higher advection velocities, augmentations of mixing and turbulent transport, thicker boundary layers, earlier laminar-turbulent transition and increased turbulent diffusion. Peak values of total pressure loss coefficients also increase dramatically as M_{ex} increases. In general, these profiles are asymmetric because the effects of surface roughness are much less apparent for positive y/cx values, downstream of the pressure sides of the vanes. This is due to different loading, different boundary layer growth, and different susceptibility to flow separation on the different vane surfaces, which also causes the suction side wakes (at negative y/cx) to be thicker than the pressure side wakes (at positive y/cx). Overall, the wakes are pushed toward smaller y/cx values as they are advected downstream (i.e., towards the vane suction side), regardless of the level, uniformity, or variability of the roughness along the surfaces of the vanes. Aside from this, the data from a vane with variable surface roughness show different quantitative and qualitative trends compared to profiles measured downstream of vanes with roughness spread uniformly over the surfaces. This is partially due to different rates of boundary layer development as different levels of roughness are encountered along the vane pressure surface.

For each value of k_s/cx, dramatic and important IAL magnitude increases are present as higher Mach numbers are present along the airfoil. IAL magnitudes also increase almost linearly as k_s/cx increases for each profile measurement location and for each value of exit Mach number. When the exit Mach number is 0.71, the normalized IAL value for the variable roughened vane is between values for the $k_s/cx=0.00108$ and $k_s/cx=0.00258$ uniformly roughened vanes. In contrast, the IAL differences obtained at each M_{ex} for $1cx$ and $0.25cx$ are relatively small compared to overall IAL loss magnitudes. This is because not much mean streamwise momentum is converted into turbulence by local shear and turbulence production as the wake is advected in the streamwise direction. When compared at the same exit Mach number, the present normalized IAL data for cambered test vanes are much higher than data obtained downstream of straight symmetric airfoils without flow turning. Overall, this means that greater losses are present with flow turning and cambered airfoils, than with symmetric airfoils.

Magnitudes of area-averaged loss coefficients Y_A generally increase as either exit Mach number or equivalent sandgrain roughness size increases. The increases in Y_A magnitudes are especially substantial as the exit Mach number increases from 0.5 to 0.7 for the smooth vane and the uniformly roughened vane with $k_s/cx=0.0108$. Mass-averaged loss coefficients Y_p show similar trends, since they also increase as normalized mean roughness height becomes larger for a particular value of vane exit Mach number.

Acknowledgment

The research reported in this paper was sponsored by the National Science Foundation (NSF Grant No. CTS-0086011). Dr. Stefan Thynell and Dr. Richard Smith were the NSF program monitors. The authors also acknowledge Dr. Mike Blair of Pratt and Whitney Corporation, Dr. Hee-Koo Moon of Solar Turbines, Inc., Dr. Ed North, Dr. Ihor Diakunchak of Siemens-Westinghouse Corp., and personnel from Pratt and Whitney – Canada Corporation for guidance and suggestions on this research effort, and for providing roughened turbine vane hardware from engines for analysis and comparison. The authors also thank Dr. Forest Ames of the University of North Dakota, Dr. Robert Boyle of NASA Glenn Research Center for their helpful and valuable suggestions on many details of the present research. Atem Khalatov of the Ukrainian Academy of Sciences is also acknowledged for several suggestions he provided on the effort.

Nomenclature

Bx = normal coordinate measured from vane leading edge
c = true chord length
cx = axial chord length
C_p = local total pressure coefficient, $(P_{oi}-P_{oe})/P_{oi}$
IAL = integrated aerodynamic losses
M_e = exit local Mach number
$M_{e,\infty}$ = exit free-stream Mach number
k = roughness height
K = dimensionless acceleration parameter, $(v/U_\infty^2)(dU_\infty/ds)$
KE = normalized local kinetic energy, $(P_{oe}-P_{se})/(P_{oe}-P_{Se})_\infty$
k_s = equivalent sand grain roughness
p = passage pitch
P_o = stagnation pressure
P_{oe} = exit local stagnation pressure
$P_{oe,m}$ = mass averaged exit stagnation pressure
$P_{oe,\infty}$ = exit freestream stagnation pressure
$P_{oe,A}$ = area averaged exit total pressure
$P_{se,A}$ = area averaged static pressure
P_{se} = exit local static pressure
P_{oi} = inlet stagnation pressure
PS = pressure side
q_e = exit local dynamic pressure
$q_{e,m}$ = exit mass-weighted dynamic pressure
s = blade surface length from leading edge of the vane
S = rough surface flat reference area
S_f = total roughness frontal area
S_s = total roughness windward wetted surface area
SS = suction side
u = exit local streamwise velocity
U_∞ = freestream velocity over the vane surface
v = kinematic viscosity
x = linear distance from vane trailing edge in direction of vane trailing edge camber line
y = normal coordinate measured from line tangent to vane trailing edge camber line
Y_A = area averaged loss coefficient used by Boyle et al. [17]
Y_P = mass averaged loss coefficient used by Kind et al. [10], $(P_{oi}-P_{oe,m})/q_{e,m}$
Λ_s = Sigal and Danberg roughness parameter
ω = total pressure loss coefficient used by Ames and Plesniak [27],$(P_{oi}-P_{oe})/(P_{oi}-P_{se})$
ρ = exit local density

Subscripts

A = area-averaged
e = exit
M = mass-averaged
∞ = freestream

References

[1] Nikuradse, J., 1933, "Laws of Flow in Rough Pipes," NACA TM 1292, National Advisory Committee on Aeronautics.
[2] Schlichting, H., 1936, "Experimental Investigation of the Problem of Surface Roughness," NACA TM-832, National Advisory Committee on Aeronautics.
[3] Coleman, H. W., Hodge, B. K., and Taylor, R. P., 1984, "A Re-Evaluation of Schlichting's Surface Roughness Experiment," ASME J. Fluids Eng., **106**, pp. 60–65.
[4] Sigal, A., and Danberg, J. E., 1990, "New Correlation of Roughness Density Effect on Turbulent Boundary Layer," AIAA J., **28**, pp. 554–556.
[5] Sigal, A., and Danberg, J. E., 1988, "Analysis of Turbulent Boundary Layer Over Roughness Surface With Application to Projectile Aerodynamics," Amy Ballistic Research Lab, Aberdeen Proving Grounds MD, Technical Report BRL-TR-2977.
[6] Van Rij, J. A., Belnap, B. J., and Ligrani, P. M., 2002, "Analysis and Experiments on Three-Dimensional, Irregular Surface Roughness." ASME J. Fluids Eng., **124**, pp. 1–7.
[7] Zhang, Q., Lee, S. W., and Ligrani, P. M., 2003, "Determination of Rough-Surface Skin Friction Coefficients From Wake Profile Measurements," Exp. Fluids, **35**, pp. 627–635.
[8] Bammert, K., and Sandstede, H., 1975, "Influence of Manufacturing Tolerances and Surface Roughness of Blades on the Performance of Turbines," ASME Paper No. 75-GT-35.
[9] Bammert, K., and Sandstede, H., 1980, "Measurements of the Boundary Layer Development Along a Turbine Blade With Rough Surfaces." ASME J. Eng. Power, **102**, pp. 978–983.
[10] Kind, R. J., Serjak, P. J., and Abbott, M. W. P., 1996, "Measurements and Prediction of the Effects of Surface Roughness on Profile Losses and Deviation in a Turbine Cascade," ASME Paper No. 95-GT-203.
[11] Bogard, D. G., Schmidt, D. L., and Tabbita, M., 1998, "Characterization and Laboratory Simulation of Turbine Airfoil Surface Roughness and Associated Heat Transfer," ASME J. Turbomach., **120**, pp. 337–342.
[12] Abuaf, N., Bunker, R. S., and Lee, C. P., 1998, "Effects of Surface Roughness on Heat Transfer and Aerodynamics Performance of Turbine Airfoils," ASME J. Turbomach., **120**, pp. 522–529.
[13] Leipold, R., Boese, M., and Fottner, L., 2000, "The Influence of Technical Surface Roughness Caused by Precision Forging on the Flow Around a Highly Loaded Compressor Cascade," ASME J. Turbomach., **122**, pp. 416–425.
[14] Sitaram, N., Govardhan, M., and Murali Krishna, V. T., 1999, "Loss Reduction by Means of Two-Dimensional Roughness Elements on the Suction Surface of a Linear Turbine Rotor Cascade, Flow, Turbul. Combust., **62**, pp. 227–248.
[15] Stripf, M., Schulz, A., and Wittig, S., 2004, "Surface Roughness Effects on External Heat Transfer of a HP Turbine Vane," *Proceedings of ASME Turbo Expo 2004*, GT2004-53114.
[16] Roberts, S. K., and Yaras, M. I., 2004, "Boundary-layer Transition Over Rough Surfaces With Elevated Free-stream Turbulence," *Proceedings of ASME Turbo Expo 2004*, GT2004-53668.
[17] Boyle, R. J., and Senyitko, R. G., 2003, "Measurements and Predictions of Surface Roughness Effects on Turbine Vane Aerodynamics," *Proceedings of ASME Turbo Expo 2003*, GT-2003-38580.
[18] Zhang, Q., Lee, S. W., and Ligrani, P. M., 2004, "Effects of Surface Roughness and Turbulence Intensity on the Aerodynamic Losses Produced by the Suction Surface of a Simulated Turbine Airfoil," ASME J. Fluids Eng., **126**, pp. 257–265.
[19] Zhang, Q., Lee, S. W., and Ligrani, P. M., 2004, "Effect of Surface Roughness and Freestream Turbulence on the Wake Turbulence Structure of a Symmetric Airfoil," Phys. Fluids, **16**, pp. 2044–2053.
[20] Zhang, Q., and Ligrani, P. M., 2004, "Effects of Mach Number and Surface Roughness on the Aerodynamic Losses of a Symmetric Transonic Turbine Airfoil," J. Propul. Power, **20**, pp. 1117–1125.
[21] Boyle, R. J., Luci, B. L., Verhoff, V. G., Camperchioli, W. P., and La, H., 1998, "Aerodynamics of a Transitioning Turbine Stator Over a Range of Reynolds Numbers," ASME Paper 98-GT-285.
[22] Boyle, R. J., 2004, private communication.
[23] Jackson, D. J., Lee, K. L., Ligrani, P. M., Johnson, P. D., 2000, "Transonic Aerodynamics Losses due to Turbine Airfoil, Suction Surface Film Cooling," ASME J. Turbomach., **122**, pp. 317–326.
[24] Furukawa, T., and Ligrani, P. M., 2002, "Transonic Film Cooling Effectiveness From Shaped Holes on a Simulated Turbine Airfoil," J. Thermophys. Heat Transfer, **16**, pp. 228–237.
[25] Kline, S. J., and McClintock, F. A., 1953, "Describing Uncertainties in Single Sample Experiments," Mech. Eng. (Am. Soc. Mech. Eng.), **75**, pp 3–8.
[26] Moffat, R. J., 1988, "Describing the Uncertainties in Experimental Results," Exp. Therm. Fluid Sci., **1**, pp. 3–17.
[27] Ames, F. E., and Plesniak, M. W., 1997, "The Influence of Large-Scale High-Intensity Turbulence on Vane Aerodynamic Losses, Wake Growth, and the Exit Turbulence Parameters," ASME J. Turbomach., **119**, pp. 182–192.
[28] Mee, D. J., Braines, N. C, Oldfield, M. L. G., and Dickens, T. E., 1992, "An Examination of the Contributions to Loss on a Transonic Turbine Blade in Cascade," ASME J. Turbomach., **114**, pp. 155–162.

Stephen T. McClain
Assistant Professor
Department of Mechanical Engineering,
The University of Alabama at Birmingham,
1530 3rd Ave. S., BEC 358B,
Birmingham, AL 35294-4461

S. Patrick Collins
Graduate Research Assistant
Department of Mechanical Engineering,
The University of Alabama at Birmingham,
1530 3rd Ave. S., BEC 257,
Birmingham, AL 35294-4461

B. Keith Hodge
Professor
Department of Mechanical Engineering,
Mississippi State University,
P.O. Box ME,
Mississippi State, MS 39762

Jeffrey P. Bons
Associate Professor
Department of Mechanical Engineering,
Brigham Young University,
435 CTB, P.O. Box 24201,
Provo, UT 84602-4201

The Importance of the Mean Elevation in Predicting Skin Friction for Flow Over Closely Packed Surface Roughness

The discrete-element surface roughness model is used to provide insight into the importance of the mean elevation of surface roughness in predicting skin friction over rough surfaces. Comparison of experimental data and extensive computational results using the discrete-element model confirm that the appropriate surface for the imposition of the no-slip condition is the mean elevation of the surface roughness. Additionally, the use of the mean elevation in the Sigal-Danberg approach relating their parameter to the equivalent sand-grain roughness height results in replacing three different piecewise expressions with a single relation. The appropriate mean elevation for closely-packed spherical roughness is also examined. [DOI: 10.1115/1.2175164]

Introduction

Historically, the two dominant methods for evaluating the effects of surface roughness on drag and heat transfer have been the equivalent sand-grain roughness model and the discrete-element model. The equivalent sand-grain roughness model, first proposed by Schlichting [1], is an empirical model in which rough surfaces with various features are compared to data from Nikuradse [2] concerning flow in pipes with varying sizes of sieved sand glued to the wetted surface. Rough surfaces are assigned a value of equivalent sand-grain roughness height based on comparisons with Nikuradse's fully rough data. Recent literature on the equivalent sand-grain roughness method has involved seeking correlations for equivalent sand-grain roughness height based on roughness metrics such as height, shape, and density. Dvorak [3], Simpson [4], Dirling [5], Sigal and Danberg [6], and Bons [7] have all proposed functions to predict the effective sand-grain roughness height based on parameters involving the roughness height, shape, and density.

Several disadvantages of the equivalent sand-grain method have been noted. A detailed discussion of these disadvantages is presented by Taylor [8]. The Sigal-Danberg parameter is determined using the relationship

$$\Lambda_s = \frac{S_{pa}}{S_f}\left(\frac{A_f}{A_s}\right)^{-1.6} \tag{1}$$

where S_{pa} is the plan area (as seen from above) of the surface and S_f is the total frontal area of the roughness elements, A_f is the frontal area of the elements, and A_s is the windward wetted surface area of the roughness elements. While the Sigal-Danberg parameter has demonstrated the most promise for correlating the available equivalent roughness height data, the best correlation based on the parameter is still limited. Bons [7] has also shown that (1) the Sigal-Danberg parameter is difficult to define for roughness elements with random spacings, shapes, and heights, (2) wind tunnel measurements of equivalent sand-grain roughness heights for randomly rough surfaces can vary as much as 40% from predicted heights using logarithmic data curve-fits based on the Sigal-Danberg parameter, and (3) different correlations are required for randomly rough surfaces and for three-dimensional uniform roughness.

Attempts to use one value of equivalent sand-grain roughness height to predict both skin friction and heat transfer have been unsuccessful. In fact, there is no reason that two surfaces with the same skin friction coefficients, which implies that they would have the same equivalent sand-grain roughness value from a friction standpoint, should have the same Stanton numbers.

The discrete-element model is an alternative to the equivalent sand-grain model. While the equivalent sand-grain model is based completely on empirical correlation, the discrete-element model evaluates the effects of roughness by considering the physical characteristics of the roughness elements in the solution of the boundary-layer equations. The discrete-element model is semi-empirical in the sense that the relationships used to determine the local drag on the roughness elements are based on empirical data including Schlichting's 1937 data set.

The basis for the discrete-element model was also described by Schlichting in his 1937 paper. In attempting to explain the effect of roughness element density on the effective sand-grain height, Schlichting suggested that the total drag on a rough surface is the sum of the skin friction on the flat part of the surface and the form drag on the individual roughness elements. Methods to solve the boundary-layer equations for flow over rough surfaces, such as Finson [9], Adams and Hodge [10], and Lin and Bywater [11], incorporated momentum sink terms into the boundary-layer equations based on Schlichting's suggestion. The form of the discrete-element roughness model presented in this paper originated in the work of Finson [9] and was rigorously derived by Taylor [8].

The discrete-element model has been validated using many data sets for surfaces with ordered roughness elements with the same

Contributed by the Fluids Engineering Division of ASME for publication in the JOURNAL OF FLUIDS ENGINEERING. Manuscript received February 4, 2005; final manuscript received October 25, 2005. Review conducted by Joseph Katz.

shape (Taylor [8], Scaggs et al. [12], Hosni [13], Chakroun [14]). Taylor et al. [15] have validated the discrete-element model for ordered roughness elements with varying shapes for completely rough flow in pipes. In most of the validation cases however, the roughness elements were sparsely spaced, and agreement between predictions and experimental measurement was better for the sparsely spaced-element rough surfaces than for the few closely packed element rough surfaces.

The discrete-element model (DEM) was also recently adapted to predict skin friction and heat transfer for flows over randomly rough surfaces [16]. In McClain et al. [16], two surfaces were generated for wind-tunnel testing that were developed from real gas-turbine surfaces with fuel deposit and erosion roughness as measured using a three-dimensional profilometer. The surface profiles were scaled and created so that when the surfaces were tested in the wind-tunnel, the ratio of roughness height to boundary-layer thickness was similar to that found during turbine operation.

In McClain et al. [16], major modifications to the discrete element model for randomly rough surfaces were the use of the mean elevation as the location of the no-slip plane and the incorporation of the element eccentricity in local roughness element drag determination. The use of the mean elevation as the location of the no-slip plane presents a significant implication for closely packed cone surfaces. Since the application of the mean elevation as the location of the no-slip surface produced excellent agreement between skin friction measurements and predictions for randomly rough surfaces, applying the mean elevation as the no-slip surface should also be applicable and appropriate for predicting skin friction for flows over surfaces with closely packed, ordered elements with the same shape.

For this study, skin friction measurements were made for two surfaces with conical roughness elements. On one of the surfaces, the elements were very closely packed. The roughness elements on the other surface were moderately packed as compared to surfaces tested by Schlichting [1], Scaggs et al. [12], Hosni [13], Chakroun [14], and Taylor et al. [15]. The two cone-roughness surfaces were created with characteristics congruent with the real random roughness described in the works by Bons [7] and McClain et al. [16]. Measurements of skin friction for turbulent flow over the conical roughness surfaces were made for comparison to predictions using the discrete-element model.

Since the DEM has been extensively validated for the aforementioned data sets and since the DEM captures the relevant physics (in the spatially averaged sense) of a wide range of roughness geometries, the DEM provides a proven tool for analysis and design procedures for turbulent flow over rough surfaces. Hence, given a detailed description of the surface roughness, the DEM has been shown to posses the capability to properly account for the surface geometry effects on the surface measurables. When incorporated into a design code the DEM will capture the salient, spatially averaged effects of the surface roughness.

The Discrete-Element Model

The discrete-element model is formulated for roughness elements with three-dimensional shapes for which the element cross section can be defined at every height, y. The differential equations including roughness effects are derived by applying the basic conservation statements for mass and momentum to a control volume such as that shown in Fig. 1. Basic to this approach is the idea that the two-dimensional, time-averaged turbulent boundary-layer equations can be applied in the flow region below the crests of the roughness elements. The flow variables are spatially averaged over the transverse (z) direction and the streamwise (x) direction. The physical effects of the roughness elements on the fluid in the control volume are modeled by considering the flow blockage, the local element heat transfer, and the local element form drag. The void factors, β, are defined as the fraction of the area open to flow. The form drag force on the control volume is

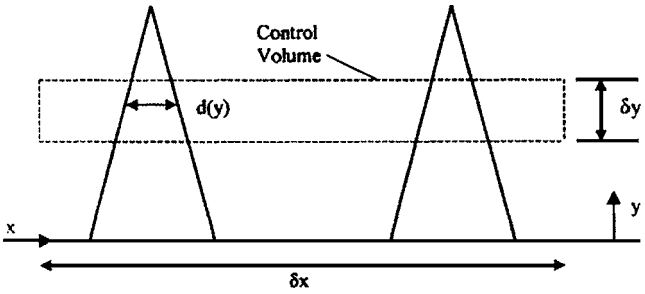

Fig. 1 The discrete-element roughness model control volume schematic

due to the portion of the roughness elements penetrating the control volume and is expressed using a local drag coefficient as

$$F_D = \tfrac{1}{2}\rho u^2 \delta y \sum_{i=1}^{N_r} C_{D,i} d_i(y) \tag{2}$$

Where N_r is the number of roughness elements in the control volume at the given height.

Using the above concept, the continuity and momentum equations for a steady, Reynolds averaged, two-dimensional turbulent boundary layer with ordered distributions of nonuniform roughness are

$$\frac{\partial}{\partial x}(\rho\beta_x u) + \frac{\partial}{\partial y}(\rho\beta_y v) = 0 \tag{3}$$

$$\beta_x \rho u \frac{\partial u}{\partial x} + \beta_y \rho v \frac{\partial u}{\partial y} = -\frac{\partial}{\partial x}(\beta_x P) + \frac{\partial}{\partial y}\left[\beta_y\left(\mu\frac{\partial u}{\partial y} - \overline{\rho u' v'}\right)\right] - \frac{1}{2}\rho\frac{u^2}{L_p L_t}\sum_{i=1}^{N_r} C_{D,i} d_i \tag{4}$$

The turbulence model is not modified to include roughness effects since the physical effects of the roughness on the flow are explicitly included in the differential equations. In this study, the Prandtl mixing length with van Driest damping is used for turbulence closure. Hence

$$-\overline{\rho u' v'} = \rho l_m^2 \left(\frac{\partial U}{\partial y}\right)\left|\frac{\partial U}{\partial y}\right| \tag{5}$$

where

$$l_m = \begin{cases} 0.41y[1-\exp(-y^+/26)] & \text{for } l_m \leqslant 0.09\delta \\ 0.09\delta & \text{otherwise} \end{cases} \tag{6}$$

In addition to the usual turbulence modeling closure requirements for $-\overline{\rho u' v'}$ and $\overline{u'^2}$, the roughness model has closure requirements for C_D. C_D is formulated as a function of the local roughness element Reynolds number

$$\mathrm{Re}_d = \frac{\rho u(y) d(y)}{\mu} \tag{7}$$

thus directly including information on the roughness element size and shape. The functional forms for C_D used in this study for circular roughness elements is

$$C_D = \begin{cases} \left(\dfrac{\mathrm{Re}_d}{1000}\right)^{-0.125} & \mathrm{Re}_d < 60{,}000 \\ 0.6 & \mathrm{Re}_d > 60{,}000 \end{cases} \tag{8}$$

The functional form for C_D was determined by extensive calibrations using a number of deterministic surface roughness data sets [8,17].

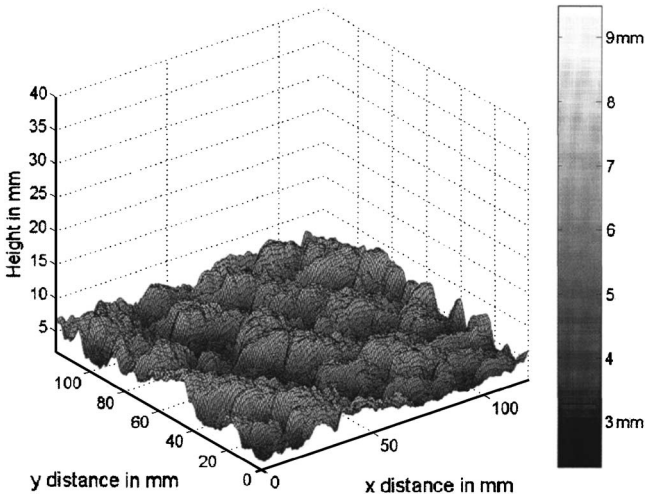

Fig. 2 A randomly rough surface

For ordered, sparse distributions of roughness elements, the boundary conditions imposed on the boundary-layer equations are

$$y = 0: u = v = 0$$

$$y \to \infty : u = U_e \tag{9}$$

Once the fluid velocity and temperature profiles are found, the skin friction relationship is

$$C_f = \frac{(1-\alpha)\mu \left.\frac{du}{dy}\right|_{y=0} + \frac{1}{2}\frac{1}{L_t L_p}\int_0^\infty \left(\rho u^2 \sum_{i=1}^{N_r} C_{D,i} d_i\right) dy}{\frac{1}{2}\rho U_e^2} \tag{10}$$

DEM Modifications for Randomly Rough Surfaces

In McClain et al. [16], the discrete element was adapted for flows over randomly rough surfaces. The adaptation made for flows over random roughness that is relevant to this study is the adoption of the mean elevation as the datum or location of the no-slip surface. Figure 2 presents a three-dimensional representation of a randomly rough surface. The most obvious difference between the surface depicted in Fig. 2 and the cone surface represented in Fig. 1, is that there is no "flat" part of the randomly rough surface from which to reference the discrete-element boundary-layer equations.

A reference or datum is needed for the application of the boundary conditions in solving the boundary-layer equations. A reference surface at the minimum elevation makes sense for the blockage-fraction evaluation, but the roughness model needs both blockage-fraction and blockage-diameter distributions. For random roughness with closely-spaced roughness features below the mean elevation, the concept of a blockage diameter is not appropriate. Because all of the blockage elements are connected, the effective diameter of the blockages becomes the length of the profilometer trace as the minimum elevation is approached.

McClain et al. [16] determined that the mean elevation serves as the computational location of the no-slip surface for randomly rough surfaces. Since the mean elevation is the mean location of the no-slip surface, applying the no-slip surface at the mean elevation is consistent when using a spatially averaged model such as the discrete-element model. Using the mean elevation as the location of the no-slip surface produced very good agreement with experimental measurements of skin friction for turbulent flows over randomly rough surfaces.

When the mean elevation is used as the datum, the boundary conditions used to solve the discrete element boundary-layer equations are

$$y = y_{me}: u = v = 0$$

$$y \to \infty : u = U_e \tag{11}$$

where y_{me} is the height of the mean elevation. Once the boundary-layer equations are solved, the skin friction coefficient is then calculated using

$$C_f = \frac{(1-\alpha)\mu \left.\frac{du}{dy}\right|_{y=y_{me}} + \frac{1}{2}\frac{1}{L_t L_p}\int_{y_{me}}^\infty \left(\rho u^2 \sum_{i=1}^{N_r} C_{D,i} d_i\right) dy}{\frac{1}{2}\rho U_e^2} \tag{12}$$

Surface Creation and Descriptions

Since the use of the mean elevation as a datum is effective for randomly rough surfaces, using the mean elevation should also applicable for rough surfaces with closely packed and ordered roughness elements of the same shape. To test the hypothesis, the skin friction coefficients were measured for two surfaces with close to moderately close arrangements of conical roughness elements. Discrete-element predictions were then made using the flat surface elevation as datum and also using the mean elevation as the datum.

Two cone surfaces were studied. The cone surfaces were generated to have characteristics congruent with two randomly rough surfaces created from scaled profilometer traces taken from real gas turbine surface roughness [7,16]. The conical roughness elements on Surface 1 were created with a height equal to three times the rms roughness height, R_q, of the deposit surface described by McClain et al. [16]. The rms roughness height, R_q is determined using

$$R_q = \sqrt{\frac{1}{N}\sum_{i=1}^{N} y_i^2} \tag{13}$$

where y_i is measured from the mean elevation of the surface. The height multiplier of three is a nominal value based on the discussion by Tolpadi and Crawford [18] regarding the relationship between the statistical parameters of a randomly rough surface and its equivalent sand-grain height.

For the deposit surface, the correlation length, λ_c, was found using Fourier decomposition. The dominant frequencies were found and the correlation length was calculated as the distance at which the autocorrelation function falls to a value of 0.1. The diameter of the cones on Surface 1 was set to one-half the correlation length, and the spacing was set equal to the correlation length.

The roughness elements on Surface 2 were created with a height equal to three times the R_q of the erosion-2 surface as described by McClain et al. [16]. The diameter of the elements on Surface 2 was set as twice the correlation length for the erosion-2 surface. The spacing of the cones was set so that distance between the rows of cones in the direction of the flow equaled the base diameter of the cones.

The two cone surfaces were generated using the three-dimensional (3D) printer and studied in the wind tunnel. A Stratasys Genisys Xs three-dimensional printer was used to create coupons of the cone roughness surfaces. The Genisys Xs printer generates 3D models with a resolution of 0.33 mm using a durable polyester. The printed surface coupons were fitted and connected together to make roughness panels to be placed in a wind tunnel for testing. Table 1 presents the measured characteristics of the cone surfaces from the three-dimensional printer.

Table 1 Summary of surface characteristics

Surface	k (mm)	d_0 (mm)	S (mm)	L_p (mm)	L_t (mm)	S/d_0
Surface 1	4.420	5.969	12.065	10.449	12.065	2.021
Surface 2	1.905	4.445	5.207	4.509	5.207	1.171

The height of the cones above the mean elevation and the diameter of the cone at the mean elevation, as depicted in Fig. 3, are calculated using Eqs. (14) and (15), respectively.

$$k_{\text{eff}} = k - \frac{\pi d_0^2 k}{12 L_p L_t} \tag{14}$$

$$d_{0,\text{eff}} = d_0 \frac{k_{\text{eff}}}{k} \tag{15}$$

The heights and diameters of the Surface 1 cones above the mean elevation are 4.093 and 5.527 mm, respectively. The heights and diameters of the cones on Surface 2 above the mean elevation are 1.485 and 3.466 mm, respectively.

Skin Friction Measurements

The wind tunnel used in this study is housed at the Air Force Research Laboratory (AFRL) at Wright-Patterson Air Force Base in Dayton, OH. The wind tunnel is an open-loop tunnel with a nominal cross section of 0.24 m by 0.38 m in the test section. For the tests presented here, the wall was adjusted to produce zero freestream acceleration [7]. Flow enters the test section through a main conditioning plenum and an entry section. As the flow exits the entry section and just before the flow enters the test section of the tunnel, the boundary layer is bled from the flow using a knife-edge boundary-layer bleed and a boundary-layer suction blower. This creates the situation where the boundary-layer thickness is zero at the entry of the test section. For all skin friction measurements, the flow was tripped turbulent using a 1.6 mm diameter cylinder placed 2.54 cm from the knife-edge. Roughness panels, 0.32 m in length, were placed 1.04 m from the knife-edge of the test section. The tunnel then continues 0.62 m beyond the trailing edge of the roughness panels. The freestream turbulence intensity, $\text{Tu} = u'_{\text{rms}}/U_e$, was measured using a hot-wire anemometry system and was found to be consistently 0.9% for all of the skin friction measurements.

The skin friction coefficients were determined by suspending the roughness panels in the wind tunnel using wires attached to the wind-tunnel framing and measuring the downstream movement of the panels during a test. Detailed information on the wind tunnel and the average skin friction coefficient determination technique can be found in Bons [7]. Bons [7] reports a systematic uncertainty (bias) of 0.00022 in the measured skin friction coefficients with a 2.8% random uncertainty (repeatability). Detailed information on the simulations and their comparisons to the experimental data can be found in McClain [19].

Skin friction measurements were made for each surface at two Reynolds numbers based on the distance from the leading edge to the center of the roughness panel: A high Re_x around 1,000,000 and a low Re_x around 500,000. Table 2 summarizes the boundary layer and freestream conditions for the rough-surface skin friction measurements. The momentum thickness and boundary-layer thickness were not measured directly in the experiments. The values of Re_θ and k/δ presented in Table 2 are based on the boundary-layer code predictions considering the roughness effects.

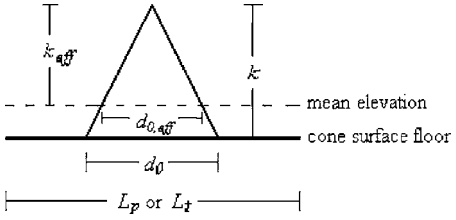

Fig. 3 Mean elevation of the cone surfaces

Table 2 Boundary-layer characteristics for the skin friction coefficient measurements for the rough surfaces

	Re_x	Re_θ	k^+	k/δ
Surface 1	944,000	2600	300.8	0.20
Surface 1	525,000	1600	171.2	0.18
Surface 2	923,000	2300	107.4	0.09
Surface 2	517,500	1400	59.0	0.08

The Reynolds numbers' designations as "high" or "low" are compared only to the Reynolds numbers used in this study. A typical turbine blade chord Re is 500,000 to 2,000,000. The finite range used in this study is in the low to mid-range of typical gas-turbine chord Reynolds numbers.

Results and Discussion

The discrete-element model was run for the cone surfaces using each of the following options:

(1) the full cones placed on the surface floor with shear acting on the surface floor
(2) the partial cones referenced to the mean elevation with shear acting on the area not blocked at the mean elevation

The discrete-element predictions using the floor of the cone surface as a reference, $C_{f,fl}$, the discrete-element predictions using the mean elevation as a reference, $C_{f,me}$, and the experimentally measured skin friction coefficients, $C_{f,\text{meas}}$, are presented in Table 3 for the high Reynolds number data and in Table 4 for the low Reynolds number data.

The C_f predictions for the smooth surface are within 3.5% of the experimentally measured values. Tables 3 and 4 also show that

Table 3 Comparison of the cone and smooth surface skin friction results and discrete-element predictions at high Reynolds numbers

Surface	$\text{Re}_{\bar{x}}$	$C_{f,\text{meas}}$	$C_{f,me}$ (% diff)	C_{ffl} (% diff)
Surface 1	944,000	0.01450	0.01396 (−3.72)	0.01514 (4.41)
Surface 2	923,000	0.01040	0.01003 (−3.56)	0.01278 (22.88)
Smooth	917,500	0.00349	n/a	0.00356 (2.0)

Table 4 Comparison of the cone and smooth surface skin friction results and discrete-element predictions at low Reynolds numbers

Surface	$\text{Re}_{\bar{x}}$	$C_{f,\text{meas}}$	$C_{f,me}$ (% diff)	C_{ffl} (% diff)
Surface 1	525,000	0.01519	0.01373 (−9.61)	0.01491 (−1.84)
Surface 2	517,500	0.01000	0.00922 (−7.8)	0.01201 (20.10)
Smooth	525,900	0.00377	n/a	0.00390 (3.4)

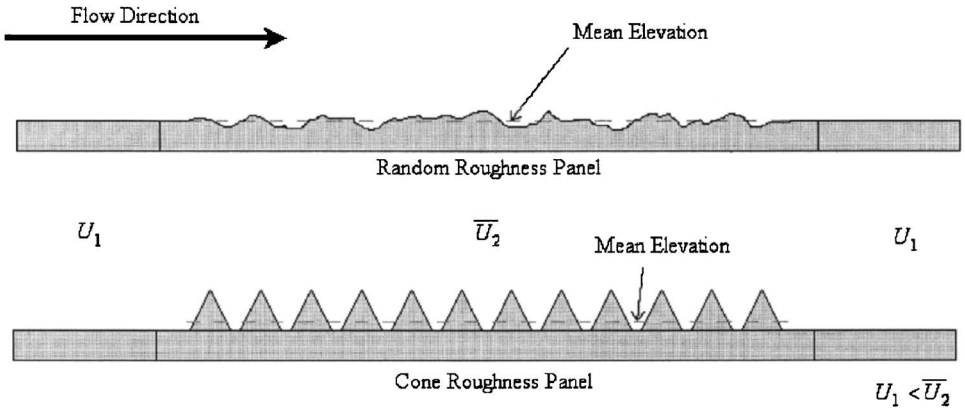

Fig. 4 Comparison of mean elevation for the random and cone roughness panels

the discrete-element predictions using the mean elevation as the reference elevation are all within 10% of the measured skin friction coefficients. While 10% agreement may not be considered acceptable for the prediction of C_f over smooth surfaces, a 10% agreement with experimental data provides a good metric for the accuracy of the DEM in comparison to the alternative prediction techniques for flows over rough surfaces.

For Surface 2, the discrete-element predictions using the floor of the cone surface as a reference overestimate the skin friction coefficients by a minimum of 20%. Using the mean elevation as a reference under predicts the skin friction coefficient by as much as 7.8% for Surface 2. Since the Surface 2 cones are closely packed, the amount of over prediction by the discrete-element model using the flat surface as a reference suggests that using the mean elevation as a reference is appropriate for closely packed surfaces.

For Surface 1, using the mean elevation underestimates the skin friction coefficients. At the low Reynolds number, using the mean elevation underestimates $C_{f,\text{meas}}$ by over 9%. At the high Reynolds number, referencing the flow to the flat part of the cone surface produces less than 5% difference from the measured skin friction coefficient. At the low Reynolds number, referencing the model to the flat part of the cone surface under predicts the skin friction coefficient by 2%.

Because using the mean elevation as a reference underestimates the skin friction coefficients for Surface 2 and because referencing the model to the flat part of the Surface 1 underestimates $C_{f,\text{meas}}$ by more than the experimental uncertainty, other factors must be influencing the flow over the cone surface as tested in the experimental apparatus. One possible cause for the higher measured skin friction coefficients is the change in mean elevation as the flow transitions from smooth surface to rough surface and back to smooth surface along the wind tunnel model. Figure 4 shows the configuration of the random roughness panels and the cone roughness panels in the experimental facility.

The randomly rough surfaces studied by Bons [7] and McClain et al. [16] were placed in the wind tunnel such that the mean elevation of the roughness panels was at the same elevation as the flat surface of the upstream Plexiglas floor of the wind tunnel. Discrete-element predictions were within ±7% of the experimentally measured skin-friction coefficients for the randomly rough surfaces [16]. However, the cone surfaces were installed in the wind tunnel with the floor of the cone surfaces at the same elevation as the upstream Plexiglas. For the cone surfaces, the placement of the roughness elements creates a situation where the mean freestream velocity accelerates as the flow transitions from smooth surface to rough surface. The freestream velocity then decelerates at the downstream portion of the roughness panel as the flow transitions from rough surface back to smooth surface. If the deceleration is strong enough, the flow will separate as found by Pinson and Wang [20] when they studied the effects of a step decrease in roughness height on the transition of flow from laminar to turbulent flow. Even if the flow does not separate, the acceleration of the fluid at the beginning of the roughness and the deceleration of the fluid at the end of the roughness creates an increase in form drag on the cone roughness elements.

Neither the effects of the extra form drag on the upstream elements below the mean elevation nor the effects of flow separation are considered in the discrete-element predictions. Taylor [8] calibrated the discrete-element model using Schlichting's corrected data and compared the discrete-element predictions to the experimental data of Healzer [21], Pimenta [22], and Coleman [23]. In each of the cases studied by Taylor, the roughness started at the "knife-edge" or start of the wind or water tunnel. Skin friction measurements were then determined using the momentum-defect method or using the measured Reynolds stresses and mean velocity profiles. In those test cases, the flow did not transition from smooth surface to rough surface and back to smooth surface. The changes in mean elevation experienced by the cone surfaces of this study cause some of the differences between the discrete-element predictions and the experimentally measured skin friction coefficients.

Implications for the Equivalent-Sand Grain Roughness Model

Since the effects of the mean elevation are clearly evident in the discrete-element predictions for flows over closely packed cone surfaces, the same effect should be evident in the data used in the equivalent sand-grain roughness approach. The most widely used correlation for using the physical characteristics of a surface to predict the equivalent sandgrain roughness height is based on the Sigal-Danberg parameter, Λ_s.

Figure 5 presents the ratio of the equivalent sand-grain height over the ratio of the roughness element height (k_s/k) versus Λ_s as traditionally defined by Sigal and Danberg [6] for the classical set of surfaces with ordered, three-dimensional roughness elements from Schlichting [1][1, as corrected in Ref. 24] and for the cones studied by Bogard et al. [25]. To investigate the effects of the mean elevation on surfaces with ordered roughness elements of the same three-dimensional shape, the Sigal-Danberg parameters were recalculated for the classical surface set using the characteristics of the roughness elements above the mean elevation. Figure 6 presents the ratio of the equivalent sand-grain roughness height to the effective height of the roughness elements above the mean elevation (k_s/k_{eff}) versus the Sigal-Danberg parameter evaluated using the characteristics of the roughness elements above the mean elevation ($\Lambda_{s,\text{eff}}$).

Figure 6 demonstrates that when the mean elevation is considered in the determination of the Sigal-Danberg parameter, the values of k_s/k_{eff} correlate well with an exponential function based on

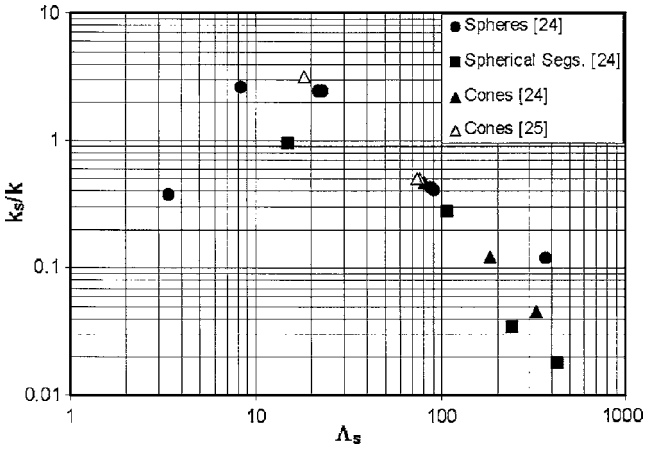

Fig. 5 k_s/k vs Λ_s for three-dimensional roughness elements

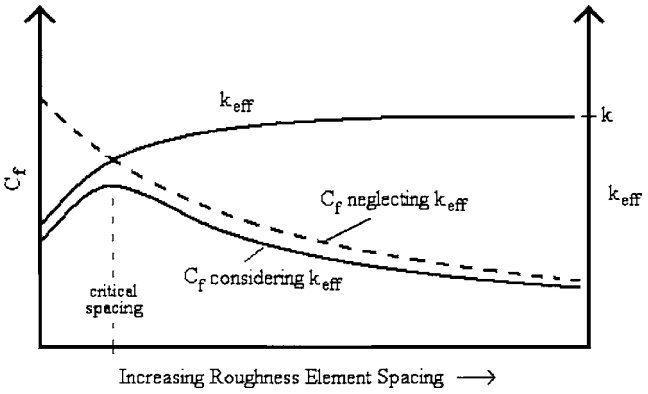

Fig. 7 Variation of skin friction coefficient and effective roughness height as functions of the roughness element spacing

$\Lambda_{s,\text{eff}}$. While really only four points are significantly affected when considering the roughness characteristics above the mean elevation, those four points are moved in-line with the other data points in Fig. 6.

Considering the mean elevation also explains why the k_s/k decreases with decreasing values of Λ_s below $\Lambda_s=20$ in Fig. 5. Schlichting [1] noticed that for roughness elements of a constant shape but with variable spacing, the maximum equivalent sand-grain roughness height did not occur at the most dense spacing but at a considerably larger spacing. Once that critical spacing was reached, the equivalent sand-grain roughness height decreased as the spacing was increased.

To explain this decreasing k_s as the spacing increased, Schlichting [1] postulated that the total drag force (F) on a rough surface was the sum of the skin friction of the flat part of the surface (F_s) and drag on the roughness elements (F_R).

$$F = F_R + F_s \tag{16}$$

Schlichting [1] then identified a resistance coefficient, C_R, of the roughness elements as

$$C_R = \frac{F_R}{\frac{1}{2}\rho u_k^2 S_f} \tag{17}$$

Where u_k is the velocity of the fluid at the highest elevation of the roughness elements and S_f is the projected frontal area of all of the roughness elements. Schlichting [1] found that the value of C_R was independent of the roughness density and the value predicted for drag coefficients of the roughness element shapes in free flow.

Following Schlichting's logic, a skin friction coefficient for the rough surface may be defined as

$$C_f = \frac{F_R + F_s}{\frac{1}{2}\rho U_\infty^2 S_{pa}} \tag{18}$$

Substituting for F_R and rearranging yields

$$C_f = C_R\left(\frac{S_f}{S_{pa}}\right)\left(\frac{u_k}{U_\infty}\right)^2 + C_{f,s}\left(\frac{A_{sm}}{S_{pa}}\right) \tag{19}$$

Inspecting Eq. (19), at a set location on a surface with roughness elements of the same size, as the roughness elements are spaced further apart, the dominant term affecting the skin friction is the ratio of the frontal area of roughness elements over the plan-form area of the surface. For a set element size, the value of S_f/S_{pa} decreases as a function of the square of the average element spacing. While u_k/U_∞ will change as the elements are spaced further apart, the value of u_k/U_∞ ranges from 0 to 1.0, and the changes will not be as big as the dramatic decrease in the value of S_f/S_{pa}.

Figure 7 demonstrates the expected variation of the skin friction coefficient at a set location on a rough surface with a fixed roughness element shape as the spacing between the roughness elements increases. If the effective height of the elements above the mean elevation were not relevant, Eq. (19) implies that the skin friction coefficient of a rough surface would start at a high value for the most closely packed configuration, then decrease as the square of the average spacing decreases. If the effective height is important, the roughness elements would appear to be much shorter to the flow than the actual height of the elements for the most closely packed configuration. Thus, the effective projected frontal area would be much less than the actual projected frontal area of the roughness elements, and u_k/U_∞, would also be significantly lower. As the roughness element spacing is increased, the combined effects of the increasing frontal area and the increasing u_k/U_∞ outpace the increases in S_{pa} until the critical spacing is reached. When the spacing increases beyond the critical spacing, the skin friction coefficient then begins to decrease. Recalling that for a constant element shape that Λ_s varies proportional to the square of the element spacing and realizing that the equivalent sand-grain roughness height is directly related to the skin friction coefficient, the curve reflecting the effect of k_{eff} on C_f in Fig. 7 explains the trends exhibited by the data in Fig. 5.

Figure 6 also demonstrates that for the surfaces with closely packed spherical roughness studied by Schlichting [1], the fluid is skimming over the roughness elements. In Fig. 6, there are two sets of points connected by arrows. The set of connected points

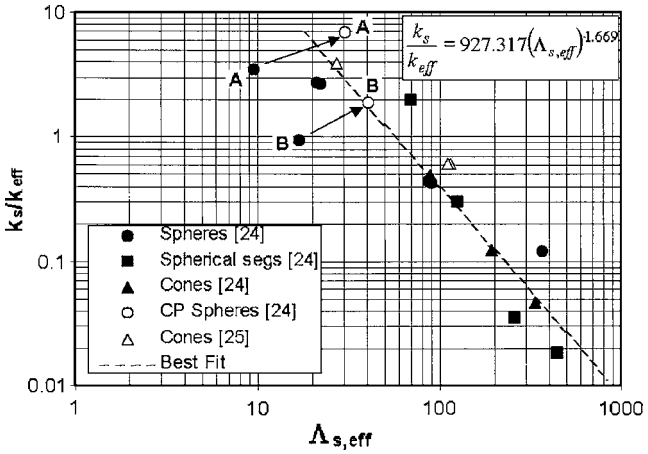

Fig. 6 k_s/k_{eff} vs Λ_s evaluated using the characteristics of the roughness elements above the mean elevation

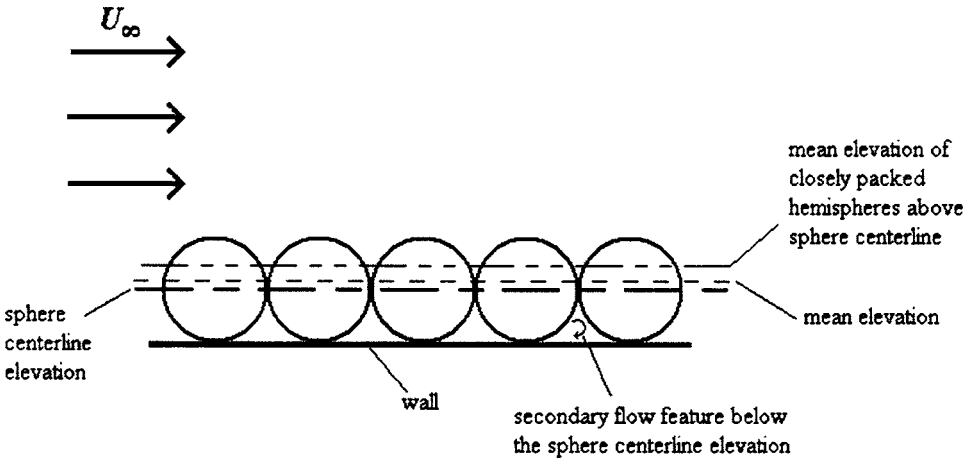

Fig. 8 Flow over closely packed spheres

labeled "**B**" represent the surface with the closest possible spacing of spheres. The spheres for the set labeled "**A**" have an average spacing over diameter ratio of 1.5. The closed-circle points at the beginnings of the arrows represent the values of k_s/k_{eff} and Λ_s evaluated for the surfaces with closely packed spheres when referenced to the mean elevation above the wall. The open-circle points at the end of the arrows represent the values of k_s/k_{eff} and Λ_s evaluated as referenced to the mean elevation above the centerline of the spheres. Figure 8 demonstrates the differences in the mean elevation used for the sets of points for the surface most closely spaced spheres.

The open-circle points referenced to the mean elevation above the sphere centerline were calculated after the values of k_s/k_{eff} and Λ_s for the most closely packed spheres based on the mean elevation above the wall were found to occur in almost the same location in Fig. 6 as do the points for the closely packed hemispheres in Fig. 5. The fact that the open-circle points line up very well with the trend of the other data representing surfaces more sparsely spaced roughness elements confirm that the flow below the centerline elevation is not contributing to skin friction. For the closely packed spheres, the flow is skimming over the spheres. Morris [26] elaborates on skimming flows similar to the flow over the closely packed spheres.

Comparing the predictions from the discrete-element model and the equivalent sand-grain model would be useful and enlightening. For the experimental situation studied, however, equivalent sand-grain model predictions could not be made using the available correlations for skin friction coefficient based on equivalent sand-grain height. In the experiments, the flow transitioned from smooth surface, to rough surface, and then back to smooth surface. The correlations available, such as the one provided by Schlichting [27],

$$C_f = \left[2.87 + 1.58 \log\left(\frac{x}{k_s}\right) \right]^{-2.5} \tag{20}$$

were developed for flows over surfaces with constant surface roughness. As discussed earlier, at the beginning of the roughness section, the skin friction is elevated as the flow adjusts to the roughness elements. At the end of the roughness section, the flow may separate depending on the magnitude of the change in mean elevation from the rough region to the smooth region. Because the correlations were not constructed to capture the transition of surface roughness, skin friction coefficient predictions constructed with the correlations for the current experimental data are much lower than either the discrete-element prediction or the experimentally measured skin friction coefficient. For example, for Surface 2, the effective Sigal-Danberg parameter is 37.38 and the corresponding value of k_s/k_{eff} 2.2 from the correlation provided on Fig. 6. From Eq. (20), the expected skin friction coefficient is 0.008, which is 20% lower than the measured skin friction coefficients at either Reynolds number tested.

Conclusions

Skin friction coefficients were measured for two cone surfaces at two turbulent Reynolds numbers. Discrete-element model predictions were made using the modifications to the DEM made for randomly rough surfaces, the most important of which being the use of the mean elevation as the location of the no-slip plane. The effects of considering the mean elevation in the evaluation of the equivalent sand-grain roughness heights and in the calculation of the Sigal-Danberg roughness density parameters was also explored. From the investigation, four major conclusions were made:

(1) The relevant surface datum for the evaluation of turbulent boundary layer skin friction over rough surfaces with either the equivalent sand-grain or the discrete-element method is the mean elevation. This is true for randomly rough and ordered roughness surfaces, though the result only becomes significant as the ordered surface elements become more closely packed.
(2) Accounting for the mean surface elevation allows for a unification of all previous ordered three-dimensional roughness element data in the literature. This implementation replaces the three different equations relating k_s/k to Λ_s, as reported by Sigal and Danberg, with one universal relation.
(3) The mean elevation must be accounted for in experimental research with densely packed roughness surfaces when there are abrupt transitions from the smooth to rough wall condition. Unless some accommodation is made, fluid acceleration over the rough wall region will create elevated levels of skin friction relative to simulations using a zero freestream velocity gradient assumption.
(4) For roughness elements that do not have continuously decreasing cross section away from the wall (e.g., spheres), close packing renders the portion of the element below the maximum cross-section insignificant for C_f determination.

Acknowledgment

This work was performed under partial sponsorship from the U. S. Department of Energy, the National Energy Technology Laboratory, and the South Carolina Institute for Energy Studies through the Advanced Land-Based Gas Turbine Systems Research Consor-

tium (AGTSR). The remainder of the support for this work was provided by Dr. Bharat K. Soni and the Department of Mechanical Engineering at the University of Alabama at Birmingham. The authors also gratefully acknowledge the assistance of Dr. Robert Taylor and Dr. Richard Rivir.

Nomenclature

A_f = frontal area of the roughness elements
A_s = windward wetted surface area of roughness elements
A_{sm} = plan area of the surface minus the plan area of the roughness elements
C_D = local element drag coefficient
C_f = skin friction coefficient
C_R = resistance coefficient
F = force
$d(y)$ = maximum transverse width of roughness element as function of distance from wall
d_0 = cone diameter at surface floor
k = roughness element height
l_m = mixing length
L_p = element spacing parameter in direction of flow
L_t = element spacing parameter transverse to the flow direction
N_r = number of roughness elements
P = pressure
R_q = root-mean-square roughness height
Re = Reynolds number
S = diagonal or average element spacing
S_{pa} = plan area of the surface
S_f = total frontal area of roughness elements
t = time
Tu = freestream turbulence
U_e = freestream velocity
u = local streamwise velocity
u_k = fluid velocity at the crest of the roughness elements
v = local velocity normal to wall
x = streamwise flow direction
y = direction normal to wall
y^+ = nondimensional y; $(y/\nu)\sqrt{(\tau_w/\rho)}$

Greek

α = blockage fraction
β = void fraction, $1-\alpha$
δ = boundary-layer thickness
Λ_s = Sigal-Danberg parameter
κ = von Karman constant
μ = dynamic viscosity
ν = kinematic viscosity
ρ = density
τ = shear
τ_w = shear at the no-slip surface

Superscripts

$'$ = turbulent fluctuating values

Subscripts

D = drag
eff = effective
fl = floor
me = mean elevation
meas = measured
rms = root-mean-square
S = flat surface

References

[1] Schlichting, H., 1936, "Experimental Investigation of the Problem of Surface Roughness," Ingenieur-Archiv, Vol. VII, No. 1, (1936), and NACA TM 823, (1937).
[2] Nikuradse, J., 1933, "Laws for Flows in Rough Pipes," *VDI-Forchungsheft 361*, Series B, Vol. 4, (1933), also as NACA TM 1292, (1950).
[3] Dvorak, F. A., 1969, "Calculation of Turbulent Boundary Layers on Rough Surfaces in Pressure Gradients," AIAA J. **7**, pp. 1752–1759.
[4] Simpson, R. L., 1973, "A Generalized Correlation of Roughness Density Effects on the Turbulent Boundary Layer AIAA J. **11**, pp. 242–244.
[5] Dirling, R. B., 1973, "A Method for Computing Rough Wall Heat Transfer Rates on Reentry Nose Tips," AIAA Pap. 73-763.
[6] Sigal, A., and Danberg, J. E., 1990, "New Correlation of Roughness Density Effect on the Turbulent Boundary Layer," AIAA J. **28**(3), pp. 554–556.
[7] Bons, J. P., 2002, "St and C_f Augmentation for Real Turbine Roughness with Elevated Freestream Turbulence," ASME J. Turbomach. **124**, pp. 632–644.
[8] Taylor, R. P., 1983, "A Discrete Element Prediction Approach for Turbulent Flow over Rough Surfaces," Ph.D. Dissertation, Department of Mechanical and Nuclear Engineering, Mississippi State University.
[9] Finson, M. L., 1982, "A Model for Rough Wall Turbulent Heating and Skin Friction," AIAA Pap. 82-0199.
[10] Adams, J. C., and Hodge, B. K., 1977, "The Calculation of Compressible Transitional Turbulent and Relaminarizational Boundary Layers over Smooth and Rough Surfaces Using an Extended Mixing-Length Hypothesis," AIAA Pap. 77-682.
[11] Lin, T. C., and Bywater, R. J., 1980, "The Evaluation of Selected Turbulence Models for High-Speed Rough-Wall Boundary Layer Calculations," AIAA Pap. 80-0132.
[12] Scaggs, W. F., Taylor, R. P., and Coleman, H. W., 1988, "Measurement and Prediction of Rough Wall Effects on Friction Factor—Uniform Roughness Results," ASME J. Fluids Eng. **110**, pp. 385–391.
[13] Hosni, M. H., 1989, "Measurement and Calculation of Surface Roughness Effects on Turbulent Flow and Heat Transfer," Ph.D. Dissertation, Department of Mechanical and Nuclear Engineering, Mississippi State.
[14] Chakroun, W., 1992, "Experimental Investigation of the Effects of Acceleration on Flow and Heat Transfer in the Turbulent Rough-Wall Boundary Layer," Ph.D. Dissertation, Department of Mechanical and Nuclear Engineering, Mississippi State University.
[15] Taylor, R. P., Scaggs, W. F., and Coleman, H. W., 1988, "Measurement and Prediction of the Effects of Nonuniform Surface Roughness on Turbulent Flow Friction Coefficients," ASME J. Fluids Eng. **110**, pp. 380–384.
[16] McClain, S. T., Hodge, B. K., and Bons, J. P., 2004, "Predicting skin Friction and Heat Transfer for Turbulent Flow over Real Gas-Turbine Surface Roughness Using the Discrete-Element Method," ASME J. Turbomach. **126**(2) pp. 259–267.
[17] Taylor, R. P., and Hodge, B. K., 1993, "A Validated Procedure for the Prediction of Fully Developed Nusselt Numbers and Friction Factors in Pipes with Three-Dimensional Roughness," J. Enhanced Heat Transfer **1**, pp. 23–35.
[18] Tolpadi, A. K., and Crawford, M. E., 1998, "Predictions of the Effect of Roughness on Heat Transfer from Turbine Airfoils," Presented at the International Gas Turbine & Aeroengine Congress & Exhibition, Stockholm, Sweden, June 2–5, 98-GT-87.
[19] McClain, S. T., 2002, "A Discrete-Element Model for Turbulent Flow over Randomly Rough Surfaces," Ph.D. Dissertation, Department of Mechanical Engineering, Mississippi State University.
[20] Pinson, M. W., and Wang, T., 2000, "Effect of Two-Scale Roughness on Boundary Layer Transition Over a Heated Flat Plate: Part 1—Surface Heat Transfer," ASME J. Turbomach. **122**, pp. 301–307.
[21] Healzer, J. M., 1974, "The Turbulent Boundary Layer on a Rough, Porous Plate: Experimental Heat Transfer with Uniform Blowing," Ph.D. Dissertation, Department of Mechanical Engineering, Stanford University.
[22] Pimenta, M. M., 1976, "The Turbulent Boundary Layer: An Experimental Study of the Transport of Momentum and Heat with the Effect of Roughness," Ph.D. Dissertation, Department of Mechanical Engineering, Stanford University.
[23] Coleman, H. W., 1979, "Momentum and Energy Transport in the Accelerated Fully Rough Turbulent Boundary Layer," Ph.D. Dissertation, Department of Mechanical Engineering, Stanford University.
[24] Coleman, H. W., Hodge, B. K., and Taylor, R. P., 1984, "A Re-evaluation of Schlichting's Surface Experiment," ASME J. Fluids Eng. **106**, pp. 60–65.
[25] Bogard, D. G., Schmidt, D. L., and Tabbita, M., 1988, "Characterization and Laboratory Simulation of Turbine Airfoil Surface Roughness and Associated Heat Transfer," ASME J. Turbomach. **120**, pp. 337–342.
[26] Morris, H. M., 1972, "*Applied Hydraulics in Engineering*," 2nd ed. The Ronald Press, New York.
[27] Schlichting, H., 1979, *Boundary-Layer Theory*, 7th ed., McGraw-Hill, New York.

Airfoil Performance at Low Reynolds Numbers in the Presence of Periodic Disturbances

S. Yarusevych[1]
University of Toronto,
Department of Mechanical and Industrial Engineering,
5 King's College Rd.,
Toronto, Ontario, M5S 3G8, Canada
e-mail: yarus@mie.utoronto.ca

J. G. Kawall
Ryerson University,
Department of Mechanical and Industrial Engineering,
350 Victoria St.,
Toronto, Ontario, M5B 2K3, Canada
e-mail: gkawall@ryerson.ca

P. E. Sullivan
University of Toronto,
Department of Mechanical and Industrial Engineering,
5 King's College Rd.,
Toronto, Ontario, M5S 3G8, Canada
e-mail: sullivan@mie.utoronto.ca

The boundary-layer separation and wake structure of a NACA 0025 airfoil and the effect of external excitations in presence of structural vibrations on airfoil performance were studied experimentally. Wind tunnel experiments were carried out for three Reynolds numbers and three angles of attack, involving hot-wire measurements and complementary surface flow visualization. The results establish that external acoustic excitation at a particular frequency and appropriate amplitude suppresses or reduces the separation region and decreases the airfoil wake, i.e., produces an increase of the lift and/or decrease of the drag. The acoustic excitation also alters characteristics of the vortical structures in the wake, decreasing the vortex length scale and coherency. Optimum excitation frequencies were found to correlate with the fundamental frequencies of the naturally amplified disturbances in the separated shear layer. The results suggest that acoustic waves play a dominant role in exciting the separated shear layer of the airfoil. Moreover, low-frequency structural vibrations are found to have a significant effect on airfoil performance, as they enhance the sound pressure levels within the test section.
[DOI: 10.1115/1.2175165]

Keywords: boundary-layer separation, low-Reynolds-number flow, wake formation, vortex shedding, flow control, acoustic excitation

1 Introduction

The performance of airfoils at low Reynolds numbers has been of interest in connection with a wide range of applications, including the operation of aircraft at low speeds and the design of micro air vehicles, compressor blades, wind turbines, and inboard sections of helicopter rotors. Several investigators have studied airfoil performance in the low Reynolds number region (e.g., [1,2]). Their findings indicate that serious aerodynamic problems occur below Reynolds number of about 200,000. Specifically, the laminar boundary layer on the upper surface of the airfoil is subjected to an adverse pressure gradient, even at low angles of attack. This often results in laminar boundary-layer separation and formation of a shear layer. At lower Reynolds numbers, the separated shear layer does not reattach to the airfoil surface, and a large wake is formed. In contrast, at higher Reynolds numbers, the separated shear layer may reattach to the airfoil surface, resulting in the formation of a separation bubble. It should be stressed that, in both cases, laminar separation has a significant detrimental effect on airfoil lift and drag. Therefore, it is of interest to improve airfoil performance by introducing a flow control mechanism to energize the boundary layer sufficiently to overcome the adverse pressure gradient and reduce or suppress the separation region. One method of flow control excites the boundary layer with an acoustic source. A number of studies have demonstrated that acoustic excitation applied at an appropriate frequency and amplitude reduces the separation region and improves airfoil characteristics [3–11]. However, the complex physical mechanism responsible for this is not yet known in detail.

At angles of attack below and in the vicinity of the stall angle, some experimental results [4–7] suggest that the optimum effect occurs when the excitation frequency matches the instability frequency of the separated shear layer. However, at angles of attack well above the stall angle, Hsiao et al. [7] have found that the most effective excitation frequency matches the vortex shedding frequency in the airfoil wake. Thus, the effect of the excitation and the corresponding control mechanism appear to be different for different ranges of the angle of attack. Furthermore, it has been concluded [5–9] that the effect and the effective frequency range of the excitation (i.e., the range of frequencies producing improvement of the airfoil characteristics) depend strongly on the excitation amplitude.

Zaman [10] has reported significant differences in the optimum excitation parameters obtained in the various experiments. The results presented show a disagreement among the experimental data, with optimum Strouhal numbers varying by as much as an order of magnitude in some cases. An increase of the external excitation amplitude was found to result in a shift of the optimum effect towards the lower Strouhal numbers. Moreover, these Strouhal numbers were much lower than those predicted by linear instability theory. Zaman [10] concluded that this is due to nonlinear and viscous effects, especially in the presence of the separation bubble. However, no analysis has yet been done to support such a conclusion.

In most of the previous experimental studies cited above, attention was concentrated on lift and drag measurements and boundary-layer behavior. Wake measurements, if any, were done at a single downstream location, involving only the streamwise velocity component, and were only briefly related to the improvement of airfoil performance. However, wake structure is also an important aspect of airfoil performance. Recent experimental results of Huang and Lin [12]and Huang and Lee [13] suggest that vortex-shedding development and characteristics are closely related to boundary-layer behavior and shear-layer instability. In fact, Yarusevych et al. [14] show that optimum values of the control parameters may be correlated with airfoil boundary-layer

[1]Corresponding author.

Contributed by the Fluids Engineering Division of ASME for publication in the JOURNAL OF FLUIDS ENGINEERING. Manuscript received March 4, 2005; final manuscript received October 10, 2005. Review conducted by Joseph Katz.

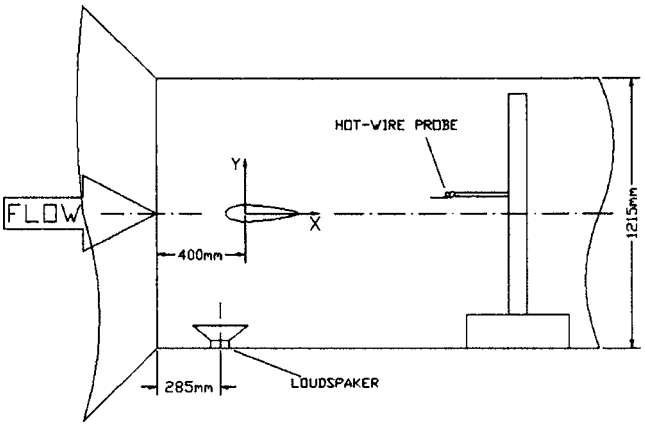

Fig. 1 Tunnel test section

and/or wake characteristics. It should be noted that the effect of airfoil vibrations has not been addressed in any of the cited references, even though such vibrations are likely to take place in most of the experiments involving acoustic excitation. In the light of this, the focus of the present work is to examine the effect of external acoustic excitation in the presence of structural vibrations on the boundary-layer separation and wake structure of a NACA 0025 symmetrical airfoil for various Reynolds numbers and angles of attack and to relate this effect to the improvement of airfoil performance.

2 Experimental Setup

Experiments were performed in a low-turbulence recirculating wind tunnel. The 5-m-long octagonal test section of this tunnel has a spanwise extent of 0.91 m and a height of 1.22 m. The flow enters the test section through seven screens and a 9:1 contraction. The operating velocity U_0 is adjustable from 2.8 to 18 m/s, with a free-stream turbulence intensity level less than 0.1% within the bandwidth from 0.1 to 2500 Hz. One wall of the test section is made of plexiglas for operational and visualization purposes. During the experiments, the free stream velocity was monitored by a pitot-static tube, with precision uncertainty estimated to be less than 2.5%.

The performance of a symmetrical NACA 0025 aluminum airfoil with a chord length c of 0.3 m and a span of 0.88 m was examined for a range of chord Reynolds numbers (Re_c) and three angles of attack (α). A schematic diagram of the test sections is shown in Fig. 1. The airfoil was mounted horizontally in the test section, 0.4 m downstream of the contraction. A Cartesian coordinate system was used, with x and y defined as shown in Fig. 1 and the origin at the centre of rotation of the airfoil.

Sound excitation was provided by means of a 250 W loudspeaker mounted on the test section floor, under the leading edge of the airfoil. The presence of the loudspeaker did not produce any measurable effect on the airfoil wake within the region of interest. The loudspeaker was driven through an amplifier by a variable-frequency wave generator and a foam-rubber pad could be installed to isolate the speaker from the test section floor. Thus, the mounting could be adjusted so as to either introduce vibrations to the structure along with sound waves or minimize the mechanical vibrations of the structure produced by the loudspeaker. A microphone and an accelerometer were employed to quantify sound excitation and airfoil surface vibrations, respectively. Based on the precision of the instruments for a frequency range of 40 to 1000 Hz, the uncertainty of the microphone measurements is approximately ±0.3 dB, and that of the accelerometer data is less than 3%.

Airfoil wake velocity data were obtained with constant temperature anemometers (Dantec 56C01 main units equipped with 56C17 CTA bridges). A Dantec 55P11 normal hot-wire probe and a Dantec 55P61 cross-wire probe were used separately to traverse vertical planes downstream of the airfoil. The probes were mounted on a remote-control traversing gear with a spatial resolution of 0.8 mm. For accurate detection of vortex-shedding frequencies, the probe was positioned in the upper part of the wake at the y/c locations corresponding to approximately one-half of the maximum velocity deficit for each Reynolds number and angle of attack. All hot-wire measurements were carried out in the vertical midspan plane of the tunnel. Based on the results of Kawall et al. [15], the maximum hot-wire measurement error was evaluated to be less than 5% and is attributed to the high turbulent intensities in the separated shear layer and near wake. Spectral analysis of the free-stream velocity signals with the model installed in the test section established that there was no periodicity associated with the approach flow.

For the spectral analysis of the velocity data sampled at 5000 Hz, the duration of a sampled signal segment was chosen to be sufficiently large to provide a frequency resolution bandwidth of 0.61 Hz, adequate for resolving narrow peaks in the spectrum. Based on the number of averages involved in obtaining the velocity spectra, the uncertainty of the spectral analysis was evaluated to be approximately 4.5%.

To qualitatively visualize boundary-layer behavior, two rows of nylon tufts were installed on the airfoil surface 0.2 m away from the midspan. Each row contained ten 2-cm-long tufts equally spaced from the leading to the trailing edge. The rows were separated by 2 cm in the spanwise direction and offset in the cordwise direction to increase spatial resolution.

3 Experimental Results

3.1 Flow Without Excitation. The results presented are for Reynolds numbers (Re_c) of 150×10^3, 100×10^3, and 57×10^3 and angles of attack (α) of 10, 5, and 0 deg. All three values of Re_c are within the low Reynolds number region, i.e., $\mathrm{Re}_c<200\times10^3$[1,2].

The surface flow visualization, which provided a qualitative picture of the boundary-layer behavior, showed that boundary-layer separation took place over a substantial portion of the upper surface of the airfoil at all three angles of attack for $\mathrm{Re}_c=57\times10^3$ and $\mathrm{Re}_c=100\times10^3$, with no boundary-layer reattachment. The separation occurred over approximately the aft 40% of the chord at $\alpha=0$ deg, increasing to 50% at $\alpha=5$ deg, and reaching 60% at $\alpha=10$ deg for these two Reynolds numbers. However, for $\mathrm{Re}_c=150\times10^3$, no clear evidence of boundary layer separation was found at $\alpha=0$ deg and $\alpha=5$ deg, and only a small separation region was detected at the trailing edge, over the aft 10% of the chord, at $\alpha=10$ deg. It should be noted that detailed boundary-layer measurements reported in [16] suggest that for this Reynolds number, the boundary layer separates on the upper surface of the airfoil and reattaches downstream to form a separation bubble over approximately 25% of the cord at all three angles of attack examined.

As a result of extensive boundary-layer separation for the two lower Reynolds numbers, wide wakes are formed behind the airfoil. Figure 2 depicts typical mean wake velocity profiles, i.e., plots of $(U_0-\bar{U})/U_0$ versus y/c, for all the three Reynolds numbers investigated at $\alpha=10$ deg. It is evident that the mean profiles for $\mathrm{Re}_c=57\times10^3$ and $\mathrm{Re}_c=100\times10^3$ differ significantly from the mean profile for $\mathrm{Re}_c=150\times10^3$. Specifically, the maximum velocity deficit of $0.24U_0$ for $\mathrm{Re}_c=57\times10^3$ decreases to $0.21U_0$ as the Reynolds number increases to $\mathrm{Re}_c=100\times10^3$. As the Reynolds number reaches 150×10^3, the wake narrows significantly with the maximum velocity deficit decreasing to $0.17U_0$. Moreover, for $\mathrm{Re}_c=150\times10^3$, the location of the minimum velocity in the wake follows the incline of the trailing edge, similar to wakes of symmetrical airfoils at high Reynolds numbers. In contrast, for the two lower Reynolds numbers examined, the vertical location

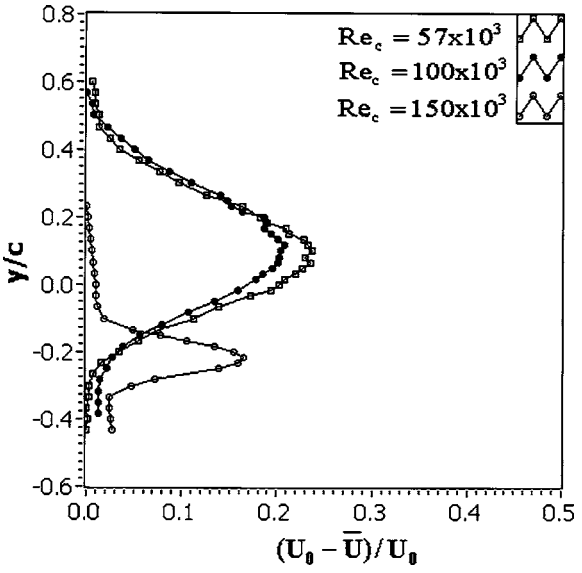

Fig. 2 Mean-velocity profiles, $x/c=1$, $\alpha=10°$

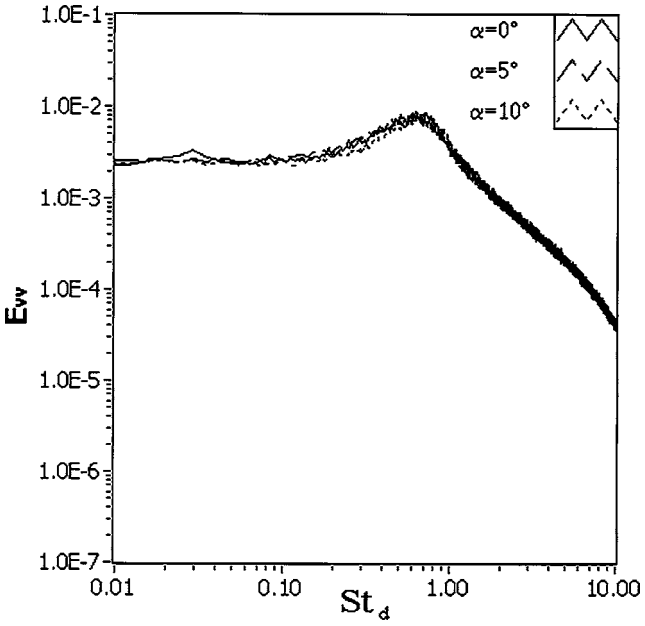

Fig. 4 E_{vv} spectra for $Re_c=150\times10^3$, $x/c=3$

of the minimum velocity in the wake is shifted upwards. This is attributable to boundary-layer separation on the upper surface of the airfoil, which governs wake formation and structure.

To gain insight into the airfoil wake structure, spectra of the wake velocity data are considered. Each of these spectra is normalized by the variance of the corresponding velocity component, so that the area under each spectrum is unity.

Figure 3 depicts spectra of the streamwise velocity component (E_{uu}) at $x/c=2$ for all Reynolds numbers and angles of attack examined. Frequency is scaled with global parameters to form a Strouhal number, $St_d=fd/U_0$, where d is the vertical length of the airfoil projection on a cross-stream plane. For the case of $Re_c=57\times10^3$, a spectral peak centered at approximately $St_d=0.21$ (8 Hz) at all three angles of attack is clear evidence of the existence of frequency-centered activity in the airfoil wake (Fig. 3(*a*)), attributable to vortex shedding. As the Strouhal numbers pertaining to the spectral peaks do not vary with angle of attack and compare well with the values reported for a circular cylinder ($St_d\approx0.2$), vortex shedding for this Reynolds number appears to be similar to that of a bluff body.

The spectral results for $Re_c=100\times10^3$ (Fig. 3(*b*)) reveal a degree of dependency of the vortex-shedding characteristics on angle of attack. At $\alpha=0$ deg, a broad peak with a maximum at $St_d=0.29$ (20 Hz) is evident. As the angle of attack increases to 5 deg, a sharp peak centered at approximately $St_d=0.29$ (20 Hz) occurs. Finally, at $\alpha=10$ deg, the vortex shedding appears to be similar to that in the wake of a circular cylinder, with the dominant spectral peak centered at $St_d=0.22$ (15 Hz). This indicates an increase in the length scale of the vortices, estimated as the ratio of free-stream velocity and the vortex-shedding frequency (U_0/f).

A detailed wake survey carried out by means of a normal hot-wire sensor did not reveal any evidence of frequency-centered activity in the airfoil wake for $Re_c=150\times10^3$ at any angle of attack, with no distinct peaks revealed in the corresponding E_{uu} spectra (Fig. 3(*c*)). This, however, does not rule out the existence of coherent structures; i.e., some sort of organized turbulent motion within the wake. As shown later for the two lower Reynolds numbers, the spectra of the vertical velocity component (E_{vv}) are more sensitive to frequency-centered activity in wakes than spectra of the streamwise velocity component (E_{uu}). Therefore, in an effort to determine whether some type of frequency-centered activity exists in the airfoil wake for $Re_c=150\times10^3$, E_{vv} spectra were measured at $x/c=3$. These spectra, presented in Fig. 4, display broad peaks, centered at approximately $St_d=0.66$ (68 Hz) at

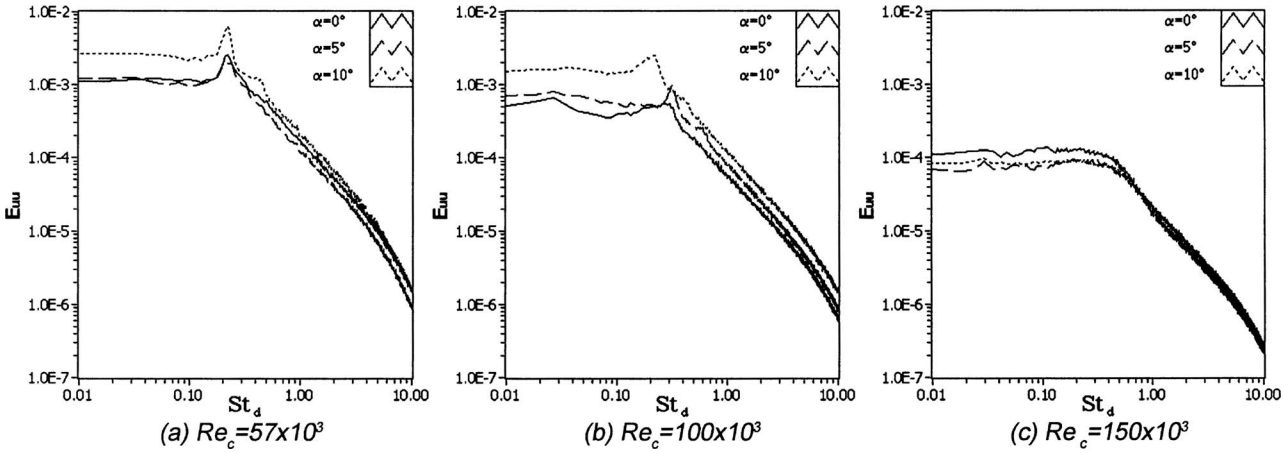

Fig. 3 E_{uu} spectra, $x/c=2$

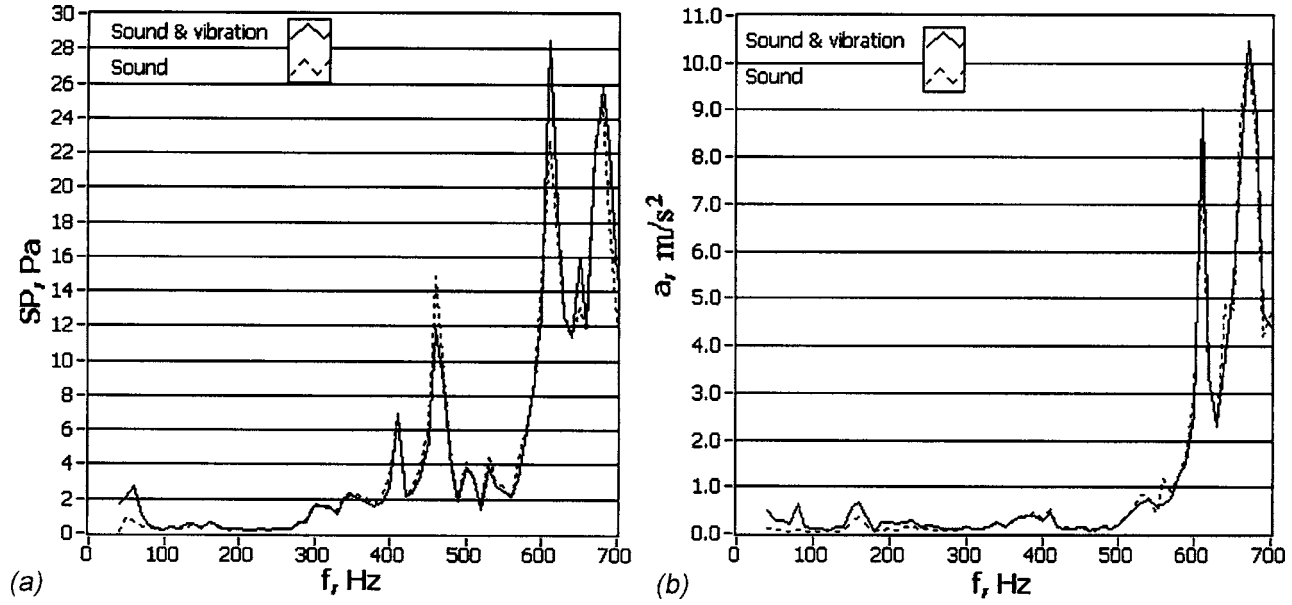

Fig. 5 Test section resonance characteristics: (a) sound pressure and (b) airfoil surface acceleration

all three angles of attack, revealing the presence of weak frequency-centered activity in the airfoil wake. It can be inferred that the coherence and length scale of the corresponding coherent structures are much lower than those of shed vortices detected for the two lower Reynolds numbers.

A distinct Reynolds number dependency of the wake structure characteristics can be detected from a comparison of Figs. 3 and 4. The vortex-shedding frequency steadily increases and length scale decreases as Reynolds number increases. Vortices become more diffuse and shedding less periodic, as peaks in the corresponding E_{uu} spectra become broader and less defined with an increase of Reynolds number. Finally, the formation of the separation bubble on the airfoil surface for $\mathrm{Re}_c = 150 \times 10^3$ results in the formation of much weaker coherent structures in the airfoil wake than the vortices observed for the two lower Reynolds numbers. Huang and Lin [12] and Huang and Lee [13] found a similar tendency in experiments with a NACA 0012 airfoil and reported the existence of a similar "transitional" regime of vortex shedding.

3.2 Excitation Parameters. Two types of excitation were considered: (i) "pure" acoustic excitation, with the loudspeaker isolated from the tunnel working section, and (ii) acoustic excitation with mechanical vibrations superimposed on the airfoil via the loudspeaker.

Since the effect of acoustic excitation depends on both excitation frequency and amplitude, wind tunnel resonance characteristics were examined at $U_0 = 0$. A microphone, positioned 40 mm above the upper surface at $x/c = 0$ in the midspan of the airfoil, was used to measure sound pressure. Airfoil vibrations were monitored with an accelerometer mounted on the airfoil surface directly under the microphone. Sound pressure (SP) and vertical airfoil acceleration (a) were acquired with constant input voltage to the speaker and varying excitation frequency (Fig. 5). The results in Fig. 5(*a*) show substantial modulations in sound pressure at frequencies from approximately 280 to 700 Hz for both types of excitation examined. Distinct peaks located within this frequency range are associated with cross-resonances within the test section. A significant amplification of vibrations occurs at frequencies above 500 Hz (Fig. 5(*b*)), where acoustic resonance frequencies match natural frequencies of the model. Both sound pressure and acceleration variations are less substantial at frequencies below 280 Hz.

Results in Fig. 5(*b*) suggest that the amplitude of airfoil surface vibrations for the case of acoustic excitation with structural vibrations is at least double that for the case of pure acoustic excitation in the range of 40 to 280 Hz. However, the results show no substantial difference in acceleration for the two types of excitation at frequencies above 280 Hz, where acoustic resonances take place. This is because vibrations at low frequency are less attenuated in the test section than those at higher frequencies. As a result, acoustic excitation with superimposed mechanical vibrations produces higher sound pressures at frequencies below about 100 Hz (Fig. 5(*a*)) and there is no substantial difference in sound pressures at higher frequencies.

To study the effect of acoustic excitation on airfoil performance, it is important to select an adequate parameter to quantify excitation amplitude. However, the choice of such a parameter is very problematic, as shown by Zaman et al. [5]. For example, their results question the suitability of sound pressure level or velocity fluctuations within the test section, as both are strongly affected not only by the resonances but also by the choice of the reference location, influence of the flow, and other factors. Following the approach taken in [4,8,9], the effect of excitation frequency in the present study was investigated with a constant voltage supplied to the speaker, as it enables assessment of the effect of structural vibrations.

The effect of external acoustic excitation on the separated boundary layer was first examined by means of flow visualization. The flow was excited at different frequencies with constant-amplitude voltage supplied to the speaker, in the presence of mechanical vibrations. For each of the cases examined, a range of frequencies (an effective-frequency range) was found to effect suppression of the separation region. As the amplitude of the excitation decreased, this range narrowed with boundary-layer reattachment finally occurring only at some "optimum" excitation frequency. Chang et al. [6] reported similar dependency of the effective-frequency range on the amplitude of the acoustic excitation. Moreover, a significant hysteresis in the suppression of the separation region by excitation was observed. Once reattachment occurred, the excitation frequency could be changed slightly from the optimum value or the excitation amplitude could be substantially lowered, with the boundary layer remaining fully attached.

The results summarized in Table 1 suggest that the optimum excitation frequency increases as Reynolds number or angle of attack increases. The effective-frequency range increases with an

Table 1 Effective-frequency ranges and optimum frequencies of acoustic excitation in presence of mechanical vibrations

	$\alpha=0$ deg			$\alpha=5$ deg			$\alpha=10$ deg		
Re_c	Effect. freq. range (Hz)	Optimum freq.	St_d	Effect. freq. range (Hz)	Optimum freq.	St_d	Effect. freq. range (Hz)	Optimum freq.	St_d
57×10^3	40–88	65	1.71	70–80	75	1.97	75–85	80	2.07
100×10^3	45–205	117	1.70	75–220	162	2.35	115–230	169	2.42
150×10^3	⋯	⋯	⋯	⋯	⋯	⋯	370–600	450	4.27

increase of Reynolds number, in agreement with [11], or a decrease of the angle of attack, similar to the trend reported in [7]. Note that all results in the table were obtained with a constant power input of 24 W to the speaker. Lack of correlation between the optimum excitation frequencies in Table 1 and acoustic resonance frequencies (Fig. 5(*a*)) suggest that excitation effect is not due to acoustic resonances in the test section. It should be noted, however, that the effective-frequency range results for $Re_c=150\times10^3$ might be influenced by the acoustic resonances that occur between 400 and 500 Hz.

The optimum excitation parameters obtained in the present study are in good agreement with those reported by Zaman and McKinzie [11] at low angles of attack ($\alpha\leqslant6.5$ deg). However, Strouhal numbers based on the optimum excitation frequency vary with Reynolds number and angle of attack (Table 1) and do not match corresponding values obtained for the vortex shedding frequency, being approximately an order of magnitude higher.

In order to gain insight into the control mechanism, spectra of the boundary layer velocity data were examined. Data were acquired in the unexcited flow at several x/c locations within the transition region in the separated shear layer at y/c positions that correspond to $0.5\bar{U}/U_0$. Figure 6 depicts spectra of the streamwise velocity for $Re_c=100\times10^3$ and $Re_c=150\times10^3$ at $\alpha=10$ deg obtained downstream of the separation. For $Re_c=100\times10^3$ (Fig. 6(*a*)), a flat laminar flow spectrum is observed shortly past the separation point. As a separated shear layer develops downstream, a band of unstable Fourier components, sometimes referred to as a wave packet, occurs centered at $St_d=2.44$, based on the fundamental frequency of the disturbances $f_0=170$ Hz. Further downstream, disturbances in this frequency band are substantially amplified and the band itself broadens, remaining centered at $St_d=2.44$; in addition, harmonics are generated. Rapid transition follows and a "classical" turbulent velocity spectrum is finally observed. A similar transition process is observed for $Re_c=150\times10^3$ (Fig. 6(*b*)), with the band of naturally amplified disturbances observed at $St_d=3.89$ ($f_0=410$ Hz).

To investigate a possible correlation between the acoustic excitation frequencies presented in Table 1 and those of the naturally amplified disturbances in the separated shear layer, the margins of the corresponding effective-frequency ranges are shown by dashed lines in Fig. 6. For both Reynolds numbers, the effective-frequency range contains the frequencies of naturally amplified disturbances in the separated shear layer. Similar results were obtained for all the cases examined, suggesting that excitations at frequencies within the band around the fundamental frequency are effective. Moreover, the Strouhal numbers based on the fundamental frequencies correlate well with the corresponding values of St_d based on the optimum excitation frequency (Table 1). For all the cases examined, the maximum deviation of the optimum frequency from the fundamental frequency did not exceed 10%, with the exception of $Re_c=10\times10^4$ at $\alpha=0$ deg, where they differ by 20%. It should be noted that these discrepancies are likely due to

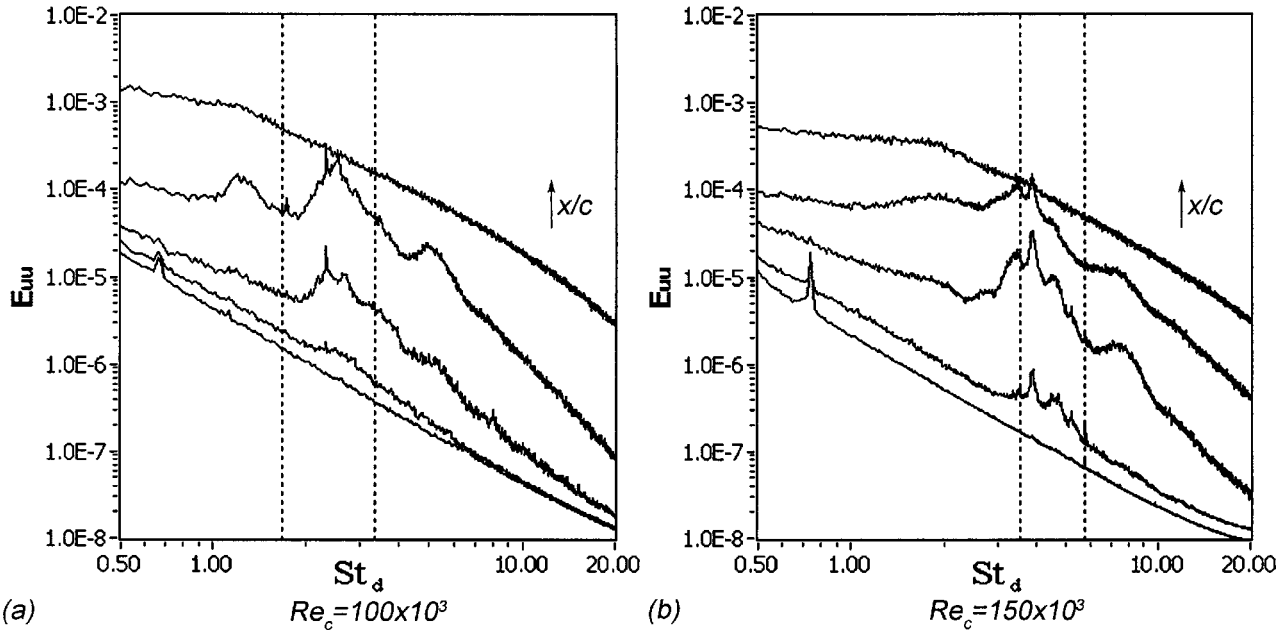

Fig. 6 Separated shear layer spectra, $\alpha=10$ deg; vertical dashed lines indicate the margins of the effective frequency ranges

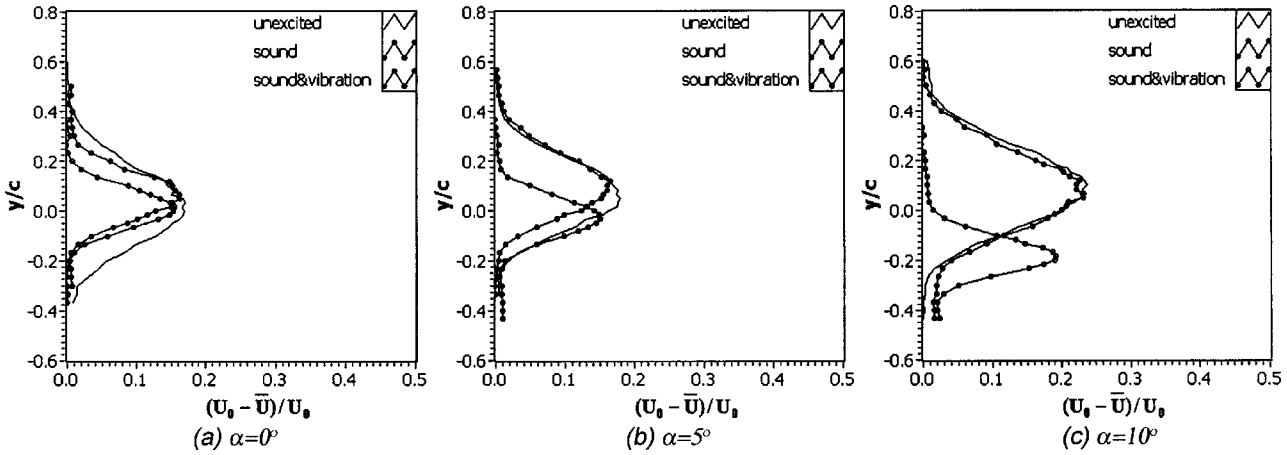

Fig. 7 Effect of excitation on mean profiles for $Re_c = 57 \times 10^3$, $x/c = 2$

the combination of several factors, such as experimental uncertainties, rather than resulting from acoustic resonance alone. Therefore, it is concluded that matching the excitation frequency with the frequency of the most amplified disturbance in the separated shear layer is the optimum method of improving airfoil performance at a given Reynolds number and angle of attack. However, acoustic resonances should be taken into account, as they may influence the results if they are present within the frequency range of interest.

3.3 Excitation Effect. The effect of the two types of excitation on the airfoil performance and wake characteristics is considered below. Note that only results pertaining to excitation applied at the optimum frequencies (Table 1) and a constant power input of 24 W are considered henceforth.

Figure 7 shows $(U_0 - \bar{U})/U_0$ profiles with and without acoustic excitations for $Re_c = 57 \times 10^3$ at $x/c = 2$. Acoustic excitation with superimposed mechanical vibrations significantly narrows the wake. Moreover, at $\alpha = 5$ deg and $\alpha = 10$ deg, the wake is shifted down following the incline of the trailing edge. For example, at $\alpha = 10$ deg (Fig. 7(*c*)), the maximum wake deficit is decreased by the excitation from $0.24U_0$ to $0.2U_0$ and its position is shifted from $y/c = 0.1$ to $y/c = -0.2$. Pure acoustic excitation is much less effective in narrowing the wake for this Reynolds number. Comparison of the profiles in Fig. 5 suggests that this type of excitation affects mainly the lower part of the wake. The wake is more affected at $\alpha = 0$ deg; i.e., it is diminished in size on both the upper and lower parts (Fig. 7(*a*)). At $\alpha = 5$ deg (Fig. 7(*b*)), this effect is only seen on the lower half of the flow with the upper half unaffected; at $\alpha = 10$ deg (Fig. 7(*c*)), the effect is slight. Comparison of the mean profiles for $Re_c = 100 \times 10^3$ at $x/c = 2$ in Fig. 8 reveals significant narrowing of the wake at all three angles of attack for both types of excitation studied. In addition, the wake shifts down following the incline of the trailing edge at $\alpha = 5$ deg and $\alpha = 10$ deg (Figs. 8(*b*) and 8(*c*)), as in the case of the excitation with superimposed vibrations for $Re_c = 57 \times 10^3$. There is no significant difference in the effect from the two types of the excitation on the profiles in Fig. 8. Similar results were obtained for $Re_c = 150 \times 10^3$ at $\alpha = 10$ deg and $x/c = 2$. However, the extent of the effect was significantly smaller for this Reynolds number due to the suppression of a smaller separation region.

A quantitative analysis of the effect of acoustic excitation on airfoil performance is based on the drag coefficient results presented in Table 2. Sound pressure levels (SPLs) and normalized surface accelerations (a/g) measured at the reference locations are also presented in the table. To facilitate data analysis, SPL and a/g values shown for the two lower Reynolds numbers are averages based on measurements at the corresponding optimum frequencies. The drag coefficients are obtained by integration of the mean-wake profiles, as described in [17], with an uncertainty estimated to be less than 5%. Note that the presence of the minor decrease of the freestream velocity at the lower part of the tunnel, which is less than 3% of U_0, was accounted for in calculating the drag coefficients. Moreover, results presented in Table 2 represent the relative reduction of airfoil drag coefficients (C_d) with respect

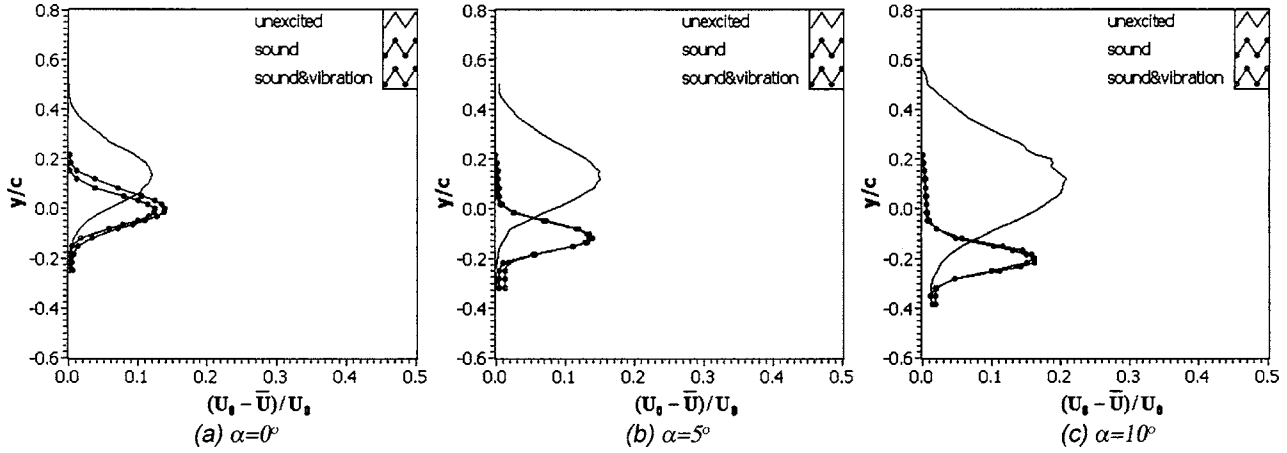

Fig. 8 Effect of excitation on mean profiles for $Re_c = 100 \times 10^3$, $x/c = 2$

Table 2 Normalized airfoil drag coefficients with excitation at optimum frequencies

					$\alpha=0$ deg		$\alpha=5$ deg		$\alpha=10$ deg	
Re_c	SPL[a] (dB)	SPL[b] (dB)	a^a/g	a^b/g	$\frac{C_{d0}-C_{da}}{C_{d0}}$	$\frac{C_{d0}-C_{db}}{C_{d0}}$	$\frac{C_{d0}-C_{da}}{C_{d0}}$	$\frac{C_{d0}-C_{db}}{C_{d0}}$	$\frac{C_{d0}-C_{da}}{C_{d0}}$	$\frac{C_{d0}-C_{db}}{C_{d0}}$
57×10^3	86	93	0.06	0.45	0.38	0.52	0.15	0.51	0.06	0.64
100×10^3	86	87	0.19	0.35	0.30	0.44	0.61	0.61	0.75	0.75
150×10^3	110	109	0.19	0.17	⋯	⋯	⋯	⋯	0.24	0.24

[a]Acoustic excitation only.
[b]Acoustic excitation with mechanical vibrations.

to the corresponding values of the drag coefficients calculated for the unexcited flow (C_{d0}), thus minimizing the effect of experimental uncertainty.

Clearly, the drag coefficients are lowered by either of the two types of excitation for all the cases examined. Note that acoustic excitation in the presence of structural vibrations produces higher sound pressure levels and more pronounced surface vibrations. There is a substantial difference between the effects of the two excitation methods for $Re_c=57\times10^3$, with the acoustic excitation in the presence of structure vibrations being more effective. For instance, at $\alpha=10$ deg, acoustic excitation of the flow with mechanical vibrations results in a decrease of the drag coefficient by 64%, whereas pure acoustic excitation results in a decrease of only 6% (Table 2).

In contrast, for $Re_c=100\times10^3$, the results suggest that there is little difference between the effects of two types of excitation on the airfoil performance. This correlates with insignificant dependency of the sound pressure level on the excitation type in this case. The most significant reduction of the drag coefficient is achieved for this Reynolds number, as the drag coefficient is reduced by 75% by both types of excitation at $\alpha=10$ deg. Note that higher vertical accelerations that occur in the case of acoustic excitation with structural vibrations do not have a measurable effect on drag coefficient.

The results demonstrate that pure acoustic excitation is more efficacious for $Re_c=100\times10^3$ than for $Re_c=57\times10^3$, despite equivalent sound pressure levels in the test section for both Reynolds numbers. This implies that higher amplitude excitations are needed to influence the airfoil performance at lower Reynolds numbers. In addition for the two lower Reynolds numbers, the drag coefficient decrease, with the exception of the result for $Re_c=57\times10^3$ at $\alpha=0$ deg, becomes more pronounced as the angle of attack increases (Table 2). This trend is due to the suppression of the separation region, which increases as angle of attack increases. Ahuja and Burrin [9] reported a similar trend with respect to the effect of acoustic excitation on the lift coefficient.

The improvement of the airfoil performance for $Re_c=150\times10^3$ is less significant than it is for the two lower Reynolds numbers. Nevertheless, a 24% decrease of the drag coefficient is achieved for both types of excitation. As in the case of $Re_c=100\times10^3$, both types of excitation produce equivalent sound pressure levels.

The results discussed above suggest that improvement of the airfoil performance is due to the amplification of the natural disturbances in the separated shear layer by periodic excitation applied at the fundamental frequency of these disturbances, which leads to boundary-layer transition and subsequent reattachment. Based on the comparative analysis of the velocity fluctuations introduced into the separated shear layer as a result of the airfoil surface vibrations and those due to acoustic excitation, it is concluded that acoustic waves have a dominant role in exciting the flow. However, structural vibrations need to be taken into account if acoustic excitation is utilized, as they can result in a higher sound pressure levels within the test section. This is especially important for flow control at lower Reynolds numbers, where higher excitation amplitudes and relatively low frequencies are required to influence airfoil performance.

To assess the effect of acoustic excitation on coherent structures in the airfoil wake, v-component velocity spectra are considered. It should be noted that peaks centered at the excitation frequencies and their harmonics appear in the E_{vv} spectra for the excited flow.

Typical E_{vv} spectra for $Re_c=57\times10^3$ at $x/c=3$ are shown in Fig. 9. The sharp peak at $St_d=0.21$ (8 Hz) in the unexcited flow at 0 deg angle of attack (Fig. 9(*a*)) is attenuated by the pure acoustic

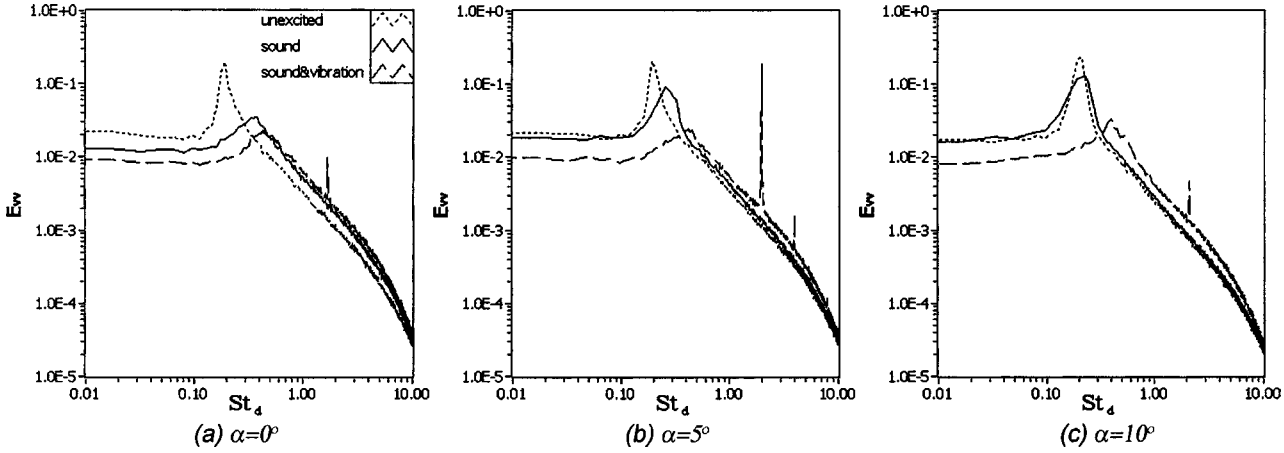

Fig. 9 Effect of excitation on E_{vv} spectra for $Re_c=57\times10^3$, $x/c=3$

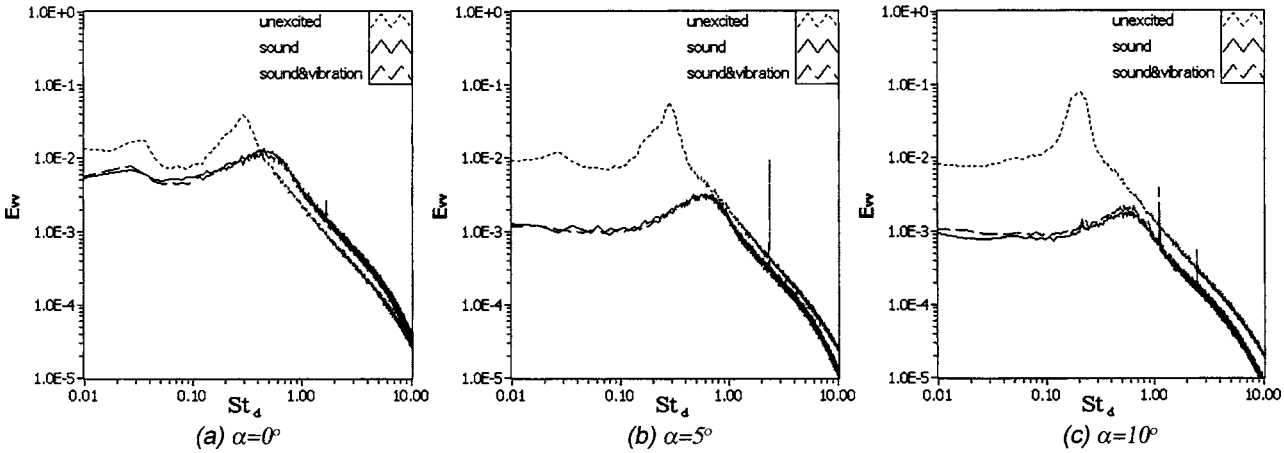

Fig. 10 Effect of excitation on E_{vv} spectra for $Re_c=100\times10^3$, $x/c=3$

excitation and is shifted to $St_d=0.37$ (14 Hz). An increase of the angle of attack to 5 deg (Fig. 9(*b*)) results in a slight attenuation of the peak, and it shifts to $St_d=0.26$ (10 Hz) from $St_d=0.21$ (8 Hz). A further increase of the angle of attack to 10 deg results in the spectrum being only slightly altered by the acoustic excitation, with the peak shifted to $St_d=0.22$ (8.5 Hz) (Fig. 9(*c*)). These observations suggest that excitation at optimum frequencies causes a decrease of the vortex length scale and coherence. The weakening of this effect with an increase of angle of attack is in good agreement with the results of Hsiao et al. [7]. As for the mean-wake velocity profiles, the effect of acoustic excitation with mechanical vibrations differs significantly from the effect of pure acoustic excitation for this Reynolds number (Fig. 9). The corresponding spectra, which are shown as long dashed curves, display diminished peaks centered at $St_d=0.43$ (16.5 Hz), $St_d=0.41$ (15.5 Hz), and $St_d=0.39$ (15 Hz) at 0, 5, and 10 deg angles of attack, respectively. The angle-of-attack effect is substantially reduced in this case, as the energy and the frequency of the peaks do not change significantly with an increase of α.

Figure 10 shows E_{vv} spectra for $Re_c=100\times10^3$ at $x/c=3$. The peaks in the spectra associated with the unexcited flow are attenuated, broadened, and shifted to higher Strouhal numbers by either of the two types of the excitation studied. Note that the extent of these effects is much greater for this case than for the $Re_c=57\times10^3$ case. The peaks corresponding to 0, 5, and 10 deg angles of attack that are centered at $St_d=0.29$ (20 Hz), $St_d=0.29$ (20 Hz), and $St_d=0.22$ (15 Hz) are strongly attenuated and shifted to $St_d=0.44$ (30 Hz), $St_d=0.58$ (40 Hz), and $St_d=0.57$ (40 Hz), respectively. These peaks resemble those obtained in the unexcited flow for $Re_c=150\times10^3$ (Fig. 4). Hence, due to the suppression of the separation region, the vortices shed in the airfoil wake when there is no excitation are replaced by coherent structures of substantially smaller length scale and coherence. As in the case of the mean velocity profiles, spectra for both types of excitation show significant overlap in Fig. 10 at corresponding angles of attack. This suggests that there is no substantial difference in the effect of these two types of excitation on the wake structure. The effect of the acoustic excitation on the vortex shedding for this Reynolds number is similar to the effect on the drag coefficient, as a more significant diminishment of the peaks in the spectra is achieved for higher angles of attack.

The results for $Re_c=150\times10^3$ at $x/c=3$ and 10 deg angle of attack are presented in Fig. 11. As for $Re_c=100\times10^3$, the broad peak centered at $St_d=0.66$ (68 Hz) in the spectrum pertaining to the unexcited flow is attenuated by both types of the excitation and is shifted to $St_d=0.76$ (80 Hz).

From the comparison of the spectral results and the drag coefficient results discussed previously, it is concluded that the magnitude of the acoustic excitation effect on the vortex shedding in the airfoil wake correlates with the improvement in the airfoil performance. Evidently, comparison of spectral results obtained with and without excitation can provide an assessment of the effect of acoustic excitation on airfoil performance.

4 Conclusions

Performance of a NACA 0025 airfoil at low Reynolds numbers was studied experimentally by means of hot-wire velocity measurements and complementary surface flow visualization.

Boundary-layer separation occurs on the upper surface of the NACA 0025 airfoil for all Reynolds numbers and angles of attack examined. For $Re_c=150\times10^3$, the separated boundary layer reattaches to the airfoil surface, forming a laminar separation bubble. However, for $Re_c=57\times10^3$ and $Re_c=100\times10^3$, the separated shear layer fails to reattach to the airfoil surface, leading to the formation of much wider wakes compared to the case for $Re_c=150\times10^3$.

Coherent structures were detected in the airfoil wake for all Reynolds numbers and angles of attack examined. The character-

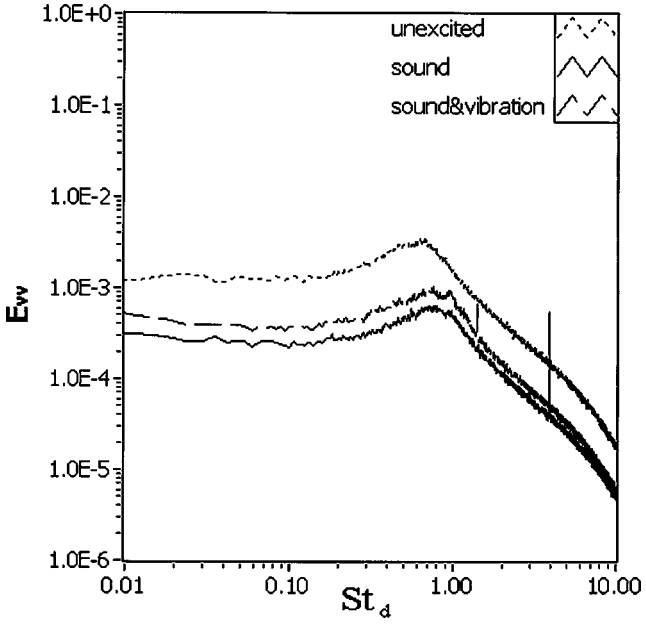

Fig. 11 Effect of excitation on E_{vv} spectrum for $Re_c=150\times10^3$ at $\alpha=10°$, $x/c=3$

istics of these structures depend strongly on boundary-layer behavior and Reynolds number. Specifically, for the two lower Reynolds numbers examined, vortex shedding occurs in the airfoil wake at all angles of attack, with the associated Strouhal number comparable to that for vortex shedding in the wake of a circular cylinder. The vortex-shedding frequency increases and the characteristic length scale and coherency decrease as Reynolds number increases. Finally, the change in the boundary-layer behavior for $\mathrm{Re}_c = 150 \times 10^3$, results in vortex shedding being replaced by the occurrence of much weaker coherent structures of substantially smaller length scale.

External acoustic excitation at particular frequencies and appropriate amplitudes with and without mechanical vibrations can substantially reduce or suppress the separation region so that a decrease in drag results. The effect of the excitation depends strongly on the excitation frequency and amplitude. In particular, the effective frequency range decreases with a decrease of the excitation amplitude. For a constant amplitude excitation, this range narrows with a decrease of the Reynolds number or increase of the angle of attack. The best effect is achieved at an optimum frequency, which increases as Reynolds number or angle of attack increases.

The results provide a definitive correlation between the optimum excitation frequencies and frequencies of naturally amplified disturbances in the separated shear layer. It is concluded that matching the excitation frequency with the frequency of the most amplified disturbance in the separated shear layer is the optimum method of improving airfoil performance at a given Reynolds number and angle of attack. The excitation promotes transition in the separated shear layer, effecting its reattachment, thus decreasing the size of the separation region.

It is concluded that acoustic waves play a dominant role in exciting the separated shear layer. However, low-frequency structural vibrations are found to have a significant effect on airfoil performance for $\mathrm{Re}_c = 57 \times 10^3$, as they result in a higher sound pressure levels within the test section, and should be considered in future experiments involving acoustic excitations.

Acoustic excitation alters the vortex-shedding characteristics, decreasing the vortex length scale and the coherency of the vortex structure. Due to the suppression of the separation region, periodic vortex shedding in the airfoil wake is replaced by the occurrence of weak coherent structures. Moreover, the magnitude of the excitation effect on the wake structure correlates with the extent of the improvement in the airfoil performance, i.e., an increase in the lift and/or a decrease in the drag.

Acknowledgment

The authors gratefully acknowledge the Natural Sciences and Engineering Research Council of Canada (NSERC) for funding this work.

Nomenclature

a = airfoil surface acceleration
C_d = airfoil drag coefficient
c = airfoil chord
d = vertical length of airfoil projection on cross-stream plane
E_{uu} = normalized energy spectrum of u
E_{vv} = normalized energy spectrum of v
f = frequency
f_0 = fundamental frequency of the disturbances
g = acceleration due to gravity
Re_c = Reynolds number, $U_0 c/\nu$
SP = sound pressure
SPL = sound pressure level
St_d = Strouhal number, fd/U_0
U_0 = free-stream velocity in the x direction
$\bar{U}$ = mean streamwise velocity
u, v = x and y fluctuating velocity components
x, y = streamwise and vertical coordinates
α = angle of attack
ν = kinematic viscosity of air

References

[1] Lissaman, P. B. S., 1983, "Low Reynolds Number Airfoils," Annu. Rev. Fluid Mech., **15**, pp. 223–239.
[2] Mueller, T. J., and DeLaurier, J. D., 2003, "Aerodynamics of Small Vehicles," Annu. Rev. Fluid Mech., **35**, pp. 89–111.
[3] Mueller, T. J., and Batill, S. M., 1982, "Experimental Studies of Separation on a Two-Dimensional Airfoil at Low Reynolds Numbers," AIAA J., **20**(4), pp. 457–464.
[4] Nishioka, M., Asai, M., and Yoshida, S., 1990, "Control of Flow Separation by Acoustic Excitation," AIAA J., **28**(11), pp. 1909–1915.
[5] Zaman, K. B. M. Q., Bar-Sever, A., and Mangalam, S. M., 1987, "Effect of Acoustic Excitation on the Flow Over a Low-Re Airfoil," J. Fluid Mech., **182**, pp. 127–148.
[6] Chang, R. C., Hsiao, F. B., and Shyu, R. N., 1992, "Forcing Level Effect of Internal Acoustic Excitation on the Improvement of Airfoil Performance," J. Aircr., **29**(5), pp. 823–829.
[7] Hsiao, F. B., Jih, J. J., and Shyu, R. N., 1997, "The Effect of Acoustics on Flow Passing a High-AOA Airfoil," J. Sound Vib., **199**(2), pp. 177–178.
[8] Collins, F. G., and Zelenevitz, J., 1975, "Influence of Sound Upon Separated Flow Over Wings," AIAA J., **13**(3), pp. 408–410.
[9] Ahuja, K. K., and Burrin, R. H., 1984, "Control of Flow Separation by Sound," AIAA Paper No. 84-2298.
[10] Zaman, K. B. M. Q., 1992, "Effect of Acoustic Excitation on Stalled Flows Over an Airfoil," AIAA J., **30**(6), pp. 1492–1499.
[11] Zaman, K. B. M. Q., and McKinzie, D. J., 1991, "Control of Laminar Separation Over Airfoils by Acoustic Excitation," AIAA J., **29**(7), pp. 1075–1083.
[12] Huang, R. F., and Lin, C. L., 1995, "Vortex Shedding and Shear-Layer Instability of Wing at Low-Reynolds Numbers," AIAA J., **33**(8), pp. 1398–1430.
[13] Huang, R. F., and Lee, H. W., 2000, "Turbulence Effect on Frequency Characteristics of Unsteady Motions in Wake of Wing," AIAA J., **38**(1), pp. 87–94.
[14] Yarusevych, S., Kawall, J. G., and Sullivan, P. E., 2003, "Effect of Acoustic Excitation on Airfoil Performance at Low Reynolds Numbers," AIAA J., **41**(8), pp. 1599–1601.
[15] Kawall, J. G., Shokr, M., and Keffer, J. F., 1983, "A Digital Technique for the Simultaneous Measurements of Streamwise and Lateral Velocities in Turbulent Flows," J. Fluid Mech., **133**, pp. 83–112.
[16] Yarusevych, S., Sullivan, P. E., and Kawall, J. G., 2004, "Investigation of Airfoil Boundary Layer and Wake Development at Low Reynolds Numbers," AIAA Paper No. 2004-2551.
[17] Lu, B., and Bragg, M. B., 2000, "Experimental Investigation of Airfoil Drag Measurement with Simulated Leading-Edge Ice Using the Wake Survey Method," AIAA Paper No. 2000-3919.

Numerical Simulation of the Particle Motion Characteristics in Boundary Layer of Gas-Solid Rotary Flow

Jingyu Ran
e-mail: ranjy@cqu.edu.cn

Li Zhang

Qiang Tang

Mingdao Xin

Institute of Thermal Power Engineering,
Chongqing University,
Chongqing 400044, China

The boundary-layer feature and the forces on the particle are analyzed in detail, and the motion parameters of the particle in the gas-solid rotary flow are divided into two parts according to the r-z meridian and r-θ cross section. The Lagrange method is then applied, the 3-D mathematical model of particle motion in the gas-solid rotary flow is presented, and the Gear integral method is applied to simulate the motion characteristics of the particles. The results show that the centrifugal force and Saffman lift force play important roles in the process of the particle being separated from the gas-solid rotary flow in the rotary boundary layer. The velocity gradient of radial direction is the biggest, and that of tangent direction is the smallest. For a higher density ratio of gas to solid, the deposition performance of the particle depends not only on the inlet flow velocity but also on the range of the particle diameter. Reasonable velocity gradient matching of the three directions (r,z,θ) in the gas-solid rotary flow is useful to improve the separation efficiency of the rotary separators. [DOI: 10.1115/1.2175166]

Keywords: gas-solid rotary flow, particle motion characteristics, boundary layer

1 Introduction

Gas-solid rotary flows are frequently observed in industrial equipment, such as dust catchers in power plants and rotary separators in environmental engineering. To improve the separator efficiency is the main object for scientific researchers and engineers. A number of investigations have been done on such gas-particle two-phase flows to elucidate the flow phenomena, such as particle behavior and the change in the gas flow due to the particles, but the results are not enough to meet the demands of the optimal designs and applications for various industrial equipment. For the purpose of improving separator efficiency, the motion characteristics of the particle in the gas-solid rotary flow are studied, considering the boundary-layer character.

While entering a rotary separator, most of the particles begin to move toward the wall and part of the particles disperse in the gas flow due to turbulence. The probability of the particle collecting on the wall is determined by the ratio of two time scales. One is migration time, which is the time for the particle to reach the wall with a radial motion, and another is flow time, which is the residence time for migration. The flow time is usually defined in terms of separate height and the average axial flow velocity, and the migration time is defined in terms of the inlet half-width and the average particle migration velocity. In an exact sense, the migration time defined as such represents the time of the particle reaching the near-wall region, namely, the boundary layer, which is not the wall surface, and most of the investigations are based on this migration time [1–5]. The velocity in the near-wall region changes very abruptly, so that the particle motion is not in equilibrium with the surrounding gas velocity. The particle migration velocity in boundary layer cannot be determined by the local conditions only; it depends on many factors, such as the motion history of the particles, the separator feature (e.g., the profile and the internal structure), operating parameters (e.g., temperature, inlet velocity, etc.), and the particle diameter, and all of these factors affect each other. Although W.S. Kim et al. [6] obtained a new relational expression of separator efficiency based on boundary-layer characteristics, the mathematical model was obtained only according to Newton's second law (Saffman, Basset, Magnus, virtual mass, pressure gradient force, etc., are not included) and could not completely present the motion characteristics of the particle for a higher density ratio of gas to solid. In addition, Basset, Magnus, and virtual mass force should be included [7]. The stochastic trajectory model of the particle in rotary flow is proposed here, and its transient motion character is researched to study methods of improving the efficiency of rotary separators.

2 Mathematical Model

Forces Acting on the Particle in the Gas-Solid Rotary Flow. The rotary separator can be divided into two regions: the turbulent-core region and the near-wall region, which is called boundary layer. When the particle is separated, it must pass through the boundary layer. The forces on a particle in the gas-solid rotary flow include the following.

Viscous Resistance. The viscous resistance is the most important force for the particle motion. While $\mathrm{Re}_{pi}=(V_{fi}-V_{pi})d_p/\upsilon_f \leqslant 1$, viscous resistance can be expressed as [7]:

$$F_{Ri} = 5.1\pi\mu_f d_p(1 + 0.15\,\mathrm{Re}_{pi}^{0.687})(V_{fi} - V_{pi}) \tag{1}$$

Gravitational and Buoyant Force. The difference between the gravitational and buoyant force can be described as:

$$F_{gi} = \frac{\pi}{6}d_p^3(\rho_p - \rho_f)g_i \tag{2}$$

Centrifugal Force. The flow in the rotary separator is strong rotary, so that the centrifugal force is written as [7]:

$$F_{ci} = \frac{\pi}{6}d_p^3\rho_p\frac{V_{\theta i}^2}{r} = m_p a_i \tag{3}$$

Contributed by the Fluids Engineering Division of ASME for publication in the JOURNAL OF FLUIDS ENGINEERING. Manuscript received March 17, 2005; final manuscript received November 9, 2005. Assoc. Editor: James A. Liburdy.

Pressure Gradient. When the diameter of a spherical particle is d_p and the pressure gradient of the gas-particle two-phase flow field is $\partial P/\partial x_i$, the force exerted by pressure gradient of the flow field is expressed by L. D. Smoot [7]:

$$F_{pi} = -\frac{1}{6}\pi d_p^3 \frac{\partial P}{\partial x_i} = -m_f \frac{1}{\rho_f}\frac{\partial P}{\partial x_i} \tag{4}$$

Virtual Mass Force. When a particle is accelerated in the flow field, not only does the velocity of the particles is increase but the velocity of the fluid surrounding the particle is also increased. The force that makes the particle move causes the kinetic energy of the particle and the fluid to increase; as a result, the force is greater than the force that accelerates particle ($m_p a_{pi}$, where a_{pi} is motion acceleration of the particle). The virtual mass force is given, and experimental coefficient K_{mi} is obtained by F. Odar [8]:

$$F_{Vmi} = -\frac{1}{12}\pi d_p^3 \rho_f \left(\frac{dV_{fi}}{d\tau} - \frac{dV_{pi}}{d\tau}\right) = K_{mi} m_f \left(\frac{dV_{fi}}{d\tau} - \frac{dV_{pi}}{d\tau}\right) \tag{5}$$

Basset Force. While a particle moves with any velocity in a separator, the Basset force is a transient flow resistance exerted by the unstable flow, [9]:

$$F_{Bi} = \frac{3}{2} d_p^2 \sqrt{\pi \rho_f \mu_f} \int_{-\infty}^{t} \left[\left(\frac{\partial V_{fi}}{d\tau} - \frac{dV_{pi}}{d\tau}\right) \Big/ \sqrt{t-\tau}\right] d\tau$$
$$= \frac{1}{4}\pi d_p^2 \rho_f K_{Bi} \sqrt{\frac{\upsilon_f}{\pi}} \int_{-\infty}^{t} \left[\left(\frac{dV_{fi}}{d\tau} - \frac{dV_{pi}}{d\tau}\right) \Big/ \sqrt{t-\tau}\right] d\tau \tag{6}$$

Saffman Force. In the gas-solid flow field with a velocity gradient, the Saffman force, which is the lift force exerted by the pressure difference acted on the whole particle surface, is described by Saffman [10]:

$$F_{si} = d_p^2 K_s \rho_f \upsilon_f^{0.5} \left|\frac{\partial F_j}{\partial x_i}\right|^{0.5} (V_{fj} - V_{pj}) \tag{7}$$

In the main flow field, Saffman force can be neglected, but in the rotary boundary layer, it cannot be neglected because of the high velocity gradient.

Magnus Force. The Magnus force, which causes the different shear forces to cause the particle to be rotary, is another lift force exerted by the collision velocity difference of the particle. The bigger the $\partial V_{fj}/\partial x_i$, the higher the rotary angular speed of the spherical particle ω'_{pi}. While the shear Reynolds number $\mathrm{Re}_{pi} = d_p^2 |\partial V_{fj}/\partial x_i| / \upsilon_f$ is lower, $\omega'_{pi} = \frac{1}{2}\nabla \times V_{fj}$. Thus, the Magnus lift force can be expressed as [7]:

$$F_{Mi} = -\frac{\pi}{8} d_p^3 \rho_f \omega'_{pi} (V_{fi} - V_{pi}) = \frac{\pi}{16} d_p^3 \rho_f (V_{fi} - V_{pi}) \left(\frac{dV_{fi}}{dx_i} - \frac{dV_{pi}}{dx_j}\right) \tag{8}$$

Particle Motion Equations in the Rotary Boundary Layer.

Motion Equations of the Particle in an Unsolicited Flow Field. According to the above analysis of the forces on the particle and Newton's second law, the differential equation of the particle motion in the unsolicited rotary flow field is described with Lagrange method:

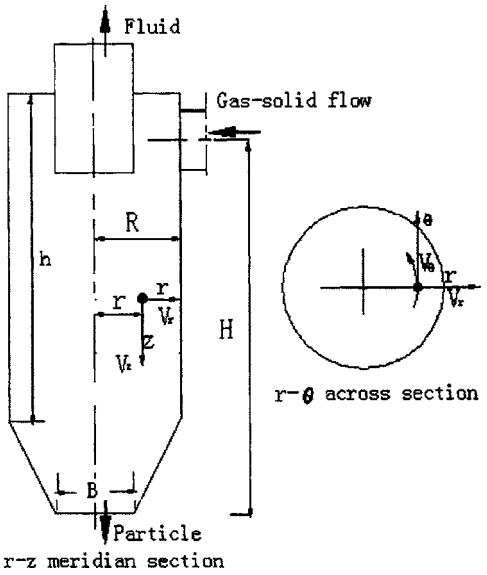

Fig. 1 The *r-z* meridian and *r-θ* across section of separator

$$(K_{mi} + \bar{m}_p)\frac{dV_{pi}}{d\tau} = \frac{30.6}{d_p^2}\upsilon_f (1 + 0.15\,\mathrm{Re}_{pi}^{0.687})(V_{fi} - V_{pi}) + (\bar{m}_p - 1) g_i$$
$$+ \bar{m}_p \frac{V_{\theta i}^2}{r} - \frac{1}{\rho_f}\frac{\partial P}{\partial x_i} + K_{mi}\frac{dV_{fi}}{d\tau}$$
$$+ \frac{3}{2d_p} K_{Bi} \sqrt{\frac{\upsilon_f}{\pi}} \int_{-\infty}^{t} \left[\left(\frac{dV_{fi}}{d\tau} - \frac{dV_{pi}}{d\tau}\right) \Big/ \sqrt{t-\tau}\right] d\tau + \frac{6}{\pi d_p} K_s \upsilon_f^{0.5} \left|\frac{\partial V_{fj}}{\partial x_i}\right|^{0.5}$$
$$\times (V_{fj} - V_{pj}) + \frac{3}{8}(V_{fi} - V_{pi}) \left(\frac{dV_{fi}}{dx_i} - \frac{dV_{pi}}{dx_j}\right) \tag{9}$$

where $\bar{m}_p = m_p/m_f = \rho_p/\rho_f$, and $\mathrm{Re}_{pi} = (V_{fi} - V_{pi}) d_p/\upsilon_f \leqslant 1$

Governing Factors and Simplified Forms

1 Wall-effecting coefficient. The coordinated system is shown in Fig. 1 according to the flow characteristics. If the free rotary of the particle is not considered, the Magnus lift force can be neglected. Brenner [11] and Maude [12] give the wall-effecting coefficient according to the Stokes resistance at the same time.

For the main flow direction:

$$C_M = \left[1 - \frac{9}{32}\frac{d_p}{R-r} + \frac{1}{64}\left(\frac{d_p}{R-r}\right)^3 - \frac{45}{4096}\left(\frac{d_p}{R-r}\right)^4 - \frac{1}{512}\left(\frac{d_p}{R-r}\right)^5\right]^{-1} \tag{10}$$

For the normal stream direction:

$$C_V = 1 + \frac{9}{16}\left(\frac{d_p}{R-r}\right) + \frac{81}{1024}\left(\frac{d_p}{R-r}\right)^2 \tag{11}$$

2 Related factors. The coefficient K_B for Basset force [9], K_s for Saffman force [7], and K_m for virtual mass force [8] are equal to 6, 1.615, and 0.5, respectively. Because $d(\,)/d\tau \approx D(\,)/D\tau$, the item $-\upsilon_f \nabla^2 V_{fi}$ exerted by pressure gradient is very small and can be neglected. Equation (12) can then be derived from Navior-Stokes equations:

$$-\frac{1}{\rho_f}\frac{\partial P}{\partial x_i}=\frac{DV_{fi}}{D\tau}-\upsilon_f\Delta V_{fi}-F_{fi} \tag{12}$$

where F_{fi} is the flow mass force.

3 Particle motion equations of r-z meridian section and r-θ cross section. The 3-D motion of the particle in the gas-solid rotary flow is divided into two 2-D flow fields, the *r-z* meridian section and *r-θ* cross section, and the particle motion equations in turbulence boundary can be expressed as follows: For the *r-z* section, the main flow direction *z*:

$$\frac{dV_{pz}}{d\tau}=\frac{C_M}{0.5+\bar{m}_p}\left\{-\frac{30.6}{d_p^2}\upsilon_f(1+0.15\,\mathrm{Re}_{pz}^{0.687})(V_{fz}-V_{pz})+\bar{m}_p g-\upsilon_f\frac{\partial^2 V_{fz}}{\partial r^2}+\frac{3}{2}\frac{dV_{fz}}{d\tau}+\frac{9}{d_p}\sqrt{\frac{\upsilon_f}{\pi}}\int_{-\infty}^{t}\times\left[\left(\frac{dV_z}{d\tau}-\frac{dV_{pz}}{d\tau}\right)\Big/\sqrt{t-\tau}\right]d\tau\right\} \tag{13}$$

normal direction r_1:

$$\frac{dV_{pr1}}{d\tau}=\frac{C_V}{0.5+\bar{m}_p}\left\{-\frac{30.6}{d_p^2}\upsilon_f(1+0.15\,\mathrm{Re}_{pr1}^{0.687})(V_{fr1}-V_{pr1})+\frac{3}{2}\frac{dV_{fr1}}{d\tau}+\frac{9}{d_p}\sqrt{\frac{\upsilon_f}{\pi}}\times\int_{-\infty}^{t}\left[\left(\frac{dV_{fr1}}{d\tau}-\frac{dV_{pr1}}{d\tau}\right)\Big/\sqrt{t-\tau}\right]d\tau+\frac{6.96}{\pi d_p}\upsilon_f^{0.5}\left|\frac{\partial V_{fz}}{\partial r}\right|^{0.5}(V_{fz}-V_{pz})\right\} \tag{14}$$

For *r-θ* section, the main flow direction *θ*:

$$\frac{dV_{p\theta}}{d\tau}=\frac{C_M}{0.5+\bar{m}_p}\left\{-\frac{30.6}{d_p^2}\upsilon_f(1+0.15\,\mathrm{Re}_{p\theta}^{0.687})(V_{f\theta}-V_{p\theta})+\frac{3}{2}\frac{dV_{f\theta}}{d\tau}+\bar{m}_p\frac{V_{p\theta}^2}{r}+\frac{9}{d_p}\sqrt{\frac{\upsilon_f}{\pi}}\int_{-\infty}^{t}\left[\left(\frac{dV_{f\theta}}{d\tau}-\frac{dV_{p\theta}}{d\tau}\right)\Big/\sqrt{t-\tau}\right]d\tau-\upsilon_f\frac{\partial^2 V_{f\theta}}{\partial r^2}\right\} \tag{15}$$

and normal direction r_2:

$$\frac{dV_{pr2}}{d\tau}=\frac{C_V}{0.5+\bar{m}_p}\left\{-\frac{30.6}{d_p^2}\upsilon_f(1+0.15\,\mathrm{Re}_{pr2}^{0.687})(V_{fr2}-V_{pr2})+\frac{3}{2}\frac{dV_{fr2}}{d\tau}+\frac{9}{d_p}\sqrt{\frac{\upsilon_f}{\pi}}\int_{-\infty}^{t}\left[\left(\frac{dV_{fr2}}{d\tau}-\frac{dV_{pr2}}{d\tau}\right)/\sqrt{t-\tau}\right]d\tau+\frac{6.96}{\pi d_p}\upsilon_f^{0.5}\left|\frac{\partial V_{f\theta}}{\partial r}\right|^{0.5}(V_{f\theta}-V_{p\theta})\right\} \tag{16}$$

3-D Dimensionless Motion Equations. The wall surface friction velocities are $u_\tau=\sqrt{\tau_w/\rho_f}$ and υ_f, respectively, so that the variables in the above equations are written as dimensionless forms: $x_i^+=x_i(u_\tau/\upsilon_f)$, $V_i^+=(V_i/u_\tau)$, $\tau^+=\tau(u_\tau^2/\upsilon_f)$, $d_p^+=d_p(u_\tau/\upsilon_f)$, $t^+=t(u_\tau^2/\upsilon_f)$, $g^+=g(u_\tau^3/\upsilon_f)$. The dimensionless motion equations derived from Eqs. (13)–(16) are then given as follows.

For the *z* direction:

$$\frac{dV_{pz}^+}{d\tau^+}=\frac{C_M}{0.5+\bar{m}_p}\times\left\{-\frac{30.6}{d_p^{+2}}(1+0.15\,\mathrm{Re}_{pz}^{0.687})(V_{fz}^+-V_{pz}^+)+\bar{m}_p g^+-\frac{\partial^2 V_{fz}^+}{\partial r^{+2}}+\frac{3}{2}\frac{dV_{fz}^+}{d\tau^+}+\frac{9}{d_p^+}\sqrt{\frac{1}{\pi}}\int_{-\infty}^{t^+}\times\left[\left(\frac{dV_{fz}^+}{d\tau^+}-\frac{dV_{pz}^+}{d\tau^+}\right)\Big/\sqrt{t^+-\tau^+}\right]d\tau^+\right\} \tag{17}$$

For the *θ* direction:

$$\frac{dV_{p\theta}^+}{d\tau^+}=\frac{C_M}{0.5+\bar{m}_p}\left\{-\frac{30.6}{d_p^{+2}}(1+0.15\,\mathrm{Re}_{p\theta}^{0.687})(V_{f\theta}^+-V_{p\theta}^+)+\frac{3}{2}\frac{dV_{f\theta}^+}{d\tau^+}+\frac{9}{d_p^+}\sqrt{\frac{1}{\pi}}\int_{-\infty}^{t^+}\left[\left(\frac{dV_{f\theta}^+}{d\tau^+}-\frac{dV_{p\theta}^+}{d\tau^+}\right)\Big/\sqrt{t^+-\tau^+}\right]d\tau^+-\frac{\partial^2 V_{f\theta}^+}{\partial r^{+2}}\right\} \tag{18}$$

For the *r* direction:

$$\frac{dV_{pr}^+}{d\tau^+}=\frac{C_V}{0.5+\bar{m}_p}\left\{-\frac{30.6}{d_p^{+2}}(1+0.15\,\mathrm{Re}_{pr}^{0.687})(V_{fr}^+-V_{pr}^+)+\bar{m}_p\frac{dV_{p\theta}^{+2}}{r^+}+\frac{3}{2}\frac{dV_{fr}^+}{d\tau^+}+\frac{9}{d_p^+}\sqrt{\frac{1}{\pi}}\int_{-\infty}^{t^+}\left[\left(\frac{dV_{fr}^+}{d\tau^+}-\frac{dV_{pr}^+}{d\tau^+}\right)\Big/\sqrt{t^+-\tau^+}\right]d\tau^+-\frac{6.96}{\pi d_p^+}\left[\left|\frac{\partial V_{fz}^+}{\partial r^+}\right|^{0.5}(V_{fz}^+-V_{pz}^+)+\left|\frac{\partial V_{f\theta}^+}{\partial r^+}\right|^{0.5}(V_{f\theta}^+-V_{p\theta}^+)\right]\right\} \tag{19}$$

The Dimensionless Particle Deposition Velocity in the Rotary Boundary Layer. The dimensionless particle deposition velocity can be obtained when the dimensionless particle tangent velocity $V_{p\theta}^+(\delta^+)$ at some point ($\delta^+=R^+-r^+$) is obtained [6]:

$$V_{pd}^+=\mathrm{T}^+\frac{V_{p\theta}^{+2}(\delta^+)}{R^{*+}} \tag{20}$$

Here, $\mathrm{T}^+=\rho_p d_p^2 C u_\tau^2/(18\mu_f\upsilon_f)$, $C=1+2/\{P_a d_u[6.32+2.01\times\exp(-0.1095P_a d_u)]\}$, P_a is the absolute pressure in cm Hg, d_u is the particle diameter in μm, $R^{*+}=R(u_\tau/\upsilon_f)$, and $R^*=((1/H)\{(H-h)/3][R^2+B^2/4+RB/2]+R^2h\})^{0.5}$.

The Flow Field in the Rotary Boundary Layer. Ideally, one needs to know the entire Lagrange time history of the turbulent boundary-layer flow in order to precisely track the motion of discrete particle. To predict or measure such information is not practical, so the approximations are employed to specify the flow field. In this study, the turbulent flow is simulated by a three-dimensional, random velocity field where the mean and rms profile is specified according to established experimental results. The fluid flow is assumed to be unaffected by the momentum of the particle phase, thus representing a dilute suspension. The mean stream velocity component is defined by the well-known law-of-the-wall relations for the viscous sublayer and logarithmic region [13]:

$$\begin{cases} V_{fk}^+ = r^+, & \text{for viscous sublayer region, } r^+ \leqslant 5 \\ V_{fk}^+ = 5.0 \ln r^+ - 3.05, & \text{for midlayer region, } 5 < r^+ < 30 \ (k = z, \theta) \\ V_{fk}^+ = 2.5 \ln r^+ + 5.5, & \text{for logarithmic region, } r^+ \geqslant 30 \end{cases} \tag{21}$$

The buffer region velocity distribution is obtained from a cubic spline interpolation, ensuring that the velocity gradient used in the lift force term is continuous throughout the boundary layer: [14,15]:

$$\begin{cases} V_{fk}^+ = -1.076 + 1.445 r^+ - 0.04885 r^{+2} + 0.0005813 r^{+3} & (k = z, \theta) \\ V_{fr}^+ = 0.005 r^{+2} (1 + 0.002923 r^{+2.218})^{-1}, & (0 < r^+ < 200) \end{cases} \tag{22}$$

The mainstream turbulence is neglected in the numerical simulation because the dominant mean velocity has little effect on the particle. The instantaneous eddy velocity that a particle encounters along its path is determined by randomizing the rms normal velocity:

$$V_{pr}^+ = V_{fr}^+ N_r \tag{23}$$

where N_T is a random number defined by Gaussian probability density distribution of zero mean and unity standard deviation.

3 Numerical Solution Method in the Rotary Boundary Layer

The differential motion equations describing each particle-eddy interaction are solved numerically by a stiff system using the Gear integral method when the initial position and velocity of a particle in the rotary boundary layer are given. The integrated item for Basset force can then be calculated:

$$\int_0^{t^+} \left(\frac{dV_{fi}^+}{d\tau^+} - \frac{dV_{pi}^+}{d\tau^+} \right) \frac{d\tau^+}{\sqrt{t^+ - \tau^+}} = 2 \sum_{k=0}^{m-1} \{ \sqrt{\Delta t^+} [V_{pi}^+(k+1) - V_{pi}^+(k) - V_{fi}^+(k) \,.\, (\sqrt{m-k} - \sqrt{m-k-1})] \} \tag{24}$$

Here, Δt^+ is dimensionless time step, m is the number of calculated points, and $V_i^+(k)$ is the particle velocity whose time is $k\Delta t^+$. The position and trace of a particle can be obtained as follows after the dimensionless velocity of a particle is decided:

$$x_{pi}^+(k) = x_{pi}^+(k-1) + \tfrac{1}{2} [V_{pi}^+(k-1) + V_{pi}^+(k)] \,.\, \Delta t^+ \tag{25}$$

The particle motion characteristics along radial direction are the composite vector of the r-z direction and the r-θ direction vector.

4 Results and Discussion

The motion characteristics of the particle in the gas-solid rotary flow ($\rho_p/\rho_f = 10$) are simulated according to the above numerical solution method. The dimensionless particle deposition velocity V_{pd}^+ and gas flow tangent velocity $V_{f\theta}^+$ along the normal direction of the boundary layer are shown in Fig. 2. When the particle moves toward the wall in the boundary layer, while $V_{p\theta 0}^+ = V_{f\theta 0}^+$, the velocity $V_{pd}^+ > V_{f\theta}^+$ always occurs, and the difference between V_{pd}^+ and $V_{f\theta}^+$ increases quickly. The dimensionless particle deposition velocity can also exceed the gas-solid flow velocity near the wall region of the separator even if $V_{p\theta 0}^+ < V_{f\theta 0}^+$. All of these show that Saffman lift force is helpful for particle deposition in the rotary boundary layer, as also shown by Kallio et al.[15] and Roahiainen et al.[16]. The relationship among the distance of the particle moving along normal direction (r^+), the particle diameter (d_p^+) and the inlet velocity (V_i) is shown in Fig. 3. For the identical particle diameter, the bigger the inlet gas-solid velocity, the longer that the distance of the particle moving in the boundary layer, and the higher the efficiency of the particle deposition. At the same inlet gas-solid flow velocity, the bigger the particle diameter, the longer the particle deposition distance, the same phenomenon described by Kim et al.[6]. Although the inlet velocity is high, the particle cannot reach the wall and its dimensionless deposition distance is short when its diameter is less than 1.5; that is $d_p^+ < 1.5$. All of these results show that the deposition performance of the particle is determined not only by the inlet gas-solid velocity, but also by the structure of the separator. As shown in Fig. 4, the tangent velocity $V_{p\theta}^+$ of a particle decreases sharply after it enters into the separator, but the change of the tangent velocity $V_{f\theta}^+$ is slight. The velocities $V_{p\theta}^+$ and $V_{f\theta}^+$ abruptly decrease in the near-wall region. The transient characteristics of the velocities V_{pr}^+ and V_{pz}^+ are shown in Figs. 5 and 6, respectively. The velocities V_{pr}^+ and V_{pz}^+ increase quickly from zero to maximum, but the dimensionless times τ^+ at the maximum velocities are not the same (while $V_{pf1}^+ = V_{fl}^+ = 18.5$, $\tau_r^+ = 25$, $\tau_z^+ = 50$), and the maximum velocities are not identical ($V_{pr}^+ < V_{pz}^+$). While V_{pr}^+ and V_{pz}^+ reach their maximum, the velocity V_{pr}^+ decreases sharply, the V_{pz}^+ decreases more slowly, and the velocity $V_{p\theta}^+$ is the slowest, as shown in Fig. 4. When the velocity V_i^+ decreases, the times τ_r^+ and τ_z^+ to reach each maximum velocity increase. All of these show that the centrifugal force and

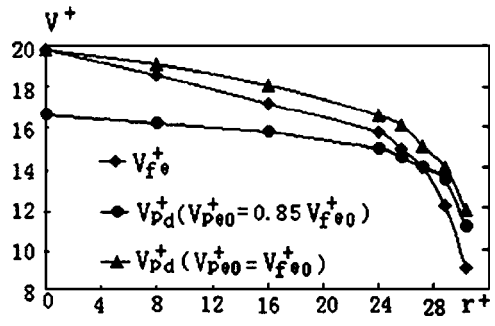

Fig. 2 The velocity $V_{f\theta}^+$ and V_{pd}^+ ($d_p^+ = 2$) under different r^+

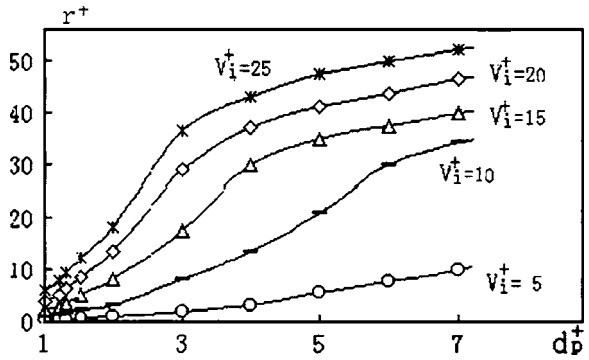

Fig. 3 The relationship among r^+, d_p^+, and V_i^+

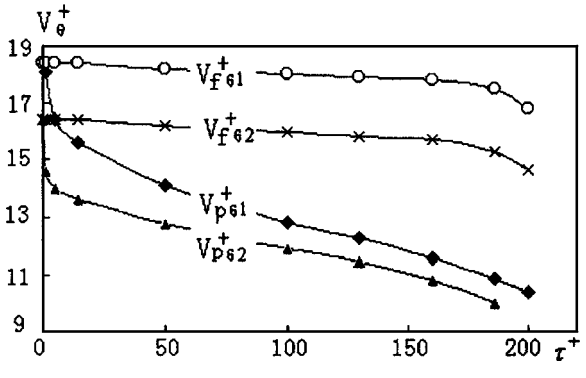

Fig. 4 The transient characteristics of the $V_{f\theta}^+$ and $V_{p\theta}^+$ (d_p^+=2)

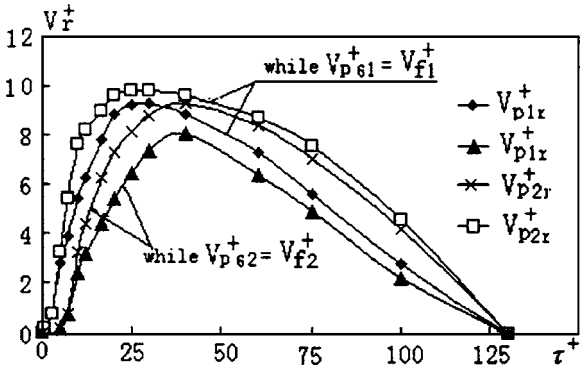

Fig. 5 The transient characteristics of the V_{pr}^+ (d_p^+=2,6) under different V_i^+

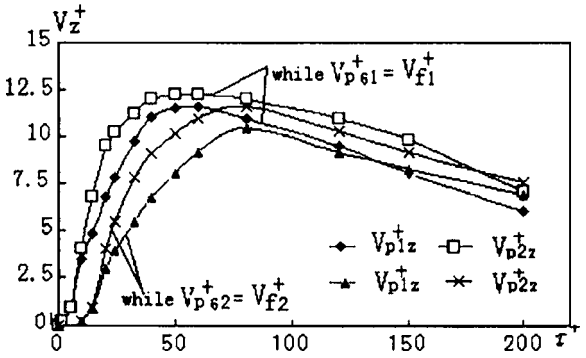

Fig. 6 The transient characteristics of the V_{pz}^+ (d_p^+=2,6) under different V_i^+

Saffman lift force play important roles in the process of the particle being separated from the gas-solid rotary flow in the rotary boundary layer. The velocity gradient of radial direction is the biggest, and the velocity gradient of tangent direction is the smallest. When $V_{pr}^+=0$, and $V_{pz}^+=0$, but $V_{p\theta}^+\neq 0$, the particle cannot be separated from the gas flow. The more reasonable the radial, axis, and tangent velocity gradient matching, the higher the separated efficiency. It is necessary to undertake more research of the optimum separator structure to ensure that the velocity gradient distribution in the three directions is reasonable. As shown in Fig. 7, the directions of the gas-solid flow line and the particle motion stay almost identical in the inlet, but the direction of particle motion gradually deflects from the gas flow line, and the bigger the diameter d_p^+, the longer the deflection distance. The deflection distance in the r direction is greater than that of z direction, but their difference decreases gradually. Because the r direction velocity gradient is bigger than that of the z direction near the wall region in the rotary boundary layer when τ^+ increases, the z direction deflection distance may be greater than that of the r direction.

5 Conclusions

(1) It is feasible to investigate the motion character of the particle in the gas-solid rotary boundary layer according to Lagrange and Gear integral calculation methods, considering Saffman, Basset, Magnus, virtual mass, pressure gradient force, etc.

(2) For the particle motion in the rotary boundary layer, while $V_{p\theta 0}^+=V_{f\theta 0}^+$, $V_{pd}^+>V_{f\theta}^+$ is always true, and their difference increases when the particle moves towards the wall. The centrifugal and Saffman lift forces are helpful for particle deposition in the rotary boundary layer.

(3) The dimensionless tangent velocity of the particle is bigger than that of gas phase. The dimensionless velocities of the particle and gas phase decrease quickly near the wall.

(4) Although the inlet velocity is high, the deposition distance of the particle ($d_p^+<1.5$) is short and the particle cannot reach the wall. When the density ratio of gas to solid is high, the deposition performance of the particles depends not only on the inlet velocity, but also on the particle diameter.

(5) In the boundary layer, the velocity gradient of radial direction is the biggest, and that of tangent direction is the smallest. The separator efficiency is high when the velocity gradients in the radial, axis, and tangent directions are reasonable and match each other.

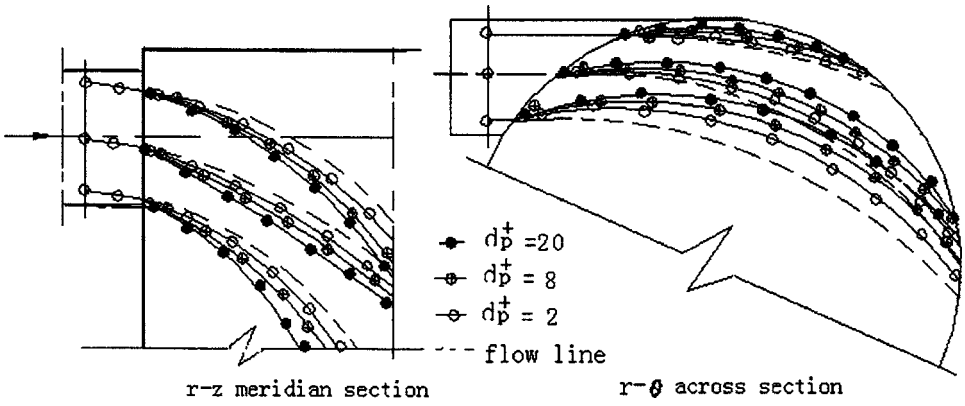

Fig. 7 The motion trace of particles on the *r-z* meridian and *r-θ* across section of cyclone

Nomenclature

a = acceleration
B = diameter of separator exit
d = diameter
F = force
g = gravitational acceleration
H = overall height of separator
h = height of separator barrel
K, C = coefficients
m = mass
P = pressure
r = radial position of particle in separator
R = radius of separator
Re = Reynolds number
t = time
u = wall surface friction velocity
V = velocity
μ = motion viscosity coefficient
υ = viscosity coefficient
ρ = density
τ = cross section force near wall, time

Subscripts

B = Basset
C = centrifugal
d = deposition
f = fluid
g = gravity
i, j, k = tensor coordinates
M = Magnus
p = particle, pressure
R = resistance
r = meridian
V = velocity
w = wall
z = axis
θ = tangent
$+$ = dimensionless

References

[1] Dietz, P. W., 1981, "Collection Efficiency of Cyclone Separator," AIChE J., **27**(6), p. 888.
[2] Enliang, L., 1989, "A New Collection Theory of Cyclone Separator," AIChE J., **35**(4), p. 666.
[3] Dirgo, J., 1985, "Cyclone Collection Efficiency: Comparison of Experimental Results With Theoretical Predictions," Aerosol Sci. Technol., **4**, p. 401.
[4] Boysan, F., 1983, "Experimental and Theoretical Studies of Cyclone Separator," Inst. Chem. Eng. Symp. Ser., **69**, p. 305.
[5] Clift, R., 1991, "A Critique of Two Models for Cyclone Performance," AIChE J., **237**(2), p. 285.
[6] Kim, W. S., and Lee, J. W., 1997, "Collection Efficiency Model Based on Boundary Layer Characteristics for Cyclones," AIChE J., **43**(10), pp. 2446–2455.
[7] Smoot, L. D., and Pratt, D. T., 1992, *Coal Combustion and Gasification*, Beijing Science Press, pp. 147–157.
[8] Odar, F., 1966, "Verification of Proposed Equation for Calculation of Forces on a Sphere Accelerating in a Viscous Fluid," J. Fluid Mech., **25**(3), pp. 591–592.
[9] Basset, A. B., 1961, *A Treatise on Hydrodynamics*, Deighton, Bell and Co., Cambridge, 1888; republished by Dover Publications, New York, p. 135.
[10] Saffman, P. G., 1968, "The Lift on a Small Sphere in a Slow Shear Flow," J. Fluid Mech., **22**(3); Correction appeared in J. Fluid Mech., **31**(3), p. 624.
[11] Brenner, H., 1961, "The Slow Motion of a Sphere Through a Viscous Fluid Towards a Plane Surface," Chem. Eng. Sci., **16**, pp. 242–251.
[12] Maude, A. D., 1961, "End Effects in a Falling-sphere Viscometer," Br. J. Appl. Phys., **12**, pp. 293–295.
[13] Hinze, J. O., 1975, *Turbulence*, 2nd ed., McGraw-Hill, New York, pp. 626–628.
[14] Hau, D., 1988, "Measurement of the Mean Force on the Particle Near a Boundary in Turbulent Flow," J. Fluid Mech., **187**, pp. 457–466.
[15] Kallio, G. A., and Reeks, M. W., 1989, "A Numerical Simulation Particle Deposition in Turbulent Boundary Layers," Int. J. Multiphase Flow, **15**, pp. 433–446.
[16] Roahiainen, P. O., and Stachiewicz, J. W., 1970, "On the Deposition of Small Particles From Turbulent Streams," J. Heat Transfer, **92**, pp. 169–177.

Miniature Single-Disk Viscous Pump (Single-DVP), Performance Characterization

Danny Blanchard

Phil Ligrani[1]
e-mail: ligrani@mech.utah.edu

Bruce Gale

Department of Mechanical Engineering,
University of Utah,
50 South Central Campus Drive, Rm. 2110,
Salt Lake City, UT 84112

The development and testing of a rotating single-disk viscous pump are described. This pump consists of a 10.16 mm *diameter spinning disk, and a pump chamber, which are separated by a small gap that forms the fluid passage. The walls of the pump chamber form a C-shaped channel with an inner radius of* 1.19 mm*, an outer radius of* 2.38 mm*, and a depth of 40, 73, 117, or* 246 μm*. Fluid inlet and outlet ports are located at the ends of the C-shaped channel. Experimental flow rate and pressure rise data are obtained for rotational speeds from* 100 to 5000 rpm*, fluid chamber heights from* 40 to 246 μm*, flow rates from* 0 to 4.75 ml/min*, pressure rises from* 0 to 31.1 kPa*, and fluid viscosities from* 1 to 62 mPa s*. An analytical expression for the net flow rate and pressure rise, as dependent on the fluid chamber geometry, disk rotational speed, and fluid viscosity, is derived and found to agree with the experimental data. The flow rate and pressure rise of the pump vary nearly linearly with rotational speed. The volumetric flow rate does not change significantly with changes in fluid viscosity for the same rotational speed and pumping circuit. Advantages of the disk pumps include simplicity, ease of manufacture, ability to produce continuous flow with a flow rate that does not vary significantly in time, and ability to pump biological samples without significant alteration or destruction of cells, protein suspension, or other delicate matter.* [DOI: 10.1115/1.2175167]

Introduction

There is a need to circulate or move fluid through macroscale and/or microscale channels in many applications, including microsensors, separation devices, drug delivery systems, electronics cooling, and other small-scale and microscale fluidic devices. Many different micropumps are proposed to meet this need, generally to fulfill specific applications [1]. These include membrane pumps [2–8] (both without check valves [2–5] and with check valves [6–8]), electrohydrodynamic pumps [9–11], electrokinetic pumps [12,13], viscous pumps [14,15], rotary pumps [16,17], peristaltic pumps [4,18–20], ultrasonic pumps [21,22], and several other types of pumps [23–26]. Many of these micropumps are fabricated using microfabrication technology. Nonmechanical pumps like the electrohydrodynamic and electrokinetic pumps do not have moving parts, which increases reliability. However, such devices are generally limited by low flow rate and pressure rise capabilities, the applications of the pump, the working fluids that can be pumped, and high supply voltage requirements [1]. Mechanical pumps like rotary pumps, peristaltic pumps, and membrane pumps have a wide variety of possible working fluids and applications. However, such mechanical micropumps are believed to be feasible only when they are greater than a certain size [1], due to the large viscous forces in the fluid at small pump geometries. At very small scales, the viscous forces are significant, and result in large pressure drops over small lengths for fluid flow through a channel [27]. One motivation of the present effort is to employ these large viscous forces to produce a millimeter-scale pump with an easily adjusted, constant flow rate.

Many variations of macroscale viscous pumps have been proposed [28–34]. Most of these pumps have a linear relationship between flow rate and pressure rise for a range of operating parameters and pump geometries. Viscous pumps are ideal for applications where high pressure rises, and low to moderate flow rates are required [34]. Uses of different viscous pumps at microscales are described by Sen et al. [15], and Kilani et al. [14]. Sen et al. [15] presents a pump that employs a shaft whose axis is perpendicular to the flow direction, and is positioned eccentrically in a channel. The difference in viscous shear between the shaft and the two channel walls produces a net pumping effect. Numerical simulations are performed by Sharatchandra et al. [35] to determine the optimal configuration. This pump is easy to fabricate, but has limited flow rates and pressure rise capabilities. Kilani et al. [14] describes a spiral pump that uses one spinning disk rotating over a single spiral channel to produce a pumping effect. Results from a macroscale version of this pump are consistent with an analytical expression for flow rate and pressure rise [14]. A small-scale version of this pump may be complex to fabricate.

A new viscous micropump is presented, called the single-disk viscous pump (single-DVP), to achieve easily controlled flow rates and pressure rises while maintaining simplicity and ease of manufacturing. An analytical equation is presented, based on the Navier-Stokes equations, which relates pressure rise and flow rate to the pump geometry, rotational speed and working fluid properties. The predicted performance of the pump from the analytical equation is compared to experimental data. The disk pump is unique because it uses viscous stress to produce a pumping effect by employing one disk and a C-shaped channel [36]. Figure 1 shows external and internal views of the single-DVP. The spinning of the disk causes a net movement of fluid due to the viscous stresses imposed on the fluid from the spinning disk. As the fluid passage height becomes smaller, the Reynolds number decreases, and the viscous forces become more significant than inertial forces. Thus, one assumption employed in the flow analysis is that the inertial or advection terms in the Navier-Stokes equations are insignificant compared to the diffusion of momentum terms. Following this analysis, the development, fabrication, and testing of the disk pump is discussed. The flow rate and pressure rise for various rotational speeds are measured experimentally and compared to analytical expressions for the flow rate and pressure rise. Based on such results, advantages of this micropump compared to other micropumps are identified and discussed, and include a wide range of possible flow rates, simplicity, planar structure, well con-

[1]Corresponding author.

Contributed by the Fluids Engineering Division of ASME for publication in the JOURNAL OF FLUIDS ENGINEERING. Manuscript received April 21, 2005; final manuscript received September 29, 2005. Review conducted by Joseph Katz.

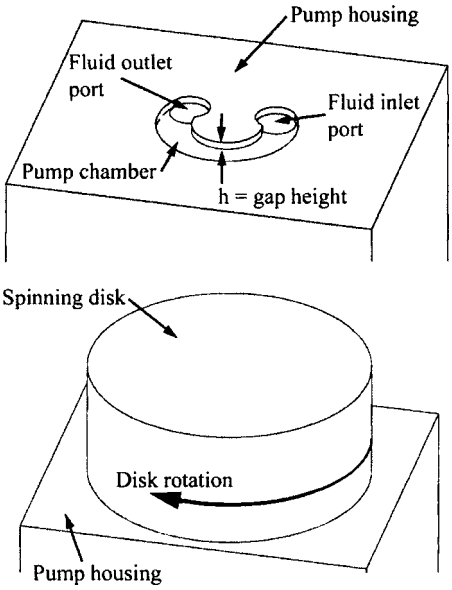

Fig. 1 External and internal views of the single-disk viscous pump

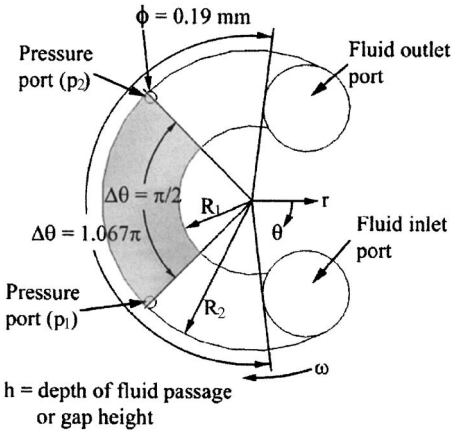

Fig. 2 Configuration of the single-disk viscous pump. The shaded region of the pump chamber is used for the flow analysis.

trolled flow rate, ease of manufacture, and ability to produce continuous flow with a flow rate that does not vary significantly in time. The device also has the ability to pump biological samples without significant alteration or destruction of cells, protein suspension, or other delicate matter. This is because shear levels produced by the present device for the present range of experimental conditions are always less than 10^5 1/s, which is the shear value when red blood cells (erythrocytes) as well as types of other biological samples begin to be damaged. With this in mind, microscale applications that may be suitable for a viscous pump include pumping of biomedical fluids, drug delivery devices, μ-TAS, fluidic sensors, and mixing devices.

Single-Disk Viscous Pump Configuration and Operation

The single-disk viscous pump (single-DVP) is comprised of a spinning disk, and a C-shaped channel that forms the pump chamber with a fluid inlet port and a fluid outlet ports located at opposite ends. Figure 1 shows an external view and an internal cross-sectional view of the single-DVP. The disk contacts the fluid chamber walls to create a seal to minimize leakage from the pump chamber. The height of the pump chamber is the distance between the disk surface and the top of the pumping chamber, and is referred to as the flow passage height of the pump. The flow passage heights used for testing in this work are 40, 73, 117, and 246 μm. As the disk spins, a rotating Couette-type flow is induced in the fluid chamber between the disk and the stationary top surface of the fluid chamber.

A circumferential pressure gradient is present in the fluid chamber mostly because of interactions between the fluid and the walls at the ends of the C-shaped channel. This interaction gives a static pressure rise with circumferential position through the pump chamber volume, such that a region of lower static pressure is present near the fluid inlet port, and a region of higher static pressure is present near the fluid outlet port. This static pressure variation then opposes the motion induced by the disk rotation and viscous forces. If the opposing circumferential static pressure variation is large enough, some of the fluid between the spinning disk and top surface of the fluid chamber will recirculate in the opposite direction of the disk rotation. For the case when the fluid outlet port is closed (or a valve on the outlet tubing is closed), there is fluid movement in the pump chamber, but the net flow rate of the fluid velocity over a cross section of the disk pump flow passage is zero. The resulting pressure rise is referred to as the maximum pressure rise.

Flow Analysis for the Single-Disk Viscous Pump

Derivation of an expression for pressure rise and flow rate in terms of pump geometry, disk rotational speed, and fluid properties is required to properly design, develop, and analyze a functional viscous disk pump. The analysis that follows leads to an expression for pressure rise and flow rate as dependent upon pump geometry, disk rotational speed, and fluid properties. Figure 2 shows a cross-sectional view of the single-DVP flow passage. The shaded region in this figure is used for the flow analysis.

In this flow analysis, an incompressible, steady flow of a Newtonian fluid, with constant density and viscosity is considered. Assuming that $h \ll (R_2 - R_1)$, edge effects near the inner radius and outer radius can be ignored. Also assume that gravity is negligible, and the rotational speed of the disks is slow enough such that the body force due to centrifugal acceleration is negligible compared to the forces produced by gradients of viscous stresses, and gradients of pressure. This assumption is valid for low Reynolds number flows. The gradients of viscous stresses are assumed to be more significant than the inertial or advection terms in the Navier-Stokes equation because the fluid motion is produced by viscous forces, and because the flow passage height is small. The Navier-Stokes equation with neglected inertial or advection terms, in cylindrical coordinates, is given by [37]

$$\frac{1}{r}\frac{\partial p}{\partial \theta} = \mu\left[\frac{\partial}{\partial r}\left(\frac{1}{r}\frac{\partial}{\partial r}(r v_\theta)\right) + \frac{1}{r^2}\frac{\partial^2 v_\theta}{\partial \theta^2} + \frac{\partial^2 v_\theta}{\partial z^2} + \frac{2}{r^2}\frac{\partial v_r}{\partial \theta}\right] \quad (1)$$

Equation (1) shows that the circumferential pressure gradient (left side) is equal to the diffusion of circumferential momentum terms (right side). Thus, the pressure gradient changes as the viscous stress imposed on the fluid by the spinning disk change. Increasing the viscous stresses then also increases the pressure gradient, for example, increasing the fluid viscosity or by increasing the disk rotational speed.

For this analysis, flow in the pumping region indicates by the shaded area in Fig. 2 is considered. For a cylindrical coordinate system, the velocity $v_\theta \gg v_z$, so that the z component of velocity at all locations can be approximated as $v_z = 0$. In addition, if it is assumed that $h \ll 3R_1\pi/2$ (circumference of the inner radius of the pump chamber), the flow in this region can be approximated as fully developed in the θ direction. Assuming incompressible, steady, fully developed flow, and the continuity equation becomes

$$\frac{1}{r}\frac{\partial}{\partial r}(rv_r) = 0 \tag{2}$$

From this equation, the value of rv_r is equal to a constant. At $r = R_1$ (inner radius wall), $v_r = 0$, which implies that $v_r = 0$ in the entire region being considered. The pressure gradients for the z and r directions are then given by

$$\frac{\partial p}{\partial z} = 0 \tag{3}$$

and

$$\frac{\partial p}{\partial r} = 0 \tag{4}$$

respectively. Equations (3) and (4) show that the pressure gradient is invariant in the z and r directions.

When the gap is thin, that is $h/(R_2 - R_1) \ll 1$, changes of v_θ across the z direction over the distance h are much larger than the changes of v_θ in the r direction over the distance $R_2 - R_1$. Therefore the first term on the right side of Eq. (1) is ignored. The second term on the right side of Eq. (1) is ignored because of the fully developed flow assumption made previously. The fourth term on the right side of Eq. (1) is ignored because $v_r = 0$. The resulting equation is then simplified as follows

$$\frac{1}{r}\frac{\partial p}{\partial \theta} = \mu\frac{\partial^2 v_\theta}{\partial z^2} \tag{5}$$

The circumferential velocity (v_θ) does not change with circumferential position, with the fully developed flow and incompressible fluid assumptions mentioned previously. Thus, because mass must be conserved, the pressure gradient on the left-hand side of Eq. (5) must be constant in the θ direction, which results in a linear pressure rise in the θ direction. The pressure gradient in the θ direction is then approximated using

$$\frac{\partial p}{\partial \theta} \approx \frac{\Delta P}{\Delta \theta} \tag{6}$$

where ΔP is the pressure rise over the angle $\Delta\theta$. The pressure rise between the two pressure ports ($p_2 - p_1$) shown in Fig. 2 is denoted as ΔP_{2-1}, and the pressure rise between the fluid inlet and outlet ports shown in Fig. 2 is denoted as ΔP_{out-in}. In addition $\Delta\theta$ is the angle between the pressure ports ($\Delta\theta = \pi/2$) or between the inlet and outlet ports ($\Delta\theta = 1.067\pi$), as shown in Fig. 2.

The velocity profile $v_\theta(r,z)$ is determined by solving the ordinary differential equation given by Eq. (5), with the following boundary conditions for the single-DVP

$$v_\theta(r,h) = 0 \tag{7}$$

$$v_\theta(r,0) = r\omega \tag{8}$$

The resulting velocity profile is given by

$$v_\theta(r,z) = \frac{h^2}{2\mu}\frac{1}{r}\frac{\Delta P}{\Delta\theta}\left[\left(\frac{z}{h}\right)^2 - \frac{z}{h}\right] + \frac{r\omega}{h}z \tag{9}$$

The volumetric flow rate is determined by integrating the velocity profile over a radial cross section of the pump chamber, from $z = 0$ to $z = h$, and from $r = R_2$ to $r = R_1$ as given by

$$Q = \int_0^h \int_{R_1}^{R_2} v_\theta(r,z)\,dr\,dz = \frac{h^3 \ln(R_1/R_2)}{12\mu}\frac{\Delta P}{\Delta\theta} + \frac{\omega h(R_2^2 - R_1^2)}{4} \tag{10}$$

Equation (10) describes the flow of the single-DVP as dependent upon pressure rise (ΔP), pump geometry (R_1, R_2, $\Delta\theta$, and h), disk angular velocity (ω), and fluid viscosity (μ).

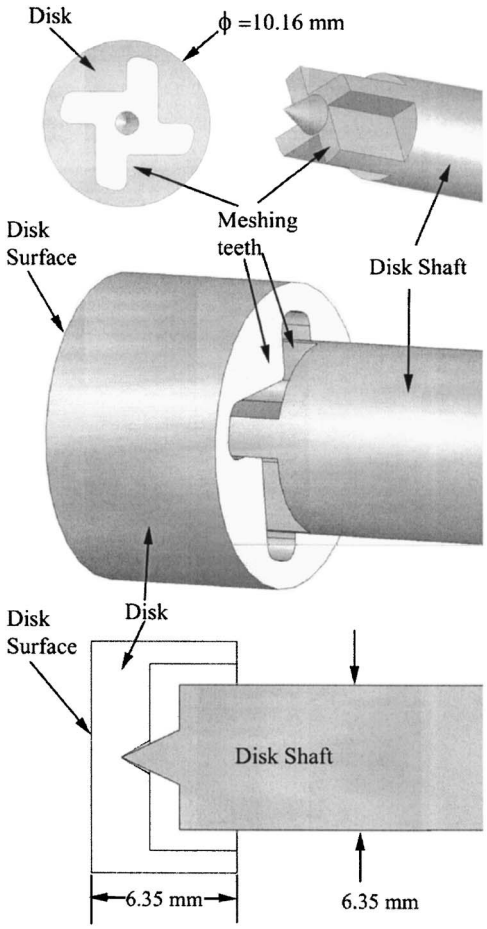

Fig. 3 Cross-sectional view and assembled view of the disk and disk shaft

Pump Component Fabrication

There are three main fabricated components of the rotary shaft pump assembly: (i) the disk, (ii) the disk shaft, and (iii) pump chamber contained within the pump housing.

The disk surface must be flat so that it is aligned with the top surface of the pump chamber, because any misalignment of the disk will result in leakage and flow passage height variation across the pump chamber. The disk surface is aligned when the disk surface is flush against the bottom of the pump housing. The disk is therefore designed to be self-aligning to ensure that the disk surface is flush against the bottom surface of the pump housing, and thus, parallel to the top of the fluid chamber (since the fluid chamber is uniform in depth). Figure 3 shows the back of the disk, the disk shaft and a cross-sectional view and assembled view of the disk and disk shaft together, all of which are designed to meet these requirements. The disk is constructed with a 60 deg cone indentation and is driven by meshing teeth on the disk shaft. The point on the cone of the disk shaft transmits a single-point axial force that holds the disk in position, while also providing a pivot point so that the disk surface can align to the bottom surface of the pump housing. Figure 3 also shows arrangements of the meshing teeth of the disk and disk shaft. The meshing teeth transmit the torque required to rotate the disk, while still allowing some movement required to keep the disk flat and aligned relative to the bottom surface of the pump housing.

Precision machining techniques are used to fabricate the disk and disk shaft. A lathe is used to obtain the desired outside diameter of the disk, and to create the disk surface. The disk is made from PEEK plastic (Ensinger Engineering Plastics, Washington

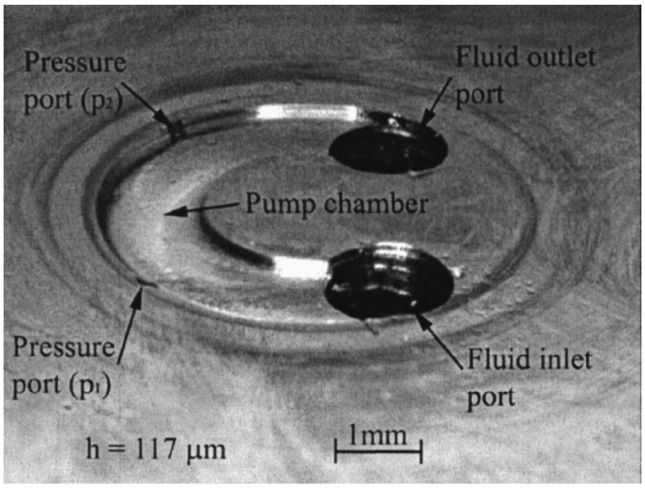

Fig. 4 Image of the single-disk viscous pump housing containing the pump chamber. The pump chamber depth or flow passage height is 117 μm, with a pump chamber outer radius of 2.38 mm.

PA) with a final outer diameter of 10.16 mm. The cone on the disk is made using a 60 deg scribe tool. The disk surface is polished to produce a smooth flat surface. The meshing teeth of the disk and disk shaft are machined with a CNC milling machine. The cone shape on the disk shaft is made using a lathe. The disk shaft is made using type 17-4 stainless steel.

The C-shaped channel that defines the pump chamber is machined into the pump housing. The inner and outer radii of the C-shaped channel are 1.19 and 2.38 mm, respectively. The pump housing is made using type 17-4 stainless steel block that is 19 mm thick. The fluid chamber is cut into the bottom face of the pump housing using a CNC milling machine. The face of the steel block is polished to produce a smooth flat surface. The final flow passage height of the fluid channel is measured with a Tencor P-10 profilometer, with a 327 μm vertical range and a resolution of 0.195 Å. The flow passage height variation across the fluid chamber, including roughness and flatness, is then less than 1.5 μm. Holes for the pressure ports are drilled with a 0.19 mm diameter drill bit. Holes for the fluid inlet and outlet ports are 1.397 mm in diameter. A photograph of the machined fluid chamber with fluid inlet and outlet ports, and pressure ports is shown in Fig. 4. Four holes are drilled from the top of the pump housing, and connect to the pressure ports and fluid inlet and outlet ports. Tubing is press fit into these four holes on the top of the pump housing to interface the fluid chamber with fluid reservoirs, and a differential pressure transducer.

Experimental Apparatus and Procedures

The disk pumps are powered by an externally mounted Maxon EC32 number 118891, brushless DC motor that is 32 mm in diameter, with an 80 W power rating. The maximum speed is 25,000 rpm, with a stall torque of 0.35 N m. The brushless motor is controlled by an Advanced Motion Controls power amplifier (Model #BE12A6). The power amplifier has a DC supply voltage of 40 V, a peak current of 12 A, and continuous current rating of 6 A. A negative feedback controller is employed to maintain constant speed for any variation in torque. The speed is controlled by adjusting a 15-turn potentiometer. The rotational speed range used for testing is 100–5,000 rpm. The motor controller determines the rotational speed from the signal from an optical encoder attached to the motor shaft. This apparatus produces a voltage signal that is proportional to speed. The voltage is measured using a National Instruments PCI-6013 data acquisition card and LABVIEW 7.0 software.

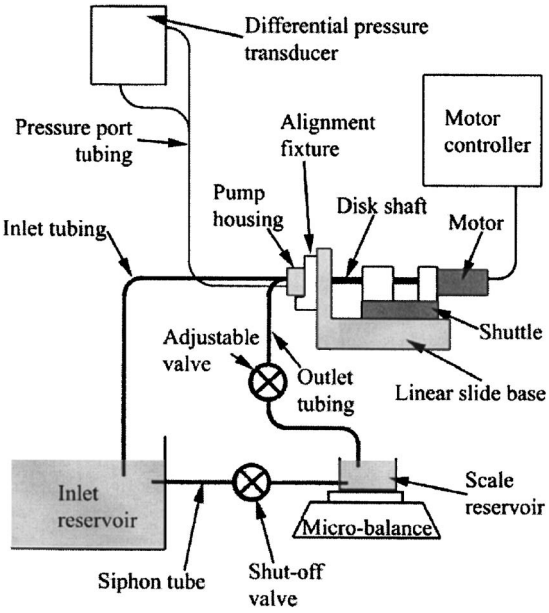

Fig. 5 Test setup for the single-disk viscous pump

The test setup is shown in Fig. 5 and includes an inlet reservoir and scale reservoir, which are large enough that the water level change during operation is negligible. The inlet reservoir is connected to the fluid inlet port by means of inlet tubing, with an inner diameter of 4.5 mm and a length of 508 mm. The inlet tubing steps down to an outer diameter of 1.59 mm, with an inner diameter of 1.397 mm, that is press-fit into the top of the pump housing. The fluid outlet port is connected to the outlet tubing, which starts with inner and outer diameters of 1.397 and 1.59 mm, respectively, that is press-fit into the top of the pump housing, and then steps up to an inner diameter of 4.5 mm. An adjustable valve is incorporated into the outlet tubing for adjustment of the flow rate through the fluid chamber. The outlet tubing drains to the scale reservoir on a Mettler AE-163 microbalance with accuracy to 0.1 mg. A siphon tube connects the water reservoir on the balance to the inlet water reservoir. A shutoff valve is incorporated into the siphon tube to allow or stop fluid flow through the siphon tube.

A DP-15 Validyne differential pressure transducer is used to measure the differential pressure between the pressure ports. Two different diaphragms are used to accommodate different ranges of pressure differentials, with maximum gauge pressures of 872 Pa and 13.8 kPa. The output signal from the pressure sensor is processed using a Celesco Model number CD10D Carrier Demodulator, which produces a voltage output that is proportional to pressure. The voltage is read by the data acquisition board and LABVIEW 7.0, mentioned previously.

The pump assembly is mounted to the base of a linear slide. The brushless motor and disk shaft are mounted to the shuttle of the linear slide as shown in Fig. 5. The disk shaft is supported with two bearings, and the distal end of the disk shaft connects to the motor shaft. Elastic bands are employed to exert a constant force on the shuttle in the direction of the pump chamber to keep the disk surface flush against the bottom of the pump housing. An alignment fixture is used to mount the pump housing and pump chamber, such that the axis of the disk aligns with the center point of the pump chamber radius. The working fluids employed are water, and 5W-30 motor oil, with properties given in Table 1. Note that 5W-30 motor oil is slightly non-Newtonian for shear rates greater than about 2500 s^{-1}. Just after assembling the disk, disk shaft, and pump chamber, and just prior to testing, the fluid inlet and outlet tubing and pressure port tubing are press-fit into

Table 1 Fluid properties of water, and oil used for experimental testing

Working fluid	ρ (kg/m^3)	μ (at 30°C) (Pas)
Water	1000	0.0010
5W-30 motor oil	857	0.0630

the top of the pump housing. The air is then bled from the pump chamber assembly using syringes filled with working fluid that are attached to the end of the inlet tubing and pressure transducer. The syringes are removed after the air is bled from the system.

After these steps are completed, testing is comprised of the following procedures. (1) The system is flushed to ensure there are no air bubbles or trapped particulates in the pump chamber. (2) The shut-off valve on the siphon tube is opened until the surface level of the inlet fluid reservoir and scale reservoir are equal. (3) The shut-off valve on the siphon tube is closed. (4) The adjustable valve on the outlet tubing is adjusted to achieve the desired flow rate. (5) The motor is activated, and adjusted to produce the desired speed. (6) The motor then continues to operate at constant speed until steady state is reached. Steady state is reached when the average pressure rise measurement is constant. (7) For testing with a net volumetric flow rate, the time is started and the scale display is recorded every minute for 3 min. Output signals related to shaft rotational speed, and pressure rise ΔP_{2-1} are recorded every minute for 3 min using the NI data acquisition card and LABVIEW 7.0 discussed previously. The flow rate is determined by dividing the amount of water collected (mass change multiplied by the fluid density) by the collection time. All data are recorded, entered, and processed using a computer.

Uncertainty Analysis

A first-order uncertainty analysis is performed using a constant-odds combination method, based on a 95% confidence level as described by Moffat [38]. The variation of flow passage height across the fluid chamber contributes most to the uncertainties associated with measurement of pressure rise and flow rate, due to the h^3 term in Eq. (10). The flow passage height variation across the fluid chamber is less than 1.5 μm, with a measured variation less than 1.1 μm ($\pm$0.55 μm) for h=40 μm, which is 2.75% of h. The value 2.75% is the maximum percent variation of flow passage height for all flow passage heights tested. The resulting uncertainty magnitudes associated with experimentally measured pressure rise, flow passage height, fluid viscosity, disk rotational speed, pump chamber radii, and flow rate are presented in Table 2.

Results and Discussion

The experimental results are presented in five sections. The first section discusses pressure rise and flow rate variations for the single-disk viscous pump (single-DVP) with a flow passage height of 117 μm. The second section presents data showing the effects of changes in rotational speed on the pressure rise and flow rate of the single-DVP. The third section gives data showing the effects of changes in flow passage height on the flow rate and pressure rise characteristics. The fourth section presents data which illustrate the effects of changes in fluid viscosity on the flow rate and pressure rise. The fifth section discusses performance of the single-DVP relative to a variety of other types of microscale pumps.

Table 2 Uncertainties associated with experimental data

Variable	Maximum percent uncertainty
ΔP_{2-1} (experimental)	5%
Q	2.5%
h	2.75%
μ	2%
ω	1.5%
R_1, R_2	1.1%

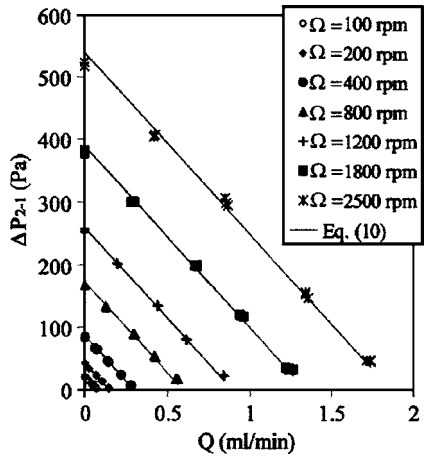

Fig. 6 Variations of pressure rise with flow rate for the single-disk viscous pump with a flow passage height of h=117 μm. Working fluid is water.

Pressure Rise and Flow Rate Variations. The dependence of pressure rise on flow rate for a flow passage height of 117 μm is illustrated by the data given in Fig. 6. These experimental data are obtained using water as the working fluid, with rotational speeds (Ω) between 100 and 2500 rpm. For a constant rotational speed, the flow rate is varied by changing the adjustable valve shown in Fig. 5. The solid lines in Fig. 6 represent theoretical values determined using Eq. (10). The data in Fig. 6 show that there is a linear relationship between the pressure rise and flow rate for the single-DVP for each different impeller rotational speed, which is consistent with results from a variety of macroscale viscous pumps [28–34]. This figure also shows that experimental data are in agreement with Eq. (10). The slopes of the data for each rotational speed in Fig. 6 are approximately the same, which means that ΔP_{2-1} versus Q slope is independent of rotational speed. The slopes of these data are characterized by the maximum pressure rise for Q=0, and the maximum flow rate at ΔP_{2-1}=0. Similar trends of pressure rise and flow rate are observed for flow passage heights of 40, 73, and 246 μm. The data given in Fig. 6 also show that the single-DVP with a flow passage height of 117 μm is useful for applications that require pressure rises from 22 to 525 Pa and flow rates up to 1.75 ml/min.

Effects of Rotational Speed. The flow rate and pressure rise are varied to meet application requirements by changing the rotational speed. The data presented previously in Fig. 6 show that the slopes of the pressure rise and flow rate characteristics of the single-DVP are characterized by the maximum pressure rise and maximum flow rate. Therefore, the maximum pressure rise variations with rotational speed for Q=0, and the maximum flow rate variations with rotational speed for ΔP_{2-1}=0 are presented.

When the flow rate is set to zero, Eq. (10) shows that the pump pressure rise varies linearly with rotational speed. Figure 7 shows such data for flow passage heights of 40, 73, 117, and 246 μm. The working fluid is water, and the rotational speed ranges between 100 and 3200 rpm for each constant flow passage height. Included is a theoretical line for each flow passage height determined from Eq. (10). The pressure rise increases linearly with rotational speed for each flow passage height in Fig. 7 and represents the maximum pressure rise between the pressure ports in the

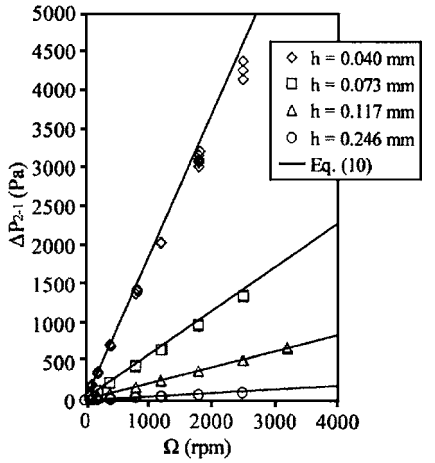

Fig. 7 Variations of pressure rise with rotational speed for the single-disk viscous pump. Working fluid is water, and $Q=0$.

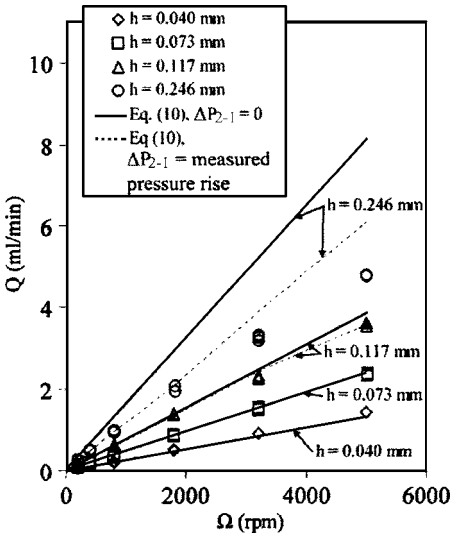

Fig. 9 Variations of maximum flow rate with rotational speed for the single-disk viscous pump. Working fluid is water.

single-DVP. Note that this maximum pressure is not the maximum pressure between the inlet and outlet ports, because the pressure continues to increase as it approaches the fluid outlet port.

Magnitudes of the viscous pump maximum pressure rise between the inlet and outlet ports (ΔP_{out-in}) are given in Fig. 8 for zero net flow rate and a flow passage height of 73 μm. Also included is the pressure rise between the pressure ports (ΔP_{2-1}). The experimental pressure rise data between the inlet and outlet ports are obtained by connecting the inlet and outlet tubing to the ports of a differential pressure transducer, which results in a zero net flow rate in the pump. This zero net flow condition is used because this arrangement gives the maximum pressure rise. The theoretical line for the pressure rise ΔP_{out-in} is obtained using $\Delta\theta=1.067\pi$ in Eq. (10) instead of $\Delta\theta=\pi/2$, where $\Delta\theta=1.067\pi$ corresponds to the angular span of the shear channel between the edges of the fluid inlet and outlet ports. Figure 8 shows that Eq. (10) gives a good representation of both ΔP_{out-in} and ΔP_{2-1}. Thus, the pressure rise between the inlet and outlet ports is approximately 2.13 times greater than the measured pressure rise between the pressure ports for this pump chamber geometry, for any given flow rate, rotational speed, or flow passage height.

Variations of maximum flow rate with rotational speed are shown in Fig. 9 for flow passage heights of 40, 73, 117, and 246 μm. These data are obtained with a fully open adjustable valve in Fig. 5. The solid lines in Fig. 9 represent theoretical values determined by setting the pressure rise $\Delta P=0$ in Eq. (10). For flow passage heights of 117 and 246 μm, experimental flow rates deviate more significantly from theoretical flow rates as the rotational speed increases. This more significant deviation is due to additional experimental fluid losses through the inlet and outlet tubing. Such loses are present for all flow passage heights tested, but the effects are negligible for flow passage heights less than about 100 μm. Better agreement between theory and experimental data in Fig. 9 is obtained when losses in the inlet and outlet tubing, represented by the experimentally measured pressure rise (ΔP_{2-1}), are included in the analysis, and is shown by the dashed lines in Fig. 9. Note that the Reynolds number for the single-DVP with a flow passage height of 246 μm is 229.3 for a rotational speed of 5000 rpm, where Reynolds number is defined as

$$\mathrm{Re}=\frac{\rho\omega(R_2+R_1)h}{2\mu} \tag{11}$$

One assumption made in deriving Eq. (10), is that the Reynolds number is small. The data in Fig. 9 suggest that Eq. (10) is valid for $\mathrm{Re}<110$ for a flow passage height of 246 μm, which corresponds to a rotational speed of 2400 rpm. This range of Reynolds number validity is a result of neglecting advection terms in Navier-Stokes Eq. (1). However, note that some of these advection terms are considered to be negligible because the flow in the passage is maintained at or near to a fully developed condition.

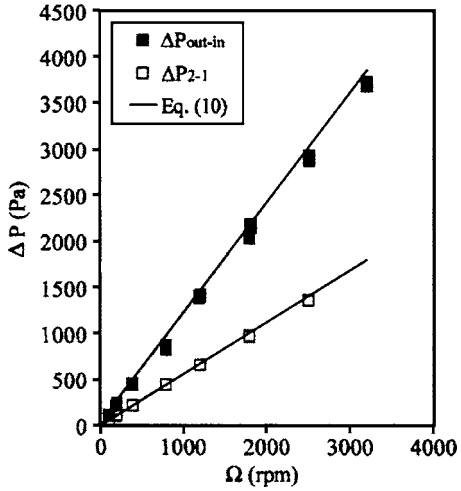

Fig. 8 Variations of pressure rise with rotational speed for the single-disk viscous pump with a flow passage height of $h=73$ μm. Working fluid is water, and $Q=0$.

Effect of Flow Passage Height. To meet application requirements, the flow rate and pressure rise are varied by changing the flow passage height. The data presented previously in Fig. 6 show that the slopes of the pressure rise and flow rate characteristics of the single-DVP are characterized by the maximum pressure rise and maximum flow rate. Therefore, the maximum pressure rise variations with rotational speed for $Q=0$, and the maximum flow rate variations with rotational speed for $\Delta P_{2-1}=0$ are presented.

Variations of pressure rise with flow passage height, for different disk rotational speeds, are shown in Fig. 10. These experimental data are obtained with a net zero flow rate in order to show the maximum pressure rise for each flow arrangement. The solid lines represent the pressure rise determined from Eq. (10), for the different flow passage heights and rotational speeds, and are in good agreement with experimental data. Note the increase in pressure rise as the flow passage height decreases for a particular disk

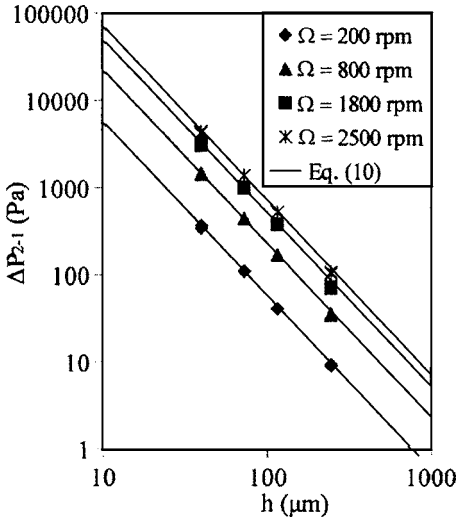

Fig. 10 Variations of maximum pressure rise with flow passage height for the single-disk viscous pump. Working fluid is water, and $Q=0$.

rotational speed. For $Q=0$, this pressure rise scales with flow passage height according to the relation given by

$$\Delta P_{2-1}(Q=0) \propto \frac{1}{h^2} \tag{12}$$

which is consistent with Eq. (10).

Variations of maximum flow rate with flow passage height are shown in Fig. 11 for rotational speeds (Ω) between 200 to 5000 rpm. Note that the flow rate decreases as flow passage height decreases for each rotational speed. The solid lines represent flow rate determined using Eq. (10) with the pressure rise set to zero. The dashed lines represent the flow rates determined using Eq. (10) including experimentally measured pressure rise contributions. The experimentally measured pressure rise is due to fluid losses through the inlet and outlet tubing. Note that the pressure rises due to these fluid losses are insignificant for flow passage heights less than or equal to about 100 μm. For the zero pressure rise condition shown in Fig. 11, flow rates scale with flow passage height according to the equation that has the form

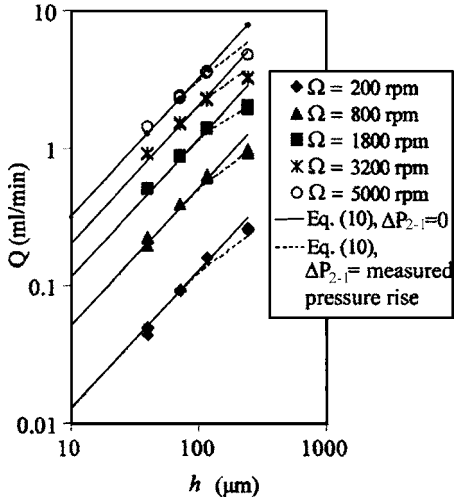

Fig. 11 Variations of maximum flow rate with flow passage height for the single-disk viscous pump. Working fluid is water.

Table 3 Shear rates for different pump chamber heights, and disk rotational speeds

h (μm)	Ω (rpm)	$\gamma_{max}(Q=0)$ (s^{-1})	$\gamma_{average}(Q=0)$ (s^{-1})	$\gamma_{max}(\Delta P=0)$ (s^{-1})	$\gamma_{average}(\Delta P=0)$ (s^{-1})
40	500	8.5×10^3	4.0×10^3	3.1×10^3	2.3×10^2
73	500	4.7×10^3	2.2×10^3	1.7×10^3	1.3×10^2
117	500	2.9×10^3	1.4×10^3	1.1×10^3	8.0×10^2
246	500	1.4×10^3	6.4×10^2	5.1×10^2	3.8×10^2
40	5000	8.5×10^4	4.0×10^4	3.1×10^4	2.3×10^4
73	5000	4.7×10^4	2.2×10^4	1.7×10^4	1.3×10^4
117	5000	2.9×10^4	1.4×10^4	1.1×10^4	8.0×10^3
246	5000	1.4×10^4	6.4×10^3	5.1×10^3	3.8×10^3

$$Q(\Delta P_{2-1}=0) \propto \frac{1}{h} \tag{13}$$

which is consistent with flow rate scaling in Couette flow between parallel plates with one translating plate [37].

Table 3 gives the maximum and average shear rates in the pump chamber for different pump chamber heights and rotational speeds. The maximum shear rate occurs on the surface of the rotating disk. The maximum and average shear rates increase linearly with rotational speed. The maximum shear rate increases as the pressure rise increases. The lowest value is present for the flow condition when $\Delta P=0$, and the highest value is present for the flow condition when $Q=0$. All shear rate values in Table 3 are below 10^5 1/s, which is the lowest shear rate that causes hemolysis of red blood cells.

Effects of Fluid Viscosity. Figure 12 shows the experimentally measured variations of flow rates and rotational speed for the single-DVP with water and oil as the working fluids, and a flow passage height of 117 μm. The solid line represents flow rates obtained using Eq. (10). The fluid properties for water and oil are given in Table 1. Note that the variation of dimensional volumetric flow rate with rotational speed is linear and independent of fluid viscosity. Figure 13 shows corresponding pressure rise data. Here, pressure rises increase linearly with rotational speed, such that values with oil as the working fluid are about two orders of magnitude larger than the values obtained with water as the working fluid.

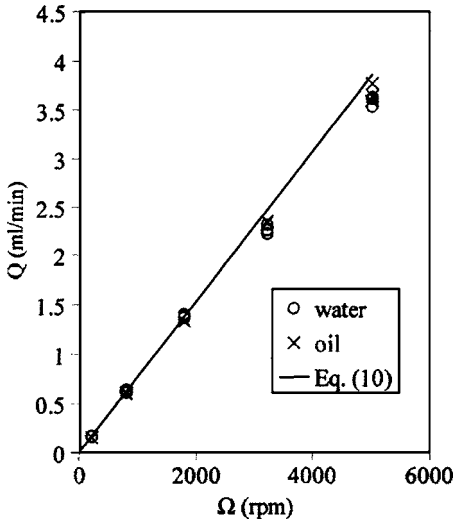

Fig. 12 Variations of maximum flow rate with rotational speed variation for the single-disk viscous pump with a flow passage height of 117 μm. Working fluid is water or 5W-30 oil.

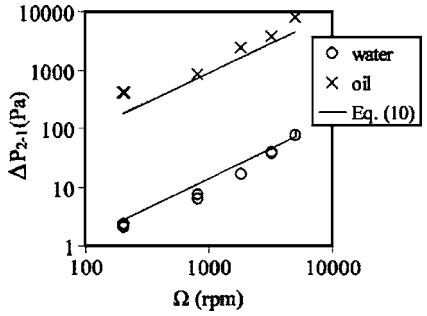

Fig. 13 Variations of pressure rise with rotational speed for the single-disk viscous pump data shown in Fig. 12. The flow passage height is 117 μm, and the working fluid is water or 5W-30 oil.

Performance of the Single-Disk Pump Relative to Other Microscale Pumps. The maximum flow rate of the single-DVP and several different micropumps are shown in Fig. 14. The typical size of the micropumps is defined as the membrane diameter, disk diameter, or channel width. The size of the actuator is not included when determining the typical size. The data points for the single-DVP are the maximum flow rate for a flow passage height of 40 and 246 μm, at a rotational speed of 2500 rpm, with water or oil as the working fluid. The viscous pump data point furthest to the right is the maximum flow rate presented by Sen [15], and the other viscous pump data point is the maximum experimental flow rate data presented by Kilani [14]. The single-DVP produces higher flow rates than many other reported micropumps of similar size.

Figure 15 shows the variations of pressure rise and flow rate of the single-DVP and several other micropumps with typical sizes less than 15 mm. The single-DVP produces higher pressure rises than many other reported micropumps for similar flow rates. The data in Fig. 15 also show that single-DVP is good for a wide range of flow rates, and pressure rises.

Summary and Conclusions

A pump called the single-disk viscous pump (single-DVP) is developed and tested. The single-DVP consists of a 10.16 mm diameter disk that rotates above a C-shaped channel with inner and outer radii of 1.19 and 2.38 mm, respectively, and a channel depth of 40, 73, 117, or 246 μm. Fluid inlet and outlet ports are located at the ends of the C-shaped channel. The advantages of this micropump compared to other micropumps and viscous pumps include analytic tractability, a wide range of possible flow rates, simplicity, constant flow, flow rate independent of fluid viscosity, planar structure, well controlled flow rate, and the ability to pump delicate fluids without disruption or damage. The design of the disk pumps is simple, and can potentially be fabricated using microfabrication technology due to the planar structure of the pump, or using injection molding techniques. The pump chamber is symmetric and the flow direction can be reversed by changing the disk rotational direction. The experimental flow rates and pressure rises are well represented by Eq. (10) for rotational speeds of 100–5000 rpm, fluid viscosities of 1–62 mPa s, flow passage heights of 40–246 μm, pressure rises of 0–31.1 kPa, and flow rates of 0–4.75 ml/min. The deviation between Eq. (10) and experimental data increases for Reynolds numbers greater than 110.

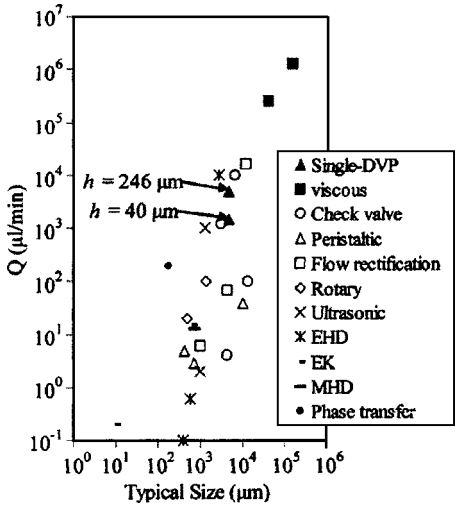

Fig. 14 Volumetric flow rate and typical size for various micropumps. Typical size is defined as the membrane diameter, disk diameter, or channel width. The data points for the single-DVP are for flow passage heights of h=40, and h=246, at a rotational speed 2500 rpm [2–26].

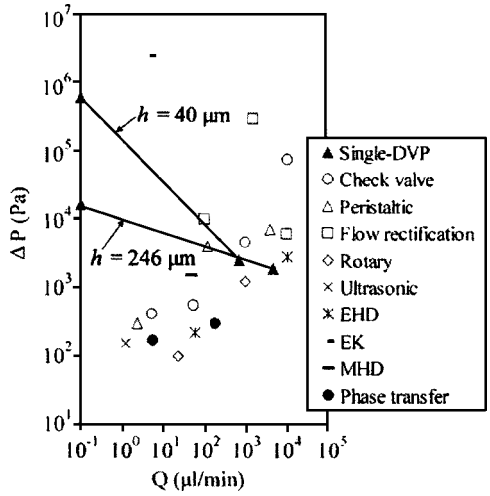

Fig. 15 Pressure rise and flow rate for various micropumps. For all points other than the single-DVP, the data corresponds to the maximum flow rate and maximum pressure. The data shown for the single-DVP are for 5W-30 motor oil at a rotational speed of 2500 rpm [2–9,11,13,16–19,22–25].

The experimental and theoretical pressure rises show a nearly linear relationship for variation in flow rate. The pressure rise variations with flow rate for the single-DVP are characterized by a straight line between the maximum pressure rise (at zero net flow) and maximum flow rate (at zero pressure rise). For Q=0, the pressure rise varies linearly with rotational speed. The pressure rise also increases as the flow passage height decreases for a particular rotational speed. For ΔP=0, the maximum volumetric flow rate is achieved, and is found to vary linearly with rotational speed. The volumetric flow rate of the single-DVP is independent of fluid viscosity for a given fluid circuit. The pressure rise through the pump chamber can be increased by increasing the rotational speed, increasing the fluid viscosity, increasing the circumferential span of the shear channel, or by decreasing the flow passage height. The flow rate through the pump chamber can be increased by increasing the flow passage height, increasing the rotational speed, or increasing the width of the pumping chamber.

The efficiency of the single-disk viscous pump can be determined using $\eta=\Delta PQ/T\omega$. A typical efficiency of the present device for a rotational speed of 1000 rpm, pump chamber height of 117 μm, and water as the working fluid is estimated to be approximately 0.25 or 25%. As such, this value does not account for any type of motor losses.

Acknowledgment

Work presented in this paper was supported by the National Science Foundation (NSF) through the IGERT Program, Grant Number DGE 9987616.

Nomenclature

h = flow passage height of the disk pump
p = static pressure
p_1 = static pressure at pressure port 1
p_2 = static pressure port 2
ΔP = static pressure rise
ΔP_{2-1} = static pressure rise between pressure ports $=(p_2-p_1)$
ΔP_{out-in} = static pressure rise between the fluid inlet and outlet ports
Q = volumetric flow rate
r = radial location
R_1 = inner radius of the pump chamber
R_2 = outer radius of the pump chamber
Re = Reynolds number
T = pump torque
v = fluid velocity
v_r = radial fluid velocity
v_z = fluid velocity in the z direction
v_θ = fluid velocity in the θ direction
z = direction normal to disk surface

Greek Symbols

μ = dynamic viscosity
ρ = fluid density
η = pump efficiency
$\gamma_{average}$ = average shear rate in pump chamber, $\gamma_{average}=[1/h(R_2-R_1)]\int_0^h\int_{R_1}^{R_2}\partial v_\theta/\partial z dr dz$
γ_{max} = maximum shear rate in pump chamber, generally located on the surface of the rotating disk
ω = rotational speed of the disk (rad/s)
Ω = rotational speed of the disk (rpm)
θ = angle
$\Delta\theta$ = angular span between two locations

References

[1] Nhuyen, N.-T., and Wereley, S. T., 2002, *Fundamentals and Applications of Microfluidics*, Artech House, Inc., Norwood, pp. 292–337.
[2] Olsson, A., Steeme, G., and Steeme, E., 1995, "A Valve-less Planar Fluid Pump With Two Pump Chambers," Sens. Actuators, A, **47**(2), pp. 549–556.
[3] Tsia, J. H., and Lin, L., 2002, "A Thermal Bubble Actuated Micro Nozzle-Diffuser Pump," J. Microelectromech. Syst., **11**(6), pp. 665–668.
[4] Nguyen, N. T., and Huang, X. Y., 2001, "Miniature Valveless Pumps Based on Printed Circuit Board Technique," Sens. Actuators, A, **88**(2), pp. 104–111.
[5] Benard, W. L., Kahn, H., Heuer, A. H., and Huff, M. S., 1998, "Thin Film Shape-Memory Alloy Actuated Micropumps," J. Microelectromech. Syst., **7**(2), pp. 245–251.
[6] Meng, E., Wang, X.-Q., Jak, H., and Tai, Y.-C., 2000, "A Check-Valved Silicone Diaphragm Pump," Proceedings of MEMS '00, 13th International Workshop Micro ElectroMechanical Systems, Japan, Jan 23–27, pp. 23–27.
[7] Gass, V., Van der Schoot, G. H., Jeanneret, S., and DeRooij, N. F., 1994, "Integrated Flow-Regulated Silicon Micropump," Sens. Actuators, A, **43**, pp. 335–338.
[8] Saggere, L., Hagood, N. W., Roberts, D. C., Li, H. Q., Steyn, J. L., Turner, K., Carretero, J. A., Yaglioglu, O., Su, Y. H., Mlcak, R., Spearing, S. M., Breuer, K. S., and Schmidt, M. A., 2000, "Design, Fabrication, and Testing of a Piezoelectrically Driven High Flow Rate Micro-pump," Proceedings of the 12th IEEE International Symposium on Applications of Ferroelectrics, Vol. 1, July–Aug, pp. 297–300.
[9] Richter, A., Plettner, A., Hofmann, K. A., and Sandmaier, H., 1991, "A Micromachined Electrohydrodynamic (EHD) Pump," Sens. Actuators, A, **29**, pp. 159–168.
[10] Fuhr, G., Hagedorn, R., Muller, T., Benecke, W., and Wagner, B., 1992, "Microfabricated Electrohydrodynamic (EHD) Pumps for Liquids of Higher Conductivity," J. Microelectromech. Syst., **1**(3), pp. 141–146.
[11] Ahn, S. H., and Kim, Y. K., 1998, "Fabrication and Experiment of a Planar Micro Ion Drag Pump," Sens. Actuators, A, **70**, pp. 1–5.
[12] Furuya, A., Shimokawa, F., Matsuura, T., and Sawada, R., 1996, "Fabrication of Fluorinated Polyimide Microgrids Using Magnetically Controlled Reactive Ion Etching (MC_RIE) and Their Applications to a Ion Drag Integrated Micropump," J. Micromech. Microeng., **6**, pp. 310–319.
[13] Zeng, S., Chen, C. H., Mikkelsen, J. C., and Santiago, J. G., 2000, "Fabrication and Characterization of Electrokinetic Micro Pumps," 7th Intersociety Conference on Thermal and Thermomechanical Phenomena in Electronic Systems, CPMT/IEEE, Las Vegas, Vol. 2, pp. 31–36.
[14] Kilani, M., Galambos, P., Haik, Y., and Chen, C. J., 2003, "Design and Analysis of a Surface Micromachined Spiral-Channel Viscous Pump," J. Fluids Eng., **125**(2), pp. 339–344.
[15] Sen, M., Wajerski, D., and Gad-El-Hak, M., 1996, "A Novel Pump for MEMS Applications," J. Fluids Eng., **118**(3), pp. 624–627.
[16] Ahn, C. H., and Allen, M. G., 1995, "Fluid Micropumps Based on Rotary Magnetic Actuators," Proceedings of MEMS 1995, Jan.–Feb., pp. 408–418.
[17] Dopper, J., Clemens, M., Ehrfeld, W., Jung, S., Kamper, K.-P., and Lehr, H., 1997, "Micro Gear Pumps for Dosing of Viscous Fluids," J. Micromech. Microeng., **7**(2), pp. 230–232.
[18] Mizoguchi, H., Ando, M., Mizuno, T., Takagi, T., and Nakajima, N., 1992, "Design and Fabrication of Light Driven Micropump," Proceedings of MEMS '92, 5th IEEE Int. Workshop MEMS, Germany, Jan. 25–28, pp. 31–36.
[19] Grosjean, C., and Tai, Y. C., 1999, "A Thermopneumatic Peristaltic Micropump," Proceedings of Transducer '99, the 10th Int. Conf. on Solid State Sensors and Actuators, Japan, June 7–10, pp. 1776–1779.
[20] Cabuz, C., Herb, W. R., Cabuz, E. I., and Lu, S. T., 2001, "The Dual Diaphragm Pump," Proceedings of MEMS '01, 14th IEEE Int. Workshop MEMS, Switzerland, Jan. 21–25, pp. 519–522.
[21] Luginbuhl, Ph., Collins, S. D., Racine, G. A., Gretillat, M. A., de Rooij, N. F., Brooks, K. G., and Setter, N., 1997, "Flexural-Plate-Wave Actuators Based on PZT Thin Films," Proceedings of MEMS '97, Jan, 1997, pp. 327–332.
[22] Miyazaki, S., Kawai, T., and Araragi, M., 1991, "A Piezoelectric Pump Driven by a Flexural Progressive Wave," Proceedings of MEMS'91, 4th International Workshop MEMS, Japan, Jan. 30–Feb. 4, pp. 283–288.
[23] Takagi, H., Maeda, R., Ozaki, K., Parameswaran, M., and Mehta, M., 1994, "Phase Transformation Type Micropump," Proceedings of International Symposium on Micro Machine and Human Sciences, Japan, Oct., pp. 199–202.
[24] Geng, X., Yuan, H., Oguz, H. N., and Prosperetti, A., 2001, "Bubble-Based Micropump for Electrically Conducting Liquids," J. Micromech. Microeng., **11**, pp. 270–276.
[25] Hatch, A., Kamholz, A. E., Holman, G., Yager, P., and Bohringer, K. F., 2001, "A Ferrofluidic Magnetic Micropump," J. Microelectromech. Syst., **10**(2), pp. 215–221.
[26] Huang, L., Wang, W., Murphy, M. C., Lian, K., and Ling, Z. G., 2000, "LIGA Fabrication and Test of a DDC Type Magnetohydrodynamic (MHD) Micropump," Microsyst. Technol., **6**, pp. 235–240.
[27] Karniadakis, G. E., and Beskok, A., 2002, *Micro Flows, Fundamentals and Simulation*, Springer, New York, pp. 1–31.
[28] Etsion, I., and Yaier, A., 1988, "Performance Analysis of a New Concept Viscous Pump," J. Tribol., **110**, pp. 93–99.
[29] Winoto, S. H., and Yohanand, K., 1994, "Analysis and Test of a Viscous Pump With Radial Pumping Grooves," Tribol. Trans., **37**(4), pp. 691–700.
[30] Arafa, H. A., and Osman, T. A., 2003, "Hydrostatic Bearings With Multiport Viscous Pumps," Proc. Inst. Mech. Eng., Part J: J. Eng. Tribol., **217**, pp. 333–342.
[31] Sato, Y., and Knight, J. D., 1992, "Performance Characteristics of Shrouded Rayleigh-step and Spiral Groove Viscous Pumps," J. Tribol., **114**, pp. 499–506.
[32] Elrod, H. G., 1973, "Some Refinements of the Theory of the Viscous Screw Pump," J. Lubr. Technol., **95**(1), pp. 82–93.
[33] Mainland, M., and Green, I., 1992, "Analysis and Optimization of Semicircular and Straight Lobe Viscous Pumps," J. Tribol., **114**(3), pp. 515–523.
[34] Hasinger, S. H., and Kehrt, L. G., 1963, "Investigation of a Shear-Force Pump," J. Eng. Power, **85**, pp. 201–207.
[35] Sharatchandra, M. C., Sen, M., and Gad-el-Hak, M., 1997, "Navier-Stokes Simulations of a Novel Viscous Pump," J. Fluids Eng., **119**, pp. 372–382.
[36] Blanchard, D., Ligrani, P., and Gale, B., 2004, "Rotary Centrifugal and Viscous Micropumps," US Patient Office, Application No. PCT\US2004\028890, September 3.
[37] Panton, R. L., 1996, *Incompressible Flow*, 2nd ed., New York, New York, pp. 148–154, 158–160, 660–664.
[38] Moffat, R. J., 1982, "Contributions to the Theory of Single-Sample Uncertainty Analysis," J. Fluids Eng., **104**, pp. 250–260.

M. Haddad
e-mail: mouloud.haddad@univ-valenciennes.fr

L. Labraga
e-mail: larbi.labraga@univ-valenciennes.fr

L. Keirsbulck
e-mail: laurent.keirsbulck@univ-valenciennes.fr

Laboratoire de Mécanique et d'Énergétique,
Université de Valenciennes et du
Hainaut-cambrésis,
59313 Valenciennes,
Cedex 9,
France

Turbulence Structures Downstream of a Localized Injection in a Fully Developed Channel Flow

The effects of localized blowing through a porous strip on a turbulent channel were studied experimentally. The measurements were conducted downstream of the porous strip for three blowing rates: 3%, 5%, and 8% (of the velocity at the centerline of the channel). It was found that the injection affects several turbulence parameters. Indeed, blowing decreases the skin friction while it increases the turbulence intensities and the Reynolds stresses. A study of cross-correlations in the streamwise and spanwise direction's showed that both inclination angles in the (x,y) *and* (x,z) *planes were increased with blowing.* [DOI: 10.1115/1.2175168]

Introduction

Since the coherent structures play a major role in turbulence production and transport, the knowledge of the evolution of these structures, especially when being manipulated, could lead to efficient active control schemes for turbulence influence.

Controlling and manipulating turbulence can be achieved by several techniques and setups. Wall injection is one of these methods. Numerous studies showed that blowing from the wall decreases the skin friction and increases the strength of the fluctuating quantities.

Sano and Hirayama [1] found in their experiments that blowing increases the shape parameter. Piomelli et al. [2] performed large eddy simulations of a transpired channel flow and reported the changes in the mean velocity and turbulence intensities. Sumitani and Kasagi [3] performed a direct numerical simulation of a fully developed turbulent channel flow with uniform injection at one wall and uniform blowing at the other wall, and calculated detailed energy budgets of various quantities. They also visualized instantaneous flow fields and found that blowing stimulates the occurrence of the coherent streamwise vortical structures. Kim et al. [4] performed a direct numerical simulation to study the characteristics of the wall pressure fluctuations after the sudden application of wall blowing or suction. With blowing, they obtained a reduction in skin friction, and they also mentioned the formation of adverse pressure gradient in front of and behind the slot, whereas the favorable pressure gradient occurred above the slot. Park and Choi [5] conducted direct numerical simulations of a low Reynolds number turbulent boundary layer subjected to injection through a slot. They observed that blowing stimulated the turbulent motion for the entire computational region downstream of the injection area. The main mechanism for the increased turbulent activity was found to be due to tilting and stretching of the streamwise vorticity. Krogstad and Kourakine [6] conducted experiments to investigate the effect on a turbulent boundary layer of weak blowing through a porous strip. They showed that blowing increases the Reynolds stresses and the mixing length. Tardu [7] performed experiments to compare a steadily blowing system and a periodically blowing system. He showed that both types of blowing led to a reduction in the skin friction. Tardu attempted to explain the response of the flow to periodic blowing in terms of physical arguments based on the vorticity dynamics near the wall. Chung et al. [8] performed numerical simulations to investigate the modulation of the near-wall turbulence with uniform blowing and suction. They found that blowing activates the transverse components of velocity fluctuations and decreases anisotropy. Park et al. [9] examined experimentally the effects of local forcing on a turbulent boundary layer, when a sinusoidal velocity fluctuation was introduced through a spanwise slot at the wall. They found that the periodic local forcing increases the boundary layer shape factor and reduces skin friction. With the highest forcing frequency they obtained the largest skin friction reduction.

Although numerous studies were devoted to determine the effects of blowing on turbulence with some attempts to explain the phenomenon occurring in the near-wall turbulence, only few studies were able to sense some of the geometrical features of the coherent structures in near-wall turbulence. The knowledge of these organized motions is paramount for a better understanding of the bursting process and for a large scale control strategy of the turbulent flows. The novelty of the present paper is the experimental determination of the effects of a local uniform blowing on the behavior of the coherent structures. This was made possible by determining the space-time correlations, the convection velocity of the coherent structures and their inclinations in (x,y) and (x,z) planes. This experimental study provides a large database that should be useful for numerical prediction.

Experimental Details

The experiments were carried out on a channel flow test section shown in Fig. 1. The dimensions of the channel cross section were 450×30 mm, providing a channel aspect ratio of 15:1. This aspect ratio was considered large enough [10], and Dean [11] recommended 7:1 to ensure the required two-dimensionality of the investigated turbulent plane-channel flows. The total length of the channel setup was 5000 mm, corresponding to $L/h\approx334$ (L is the total length of channel and h is the channel half-height). The actual measurement locations and the control device were taken at $268h$ from the channel inlet. This length was considered sufficient to ensure a fully developed turbulent channel flow. The blowing section consisted of 10 mm (170 wall units) long porous strip spanning the entire width of the test section. The strip was made of sintered bronze with pore sizes in 100–200 μm range. The injected air was supplied by a compressor. Air was supplied to the

Contributed by the Fluids Engineering Division of ASME for publication in the JOURNAL OF FLUIDS ENGINEERING. Manuscript received June 9, 2005; final manuscript received October 19, 2005. Assoc. Editor: Phillip M. Ligrani.

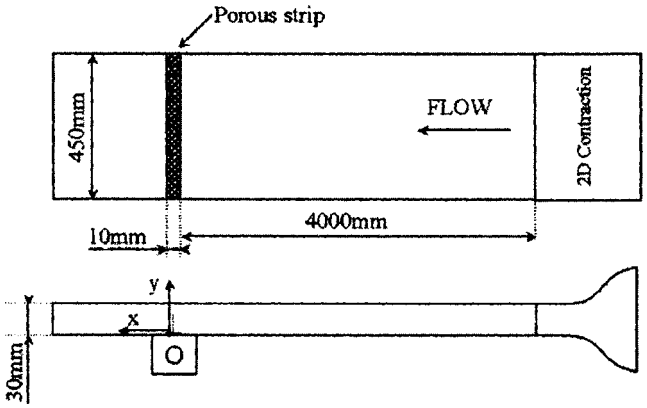

Fig. 1 Nonscaled experimental setup

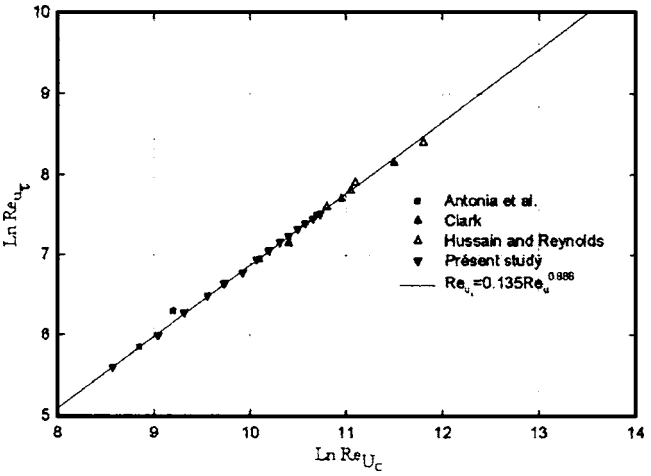

Fig. 2 Global characteristics of fully developed flow

plenum chamber by uniformly perforated tube where filter material is filled to generate an uniform velocity distribution across the porous strip.

The origin of the coordinate system was located at the center of the porous strip. Measurements were performed along the centerline of the channel at two stations $x/b=11.5$ and $x/b=31.5$ (b is the porous strip width) downstream of the injection strip. Measurements were carried out for four blowing rates: $C_q=v_w/U_c=0$, 0.03, 0.05, and 0.08, where v_w is the exit injection velocity and U_c the velocity at the centerline of the channel. The blowing rates were less than 10% in order to show that the turbulent structures may be significantly affected even though the perturbations are quite small. The ratio of momentum flux gain due to the blowing and momentum flux of the incoming channel flow is defined as $\sigma=v_w b/U_c\delta_{20}=C_q b/\delta_{20}$, where δ_{20} is the momentum thickness of the unperturbed flow. The corresponding values of σ for $C_q=0.03$, 0.05 and 0.08 are, respectively, 0.22, 0.36, and 0.58. The local wall shear stress τ_w was measured with a Preston tube (the outer diameter is 15 wall units). Pressure variations were measured by a micromanometer ($0-10\pm0.01$ mm$_{H_2O}$). The Preston tube was calibrated in the present fully developed channel flow according to the method described by Head and Ram [12]. The friction velocity u_τ can be determined with reasonable confidence and accuracy from relation $\tau_w=-h[dp(x)/dx]$, where $p(x)$ is the static pressure along the fully developed channel section. Experiments are carried out using DANTEC 55M10 constant temperature hot-wire anemometry (CTA) system. The output signal was transferred by an A/D digital card connected to a PC. The STREAMLINE soft supplied by DANTEC was used to acquire and store data. A single-wire probe DANTEC 55P15 and X cross-wires probe 55P61 were used. The sensors of both probes consisted of platinum-tungsten wires. The length of the sensors was 17 wall units and the length of the hot-wire was about 200 times the diameter which was sufficient to obtain accurate measurements according to Ligrani and Bradshaw recommendations [13]. The anemometer voltages were calibrated with the velocities using a fifth-degree polynomial fit with an accuracy better than ±1% for the simple probe and ±3% for the X cross-wires. The directional calibration of the velocity with the yaw angle was performed according to the technique described by Jørgensen [14]. All calibrations and measurements were performed with an overheat ratio of 1.8. To ensure that the original calibration curve was maintained during one entire set of hot-wire measurements, the calibration curves were rechecked after each set of measurements covering the entire range of velocities experienced in the channel for each flow case investigated. Streamwise, vertical, and spanwise displacements of the probes were made using a manually controlled mechanism.

The signals from the CTA were filtered and amplified to give signals that covered most of the ±10 V range of the A/D converter. The sampling frequency was chosen to be equal to the viscous frequency ($f_v=u_\tau^2/\nu$).

Pressure measurements were carried out to obtain the wall shear stress and to verify the fully development of turbulence in the channel. For this purpose, 25 pressure trappings were set along the test section every 20 cm. Care was taken to ensure the smoothness of the inner surface of the channel wall. The mean static pressure measurements were used to evaluate the static pressure gradient dp/dx, which in turn was used to obtain the wall shear stress τ_w and the friction velocity, u_τ, as follows:

$$\tau_w=-h\left(\frac{dp}{dx}\right);\quad u_\tau=\sqrt{\frac{\tau_w}{\rho}}.$$

The friction velocity is obtained with an uncertainty less than ±1%. Figure 2 shows the evolution of the Reynolds number based on the friction velocity Re $u_\tau=u_\tau h/\nu$ as a function of the Reynolds number based on the velocity in the centerline of the channel Re $u_c=U_c h/\nu$ at a section where the flow is fully developed. The comparison of the present results in Fig. 2 with those of the literature [15–17] show good agreement. We note that all these authors studied a fully turbulent flow in a two-dimensional channel at least at $50h$ from the channel's leading edge. The plot of static pressure and statistical moments profiles (not reported here) showed that the profiles of the mean and fluctuating velocities, the skewness, and flatness factors are established. Indeed, the profiles are similar at $x/b=11.5$ and 31.5 stations and show the same behavior. The profiles are found to be very close to those of Durst et al. [18].

Experimental Uncertainties

Statistical Uncertainties Due to Finite Sample Size. The statistical errors encountered due to a finite sample size are estimated following the approach presented by Bendat and Piersol [19]. We used a typical sample size of 500,000 for a total sampling time of 83 s. The statistical uncertainties for mean and rms velocity measurements were estimated to be ±0.05% and ±0.8%, respectively. The uncertainty due to the calibration of the cross-wire probe was found to be less than 3%. The overall uncertainties for the cross-wire probe were then estimated to be ±3.05% for the mean velocity and ±3.8% for the rms velocity. In the same manner, the total uncertainties for the single hot-wire were found to be less than ±1.05% and ±1.8% for mean and rms velocities, respectively.

Positional Accuracy. The displacement of the the hot-wire probes is ensured by a traversing system. This system consists in a transmission screw whose function is to produce a rectilinear

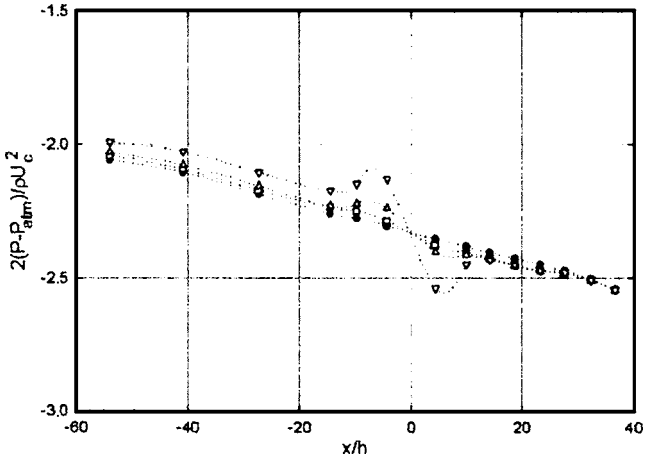

Fig. 3 Effect of blowing on static pressure profiles: ●, C_q=0; □, C_q=0.03; △, C_q=0.05; ▽, C_q=0.08

movement. The entire revolution of the screw produces a displacement of 0.5 mm. The resolution of this device is 0.01 mm.

Effects of Blowing on the Turbulent Channel Flow

One-Point Measurements

Mean Flow Field. Figure 3 shows the variations of the static pressure at the wall due to belowing. It is seen that the static pressure changes very quickly near the porous strip. With blowing, adverse pressure gradient occurs in front of and behind the strip. However, above the strip a favorable pressure gradient appears. These observations were also reported by Kim et al. [4] and Park and Choi [5].

Figure 4 shows the effect of blowing on the evolution of the skin friction downstream of the porous strip. The measurements were carried out by using a Preston tube. According to the study of Sutardi and Ching [20] concerning the effect of the Preston tube diameter on the accuracy of measuring the skin friction and according to Antonia et al. [21], who showed that the Preston tube provides convenient measurements when the wall region is disturbed, the present data of C_f are obtained with ±5% uncertainty. It is seen that the skin friction without blowing remains constant due to the establishment of the turbulent flow. In the vicinity of the injection strip, the skin friction sharply decreases, however, the effect of blowing is weaker far downstream of the porous strip. It is seen that the deviation of the skin friction coefficient from the value of the unperturbed case becomes larger with higher blowing rates. At $x/b \approx 20$, the reduction in C_f is about 20% with the highest blowing rate C_q=0.08. The tendency of the present distribution of the skin friction is consistent with that found in the steady forcing cases [1,5] and the periodic blowing case [22]. Park and Choi [5] attributed the reduction of skin friction to the liftup of the streamwise vortices.

Figure 5 shows the mean streamwise velocity profiles, respectively, at x/b=11.5 and x/b=31.5 with and without blowing. Here the velocity profiles measured for three blowing rates have been scaled with the friction velocity of the unforced case, so that the part of the profile affected by injection is clearly detected [6].

In the disturbed mean velocity profiles, especially at x/b =11.5, a delayed flow region appears, whereas the region close to the wall and the upper logarithmic region $y^+ > 200$ seem to be less sensitive to the effect of blowing. At x/b=31.5, the delayed flow becomes weaker and the velocity profiles converge towards the undisturbed one. A similar decaying tendency of the delayed profiles was observed in the steady blowing of Sano and Hirayama [1]. This delayed flow is typical of the characteristic phenomena of flows with reduced skin friction [6,9]. In Table 1, the displacement thickness δ_1, the momentum thickness δ_2, and the shape factor H increase with increasing injection rate. This observation was also mentioned by Sano and Hirayama [1].

Fluctuating Flow Field. In Fig. 6, the turbulence intensities of the velocity fluctuations measured at x/b=11.5 and at x/b=31.5 are shown, and the effects of injection are clearly identified. The turbulence intensities in the x direction are significantly modified with blowing. The profiles of u' (prime denotes the rms value) with wall-forcing show an increase in the turbulence intensities, more visible when $y^+ > 50$. One of the most notable features is the appearance of a peak at $y^+ \approx 100$ in the profiles of u', which is in agreement with results of Park and Choi [5]. Park et al. [9] explained that this peak denotes the center of the spanwise vortices. For $y^+ < 50$, a slight increase in the streamwise fluctuations u' is observed.

The Reynolds stress profiles $-\overline{uv}$ are plotted in Fig. 7. At Cq =0, the present results are in good agreement with the results of Kim et al. [23] and Günther et al. [24]. A similar overall increase

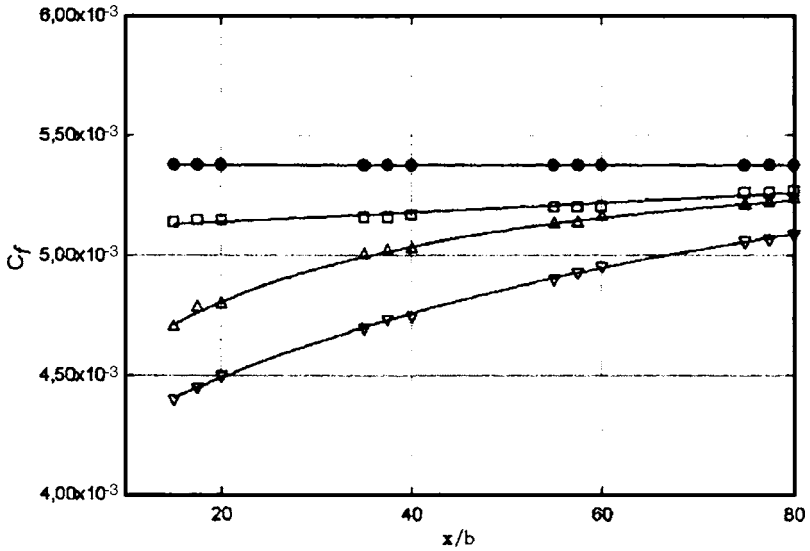

Fig. 4 Effect of blowing on skin friction coefficient. Symbols are the same as in Fig. 3.

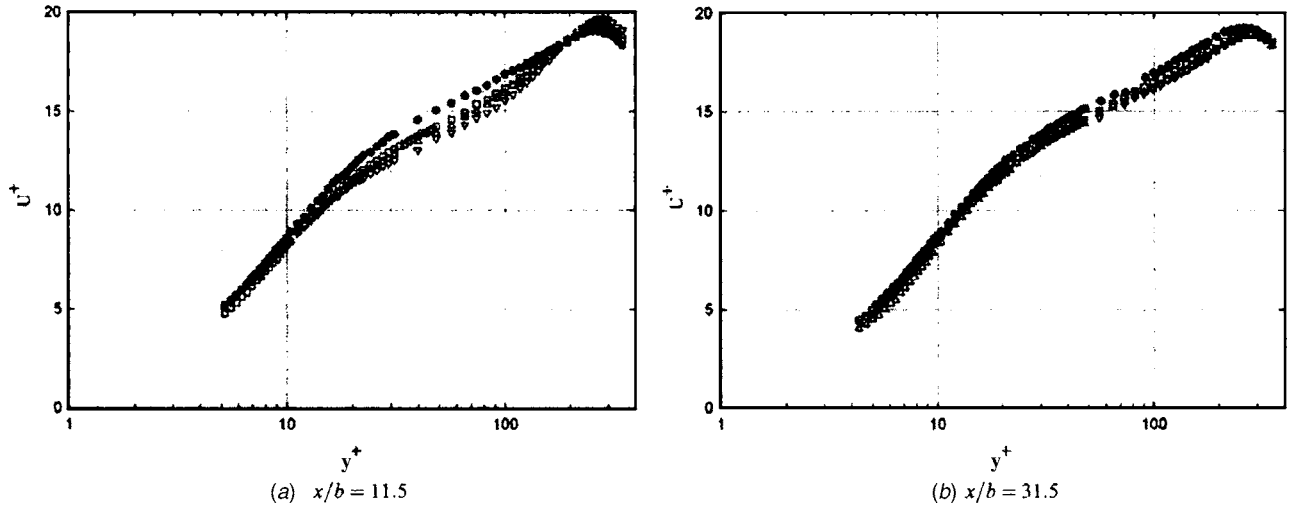

Fig. 5 Effect of blowing on mean velocity profiles. The data have been scaled with u_τ from the unforced case. Symbols are the same as in Fig. 3.

in Reynolds stress profiles with forcing is found as in u'. At $x/b=11.5$ downstream of the porous strip, a peak appears in the profile of $-\overline{uv}$ at $y/h=0.4$ from the wall. This peak occurs at the same distance from the wall as the one observed in the profile of u'. At $x/b=11.5$, the Reynolds stresses are significantly increased in a bounded region $y/h<0.9$, compared to the $x/b=11.5$ location, where the effect of blowing is weaker but extends over a broad region of the profile.

Auto-correlation obtained from the hot-wire probe measurements is a statistical characteristic of the turbulence. The integral scale deduced from the auto-correlation is shown in Fig. 8. The integral scale appears to be highly sensitive to the effect of blowing. Indeed, Fig. 8 shows that the integral scale decreases with increasing blowing rate. The decrease is clearly identified in the region $10<y^+<100$. This means that blowing reduces the eddy scale. The behavior of the integral scale profile is in good agreement with the observations of Sano and Hirayama [1] and Senda et al. [25].

Table 1 Shape parameters of channel flow

C_q [%]	σ	δ_1 [mm]	δ_2 [mm]	H
0	0	2.06	1.37	1.50
3	0.22	2.31	1.51	1.53
5	0.36	2.55	1.67	1.53
8	0.58	2.85	1.85	1.55

Two-Point Measurements

Correlation Measurements in Streamwise and y Directions. To investigate the effect of blowing on the coherent structures, space-time correlations were performed. One hot-wire probe was kept at a fixed position on the centerline of the channel $x/b=11.5$ downstream of the porous strip at about $y^+=15$. The free hot-wire probe was initially positioned close to the fixed one ($\Delta Y^+=7$) with no streamwise separation, as shown in Fig. 9. The free probe was then moved downstream in $\Delta X^+=3.4$ steps.

The convection speed of the coherent structures is obtained from Fig. 10, which depicts the offset location $T^+_{\max}$ of the streamwise correlation $(R_{uu})_x$ peaks as a function of the hot-wire separation ΔX. Plotting $T^+_{\max}$ with respect to ΔX^+ leads to a straight line. The convection velocity corresponds to the slope of this line $u_c^+=\Delta X^+/T^+_{\max}$.

In Fig. 10, both the undisturbed and disturbed cases show the slope leading to u_c convection velocity at $y^+\approx 20$. In the no-

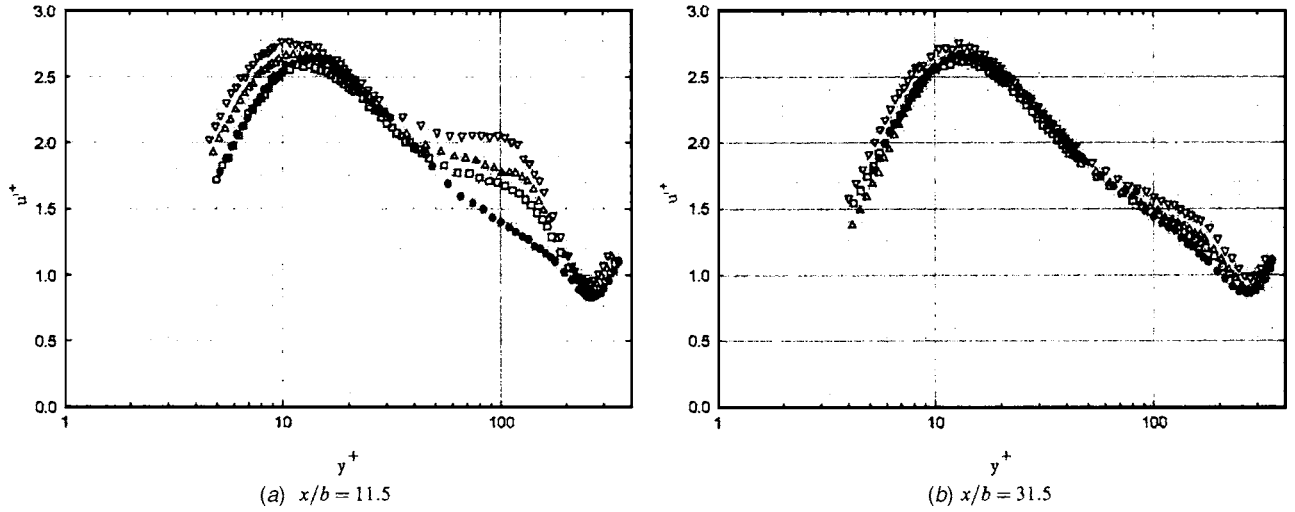

Fig. 6 Effect of blowing on the turbulence intensities. Symbols are the same as in Fig. 3.

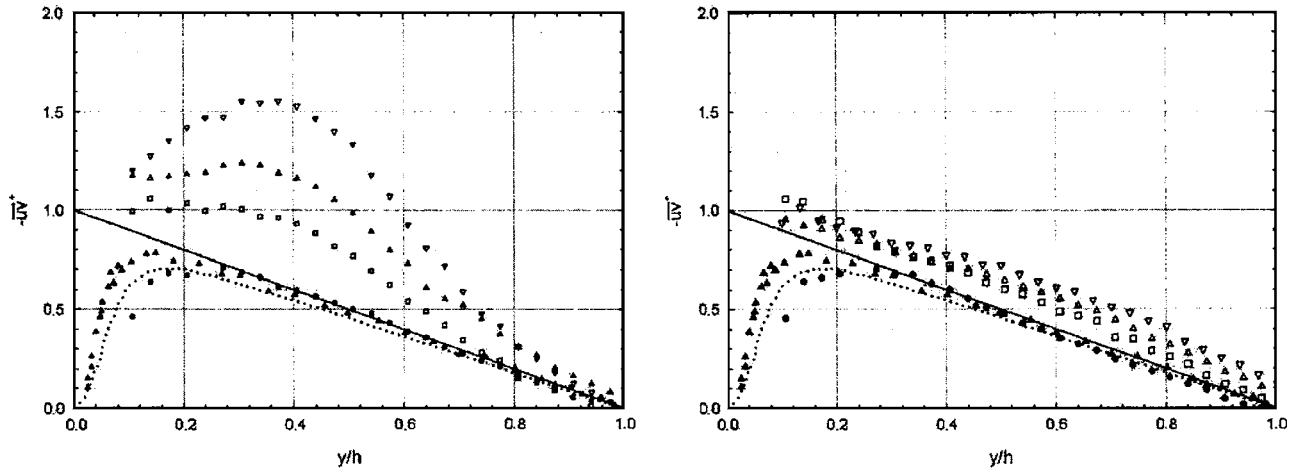

Fig. 7 Effect of blowing on Reynolds stress profiles. Symbols are the same as in Fig. 3;…, Kim et al. [23]; ▲ Günther et al. [24].

blowing case, the convection velocity is found to be approximately $11u_\tau \pm 0.5u_\tau$. With blowing, u_c is about $10.2u_\tau$ and remains fairly constant independent of the blowing rate. The value of u_c found here, is in good agreement with those reported in the literature [26–29].

In order to determine the effect of blowing on the inclination angle θ of the coherent structures in the (x,y) plane, further measurements of the streamwise correlations were made by changing the position of the free hot-wire probe in the y direction.

With the convection velocity u_c found previously, the average inclination angle of the coherent structures at the height between the two hot-wire probes is given by $\theta=\tan^{-1}(\Delta Y^+/\Delta X^+)$. Figure 11 shows the effect of blowing on the inclination angle of the coherent structures.

For the no-blowing case, the inclination angle θ is about 14.5°; this result is consistent with that found by Labraga et al. [30]. With blowing, the inclination angle is found to be greater. For injection rates of $C_q=0.03$, $C_q=0.05$, and $C_q=0.08$, the respective inclination angles are 17.5°, 19°, and 21° with an uncertainty of ±1°. The inclination angle in the near-wall region needs to be investigated by using a correlation analysis between a moving probe and a wall shear stress probe. This will be reported elsewhere.

Correlation Measurements in the Spanwise Direction. Cross-correlations between the velocity given by a fixed wire and that supplied by a moving wire in the spanwise direction are investigated. The velocity-velocity correlations were achieved by positioning the free hot-wire probe next to the fixed probe at the same location $x/b=11.5$ and at $y^+=15$ from the wall. The given spanwise distance ΔZ^+ is taken from centerline to centerline of the hot-wire probes, hence, the initial ΔZ^+ is 24.65. The free hot-wire probe was traversed in steps of approximately 3.4 wall units on one side of the channel centerline.

Plotting several cross-correlation data in the z direction for the undisturbed and disturbed case shows the development of this

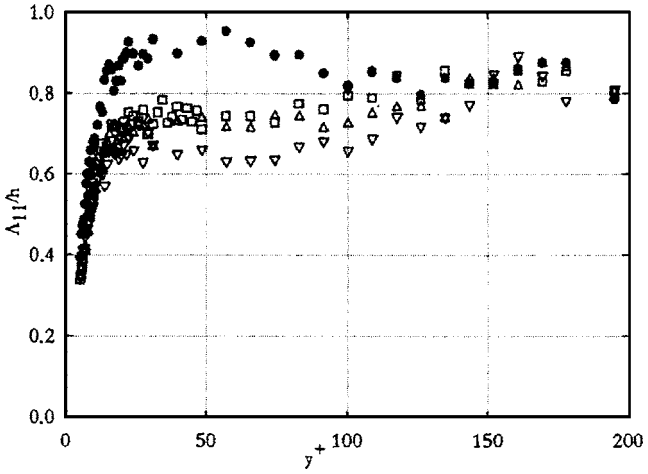

Fig. 8 Effect of blowing on the integral scale at $x/b=11.5$. Symbols are the same as in Fig. 3.

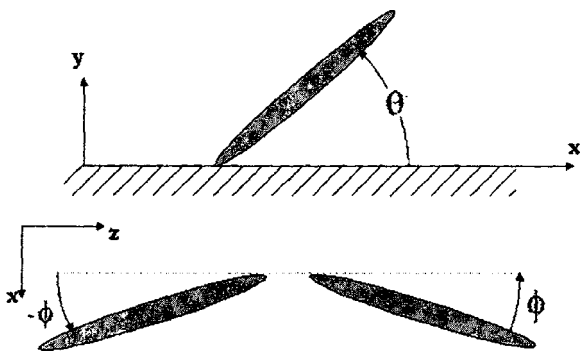

Fig. 9 Measurement procedure for acquiring cross-correlation data

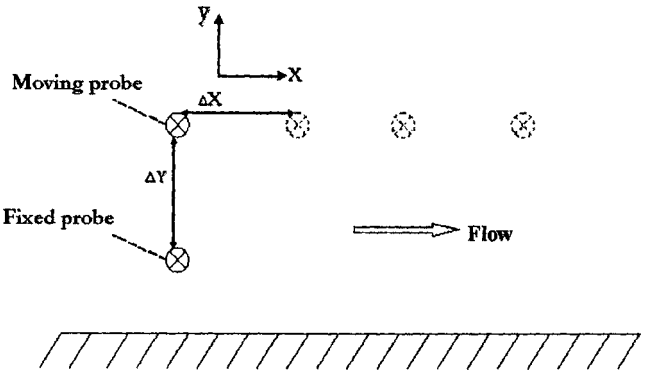

Fig. 10 Time shift of maximum correlation coefficients. Symbols are the same as in Fig. 3.

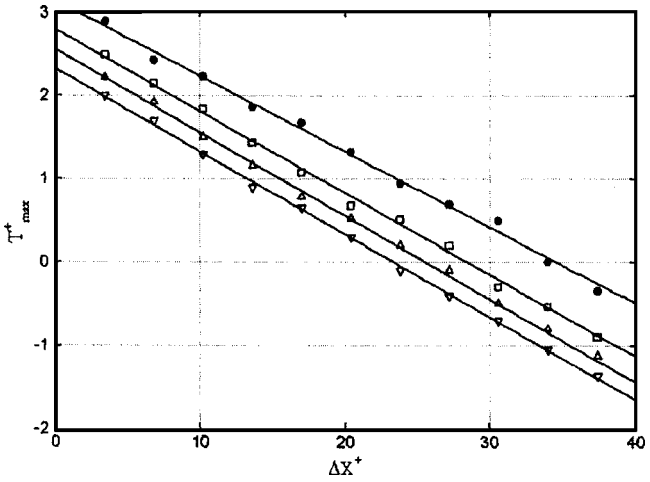

Fig. 11 Effect of blowing on the coherent structures inclination angle in the (x,y) plane. Symbols are the same as in Fig. 3.

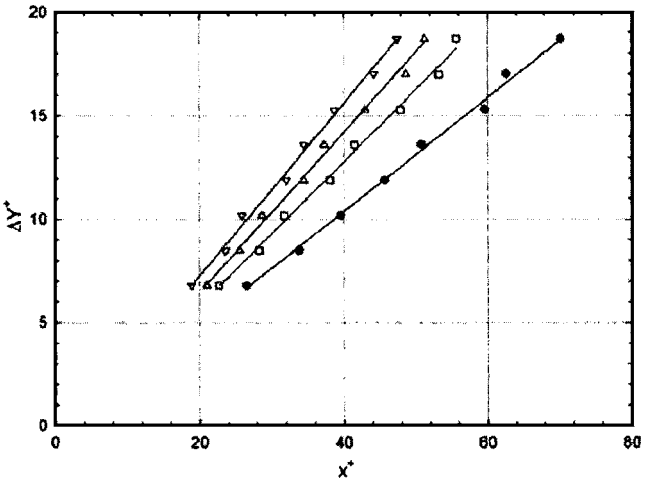

Fig. 12 Sketch of the inclination angle of the coherent structures. (*a*) (x,y) plane. (*b*) (x,z) plane.

behavior.

The magnitude of the correlation decreases rapidly as the spanwise separation of the probes increases. The most notable feature of the spanwise space-time correlations is the emergence of a double peak in the correlation curves. One of the peaks results from the inclination of the structures in the (x,z) plane at ϕ angle. The second peak is generated by the structures inclined at $-\phi$ angle (Fig. 12). For $C_q=0$, this angle is found to be $\approx 6°$ with an uncertainty of $\pm 1°$. This result is consistent with that found by Lagraa et al. [31], who used an array of electrochemical probes and space-time correlations of the wall shear stress. The double peak is detected earlier in the no-blowing case (i.e., the double peak appears for $\Delta Z^+=24.65$ when $C_q=0$, while it appears for $\Delta Z^+\approx 31.5$ when $C_q=0.08$). This suggests that a slight increase in the inclination is observed when blowing is applied.

The inclination angle ϕ was estimated from the spanwise separation between the probes with the lag time of the correlation peaks and the convection velocity. The inclination angle without injection is found to be $\phi\approx\pm 6°$. The structures can be tilted to one side or the other, leading to the two peaks in the spanwise correlation curves (Fig. 13). The value of ϕ for $C_q=0$ agrees with the results found in the literature [30–32]. In the case of blowing, the spanwise inclination increases and reaches $\pm 8°$ with the highest blowing rate. The slight increase in the yaw angle of the coherent structures when being manipulated could explain the earlier detection of the two peaks in the spanwise correlation.

The streak spacing extent λ^+ of the coherent structures can be estimated by plotting the magnitude of the correlations $(R_{uu})_z$ at $T^+=0$ with the corresponding spanwise separation ΔZ^+, as shown in Fig. 14. Figure 14 shows that the correlation decreases rapidly and a broad minimum is found at $\Delta Z^+\approx 60$ in the absence of blowing, hence, the half-streak spacing of the coherent structures is about $\lambda^+\approx 60$, which is in agreement with the results found in the literature [31]. By applying blowing, the half-streak spacing increases up to $\lambda^+\approx 80$ when $C_q=0.03$, however, for the blowing rates of 0.05 and 0.08, the minimum is not clearly visible.

Conclusion

Injection on a fully developed turbulent channel using a porous strip was investigated. The effect on the flow statistics as well as the coherent structures present in the turbulent channel flow were studied downstream the blowing strip. Hot-wire anemometry and two-point space-time correlation measurements were performed to characterize the flow field.

It was found that blowing reduces the skin friction by approximatively 20% for the largest blowing rate at $x/b=15$. The pres-

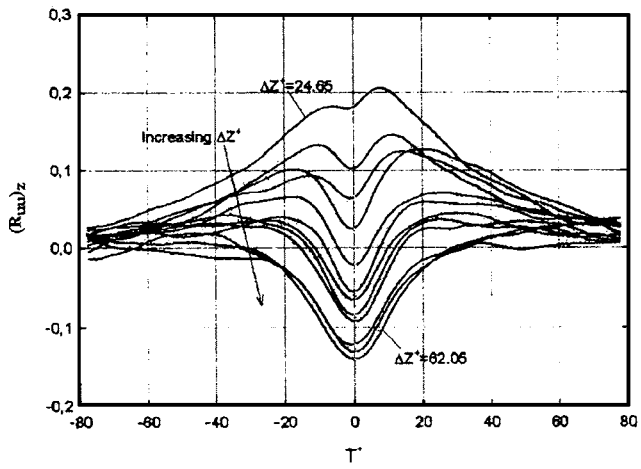

(*a*) $C_q=0$

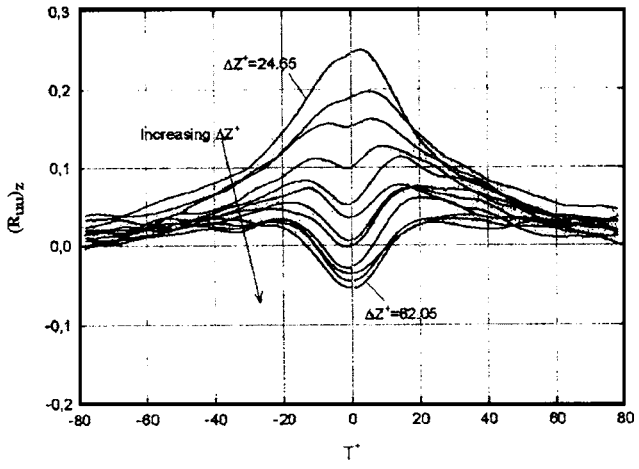

(*b*) $C_q=0.08$

Fig. 13 Effect of blowing on spanwise cross-correlations

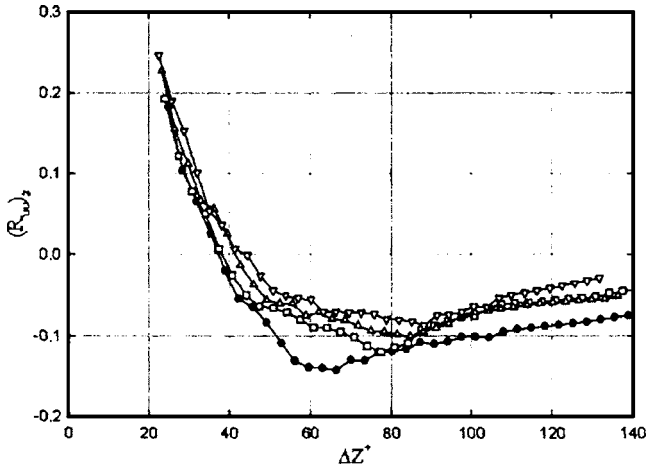

Fig. 14 Spanwise spatial correlations at $T^+=0$. Symbols are the same as in Fig. 3.

sure profiles were modified by an adverse pressure gradient in front of and behind the blowing porous strip, while a favorable pressure gradient occurs above the injection strip.

A delayed flow clearly appears in the mean velocity profiles downstream of the injection. The effect of blowing gradually decreases with an increasing distance from the porous strip. The turbulence intensities and Reynolds stresses are strongly increased, especially in the vicinity of the porous strip. The integral scale is significantly reduced in the presence of the wall injection.

The convection velocity depends a little on blowing and is nearly $u_c=11u_\tau$ in the no-blowing case. It decreases up to approximately $u_c=10.2u_\tau$ in the blowing case. The inclination angle in (x,y) plane was found to increase from 14% to 21% when blowing was applied from 0% to 8% at the outer region.

The inclination angle of the coherent structures in (x,z) plane was about $\pm 6°$ in the undisturbed case and increased slightly when injection is applied. Moreover, the effect of blowing is also to increase the streak spacing.

References

[1] Sano, M., and Hirayama, N., 1985, "Turbulent Boundary Layers With Injection and Suction Through a Slit," Bull. JSME, **28**, pp. 807–814.

[2] Piomelli, U., Ferziger, J., Moin, P., and Kim, J., 1989, "New Approximate Boundary Conditions for Large Eddy Simulation of Wall-Bounded Flows," Phys. Fluids A, **1**, pp. 1061–1068.

[3] Sumitani, Y., and Kasagi, N., 1995, "Direct Numerical Simulation of Turbulent Transport With Uniform Wall Injection and Suction," AIAA J., **33**, pp. 1220–1228.

[4] Kim, J., Kim, K., and Sung, H. J., 2003, "Wall Pressure Fluctuations in a Turbulent Boundary Layer After Blowing or Suction," AIAA J., **41**, pp. 1697–1704.

[5] Park, J., and Choi, H., 1999, "Effects of Uniform Blowing or Suction From a Spanwise Slot on a Turbulent Boundary Layer Flow," Phys. Fluids, **11**, pp. 3095–3105.

[6] Krogstad, P. Å., and Kourakine, A., 2000, "Some Effects of Localized Injection on the Turbulence Structure in a Boundary Layer," Phys. Fluids, **12**, pp. 2990–2999.

[7] Tardu, S., 2001, "Active Control of Near-Wall Turbulence by Local Oscillating Blowing," J. Fluid Mech., **439**, pp. 217–253.

[8] Chung, Y. M., Sung, H. J., and Krogstad, P. Å., 2002, "Modulation of Near Wall-Wall Turbulence Structure With Wall Blowing and Suction," AIAA J., **40**, pp. 1529–1535.

[9] Park, S.-H., Lee, I., and Sung, H. J., 2001, "Effect of Local Forcing on a Turbulent Boundary Layer," Exp. Fluids, **31**, pp. 384–393.

[10] Zanoun, E. S., Durst, F., and Nagib, H., 2003, "Evaluating the Law of the Wall in Two-Dimensional Fully Developed Turbulent Channel Flows," Phys. Fluids, **15**, pp. 3079–3089.

[11] Dean, R. B., 1978, "Reynolds Number Dependence of Skin Friction and Other Bulk Flow Variables in Two-Dimensional Rectangular Duct Flow," J. Fluids Eng., **100**, pp. 215–223.

[12] Head, M. R., and Ram, V. V., 1971, "Simplified Presentation of Preston Tube Calibration," Aeronaut. Q., **22**, pp. 295–300.

[13] Ligrani, P. M., and Bradshaw, P., 1987, "Spatial Resolution and Measurement of Small-Scale Turbulence in the Viscous Sublayer Using Subminiature Hot-Wire Probes," Exp. Fluids, **5**, pp. 407–417.

[14] Jørgensen, F. E., 1971, "Directional Sensitivity of Wire and Fibre-Film Probes," DISA Inf., **11**, pp. 31–37.

[15] Antonia, R. A., Teitel, M., Kim, J., and Brown, L. W. B., 1992, "Low-Reynolds-Number Effects in a Fully Developed Turbulent Channel Flow," J. Fluid Mech., **236**, pp. 579–605.

[16] Clark, J. A., 1968, "A Study of Incompressible Turbulent Boundary Layers in Channel Flow," ASME J. Basic Eng., **90**, pp. 455–468.

[17] Hussain, A. K. M. F., and Reynolds, W. C., 1975, "Measurements in Fully Developed Turbulent Channel Flow," J. Fluids Eng., **97**, pp. 568–580.

[18] Durst, F., Fischer, M., Jovanović, J., and Kikura, H., 1998, "Methods to Set Up and Investigate Low Reynolds Number, Fully Developed Turbulent Plane Channel Flows," J. Fluids Eng., **120**, pp. 496–503.

[19] Bendat, J. S., and Piersol, A. G., 2001, *Random Data Analysis and Measurement Procedures*, Wiley, New York.

[20] Sutardi, and Ching, Y. C., 2001, "Effect of Tube Diameter on Preston Tube Calibration Curves for the Measurement of Wall Shear Stress," Exp. Therm. Fluid Sci., **24**, pp. 93–97.

[21] Antonia, R. A., Zhu, Y., and Sokolov, M., 1995, "Effect of Concentrated Wall Suction on a Turbulent Boundary Layer," Phys. Fluids, **7**, pp. 2465–2474.

[22] Tardu, S., 1998, "Near Wall Turbulence Control by Local Time Periodical Blowing," Exp. Therm. Fluid Sci., **16**, pp. 141–53.

[23] Kim, J., Moin, P., and Moser, R., 1987, "Turbulence Statistics in Fully Developed Channel Flow at Low Reynolds Numbers," J. Fluid Mech., **177**, pp. 133–166.

[24] Gunther, A., Papavassiliou, D. V., Warholic, M. D., and Hanratty, T. J., 1998, "Turbulent Flow in a Channel at a Low Reynolds Number," Exp. Fluids, **25**, pp. 503–511.

[25] Senda, M., Kawaguchi, Y., Suzuki, K., and Sato, T., 1981, "Study on Turbulent Boundary Layer With Injection," Bull. JSME, **24**, pp. 1748–1755.

[26] Johansson, A. V., Alfredsson, P. H., and Eckelmann, H., 1987, "On the Evolution of Shear Layer Structures in Near Wall Turbulence," in *Advances in Turbulence*, Springer Verlag, Berlin, pp. 383–390.

[27] Xu, C., Zhang, Z., Toonder, J. M. J., and Nieuwstadt, F. T. M., 1996, "Origin of High Kurtosis Levels in the Viscous Sublayer Direct Numerical Simulation and Experiment," Phys. Fluids, **8**, pp. 1938–1944.

[28] Kim, J., and Hussain, F., 1993, "Propagation Velocity of Perturbations in Turbulent Channel Flow," Phys. Fluids A, **5**, pp. 695–706.

[29] Krogstad, P. Å., Kaspersen, J. H., and Rimestad, S., 1998, "Convection Velocities in a Turbulent Boundary Layer," Phys. Fluids, **10**, pp. 949–957.

[30] Labraga, L., Lagraa, B., Mazouz, A., and Keirsbulck, L., 2002, "Propagation of Shear-Layer Structures in the Near-Wall Region of a Turbulent Boundary Layer," Exp. Fluids, **33**, pp. 670–676.

[31] Lagraa, B., Labraga, L., and Mazouz, A., 2004, "Characterization of Low-Speed Streaks in the Near-Wall Region of a Turbulent Boundary Layer," Eur. J. Mech. B/Fluids, **23**, pp. 587–599.

[32] Jeong, J., Hussain, F., Schoppa, W., and Kim, J., 1997, "Coherent Structures Near the Wall in a Turbulent Channel Flow," J. Fluid Mech., **332**, pp. 185–214.

Effect of Channel Aspect Ratio on the Flow Performance of a Spiral-Channel Viscous Micropump

M. I. Kilani[1]
Assistant Professor
e-mail: mkilani@ju.edu.jo

A. Al-Salaymeh
Assistant Professor
e-mail: salaymeh@ju.edu.jo

A. T. Al-Halhouli

Mechanical Engineering Department,
University of Jordan,
Amman 11942, Jordan

The paper investigates the effect of channel aspect ratio on the flow performance of a newly introduced spiral-channel viscous micropump. An approximate 2D analytical solution for the flow field, which ignores channel curvature but accounts for a finite wall height, is first developed at the lubrication limit. A number of 3D models for spiral pumps with different aspect ratios are then built and analyzed using the finite volume method. Numerical and analytical results are in good agreement and tend to support one another. The results are compared with an approximate 2D analytical solution developed for infinite aspect ratio, which neglects the effect of side walls, and assumes uniform velocity distribution across the channel width. The error in this approximation was found to exceed 5% for aspect ratios less than 10. Pressure and drag shape factors were introduced in the present work to express the effect of the pressure difference and boundary velocity on the flow rate at various aspect ratios for both moving and stationary walls. Also, it has been found numerically that the flow rate varies linearly with both the pressure difference and boundary velocity, which supports the validity of the linear lubrication model employed. [DOI: 10.1115/1.2175169]

Keywords: spiral micropumps, flow field solution, channel aspect ratio, lubrication model

1 Introduction

Over the last decade, micromachining technologies have been used to advance the area of microfluidic systems. These technologies have promoted the miniaturization of systems such as gas chromatography [1], liquid chromatography [2], electrophoresis [3], polymer chain reaction [4], chemical analysis systems [5], and microreactors [6]. All of these systems require the use of miniaturized channels for liquid or gas delivery and/or chemical reactions. One of the basic components in microfluidic systems is micropumps, which are used for the controlled delivery of reagents within the system.

Research on micropumps was initiated in the 1980s [7], and their development has been governed by the physics of microscale flow, which is characterized by large surface areas to volume ratio, fast and uniform heat transfer, increased surface tension, dominating viscous forces over inertia, large diffusion to convection ratio and laminar flows. Several different micropumps have been developed based on different pump principles and using different actuation principles [8–10]. Viscous drag micropumps have been investigated by several researchers and this investigation has been motivated by the ability of generating significant pressure heads in the viscosity dominated microchannels by the simple rotation of a rigid element contiguous to the flow field [11]. A number of analytical and numerical simulations have been conducted on such pumps [12,13]. Viscous drag micropumps are attractive because they are easy to fabricate, capable of handling a wide variety of fluids, and can operate with no valves allowing them to handle particle-laden fluids.

A spiral viscous pump which works by rotating a disk with spiral groove at a close proximity over a stationary plate, using a planar mechanism has recently been proposed by Kilani et al. [14]. As illustrated in Fig. 1, the pump works with no valves, and fluid contained in the spiral channel between the disk and the plate is subjected to a net tangential viscous stress on its boundaries and a positive pressure gradient is established in the direction of flow. Two holes at either end of the spiral channel provide the required inlet and outlet for the pumped fluid.

An approximate analytical solution for the flow field in the spiral micropump has been presented in [14]. This approximation neglects the curvature of the spiral and treats it as a straight channel with a stationary bottom wall and moving top and side walls. The validity of this "unfolding approximation" for flows in curved geometry has been first investigated by Dean in 1927 [15] who has shown that for low values of Re the approximation is valid when the channel width is small compared to its radius of curvature. Using a perturbation analysis of the Navier-Stokes equations it may be demonstrated that the leading-order error in the axial velocity due to the unfolding approximation is proportional to the square of Re, which is small in the viscosity dominated microscale flow fields. Further quantitative discussion on these parameters is presented in [14], and it is demonstrated that both Re and the ratio of channel width to its radius of curvature are small for the problem addressed in this study.

The straight channel model is further simplified using symmetry into the 2D flow in the middle plane of the channel by considering a large aspect ratio $w/h \to \infty$, which neglects the effect of the side walls of the spiral channel. The obtained model closely resembles the classical Couette-Poiseuille model, and was solved analytically for the velocity and pressure fields. For a spiral pump with channel height h, channel width w, wall thickness w_t, initial radius r_o, angular span $\Delta\theta$, polar slope k, and angular velocity ω, the modeling parameters and the performance relations of the approximate model are summarized in Tables 1 and 2.

This paper presents an analytical solution and a numerical investigation for the flow in the spiral pump which considers a finite

[1]Corresponding author.

Contributed by the Fluids Engineering Division of ASME for publication in the JOURNAL OF FLUIDS ENGINEERING. Manuscript received May 7, 2005; final manuscript received November 1, 2005. Assoc. Editor: Yu-Tai Lee.

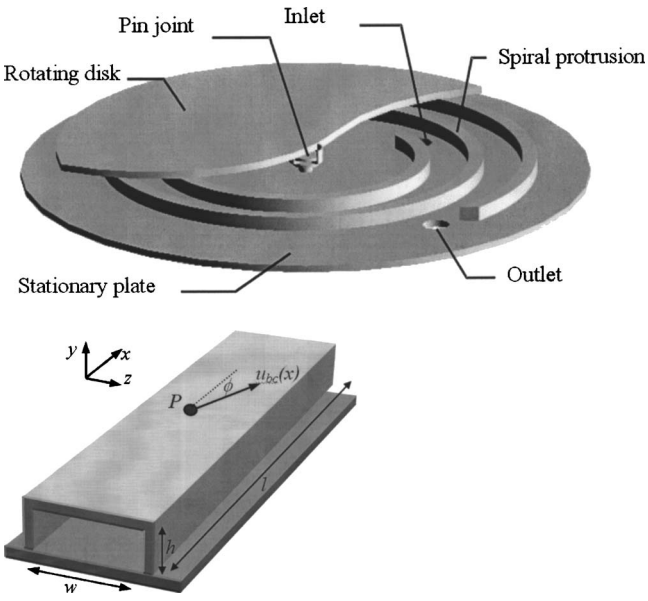

Fig. 1 A schematic illustration of the spiral pump design [14]

wall height. Numerical simulations have been carried out using the finite volume method for the viscous spiral micropump. The effect of channel aspect ratio on the flow field at various pressure gradients and angular velocities was investigated. The numerical results were compared with the analytical solution and a very good agreement has been shown for aspect ratios ranging from 0 to ∞. Shape factors that describe the effect of the pressure difference and drag velocity on the flow rate for moving walls and stationary walls at various aspect ratios were developed to account for the deviation of the flow rate from the simple approximate model.

Table 1 Straight channel model parameters

Quantity	Formula
Straight channel width, w	$2\pi k - w_t$
Straight channel length, l	$(r_o + k\Delta\theta/2)\Delta\theta = r_a\Delta\theta$
Straight channel height, h	h
Channel boundary velocity	$u_{\mathrm{ch}}(x) = \omega r_o + \dfrac{k\omega}{r_a} x$
Channel boundary mean velocity	$\bar{u}_{\mathrm{ch}}(x) = (1/l)\int_0^l u_{\mathrm{ch}}(x)dx$

2 Analytical Formulation

To study the effect of channel aspect ratio on the flow field in a spiral-channel viscous micropump, the basic governing equations for mass, momentum, and energy conservation have been normalized in order to reveal the nondimensional parameters relevant to the particular flow situation. The conservation of mass (continuity) equation can be written in the general form as:

$$\frac{\partial \rho}{\partial t} + \frac{\partial}{\partial x_i}(\rho U_i) = 0, \quad i = 1,2,3 \tag{1}$$

where ρ is the density, t is the time, U_i is the Cartesian velocity components, and x_i is the Cartesian coordinates.

The Navier-Stokes equations for the conservation of momentum can be written as

$$\rho\left[\frac{\partial U_j}{\partial t} + U_j \cdot \frac{\partial U_j}{\partial x_i}\right] = -\frac{\partial P}{\partial x_j} + \frac{\partial \tau_{ij}}{\partial x_i} + \rho g_j \tag{2}$$

where P is the pressure, τ_{ij} is the shear stress term, and g_j is the gravitational acceleration in the direction x_j. The shear stress term for a Newtonian fluid can be written in general as

$$\tau_{ij} = \mu\left[\frac{\partial U_j}{\partial x_i} + \frac{\partial U_i}{\partial x_j} - \frac{2}{3}\delta_{ij}\frac{\partial U_k}{\partial x_k}\right] \tag{3}$$

where μ is the dynamic viscosity and δ_{ij} is the Kronecker delta.

The flows in a spiral-channel viscous micropump in our work are considered as steady, incompressible homogeneous flows so the above continuity and momentum equations can be rewritten in indicial notations as:

$$\frac{\partial}{\partial x_i}(U_i) = 0.0 \tag{4}$$

While the momentum equation can be written as:

$$\rho\left[U_j \cdot \frac{\partial U_j}{\partial x_i}\right] = -\frac{\partial P}{\partial x_j} + \mu\frac{\partial^2 U_j}{\partial x_i^2} + \rho g_j \tag{5}$$

to introduce characteristic quantities for all the terms in the continuity and momentum equations, the following nondimensional parameters can be introduced:

Table 2 Performance relations for the approximate analytical model

Quantity	Accelerate Couette model
Axial velocity	$u = u_{\mathrm{ch}}(x)\dfrac{y}{h} - \left(\dfrac{h^2}{2\mu}\dfrac{\Delta P}{l} + 3(u_{\mathrm{ch}}(x) - \bar{u}_{\mathrm{ch}})\right) \times\left(\dfrac{y}{h} - \left(\dfrac{y}{h}\right)^2\right)$
Vertical velocity	$v = hu'_{\mathrm{ch}}((y/h)^2 - (y/h)^3)$
Pressure	$p(x) = \dfrac{6\mu}{h^2}\displaystyle\int_0^x \delta(x)dx + \Delta p\dfrac{x}{l} + p_0$
Volume flow rate per unit channel width	$q = \dfrac{h\bar{u}_{\mathrm{ch}}}{2} - \dfrac{h^3}{12\mu l}\Delta p$

$$\rho = \rho_o \cdot \rho^*; \quad U_j = \bar{U} \cdot U_j^*; \quad x_i = l_o \cdot x_i^*; \quad P = \Delta P_o \cdot P^*;$$
$$\mu = \mu_o \cdot \mu^*; \quad \text{and } g_j = g_j^* \cdot g_o \tag{6}$$

to yield:

$$\frac{\partial(U_i^*)}{\partial x_i^*} = 0.0 \tag{7}$$

$$\rho^* \left[U_j^* \cdot \frac{\partial U_j^*}{\partial x_i^*} \right] = -\left(\frac{\Delta P_o}{\rho_o \bar{U}^2} \right) \frac{\partial P^*}{\partial x_j^*} + \left(\frac{\mu_o \mu^*}{\bar{U} \rho_o l_c} \right) \frac{\partial^2 U_j^*}{\partial x_i^{*2}} + \frac{l_c g_o}{\bar{U}^2} \rho^* g_j^* \tag{8}$$

Define the nondimensional numbers: Reynolds number: $\mathrm{Re} = \rho \bar{U} l_o / \mu$, Euler number: $\mathrm{Eu} = \Delta P_o / \rho_o \bar{U}^2$, and Froude number: $\mathrm{Fr} = \bar{U} / \sqrt{g_o l_o}$.

Then, Eq. (8) becomes

$$\rho^* \left[U_j^* \cdot \frac{\partial U_j^*}{\partial x_i^*} \right] = -\mathrm{Eu} \frac{\partial P^*}{\partial x_j^*} + \frac{1}{\mathrm{Re}} \mu^* \frac{\partial^2 U_j^*}{\partial x_i^{*2}} + \frac{1}{\mathrm{Fr}^2} \rho^* g_j^* \tag{9}$$

Multiplying Eq. (9) by Re, results in

$$\mathrm{Re} \cdot \rho^* \left[U_j^* \cdot \frac{\partial U_j^*}{\partial x_i^*} \right] = -\mathrm{Re} \cdot \mathrm{Eu} \frac{\partial P^*}{\partial x_j^*} + \mu^* \frac{\partial^2 U_j^*}{\partial x_i^{*2}} + \frac{\mathrm{Re}}{\mathrm{Fr}^2} \rho^* g_j^* \tag{10}$$

In the case of the viscosity dominated flow in the microscale channels considered in the present analysis (viscous micropump), the viscosity forces are considerably larger than the inertial forces. The inertial and body terms can therefore be completely neglected, so that Eq. (10) may be reduced to:

$$\mu^* \frac{\partial^2 U_j^*}{\partial x_i^{*2}} = \mathrm{Re} \cdot \mathrm{Eu} \frac{\partial P^*}{\partial x_j^*} \tag{11}$$

which is a linear differential equation. Since $\partial P / \partial y = 0$ ($P = P_{\text{motion}}$ is here the pressure due to the motion only), the pressure is therefore only dependent on x. This observation along with the small value of Re reduces the momentum equations, respectively, into a form of the Navier-Stokes equation known as the lubrication flow model, and is encountered in the hydrodynamic theory of lubrication [16], which is also characterized by narrow, thin channels

$$\mu \left(\frac{\partial^2 u}{\partial y^2} + \frac{\partial^2 u}{\partial z^2} \right) = \frac{\partial P}{\partial x} \tag{12}$$

Additional insight into the equations above may be reached by comparing the inertia force to the viscous force in the channel as follows: With reference to Eq. (10), it may be seen that the largest inertia force in such geometries is proportional to $[U_i^* \cdot (\partial U_j^* / \partial x_i^*)]$, while the viscous term is proportional to $\mu^* (\partial^2 U_j^* / \partial x_i^{*2})$. Hence, the ratio between those forces is

$$\frac{\text{inertia force}}{\text{viscous force}} = \frac{U_i^* \partial U_j^* / \partial x_i^*}{v \partial^2 U_j^* / \partial x_i^{*2}} = \frac{\bar{U}^2 / l}{v \bar{U} / h^2} = \frac{\bar{U} h}{v} \left(\frac{h}{l} \right) = \overline{\mathrm{Re}} \tag{13}$$

The ratio is known as the reduced Reynolds number $\overline{\mathrm{Re}}$, and is considered the characteristic dimensionless number in flow fields in thin, narrow channels. In the geometry considered in the present analysis we have $\overline{\mathrm{Re}} = \mathrm{Re}_h . (h/l)$ and $\overline{\mathrm{Re}} \square 1$.

3 Effect of Aspect Ratio

The flow model in the solution of Table 2 assumed that $w/h \to \infty$, which allowed the solution in the plane of symmetry to be applied across the channel. If this condition is not met, such as in microchannels produced using deep reaction ion etching (DRIE) technology, the effect of channel height on the flow rate becomes significant. This effect may be estimated by accounting for $\partial^2 u / \partial z^2$ in the x momentum equation of the Stokes model, as shown in Eq. (12). We consider two situations, the first is when the spiral wall is attached to the stationary plate rather than rotating with the rotating disk (stationary walls) and the second is when the spiral wall is rotating with the rotating disk rather than attached to the stationary plate (rotating walls).

The boundary conditions for the stationary walls on Eq. (12) are

$$u(0,z) = u(y,w) = u(y,0) = 0.0, \quad u(h,z) = \bar{U}_{\text{ch}} \tag{14}$$

and for the moving walls are

$$u(y,0) = u(y,w) = u(h,z) = \bar{U}_{\text{ch}}, \quad u(0,z) = 0.0 \tag{15}$$

An exact solution for the system above may be obtained by writing the solution as the sum of a drag component u_D and a pressure component u_P as

$$u = u_D + u_P \tag{16}$$

The solutions of these equations for the two situations are as follows: The PDE and B.Cs for u_D in the stationary situation are

$$\frac{\partial^2 u_D}{\partial y^2} + \frac{\partial^2 u_D}{\partial z^2} = 0 \tag{17}$$

$$u_D(0,z) = u_D(y,w) = u_D(y,0) = 0.0, \quad u_D(h,z) = \bar{U}_{\text{ch}} \tag{18}$$

while for u_P we have

$$\frac{\partial^2 u_P}{\partial y^2} + \frac{\partial^2 u_P}{\partial z^2} = \frac{1}{\mu} \frac{\Delta p}{l} \tag{19}$$

$$u_P(0,z) = u_P(h,z) = u_P(y,0) = u_P(y,w) = 0.0 \tag{20}$$

Using separation of variables, the general solution of the homogeneous PDE in Eq. (17) satisfying the homogeneous B.Cs in Eq. (18) is

$$u_D = \sum_{n=0}^{\infty} A_n \sinh(n\pi y/w) \sin(n\pi z/w) \tag{21}$$

The coefficients A_n are determined using the theory of Fourier cosine series and using the nonhomogeneous B.Cs in Eq. (18), the solution for u_D may be written as

$$u_D = -\frac{2\bar{U}_{\text{ch}}}{\pi} \sum_{n=0}^{\infty} \frac{((-1)^n - 1)}{n} \frac{\sinh(n\pi y/w)}{\sinh(n\pi h/w)} \sin(n\pi z/w) \tag{22}$$

For u_P, the solution of the nonhomogeneous PDE in Eq. (19) is found to be:

$$u_P(y,z) = \frac{\Delta p}{2\mu l} \left[z^2 - wz - \frac{4w^2}{\pi^3} \sum_{n=0}^{\infty} \left(\frac{((-1)^n - 1)}{n^3} \right) \times \frac{\sinh(n\pi y/w) + \sinh(n\pi(h-y)/w)}{\sinh(n\pi h/w)} \sin(n\pi z/w) \right] \tag{23}$$

The volumetric flow per unit width

$$\frac{1}{w} \int_0^w \int_0^h (u_D + u_P) dy dz$$

is thus found to be

$$q = \frac{\bar{U}_{\text{ch}} h}{2} F_D - \frac{h^3 \Delta p}{12 \mu l} Fp \tag{24}$$

$$q^* = \frac{1}{2}F_D - \frac{1}{12}\overline{\mathrm{Re}}\,\mathrm{Eu}\,Fp \tag{25}$$

Equation (24) has the same general form as that of q in Table 1. The coefficients F_D and F_P are shape factors that depend on the aspect ratio w/h and are defined by

$$F_D = \frac{4w/h}{\pi^3}\sum_{n=1}^{\infty}\frac{((-1)^n-1)^2}{n^3}\frac{\cosh(n\pi h/w)-1}{\sinh(n\pi h/w)} \tag{26}$$

$$F_P = (w/h)^2 - \frac{48(w/h)^3}{\pi^5}\sum_{n=1}^{\infty}\frac{((-1)^n-1)^2}{n^5}\frac{\cosh(n\pi h/w)-1}{\sinh(n\pi h/w)} \tag{27}$$

In the moving wall situation the same procedure is used to derive the drag velocity component and its shape factor, imposing new boundary conditions, while the same results will be considered for the pressure velocity component and shape factor since there is no change on the B.Cs. So, the new boundary conditions for u_D are as follows

$$u_D(h,z) = u_D(y,w) = u_D(y,0) = \bar{U}_{\mathrm{ch}}, \quad u_D(0,z) = 0 \tag{28}$$

Using separation of variables, the general solution of the homogeneous PDE in Eq. (17), which satisfies the B.Cs in Eq. (28), may be found using the superposition to be:

$$u_D = \sum_{n=0}^{\infty} C_n \sinh(n\pi(h-y)/w)\sin(n\pi z/w) - \bar{U}_{\mathrm{ch}} \tag{29}$$

The coefficients C_n are determined using Fourier cosine series and the nonhomogeneous B.C in Eq. (28), which leads to the following solution on u_D:

$$u_D = \bar{U}_{\mathrm{ch}}\left(1 + \frac{4}{\pi}\sum_{n=0}^{\infty}\frac{(-1)^n}{(2n+1)}\frac{\sinh((2n+1)\pi(h-y)/w)}{\sinh((2n+1)\pi h/w)} \times \sin((2n+1)\pi z/w)\right) \tag{30}$$

Solving for the volumetric flow per unit width in Eq. (24), F_D is found to be

$$F_D = 2 + \frac{4w/h}{\pi^3}\sum_{n=1}^{\infty}\frac{((-1)^n-1)^2}{n^3}\frac{1-\cosh(n\pi h/w)}{\sinh(n\pi h/w)} \tag{31}$$

while F_P is still given by Eq. (27).

4 Numerical Modeling

The computational fluid dynamics (CFD) simulations of a spiral grooved micropump presented in this section have been carried out using Fluent 6.1. This CFD package uses the finite volume method (FVM) for solving the Navier-Stokes equations. It also enables the use of different discretization schemes and solution algorithms, together with different types of boundary conditions.

4.1 Model Setup. For the CFD simulations a full 3D model of the spiral micropump has been built for different aspect ratios, and at constant polar slope, starting radius, and angular span. Obtained geometry was exported to the preprocessor of the CFD package, Gambit, which is investigated to generate the mesh and name the faces as the boundary conditions are.

4.2 Mesh Generation and Boundary Conditions. A structured grid with hexahedral elements is used. The inlet face is firstly meshed by dividing the height and width edges into regular divisions with one unit length which is scaled later to 1 μm. Then, the spiral edge of the moving wall is divided into 360 units. After that the volume is meshed with the hexahedral elements. Different meshes were used to determine the element size, shape, and arrangement to ensure grid independent solution. This independent solution is assured by increasing the number of edge grid points by 10% or 20% per trial until the outlet mass fluxes and the velocity components through the micropump channel varied by less than 0.2%. For example, when $w/h=0.5$ the number of grid points was increased from 18,000 to 23,760 and the flow rate varied by less than 0.154%.

The boundary conditions were defined for Fluent 5/6 at the inlet to the spiral channel to be pressure inlet, and pressure outlet at the exit. For the moving situation, the upper, interior and exterior walls were defined as a wall, labeled moving and the bottom wall was also defined as a wall, but labeled stationary as shown in Fig. 2, while for the stationary situation the upper wall was defined as a wall, labeled moving and the bottom, interior and exterior walls were also defined as a wall, but labeled stationary. After saving the models, they have been exported to fluent.

4.3 Physical Modeling. After reading the mesh file and scaling it to the micrometer scale, a check for the grid was carried out to ensure that no negative minimum volume value existed. Then the model is employed to be steady, viscous, laminar, without considering the energy equation, and the solver to be segregated. SAE10W30 motor oil with 825 kg/m^3 density and 0.0901 kg/m s viscosity were defined as the interior fluid. In the boundary conditions menu the values for the outlet pressure and moving walls were assigned for each case. The Simple-Consistent algorithm was used for the pressure velocity coupling, which has the same steps as the SIMPLE algorithm [17], with the difference that the momentum equations are manipulated so that the SIMPLEC velocity correction equations omit terms that are less significant than those omitted in SIMPLE. In addition, a second order upwind scheme was used for the momentum equations while a second order pressure interpolation scheme is used for pressure.

In the present work the scaled residual for the continuity and momentum equations was used because it is much simpler to judge the convergence of the scaled over the unscaled equations and it is an appropriate indicator for most problems. The solver iterated the equations until the scaled residuals were less than 10^{-5} or until it stabilized at a constant value, which is still small enough to ensure convergence, this can be best viewed by plotting the residuals of the simulation versus the iterations for the continuity equation and the velocity components as appeared in Fig. 3. In the segregated solver, the mass imbalance is used to monitor the convergence of the solution. This quantity should be small compared to the average mass flow rate. For example, when $w/h=0.5$ the mass imbalance was 6.729×10^{-8} nl/s while the inlet mass flow rate was 0.4815 nl/s and this value is very small compared to inlet mass flow rate.

Also, for the purpose of judging convergence together with grid independence the area-weighted average values was estimated at a surface with $\theta=90$ deg from the inlet. For the x velocity this quantity was found to be 5.0053×10^{-10} in dimensionless form with respect to the velocity of the perimeter of the disk. The grid was then adapted and the solution was reconverged. It was noticed that the area-weighted average became closer to 5.0371×10^{-10}. This verifies the convergence of the solution and indicates that it is grid independent.

5 Results and Discussion

To investigate the effect of aspect ratio on pump performance, an analytical solution has been developed, which accounts for the aspect ratio in the spiral channel, and a number of 3D finite volume numerical models were built with different aspect ratios. Obtained numerical results can be used to verify the assumptions employed in the analytical solutions. By examining the axial velocity field at different cross sections along the channel, as illustrated in Figs. 4(a) and 4(b), it may be seen that the axial velocity contour plots are symmetric around the axial middle plane of the

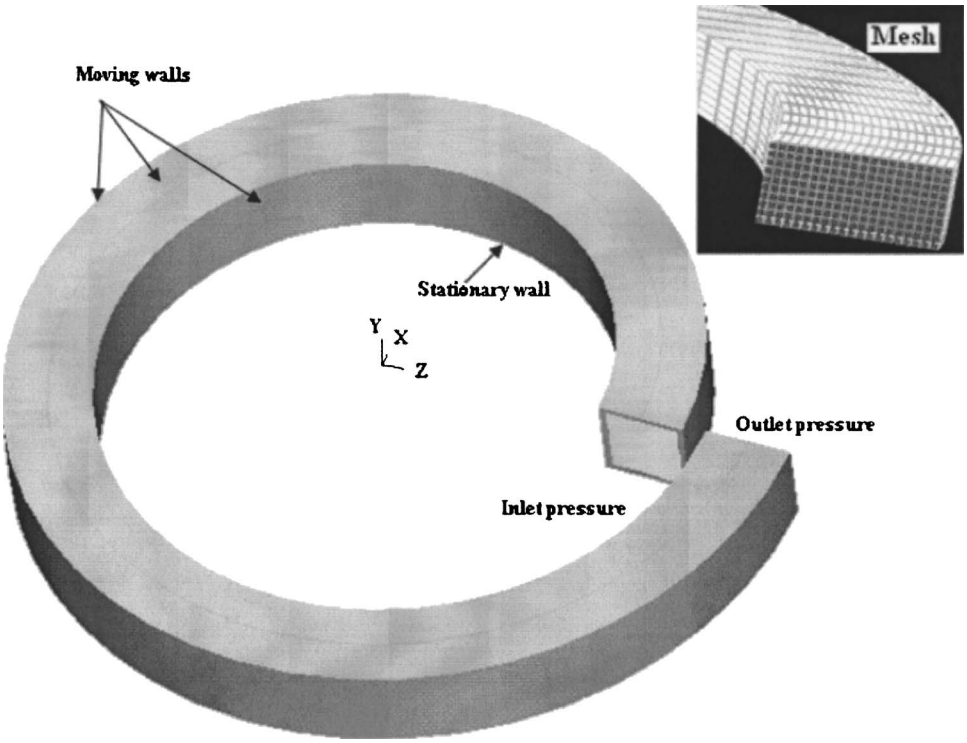

Fig. 2 Three-dimensional flow model

channel for different values of pressure head. Such a profile is repeated for different sections along the channel, and verifies that the flow field is symmetric around the middle axial plane of the channel.

A plot of two streamlines taken along the channel from the inlet to the outlet is shown in Fig. 5. It is seen that the streamlines are parallel to one another and parallel to the channel boundary. This verifies that the curvature of the spiral can be neglected, which allowed neglecting the centrifugal forces in the analytical solution. If the curvature effect was significant, then the centrifugal forces would shift the stream lines in Fig. 5 close to one another at the end of the channel.

Table 3 present a comparison between the dimensionaless analytical flow rates obtained from Eq. (26), and the corresponding values obtained from the numerical simulations for the stationary walls situation, while Table 4 presents the same comparison for the case of moving walls. Figures 6 and 7 show a graphical representation of these results. Numerical and analytical predictions

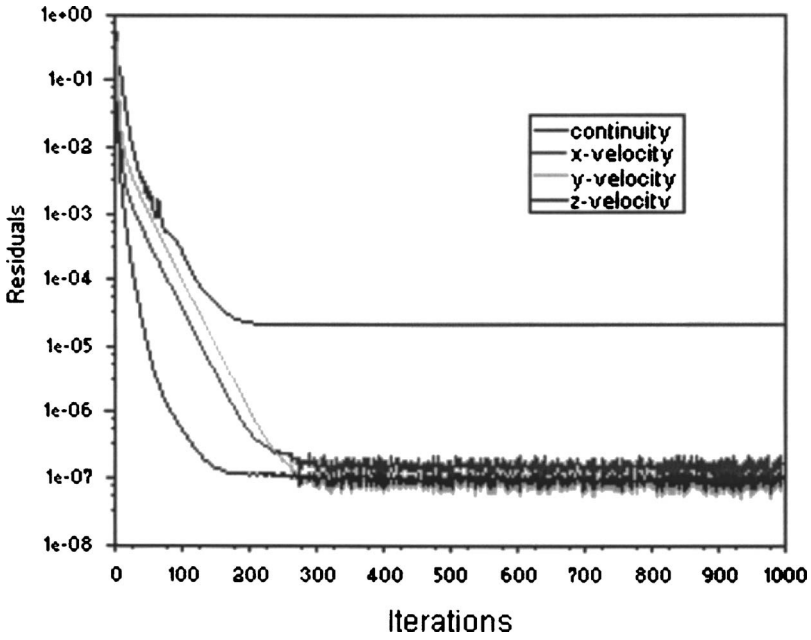

Fig. 3 Residuals of the numerical simulations after 1000 iterations

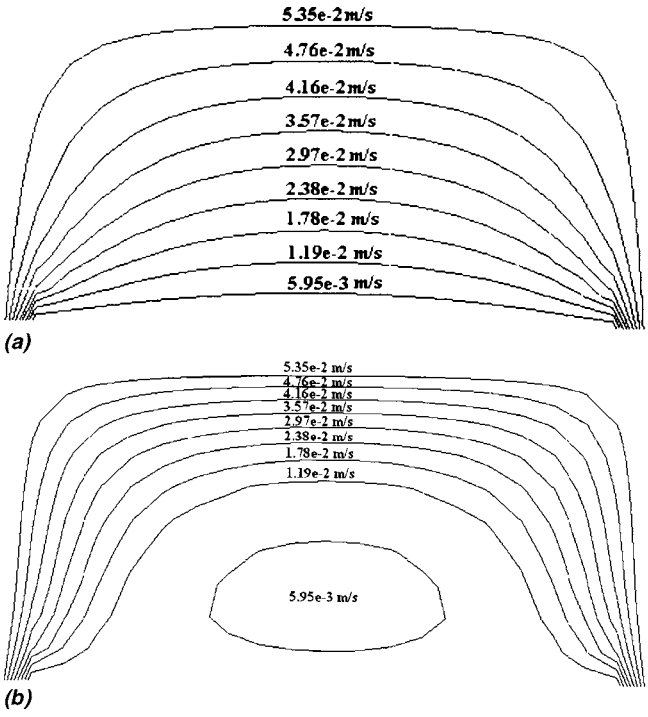

Fig. 4 (*a*) Contour lines for the axial velocity field across the channel ($w/h=2$, $\omega=500$ rpm, and $\Delta P=0.0$ kPa). (*b*) Contour lines for the axial velocity field across the channel ($w/h=2$, $\omega=500$ rpm, and $\Delta P=1750$ kPa).

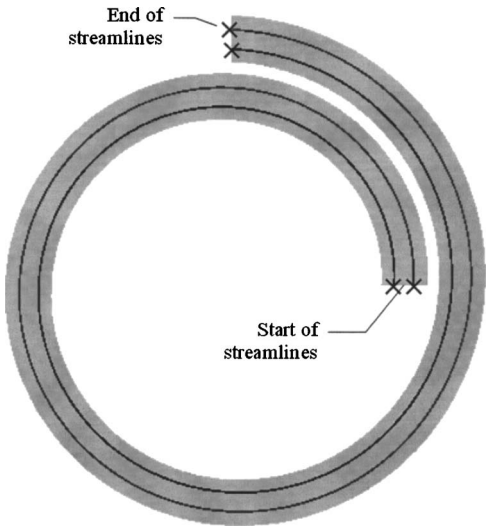

Fig. 5 Streamline plots along the channel

are in very good agreement for the full range of aspect ratios considered, and show that the effect of sidewalls could be neglected when $w/h \geq 10$. For $w/h < 10$, neglecting the effect of sidewalls leads to an error in the analytical flow rate predictions which exceeds 5%. The approximate 2D analytical solution [14] developed for infinite aspect ratio, neglects the effect of side walls and assumes uniform velocity distribution across the channel width and has such an error. The error of the analytical solution presented in this study is summarized in Tables 3 and 4 for the cases of stationary and moving walls and is found to be less than 4% for the whole range of w/h.

The value of the acceptable error in flow rate predictions depends on the specific applications for which the micropump is used. For example, the accuracy required in pharmaceutical and medical microdevices will generally be higher than that needed in electronics cooling or inkjet printing applications. The aspect ratio achievable depends on the used fabrication technology. For example, surface micromachining allows very shallow channels usually less than 10 microns in height giving an aspect ratio value larger than 10. Deep reactive ion etching (DRIE), on the other hand, allows very deep channels reaching hundreds of microns in height and an aspect ratio of 0.5 or less may easily be achieved.

For both the stationary and moving wall situations, Figs. 6 and 7 show that the flow rate varies linearly with both the pressure difference and boundary velocity. This is consistent with the linear lubrication model employed. On the other hand, as $w/h \rightarrow 0.0$, the values of q^* approaches zero for the stationary walls situation and approaches the plug flow value ($q^*=1$) for the moving walls situation for the whole range of $\overline{\mathrm{Re}}\,\mathrm{Eu}$. When $w/h \rightarrow \infty$, q^* drops linearly from a value of 0.5 at $\overline{\mathrm{Re}}\,\mathrm{Eu}=0.0$ to a value of zero at $\overline{\mathrm{Re}}\,\mathrm{Eu}=6.0$ in both the stationary and the moving walls solutions.

The available experimental data for the macroscale model [14] has a high viscous dissipation effect which causes a temperature rise in the pumped fluid and in turn decreases its viscosity. This causes the experimental flow rate to be lower than that the analytical or numerical predictions, particularly for high values of $\overline{\mathrm{Re}}\,\mathrm{Eu}$. Figure 8 shows the experimental, analytical, and numerical flow rates for $w/h=3.2$ for the case of moving walls. The figure shows a close agreement between the experimental and the theoretical results for low values of $\overline{\mathrm{Re}}\,\mathrm{Eu}$. At high values of $\overline{\mathrm{Re}}\,\mathrm{Eu}$, a large deviation between the experimental and the theoretical results is observed. This deviation can be attributed to the effect of viscous dissipation and the effect of cross flow in the gap below the spiral wall in the scaled up model, which is increased with increasing pressure difference.

The differences between the approximate 2D analytical solution for infinite aspect ratio and the numerical solution is referred to the approximations considered in the approximate analytical solution that neglects the curvature of the spiral and replaces it with an equivalent straight channel, which is further simplified using symmetry into the 2D flow in its middle plane. The three-dimensional consideration in solving the Navier-Stokes equations numerically

Table 3 Volumetric flow rates for different values of w/h and $\overline{\mathrm{Re}}\,\mathrm{Eu}$ (stationary wall)

w/h	$\overline{\mathrm{Re}}\,\mathrm{Eu}$	q^*_{num}	q^*_{ana}	% error	w/h	$\overline{\mathrm{Re}}\,\mathrm{Eu}$	q^*_{num}	q^*_{ana}	% error
0.1	0.0	0.017	0.027	37.04	2.00	0.0	0.366	0.364	0.55
	1.5	0.016	0.026	38.46		1.5	0.278	0.279	0.36
	3.0	0.014	0.025	44.00		3.0	0.191	0.193	1.036
	4.5	0.013	0.024	45.83		4.5	0.103	0.108	4.63
0.5	0.0	0.137	0.135	1.48	5.00	0.0	0.447	0.445	0.45
	1.5	0.113	0.114	0.877		1.5	0.336	0.336	0
	3.0	0.090	0.092	2.174		3.0	0.224	0.227	1.322
	4.5	0.066	0.071	7.042		4.5	0.113	0.118	4.2373
1.0	0.0	0.251	0.250	0.40	10.0	0.0	0.475	0.471	0.8493
	1.5	0.196	0.197	0.508		1.5	0.415	0.413	0.4843
	3.0	0.142	0.145	2.07		3.0	0.355	0.354	0.2825
	4.5	0.087	0.092	5.435		4.5	0.236	0.237	0.4219

Table 4 Volumetric flow rates for different values of w/h and $\overline{\mathrm{Re}}\,\mathrm{Eu}$ (moving wall)

w/h	$\overline{\mathrm{Re}}\,\mathrm{Eu}$	q^*_{num}	q^*_{ana}	% error	w/h	$\overline{\mathrm{Re}}\,\mathrm{Eu}$	q^*_{num}	q^*_{ana}	% error
0.1	0.0	0.987	0.973	1.44	2.00	0.0	0.638	0.636	0.315
	1.5	0.985	0.972	1.34		1.5	0.550	0.550	0.00
	3.0	0.980	0.971	0.93		3.0	0.462	0.464	0.431
	4.5	0.980	0.969	1.14		4.5	0.375	0.379	1.06
0.5	0.0	0.867	0.865	0.23	5.00	0.0	0.556	0.555	0.18
	1.5	0.843	0.843	0.00		1.5	0.445	0.446	0.224
	3.0	0.820	0.822	0.243		3.0	0.334	0.337	0.89
	4.5	0.796	0.801	0.624		4.5	0.222	0.228	2.63
1.0	0.0	0.753	0.750	0.40	10.0	0.0	0.529	0.529	0.00
	1.5	0.698	0.698	0.00		1.5	0.410	0.412	0.485
	3.0	0.644	0.645	0.155		3.0	0.290	0.295	1.70
	4.5	0.589	0.592	0.507		4.5	0.171	0.178	3.93

Table 5 Effect of channel aspect ratio on the drag and pressure shape factors. Analytical and numerical results are compared.

	Moving walls			Stationary walls			Moving and stationary walls		
w/h	$F_{d,\mathrm{num}}$	$F_{d,\mathrm{ana}}$	% error	$F_{d,\mathrm{num}}$	$F_{d,\mathrm{ana}}$	% error	$F_{p,\mathrm{num}}$	$F_{p,\mathrm{ana}}$	% error
0.5	1.734	1.7297	0.249	0.274	0.2703	1.369	0.1703	0.1715	0.6997
1.0	1.506	1.5003	0.38	0.502	0.4997	0.460	0.4365	0.4217	3.510
2.0	1.276	1.2711	0.386	0.732	0.7289	0.425	0.6858	0.686	0.029
5.0	1.112	1.1107	0.117	0.894	0.8898	0.472	0.8921	0.8739	2.082
10.0	1.058	1.0575	0.047	0.95	0.9425	0.796	0.9568	0.9371	2.102
15.0	1.03	1.041	1.057	0.958	0.959	0.104	0.9976	0.9588	4.047

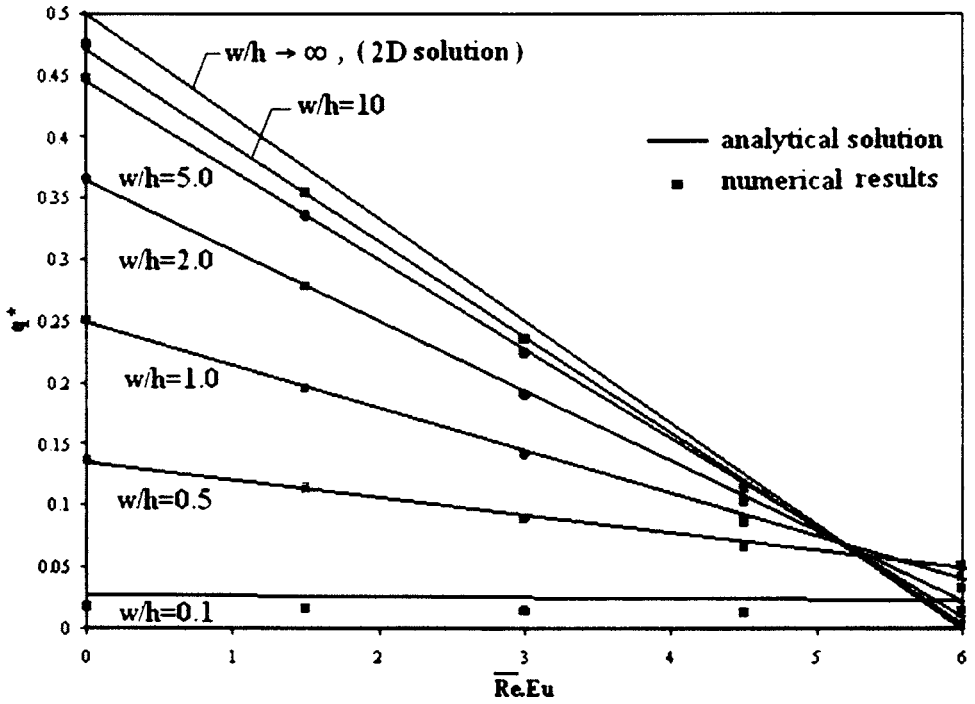

Fig. 6 Flow rate versus pressure head (stationary walls)

is also a source of results differences. So, the 2D analytical solution can be applied for aspect ratios of 10 or greater.

It is also interesting to consider the case where the direction of disk rotation is reversed while the pressure at the inlet and outlet are maintained the same. This situation may be encountered for examples in situations where the pump is used to accelerate a naturally occurring flow from high to low pressure. Considering the assumptions used to arrive at Eq. (24) for the volumetric flow rate and Eq. (30) for the velocity distribution; it is noted that reversing the direction of the disk rotation will only reverse the

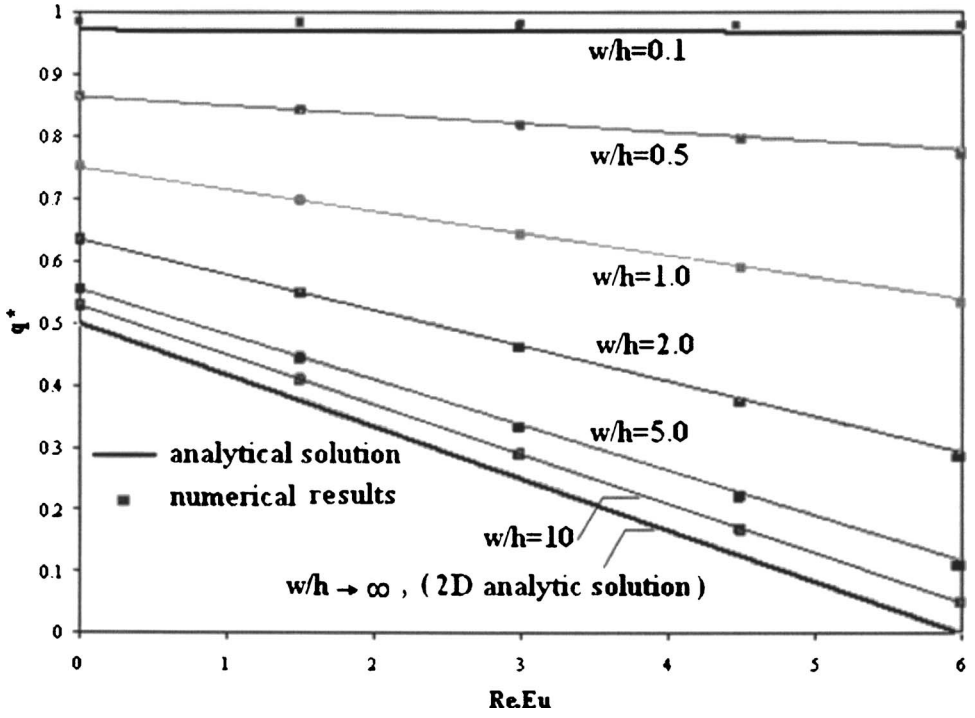

Fig. 7 Flow rate versus pressure head (moving walls)

sign of $\bar{U}_{ch}$. If the disk rotates in the clockwise (CW) direction instead of counterclockwise (CCW) direction, the nondimensional flow rate equation becomes

$$q^* = -\frac{1}{2}F_D - \frac{1}{12}\overline{\mathrm{Re}}\,\mathrm{Eu}\,Fp \tag{32}$$

which indicates that reversing disk rotation will merely shift the flow lines in Figs. 6 and 7 by $-F_d$ along the y-axis. This is shown in Fig. 9 for the moving wall situation both numerically and analytically.

Table 5 presents the effect of aspect ratio on the drag and pressure shape factors for the analytical and numerical results at the moving and stationary walls situations. Those results are also shown graphically in Figs. 10 and 11. Theoretical results showed that the drag shape factor approaches unity as $w/h \to \infty$, and that the numerical results are best fitted with that. It is also shown that as $w/h \to 0$, F_d has a value of 2 in the moving walls case and a value of zero at the stationary case. Meanwhile F_p has the same trend in both cases since there is no effect of moving boundary on this shape factor. Figure 11 shows that the value of F_P increases with increasing w/h, and goes to unity at high values of aspect ratio. Numerical values for F_d and F_P are in very good agreement with the analytical values.

In the 3D straight channel flow problems, the flow may be treated as a 2D flow when the channel height is very small compared to its width. In the present study, the numerical solution has been carried out on the full 3D geometry, taking into account the effect of sidewalls and the spiral curvature for the whole range of aspect ratios ($0 < w/h < \infty$). In the analytical solution, however, the flow field in the middle cross plane was analyzed, and the boundary conditions for the top and sides were taken from their value in that plane. The y- and z-coordinates in Eq. (12) represent

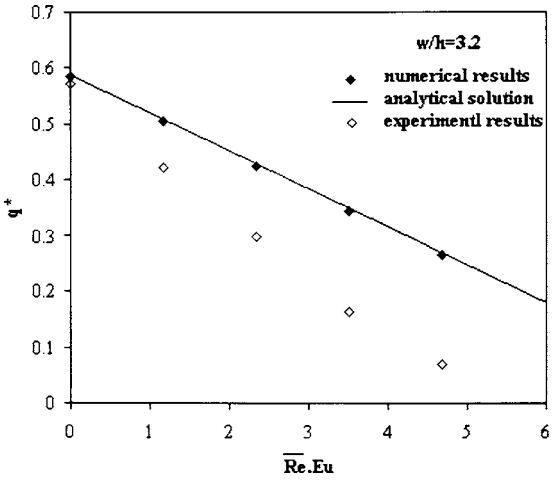

Fig. 8 Experimental, numerical, and analytical flow rate versus pressure head (moving walls)

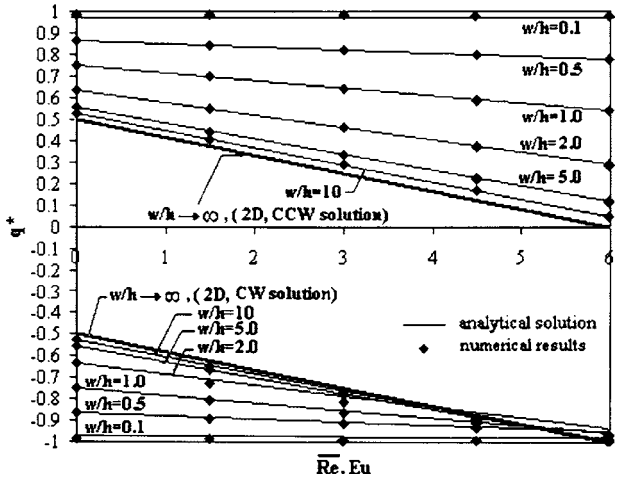

Fig. 9 Flow rate versus pressure head for CW and CCW disk rotation (moving walls)

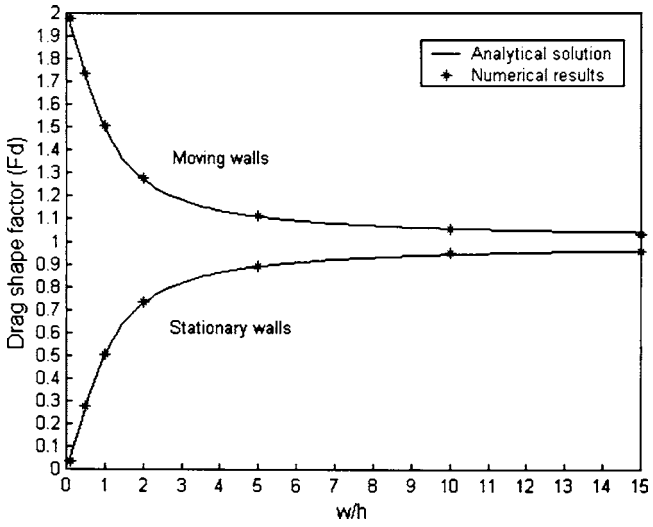

Fig. 10 Effect of aspect ratio on the drag shape factor (moving and stationary walls)

the width and height of the channel, respectively. Equation (26) provides a general analytical solution for the flow rate through the spiral channel for the full range of aspect ratios in terms of pressure and drag shape factors F_d and F_p. The flow rate values given by this equation were found in very good agreement with the numerical solutions for the considered assumptions on Re and the spiral curvatures. Figures 10 and 11 show the analytical values of F_d and F_p for the full range of w/h and the numerical values of these parameters for $w/h=0.1$, 0.5, 1.0, 2.0, 5.0, and 10.0 at moving and stationary walls.

When $w/h \to \infty$, the basic difference between the channel model investigated in this study, and that of the classical Couette-Poiseuille model, is that the upper boundary velocity is not constant but is a function of axial distance along the channel. However, since the flow field in this problem is described by the linear lubrication model, the flow rate is found to be equivalent to that of a Couette-Poiseuille flow with an upper boundary velocity equal to the average velocity of the spiral channel.

To investigate the range of Reynolds number where the analytical model can be successfully applied, Table 6 shows the numerical and analytical values of q^* for various values of $\overline{\mathrm{Re}}$ at $w/h=1$ and at $w/h=5$. The table shows that the analytical solution can be successfully applied for $\overline{\mathrm{Re}} \leq 1$, where the error is less than 6%. For $\overline{\mathrm{Re}}=10$, the error in the analytical solution reaches 12%.

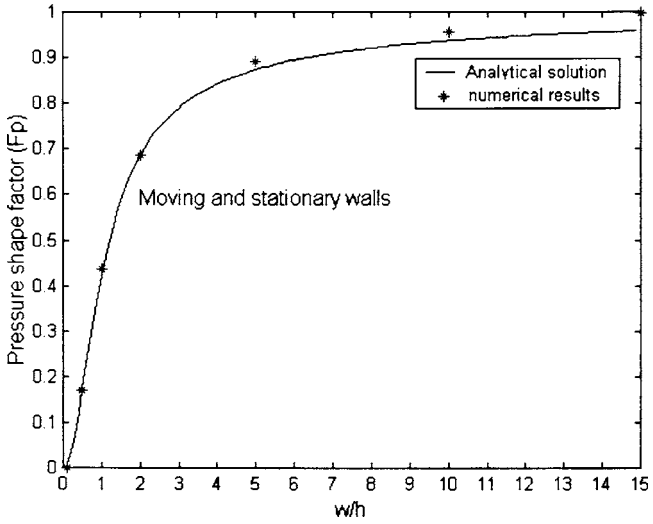

Fig. 11 Effect of aspect ratio on the pressure shape factor

Table 6 Effect of $\overline{\mathrm{Re}}$ on analytical and numerical flow rates

w/h	$\overline{\mathrm{Re}}$	$q^*_{\mathrm{numerical}}$	$q^*_{\mathrm{analytical}}$	% error
1.00	0.05	0.753	0.75	0.400
	0.20	0.751	0.75	0.133
	0.50	0.745	0.75	0.667
	1.00	0.733	0.75	2.267
	6.25	0.681	0.75	9.200
	8.50	0.669	0.75	10.80
	10.0	0.660	0.75	12.00
5.00	0.05	0.556	0.555	0.180
	0.20	0.553	0.555	0.360
	0.50	0.543	0.555	2.162
	1.00	0.524	0.555	5.586
	6.25	0.505	0.555	9.01
	8.50	0.495	0.555	10.81
	10.0	0.487	0.555	12.25

6 Conclusions

Viscous drag micropumps are attractive because they are easy to fabricate, capable of handling a wide variety of fluids, and can operate with no valves allowing them to handle particle-laden fluids. This paper has presented an investigation for the effect of channel aspect ratio on the flow performance of a newly introduced spiral-channel viscous micropump. Both stationary walls and moving walls configurations were studied. Based on the assumption that the inertia terms are negligible compared to the viscous terms, the Navier-Stokes equation could be reduced into the linear form known as the lubrication model. This assumption was verified numerically for the full range of aspect ratios investigated, and an analytical solution for the flow field was developed, which accounts for a finite wall height. The analytical flow rates were compared with those obtained from a numerical finite volume solution for several 3D models of the spiral pump at different aspect ratios, and were found in good agreement and tend to support one another. The results are also compared to an approximate 2D analytical solution developed for infinite aspect ratio, which neglects the effect of sidewalls, and assumes uniform velocity distribution across the channel width. The error in this approximation was found to exceed 5% for $w/h \leq 10$. The deviation of the flow rate from the 2D approximate solution could be expressed analytically using pressure and drag and shape factors, which describe the effect of pressure difference and boundary velocity on the flow rate at various aspect ratios. Also, it has been found that the flow rate varies linearly with both the pressure difference and boundary velocity, which supports the validity of the linear lubrication model employed. Comparing numerical and analytical values of q^* for various values of $\overline{\mathrm{Re}}$ and w/h shows that the developed analytical solution can be successfully applied for $\overline{\mathrm{Re}} \leq 1$, where the error is less than 6%.

Acknowledgment

The authors wish to acknowledge the support received from the Deanship of Scientific Research, and the Mechanical Engineering Department at the University of Jordan.

Nomenclature

Eu = Euler number
Fr = Froude number
F_D = drag shape factor
F_P = pressure shape factor
g = gravitational acceleration
h = height
k = polar slope

l = spiral curvature length
q = volume flow rate per unit width
P = pressure
r = spiral radius
Re = Reynolds Number
t = time
u = x-velocity component
u_{ch} = channel boundary velocity
u_D = drag velocity component
u_P = pressure velocity component
U = fluid velocity
$\bar{U}_{ch}$ = average channel velocity
v = y-velocity components
w = channel width
w_t = wall thickness
x,y,z = Cartesian coordinates

Greek Symbols

δ_{ij} = Kronecker delta
Δ = difference operator
ρ = fluid density
τ_{ij} = shear stress tensor
μ = dynamic viscosity
ω = angular velocity
θ = spiral angle

Subscripts

a = average
ch = channel
i,j,k = coordinate direction indices
D = drag
o = initial/characteristic
P = pressure

Superscript

$()^*$ = nondimensional variable
$()'$ = first derivative
$\bar{()}$ = average/reduced

References

[1] Terry, S. C., Jerman, J. H., and Angell, J. B., 1979, "A Gas Chromatographic Air Analyzer Fabricated on a Silicon Wafer," IEEE Trans. Electron Devices, **ED-26**(12), pp. 1880–1886.

[2] Manz, A., Miyahara, Y., Miura, J., Watanabe, Y., Miyagi, H., and Sato, K., 1990, "Design of an Open-Tubular Column Liquid Chromatograph Using Silicon Chip Technology," Sens. Actuators B, **1**, pp. 249–255.

[3] Harrison, D. J., Manz, A., Fan, Z., Ludi, H., and Widmer, H. M., 1992, "Capillary Electrophoresis and Sample Injection Systems Integrated on a Planar Glass Chip," Anal. Chem., **64**, pp. 1926–1932.

[4] Wilding, P., Shoffner, M. A., and Kricka, L. J., 1994, "PCR in a Silicon Microstructure," Clin. Chem., **40**(9), pp. 1815–1818.

[5] Kaplan, W., Elderstig, H., and Vieider, C., 1994, "A Novel Fabrication Method of Capillary Tubes on Quartz for Chemical Analysis Applications," *Proc. IEEE MEMS '94, Int. Conf. MEMS*, Oiso, Japan, pp. 63–68.

[6] Srinivasan, R., Firebaugh, S. L., Hsing, I., Ryley, J., Harold, M. P., Jensen, K. F., and Schmidt, M. A., 1997, "Chemical Performance and High Temperature Characterization of Micromachined Chemical Reactors," *Proc. Transducers '97*, Chicago, IL, Vol. 1, pp. 163–166.

[7] Smits, J., 1985, "Piezoelectric Pump for Peristaltic Fluid Displacements," Dutch Patent No. 8 302 860.

[8] Van Lintel, H., Van de Pol, F., and Bouwstra, S., 1988, "A Piezoelectric Micropump Based on Micromachining of Silicon," Sens. Actuators, **15**(2), pp. 153–167.

[9] Manz, A., Effenhauser, C., Burggraf, N., Harrison, D., Seiler, K., and Fluri, K., 1994, "Electroosmotic Pumping and Electrophoretic Separations for Miniaturized Chemical Analysis Systems," J. Micromech. Microeng., **4**(4), pp. 257–265.

[10] Woias, P., 2005, "Micropumps-Past, Progress and Future Prospects," Sens. Actuators B, **105**, pp. 28–38.

[11] Sen, M., Wajerski, D., and Gad-El-Hak, M., 1996, "A Novel Pump for MEMS Applications," ASME J. Fluids Eng., **118**(3), pp. 624–627.

[12] Day, R., and Stone, H., 2000, "Lubrication Analysis and Boundary Integral Simulations of a Viscous Micropump," J. Fluid Mech., **416**, pp. 197–216.

[13] Darabi, J., Ohadi, M., and De Voe, D., 2001, "An Electrohydrodynamic Polarization Micropump for Electronic Cooling," J. Microelectromech. Syst., **10**(1), pp. 98–106.

[14] Kilani, M. I., Galambos, P. C., Haik, Y. S., and Chen, C. J., 2003, "Design and Analysis of a Surface Micromachined Spiral-Channel Viscous Pump," ASME J. Fluids Eng., **125**, pp. 339–344.

[15] Dean, W. R., 1927, "Note on the Motion of Fluid in a Curved Pipe," Philos. Mag., **4**, pp. 208–219.

[16] Schlichting, H., 1951, *Boundary Layer Theory*, McGraw-Hill, New York.

[17] Patankar, S. V., 1980, *Numerical Heat Transfer and Fluid Flow*, Hemisphere Publishing, Taylor and Francis Group, New York.

Journal of Fluids Engineering

Technical Briefs

Semi-circular Rods Used to Control Turbulent Boundary Layer Separation at Cylindrical Surface

Andrzej P. Szumowski
e-mail: aszum@meil.pw.edu.pl

Jan Wojciechowski

Institute of Aeronautics and Applied Mechanics,
Warsaw University of Technology,
ul. Nowowiejska 24,
00-665 Warsaw, Poland

Introduction

Flows in the boundary layer are retarded due to skin friction at the body surface. This, in the case of an adverse pressure gradient being present in the flow, leads to boundary layer separation (airplane wings, engine diffusers, axial compressors). To prevent or at least delay this phenomenon, the streamwise momentum of air particles in the boundary layer should be continuously supplemented with the momentum of external flow. Numerous investigations conducted hitherto show that the streamwise vortices generated at the surface appear to be a favorable means of transverse streamwise momentum exchange. Due to such vortices, fluid particles with high momentum are swept toward the surface to mix with the retarded air at the surface, which in turn is swept away from the surface. The mean streamwise momentum of the fluid particles in the boundary layer is thereby increased. Various vortex generators were employed to induce partially helical flow at the boundary layer. Fixed solid vortex generators of both the vane and wing types were used over a long period because of their simplicity and low cost [1–7]. They form an array of small plates or wings projected normally (in the former case) or parallel to the surface (in the latter case) at an angle of incidence to the flow.

Low-profile vortex generators in the form of triangular ramps (Wheeler generators, [8,9]) and the like have been developed in recent years to reduce parasitic drag. Low-profile generators have been observed to possess drag about twice as low as the conventional vane-type generator of the same relative height ($h/\delta=0.4$, where δ is boundary layer thickness).

Streamwise vortices were generated also by means of normal and oblique air jets injected through the wall to the main flow [10,11]. It was observed that this injection is more efficient when normal jets are vigorously swirled to induce the vortex breakdown phenomenon [12] (in each jet). As a result of this, the air of the jets spreads around the orifices, and in this way disturbs only the flow, which is close to the wall.

In the present experimental study a fixed solid generator in the form of semi-circular rods settled on the surface at an oblique angle to the main stream is considered. It is expected that a generator of this type demonstrate high efficiency. This supposition results from following observations: (i) Air particles which pass over the top of the rod (like over a bump) accelerate and reach velocity larger then the external flow velocity. (ii) The streamwise momentum of air locally enhanced in this way, is transferred with a streamwise vortex to the near wall flow region.

The considered generator was examined in delaying the boundary layer separation at a convex cylindrical surface. Such a surface is appropriate to the present basic investigations because the flow over the cylindrical surface is separated for each Reynolds number, which is of practical significance.

Apparatus and Measuring Technique

The experiments were conducted in an open circuit wind tunnel of rectangular cross section 1×1 m. In its aft section there was a bump composed of two cylindrical surfaces joined together with a plane surface (Fig. 1). Due to this location, the flow which separated at the downstream cylindrical surface (test surface) did not reattached to the tunnel floor. The fully developed turbulent boundary layer of 18 mm in thickness existed at the end of the plane surface of the bump.

In the majority of experiments the semi-circular rods used to generate streamwise vortices were set up in a continuous tooth line (tooth generator). Several tests were also conducted with an array of V-generators of various pitch distance. In both cases the generators were settled on the trailing part of the plane section preceding the cylindrical surface.

The main of results, which enabled the authors to estimate the effect of the vortex generator, were obtained from pressure measurements at several points distributed along the cylindrical surface in the symmetry plane of the test section of the tunnel. Complementary data were collected from surface visualization with a suspension of titanium white in oil.

Results

Figure 2 shows streamwise pressure distributions along the cylindrical surface for several values of Reynolds number, based on the radius of the cylindrical surface, in the case when the vortex generator was absent (here, p is the relative pressure related to p_∞ and $q=\rho V_\infty^2/2$). As can be seen in this figure, the surface pressure initially decreases, reaches a minimum and then increases again as long as the boundary layer is attached to the cylinder surface. There are two opposite reasons for this behavior. The first one is a result of the air particles that initially move parallel to the plane section of the bump, and then turn to follow the cylinder surface. As a result, the pressure increases across the streamlines in a radial direction, and as a consequence of this the wall pressure drops below the pressure in the preceding plane section. The sec-

Contributed by the Fluids Engineering Division of ASME for publication in the JOURNAL OF FLUIDS ENGINEERING. Manuscript received May 23, 2005; final manuscript received October 13, 2005. Assoc. Editor: James A. Liburdy.

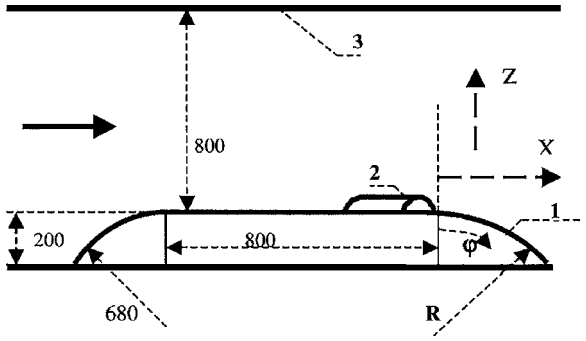

Fig. 1 Aft section of wind tunnel. 1—test contour, 2—vortex generator, 3—roof of wind tunnel; dimensions in mm.

ond reason is a result of the divergence of streamlines; this results in an increase in wall pressure. The former is dominant over the latter one in the leading section of the cylinder. It can be noted that the streamwise pressure distribution and thereby location of separation remains independent of the Reynolds number in the range under consideration. Analogous behavior shows the flow over a free cylinder in the case of turbulent boundary layer separation.

Pressure distribution $p(\varphi)$ changes considerably when the tooth vortex generator is installed ahead of the cylindrical test contour (Fig. 3). The minimum pressure decreases and its location shifts downstream. Simultaneously the maximum positive pressure gradient decreases. In this way the site where the surface pressure reaches pressure in infinity p_∞ is delayed. The delay increases as the height (h) of the generator is increased within the range of 0–0.5 of boundary layer thickness; for higher generators the delay remains nearly constant. This effect is justified when the flow velocity profile in the boundary layer at $x=0$ is taken into account where the flow velocity at $z/\delta=0.5$ reaches 95% of external flow velocity.

The curve marked "SCR" in Fig. 3(b) displays the time mean pressure distributions obtained in the case when a semi-cylindrical rod of a diameter $d=24$ mm was settled across the flow, instead of a tooth generator. In this case, spanwise vortices in shear layer are generated and shed downstream; now the flow is separated practically at the entire cylindrical surface.

Taking into account the pressure distribution $p(\varphi)$ for any case (with or without a vortex generator of any height), we estimate the separation forepart to be the point where the tangential for the maximal $dp/d\varphi$ crosses the line $p=0$. Figure 4 shows the angular

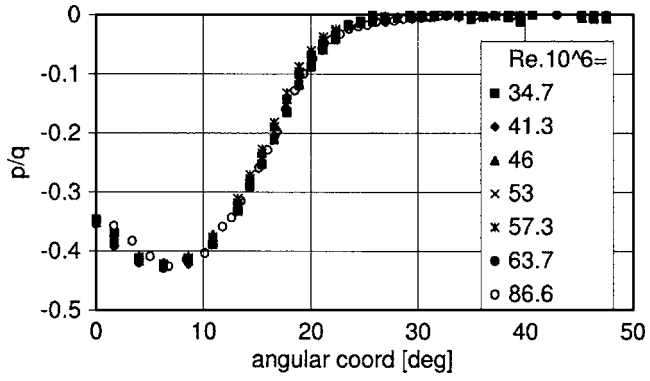

Fig. 2 Streamwise surface pressure distribution for nonmanipulated boundary layer. Reynolds number referred to the cylinder radius *R*. Open symbol ○: *R*=680 mm; remaining symbols *R*=500 mm. Symbols ○ and ● correspond to the same flow velocity: *V*=19.1 m/s.

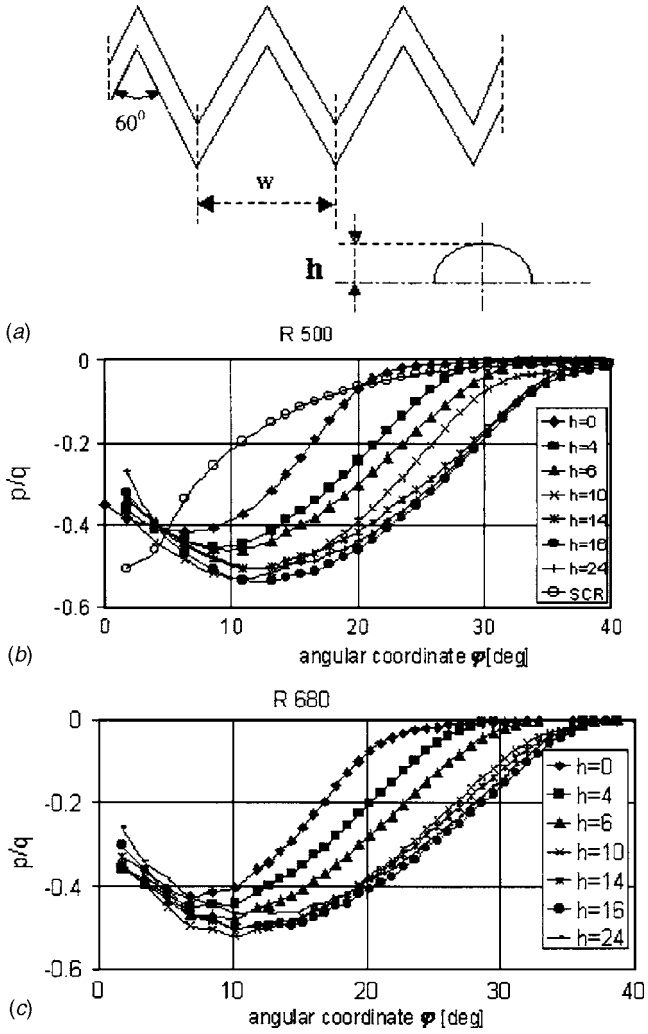

Fig. 3 Tooth vortex generator (a), streamwise surface pressure distribution *R*=500 mm (b), and 680 mm (c). *w*/*h*=10, $q=\rho V^2/2$; symbol ○: (SCR)—singular semi-circular rod across the flow.

coordinate of a point defined as above (called below as the separation angle φ_s) obtained in this way as a function of the height of the tooth generator for two cylinders $R=500$ and $R=680$ mm.

It is observed for both cylinders that the separation angle in the case when the vortex generator was absent does not show any distinguishable difference, and it is about 22°. In the case when the vortex generator is used, φ_s is slightly larger for $R=500$ mm than φ_s for $R=680$ mm. This occurs because the distance at which the vortex decays is, to some extent, independent of the cylinder radius. The same distance corresponds to the larger angle in the case of a lower R. As a consequence, φ_s for $R=500$ is larger than

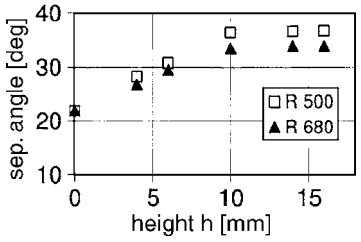

Fig. 4 Angular coordinate of separation point

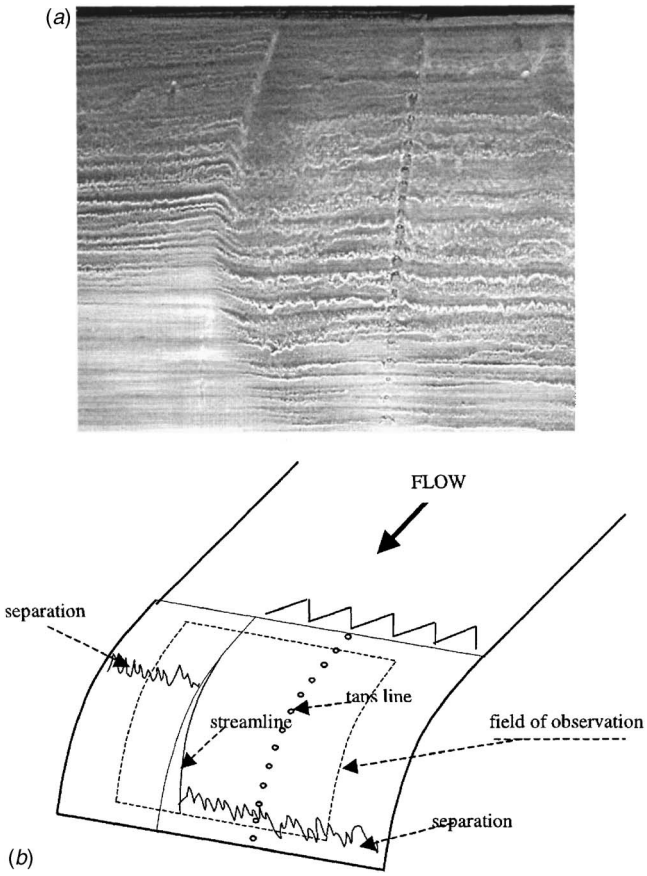

Fig. 5 Photograph of the oil layer on the cylindrical surface (a) and its explanation (b)

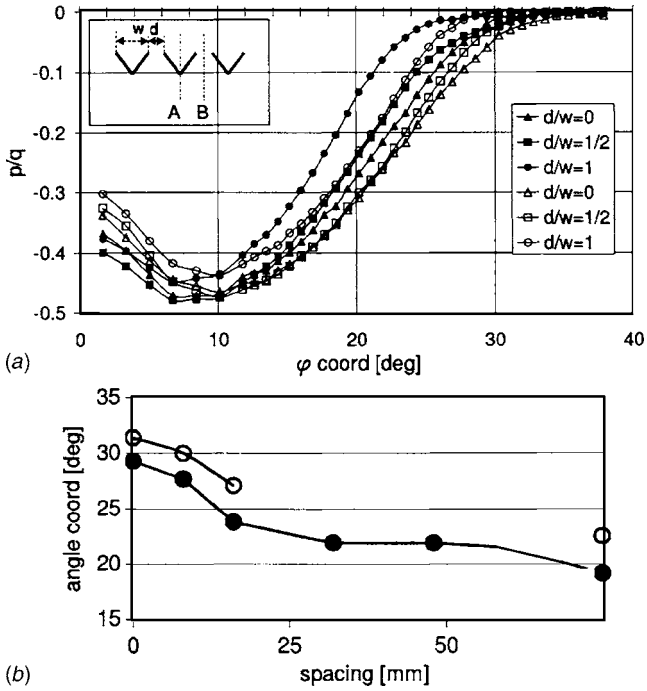

Fig. 6 Streamwise pressure distribution for array of V-generators (a) and angles of separation (b); empty symbols—downstream edge (line A); filled symbols—symmetry plane (line B); h=14 mm

φ_s for R=680 mm, in spite of the larger pressure gradient dp/ds (s is the coordinate along the cylinder contour) for a lower cylinder.

The visual effect of the vortex generator can be observed in the photograph in Fig. 5(a). It shows a section of the cylindrical surface, initially covered with oil, photographed 20 s after switching on the wind tunnel. During such a short period, washing the oil down an inclined cylindrical surface, which is enhanced by gravity, was not remarkable. The oil particles in the region of attached flow were only slightly moved. The photograph shows two sections divided by a distinct bow line (streamline). The left- and the right-hand sections display the nonmanipulated and manipulated boundary layers, respectively. (the vortex generator in the left section was absent). An explanation of the photograph is given in Fig. 5(b). The curvature of the streamline showing the boundary between the left and right sections is caused by overpressure in the former section with respect to the latter at the same angular coordinate in the range of $\varphi > \approx 5°$ (see pressure distributions for h=0 and h=10 mm in Fig. 3).

The tooth generator can be considered to be an array of V-generators without spacing between them. Figure 6(a) presents surface pressure distributions when the V-generators are spaced out. The pressure distributions were measured along a line drawn through the trailing point of the generator and a line of symmetry between the neighboring generators. Taking these distributions into account, the separation angles (φ_s) defined as above were obtained (Fig. 5(b)). It can be noted that the φ_s obtained from streamwise pressure distribution in the symmetry plane between V-generators is lower than that from pressure distribution downstream of the trailing point.

Concluding Remarks

Streamwise vortices produced by oblique semi-circular rods have been used successfully to transfer the streamwise momentum of external flow to retarded air in the turbulent boundary layer. This occurs as a result of the high velocity of air particles, which accelerate when they pass over the top of the rod and are convected toward the surface. It was observed that a vortex generator consisting of semi-circular rods set up in a tooth line enables one to lengthen the distance of the attached flow at the cylindrical surface by nearly 50% in comparison with the case of a nonmanipulated boundary layer. To attain this, it is sufficient for the height of the vortex generator (radius of semi-circular rods) to be half of the boundary layer thickness. The generator need not be located close before the separation point of the nonmanipulated boundary layer as is recommended for exciting-type generators (Helmholtz resonator [13] or other means of periodic excitation [14]). As a result, the semi-circular rod generators can be used successively in cases in which the location of the separation point cannot be predicted exactly.

The efficiency of the V-generators set up in an array depends on the pitch distance. When it is larger than the width of the generator, the boundary layer in the section of the cylinder corresponding to the spacing between neighboring generators is slightly affected.

References

[1] Lachmann, G. V., 1961, *Boundary Layer and Flow Control. Its Principles and Application*, Pergamon Press, New York.
[2] Simpson, R. J., 1966, "Aspects of Turbulent Boundary Layer Separation," Prog. Aeronaut. Sci., **32**, pp. 457–521.
[3] Chang, P. K., 1976, *Control of Boundary Layer Separation*, McGraw-Hill, New York.
[4] Bragg, M. B., and Gregorek, G. M., 1987, "Experimental Study of Airfoil Performance with Vortex Generators," J. Aircr., **4**, pp. 305–309.

[5] Simpson, R. Y., 1989, "Turbulent Boundary Layer Separation," Annu. Rev. Fluid Mech., **21**, pp. 205–234.
[6] Gad-el-Haq, M., and Bushnell, D. M., 1991, "Separation Control: Review," J. Fluids Eng., **113**, pp. 1–28.
[7] Gad-el-Haq, M., 2000, *Flow Control*, Cambridge University Press, Cambridge, UK.
[8] Rao, D. M., and Koriya, 1988, "Boundary-Layer Submerged Vortex Generators for Separation Control—An Exploratory Study," AIAA Paper 88-3546CP, pp. 839–846.
[9] McCormick, D. C., 1993, "Shock/Boundary-Layer Interaction Control with Vortex Generation and Passive Cavity," AIAA J., **31**(1), pp. 91–96.
[10] Wallis, R. A., and Stuard, C. M., 1962, "On the Control of Shock-Induced Boundary Layer Separation with Discrete Air Jets," Aerodynamic Research Council C.P. No. 595.
[11] Johnson, J. P., and Nishi, M., 1990, "Vortex Generator Jets—Means for Flow Separation Control," AIAA J., **28**(6), pp. 989–994.
[12] Szumowski, A., and Wojciechowski, J., 2005, "Use of Vortex Generators to Control Internal Supersonic Flow Separation," AIAA J., **43**(1), pp. 216–218.
[13] Urzynicok, F., 2003, "Separation Control by Flow-Induced Oscillations of a Resonator," Ph.D. thesis, T.U. Berlin, D83; edocs.tu-berlin.de/diss/2003/urzynicko_frank.htm
[14] Greenblatt, D., and Wygnanski, I. J., 2000, "The Control of Flow Separation by Periodic Oscillation," Prog. Aerosp. Sci., **36**, pp. 487–545.

Pressure Drop of Fully Developed, Laminar Flow in Rough Microtubes

M. Bahrami
Post Doctoral Fellow
Mem. ASME
e-mail: majid@mhtlab.uwaterloo.ca

M. M. Yovanovich
Distinguished Professor Emeritus
Fellow ASME

J. R. Culham[1]
Associate Professor
Mem. ASME

Microelectronics Heat Transfer Laboratory,
Department of Mechanical Engineering,
University of Waterloo,
Waterloo, Ontorio, Canada N2L 3G1

1 Introduction

Advances in fabrication methods in microelectromechanical systems (MEMS) have generated significant interest in the area of microscale heat transfer and fluid flow. Microchannel heat exchangers can dissipate high heat fluxes which make them well suited for a wide variety of unique cooling applications. Microchannels can also be integrated directly within the heat generating component; thus, the thermal contact resistance at the interface of a heat-generating component and heat sink is eliminated. This feature leads to lower substrate temperatures and smaller temperature gradients that make microchannels attractive for microelectronics cooling applications [1]. In addition, microchannels are being used in other applications, such as reactant delivery, physical particle separation, and inkjet print heads.

Microchannels can be defined as tubes/channels whose diameters are less than 1 mm. There are many techniques used to manufacture microchannels, but the following four processes are more common [2]: (i) Micromechanical machining, e.g., diamond machining, laser processes, microdrilling; (ii) x-ray machining (such as LIGA LIthographie-Galvanoforming-Abformung). (iii) photohthographic-based techniques such as Si chemical etching; and (iv) surface and surface-proximity micromachining.

Many researchers have conducted experiments and reported friction factors higher than the values predicted by conventional theory (smooth pipes) for liquids in microchannels during the last 15 years (see survey articles [1,2]). Tuckerman [3] was the first to experimentally investigate the liquid flow and heat transfer in microchannels. He reported that the flow approximately followed the Hagen-Poiseuille theory. Pfahler et al. [4,5] conducted experimental studies on the fluid flow in microchannels. They observed that in the relatively large channels, the experimental observations were in general agreement with the predictions from conventional equations. However, in the smallest of the channels, they observed a significant deviation from the classical predictions. Mala and Li [6] measured the friction factor of water in microtubes with diameters ranging from 50 to 254 μm. They also reported good agreement with the classical theory in large diameters microtubes. They proposed a roughness-viscosity model to explain the increase in the friction factor of the microchannels. The model of [6], however, did not encompass the physical mechanism and the effect of wall roughness. Li et al. [7] experimentally studied the frictional resistance for deionized water flow in microtubes. They reported a 15%–37% higher friction factor than the classical theory for rough microtubes. They concluded that the effect of wall roughness cannot be neglected for microtubes. However, they did not propose any models to explain the higher friction factors observed experimentally.

Kleinstreuer and Koo [8] proposed a computational model to consider the effect of wall roughness on liquid flow in microchannels. They modeled roughness by considering a *porous medium layer* (PML) near the wall. They showed good agreement with experimental data when the relative roughness was relatively large. The PML model of [8] requires parameters such as permeability and porosity for the "porous layer" which must be supplied to their numerical code. These parameters cannot be measured directly; no relationship was proposed for determining these parameters in [8].

As the diameter of (micro-) tubes decreases, the surface to volume ratio, which is equal to $2/r$, increases rapidly. As a result, the surface phenomena, including the effect of roughness, become more significant. There is a need for a better understanding of the effect of wall roughness on fluid characteristics in microtubes. This paper is the first attempt to develop an analytical model to predict the pressure drop of the fully developed, laminar, incompressible flows in rough microtubes.

2 Frictional Resistance

Consider *pressure-driven* flow in a long microtube. The Reynolds number associated with the flow is in general small, due to the small radii, therefore the flow is laminar. Applying a force balance and the no-slip boundary condition, one can find a relationship between the mass flow rate $\dot{m}$, and the pressure drop ΔP for a smooth circular tube of radius a, as follows (Hagen-Poiseuille flow):

$$\dot{m} = \frac{\pi a^4}{8}\frac{\rho \Delta P}{\mu L} \tag{1}$$

where the mean velocity of the fluid is, $\bar{u}=\dot{m}/\pi\rho a^2$. The relationship between the pressure gradient and the mean velocity is $\Delta P/L=8\mu\bar{u}/a^2$. It can easily be shown that $f=64/\mathrm{Re}_D$, where f is the Darcy's friction factor.

With an electrical network analogy in mind, we introduce a frictional resistance as:

$$\dot{m} = \frac{\Delta P}{R_{f,0}} \tag{2}$$

where $R_{f,0}$ is the frictional resistance of a smooth microtube of radius a and length L:

$$R_{f,0} = \frac{8\mu L}{\pi \rho a^4} \tag{3}$$

Note that the frictional resistance is not linearly proportional to the radius. The relationship between the frictional resistance, defined in this study, and Darcy's friction factor f is

$$f = \frac{4\pi a^3}{\bar{u}L} R_{f,0} \tag{4}$$

The concept of frictional resistance, introduced in Eq. (2), can also be used to construct frictional resistance networks to analyze more complex systems.

3 Wall Roughness

Roughness or surface texture can be thought of as the surface deviation from the nominal topography. The term *Gaussian* is

[1]Associate Professor, Director, Microelectronics Heat Transfer Laboratory.

Contributed by the Fluids Engineering Division of ASME for publication in the JOURNAL OF FLUIDS ENGINEERING. Manuscript received March 11, 2005; final manuscript received October 7, 2005. Assoc. Editor: Kenneth Breuer. Paper presented at the 3rd International Conference on Microchannels and Minichannels (ICMM2005), June 13–15, 2005, Toronto, Ontario, Canada.

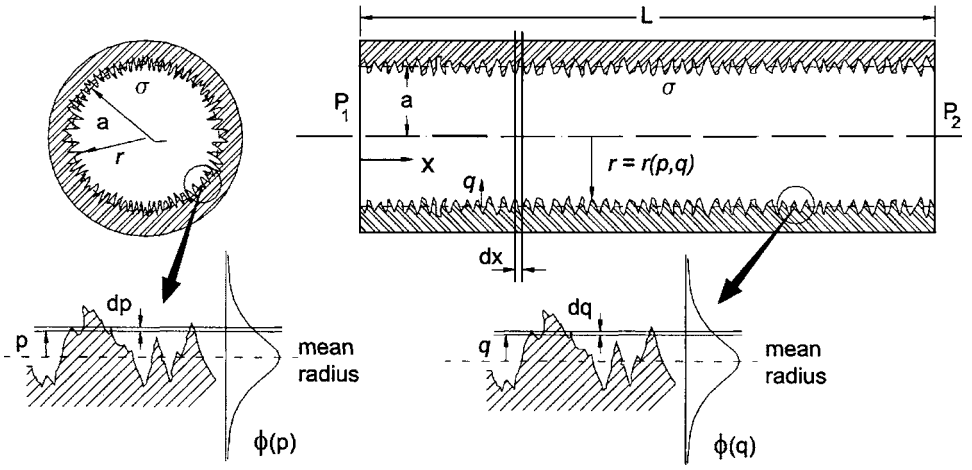

Fig. 1 Random rough microtube: wall roughness and Gaussian distribution

used to describe a surface in which its asperities are isotropic and randomly distributed over the surface. It is not easy to produce a wholly isotropic roughness.

According to Liu et al. [9], five types of instruments are currently available for measuring the surface topography: (i) stylus-type surface profilometer, (ii) optical (white-light interference) measurements, (iii) scanning electron microscope, (iv) atomic force microscope, and (v) scanning tunneling microscope. Among these, the first two instruments are usually used for macro-to-macro asperity measurements, whereas the others may be used for micro- or nanometric measurements. Surface texture is most commonly measured by a profilometer, which draws a stylus over a sample length of the surface. A datum or centerline is established by finding the straight line, or circular arc in the case of round components, from which the mean square deviation is a minimum. The arithmetic average of the absolute values of the measured profile height deviations, R_a, taken within a sampling length from the graphical centerline [10]. The value of R_a is

$$R_a = \frac{1}{l}\int_0^l |z(x)|dx \tag{5}$$

where l is the sampling length in the x direction and z is the measured value of the surface heights along this length. When the surface is Gaussian, the standard deviation σ is identical to the rms value R_q:

$$\sigma = R_q = \sqrt{\frac{1}{l}\int_0^l z^2(x)dx} \tag{6}$$

For a Gaussian surface, it can be shown that the average and rms values are related as follows:

$$R_q \approx \sqrt{\frac{\pi}{2}}R_a \approx 1.25R_a \tag{7}$$

4 Frictional Resistance of Rough Microtubes

The assumptions of the present model can be summarized as:

- The fully-developed laminar flow is modeled. The fluid is forced to move by a pressure gradient applied to the ends of the microtubes; i.e., pressure-driven flow.
- The fluid is Newtonian and the microtube cross section is circular.
- The microtube walls are rough; the roughness is assumed to be Gaussian, i.e., isotropic in all directions. In addition, there are no *macro* deviations or *waviness* inside the microtubes.
- Rarefaction, compressibility, and slip-on-walls effects are negligible.
- Fluid properties are constant.

Some researchers have reported that the transition from laminar to turbulent flow regimes starts at lower Reynolds numbers in microchannels. However, this early transition has not been observed by Judy et al. [11]. In addition, Obot [12] presented a critical review of published data and concluded that there is hardly any evidence to support the occurrence of transition to turbulence in smooth microchannels for $\mathrm{Re} < 1000$. Therefore, the focus of this study is on the laminar flow regime and the transition will not be discussed.

Consider a long rough microtube with the mean radius of a and length $L \gg a$ (Fig. 1). As shown schematically in the figure, the wall roughness of the microtube is assumed to posses a Gaussian distribution in both the angular and longitudinal directions. Owing to the random nature of the wall roughness, an exact value of the local radius r cannot be used for rough microtubes. Instead, probabilities of occurring different radii should be computed. A random variable p is used to represent the deviations of the local radius r in the angular direction. The standard deviation of p is the wall roughness σ_θ and has the following Gaussian distribution:

$$\phi(p) = \frac{1}{\sqrt{2\pi}\sigma_\theta}\exp\left(-\frac{p^2}{2\sigma_\theta^2}\right) \tag{8}$$

The local radius can vary over a wide range of values from much larger to much smaller radii than the mean radius a (valleys and hills in Fig. 1) with the Gaussian probability distribution shown in Eq. (8). The microtube wall also has roughness in the longitudinal direction x (see Fig. 1). The variations of the local radius of the microtube r in the longitudinal direction is shown by another random variable q, with the same Gaussian distribution as in the angular direction;

$$\phi(q) = \frac{1}{\sqrt{2\pi}\sigma_x}\exp\left(-\frac{q^2}{2\sigma_x^2}\right) \tag{9}$$

The local radius of the microtube can be written as

$$r = a + p + q \tag{10}$$

where a is the mean statistical value of the local radius r over the cross sections over the entire length L of the microtube.

To better understand Eq. (10), consider cross sections of a rough microtube at different longitudinal locations. These cross sections have different mean radii where the probability of these radii occurring can be determined from Eq. (9): $a+q$. Meanwhile, the actual radius at each cross section varies around the mean

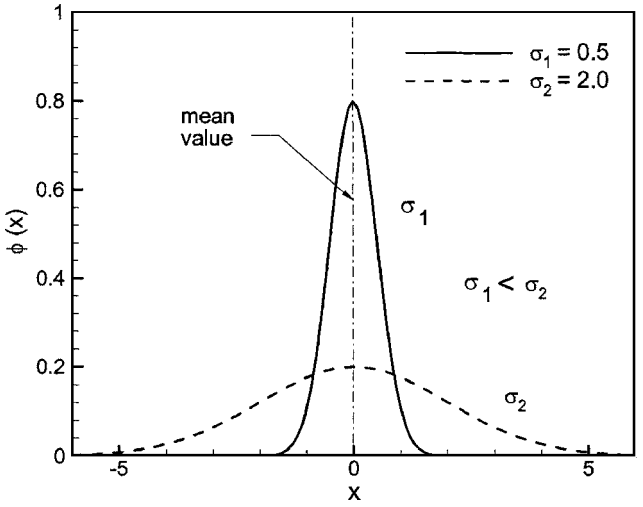

Fig. 2 Gaussian distribution

radius, $a+q$, in the angular direction (variations of p) with the probability distribution expressed in Eq. (8). Therefore, the local radius r of a microtube is a function of both random variables p and q; i.e., $r=r(p,q)$. We assume that the local radius is the *superposition* of the two random variables, as shown in Eq. (10). Note that the variables p and q are independent. For argument's sake, consider an imaginary case in which a microtube has roughness only in the angular direction; thus, one can write $r=r(p)$. As a result, an average of these variables $(r=a+(p+q)/2)$ is not correct.

In the general case, the standard deviations σ_θ and σ_x might be different. However in this study, we assume $\sigma_\theta=\sigma_x=\sigma$. This assumption is based on the premise that the texture of microtubes (surface properties) is isotropic which is the case in most MEMS fabrication techniques.

The frictional resistance dR_f for an infinitesimal element dx can be written using Eq. (3) as:

$$dR_f = \frac{8\mu dx}{\pi\rho}\int_{-\infty}^{+\infty}\int_{-\infty}^{+\infty}\frac{\phi(p)\phi(q)}{r^4}dp\,dq \tag{11}$$

Equation (11) considers the probabilities of all values of radius r occurring according to the Gaussian distribution. It should be noted that it is mathematically possible for the variables p and q to have values ranging from $-\infty$ to $+\infty$ (see Eqs. (8) and (9)). However, the probability of occurrence of much larger/smaller radii than the mean radius a, are quite small (see Fig. 2).

The total frictional resistance over the length L is

$$R_f = \frac{4\mu}{\pi^2\rho\sigma^2}\int_0^L\int_{-\infty}^{+\infty}\int_{-\infty}^{+\infty}\frac{\phi(p)\phi(q)}{(a+p+q)^4}dp\,dq\,dx \tag{12}$$

Equation (12) is used to calculate an *effective* frictional resistance for rough microtubes. Integrating over the length L, one finds

$$R_f = \underbrace{\frac{8\mu L}{\pi\rho a^4}}_{R_{f,0}}\underbrace{\left\{\frac{1}{2\pi\sigma^2}\int_{-\infty}^{+\infty}\int_{-\infty}^{+\infty}\frac{\phi(p)\phi(q)}{(1+p/a+q/a)^4}dp\,dq\right\}}_{\text{effect of wall roughness on frictional resistance}} \tag{13}$$

where $R_{f,0}$ is the frictional resistance of the smooth microtube, where no roughness exists (see Eq. (3)). Thus, the effect of wall roughness on the frictional resistance can be presented as a normalized frictional resistance or a correction factor, i.e., $R_f^*=R_f/R_{f0}$. After changing variables and simplifying, one finds

$$R_f^* = \frac{1}{2\pi}\int_{-\infty}^{+\infty}\int_{-\infty}^{+\infty}\frac{\exp(-u^2/2)\exp(-v^2/2)}{[1+\epsilon(u+v)]^4}du\,dv \tag{14}$$

where ϵ is the relative wall roughness

$$\epsilon = \frac{\sigma}{a} \tag{15}$$

Note that in this study, the relative roughness ϵ, is defined as the rms wall roughness over the *radius* of the microtube.

The integral in Eq. (14) cannot be solved analytically; thus, it is solved numerically over a range of relative roughness. It can be shown that $[1+\epsilon(u+v)]^4\cong(1+\epsilon u)^4(1+\epsilon v)^4$, where $\epsilon\ll1$; thus, Eq. (14) can be simplified to

$$R_f^* = \frac{1}{2\pi}\left\{\int_{-\infty}^{+\infty}\frac{\exp(-u^2/2)}{[1+\epsilon u]^4}du\right\}^2, \quad \epsilon\ll1 \tag{16}$$

The numerical solution to Eq. (14) is curve fitted and the following correlations can be used to calculate R_f^*:

$$R_f^* = \begin{cases}\dfrac{1}{1-23\epsilon^2}, & \epsilon\leqslant0.1\\[2ex] \dfrac{1}{1-50\epsilon^{2.4}}, & 0.1<\epsilon<0.15\end{cases} \tag{17}$$

The maximum relative difference between the numerical values and the above correlation is less than 3%. Note that in the limit where roughness goes to zero, the effective frictional resistance predicted by the present model approaches the Hagen-Poiseuille theory.

Figure 3 illustrates the trend of the normalized frictional resistance R_f^* as relative roughness ϵ is varied. From Eq. (4), it can be seen that the effect of wall roughness on the friction factor f is the same as the frictional resistance, i.e.,

$$f^* = \frac{f}{f_0} = R_f^* \tag{18}$$

Equations (17) and (18) can be employed to calculate Darcy's friction factor for rough microtubes.

Based on Eq. (17), the effect of roughness is negligible for relative roughness values $\epsilon<0.03$. However, as relative roughness increases the correction factor R_f^* increases rapidly, e.g., for a microtube with a relative roughness of 0.08, an increase of $\approx$17% in frictional resistance is predicted by the present model. As ϵ increases to approximately 0.2, the normalized frictional resistance approaches infinity.

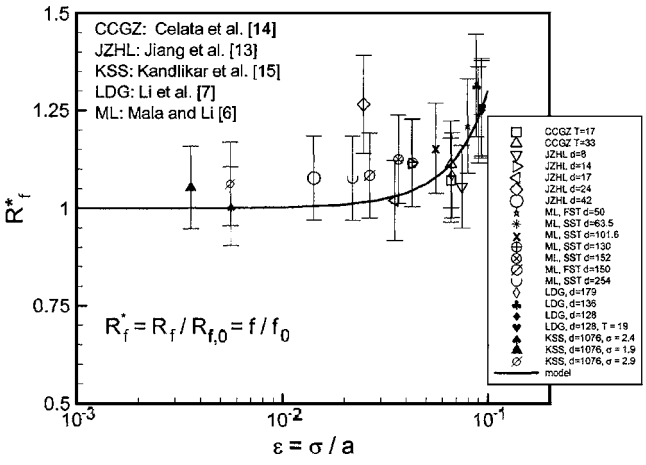

Fig. 3 Effect of relative roughness on pressure drop of microtubes: comparison of present model with all data

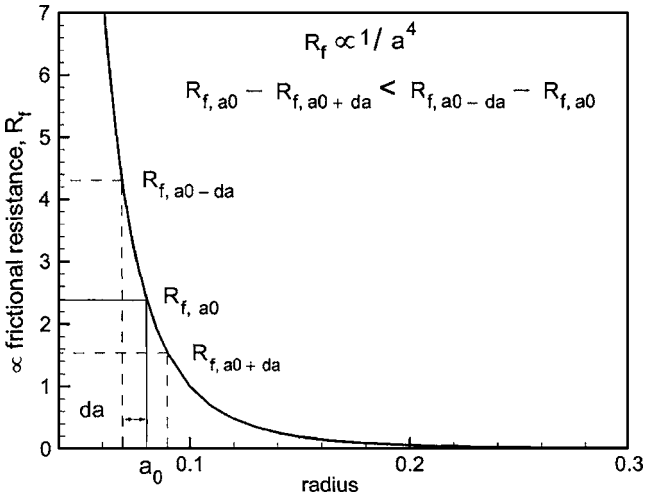

Fig. 4 Relationship between frictional resistance and radius of rough microtubes

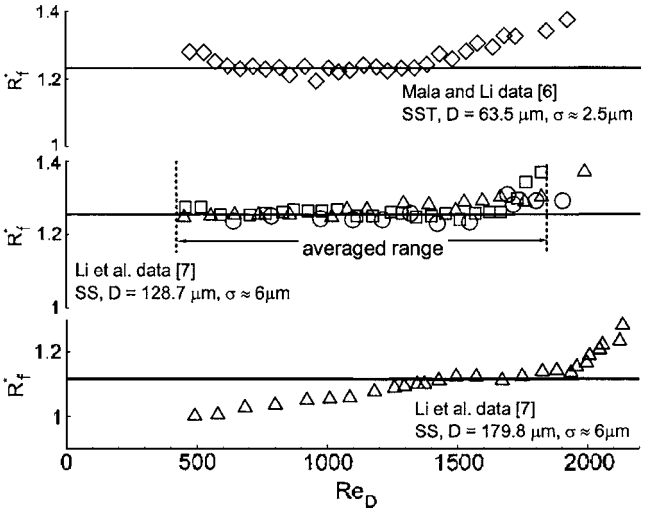

Fig. 5 Comparison of present model to Li et al. [7] and Mala and Li [6] data

It should be noted that the relative roughness of 0.2 is extremely high—imagine a microtube where the standard deviation of its wall roughness is 1/5 of its radius. It is also worth noting that in the Gaussian distribution as the standard deviation increases, the probability of occurring radii with larger deviations from the mean radius becomes higher (see Fig. 2). In other words, in rougher microtubes (higher values of σ) the probability of occurring smaller radii is higher, which leads to higher pressure drops.

Increasing roughness, while all other parameters are kept constant, results in an increase in the frictional resistance or equivalently the pressure drop (see Eq. (17)). We know that by assuming the Gaussian distribution, the probabilities of having smaller and/or larger radii microtubes (than the mean radius a) are identical; the mean statistical radius of the microtube also remains unchanged as the roughness is increased. The question may then arise as to why the frictional resistance increases as roughness increases. The answer to this question lies in the relationship between the frictional resistance and the radius of microtube (Eq. (3)). The frictional resistance is inversely proportional to the radius to the fourth power: $R_f \propto 1/a^4$. Figure 4 illustrates the frictional resistance as a function of the radius. The frictional resistance of a slightly smaller radius (a_0-da) is much larger than the resistance of a slightly larger radius (a_0+da) (see Fig. 4). Therefore, the resistance of smaller radii microtubes controls the effective frictional resistance and the effective frictional resistance increases as a microtube becomes rougher.

5 Comparison with Data

The present model is compared against experimental data conducted by several researchers. A constant roughness value is used for the same microtube material for all radii reported in each reference. In other words, the roughness is assumed *not* to be a function of the microtube radius. This assumption may not be strictly correct, unfortunately, none of the available experimental studies reported the wall roughness for different radii of microtubes. Different values for the uncertainty of the experimental data were reported by different researchers, in the vicinity of 10%; thus, a constant error bound of 10% is considered for all data.

Li et al. [7] tested glass, silicon, and stainless steel microtubes with diameters ranging from 79.9 to 166.3 μm, from 100.25 to 205.3 μm, and from 128.76 to 179.8 μm, respectively. The Reynolds number was varied over $500<\mathrm{Re}<2500$. To determine the wall conditions, the three types of microtubes were milled open along the axial direction. The wall roughness was measured using a Talysurf-120 profilometer. The wall roughness of glass and silicon microtubes were reported in order of 0.05 μm; thus the glass and the silicon microtubes can be considered as smooth microtubes. However, the stainless steel microtubes exhibited a relatively large wall roughness. They [7] did not report the exact value of R_q or R_a for wall roughness; only a "peak-valley roughness" in the order of $\approx$5.5 μm was reported for stainless steel microtubes. Through experiments, Li et al. [7] showed that for glass and silicon microtubes the conventional theory in the laminar regime holds. For stainless steel microtubes the friction factors were higher than the prediction of the classical theory.

Mala and Li [6] studied experimentally the flow of deionized water through circular microtubes of fused silica and stainless steel with Reynolds numbers in the range $100<\mathrm{Re}<2500$ and with diameters ranging between 50 to 254 μm. They reported a strange nonlinear trend between pressure drop and flow rate for low Reynolds numbers, and that the friction factors were consistently higher than the conventional values.

Figure 5 shows the comparison between the present model, Eq. (17), and two sets of data from Li et al. [7] and one set of data from Mala and Li [6]. As can be seen, the model agrees well with these data.

Jiang et al. [13] studied the trend of water flow through glass microtubes. Their circular microtubes were fabricated by the glass drawn process, with wall roughness in the order of 0.3 μm. The microtubes diameters ranged from 8 to 42 μm with Reynolds numbers in the range $0.12<\mathrm{Re}<3$. The range of the Reynolds number, in which their experiments were conducted, was very low. However, they did not report any trends similar to those of Mala and Li [6]. Figure 6 shows the comparison between the present model and a set of the [13] data.

Celata et al. [14] performed an experimental analysis of the friction factor in stainless steel capillary tubes with a diameter of 130 μm with R114 as the fluid with Reynolds numbers in the range $100<\mathrm{Re}<8000$. Their reported values of R_a have been converted to $\sigma=R_q$, using Eq. (7), to be used in the comparison.

Kandlikar et al. [15] investigated experimentally the role of the wall roughness on the pressure drop in two microtubes with Reynolds numbers in the range $500<\mathrm{Re}<2500$ and with different diameters 1067 and 620 μm. The wall roughness of the microtube walls was changed by etching with an acid solution. A micrograph scan of the microtubes was used to measure the average roughness R_a (see Eq. (5)). Their reported values of R_a have been converted to $\sigma=R_q$, using Eq. (7), to be used in the comparison.

The frictional resistance constant, $C=f\,\mathrm{Re}_D$, is not a function of

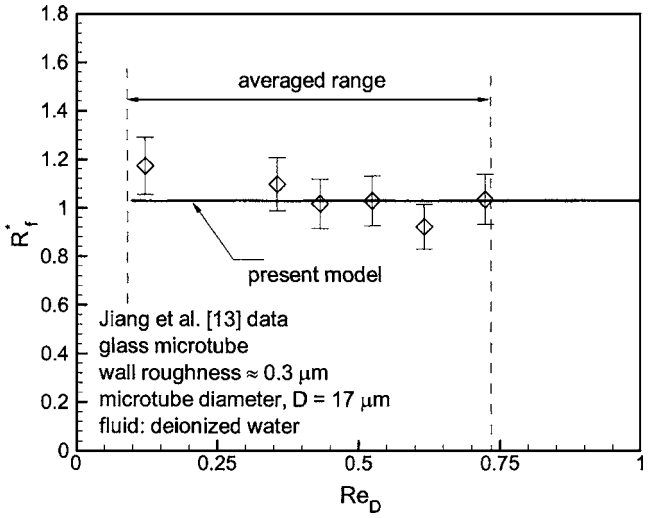

Fig. 6 Comparison of present model to Jiang et al. [13]

Reynolds number and remains unchanged for the laminar regime. Therefore, the experimental data are averaged over the laminar region; the transitional data are *not* included in the comparison. For each data set, the relative roughness is calculated using $\epsilon = \sigma/a$. As a result, for each experimental data set, a relative roughness and a normalized frictional resistance can be obtained, dashed lines in Figs. 5 and 6 demarcate the averaged ranges.

Figure 3 shows the comparison between the experimental data (normalized frictional resistance as a function of relative roughness) and the present model (Eq. (17)). As previously mentioned, the nonlinear trend of Mala and Li [6] data (at low Reynolds numbers) has not been observed by any other researchers. Therefore, those data points are not included in the averaged values shown in Fig. 3. The agreement between the model and the data is relatively good; within the 10% for most of data points. More importantly, the present model captures the trends of the data as relative roughness increases.

6 Summary and Conclusions

The influence of wall roughness on the laminar, fully developed, incompressible flow in microtubes is studied and a new model is proposed. The concept of frictional resistance is introduced and its relation to the Darcy's friction coefficient is derived.

The present model assumes an isotropic Gaussian distribution for wall roughness. In addition, the rarefaction, compressibility, and slip-on-wall effects are assumed to be negligible. Owing to the random nature of the wall roughness, an exact value of the local radius cannot be used for rough microtubes. Instead, probabilities of different radii occurring should be computed. Two independent random variables are considered to account for the deviations of the local radius in the angular and longitudinal directions. The local radius of a microtube is a function of these two random variables. In the present model, the local radius is assumed to be the superposition of the two random variables. The effect of wall roughness on the frictional resistance is presented as a normalized frictional resistance or a correction factor; the final results are reported in the form of a compact correlation. It is found that the effect of roughness is to increase the pressure drop in microtubes. The effect of roughness can be neglected when relative roughness is less than 3%. It is observed that the constant in the conventional frictional resistance, $C = f\,\mathrm{Re}_D$, is a function of relative roughness, i.e., $C = C(\epsilon)$. The published experimental data, in which the roughness is reported, are collected and compared with the present model. The present model exhibits the influence of roughness and predicts the pressure drop within the uncertainty of data.

There is a need for carefully designed experimentation aimed at more comprehensive wall roughness and pressure drop measurements. For most conventional microtubes, the relative roughness is small, in the order of a few percent. According to the model, the increase in the pressure drop for these microtubes are within the uncertainty of the current experimental arrangements, i.e., 10%. This makes the validation of the present model a difficult task for relatively smooth microtube.

Acknowledgment

The authors gratefully acknowledge the financial support of the Centre for Microelectronics Assembly and Packaging, CMAP and the Natural Sciences and Engineering Research Council of Canada, NSERC. Our thanks go to Mr. K. Narimani for his helpful comments on Sec. 4.

Nomenclature

a = mean radius of rough microtube, m
C = Darcy's friction coefficient, $f\,\mathrm{Re}_D$
D = microtube inside diameter, m
f = Darcy's friction factor, (–)
f^* = normalized friction factor, f/f_0
L = microtube length, m
$\dot{m}$ = mass flow rate, kg/s
p, q = random variables, m
R_a = arithmetic average wall roughness, m
r = radius, m
Re_D = Reynolds number, $\rho\bar{u}D/\mu$
R_f = frictional resistance, $\mathrm{m}^{-1}\mathrm{s}^{-1}$
R_f^* = normalized frictional resistance, $R_f/R_{f,0}$
R_q = rms wall roughness, m
T = mean fluid temperature, °C
$\bar{u}$ = mean fluid velocity, m/s
z = measured values of surface heights, m

Greek

ϵ = relative roughness, $\equiv\sigma/a$
ρ = fluid density, $\mathrm{kg/m}^3$
μ = fluid viscosity, kg/m s
σ = roughness standard deviation, m
ΔP = pressure gradient, Pa

Subscripts

0 = reference value, smooth microtube
θ = in angular direction
x = in longitudinal direction

References

[1] Sobhan, C. B., and Garimella, S. V., 2001, "A Comparative Analysis of Studies on Heat Transfer and Fluid Flow in Microchannels," Microscale Thermophys. Eng., **5**(4), pp. 293–311.
[2] Morini, G. L., 2004, "Single-Phase Convective Heat Transfer in Microchannels: A Review of Experimental Results," Int. J. Therm. Sci., **43**, pp. 631–651.
[3] Tuckerman, D. B., 1984, Heat Transfer Microstructures for Integrated Circuits, Ph.D. thesis, Stanford University, Dept. of Electrical Eng., California.
[4] Pfahler, J., Harley, J., Bau, H. H., and Zemel, J., 1990, "Liquid and Gas Transport in Small Channels," *ASME Dynamic Systems and Control Division—DSC, Microstructures, Sensors, and Actuators*, Vol. **19**, pp. 149–157.
[5] Pfahler, J., Harley, J., and Zemel, H. H., 1991, "Gas and Liquid Flow in Small Channels," *ASME Dynamic Systems and Control Division—DSC, Microstructures, Sensors, and Actuators*, Vol. **32**, pp. 49–60.
[6] Mala, G. M., and Li, D. Q., 1999, "Flow Characteristics of Water in Microtubes," Int. J. Heat Fluid Flow, **20**(2), pp. 142–148.
[7] Li, Z., Du, D., and Guo, Z., 2003, "Experimental Study on Flow Characteristics of Liquid in Circular Microtubes," Microscale Thermophys. Eng., **7**(3), pp. 253–265.

[8] Kleinstreuer, C., and Koo, J., 2004, "Computational Analysis of Wall Roughness Effects for Liquid Flow in Micro-conduits," ASME J. Fluids Eng., **126**, pp. 1–9.
[9] Liu, G., Wang, Q., and Ling, C., 1999, "A Survey of Current Models for Simulating Contact Between Rough Surfaces," Tribol. Trans., **42**(3), pp. 581–591.
[10] ANSI b46.1,1985, "Surface texture: Surface Roughness, Waviness and Lay."
[11] Judy, J., Maynes, D., and Webb, B. W., 2002, "Characterization of Frictional Pressure Drop for Liquid Flows Through Microchannels," Int. J. Heat Mass Transfer, **45**, pp. 3477–3489.
[12] Obot, N. T., 2002, "Toward a Better Understanding of Friction and Heat/Mass Transfer in Microchannels—A Literature Review," Microscale Thermophys. Eng., **6**, pp. 155–173.
[13] Jiang, X. N., Huang, X. Y., and Liu, C. Y., 1997, "Laminar Flow Through Microchannels Used for Microscale Cooling Systems," *IEEE CPMT Electronic Packaging Technology Conference*, pp. 119–122.
[14] Celata, G., Cumo, M., Guglielmi, M., and Zummo, G., 2002, "Experimental Investigation of Hydraulic and Single Phase Heat Transfer in 0.130 mm Capillary Tube," Microscale Thermophys. Eng., **6**, pp. 85–97.
[15] Kandlikar, S. G., Joshi, S., and Tian, S., 2001, "Effect of Channel Roughness on Heat transfer and Fluid Flow Characteristics at Low Reynolds Numbers in Small Diameter Tubes," *Proceedings of the National Heat Transfer Conference, ASME*, Vol. **2**, pp. 1609–1618.

Permeability and Form Coefficient Measurement of Porous Inserts With Non-Darcy Model Using Non-Plug Flow Experiments

L. Wilson
Research Scholar

Arunn Narasimhan
Assistant Professor
e-mail: arunn@iitm.ac.in

S. P. Venkateshan
Professor
e-mail: spv@iitm.ac.in

Heat Transfer and Thermal Power Laboratory,
Department of Mechanical Engineering,
Indian Institute of Technology Madras,
Chennai, Tamil Nadu 600036, India

Permeability (K) *and form coefficient* (C) *are the characteristic hydraulic properties of any porous medium. They are determined simultaneously, for known fluid thermo-physical properties by using the Hazen-Dupuit-Darcy model (HDD) to curve-fit the longitudinal global pressure-drop versus average fluid speed data from an isothermal, steady flow, hydraulic experiment across a test section of the porous medium. The K and C thus measured are global parameters, i.e., valid for the entire porous medium and universal provided the flow throughout the porous medium is of plug flow nature. We report here experimental evidence on the influence of non-plug flow velocity profiles at the inlet, on the simultaneous determination of K and C of fissure- and rod bundle-type porous inserts. Although variation in K is minimal, as much as 12.1% variation in C is observed, when going from a fully developed velocity profile to a plug flow profile at the inlet.*
[DOI: 10.1115/1.2175172]

Introduction

The hydraulic properties that characterize a porous medium are its permeability (K, m^2) and form coefficient (C, m^{-1}). In line with the original experiments of Darcy, the permeability of a porous medium can be determined [1] from Darcy's law, expressed as

$$\Delta P/L = (\mu/K)U \tag{1}$$

A curve fit of longitudinal global pressure drop ($\Delta P/L$, Pa/m) versus average fluid speed (U, m/s) obtained from an isothermal, steady flow, laboratory experiment, for known fluid viscosity ($\mu, \mathrm{N\,s\,m}^{-2}$) will accomplish this. Such an experiment must be prescribed at lower fluid speeds (pore diameter based Re is less than 0.1) for better accuracy of the measured permeability, as form effects (due to shape of the solid matrix) dominate at higher fluid speeds [2]. On the other hand, to simultaneously determine K and C for a porous medium, the accepted practice [3–5] is to use the Hazen-Dupuit-Darcy (HDD) model, expressed as

$$\frac{\Delta P}{L} = \frac{\mu}{K}U + C\rho U^2 \tag{2}$$

The K and C obtained from curve fit are global parameters (valid for the entire porous medium) and under isothermal conditions, are independent of the properties and flow conditions of the fluid flowing through the porous medium. Consequently, they can be used with the HDD model on all subsequent occasions in the determination of the unknown global pressure drop for a particular flow speed across a configuration using that porous medium [2].

However, the universality of the K and C measurements (independent of the flow and geometry) found using the standard porous pipe flow hydraulic experiment is doubtful. For instance, for a chosen porous medium, the global HDD model (Eq. (2)) and the differential HDD model, $dp/dx=(\mu/K)u+\rho Cu^2$, would yield identical results for K and C, only for the plug flow (PF) profile. This means, as shown in [6], non-PF profiles achieved through spatial variation of properties and local velocities inside a nonisothermal porous medium could affect K and C measurement. Hence, the present experimental study investigates, under isothermal conditions, the influence of non-PF profile (say, fully developed flow (FDF) profile) on the simultaneous determination of K and C for porous inserts in rectangular channels, by using the HDD model.

Experimental Apparatus

Figures 1(*a*) and 1(*b*) show the experimental apparatus. The Mono Bloc pump provides a steady continuous discharge of water with minimum agitation and the constant head water tank maintains a 1.5 m head for all of the experiments, using an adjustable pipe arrangement. The discharge from the tank is sent to the test section with the porous insert via an initial section of sufficient length (3 m) to ensure laminar flow conditions for the aspect ratio (L/D_h) of the chosen configuration. The test section A is a flow channel of rectangular cross section into which the porous inserts are placed. An exit section is provided at the end of the test section for undisturbed exit flow. Pressure measurements across the test section A are done using static pressure taps (made of 1 mm bore stainless steel tubes), two each, on the upper wall of the flow channel connected to two differential pressure transmitters (make: Fisher Rose Mount, range: 0 to 50 mbar, accuracy: 0.2%; and make: Instrumentation Ltd., range: 0 to 80 mm H_2O column, accuracy: 0.25%). As this procedure could "capture" the inlet and outlet pressure drops, special care (as suggested in [3]) is paid to ensure that the porous medium (inside test section A) pressure-drop component is much larger than the pressure-drop component of the inlet/outlet portions of section A. Discharge measurements were carried out by collecting water in a measuring can (Fig. 1) at the exit for a known period. The flow measured covered a range of flow rates from 3.3×10^{-6} to 1.7×10^{-4} m^3/s, corresponding to U between 0.01 to 0.12 m/s. The water temperature at the inlet and outlet of the test section are measured using thermocouples connected to an indicator (make: Thermal Systems, model: DQ 100) and the difference is found negligible ($<0.1\,^\circ\mathrm{C}$) ensuring isothermal conditions. Further details of the experiment, along with the validation of the setup, are available in [7].

Plug Flow Generation

Next, we report on the method adopted to generate plug flow (PF) at the entry of the test section A. An initial section B (see Fig. 1(*b*)) with a mesh-type porous insert (of individual pore size of 10^{-4} m, always an order of magnitude less than that of the pores of the porous inserts kept inside test section A) is fitted just before the actual test section A in which the currently reported pressure-drop measurements are carried out. This initial section B has a length (4.5 cm) greater than the length (2 cm) necessary for an inlet flow of FDF nature to become fully PF ($u(y)=U$) type. This

Contributed by the Fluids Engineering Division of ASME for publication in the JOURNAL OF FLUIDS ENGINEERING. Manuscript received February 10, 2005; final manuscript received September 24, 2005. Assoc. Editor: Dennis Siginer.

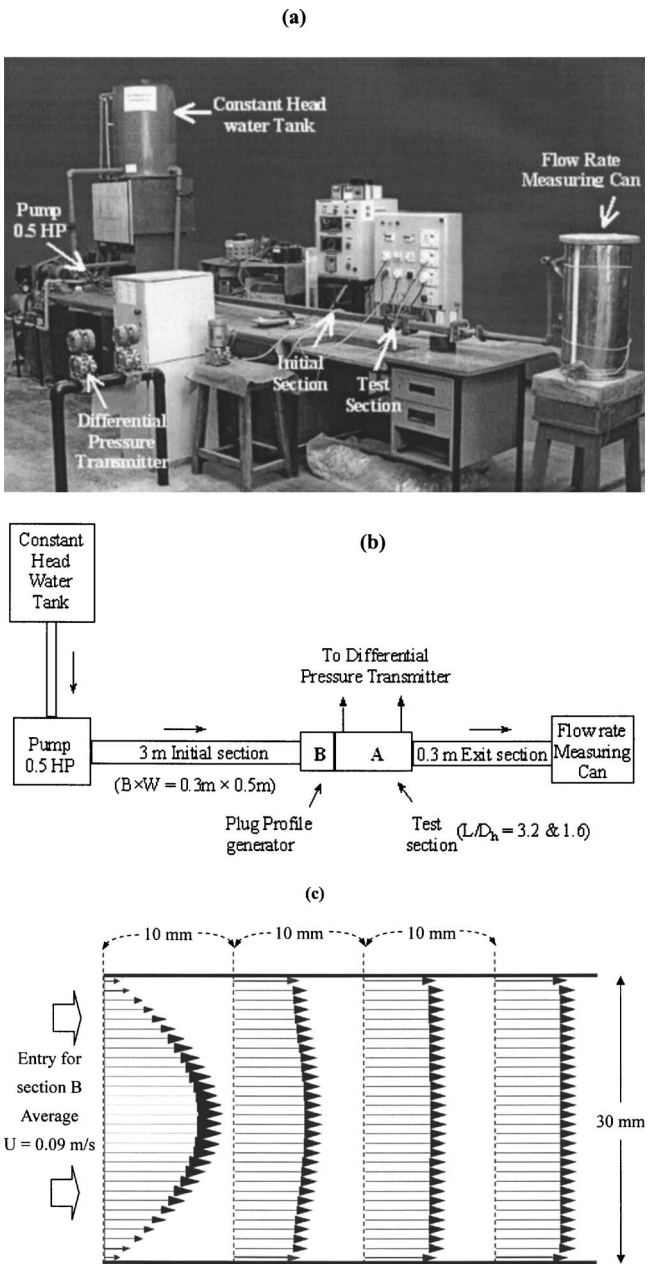

Fig. 1 (*a*) Picture and (*b*) schematic of experimental apparatus. (*c*) Simulation results for determining the length necessary to generate plug flow at the exit of the plug flow generator.

length is obtained from a "numerical simulation experiment" (see Fig. 1(*c*)) conducted using an isotropic porous medium model (solving a differential form of Eq. (2), with K and C taken as known; further details of the numerical procedure, tested for grid independence and numerical accuracy, can be found in [6]) inside B, and finding the sufficient length for which the FDF profile at the inlet of B, becomes PF type. Hence, in the actual experiment of Fig. 1, a FDF profile is always ensured at the inlet to this mesh-type porous medium inserted section B by an initial channel of length $L=3$ m. The outlet flow from section B is practically PF $(u(y)=U)$ type, which consequently is sent as the inlet to the test section A. For all the FDF experiments conducted, this "plug flow generator," i.e., section B in Fig. 1, is manually removed from the test setup, ensuring the FDF profile from the initial section to enter test section A.

Measurement Uncertainties

Laminar flow experiments using water were performed on four different porous medium inserts placed inside the test section A of Fig. 1. Figure 2 provides the details of the types of inserts used. The pressure measurements for obtaining the pressure drop across the test section A are done immediately before and after the section A, using the pressure tapping (one each, before and after the test section A) made in the top wall of the left and right flanges of the test section A. The individual uncertainties in calculating the area of the test section A and hydraulic diameter of the duct (D_h) are 0.24% and 0.27%, respectively. The uncertainty in discharge and pressure-drop measurement using the differential pressure transmitter is 0.5% and 0.25%, respectively. The pressure-drop and average velocity measurements (obtained from the discharge measurements) for all of the experiments, are curve fit using the HDD model (Eq. (2)) to obtain the permeability K and form coefficient C of the porous medium, for known values of μ and ρ of water (values are taken from [8], with less than 2% uncertainty). The uncertainty u of a quantity R, which is a function of several variables $x_1 \ldots x_N$, can be found using root-sum-square combination [9] as $u_R=[\Sigma_{i=1}^{N}((\partial R/\partial x_i)u_i)^2]^{0.5}$, where u_i is the uncertainty in the generic variable x_i. We use this relation along with the standard procedure [1,3,4] to calculate the uncertainty in simultaneous K and C determination through experimental pressure-drop measurements (reported in Table 1).

Results and Discussion

Figure 3(*a*) show data for the pressure-drop versus cross-section averaged fluid speed results for two different velocity profiles (PF and FDF) at the inlet to the test section (A in Fig. 1) having aluminum rod bundles as the porous insert (Fig. 2(*a*)). The continuous curves represent the dimensional HDD model (Eq. (2)), curve fit of the data in the full range of the flow rates tested, in order to determine simultaneously the K and C of the porous medium. Comparing the two HDD model curve fits we can observe a mild but consistent deviation of the FDF profile curve fit from that of the PF curve fit. The variation in K between the two curve fits is close to 0.52%—the same as that of the uncertainty in the determination of K. The variation in C is about 7.5%—more than twice that of 2.90%, the respective uncertainty in the determination of C (Table 1). Proceeding from left to right in Fig. 3(*a*) the plot show that the variation between the curve fits for FDF and PF profiles increases for higher average inlet velocities (U). This suggests that the variation will be seen more in the values of C obtained from the two curve fits for higher average velocities, when the flow through the porous medium is form-drag dominated [10].

However, from Fig. 2(*a*), it is evident that the rod bundle porous insert allows the porosity to spike up near the bounding walls, resulting in the effect documented in porous medium literature [10,11] as wall channeling. Because of the local increase in porosity, a higher mass efflux is anticipated near the walls. Hence, a flow entering either as PF or FDF in the porous test section A, leaves it with a higher local velocity near the walls (at the wall it is still zero—no slip). This results in a higher local pressure drop across the porous test section near the walls than that of the case when the wall channeling effect was absent. The pressure tapping on the walls before and after the test section measure the pressure drop influenced by this wall channeling effect. Therefore, in Fig. 3(*a*), the pressure-drop data for both PF and FDF conditions (thereby the curve fits) are higher than what they actually would be if the wall channeling effect were absent.

From the above discussion it is clear that there are two velocity profile variation effects: one imposed at the inlet and the other due to the porous medium itself. To reduce the wall channeling we reduced the diameter of the rods used in the rod bundles from 3 to 1 mm, as shown in Fig. 2(*b*). The corresponding experimental data set and curve fits are shown in Fig. 3(*b*). For identical

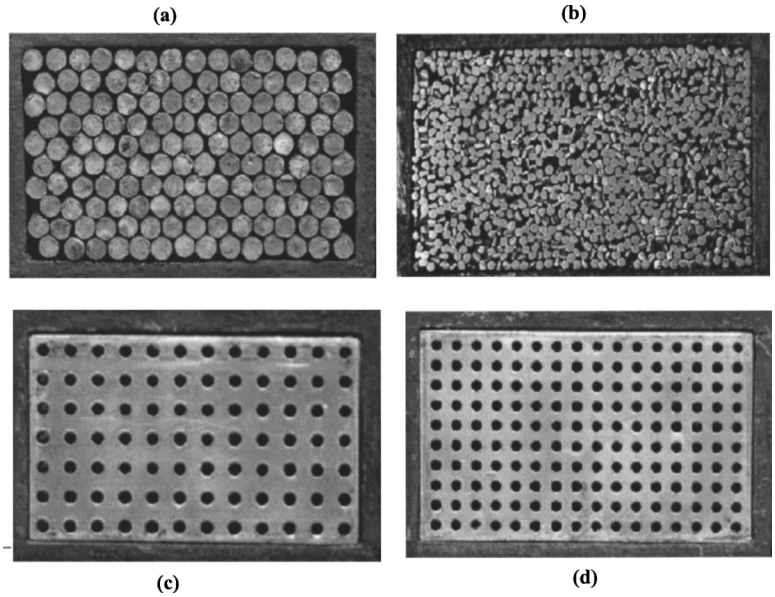

Fig. 2 Cross-sectional pictures of the porous inserts used: Types (*a*) through (*d*) are serialized as nos. 1 through 4, respectively, in Table 1

velocity range of the experiment on the abscissa, the pressure drop across the porous inserts is observed to increase by an order of magnitude on the ordinate. As expected [10], the value of K decreases as greater surface area resisting the flow leads to greater viscous friction. However, the variation in K for the two velocity profiles is minimal, as found by the HDD model curve fits. Even in this configuration of reduced wall channeling, the effect of the inlet velocity profiles is significant on the estimation of C. Since the local velocity profile is changing inside the channel, it leads to greater local variations in the form effect, which depends on the local velocity and form (shape) of the medium [2,10], in this case of 990 rods (Fig. 2(*b*)). This is reflected in the variation of the global form coefficient C, obtained from a global HDD model (Eq. (2)), curve fit of the global pressure drop versus average velocity.

Figures 4(*a*) and 4(*b*) depict the results for fissure-type porous inserts of Figs. 2(*c*) and 2(*d*) respectively, which are, complementary to the rod bundles, blocks with holes drilled through them. In addition, $L/D_h=1.6$, with the pressure drop measured across the reduced L. As the gaps between the blocks and the bounding channel wall is sealed, the wall channeling effect is absent in these porous inserts. As the wall channeling inside the porous medium is absent, the result support the earlier conjecture of how the C is influenced by the local velocity profile ($u(y)$) variation through the variation in local form effects inside the porous insert.

Table 1 summarizes the results of K and C evaluation for all of the reported experiments. Using the appropriate method of HDD model (Eq. (2)) curve-fit procedure, the variation in K is mostly comparable to the uncertainties of its measurement except for the

Table 1 Permeability and form coefficient results using non-slug flow experiments

S. no.	Types of aluminum porous inserts	Aspect ratio (L/D_h)	Inlet velocity profile	HDD model (Eq. (2)) $K\times10^{-8}$ m^2	HDD model (Eq. (2)) $C\times10^{-2}$ m^{-1}	Percentage variation from PF to FD flow K	Percentage variation from PF to FD flow C	Percentage uncertainties K	Percentage uncertainties C
1	Rods $\varepsilon=0.25$, 140 rods, $d=3$ mm	3.2	PF	1.92	3.60	0.52	7.50	0.50	2.90
			FDF	1.91	3.33				
2	Rods $\varepsilon=0.21$, 990 rods, $d=1$ mm	3.2	PF	0.173	21.9	0.57	12.10	0.50	5.20
			FDF	0.172	19.2				
3	Block $\varepsilon=0.176$, 84 holes, $d=2$ mm	1.6	PF	5.52	1.84	0.72	7.60	0.77	1.09
			FDF	5.48	1.70				
4	Block $\varepsilon=0.187$, 159 holes, $d=1.5$ mm	1.6	PF	4.76	1.90	2.00	10.4	0.76	4.50
			FDF	4.86	2.12				

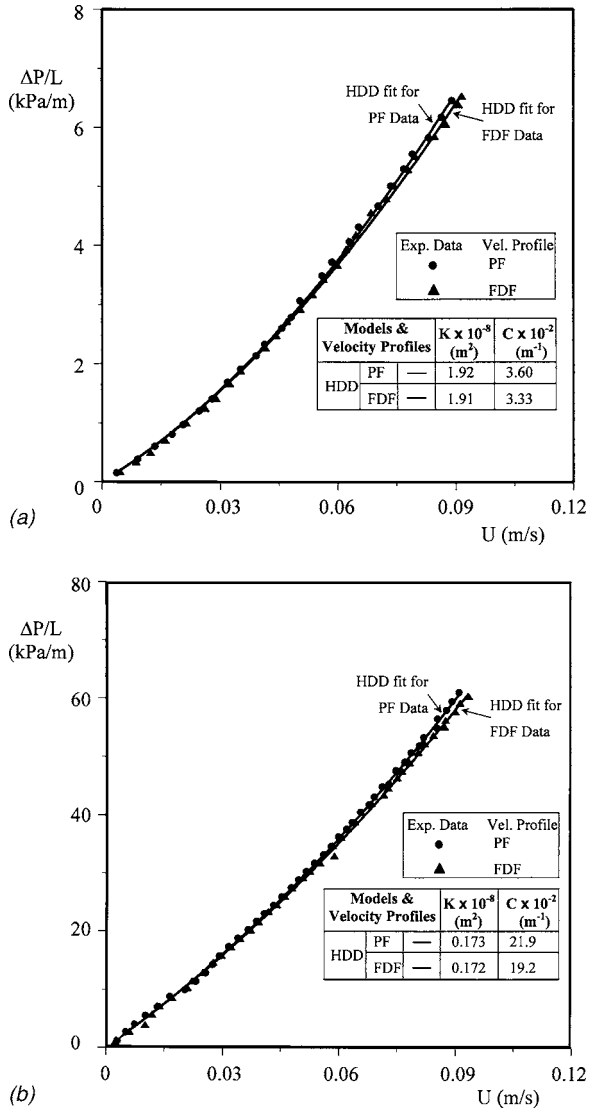

Fig. 3 Longitudinal pressure drop versus average fluid velocity for (*a*) aluminum rod bundle inserts for porosity $\varepsilon=0.25$, 140 rods of $d=3$ mm, $L/D_h=3.2$. Experiment done at $T=30°C$, with water of $\mu=792.4\times10^{-6}$ N s m^{-2} and $\rho=995.7$ kg/m^3; (*b*) aluminum rod bundle inserts for porosity $\varepsilon=0.21$, 990 rods of $d=1$ mm, $L/D_h=3.2$. Experiment done at $T=31°C$, with water of $\mu=811.4\times10^{-6}$ N s m^{-2} and $\rho=997.25$ kg/m^3.

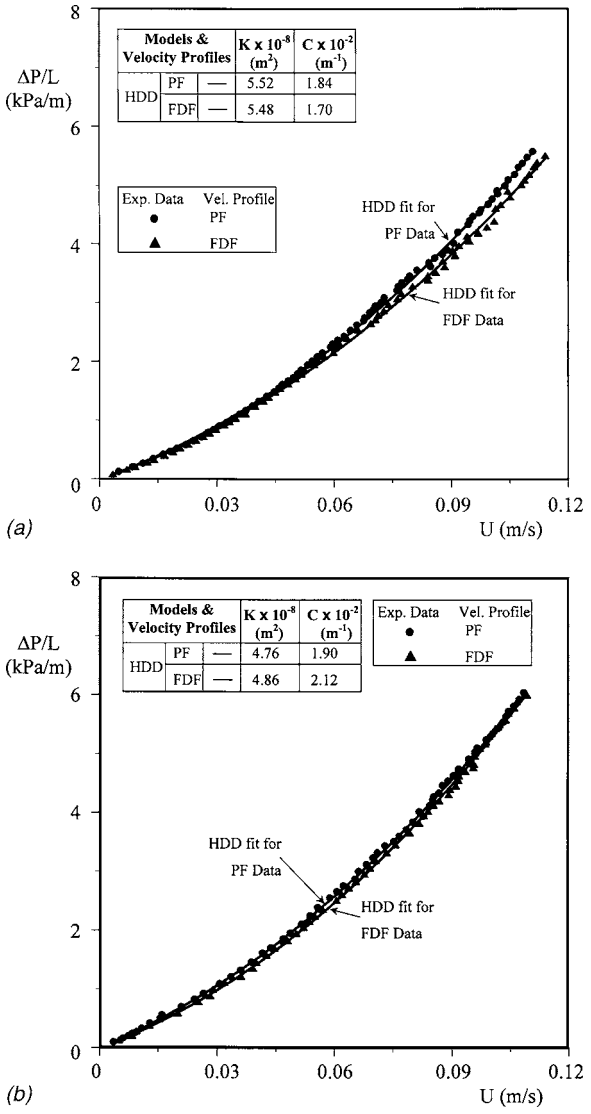

Fig. 4 Longitudinal pressure drop versus average fluid velocity for (*a*) aluminum block inserts porosity $\varepsilon=0.18$, 84 holes of $d=2$ mm, $L/D_h=1.6$. Experiment done at $T=25°C$, with water of $\mu=935.06\times10^{-6}$ N s m^{-2} and $\rho=999$ kg/m^3; (*b*) aluminum block inserts porosity $\varepsilon=0.18$, 159 holes of $d=1.5$ mm, $L/D_h=1.6$. Experiment done at $T=27°C$, with water of $\mu=882.6\times10^{-6}$ N s m^{-2} and $\rho=998.25$ kg/m^3.

block-type porous insert with 159 holes of 1.5 mm (last row), in which case, it is about twice that of the uncertainty. In contrast, the variation in C is consistently more than twice that of the respective uncertainties in measurements for all of the inserts (and is almost four times for the block-type insert in the third row). Further, it is amplified from 7.5% to 12.1% for the rod bundle inserts and from 7.6% to 10.4% for the block-type inserts; i.e., the C variation increases as we proceed towards more porous medium behavior (pore scale, $\sim10^{-6}$ m^2, very small when compared to the global length scale—here, the channel cross section, 1.5×10^{-3} m^2). Altering the inlet velocity profile from PF to FDF profile allows the flow while traversing through the porous medium to have local (macroscopic, porous continuum level) variation in velocities $[u(y)\neq U]$, at least for sufficient initial length of the porous medium test section. This local velocity variation affects more the form drag, hence C, which depends on the square of the velocity. Further, the deviation becomes pronounced for higher velocities and also while approaching strong porous medium behavior.

The results of Figs. 3 and 4 can be interpreted using a Reynolds number and friction factor, defined using length scales, which are functions of K or the pore diameter (D_p) of the porous medium [10]. Although limited in applicability in the context of determining flow regimes [2,4,6,12], for instance, this approach has been elegantly used in [13] to "collapse" data onto a single curve, for fibrous porous media. However, if this approach is followed for the data in Figs. 3 and 4, confusion could result over which K and C (either for PF or FDF velocity profile) is to be used to define Re and the friction factor. In addition, the experimental data of Fig. 3 and 4 (generated within identical flow rate values), if interpreted using an aforementioned Re and friction factor plot, would not collapse into a single curve.

Conclusions

Isothermal, laminar, steady flow, hydrodynamic pressure-drop experiments through different porous inserts using water flowing with two different velocity profile conditions; viz., plug flow (PF) and fully developed flow (FDF) at the inlet of the test section were performed. The effects of these velocity profile variations on the simultaneous determination of the permeability K and form coefficient C of the porous inserts were studied. Altering the inlet velocity profile from PF to FDF profile affects more the form drag (hence C, which depends on the square of the velocity) than the viscous drag, as observed from the 12.1% variation reported in Table 1, in the determination of C using the HDD model curve fit.

Inlet velocity profile variation effect could be countered by the effect of porous medium test section length increase. While performing a laboratory experiment to determine the K and C, a PF profile at the inlet to the test section should be ensured. Otherwise, sufficient length of the test section should be provided such that any velocity profile at the inlet "develops" into a plug flow well before the exit. As shown by the preliminary yet fundamental results of this paper, use of porous medium in practical locations of altered inlet velocity profiles (such as a FDF profile), will result in an experimental pressure drop different from the pressure drop obtained from the HDD model using the K and C obtained from a standard plug flow experiment in the lab. An experimental database, amplifying the effects noticed in this paper, is required to enunciate appropriate correction factors to standardize K and C measurements.

References

[1] Antohe, B. V., Lage, J. L., Price, D. C., and Weber, R. M., 1997, "Experimental Determination of Permeability and Inertia Co-efficient of Mechanically Compressed Aluminum Porous Matrices," ASME J. Fluids Eng., **119**, pp. 404–412.

[2] Lage, J. L., Krueger, P. S., and Narasimhan, A., 2005, "Protocol for Measuring Permeability and Form Coefficient of Porous Media," Phys. Fluids, **17**, p. 088101.

[3] Lage, J. L., Antohe, B. V., and Nield, D. A., 1997, "Two Types of Nonlinear Pressure-Drop Versus Flow-Rate Relation Observed for Saturated Porous Media," ASME J. Fluids Eng., **119**, pp. 700–706.

[4] Lage, J. L., and Antohe, B. V., 2000, "Darcy's Experiments and the Deviation to Nonlinear Flow Regime," ASME J. Fluids Eng., **122**, pp. 619–625.

[5] Boomsma, K., and Poulikakos, D., 2002, "The Effects of Compression and Pore Size Variations on the Liquid Flow Characteristics in Metal Foams," ASME J. Fluids Eng., **124**, pp. 263–271.

[6] Narasimhan, A., and Lage, J. L., 2001, "Modified Hazen-Dupuit-Darcy Model for Forced Convection of a Fluid with Temperature-Dependent Viscosity," ASME J. Heat Transfer, **123**, pp. 31–38.

[7] Wilson, L., 2005, "Hydrodynamic and Heat Transfer Experiments Using Rod Bundles and Porous Medium Inserts," Ph.D. thesis, IIT Madras, Chennai, India.

[8] Perry, R. H., and Chilton, C. H., 1975, *Chemical Engineers Handbook*, McGraw Hill, New York.

[9] Holman, J. P., 2001, *Experimental Methods for Engineers*, 7th ed., McGraw Hill, New York.

[10] Nield, D. A., and Bejan, A., 1999, *Convection in Porous Media*, 2nd ed., Springer-Verlag, Berlin.

[11] Georgiadis, J., and Catton, I., 1987, "Stochastic Modeling of Unidirectional Fluid Transport in Uniform and Random Packed Beds," Phys. Fluids, **30**, pp. 1017–1022.

[12] Wilson, L., Narasimhan, A., and Venkateshan, S. P., 2004, "Turbulent Flow Hydrodynamic Experiments in Near-Compact Heat Exchanger Models with Aligned Tubes," ASME J. Fluids Eng., **126**, pp. 990–996.

[13] Papathanasioua, T. D., Markicevic, B., and Dendy, E. D., 2001, "A Computational Evaluation of the Ergun and Forchheimer Equations for Fibrous Porous Media," Phys. Fluids, **13**(10), pp. 2795–2804.

Journal of Fluids Engineering

Discussion

Discussion: "Three-Dimensional Vortex Method for Gas-Particle Two-Phase Compound Round Jet" (Uchiyama, T., and Fukase, A., 2005, ASME J. Fluids Eng., 127, pp. 32–40)

L. A. Barba
Department of Mathematics,
University of Bristol,
Bristol BS8 1TW, UK

The paper by Uchiyama and Fukase [1] proposes a three-dimensional vortex method for particulate flows, which is applied to a circular jet of air laden with glass particles. The numerical method presented has the following characteristics: (1) it includes the two-way coupling of the particles and the fluid, (2) it discretizes the vorticity in the gas phase in the usual manner when vortex blob methods are used, and (3) it accounts for the effects of viscosity in the fluid by means of the less-than-usual core spreading method.

The method presented in the paper under discussion is claimed to be a 3D extension of the two-dimensional vortex method for particle-laden flows proposed by Uchiyama and Naruse [2]. Upon reading this previous work, however, one notes important differences in the core spreading viscous scheme. There is an apparent inconsistency in the paper in relation to the implementation of the vortex method, which will be discussed below. There are three issues that should be made clear.

1. The core spreading formula presented is not the same as used in the previous work by Uchiyama and Naruse [2] (and several subsequent works by Uchiyama and others). The extension to 3D of [1] refers to the particle-fluid coupling only.
2. The core spreading scheme in [1] corresponds to that presented by Leonard [3]; that scheme is derived for simple Gaussian vortex blobs, whereas in [1] a *cubic* Gaussian is used. This is a severe inconsistency, and readers should be made aware that core spreading is derived for a *specific* blob distribution.
3. The core spreading method used in [1] (Leonard's) is a two-dimensional scheme, derived from an exact solution to the 2D Navier-Stokes equation. It is unclear how the authors are applying the scheme for 3D flows; in fact, the mere application of this scheme to 3D is questionable.

The 2D antecessor [2] of the method presented in [1] incorporated the two-way coupling for particles and fluid, by means of turning the force of particles acting on the fluid into a source term in the vorticity transport equation. This technique was well known at the time. The generation of vorticity due to the presence of the particles and by the action of the drag force was pointed out in the review by Crowe et al. [4]. The concept was implemented successfully in a vortex-based method in [5].

The salient feature of the 2D method of Uchiyama and Naruse [2] is the use of the core spreading method for viscous effects in the gas phase. The core spreading method has not been used often, due to it falling out of favor with vortex methods workers when consistency objections were raised [6]. The scheme was presented by Leonard [3], and consists of the idea that elementary vortex blobs can be made to grow in time to simulate viscosity.

The consistency issues with the core spreading vortex method stem from the fact that the vortex blobs are advected without deformation, and thus they cannot be allowed to grow larger and larger in time. Basically, the size of the blobs represents the smallest scales that the vortex blob method can resolve. If the size of the vortex blobs is σ, then the truncation error of the vortex method grows with σ^2, as proved in [3]. Moreover, since the vorticity is advected with an average velocity and not with the actual local velocity, the convection of vorticity is incorrect even in the limit of infinitely many particles, as proved by [6]. These issues were successfully addressed by Rossi [7], who proposed a vortex splitting technique to control the core sizes, and proved it to be convergent. This result prompted new recent work with the core spreading method [8,9]. Most recently, a new formulation for the vortex method with core spreading has been developed, in which the core size control necessary for consistency and convergence is provided (without splitting) in a spatial adaption scheme using radial basis function interpolation [10].

In the paper under discussion, and the previous work of Uchiyama and co-workers, starting with [2], no correction is provided for the consistency problem of the core spreading method. As far as can be inferred from their publications, they allow the vortex blobs to grow uncontrolled throughout a time marching calculation. This is acceptable if the Reynolds number is large and the simulations short, but it is important to underscore that the algorithm is inconsistent if applied to another flow situation.

Going into more detail, in [2] the authors cite as their source for the core spreading method the scheme proposed by Nakanishi and Kamemoto [11], and thus the core sizes are grown in time following the rule:

$$\frac{d\sigma}{dt} = \frac{\nu c^2}{2\sigma} \tag{1}$$

where the constant c takes the numeric value of 2.242; this is Eq. 15 of [2], taken from Eq. 10 of [11] with changes in notation.

The cited work [11] contains a rather scant derivation, and is easy to question. They claim to obtain the above formula for the change in blob radius due to viscosity in three dimensions by *approximating it by two-dimensional viscous diffusion "for convenience."* They seem to take the 3D vortex blobs, with spherical symmetry, and approximate these with a cylinder of equal volume, then use 2D core spreading to diffuse the (finite-length!)

Contributed by the Fluids Engineering Division of ASME for publication in the JOURNAL OF FLUIDS ENGINEERING. Manuscript received July 22, 2005; final manuscript received October 25, 2005. Assoc. Editor: Georges L. Chahine.

cylindrical vortex. Apparently they then switch back to a spherical blob of volume equal to the "diffused" cylindrical one.

The first question that comes to mind is, what may be the accuracy of the approximation of spherical blobs with cylinders, and of using a 2D viscous scheme in a 3D method? Secondly, and more importantly, how is the 2D core spreading formula given by (1) obtained, and what is its accuracy? The authors of [11] claim that the numeric value of the constant c in the formula is "obtained using an exact solution of Navier-Stokes equation for a straight and infinitely long vortex filament of fluid." Indeed, this is the concept behind the core spreading method that is well known by the rest of the community. In [11], strangely, the blob distribution function is an *algebraic* cutoff, given by:

$$\zeta(\rho) = \frac{15}{8\pi} \frac{1}{(\rho^2+1)^{7/2}} \tag{2}$$

where $\rho = |\mathbf{x}-\mathbf{x}_i|^2/\sigma^2$, and the vorticity distribution of each blob is $(1/\sigma^2)\zeta(\rho)$. The above cutoff function is certainly not an exact solution of the Navier-Stokes equations. How this spherical distribution of vorticity is turned into a "straight and infinitely long filament" to obtain the core spreading formula is simply not explained.

Turning our attention back to the work by Uchiyama and coworkers, we note that in [2] they have used the core spreading formula given by (1), but they utilize a *different cutoff function* (Chorin's). This is disconcerting, as the core spreading method is explicitly tied to the cutoff function. In subsequent papers [12–14], the authors continue to give the same core spreading formula as above, and continue to use Chorin's cutoff function. This cutoff was introduced in [15] and is the following:

$$\zeta(\rho) = \begin{cases} \dfrac{1}{2\pi\rho}, & \rho \leqslant 1 \\ 0, & \rho > 1 \end{cases} \tag{3}$$

The above is a 2D blob function and indeed the work of [2,12–14] is always in two dimensions. However, recall that the method of [11] is a *3D method*, where an algebraic cutoff is used, and some transformations between spherical and cylindrical symmetry are applied to obtain the formula given by (1).

Subsequently, in [16], the authors no longer reference [11] but instead cite [3] for the core spreading method. They now use a Gaussian blob distribution function, and present the following formula for core spreading:

$$\frac{d\sigma}{dt} = \frac{2\nu}{\sigma} \tag{4}$$

One can see that the formula above is equivalent to (1) if one takes $c=2$, and it is also equivalent to the core spreading formula more familiar to the community, as presented by [3]:

$$\frac{d\sigma^2}{dt} = 4\nu \tag{5}$$

The factor 4 in the above equation is sometimes replaced by 2, or even 1, depending on the normalization of the Gaussian cutoff used.

In deriving the core spreading scheme, the viscous term of the vorticity equation is satisfied identically, using the classical exact solution of the Navier-Stokes equation known as "spreading line vortex" ([[17], p. 204). This exact solution is given by

$$\omega(\mathbf{x},t) = \frac{\Gamma}{4\pi\nu t} \exp(-|\mathbf{x}|^2/4\nu t) \tag{6}$$

With the 2D Gaussian cutoff used by Leonard,

$$\zeta(\rho) = \frac{1}{\pi} \exp(-\rho^2) \tag{7}$$

clearly the diffusion equation is satisfied *exactly* by each blob when making σ^2 grow linearly according to (5). Since the diffusion equation is linear, the discretized vorticity field in 2D can be seen as a superposition of spreading line vortices of different strengths (circulation). This is the essence of the core spreading vortex method.

In the three-dimensional extension of the the method presented in the paper under discussion, the authors give the core spreading formula as in (5), citing Leonard. This time, however, they use a cubic Gaussian cutoff function, given by:

$$\zeta(\rho) = \frac{3}{4\pi} \exp(-\rho^3) \tag{8}$$

It is not explained how the authors use the two-dimensional core spreading formula with a three-dimensional cutoff function. It is also not clear why the standard core spreading formula is given, which applies only to simple Gaussian blobs, like (7).

The compilation of articles by Uchiyama and co-workers, from [2] to the paper under discussion, seems to indicate that the core spreading method has been misinterpreted. I tend to believe that the method that has been implemented is rather like a point vortex model, regularized. It seems quite probable that viscous effects are incorrectly modeled; the method seems to be mathematically inconsistent.

It is important, in my opinion, to discuss and acknowledge the problems just examined. The vortex method has sometimes suffered the reputation of being only a modeling approach for unsteady flows. It is a fact that the vortex method can produce direct numerical simulation results, and many researchers have shown accuracy in competition with finite difference methods and even spectral methods (see, for example, [18–22]). One should not, under the cover of considering the "application to engineering problems," fail to have concern for numerical consistency and accuracy.

Acknowledgment

For reading an early draft of this discussion, thanks to A. Leonard, C. Meneveau, and L. F. Rossi.

References

[1] Uchiyama, T., and Fukase, A., 2005, "Three-dimensional Vortex Method for Gas-Particle Two-Phase Compound Round Jet," J. Fluids Eng., **127**(1), pp. 32–40.
[2] Uchiyama, T., and Naruse, M., 2001, "A Numerical Method for Gas-Solid Two-Phase Free Turbulent Flow Using a Vortex Method," Powder Technol., **119**(2–3), pp. 206–214.
[3] Leonard, A., 1980, "Vortex Methods for Flow Simulation," J. Comput. Phys., **37**, pp. 289–335.
[4] Crowe, C. T., Troutt, T. R., and Chung, J. N., 1996, "Numerical Models for Two-Phase Turbulent Flows," Annu. Rev. Fluid Mech., **28**, pp. 11–43.
[5] Chen, H., and Marshall, J. S., 1999, "A Lagrangian Vorticity Method for Two-Phase Particulate Flows With Two-Way Phase Coupling," J. Comput. Phys., **148**(1), pp. 169–198.
[6] Greengard, C., 1985, "The Core Spreading Vortex Method Approximates the Wrong Equation," J. Comput. Phys., **61**, pp. 345–348.
[7] Rossi, L. F., 1996, "Resurrecting Core Spreading Vortex Methods: A New Scheme That is Both Deterministic and Convergent," SIAM J. Sci. Comput., **17**, pp. 370–397.
[8] Shiels, D., and Leonard, A., 2001, "Investigation of a Drag Reduction on a Circular Cylinder in Rotary Oscillation," J. Fluid Mech., **431**, pp. 297–322.
[9] Moeleker, P., and Leonard, A., 2001, "Lagrangian Methods for the Tensor-Diffusivity Subgrid Model," J. Comput. Phys., **167**(1), pp. 1–21.
[10] Barba, L. A., Leonard, A., and Allen, C. B., 2005, "Advances in Viscous Vortex Methods—Meshless Spatial Adaption Based on Radial Basis Function Interpolation," Int. J. Numer. Methods Fluids, **47**(5), pp. 387–421.
[11] Nakanishi, Y., and Kamemoto, K., 1993, "Numerical Simulation of Flow Around a Sphere With Vortex Blobs," J. Wind. Eng. Ind. Aerodyn., **46–47**, pp. 363–369.
[12] Uchiyama, T., and Naruse, M., 2002, "Numerical Simulation of Gas-Particle Two-Phase Mixing Layer by Vortex Method," Powder Technol., **125**(2–3), pp. 111–121.
[13] Uchiyama, T., and Okita, T., 2003, "Numerical Prediction of a Plume Diffusion Field Around a Circular Cylinder by the Particle Method," Adv. Environ. Res., **7**(2), pp. 573–581.
[14] Uchiyama, T., and Naruse, M., 2003, "Vortex Simulation of Slit Nozzle Gas-Particle Two-Phase Jet," Powder Technol., **131**(2–3), pp. 156–165.

[15] Chorin, A. J., 1973, "Numerical Study of Slightly Viscous Flow," J. Fluid Mech., **57**, pp. 785–796.
[16] Uchiyama, T., and Naruse, M., 2004, "Numerical Simulation for Gas-Particle Two-Phase Free Turbulent Flow Based on Vortex in Cell Method," Powder Technol., **142**(2–3), pp. 193–208.
[17] Batchelor, G. K., 1967, *An Introduction to Fluid Dynamics*, Cambridge University Press, Cambridge, UK.
[18] Cottet, G.-H., and Poncet, P., 2004, "Advances in Direct Numerical Simulations of 3D Wall-Bounded Flows by Vortex-in-Cell Methods," J. Comput. Phys., **193**(1), pp. 136–158.
[19] Cottet, G.-H., Michaux, B., Ossia, S., and VanderLinden, G., 2002, "A Comparison of Spectral and Vortex Methods in Three-dimensional Incompressible Flows," J. Comput. Phys., **175**, pp. 702–712.
[20] Ploumhans, P., Winckelmans, G. S., Salmon, J. K., Leonard, A., and Warren, M. S., 2002, "Vortex Methods for Direct Numerical Simulation of Three-Dimensional Bluff Body Flows: Application to the Sphere at Re=300, 500 and 1000," J. Comput. Phys., **178**, pp. 427–463.
[21] Cottel, G.-H., and Koumoutsakos, P., 2000, *Vortex Methods. Theory and Practice*, Cambridge University Press, Cambridge, UK.
[22] Ploumhans, P., and Winckelmans, G. S., 2000, "Vortex Methods for High-Resolution Simulations of Viscous Flow Past Bluff Bodies of General Geometry," J. Comput. Phys., **165**, pp. 354–406.